

This item is held in Loughborough University's Institutional Repository (<https://dspace.lboro.ac.uk/>) and was harvested from the British Library's EThOS service (<http://www.ethos.bl.uk/>). It is made available under the following Creative Commons Licence conditions.



For the full text of this licence, please go to:
<http://creativecommons.org/licenses/by-nc-nd/2.5/>

Microstructural and Mechanical Property Modelling for the Processing of Al-Si Alloys

By
Wendy Mair Edwards

Institute of Polymer Technology and Materials Engineering
Loughborough University

A doctoral thesis submitted in partial fulfilment of the requirements for the
award of Doctor of Philosophy

October 2002

© W. M. Edwards, 2002

Acknowledgements

I wish to thank Dr. R. Thomson for her enduring encouragement and support, and for the guidance and enthusiasm in “pushing back the frontiers of science”.

I am grateful to both Federal-Mogul Technology and the Engineering and Physical Sciences Research Council for providing financial support for this project, and to the Materials Thermochemistry department of the National Physical Laboratory, Teddington, for the provision of MTDATA and advice on its use. I would also like to acknowledge TexSEM Laboratories, Utah, in particular Dr. D. Dingley, for their assistance with EBSD.

I would like to thank all those involved in this collaborative project for their invaluable discussions and advice: Drs. S. and S. Barnes at Federal-Mogul Technology (now Federal-Mogul Powertrain Systems, Germany); Dr. A. Dinsdale at the National Physical Laboratory; Drs. E. R. Wallach and R. Qin at Cambridge University; Drs. P. Reed, C. Styles and M. Joyce at Southampton University; Dr. R. Wood and D. Price at Loughborough University; and Mr. J. Woodthorpe and Mr. J. Philby (formerly of Federal-Mogul).

Thanks are also extended to the technical staff in the Institute of Polymer Technology and Materials Engineering at Loughborough University for their help. In particular Mr. T. Atkinson for his advice on sample preparation and photographic techniques, and Mr. J. Bates and Mr. F. Page for their help with the electron microscopy units.

I must also thank my friends and colleagues in the department, particularly the I.P.T.M.E. cricket team, for making my time at Loughborough a more enjoyable experience.

Finally, to my family and wonderful fiancé, for their unfailing support, encouragement and love throughout – Thankyou.

Abstract

The components of a modern internal combustion engine are required to give extreme reliability over extended periods of operation and none is exposed to more arduous conditions than the piston, especially in the pin boss and crown regions of pistons for diesel engines. The increasing emissions requirements and performance targets demanded of direct injection diesel engines has resulted in steep increases in both specific powers and maximum cylinder pressures. This has in turn lead to greater temperatures and pressures being felt by the piston. The adaptation of the piston design to these increasingly demanding load and temperature conditions has required a continuous improvement and innovation in the field of materials and process technologies.

The vast majority of the internal combustion engine pistons produced globally are made by a gravity die casting process using Al-Si based alloys. Although Al-Si alloys have been the subject of a great deal of research over the last 30 years, the majority of work has been based on fairly rudimentary characterisation of the microstructures as a function of alloy chemistry and cooling rate. Most of the attention has been paid to the silicon morphology and distribution rather than on a fundamental knowledge of the development of the complex microstructures and intermetallic phases that arise in commercial alloys. However, the properties of cast near-eutectic aluminium-silicon alloys are very strongly influenced by the microstructure, i.e. the primary aluminium, and the interdendritic microconstituents such as secondary phases, intermetallics, inclusions and porosity. A fine and uniform grain size is often desired as it improves mechanical properties of castings such as tensile strength, ductility and fatigue resistance, and at the same time aids castability, improves porosity distributions and reduces hot tearing susceptibility.

A thorough phase characterisation has been carried out using a number of techniques including optical and electron microscopy with electron backscatter diffraction (EBSD), and image analysis. Use was also made of thermodynamic modelling to predict the volume fraction and distribution of phases within the microstructure as a function of chemical composition and process parameters. From this analysis a detailed understanding of the

phases occurring in multicomponent Al-Si alloys was established. Furthermore, additions associated with grain refining, i.e. Ti, Zr and V, have been investigated systematically using commercial and model alloy systems. All three additions were observed to refine the structure of the castings through the formation of the phase Al_3Ti , although combined additions with Zr were found to be less efficient due to a ‘poisoning’ effect on the Al_3Ti . It was also established that there is a strong competition between the effects of grain refiners and P, with the formation of Al_3Ti reducing the nucleating efficiency of AlP to silicon. The nucleation and growth of the primary silicon phase were thus examined by EBSD. AlP was confirmed as nucleating the silicon epitaxially, after which growth continues by surface nucleation, although the presence of twins were seen to influence the shape of the crystal. Finally, suggestions have been made as a consequence of this work for the future development of piston alloys.

Contents

Acknowledgements	i
Abstract	ii
Contents	iv
1 Introduction	1
2 The Automotive Piston	4
2.1 Introduction	4
2.2 The Piston Engine	4
2.3 The Piston Assembly	5
2.4 Piston Design	9
2.5 Material Requirements	10
2.6 Development of Commercial Alloys	15
2.7 Summary	19
3 Aluminium-Silicon Alloys	20
3.1 Introduction	20
3.2 Fundamentals of Solidification	20
3.2.1 Nucleation	22
3.2.2 Growth	28
3.3 Solidification of Aluminium-Silicon Alloys	33
3.3.1 Primary Aluminium	36
3.3.2 Primary Silicon	36
3.3.3 Eutectic Silicon	40
3.4 The Structure of Castings	43
3.4.1 Solidification Zones	43
3.4.2 The Columnar to Equiaxed Transition	47
3.5 Grain Refinement	52
3.5.1 Mechanisms of Grain Refinement	56
3.5.2 Effect of Additions on the Grain Refining Ability of Ti and Ti+B	60
3.5.3 Additional Effects on Grain Refinement Ability	62
3.5.4 Quantification of Grain Refining Ability	64
3.6 Controlling the Microstructure	64
3.6.1 Modification	65
3.6.2 The Effect of Cooling Rate	68
3.7 Summary	70
4 Experimental Procedure	71
4.1 Introduction	71
4.2 Alloy Compositions, Casting Methods, and Heat Treatments	71
4.2.1 Cylindrical Mould: Model Alloys 5, 7 to 11	71
4.2.2 Keel Bars	75
4.2.3 Commercial Alloy AE160 and Model Alloys 24, 25 and 38	77
4.2.4 Stepped Mould: Model Alloys 83 to 90	78
4.2.5 Stepped Mould: Model Alloys 3	80
4.3 Analysis Techniques	81
4.3.1 Sample Preparation	81
4.3.2 Optical Microscopy	82
4.3.3 Image Analysis	82
4.3.4 Transmission Electron Microscopy	83
4.3.5 Scanning Electron Microscopy	84
4.3.6 High Temperature Differential Scanning Calorimetry	92
4.4 Thermodynamic Calculations	94
4.4.1 The Theory of Modelling Multicomponent Equilibria	94
4.4.2 Prediction of Phase Equilibria	98
4.4.3 Solidification Simulations	99

4.4.4 Thermodynamic Modelling Software: MTDATA	104
4.4.5 Thermochemical Databases	106
4.4.6 Calculation Methodology	108
5 Phase Analysis	109
5.1 Introduction	109
5.2 Verification of Thermodynamic Modelling	109
5.2.1 Comparison of Databases	110
5.2.2 Comparison of Equilibrium and Scheil Simulations	114
5.2.3 Comparison of Observed Phases and Equilibrium Predictions	118
5.2.4 Summary	121
5.3 Phase Analysis of AE160	122
5.3.1 Aluminium Matrix	123
5.3.2 Silicon	128
5.3.3 Al_3Ti	132
5.3.4 AlP	135
5.3.5 $\theta(Al_2Cu)$	138
5.3.6 Mg_2Si	140
5.3.7 Al_3Ni	143
5.3.8 $Al_3(Cu,Ni)_2$	146
5.3.9 Al_7Cu_4Ni	148
5.3.10 $\beta(AlFeSi)$	150
5.3.11 Al_9FeNi	151
5.3.12 $\lambda(Al_5Cu_2Mg_8Si_6)$	154
5.3.13 $\pi(Al_8FeMg_3Si_6)$	157
5.3.14 $\alpha(AlFeMnSi)$	159
5.3.15 New Quinary Phase	161
5.4 Phase Mapping	164
5.5 Summary	168
6 Grain Refinement	169
6.1 Introduction	169
6.2 Commercial Alloy AE160 and Model Alloys 24, 25, and 38	170
6.2.1 Microstructural Characterisation	170
6.2.2 Thermodynamic Predictions of Ti, Zr, and V Additions	172
6.2.3 Summary	181
6.3 Stepped Mould: Model Alloys 83 to 90	183
6.3.1 Grain Structures	183
6.3.2 Microstructural Analysis	185
6.3.3 Heat Treated Model Alloys	202
6.3.4 Summary	204
6.4 Keel Bar Alloys	205
6.4.1 Grain Structures	206
6.4.2 Microstructural Characterisation	211
6.4.3 Summary	218
6.5 Stepped Mould: Model Alloys 3/1 to 3/6	219
6.5.1 Characterising the Structure	221
6.5.2 Electron Microscopy.....	229
6.5.3 The Columnar to Equiaxed Transition	234
6.5.4 Modelling the Columnar to Equiaxed Transition	235
6.5.5 Summary	239
6.6 Discussion	239
7 Silicon: Nucleation and Growth	246
7.1 Introduction	246
7.2 Nucleation of Silicon Crystals	246
7.2.1 Identification of AlP Particles	247
7.2.2 Thermodynamic Data for AlP	249
7.3 Silicon Growth	255
7.4 Fatigue: Relationship Between Silicon Particles and Crack Nucleation and Growth	259

7.5 Summary	260
8 Piston Materials for the Future	262
8.1 Introduction	262
8.2 Alloy Database	262
8.2.1 Mechanical Properties	263
8.2.2 Physical Properties	267
8.3 Thermodynamic Phase Predictions	268
8.3.1 FMS2N	268
8.3.2 Addition of Silicon	269
8.3.3 Addition of Copper	270
8.3.4 Addition of Nickel	271
8.3.5 Addition of Iron	272
8.4 Elemental Database	273
8.4.1 Beryllium	275
8.4.2 Rare Earth Additions	276
8.5 Summary	277
9 Conclusions and Further Work	279
9.1 Conclusions	279
9.2 Further Work	280
References	
Appendices	
A Columnar to Equiaxed Growth Model	
B Image Analysis Data Collection Macro	
C Image Analysis Data Analysis Macro	
D Image Analysis t-Table	
E Orientation Space Charts	
F Image Analysis Results	
G Alloy Database	

Chapter 1

Introduction

This work has been carried out through a Project Studentship with the Engineering and Physical Sciences Research Council (EPSRC), with additional support from Federal-Mogul Technology (FMT) and the National Physical Laboratory (NPL). In collaboration with Cambridge (kinetic modelling) and Southampton (fatigue work) Universities, and Manufacturing Engineering at Loughborough (combined model), the project aims to develop a combined model to predict microstructural development for alloys typical of those used in automotive piston applications. This approach uses thermodynamic and kinetic modelling to predict the volume fraction and distribution of phases within the microstructure as a function of chemical composition and process parameters, with the ultimate aim of predicting mechanical properties. The research reported in this thesis focuses on microstructural characterisation and thermodynamic modelling, and addresses a number of issues concerning multicomponent, near-eutectic Al-Si casting alloys for piston applications.

The components of a modern internal combustion engine are required to give extreme reliability over extended periods of operation and none is exposed to more arduous conditions than the piston, especially in the pin boss and crown regions. Most automotive petrol engine pistons currently run at up to 350 °C, with diesel engines running even hotter. Increasing specific loads, new optimisation approaches for combustion processes, cost reduction programs, and a growing demand for increased service life for the equipment and its components, mean that pistons constantly require changes in design. In particular, the processing and high temperature performance of piston alloys are of considerable significance and need to be addressed.

Chapter 2 introduces the piston and its components, and describes how adaptation of the piston design to meet changing and more demanding load conditions, as is necessary for new engine development, requires a continuous improvement and innovation in the field of materials and process technologies. It has long since become established practice for the

pistons to be cast from multicomponent, near eutectic, aluminium-silicon alloys, which combine lightness in weight with high thermal conductivity. The moderate silicon content ensures that their mechanical strength is better maintained at high operating temperatures, whilst their coefficient of thermal expansion is lower than that usually associated with aluminium alloys. Although Al-Si alloys have been the subject of a great deal of research over the last 30 years, the majority of work has been based on fairly rudimentary characterisation of silicon morphology and distribution, rather than on a fundamental knowledge of the development of the complex microstructures and intermetallic phases that arise in commercial alloys.

The first step in alloy optimisation is thus to obtain a detailed understanding of the microstructures observed in commercial Al-Si alloys and the solidification processes by which they form. In Chapter 3 the nucleation and growth aspects of solidification are discussed with respect to both fundamental thermodynamics and the solidification of the Al-Si system. The chapter then considers the various casting practices developed to control the solidification of Al-Si alloys. An example is grain refinement, which is typically described as the addition of an element, such as Ti in the form of Al_3Ti , which acts as a nucleant for the aluminium phase, promoting a change in nucleation and growth mechanisms, and hence determining the final structure of the casting. In modification of the silicon phase, on the other hand, elements are added to hinder the growth of the silicon and produce fine, non-acicular particles less detrimental to the material properties. Thus, the final microstructure in a multicomponent Al-Si alloy is a complex function of alloy composition and casting conditions.

Using a range of well-established and novel analysis techniques, a thorough characterisation of both commercial and model alloy systems has been carried out as described in Chapter 4, and discussed in Chapter 5. Thermodynamic modelling methods are scrutinised in order to validate equilibrium and non-equilibrium (Scheil) simulations. It is found that both are representative of an as-cast alloy, although Scheil has the added capability of predicting minor phases characteristic of segregated regions of a casting. The thermodynamic predictions are then used in combination with optical and electron microscopy to produce a detailed analysis of the phases in multicomponent Al-Si alloys, consisting of information on phase morphology, composition, stability as a function of temperature, and crystallographic data.

Chapter 6 investigates the commercial practice of grain refinement, typically carried out to control the aluminium structure and hence improve mechanical properties. This is done through a series of theoretical and experimental analyses. In the casting process, a master alloy containing inoculant particles embedded in an Al matrix is added to the melt prior to pouring, where it typically dissolves completely apart from the inoculant particles which are dispersed in the melt. These subsequently act as nucleants for the Al phase during solidification, which can lead to a range of grain shapes and sizes depending of the casting conditions. Although used widely in refinement of casting alloys, the addition of grain refiners such as Al_3Ti has been borrowed completely from wrought aluminium practice, without extensive research. The aim of this chapter is, therefore, to explain some of the underlying mechanisms, including aspects of nucleation and growth.

The silicon phase can also adopt a number of morphologies depending on the alloy composition and casting conditions, as is discussed in Chapter 7. In particular, the primary silicon is of interest as it has been studied in much less detail than the modification of the eutectic silicon in the past, despite its importance to the mechanical properties of the alloy. Through electron backscatter diffraction, the nucleation and growth of primary silicon are investigated. AlP is identified as a nucleant for primary silicon, often found in the centre of the silicon particles. However, the growth of the silicon phase appears to be complex, comprising of both twinning and surface nucleation on the $\{111\}$ planes to produce a wide range of polygonal morphologies.

Finally, the concluding part (Chapter 8) of this study draws on the knowledge presented in the previous chapters, to suggest developments for future piston alloys. Drawing on information regarding the effect of alloying additions on the stability of intermetallic phases, and in turn, the effect of intermetallic phases on the mechanical properties of Al-Si alloys, recommendations for possible new alloying additions are proposed for a new generation of piston alloys.

Chapter 2

The Automotive Piston

2.1 Introduction

The continuous development in the field of automotive engines requires constant optimisation and improvement for all engine components, in particular the pistons. In this chapter the role of the pistons in the modern internal combustion engine will be discussed, detailing important components and the demands placed upon them. Some aspects relevant to piston design, and adaptation to the increasing requirements imposed on the piston will be outlined, with attention being paid to important properties and the evolution of piston materials to meet these growing demands.

2.2 The Piston Engine

The piston engine is known as an internal combustion engine, and almost all automotive vehicles use what is termed a four-stroke combustion cycle (intake, compression, combustion, exhaust) to convert the fuel into motion. However, the way in which petrol and diesel engines perform this process differs slightly. In petrol engines the concept is that a supply of air-and-fuel mixture is fed to the inside of the cylinder where it is compressed and ignited with a spark. A diesel engine, on the other hand, takes in only air, compresses it, and then injects fuel into the compressed air (direct fuel injection); the heat of the compressed air being enough to spontaneously light the fuel. Both methods of internal combustion release heat energy which is converted into useful mechanical work when the resultant high gas pressures force the piston to move along its stroke in the cylinder, although diesel fuel has a higher energy density than gasoline and therefore obtains better mileage ^[Bra02].

2.3 The Piston Assembly

Figure 2.1 shows a cross section of the piston assembly common to both petrol and diesel engines. The piston itself is a pressure-tight cylindrical plunger which converts the gas pressure generated from the heat energy of combustion into mechanical work as a concentrated driving thrust along the connecting rod. The connecting rod is linked to the crankshaft whose function is to convert the linear piston motion in the cylinder to a rotary crankshaft movement. The backward and forward displacement of the piston is generally referred to as the reciprocating motion of the piston.

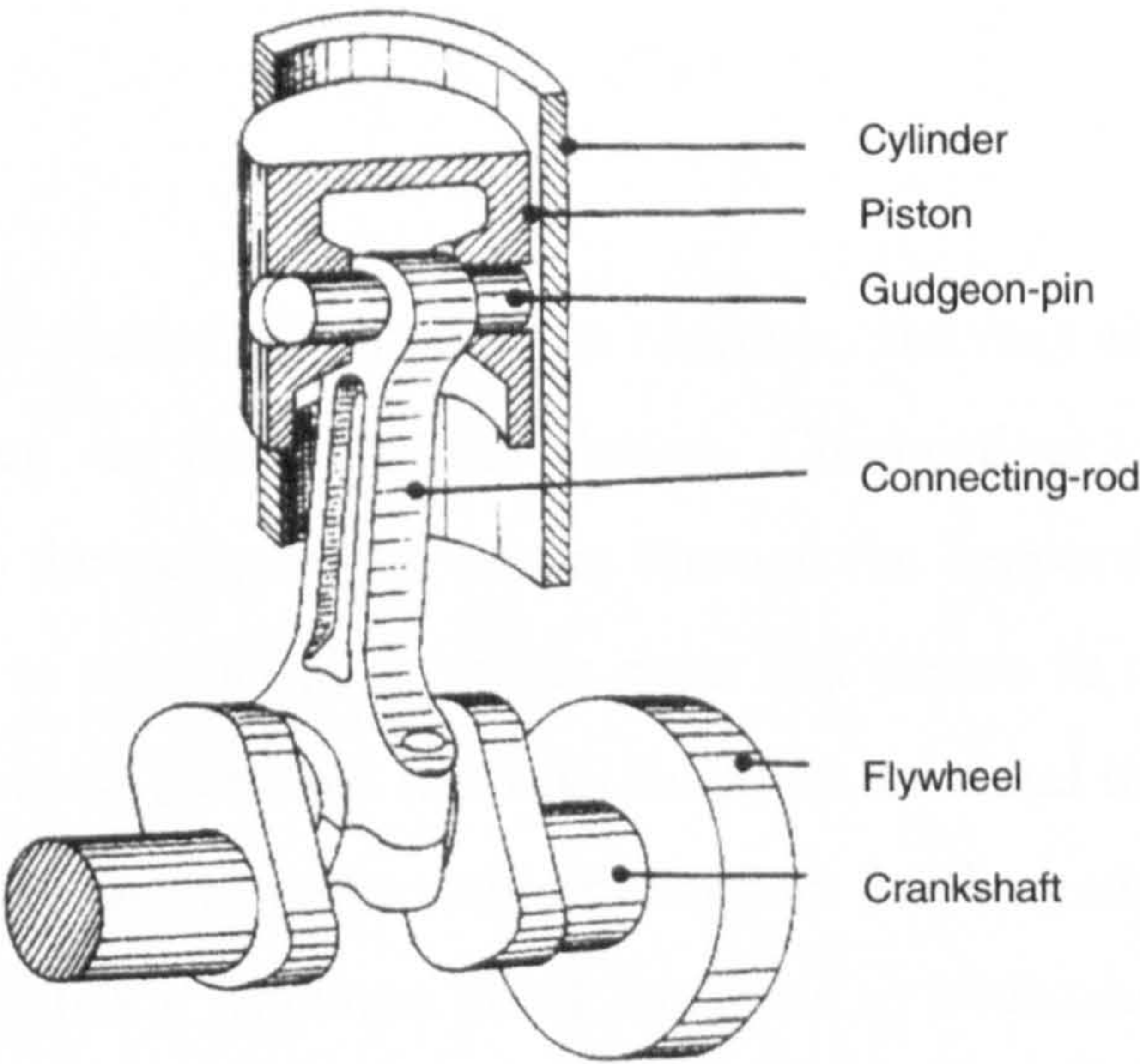


Figure 2.1 Schematic diagram of a piston assembly, after Heisler ^[Hei99]

A diagram of the components that make up the piston assembly is given in Figure 2.2. The individual components are outlined now, with an emphasis on how heat and force are transmitted through the piston, and the fundamental differences between petrol and diesel engines ^[Deu97, Hei99, Nun98].

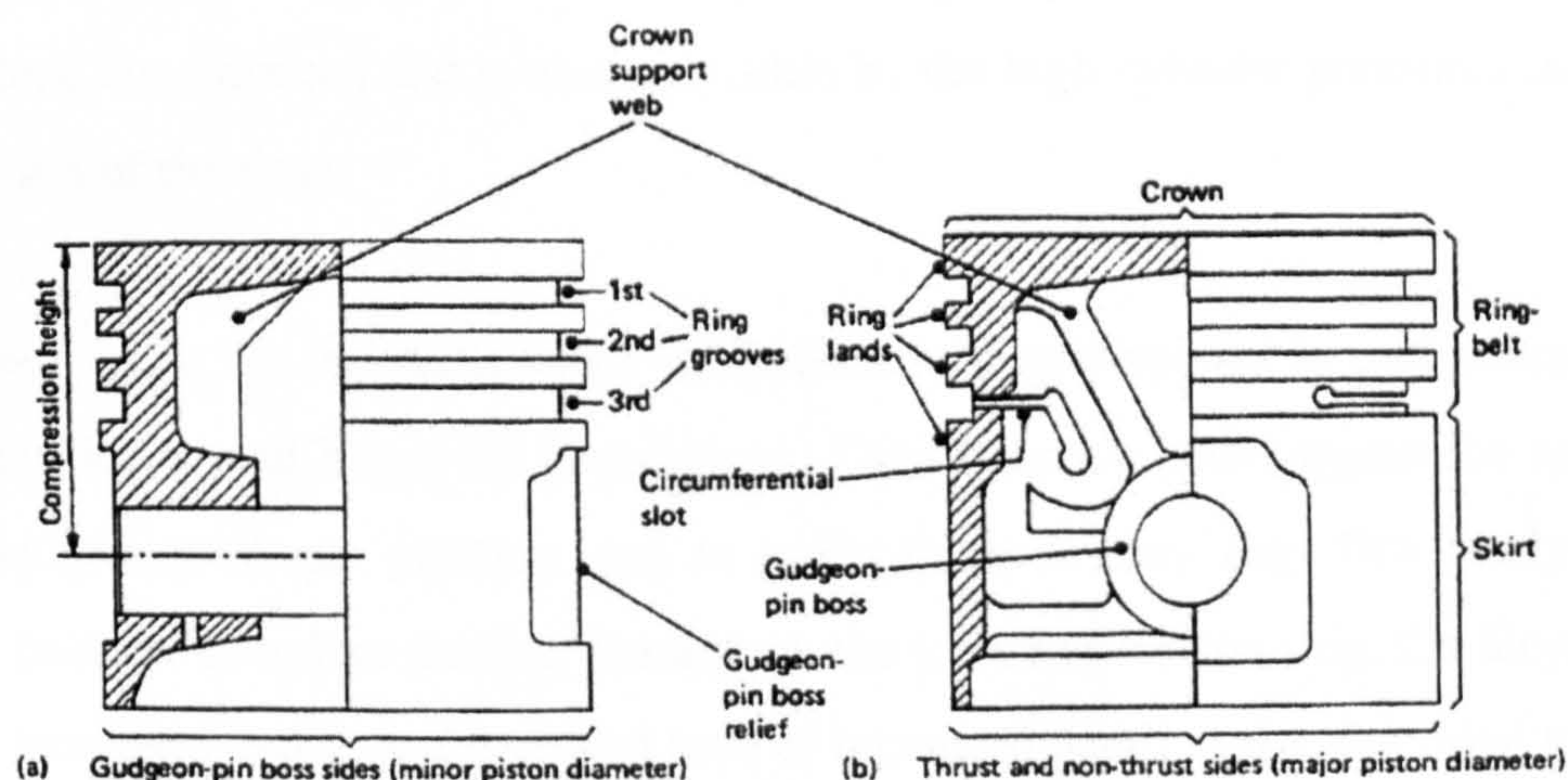


Figure 2.2 Schematic diagram of the piston components, after Heisler ^[Hei99]

Piston crown

The piston crown forms one wall of the combustion chamber, and may either be flat topped or specially shaped depending on the particular design. Combustion loads are transmitted directly from the crown to the gudgeon-pin bosses through the supporting webs, which also facilitate the flow of heat to the encircling piston rings and thence to the cylinder walls. In diesel engine pistons there is an increased sectional thickness of metal in the upper portion of the piston for better heat dissipation and maximum support for the gudgeon-pin bosses. The crown section of the piston has a generous metal thickness to withstand the higher cylinder gas pressures without distorting and to provide a ready path for heat to flow to the rings without cracking.

Piston rings and the ring belt

Piston rings are circular rings which seal the gaps made between the piston and the cylinder. Their purpose is to prevent the fuel/air mixture and exhaust gases escaping from the combustion chamber, and similarly to control the amount of lubricant that is allowed to reach the top of the cylinder and keep it from reaching the chamber. These are designated the compression and oil control rings, respectively. The diesel engine piston has generally been equipped to carry more rings than those on a petrol piston, with three instead of two compression rings, and two rather than one oil-control ring. More recently, however, there has been a definite trend to reduce the numbers of both compression and oil-control rings to the

same combination as that used in modern petrol engine practice. This is desirable as fewer rings produce less friction, and is made possible by the high cylinder pressures increasing the sealing action of the rings.

The ring belt lands are the metal strips left between the grooves cut in and around the top of the piston to locate and house the piston rings. Their function is to support the rings squarely against the generated gas pressure and to guide them so they may flex freely in a radial direction. In order to reduce thermal loading on the top compression ring, the diesel piston top land is of increased depth, and a second land of increased depth is also provided to contain the higher mechanical loading on the top ring.

The ring belt is the zone in which the rings and lands are grouped together. The crown relieves the ring belt of loads that would otherwise tend to deform its grooves; any closing of the grooves would prevent the rings moving freely, thus impairing their sealing ability. In diesel engines where high cylinder pressure and temperature conditions are expected, the piston can also include a bonded insert in the top ring carrier. A cast iron ring is cast into the aluminium alloy and forms a wear resistant carrier for the top, and sometimes also the second, compression ring. The insert has hot expansion characteristics that closely match those of aluminium, and is of tapered form to ensure the piston alloy grips it on cooling and contraction in diameter.

Skirt

The piston skirt is the portion of the piston that continues below the ring-belt. Its function is to form a guide capable of absorbing pressures created by the angle made by the connecting rod relative to the cylinder axis. Piston skirts are made as close fitting as possible in the cylinder, separated by a thin film of oil to ensure quiet operation and to assist with heat dissipation. Although the skirt should be internally structured to support the gudgeon-pin boss and sufficiently long enough to resist tilting of the piston under load, it is not designed to support the piston crown against compressive loads. Making the piston skirt longer in relation to the diameter spreads the side thrust forces over an increased surface area. Hence, the unit pressure is reduced so that separation between the piston and the cylinder wall is better maintained by the film of lubricating oil, and wear through direct contact is minimised.

Piston webs, bosses and relief

Piston webs are cast inside the piston between the crown and the gudgeon-pin bosses. They act as struts along which the compressive loads can be transmitted from the piston crown to the gudgeon-pin bosses, and then through the gudgeon pin to the connecting rod. Unfortunately the thick web sections form heat paths from the crown to the gudgeon-pin bosses which can lead to expansion problems if they are not carefully designed. The gudgeon-pin bosses are designed to transfer a large amount of heat from the piston crown to the cylinder walls so additional clearance must be provided. The skirt adjacent to these bosses is often recessed to provide a permanent relief and the necessary clearance.

Compression height

The compression height is the distance between the gudgeon-pin centre axis and the top of the piston crown. Engine manufacturers may offer different compression-ratios for the same basic engine and, to achieve this, a series of pistons may be made which are identical except for their compression heights. Fast-running direct-injection diesel engines have a comparatively low compression height and therefore reach very high boss temperatures of over 200 °C, with temperatures at the rim of the combustion chamber trough currently reaching over 350 °C, although this temperature is expected to increase to over 400 °C in future engines.

Surface finish and oil cooling

To ensure freedom from piston scuffing on cold starting or hot running conditions, it is important that the surface finish of the piston is oil retentive, and that the fitting clearance is always sufficient to maintain an oil film during engine operation, thereby prevent scuffing or seizure of the piston in the cylinder bore. The piston requires oil cooling as most of the combustion heat, to which the piston is exposed, flows through the rings to the cylinder, the piston itself being cooled only by contact with the cylinder wall and a constantly renewing thin film of oil. The oil, which has originally been pumped from the sump, acts as a medium for transferring excess heat away from the piston.

2.4 Piston Design

It has been stated that fast-running direct-injection diesel engines have a comparatively low compression height and therefore reach very high temperatures in the gudgeon-pin boss and rim of the combustion chamber trough. In addition, ignition pressures currently of around 13 MPa, but increasing to 20 MPa in the future, can lead to cracks in the boss and rim zones in aluminium pistons ^[Deu97]. The design of pistons requires the consideration of engine related boundary conditions such as compression height, connecting rod geometry and combustion bowl design, as well as the expected mechanical and thermal loads. These are essentially related to the specific cylinder output and the combustion process used. Small variations of these factors can result in enormous effects and, as Figure 2.3 indicates, such a difference can mean a drastic change in service life ^[Koe96].

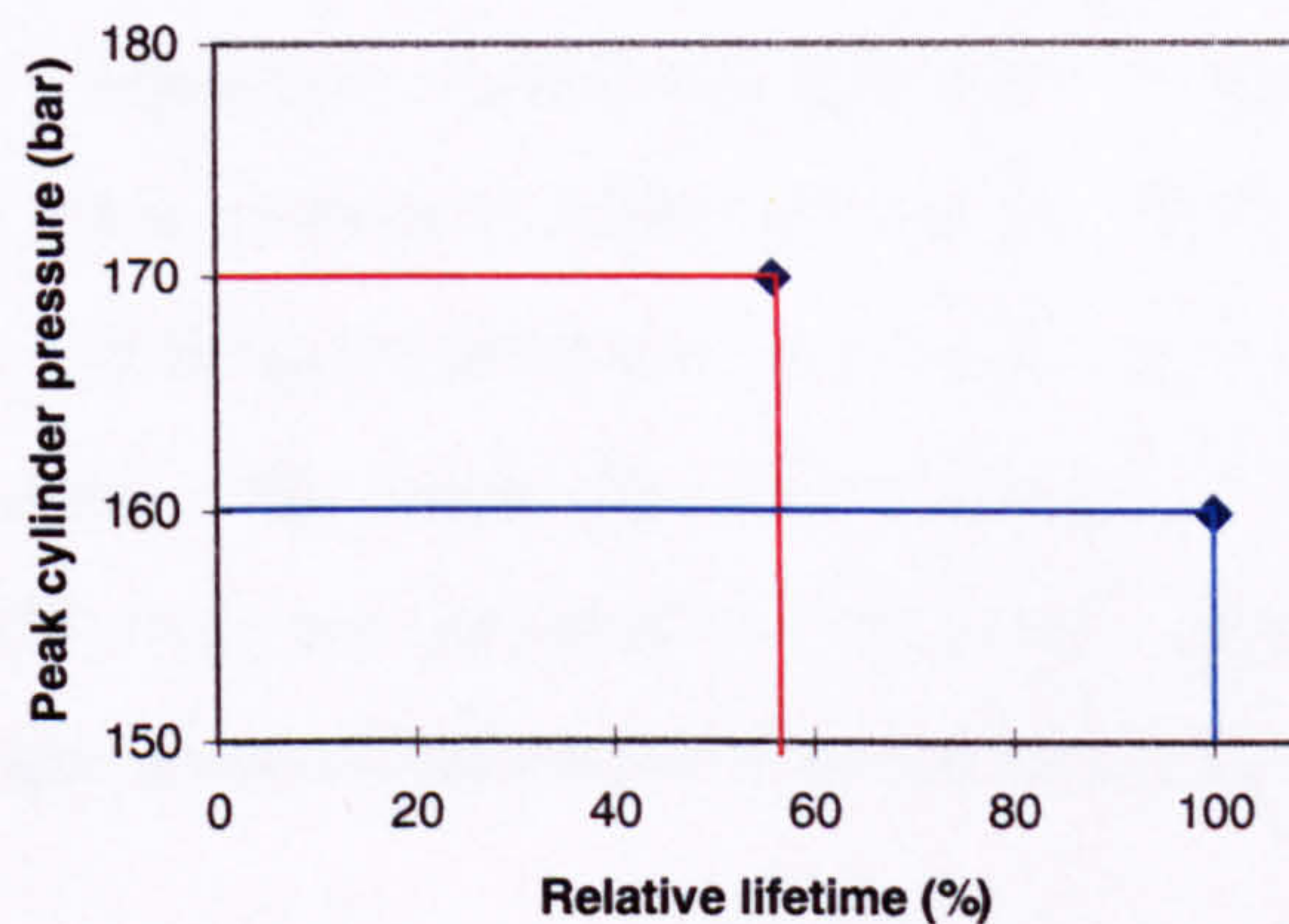


Figure 2.3 Estimated lifetime of an aluminium piston as a function of maximum cylinder pressure, based on data from Koehnert and Issler ^[Koe96]

Increasing demands on the engine and its components include:

- the increase of specific loads such as power output, torque, and peak cylinder pressure;
- new optimisation approaches for combustion processes regarding emissions, specific fuel consumption, reduced oil consumption etc.;
- requirements for noise reduction;
- the need for cost optimisation with the lowest possible weight; and
- a growing demand for increased service life for the equipment and its components.

The adaptation of the piston design to these changing and more demanding load conditions, as is necessary for new engine developments, requires a continuous improvement and innovation in the field of materials and process technologies. This is the only way to reach the goal of extended service life in an increasingly more severe environment at the lowest possible costs.

2.5 Material Requirements

It has been shown that modern internal combustion engine components are required to give reliability over extended periods of operation in an extremely severe environment. The pistons are exposed to more arduous conditions than most, especially in the pin boss and crown regions. In low-speed engines of early design, pistons were made from cast iron to match the cylinders. However, with increasing engine speeds and output, it has long since become established practice for the pistons to be cast from aluminium alloys, such alloys offering a good general balance of properties, combining lightness in weight with high thermal conductivity. They usually have a moderate silicon content so that their mechanical strength is better maintained at high operating temperatures, which may soon exceed 300 °C for petrol and 400 °C for diesel engines. This means that eutectic Al-Si alloys, which have relatively low melting points (~575 °C), are required to withstand considerable thermal and/or mechanical stresses at temperatures as high as 85 % of their absolute melting points ^[Sma82].

The fact that automotive pistons operate as well as they do under these circumstances represents a considerable technical achievement. Clearly, however, there could be advantages in changing to a higher melting point alloy. Indeed, there is growing use of ferrous pistons for highly rated diesel engine pistons, and there is on-going research aimed at the development of more heat resistant piston crowns. However, for the majority of engine applications, the disadvantages of departing very far from the usual Al-Si composition outweigh the advantages, and for this reason Al-Si continues to dominate piston production.

A satisfactory piston material must therefore possess a range of properties, and although some of the requirements are complementary, others are not. As in most engineering, some compromise has generally to be accepted in the final product. The most important properties are considered below.

Mass

For high speeds, the reciprocating forces created by the pistons reversing their direction of motion must be as small as possible. This has made it necessary to turn to lighter materials than the cast iron and steel that were used in early slow-speed engines. The obvious choice of the light metals was aluminium, which has a relative density of 2.6 compared with 7.8 for cast iron, and thus for a given volume, aluminium is one third of the mass of cast iron. This reduces the mass of the piston in proportion, but to maintain the rigidity of cast iron, the sections of the aluminium structures have to be larger, offsetting the advantage to some extent. By alloying aluminium with small amounts of other elements such as copper or silicon (relative densities of 8.9 and 2.3 respectively) the strength-to-mass ratio of the pistons is considerably improved, whilst only marginally altering the mass compared to a piston made of pure aluminium ^[Hei99].

High fatigue strength

Fatigue behaviour is highly sensitive to a number of variables, with failure normally occurring after a lengthy period of repeated stress or strain cycling. Work by Chave ^[Cha95] defined the three major inputs that are key components in fatigue life of pistons to be loading history (thermal and mechanical), component geometry, and materials properties. Firstly, knowledge of the in-service loads on a component are important in order to recreate in the model the stress levels experienced by the piston. There are two load cases to consider: the first is mechanically induced, and the second is that from the residual thermal stresses. Secondly, component geometry must be incorporated into the procedure due to the stress concentrating effects of notches and holes. And thirdly, materials properties are important in determining the levels of stress a component can safely withstand.

Thermal considerations

The whole piston assembly absorbs in the region of 50 to 60 % of the mechanical losses of the engine. For a typical piston with three rings, the first compression ring accounts for 60 % of the friction work, the second compression ring for 30 %, and the third oil-control ring for only 10 %. The energy from the combustion increases the temperature of the crown of the piston, and this heat has to be dissipated by way of the ring zone and skirt (see Figure 2.4). Approximately 50 to 60 % of the crown heat energy is transferred from the piston to the rings and then to the cylinder walls. The remaining heat-flow distribution is of the order of 20 %

through the ring lands and 20 to 30 % through the skirt, with 5 % of this heat being carried away by the gas and oil but most being conducted through the cylinder walls ^[Hei99].

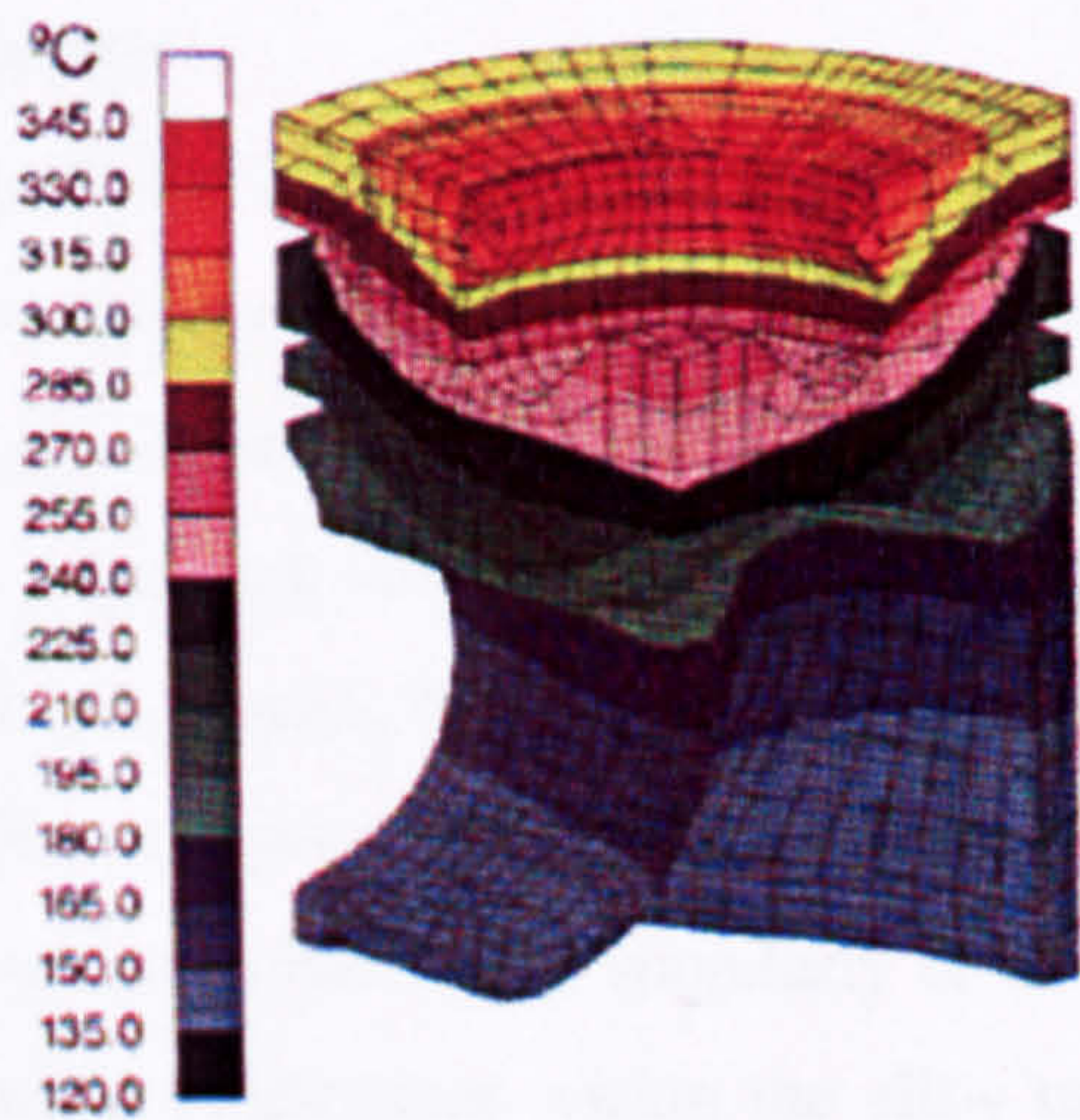


Figure 2.4 Temperature field from a finite element analysis of a piston, after Mahle ^[Mah98]

Low expansion coefficient

Although the aluminium alloys chosen for piston materials expand less when heated than most other light alloys, they nevertheless expand at nearly twice the rate of the cast iron used for most engine cylinders. Therefore, extra clearance between the piston and cylinder at room temperature has to be provided, otherwise the piston would become tight and seize under operating conditions. However, this clearance usually gives rise to piston ‘slap’ when the engine is cold and consequently rapid wear. The development of alloys with low expansion coefficients, often with additions of nickel, has helped to reduce this problem by keeping piston-to-cylinder clearance to a minimum.

High thermal conductivity

A high thermal conductivity is needed to keep down piston temperatures. Considering silver as 100 %, aluminium and cast iron have relative thermal conductivities of 38 % and 11.9 % respectively, making aluminium a much better conductor than cast iron. The aluminium can conduct 3.2 times more heat away in a given period, and since Al-alloy pistons have thicker sections than cast-iron pistons (see *mass considerations*), heat transfer is superior with these

light pistons. The enhanced heat dissipation of an aluminium alloy compared to cast-iron pistons greatly reduces the maximum piston-crown operating temperature, which has been stated as in excess of 350 °C for Al-alloy pistons and 400 to 500 °C for cast iron.

Strength and wear considerations

Pure aluminium is not strong enough for use as a piston material due to its low tensile strength of about 92 to 124 MPa at room temperature, falling off progressively to about 31 MPa at 300 °C (roughly the operating temperature of the piston crown). Furthermore, the soft aluminium has very little resistance to wear and scores readily. To overcome these limitations, near eutectic Al-Si alloys are generally used, the silicon providing some of the wear resistance required. In addition, small percentages of other elements such as copper, nickel, magnesium, and manganese, may be alloyed with the Al-Si, singularly or in various combinations. These elements form hard intermetallic precipitates within the alloy to produce not only improved strength over the operating temperature range, but also improved resistance to wear.

Good castability

The molten metal must have good castability (the ease with which the metal can be poured into a mould without producing defects) in order to minimise porosity and avoid shrinkage that can accompany cooling and solidification of the molten aluminium, and achieve the accuracy and surface finish derived from the intimate contact between the aluminium and the die. It is also very important to be able to use the current production route, gravity die casting, because introducing a new process would mean huge investment and expense. Certain elements, added to improve some of the aforementioned properties, result in a decrease in the castability and hot tear resistance (ability to withstand distortion during solidification) of the casting through the formation of sludge phases. These elements include copper and iron, which is the main impurity in these alloys, although additions of elements such as manganese can often be added to control intermetallic formation and to some extent rectify the deterioration in castability.

Low cost

As always, low manufacturing costs are crucial for mass production and there are several ways in which cost can be kept down. Over the last 40 years the size of pistons has decreased, a change that can be seen clearly in Figure 2.5. With this decrease in piston size follows a

reduction in the mass of material used, and consequently a reduction in the cost of material needed for production.

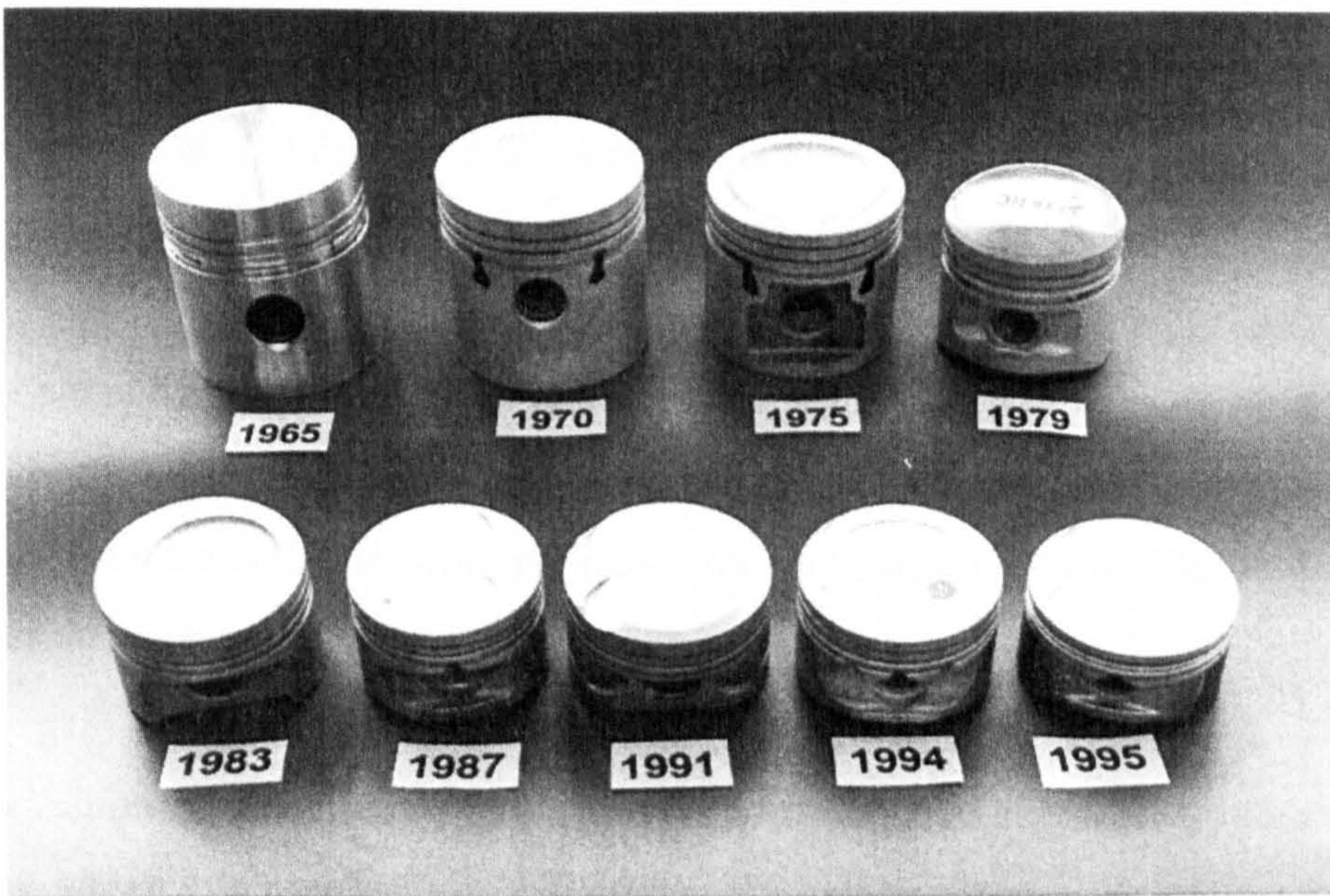


Figure 2.5 Change in piston size from 1965 to 1995, courtesy of Federal-Mogul

The development of pistons with improved properties has been partly aided by increasing the amount and number of elements added to the alloy. However, the cost of alloying additions can be high and so there has to be a balance between increased cost and improved properties, although the consumer is often prepared to pay more for a product with significantly improved properties and hence better performance.

Finally, scrap minimisation helps reduce cost by keeping material costs to a minimum. Firstly, the mould is designed as close as possible to the final shape required in order to reduce the amount of waste produced through machining, and secondly, waste produced through machining, swarf and risers, is generally sent away for recycling.

2.6 Development of Commercial Alloys

It has been explained that piston materials have developed from cast iron to aluminium-silicon alloys in order to adapt to constantly increasing demands on the piston. However, continuous materials development is required in order to compete in the market against the other piston manufacturers. The addition of alloying elements is one way of improving the properties of an Al-Si casting alloy, and much work has been carried out to investigate the effects of the major additions. Many of the properties discussed, however, are strongly influenced by the macroscopic and microscopic grain structure. In particular, a fine, uniform grain size is known to improve the strength of Al-Si alloys, and so small additions of elements such as titanium and phosphorus are added to promote nucleation and restrict growth. This is discussed further in the following chapter (Chapter 3).

Piston development led, in 1997 to a major competitor in the piston alloy market introducing a new alloy which was claimed to have improved properties to previous alloys being marketed for LVD (Light Vehicle Diesel) applications. Through detailed characterisation of existing alloys ^[Day98] together with an understanding of the behaviour of commercial alloys, a new alloy, AE160, was designed and put into production by Federal-Mogul. This section outlines the most recent advancements in piston materials, and explains how the development of new alloys evolves.

Predecessors to AE160

The three piston alloys in production by Federal-Mogul prior to the development of AE160 are briefly outlined below. These are AE413P, AE135, and AE113, and their compositions are given in Table 2.1.

AE413P was a phosphorus refined, near-eutectic, aluminium-silicon casting alloy (all other additions at less than 1 wt.%) designed for gasoline and light duty diesel piston applications. The microstructure consisted of primarily silicon cuboids with dispersed intermetallics in an acicular Al/Si matrix. The alloy could be both solution treated and/or aged (at lower temperatures) depending on the application.

AE135 was a superior grade, phosphorous treated aluminium alloy for premium gasoline pistons. As a new, higher copper version of AE413P (~ 5 wt. % compared with 1.2 wt. % in AE413P), AE135 had a number of improved properties, including hardness and yield strength.

Finally, AE113 was the premium diesel piston in use before AE160 was developed. It had a moderate Cu content (~ 3 wt. %) with all other additions generally at less than 1 wt. %.

Competitors

Two piston alloys in production by major competitors in the piston market were also analysed by Daykin ^[Day98]. The details of the alloys, Nüral S2 and Mahle 142, are given in Table 2.1.

During 1996, a great deal of interest was shown in piston alloys with a significantly higher nickel content than traditional alloys. Such an alloy, Nüral S2, was found to essentially be a higher Ni version of AE113 for use in diesel engines, with 2.3 and ~ 1 wt. % Ni respectively. Nüral S2 was reported to possess better toughness, higher hot tensile strength, increased temperature yield strength, and a lower hot elongation at rupture in comparison to Nüral's previous alloy, 3210 (similar to AE413P). The stated properties made the material ideal for the fast running direct injection (DI) diesel engines, where the rim of the combustion chamber can reach temperatures of over 300 °C.

The piston alloy, Mahle 142, was brought out in late 1997 as Mahle's new LVD (light vehicle diesel) piston, also for use in the small end of the MRD (medium range diesel) range, as well as gasoline applications. This is the same market as Nüral S2 and AE113 were designed for. In the publicity material Mahle claimed that "*Mahle 142 eutectic alloy offers better thermal properties and provides greater wear and deformation resistance compared to previous piston alloys*". More explicitly, it was reported that Mahle 142 offers improved creep resistance, yield strength at elevated temperatures, fatigue strength above 250 °C, thermal and dimensional stability, and wear and deformation resistance.

Analysis by Federal-Mogul of the Mahle 142 alloy discovered that, in comparison to AE113, Mahle 142 showed significant improvements at 350 °C as a result of the increased Ni content of the alloy, together with titanium, zirconium and vanadium additions known to act as grain refiners. Additions of the grain refiners were believed to produce a dispersion of relatively

fine, thermally stable Ni intermetallics in combination with a relatively fine grain size, which was thought to influence piston alloy properties (see Chapter 3). Image analysis determined that the particle size and distribution of primary Si particles was also reduced in comparison to the current Federal-Mogul alloys. On investigation of the macrostructure, the grain sizes within the Mahle 142 were found to be considerably smaller than those in AE113 pistons.

AE160 and subsequent alloys

AE160 was promoted as Federal-Mogul's new light vehicle diesel and heavy-duty diesel piston alloy (e.g. 1.9 TD VW Golf, Audi A6) with a 15 % improvement in 350 °C fatigue strength over the current alloy. Spark analysis was carried out at Federal-Mogul to determine the composition given in Table 2.1. Initial tests were carried out to ensure the material could withstand the operating conditions to which it would be subjected in service. The thermal properties are given in Table 2.2 along with the same properties of competitor and predecessor alloys in order for a comparison to be made. From these measurements it can be seen that the properties of AE160 are comparable to the other materials, particularly at 350 °C.

Since the launch of AE160, Federal-Mogul have merged with Nüral (producer of Nüral S2) making it necessary to integrate the two commercial alloys each company had in production. Although the compositions of AE160 and Nüral S2 are similar, the methods by which the two alloys are cast differs; Federal-Mogul cast their pistons upright, Nüral cast theirs on the side. This has an effect on the amount of certain elements added to the alloy, for example Nüral S2 contains considerably less Ti than AE160 as it is believed to reduce castability when the pistons are cast on their side. Therefore, a rationalisation of the two alloys was carried out resulting in the recent development of FMS2N, composition given in Table 2.1.

Initial tests have shown that FMS2N has improved properties compared to alloys with similar Cu and Ni levels, indicating that Ti, Zr and V additions are especially important factors. However, without complete understanding of how the microstructure influences the material properties, it is difficult to build a relationship between the two. Also in development is the alloy FMB2, a higher Si and Cu version of FMS2N (composition given in Table 2.1). At present initial fatigue tests have proven inconclusive and the alloy is close to the limit for production castability. The effects of alloying elements V, Zr and Ti are also explored in detail in Chapter 6.

Table 2.1 Compositions of commercial piston alloys

	Wt. % element													ppm
Alloy	Si	Mg	Cu	Ni	Mn	Fe	Sn	Pb	Zn	Ti	Zr	V	P	
AE413P	12.3	1.0	1.2	0.82	0.22	0.6	0.01	0.03	0.1	0.07	-	-	15	
AE135	12.5-14.0	0.8-1.3	4.5-5.5	0.8-1.3	0.1	0.5	0.1	0.1	0.2	0.2	-	-	30	
AE113	10.5-12.5	0.8-1.2	2.5-3.5	0.7-1.3	0.15	0.4	0.1	0.1	0.1	0.2	-	-	30	
AE160	11.2	1.05	3.1	2.27	0.08	0.3	-	-	-	0.17	0.15	0.06	53	
Nüral S2	12.0	1.1	3.4	2.3	0.1	0.4	-	-	0.05	0.01	-	-	-	
Mahle142	12.0	0.75	3.5	2.5		0.3	-	-	-	0.15	0.15	0.1	0.02	
FMS2N	12.3	1.0	3.6	2.5	0.2	0.5	-	-	-	0.05	0.16	0.08	-	
FMB2	14.5	1.0	4.2	3.1	0.15	0.5	-	-	-	0.05	0.07	0.07	-	

Table 2.2 Thermal properties of AE160 and its competitors

Alloy	Thermal conductivity at		Thermal conductivity at	Thermal expansion coefficient	Thermal expansion coefficient
	200 °C (W/mK)		350 °C (W/mK)	at 200 °C (1/K)	at 350 °C (1/K)
AE160	128		136	21.0	21.5
AE113	144		145	20.8	22.0
Mahle 142	130		135	21.2	22.4

2.7 Summary

This chapter has not only provided the reader with a background to automotive pistons, but also an indication of how the area of piston development is constantly changing. There is a specific need to understand the piston materials used in order to be able to continuously improve and develop alloy systems. The section on commercial alloys, in particular, demonstrated how a detailed understanding of the effect of alloying additions on the microstructure, and hence mechanical properties is essential in the design of new alloys. This is, therefore, the primary aim of the research described in the following chapters. In addition, generic modelling approaches will be developed to enable prediction of microstructural evolution, eliminating the need for expensive experimental 'trial and error' approaches.

19

Chapter 3

Aluminium-Silicon Alloys

3.1 Introduction

Chapter 2 described how piston materials have developed from cast iron to aluminium-silicon alloys in order to adapt to the ever-increasing demands on the piston. This chapter investigates the aluminium-silicon system further, with particular attention to some of the basic concepts of solidification, including nucleation and growth of crystals. A fundamental understanding of the mechanism of solidification and how it is affected by such parameters as temperature distribution, cooling rate, and alloying is proven to be essential in the control of mechanical properties of cast metals. Thus, casting practices developed for the control of structures on both a microscopic and macroscopic scale are considered.

3.2 Fundamentals of Solidification

This section is aimed at providing a generic explanation of some of the basic concepts of the solidification process, whereby the solidification of a liquid metal is promoted by heat removal, initiated by nucleation, and completed by the growth of the nuclei into the remaining melt. Thus, by understanding the individual mechanisms it should be possible to control the solidification of a casting and hence the resultant mechanical properties.

Throughout the analysis of solidification, thermodynamics is used to judge the alloy phase constitution, to describe the solidification path and composition changes in terms of partition coefficients and the slopes of the liquidus and solidus phase boundaries, and to account for the free energy changes involved in various solidification processes. In most castings, the equilibrium condition associated with a uniform phase composition does not occur throughout the ingot. It is often valid, therefore, to take the liquid and solid compositions at the solidification front to be represented by the liquidus and solidus compositions determined by the end points of a tie line at a given temperature on the phase diagram. This concept is called

local interfacial equilibrium, and it has been successfully applied to the description of casting processes in which the rate of diffusion, particularly in the solid, is too slow to achieve uniform phase compositions.

The thermodynamic description of solidification can be quantified by recalling that for a pure metal at the equilibrium melting temperature, T_m , the change in Gibbs free energy of a system, ΔG , is given by;

$$\Delta G = \Delta H - T_m \cdot \Delta S = 0 \quad [3.1]$$

so that:

$$\Delta S = \Delta H / T_m \quad [3.2]$$

where ΔH and ΔS are the differences in enthalpy and entropy respectively between the liquid and solid states. At T_1 , a temperature other than T_m where $\Delta G \neq 0$, Equations 3.1 and 3.2 can be combined to yield:

$$\Delta G = \frac{\Delta H \cdot (T_m - T_1)}{T_m} = \frac{\Delta H \cdot \Delta T}{T_m} \quad [3.3]$$

when the small correction due to heat capacity is neglected. Based on Equation 3.3 there is a direct relationship between ΔG and the supercooling ΔT , as can be seen in Figure 3.1.

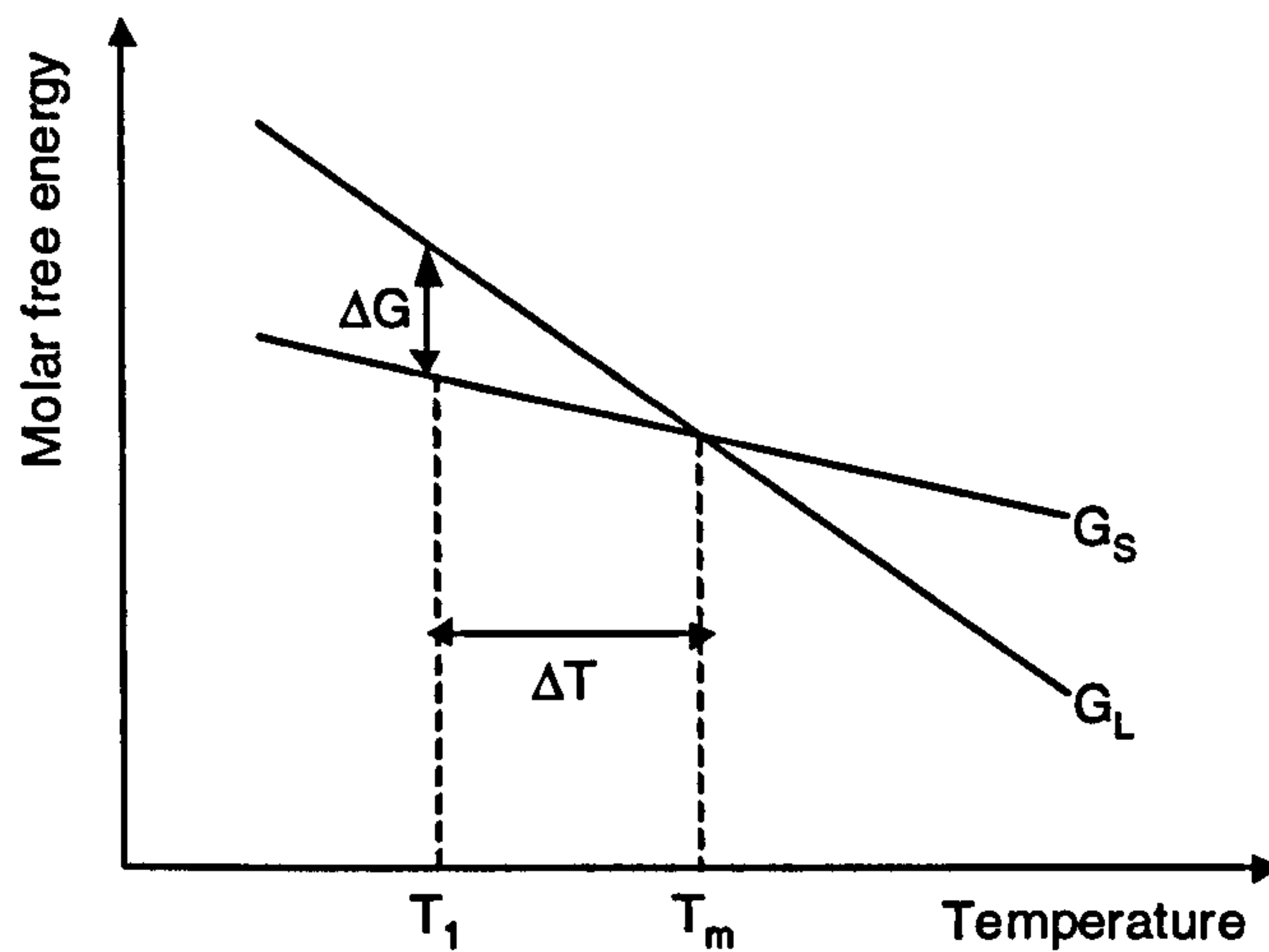


Figure 3.1 Difference in free energy between the liquid and solid close to the melting point (curvature of the lines has been ignored)

3.2.1 Nucleation

If a liquid is cooled below its equilibrium melting temperature (T_m) there is a driving force for solidification (ΔG) and it might be expected that the liquid phase would spontaneously solidify [Por81]. However, this is generally not the case and, depending on the conditions, the solidification temperature corresponding to the onset of freezing is often significantly less than the melting point or equilibrium liquidus temperature. The offset of the solidification temperature with respect to the equilibrium temperature is called the undercooling or supercooling, ΔT , and plays a vital role in the overall description of the initial stage of solidification that is controlled by nucleation. The level of melt supercooling at the onset of solidification is particularly important in developing an understanding in the grain refinement practice as is discussed later in Section 3.5.

Homogeneous Nucleation

It is possible to supercool a liquid because the initial stage in the formation of a crystal is the spontaneous aggregation of a few hundred atoms of the liquid in the geometrical pattern characteristic of the crystal, forming what is termed an embryo. In order to be sufficiently stable enough to have a reasonable chance of growing, the embryo must reach a certain size, dependent on the temperature, when it is called a nucleus. This type of nucleation is referred to as homogeneous. It has been shown, both theoretically and experimentally, that a pure metal does not spontaneously form nuclei unless it is supercooled by a very large amount. For example, in aluminium, which has a melting point of 660 °C, spontaneous homogeneous

nucleation is believed to occur at around 465 °C, although it is usually found that solidification starts at a much reduced supercooling than this in practice.

In alloys, the driving force for nucleation is a function of both composition and temperature, as well as having to take into account the role played by interfacial free energy. During the formation of the embryo, from which the nucleus grows, there is a significant increase in the interphase boundary area. The resultant increase in interfacial free energy is necessary in determining whether the transformation proceeds with a reduction in the free energy of the system. The free energy change accompanying the formation of an embryo at a temperature, T_1 , below T_m , is the difference between the change in volume free energy of the two phases, ΔG_V , and the interfacial free energy, γ_{SL} , required to form the new solid-liquid interface. For a spherical embryo of radius, r , this change is given by:

$$\Delta G = (4 \cdot \pi \cdot r^2 \cdot \gamma_{SL}) - \left(\frac{4}{3} \cdot \pi \cdot r^3 \cdot \Delta G_V \right) \quad [3.4]$$

and is illustrated in Figure 3.2.

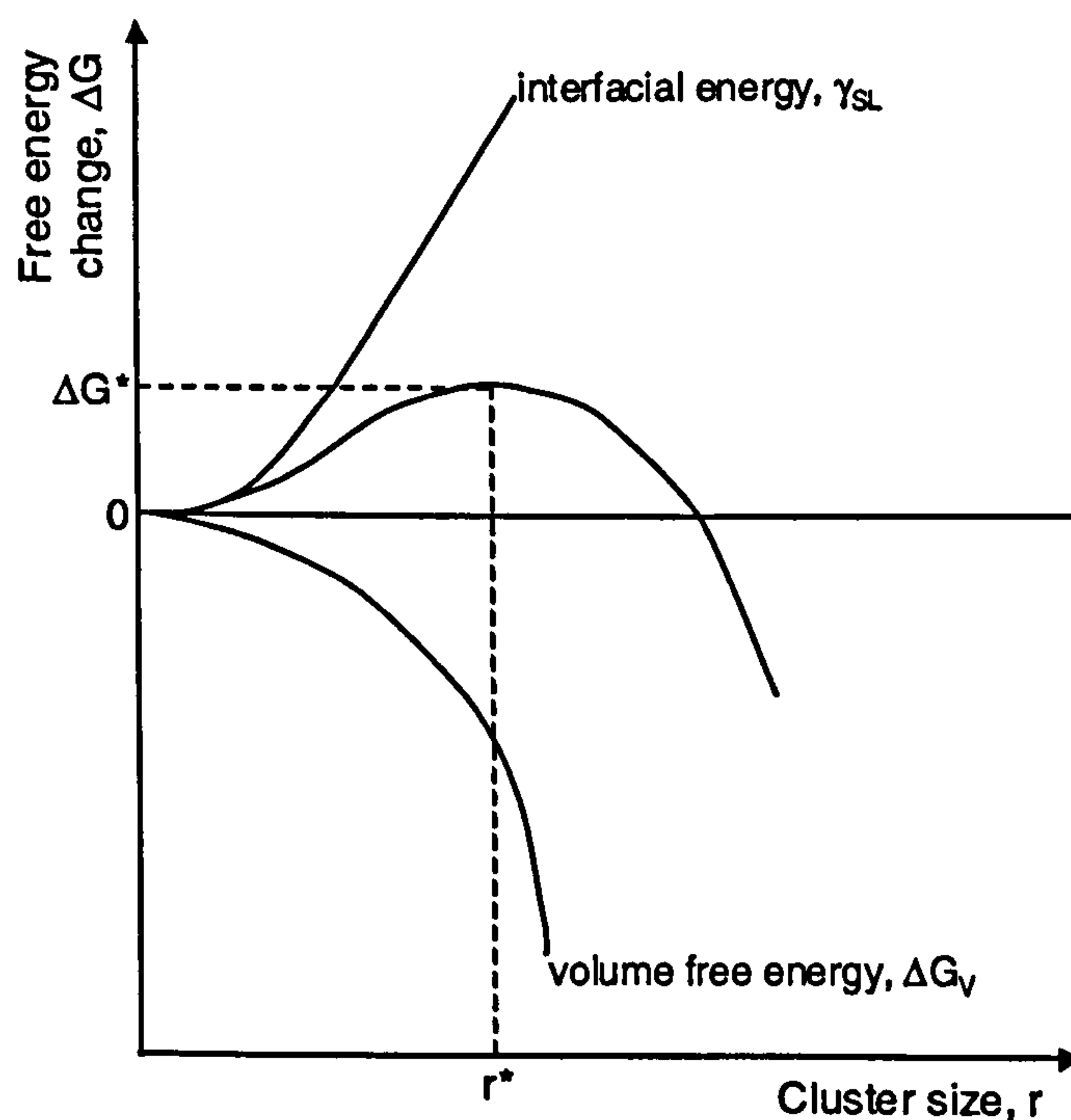


Figure 3.2 Diagram of the free energy change associated with homogeneous nucleation of a sphere of radius, r

The condition for homogeneous nucleation is that the metastable embryo should continue to grow into a stable nucleus. This occurs when the embryo radius exceeds r^* when further transformations are accompanied by a continuous decrease in free energy and spontaneous growth, as seen in Figure 3.2. The critical value r^* corresponds to the differential of Equation 3.4 which gives

$$r^* = \frac{2 \cdot \gamma_{SL}}{\Delta G_V} \quad \text{and} \quad \Delta G^* = \frac{16 \cdot \pi \cdot \gamma_{SL}^3}{3 \cdot (\Delta G_V)^2} \quad [3.5]$$

where ΔG_V increases as the temperature decreases according to

$$\Delta G_V = \frac{\Delta H_f \cdot \Delta T}{T_m} \quad [3.6]$$

just as r^* varies inversely with ΔT according to

$$r^* = \frac{2 \cdot \gamma_{SL} \cdot T_m}{\Delta H_f \cdot \Delta T} \quad [3.7]$$

Thus, prior to nucleation, the liquid phase supercools until it reaches a temperature at which the critical embryo size, r^* , falls into the range of cluster sizes present in the liquid. The rate of nucleation, I_{hom} , depends on the number of these critically sized embryos per unit volume, n_{r^*} , and the frequency with which atoms join them from the melt. Although Figure 3.2 shows that the formation of an embryo is accompanied by an increase in energy, an equilibrium concentration of embryos of all sizes exist in the liquid. On average the number of spherical clusters of radius r is given by

$$n_{r^*} = n \cdot \exp\left(\frac{-\Delta G^*}{k \cdot T}\right) \quad [3.8]$$

where n is the total number of atoms per unit volume, The frequency of transfer of atoms is inversely proportional to the viscosity or may be described by $(k \cdot T/h) \cdot \exp(-\Delta G_D/k \cdot T)$

where ΔG_D is identified with the activation energy for diffusion, k is Boltzmann's constant and h is the Planck constant. The rate of homogeneous nucleation is given by

$$I_{\text{hom}} = \frac{n \cdot k \cdot T}{h} \cdot \exp\left(-\frac{\Delta G^* + \Delta G_D}{k \cdot T}\right) \quad [3.9]$$

However, homogeneous nucleation does not occur in normal casting processes and is observed only when precautions are taken to eliminate the effect of impurities or to restrict their influence to a small volume in the melt.

Heterogeneous Nucleation

Normally nucleation is greatly assisted by the presence of suitable solid particles suspended in the melt known as 'nucleation catalysts', which make nucleation easier by acting as a substrate on which embryos can form and become a nuclei at much less supercooling than would otherwise be necessary. This is known as heterogeneous nucleation. The source of such particles is debatable, many originating as impurities common in alloy melts, but also from deliberate additions and even broken-off pieces of solid having been washed into the melt by turbulence during pouring.

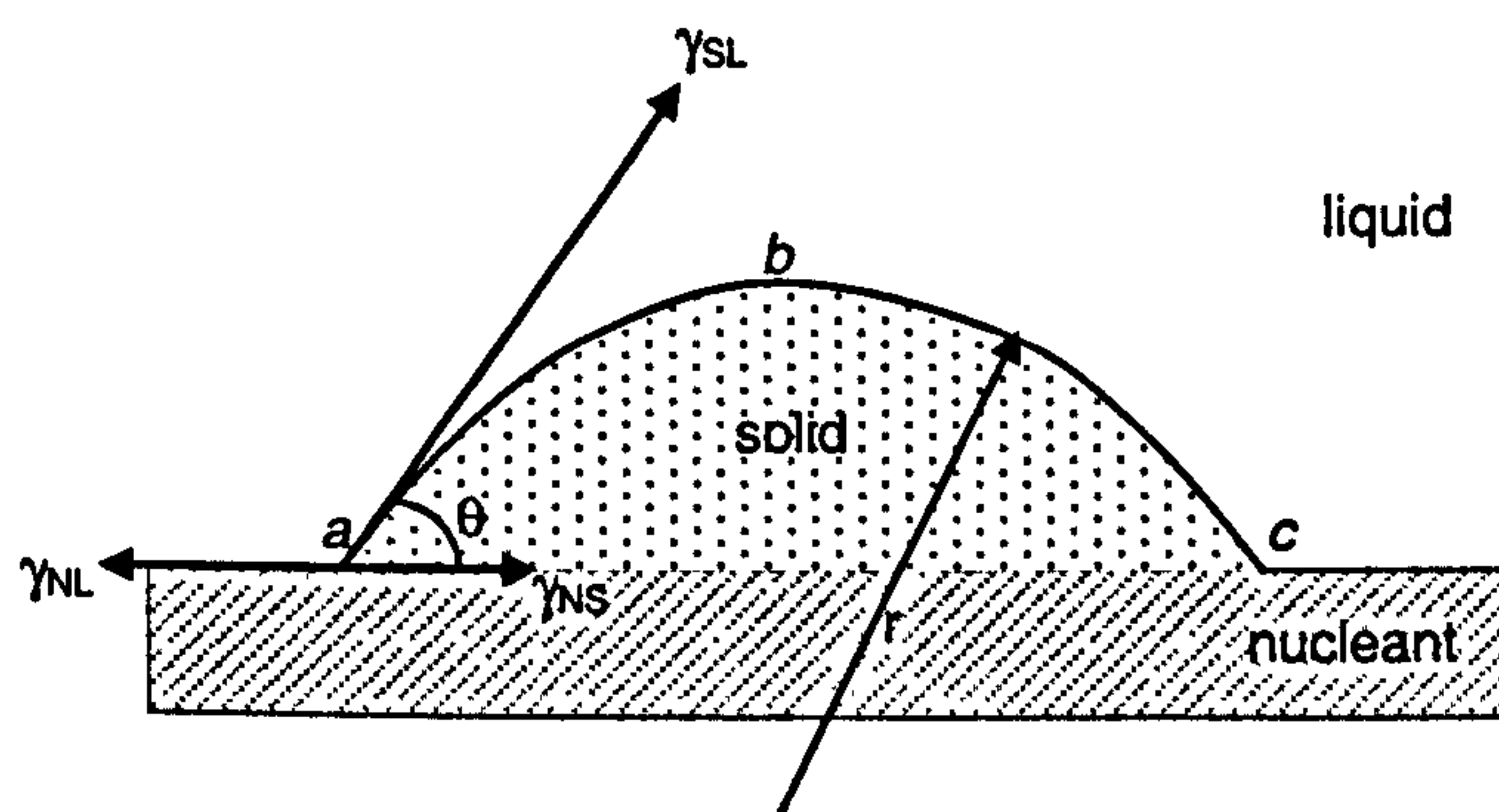


Figure 3.3 Schematic representation of a capped shaped nucleus for heterogeneous nucleation

For homogeneous nucleation the formation of a spherical cluster of atoms of a critical size is considered, although it is not necessary for the nucleus to be a complete sphere. Consider Figure 3.3. If the surface of the cap-shaped embryo is stabilised by a nucleant, depicted here

as a flat substrate, the cluster can grow into a nucleus by expansion of its surface to abc . A nucleus formed in this way will contain fewer atoms than a spherical one, and consequently the supercooling required for the formation of a capped-shaped nucleus is less than that required for homogeneous nucleation. The same critical radius is required for nucleation in both cases, but the driving force for heterogeneous nucleation is less because the presence of the nucleant lowers the total interfacial free energy, which in turn reduces the energy barrier. This may be expressed mathematically in a similar manner to that in Equation 3.4 for homogeneous nucleation. The free energy change accompanying heterogeneous nucleation comprises the volume free energy change, the interfacial free energy acting over the base of the cap, and that acting over the solid-liquid interface. Hence

$$\Delta G = (\pi \cdot r^2 \cdot \sin^2 \theta) \cdot (\gamma_{SN} - \gamma_{NL}) + (2 \cdot \pi \cdot r^2 \cdot \gamma_{SL}) \cdot (1 - \cos \theta) - \left(\frac{\pi \cdot r^3}{3} \cdot \Delta G_v \left[(1 - \cos \theta)^2 (2 + \cos \theta) \right] \right)$$

(Equation 3.10) which gives

$$\Delta G = \pi \cdot r^2 \cdot \left[(2 + \cos \theta) \cdot (1 - \cos \theta)^2 \right] \cdot \left(\gamma_{SL} - \frac{1}{3} \cdot \Delta G_v \cdot r \right) \quad [3.11]$$

Differentiation yields

$$\frac{\delta \cdot \Delta G}{\delta \cdot r} = \left[2 \cdot \pi \cdot r \cdot (2 + \cos \theta) \cdot (1 - \cos \theta)^2 \right] \cdot \left(\gamma_{SL} - \frac{1}{2} \cdot \Delta G_v \cdot r \right) \quad [3.12]$$

hence

$$r^* = \frac{2 \cdot \gamma_{SL}}{\Delta G_v} \quad [3.13]$$

and

$$\Delta G^* = \frac{16 \cdot \pi \cdot \gamma_{SL}^3}{3 \cdot \Delta G_v^2} \cdot \left[\frac{(2 + \cos \theta) \cdot (1 - \cos \theta)^2}{4} \right] \quad [3.14]$$

Thus, the free energy barrier for heterogeneous nucleation is that for homogeneous nucleation modified by a factor $[(2 + \cos\theta)(1 - \cos\theta)^2] / 4$. As $\theta \rightarrow 0$, the free energy barrier opposing nucleation disappears and the effectiveness of the nucleant increases, although the critical nucleus size, r^* , is unaffected by the catalyst and only depends on the supercooling. This relationship can be seen in Figure 3.4.

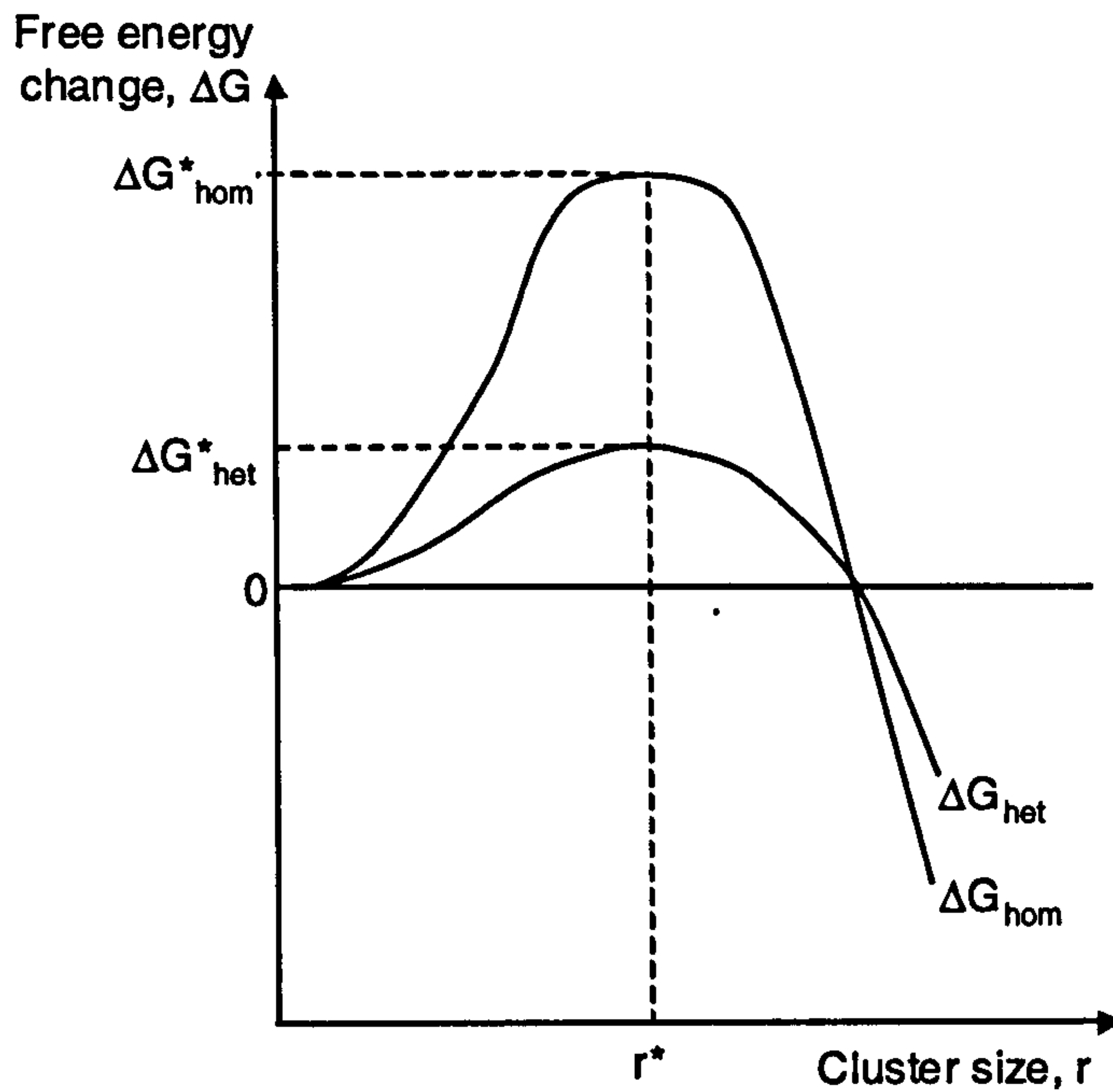


Figure 3.4 Comparison of free energy change for homogeneous and heterogeneous nucleation

The rate of heterogeneous nucleation is expressed in the same way as for homogeneous nucleation

$$I_{het} = \frac{n \cdot k \cdot T}{h} \cdot \exp - \left(\frac{(2 + \cos\theta) \cdot (1 - \cos\theta)^2}{4 \cdot k \cdot T} \cdot \frac{\Delta G^* + \Delta G_D}{k \cdot T} \right) \quad [3.15]$$

In the simple analysis of heterogeneous nucleation described above the effectiveness of a nucleant can be related to the contact angle, θ . However, in practice the contact angle approach is of limited use as not only are there doubts regarding the shape of the nucleus, but experimentally it is difficult to measure θ and the interfacial free energy. As a result, several

attempts have been made to correlate the effectiveness of a nucleant with the parameter γ_{SN} (Equation 3.16). The most reported of these uses the entrained droplet technique whereby liquid droplets and nucleant surface are formed internally in a chill cast alloy during heat treatment ^[Sou78]. Results from these experiments have been analysed in terms of nucleation theory to calculate the operative contact angles derived from

$$\cos \theta = \frac{T_{m(N)}}{T_{m(S)}} - \frac{\gamma_{SN}}{\alpha \cdot T_{m(S)}} \quad [3.16]$$

where $T_{m(N)}$ and $T_{m(S)}$ are the melting points of the nucleant and solid respectively, and α is a constant. Other results suggest that a strong correlation exists between $\cos \theta$ (nucleant effectiveness) and the ratio of melting points. Thus, the clean heterogeneous nucleation observations suggest that a nucleant will be effective for a solid if:

- the nucleant shows metallic bonding;
- there is a high melting point ratio;
- a low nucleant-solid interfacial energy exists.

Although these conditions may define a potential nucleant, other factors may over-ride the specified criterion. For example, as will be discussed in full in Section 3.5, analysis of the grain refinement of Al alloys has shown that not all potentially good nucleants are effective, and this was attributed to constitutional supercooling effects which permit a high nucleation rate prior to recalescence. These observations add a further condition that however good a nucleant might be potentially, if it is insoluble in the metal, its potential refining action will be precluded if the growth temperature is not depressed significantly below the freezing point.

3.2.2 Growth

The solidification process is completed by the growth of the nuclei into the surrounding liquid. The driving force for this process is supercooling, which is controlled by the rate of heat extraction.

Consider first the idealistic condition of a planar interface in an alloy bar where there is complete mixing of solute in the solid and liquid phases at all stages of the solidification process. For a temperature, T , in the alloy freezing range, the solid of uniform composition,

C_S , is in equilibrium with the liquid of composition C_L . The solute also partitions between solid and liquid at the interface according to the equilibrium partition coefficient, k_0 , defined as

$$k_0 = \frac{C_S}{C_L} \quad [3.17]$$

where C_S and C_L are the mole fractions of solute in the solid and liquid in equilibrium at a given temperature. For the simple case shown in Figure 3.5, k_0 is independent of temperature. As growth progresses the composition of the solid and liquid phases changes continuously according to the liquidus and solidus lines in the relevant equilibrium phase diagram.

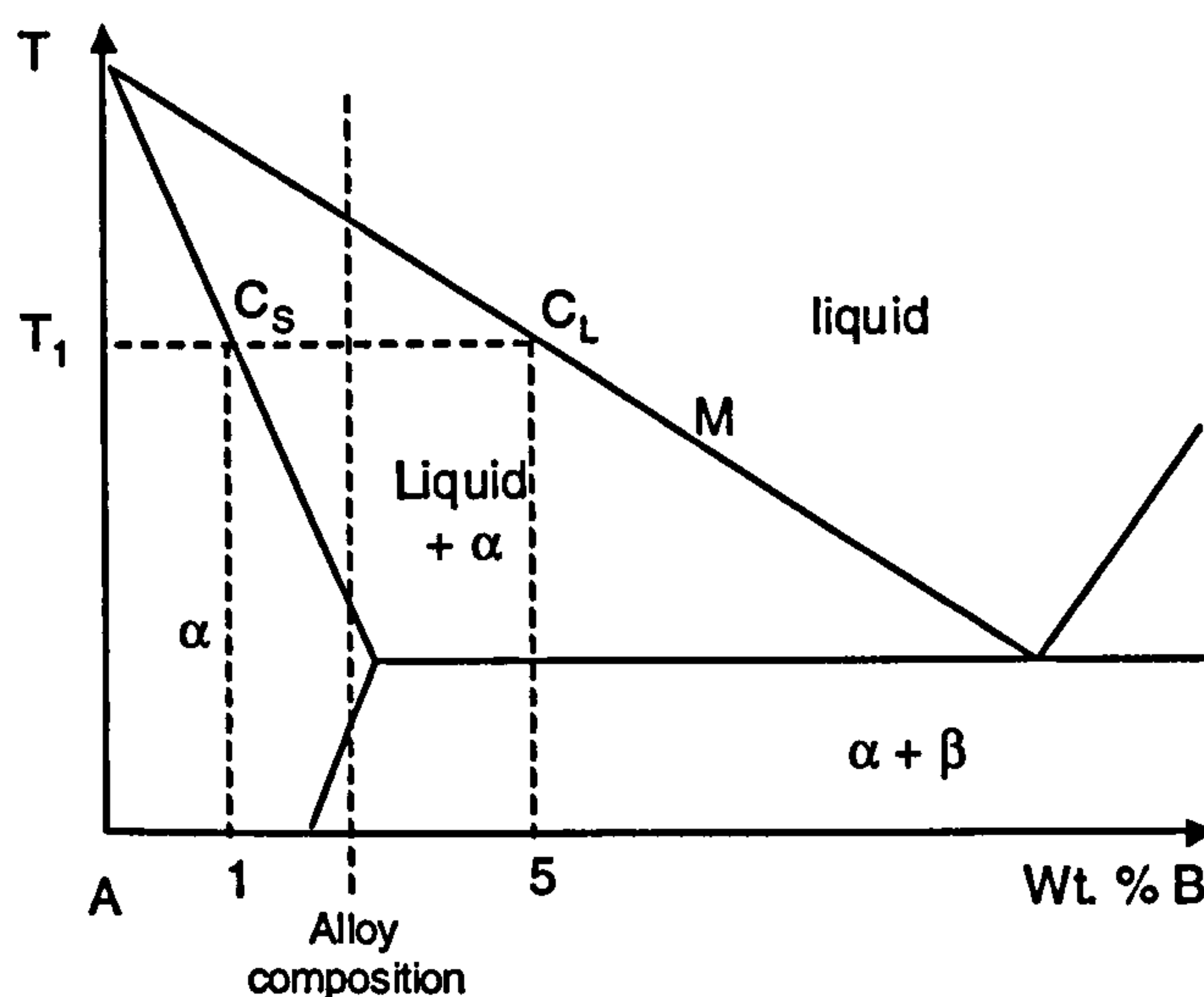


Figure 3.5 Example of a typical eutectic binary equilibrium phase diagram

However, solute diffusion plays an important role in the solidification of alloys with the transformation being both a heat and solute flow problem in eutectic alloys. It is necessary, therefore, to consider the more realistic situation of a finite growth rate where no solute diffusion occurs in the solid phase, but with complete mixing achieved in the liquid. These conditions are achieved in practice by having a slow solidification rate and/or by vigorously stirring the liquid. The growth rate is sufficiently slow for equilibrium conditions to be reached at the interface during growth although, as there is no diffusion in the solid; the composition of the solid formed in the initial stages of freezing remains unchanged. A

quantitative expression may be derived for the composition of the solid C_s as a function of the fraction of solid, f_s , by equating the solute rejected when a small amount of solid forms to the resulting increase in the liquid.

$$C_s = k_0 \cdot C_0 \cdot (1 - f_s)^{k_0 - 1} \quad [3.18]$$

This is the classical non-equilibrium lever rule or Scheil equation whereby all the solute rejected at the solid-liquid interface is immediately mixed uniformly throughout the liquid.

In practice, however, the solute rejected from the solid is transported away from the interface by both liquid diffusion and limited stirring as a result of turbulence or convection effects. Hence, there will be a build-up of solute ahead of the solid, which decreases with distance from the interface. This means that the solid that forms generally has a different composition to that of the liquid that is immediately in contact with it. Considering an alloy system AB, the relevant part of the equilibrium phase diagram is given in Figure 3.5, which can be thought of as a typical eutectic binary alloy system which has been idealised by assuming that the solidus and liquidus are straight lines. At a temperature, T_1 , the liquid containing 5 wt. % B (C_L) is in equilibrium with the solid α containing 1 wt. % B (C_s). Therefore, for every 1 gram of liquid solidified, the solid will contain 1/100 grams of B whilst the liquid from which it was formed will contained 5/100 grams of B. It follows that 4/100 grams of B are rejected back into the melt during the solidification of 1 gram of alloy. The rejected solute is initially localised in the liquid adjacent to the solid-liquid interface, and despite slow dispersion by diffusion, convection or stirring, there remains an excess of solute at the interface compared with more remote liquid. The rejection has two main consequences:

- i) the solute cannot be uniformly distributed in the solid and, therefore, there must be some segregation, and;
- ii) the enrichment of the liquid at the solid-liquid interface lowers the equilibrium temperature as the composition moves towards M (Figure 3.5). As the process continues, the depression of the temperature of the solid-liquid interface also continues.

Indeed, as the crystals grow there is a rejection of solute ahead of the growing crystals that causes a progressive drop in the temperature of the solid-liquid interface, and therefore of the liquid which still exists in the interior. The liquid in the interior supercools because of the depression of the freezing point, and consequently the temperature of the layer of ‘alloy enriched’ liquid at the interface. The bulk of the liquid, being unchanged in composition, does not undergo any change in liquidus temperature, and so is below its own liquidus temperature. Supercooling that originates from this depression of the freezing temperature by rejection of solute at an advancing interface is called ‘constitutional supercooling’.

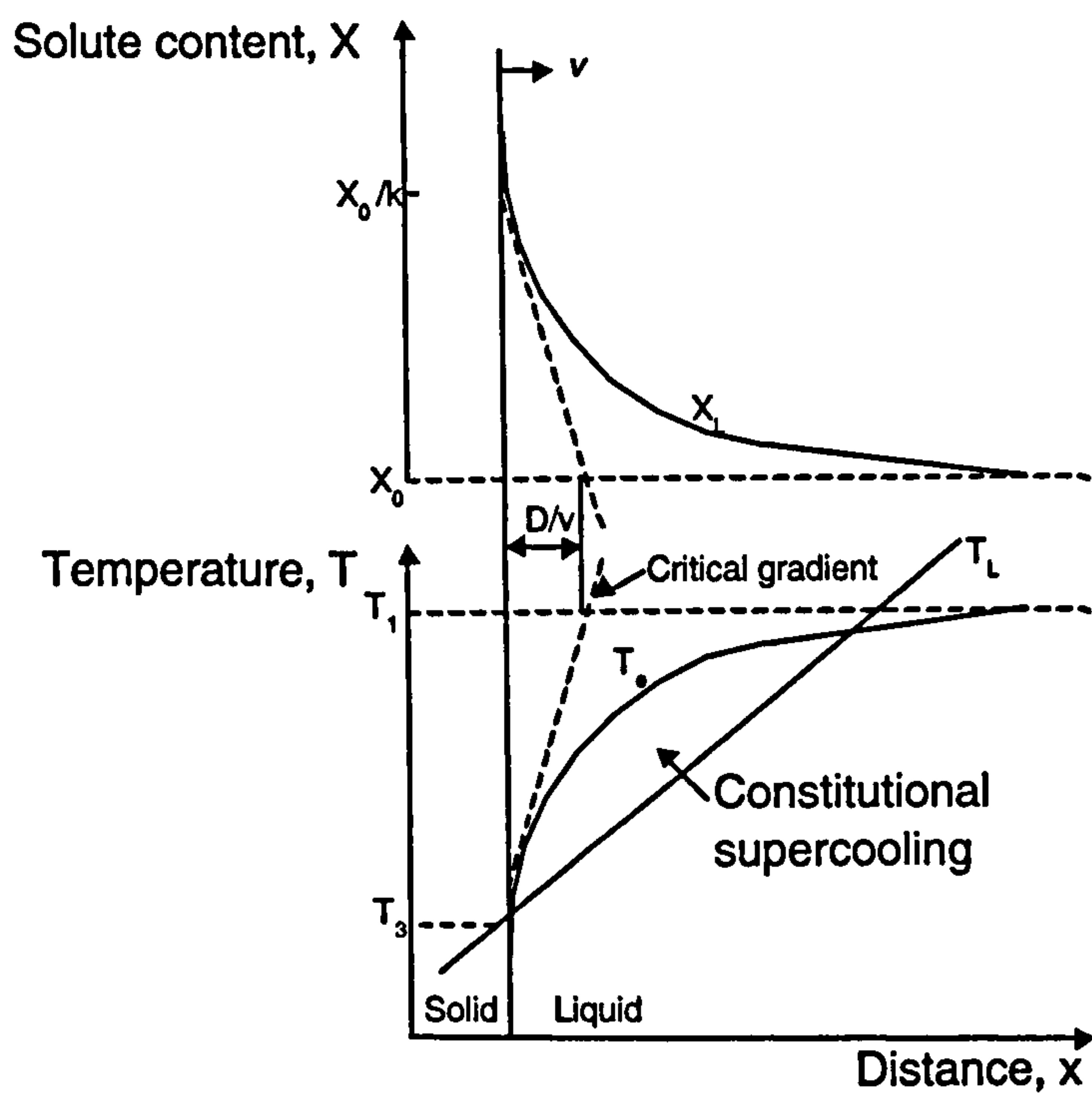


Figure 3.6 The origin of constitutional supercooling ahead of a planar solidification front considering both the composition profile across the solid/liquid interface during steady-state solidification and the temperature of the liquid ahead of the solidification front follows line T_L . The equilibrium liquidus temperature for the liquid adjacent to the interface varies as T_0 . Constitutional supercooling arises when T_L lies under the critical gradient.

Figure 3.6 considers the condition of constitutional supercooling during steady-state solidification at a planar interface where there is a variation of the equilibrium solidification, or liquidus temperature (line T_m) as a result of the varying solute content ahead of the solidification front. Apart from the temperature of the interface, which is fixed due to local equilibrium requirements, the temperature of the liquid can follow any line such as T_L ,

although at the interface $T_m = T_L = T_3$. If the temperature gradient is less than the critical value shown in Figure 3.5 the liquid ahead of the solidification front exists below its equilibrium freezing temperature due to constitutional effects i.e. it is constitutionally supercooled.

The exact mechanism by which atoms attach themselves to the solid from the liquid rarely occurs as a planar interface as previously described. There are basically two types of atomic structure for solid-liquid interfaces. In pure solids, the solid-liquid interface is usually either atomically flat close-packed or sharply defined (planar) often associated with non-metals. Here the transition from liquid to solid occurs over a narrow transition zone approximately one atom layer thick. Such an interface can also be described as smooth, faceted or sharp. The other type of interface is atomically rough or diffuse (dendritic) associated with metallic systems. In this case the liquid to solid transition takes place over several atomic layers. There is a gradual weakening of the interatomic bonds and an increasing disorder across the interface into the liquid. Diffuse interfaces are also known as rough or non-faceted. The type of structure chosen by a particular system will be that which minimises the interfacial free energy.

In fact it has been found that there are four recognisable morphologies that the solid-liquid interface can assume, depending on the composition of the alloy and the thermal conditions. These are smooth (or planar), cellular, cellular-dendritic, and dendritic as shown in Figure 3.7. In most alloys (and impure metals) crystals grow as cellular dendrites ^[Cha63], although often there is a continuous transition from one of these interface morphologies to another, particularly in alloys of metal-non metal composition such as Al-Si.

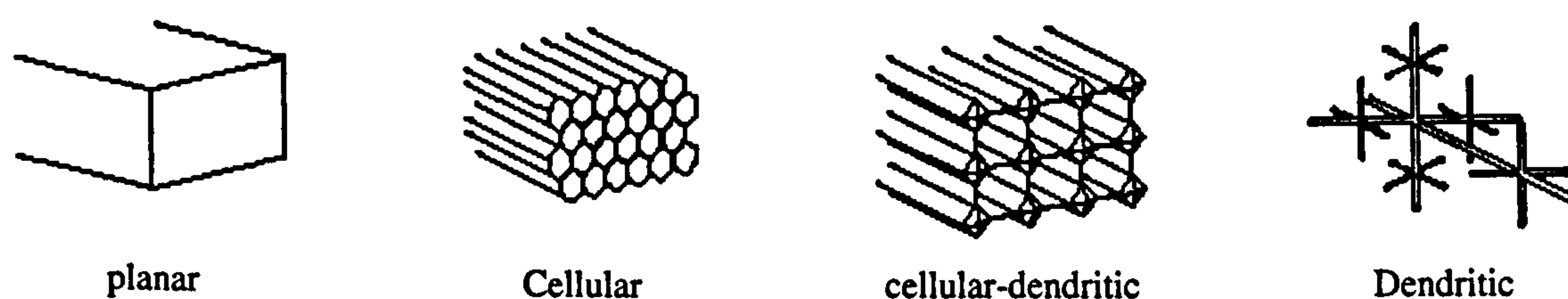


Figure 3.7 Solid-liquid interface morphologies

A planar front arises when a well-inoculated liquid cools under equilibrium conditions, where the temperature of the liquid is greater than the temperature of the solid which is at or below

the freezing temperature. During solidification, the latent heat of fusion is removed by conduction from the solid-liquid interface through the solid to the surrounding mould. Any small protuberance that begins to grow on the interface is surrounded by liquid above the freezing temperature which therefore restricts further growth until the rest of the interface has caught up.

A dendritic interface, on the other hand, occurs when nucleation is poor and the liquid supercools before the solid forms. Under these conditions a small protuberance of the solid growth front is encouraged to grow as the latent heat is conducted away either through the solid or into the supercooled liquid. The structure of the dendrite depends on the way in which the latent heat is carried away from the interface. Directional (or constrained) growth occurs in the direction of the heat flow when the latent heat is dissipated through the solid, whilst equiaxed dendritic crystals grow from a supercooled melt where the latent heat is dissipated through the cooler liquid ahead of the interface. Secondary and tertiary dendrite arms can also form on the primary stalks to speed up the evolution of the latent heat [Ask96, Tri94]. Many attempts have been made to relate dendritic solidification to casting conditions for aluminium alloys with respect to dendrite arm spacing [McC81, Gho93], dendrite tip temperatures [Bur74 I and II, Tas76], and constitutional effects [Win54, Bro66], as these factors are prominent in determining the properties of the material. Indeed, there has also been a great deal of interest in modelling dendritic solidification, however, due to the wide extent of these studies they will not be covered in detail this work.

3.3 Solidification of Aluminium-Silicon Alloys

Eutectic or near-eutectic alloys are extremely important in the casting industry owing to their low melting points compared to those of the pure components, their excellent flow properties, and the composite properties gained from the two phases. In the solidification of a binary eutectic alloy two solid phases form co-operatively from the liquid, i.e. $L \rightarrow \alpha + \beta$. Two main types of eutectic growth are possible and these are usually classified as normal, where the two phases both have low entropies of melting, and anomalous, in which one phase has a high and the other phase has a low entropy of melting [Hun66, Kur79, Ell84]. In normal systems nucleation moves from the liquid composition into the coupled $\alpha + \beta$ zone (see Figure 3.8 a) where the two non-faceting phases appear as regular lamellae, or rods of the minor phase embedded in

the major phase ^[Jac66]. Both phases grow together simultaneously behind an essentially planar solid-liquid interface: examples are Pb-Sn, Pb-Cd, and Al-Zn.

Anomalous structures, on the other hand, occur in systems where one of the solid phases is capable of faceting (i.e. has a high entropy of melting) and therefore experiences difficulty adding new solid to the existing layer at the interface during growth. This means that at the same supercooling, a low entropy phase will usually grow at a higher velocity than a high entropy phase ^[Ell84]. Thus, in an anomalous system the nucleation moves from the liquid composition into the $\alpha + \beta$ region outside the coupled zone (see Figure 3.8 b), and exhibits a wide range of microstructures where one phase may grow as a faceted crystal while the other grows dendritically. Many casting alloys, including the Al-Si system, display anomalous eutectic structures and, therefore, growth of the anomalous structure shall be considered henceforth.

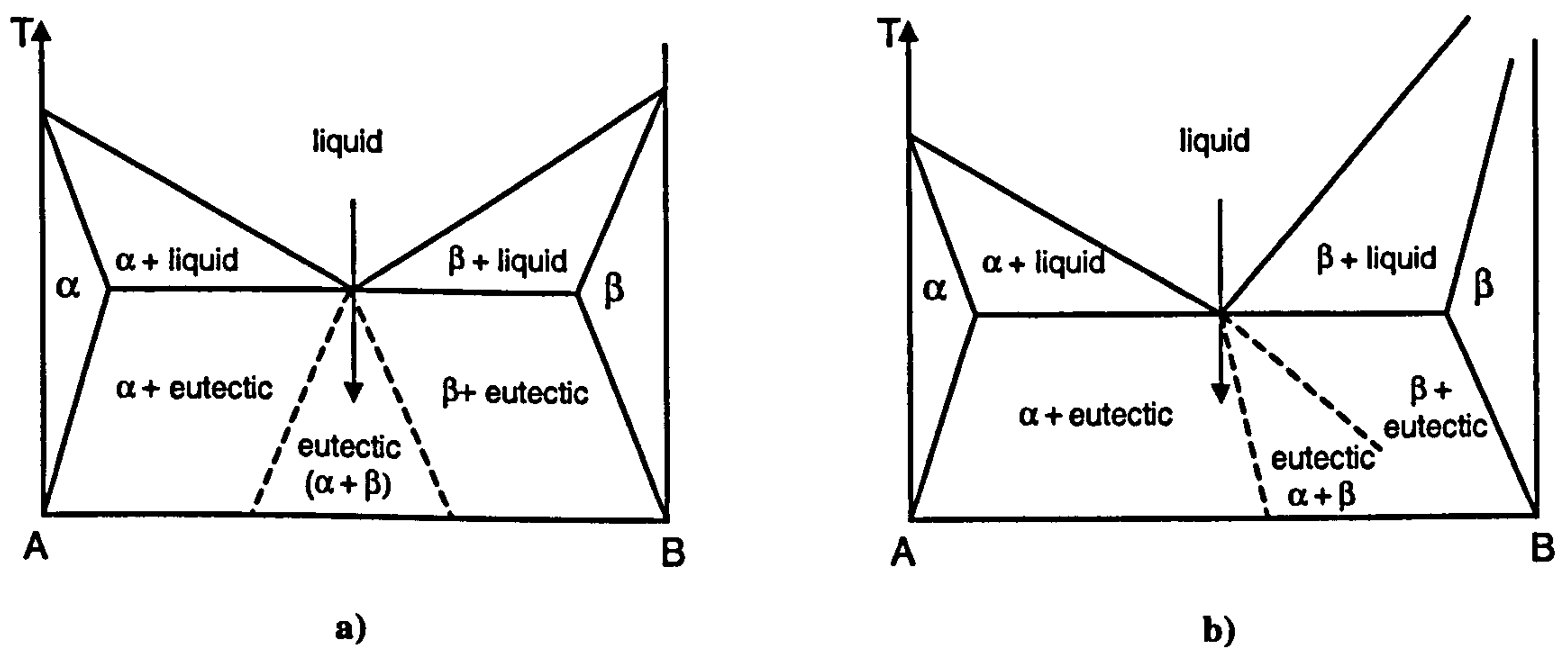


Figure 3.8 Phase diagrams typical of systems showing a) a normal eutectic structure and b) an anomalous eutectic structure

The binary Al-Si system is a simple, anomalous eutectic with two solid solution phases; FCC (Al) and diamond cubic (Si) as shown in Figure 3.9. The eutectic is formed between an aluminium solid solution containing just over 1.5 % silicon and virtually pure silicon as the second phase. The eutectic composition has been a matter of debate but is now generally accepted as 11.7 wt. % Si ^[Mur86, Pol95, Bac90, Mon76] at the eutectic temperature, 577 °C.

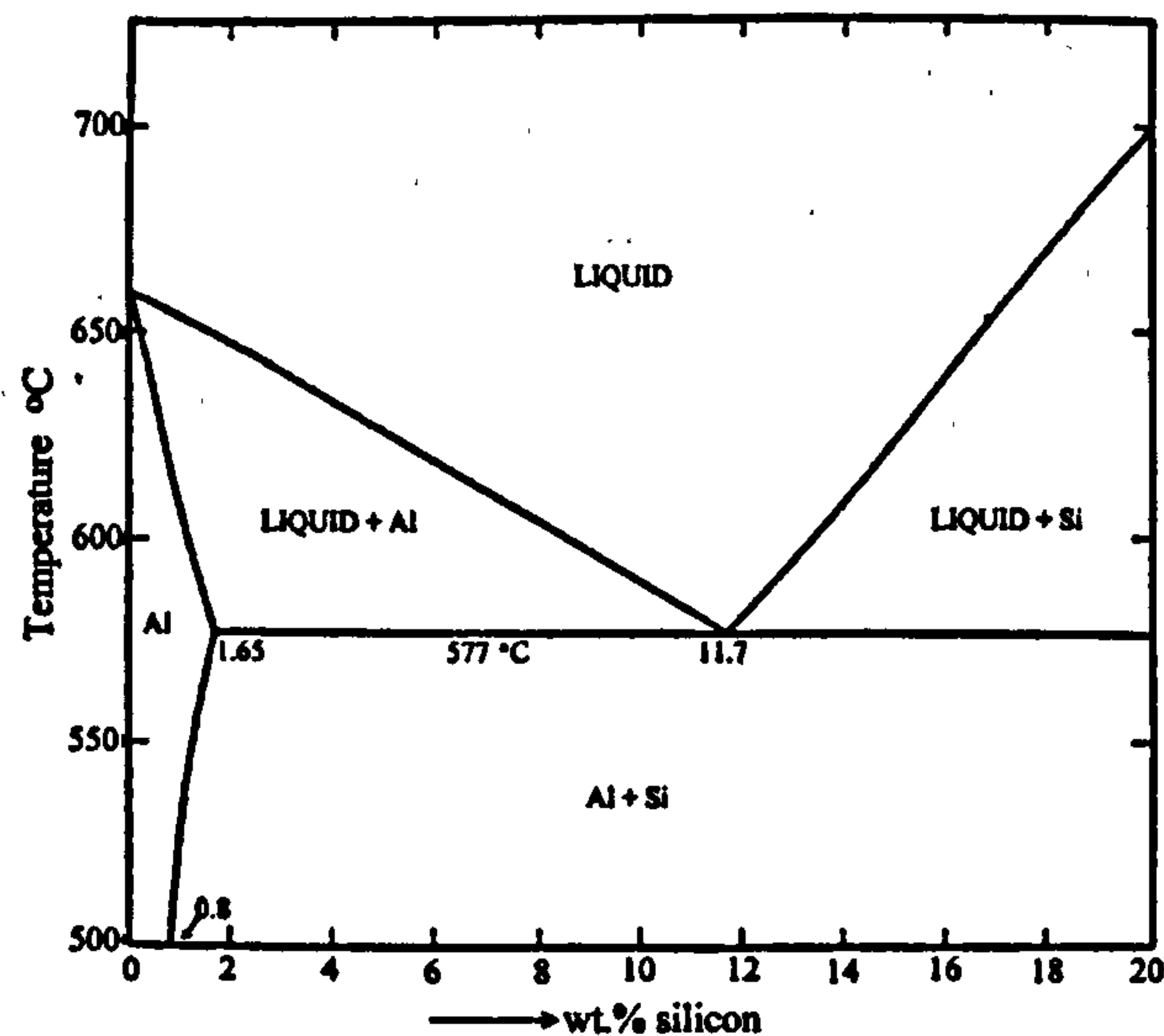


Figure 3.9 Aluminium-Silicon binary phase diagram, after Phillips [Phi59]

Depending on the composition of the alloy and the cooling conditions, the microstructure of an Al-Si casting will essentially comprise mixtures of aluminium grains, silicon crystals and aluminium-silicon eutectic, as well as various intermetallic phases formed from other alloying additions. In a simple Al-Si binary alloy, when the eutectic point is reached there must be simultaneous solidification of the aluminium and silicon solid phases. In its simplest form this leads to a eutectic (lamellar) structure consisting of plates of silicon in an aluminium matrix. Commercial alloys are available with hypoeutectic, eutectic and hypereutectic compositions. If the alloy is at all hypoeutectic (less than 12 wt. % Si) then primary aluminium dendrites would be expected to form, and for hypereutectic (greater than 12 wt. % Si) primary silicon cuboids are anticipated, each being the primary phases at the relevant compositions.

In practice, however, high cooling rates produce growth far from the equilibrium and microstructures which do not reflect the characteristics of the phase diagram. The final structure of a near eutectic Al-Si alloy, therefore, usually consists of aluminium matrix with both primary (cuboidal) and secondary (eutectic) silicon particles within it depending on the composition and casting conditions. As the coupled region of the Al-Si system is relatively narrow the growth conditions during solidification may change from those favouring one type of primary phase to those favouring the other. Therefore, primary crystals of both aluminium and silicon can occur in the same casting [Ste72].

3.3.1 Primary Aluminium

The solidification structure of the primary aluminium phase in most aluminium alloys tends to be dendritic, as discussed previously in Section 3.2.2, and forms the macrostructure of a casting as discussed in Section 3.3. Thus, the aluminium phase is considered in more detail later with respect to columnar and equiaxed growth. However, it is also important to understand the solidification of aluminium in relation to growth of the minor phases. Work by Shamsuzzoha and Hogan ^[Sha86] investigated the growth of the aluminium phase in an Al-Si eutectic alloy to determine whether there was any evidence of preferred orientation relationship between the eutectic phases. This, and subsequent research ^[Hog87], concluded that in a simple Al-Si system solidified at moderate freezing rates, silicon is a favoured site for aluminium nucleation, with the aluminium phase repeatedly nucleating during growth of the eutectic.

At high cooling rates, on the other hand, the silicon structure has been reported to be surrounded by aluminium dendrites ^[Han84, Gho64]. For slightly hypereutectic alloys where the primary silicon is the first phase to solidify, high growth velocities can induce an aluminium ‘halo’ formation around the silicon particle. This is a result of constitutional supercooling whereby the growing silicon phase rejects aluminium into the surrounding melt until such a point as the aluminium solidifies forming what appears as a halo around the silicon. The process continues as the halo then grows, enriching the surrounding liquid with silicon until the composition is displaced such that the eutectic silicon will nucleate and grow on the halo ^[Yil84].

3.3.2 Primary Silicon

The number and size of primary silicon particles can be controlled by the addition of particles that facilitate the nucleation of silicon crystals. One of the most efficient substrates on which silicon may nucleate is the compound AlP (aluminium phosphide), which has the same diamond cubic structure and crystal parameters close to those of silicon. AlP is naturally present in most aluminium-silicon alloys when phosphorous reacts with aluminium to form small, insoluble particles of AlP which then act as nuclei on which the silicon forms ^[Zho94, Ho95]. To further improve the nucleating effect an additional amount of phosphorous may be added to the melt before casting, thus increasing the number of AlP particles ^[Bac90]. However, excess holding times (> 5 hours) can allow AlP to agglomerate, resulting in a drop in the number of nucleation sites and a corresponding increase in particle size.

Primary silicon grows in a faceted manner developing a variety of complex polygonal shapes depending upon the solidification rates to which the melt is subjected ^[Mah93]. Fredriksson ^[Fre73] defined a variety of morphologies as: plate-like shaped crystals of hexagonal form; equiaxed crystals containing varying numbers of parallel twins; star-like crystals containing up to five radiating twin planes; and spheroidal crystals. The most likely explanation for such a range of crystal shapes is the possible existence of a number of different growth mechanisms that arise depending on solidification conditions.

The unaided growth of a faceted phase, such as silicon, occurs by a layer deposition involving step propagation cross the liquid-solid interface, and requires a large supersaturation of the melt. The rate at which this occurs depends on the interface orientation. Normally crystal growth in diamond cubic systems tends to be highly anisotropic leading to the plate or flake form. This anisotropy is usually sufficient for a multi-faced nucleus to grow into a faceted primary phase bound by the slowest growing faces. These tend to be the {111} planes in silicon as this is the densely packed cleavage plane in the diamond cubic structure, and a continuous faceted octahedral growth habit is frequently observed ^[Fre73]. Sectioning the octahedron at random angles gives rise to various crystal shapes including trapezoidal, hexagonal (Figure 3.10 a), and twinned (Figure 3.10 b), as well as polyhedral, which tend to be clusters of several crystals.

Several authors ^[Ata87, Wan95] have observed primary silicon morphologies and found that the octahedral crystals, both twinned and twin free, predominate. They can nucleate and grow with very little supercooling below the silicon liquidus temperature and over a wide range of growth velocities. However, certain geometrical factors can facilitate the formation of new atomic layers on a facet. The first is the emergence of dislocations on the facet surface which promote continuous spiral growth of successive atom layers. Bauser and Strunk ^[Bau83] suggested that dislocations emerging from the surface form growth spirals and, when the deposited layer is parallel too {111}, the spiral step formed is one micron high. However, when the growing solid surface deviates from {111} by a small angle, of the order of 1 °, new solid layers are formed by the advance of multi-layered steps across the facets. Solute was observed to segregate to the base of each multi-layer forming striations parallel to the {111} planes, which could be revealed by etching.

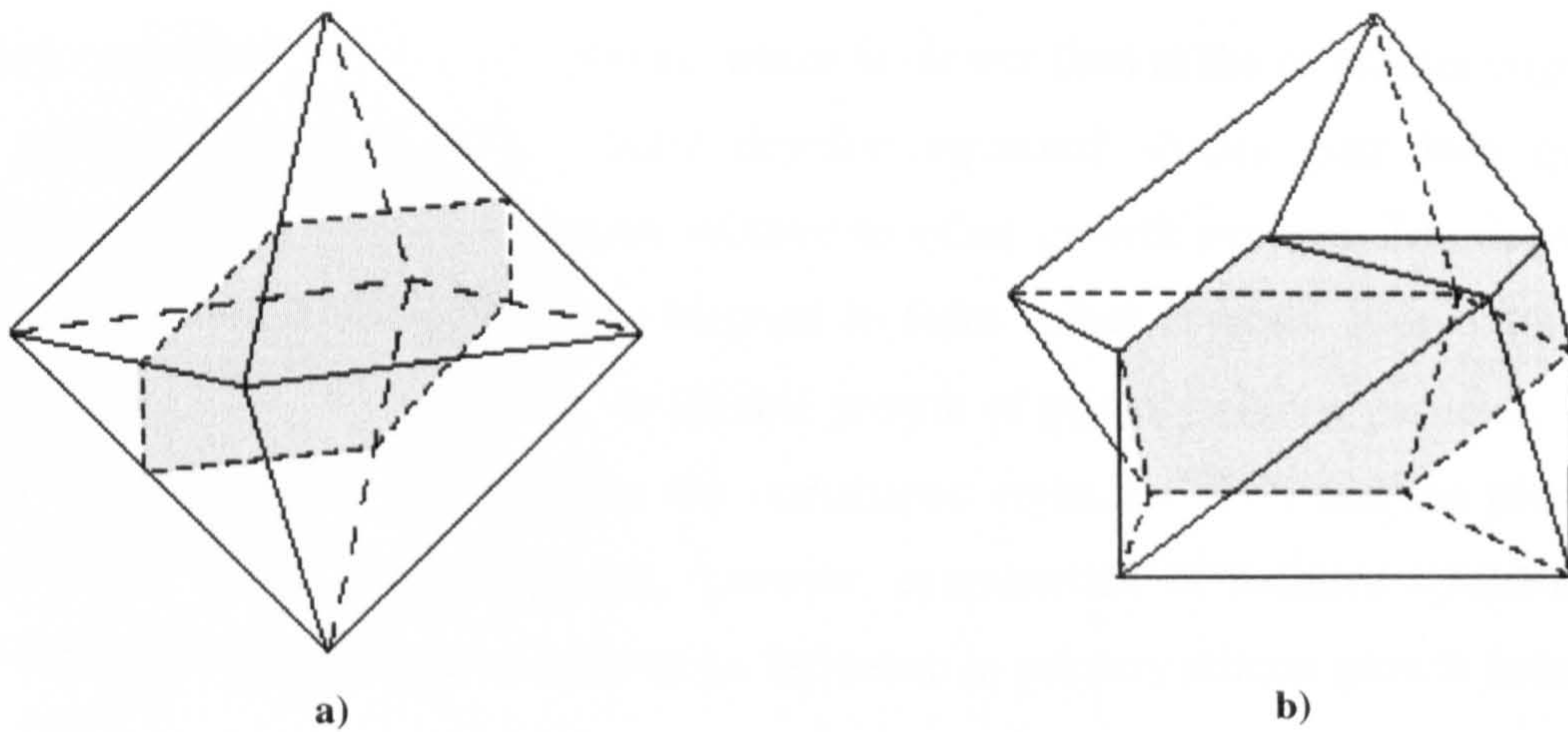


Figure 3.10 Schematic diagrams of **a)** an octahedral crystal showing a section through a $\{111\}$ plane parallel to an external facet (shaded), and **b)** a spinel crystal showing twinning about a $\{111\}$ plane (shaded) with 141° grooves and opposing 219° ridges

Later work investigated the growth of InSb ^[Mor66] crystals, and primary silicon particles ^[Wan95, Wan97, Wan99] through the observation and measurement of growth traces. Such concentric traces are exposed by etching polished surfaces to reveal the shape of a given crystal at successive stages in its growth. It is suggested that during solidification the convection flows, which can occur with cyclic regularity, produce temperature fluctuation and impurity layer deposition on the surface of a crystal at intervals to disturb the growth process repeatedly. Hence, the traces reveal the shape of a given crystal at successive stages of growth from the melt showing the intersection of the facets with the plane of section. One particularly important feature was that of the variation in spacing between successive traces on different facets, which were used to measure the variation in growth rates in different $\langle 111 \rangle$ directions during growth of any one crystal.

The second geometrical factor is the observation of twin planes which are often found ^[Fre73]. The twin boundary has a hexagonal shape with three of its sides forming protruding edges on the crystal and three forming re-entrant edges as seen in Figure 3.10 b. The twin plane reentrant (TPRE) mechanism is explained in detail in the explanation of eutectic silicon growth as it is considered a more dominant growth mode for eutectic than primary silicon. Twinning was also observed to occur during growth without influencing the growth mechanism and Wagner ^[Wag60] concluded that if only one, or no, twin plane is present (twins originating from the nucleus), growth will be slow and polyhedral as it is controlled by

surface nucleation on the {111} planes, which is slower than at the re-entrant edges. The fact that primary silicon crystals usually develop equiaxed shapes puts into question the importance of the TPPE mechanism relative to other growth systems. Moreover, although primary silicon octahedra are often twinned to form spinel crystals, it is unlikely that the TPPE mechanism operates in the octahedral growth of primary silicon particles. There is no doubt that twin planes can nucleate the star-shaped crystals [Wan95], and the plate like form characteristic of the eutectic silicon, however, examination of twinned spinel crystals has established that the twins have little or no influence in primary silicon growth behaviour [Ell83, Ata84, Wan97].

Thus, whilst the alloy composition controls the fraction of primary silicon formed, the size, shape, and distribution of primary silicon in the matrix depends largely on the foundry parameters such as cooling rate and modifying techniques (discussed later in section 3.6). Indeed, high G/V (temperature gradient/ growth velocity) ratios have been reported to suppress the formation of the primary silicon phase altogether [Ata84].

The primary silicon phase is important to certain mechanical properties. Research on the mechanism of wear in cast aluminium alloys has shown that intense bands of shear develop beneath and parallel to the wearing surface. Cracks may then initiate and propagate along these shear bands until a small wedge or laminate above them detaches itself from the surface [Pol89]. Certain microstructural features are known to augment the wear process including primary silicon particles. Indeed, in work by Styles and Reed [Sty00] investigating the mechanical properties of an Al-Si casting alloy, they determined that primary silicon particles were generally responsible for controlling the fatigue crack initiation and growth, in a room temperature plain bend bar test at a frequency of 15 Hz. Such a silicon particle was revealed to be the initiating particle of the fatigue crack in Figure 3.11. Further work concluded [Joy02] that changes in fatigue crack growth resistance were linked to a change in crack growth mechanism regarding the polyhedral primary silicon. The transition was characterised as a switch from preferential fracture to decohesion of the silicon particles, dependant on both the temperature and microstructure.

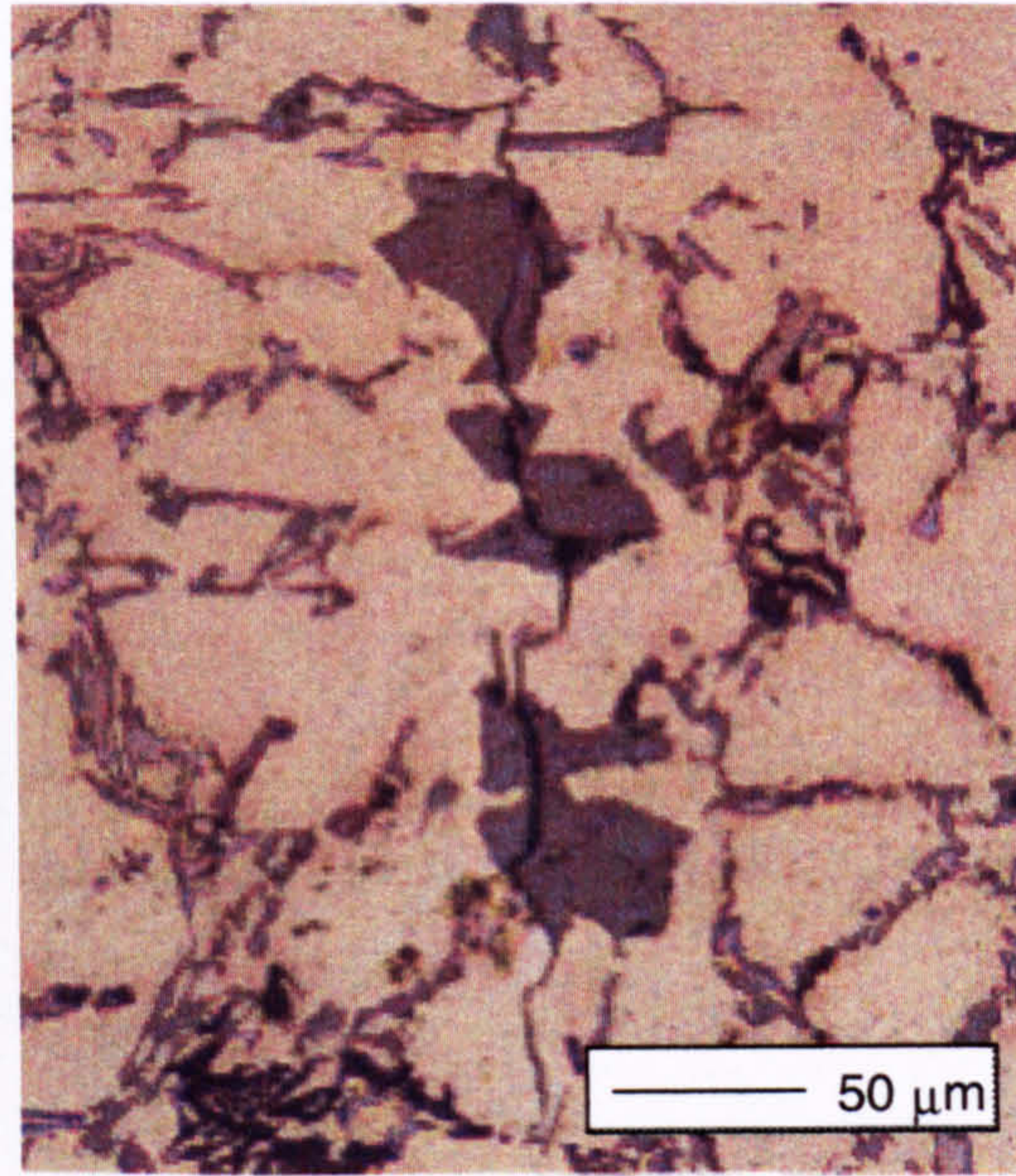


Figure 3.11 Optical micrograph of a fatigue crack propagating through primary silicon particles, courtesy of M. Joyce

3.3.3 Eutectic Silicon

As the Al-Si system is anomalous, the structures of the eutectic phase are very sensitive to solidification conditions and impurities, and several structures, each with its own properties, may form in an Al – 12.7 wt. % Si alloy. Directional solidification studies^[Day68, Ste72, Ata84, Ata87, Mag91, Kha93] have led to a clearer understanding of the various structures resulting in Figure 3.12 showing the range of microstructures in a directionally solidified Al-Si eutectic alloy. It can be seen that the different structures were found to change depending on the growth velocity, V , and temperature gradient, G , in the liquid at the interface during solidification. Area A is the massive eutectic structure which forms due to long range diffusion between the faceted Si particles at a planar Al interface. Here, the very high G/V ratio prevents constitutional supercooling and the two phases grow independently of each other. Area B determines rod or angular Si where a low G/V ratio renders the interface unstable leading to semi-coupled growth of the two phases by short-range diffusion. The silicon morphology is sensitive to the solidification conditions, developing rods or angular plates at high and low temperature gradients respectively. C is the flake Si where there is again short-range diffusion between the Si flakes and Al, but the growth here is only partially coupled. Finally, area D is the fibrous Si which grows coupled with the Al due to short range diffusion between the two phases at higher growth velocities, such as occurs during quench modification^[Ell84, Ell83].

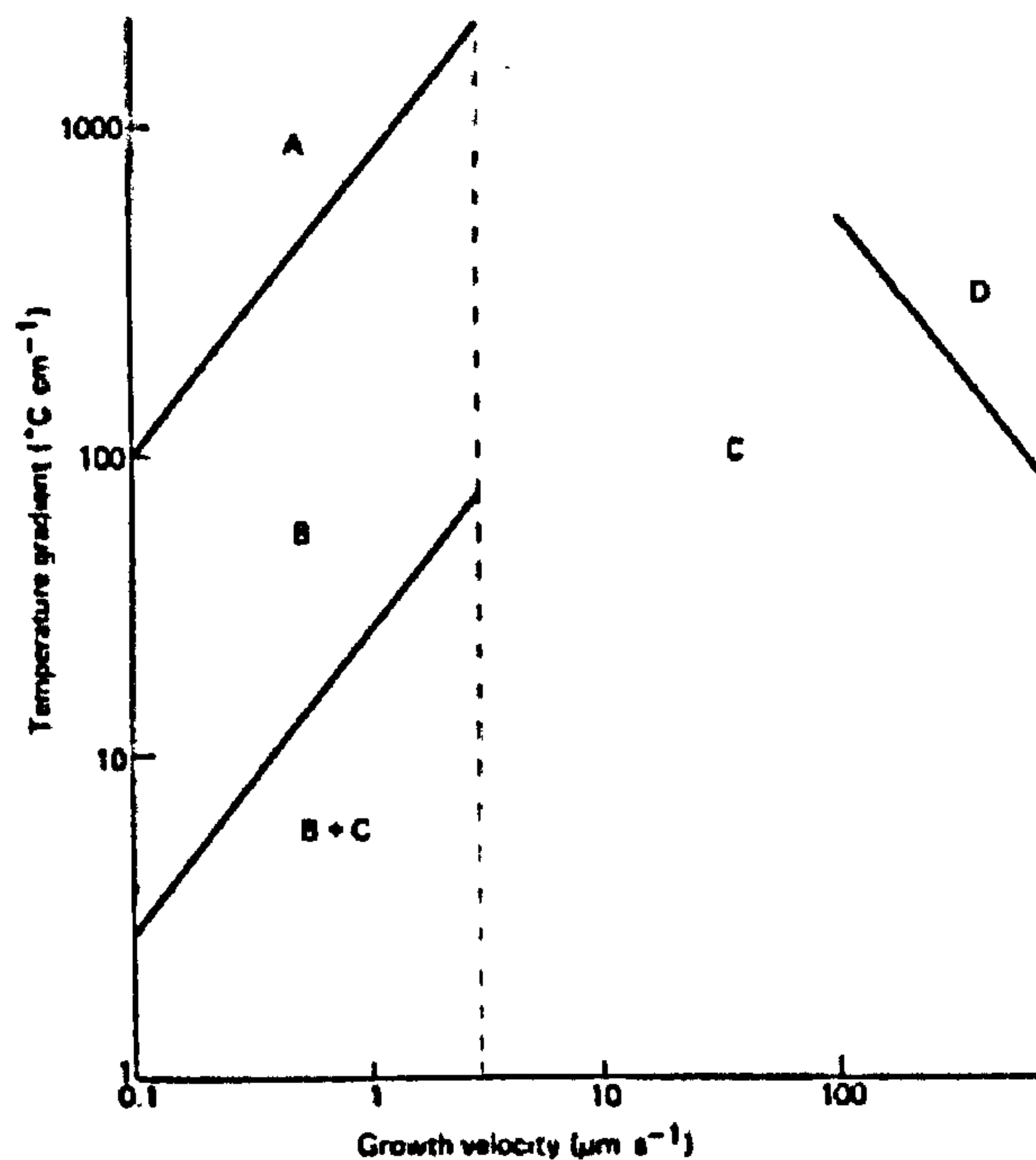


Figure 3.12 Range of microstructures in directionally solidified eutectic Al-Si alloys:
A is massive Si particles, B rod or angular silicon, C flake Si, and D fibrous Si, after Elliott ^[Eli83]

The most common unmodified Al-Si eutectic microstructure observed in casting alloys of interest in this work is that of the flake morphology. This is because the growth conditions in region C are closest to those encountered in normal foundry practice. Eutectic silicon has been observed ^[Ata84] to grow by a layer deposition mechanism although Si flakes have also been found to contain numerous multiple {111} twins. The twinning occurs as a result of growth accidents during the extension of existing close packed atomic planes, or during the nucleation of new growth steps. As their formation requires a certain activation energy or supercooling, significant growth occurs only at flake edges where twin planes aligned in the growth direction of the flake provide self-perpetuating growth steps at the interface. This is known as the twin plane re-entrant (TPRE) growth mechanism ^[Wag60, Ham60].

The TPRE mechanism can be understood with reference to Figure 3.13 ^[Eli83, Sha89]. This shows a silicon particle containing two twin planes bound by {111} planes in the early stage of growth. Each twin plane creates a 141° re-entrant angle and a 219° ridge at the edge of the particle. The energy required for the deposition of a new atomic layer initiated at the re-entrant corner is approximately half of that required to deposit a new layer on an atomically smooth interface. Consequently, the re-entrant corner is a favourable site for atomic additions.

The particle will continue to grow in this manner until it is bound by the {111} ridge at the growth front, when the growth rate will fall because further growth can only occur by layer deposition on {111} planes. Two parallel twin planes is the minimum requirement to ensure the continued presence of the re-entrant corner in the growth direction, with growth able to proceed preferentially in any or all of the six $\langle 211 \rangle$ directions depending on the heat flow.

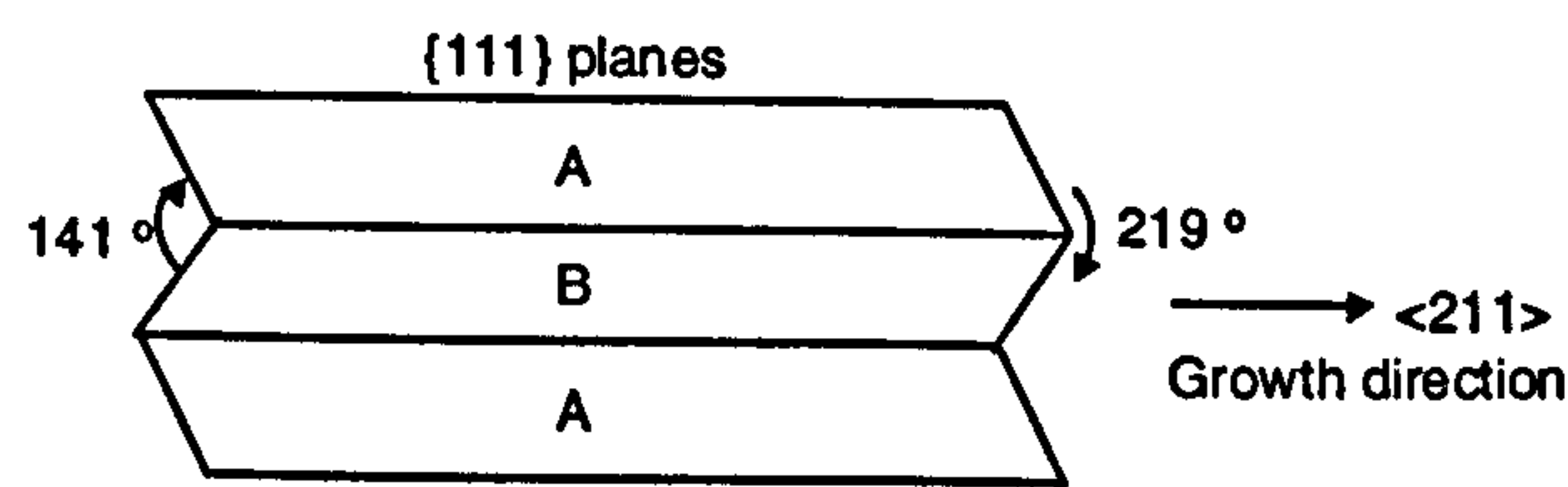


Figure 3.13 Schematic diagram showing the twin plane re-entrant (TPRE) growth mechanism for a silicon plate.

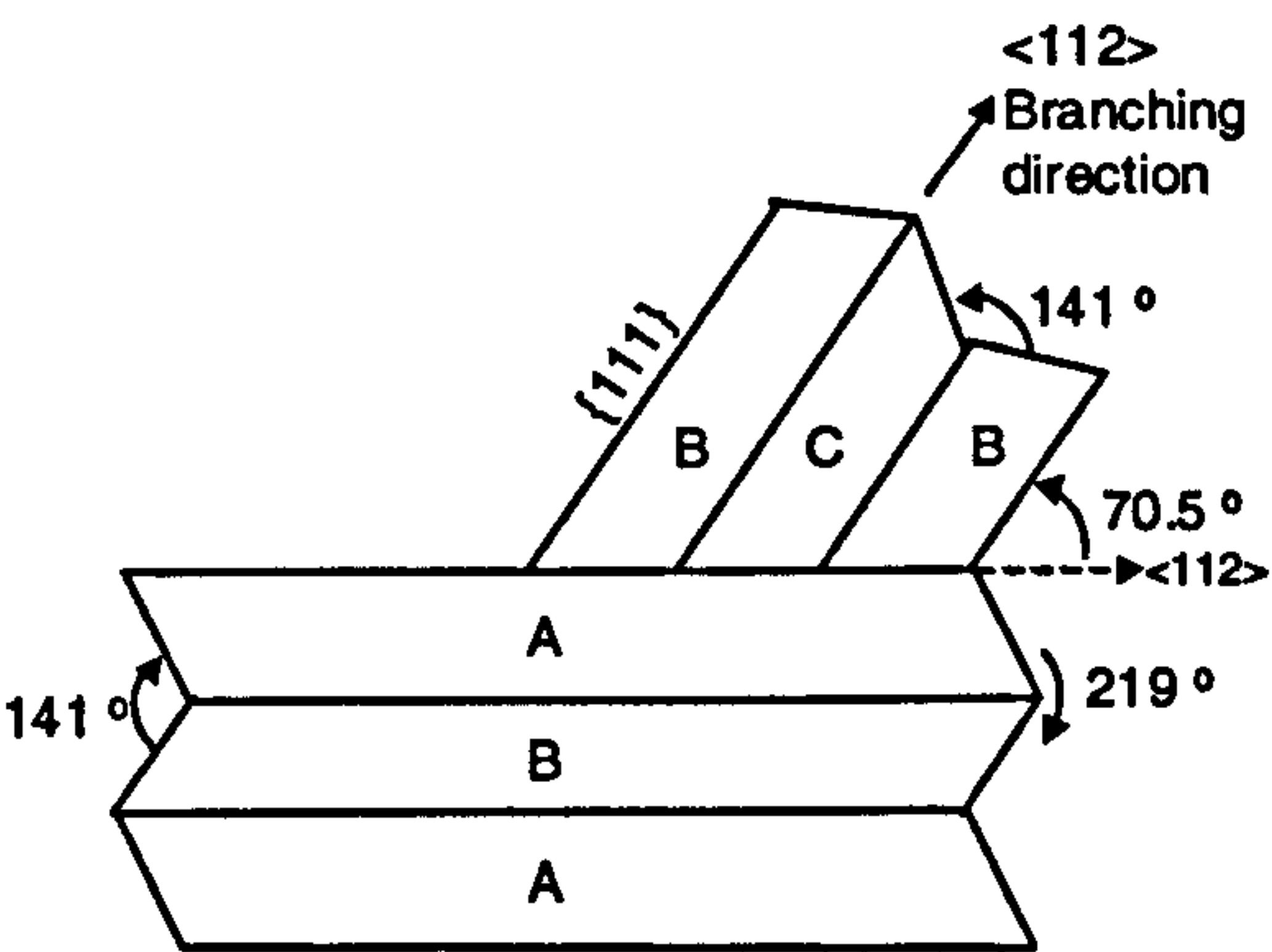


Figure 3.14 Schematic diagram showing the large angle branching in a silicon plate

At certain temperature gradients eutectic silicon is often found to be branched [Sha86]. As can be seen in Figure 3.14 new twins can form on the flat {111} growth plane of the original plate to produce a new segment in a new orientation. If the new twin, denoted C, has a twinned relationship to B which is repeated on either side of the crystal, then a new TPRE site is formed and growth can continue in a new $\langle 112 \rangle$ direction. This new direction is at 70.5° to the original growth direction, although occasionally small angle branching at less than 70.5° has been observed. Irrespective of the angle at which the new twin has formed, in any one branched silicon plate all twins are in the same zone i.e. they share a common $\langle 101 \rangle$ direction.

The shape and size of the crystals formed on solidification will also vary for both aluminium and silicon phases, and this can have a significant effect on the filling and mechanical properties of castings. Thus, the grain structure must be controlled to achieve the desired properties; this refinement is discussed in Chapter 6, whilst the nucleation and growth of the silicon phase is examined in Chapter 7.

3.4 The Structure of Castings

When a metal or alloy is poured into a mould and allowed to solidify, it may do so in various ways. Process variables related to both the alloy (composition, nucleation characteristics, pouring temperature etc.) and mould (thermal properties, temperature, and geometry etc.) can vary greatly between castings making the structure of a casting difficult to quantify. Although under certain conditions the primary aluminium dendrites are seen clearly in the microstructure, due to their large size they are more often viewed by observation of the macrostructure. Thus it is the α -aluminium grains which are considered in this section, and which give rise to the practice of grain refinement in controlling the final cast structure.

3.4.1 Solidification Zones

In general, three different zones can be distinguished in solidified alloy castings, as can be seen in Figure 3.15. These are (i) an outer chill zone of equiaxed crystals, (ii) a columnar zone of elongated or column-like grains, and (iii) a central equiaxed zone. Twinned columnar grains (TCG's) can also occur in certain alloy systems at critical cooling rates but are much less common than the other morphologies and will not be considered here.

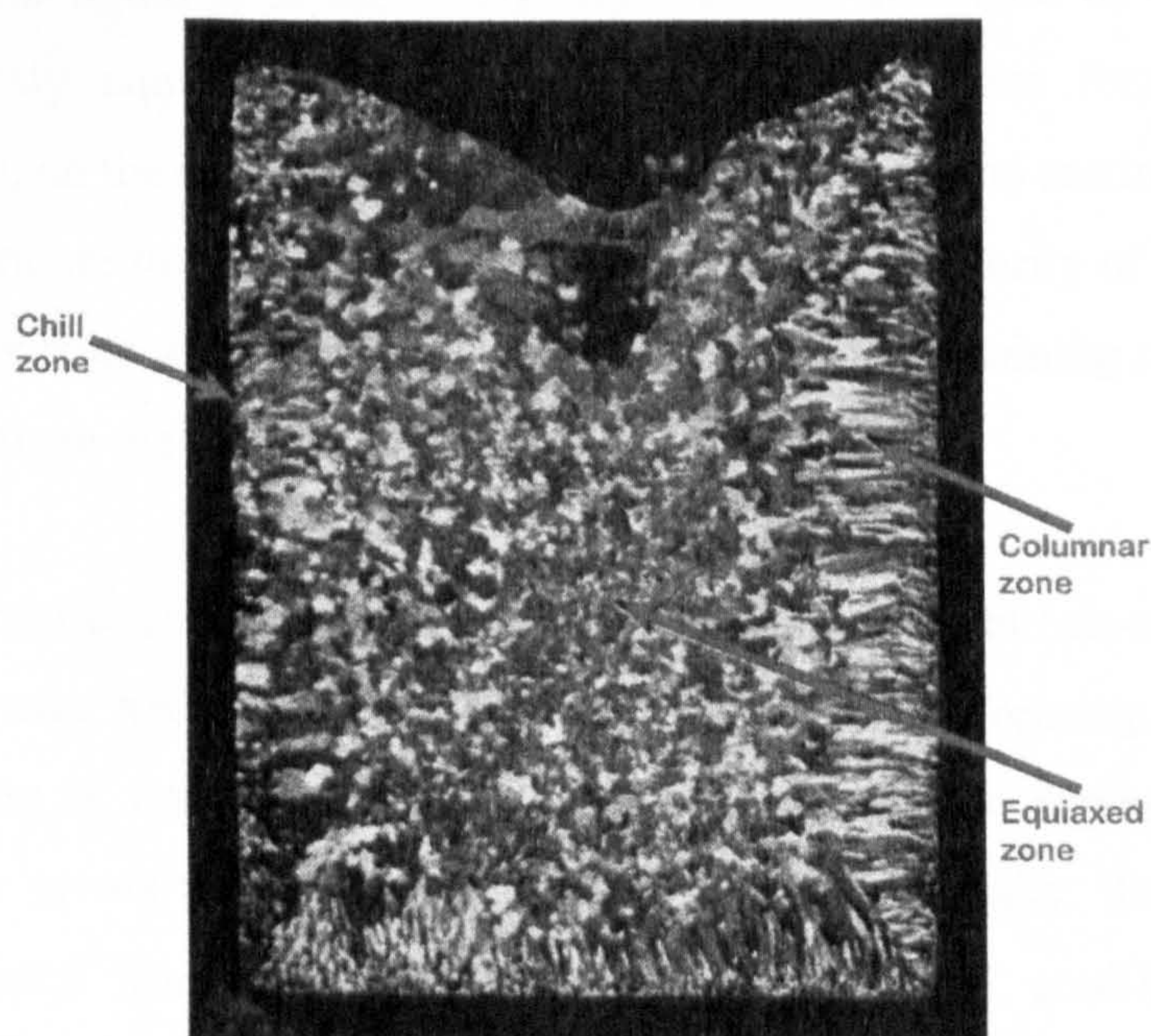


Figure 3.15 Casting showing the three solidification zones; chill, columnar and equiaxed, after Chalmers ^[Cha63]

Chill Zone

When the molten metal enters the mould, which is below the melting temperature of the metal, the chilling action of the mould wall results in the formation of a thin 'skin' of solid metal surrounding the liquid. The layer of metal in contact with the mould wall is chilled to such a degree that copious nucleation takes place in it as explained previously in section 3.2.1. The number of crystals nucleated depends upon the effectiveness of the nucleants, the rate of heat extraction, and the volume of chilled liquid. Crystals nucleate heterogeneously with the presence of foreign nuclei in the melt giving a range of nucleation temperatures involving progressively less supercooling of the liquid for more effective nuclei. The grains then grow rapidly in the chill zone although supercooling, resulting from the high cooling rate, speeds up nucleation even more than crystal growth, so that many fine-grained equiaxed crystals are formed. As the shell of solid metal thickens, the temperature gradient from the liquid to the mould becomes less sharp and the liquid next to this shell cools more slowly and supercools less, with the result that crystal growth rather than nucleation is then favoured.

However, as the mould wall warms up it is possible for many of these solidified crystals to break away from the wall under the influence of the turbulent melt. If the pouring temperature is low, the whole of the liquid will be rapidly cooled below the liquidus temperature and the crystals swept into the melt may be able to continue to grow. This is known as 'big bang' nucleation since the liquid is immediately filled with a multitude of crystals ^[Flo86]. This produces an entirely equiaxed structure i.e. no columnar zone forms. If the pouring temperature is high, on the other hand, the liquid in the centre of the casting will remain above the liquidus temperature for a long time and consequently the majority of crystals soon remelt after breaking away from the mould wall. Only those crystals remaining close to the wall will be able to grow to form the chill zone.

If the liquid is poured at a temperature well above its melting point (superheated) the initially formed chill zone may remelt and disappear completely. When freezing begins again, at the surface, the cooling is much slower and only a few nuclei are formed, so that a coarse columnar structure grows inwards from the surface. If, additionally, the actual temperature gradient is prevented from becoming too flat, e.g. by water cooling the mould, then constitutional undercooling is reduced and the columnar structure may continue right to the centre.

Columnar Growth

The columnar zone consists of crystals that have nucleated on or near the mould wall and have grown dendritically against the heat flow forming long, column-like grains often by constitutional supercooling. The crystals grow in competition with each other and a preferred orientation perpendicular to the mould wall develops ($\langle 100 \rangle$ for fcc and bcc, $\langle 1010 \rangle$ for hcp) at the expense of those crystals that are less favourably oriented. As the number of crystals decreases, the cross section of those remaining increases and having grown faster and larger the remaining crystals also have more sides (8 compared with an average 6). The crystals with more sides tend to increase in size because the equilibrium dihedral angle (120°) between faces can be maintained by tilting the 3-grain intersection outward as the crystal grows. The finally established columnar grains are much wider, as well as longer than those of the chill zone ^[Por81].

Equiaxed Growth

The origin of the equiaxed zone in the interior is not as well established as that of the chill and columnar zones which have long been understood as discussed above. It is known that during equiaxed growth dendritic arms grow radially outwards from many different centres to form relatively round, randomly oriented crystals, however, the nucleation of such crystals has long been a source for debate. Early work by Winegard and Chalmers ^[Win54] suggested that the equiaxed grains in the interior nucleate, after the columnar zone has formed, as a result of the constitutional supercooling of the remaining liquid. New crystals are formed when the temperature of the remaining liquid falls to that at which the existing nucleation catalyst particles are effective.

However, further work by Chalmers ^[Cha63] pointed out that there were several objections to this early proposal, and that consideration should be given to the possibility that all the crystals, equiaxed as well as columnar, originate during the initial chilling of the part of the liquid in contact with the mould. It was suggested that constitutional supercooling protects some of the nuclei not in contact with the wall, so that they do not melt. All nuclei that survive when the liquid falls to the interface temperature drift away from the interface by convective motion of the liquid and are then able to grow at a rate controlled by their own rejection of solute and liberation of latent heat. Since they are in supercooled liquid they grow dendritically and their growth ceases when the temperature and composition of the liquid are

such that it is in equilibrium with the crystals. By this time, the dendritic equiaxed crystals may have formed a skeleton-network throughout the liquid.

In the absence of a hot mould top (as is assumed in theories mentioned previously), crystal fall out from the superficial frozen layer may contribute to the formation of the equiaxed zone. In 1967 an investigation by Southin ^[Sou67] showed the presence of a fourth zone consisting of large coarsely dendritic grains and taking the form of a layer over the top surface. These grains are believed to nucleate independently from the solid growing from the mould walls, the liquid in which they nucleate must, therefore, be supercooled. The heat loss for this is presumably due to radiation, with conduction and convection playing a minor role. Since heat loss by this mechanism would be much lower than through the mould wall, fewer nuclei are produced, with the resultant larger grain size in the layer. Southin also found the equiaxed grains to have a comet shape consisting of a dendritic head and a tail that grows in the same manner as the columnar grains, i.e. cellular or cellular-dendritic. The tail also grows in the same direction as a columnar grain, i.e., opposite to the direction of heat flow. It is believed that the nucleation of the equiaxed zone in this instance is caused by the showering of dendritic particles from this surface dendrite layer to form the heads found in the comet grains.

It is generally accepted that nuclei are always present in the melt and that they await propitious conditions to grow. One condition in particular seems clear; the presence of the equiaxed zone is closely linked with the existence of natural convection free systems. There is no doubt that some constitutional supercooling does exist, but it is doubtful in the liquid. Work by several authors ^[Bil68, Mor70] was carried out on convection free systems to emphasize the importance of thermal convection on equiaxed growth. For convection that there is an influential build-up far ahead of an advancing (solidifying) dendritic interface. When strong fluid flow is present the question of constitutional supercooling is rather immaterial, since any structure transitions are better attributable to other mechanisms. It is most likely that the nuclei for the equiaxed grains occur only at the time of pouring, although the precise means by which these crystal fragments are produced is difficult to explain quantitatively.

Currently all theories involve one of two possible sources; i) they form heterogeneously on insoluble extraneous solids (nucleation catalysts), or ii) they originate as a result of fragmentation of dendritic crystals at some stage of solidification. Both of these mechanisms

of nucleation at the onset of casting as proposed by Chalmers ^[Cha63] and dendrite melting are notably inoperative in a convection-free system, as initial nuclei cannot be transported within the ingot, and insufficient fluid flows are available to break or remelt portions of the columnar dendritic interface by transport of hotter liquid. An ingot solidifying under a sufficiently large magnetic field can then only produce a central zone of equiaxed grains by the Winegard and Chalmers ^[Win54] or the Southin ^[Sou67] mechanisms.

The amount of solute present in the melt is also an important parameter influencing the microstructure. In an investigation by Tarshis ^[Tar71] catalytically clean metals and alloys were used in order to avoid any heterogeneous nucleation. This way they were able to relate alloying effects to variables obtainable from equilibrium phase diagrams, such as the equilibrium liquidus slope and solute distribution coefficient. This is described fully later when it is used to model the columnar to equiaxed transition. In the absence of any other theoretical explanations being viable, the mechanism of dendrite fragmentation was supported, where new grains are introduced into the solidifying alloy by some 'grain multiplication' process distinctly different from heterogeneous nucleation.

In summary, to date two main hypotheses have been put forward to explain the origin of the equiaxed zone: i) heterogeneous nucleation; and ii) fragmentation of existing dendrites. The heterogeneous nucleation model has two variants; firstly that nucleation can occur any time during solidification due to residual constitutional supercooling, or alternatively during the initial pouring into the mould when the metal is drastically chilled – the so-called 'big bang' model. The dendrite fragmentation model also has several variants – dendrite arm melt-off due to thermal effects such as convection, or fragmentation due to mechanical damage or fallout from the upper surface of the ingot.

3.4.2 The Columnar to Equiaxed Transition

The columnar to equiaxed transition (CET) has been the subject of much solidification research to understand the parameters that influence it. It seems that two conditions must first be met; the first being that numerous potent substrates must be present in the melt, upon which heterogeneous nucleation can occur. Secondly, the constitutional, and heat and fluid flow conditions must be such that many of these substrates are allowed to become active and nucleate solid which grows to form a network of equiaxed grains. So far the main attention has been devoted to the mechanism of nucleation of the central equiaxed grains, the means by

which the continued growth of the columnar grains is impeded by the equiaxed grains has been discussed in much less detail.

In early work it was generally agreed that the transition occurs when equiaxed crystals, forming in the melt ahead of the columnar grains, have grown sufficiently in size and number. This seems to imply that the transition occurs when the equiaxed crystals in the melt have formed a mushy state or even something like a skeleton network as suggested by Chalmers [Cha63]. The columnar interface has continued to move inwards from the mould wall as a result of the extraction of heat by the mould, and this continues until the columnar crystals impinge upon the dendritic crystals that have formed. From then on growth continues by the advance of the interface in the interdendritic liquid, each dendrite crystal 'filling in' as the interface goes by.

However, Fredriksson [Fre72] suggested that the equiaxed grains are floating in the melt and adhere to the vertical solidification front if conditions are favourable. The interruption of the columnar grains by the adhesion and further growth of crystals may depend upon interplay between the number and sizes of floating crystals in the melt on one hand, and the shape of the solidification front on the other. A more 'jagged' front may catch floating crystals more efficiently than a smooth front. During solidification of a casting, the shape of the vertical solidification front changes gradually from very smooth to more jagged as a consequence of the decreasing thermal gradient and the chance of a CET occurring will thus increase. It is therefore concluded that the CET is caused either when the columnar zone encounters an existing skeleton of the equiaxed zone or by attachment of equiaxed grains from the liquid to the columnar front. Whichever mechanism is accepted, both depend on a rapid rate of growth of equiaxed grains in the liquid and thus two aspects to the problems of CET are defined. Firstly, the nuclei can only grow if the latent heat can be conducted out to the mould wall past the tips of the columnar dendrites so the equiaxed grains must grow at a higher temperature than the columnar grains. The second aspect of the problem is how the equiaxed grains can halt the columnar growth.

It is now clear that dendritic growth occurs with some residual supercooling. Two different types of dendrite supercooling have been identified: one occurring with dendrite growth into an imposed temperature gradient (cellular dendritic growth) in which the supercooling decreases for faster dendritic growth; and the second (dendritic growth) with no temperature

gradient in which the supercooling increases with faster growth. The role of the temperature gradient in causing this difference was suggested by Doherty [Doh77] and investigated experimentally and theoretically by Burden and Hunt [Bur74 I and II]. The latter authors were able to show that columnar dendrite tips grow with a supercooling dependent on their velocity and the temperature gradient in which they develop (Figure 3.16). In the absence of a temperature gradient ($G = 0$), greater supercooling was required for faster dendritic growth. However, with a steep temperature gradient ($G = G_1, G_2$ where $1 < 2$) large supercoolings were found with the slowest growth rate. The supercooling in the limits of very slow cooling should approach the freezing range of the alloy for plane front solidification. As the dendrite velocity increased for an imposed temperature gradient the supercooling decreased (the tip temperature approaching the liquidus temperature) but then passed a minimum in supercooling and joined the rising curve for increasing supercooling with faster growth of the free dendrite behaviour.

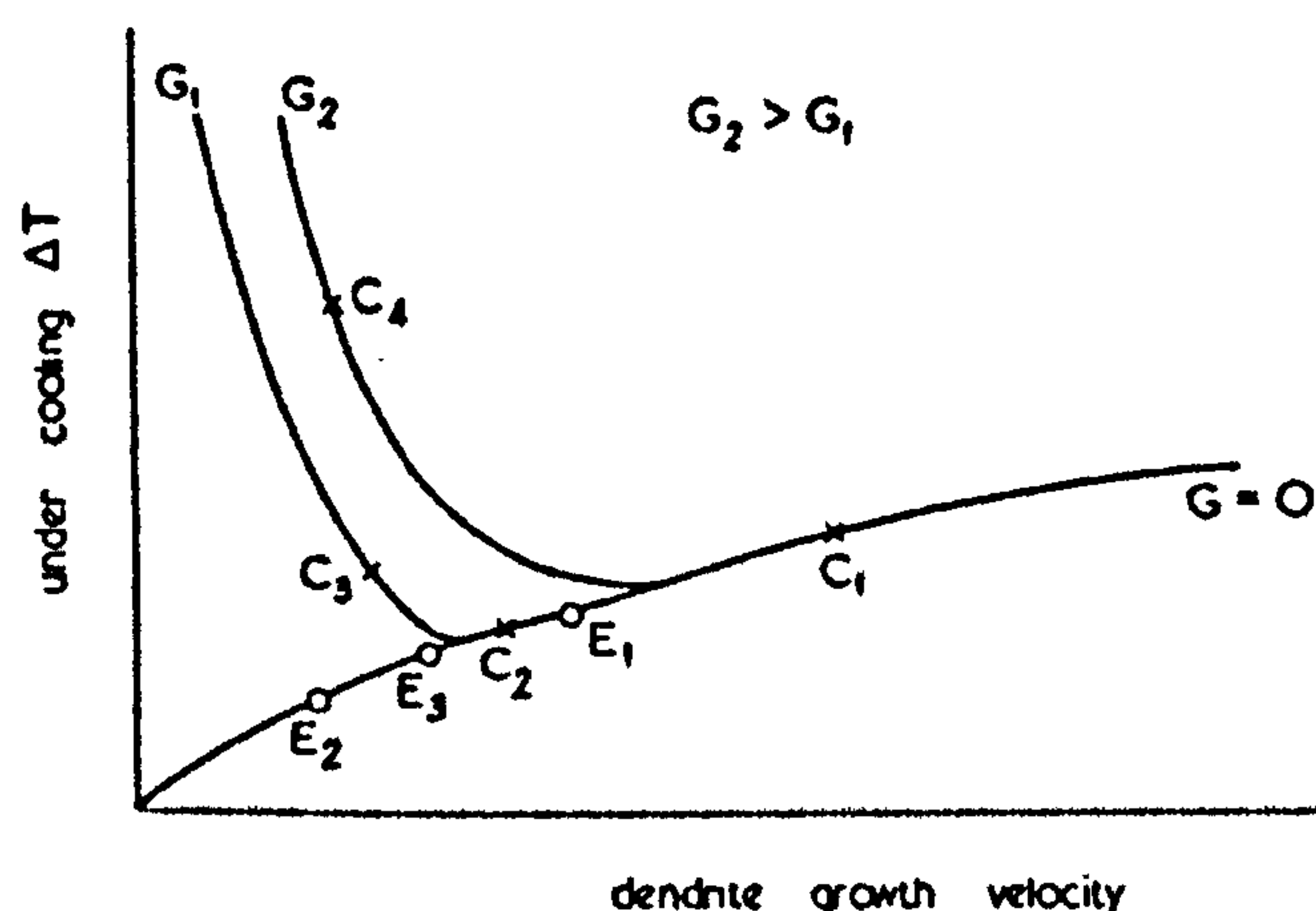


Figure 3.16 Supercooling of a columnar tip as a function of growth velocity and temperature gradient, after Burden and Hunt [Bur74]

Based on this behaviour Burden and Hunt [Bur74] were able to produce an explanation of the sharpness of the CET. They pointed out that during initial growth of the columnar dendrites at a high velocity, once the superheat of the liquid metal was lost, the fast columnar growth C_1 would require a high supercooling so allowing the slow growth of the equiaxed grains E_1 . As the columnar growth continued at a slower velocity C_2 the equiaxed grain would for thermal reasons also have to grow more slowly, E_2 , and it is difficult to see how the process of slower equiaxed than columnar growth would enable the CET to occur. However, if there is a sufficient density of slowly growing equiaxed dendrites just ahead of the growing columnar

front, then the equiaxed grains should generate a sufficient thermal gradient to increase the columnar supercooling C_3 , so allowing more rapid equiaxed growth and thus an increased gradient which will further impede columnar growth leading to the CET ^[Doh77].

From this a theoretical model of dendritic and cellular growth was proposed and a possible mechanism for the CET suggested ^[Bur74]. If a certain amount of equiaxed crystals manage to grow in front of the columnar interface, the temperature gradient will increase and the velocity decrease. This mechanism will lead to the fall in the temperature of the columnar dendrites, therefore promoting further equiaxed growth. However, this mechanism neither explains the initial amount of equiaxed crystals nor accounts for the fact that an equiaxed zone is always associated with liquid convection. Further work by Hunt ^[Hun84] incorporated these factors in an attempt to model columnar and equiaxed growth under realistic casting conditions. The columnar front usually associated, but not necessarily exclusively, with directional growth was rejected in favour of simple steady state equiaxed growth (assumes that at each temperature the number and size of the equiaxed grains remains unchanged with time) for both dendritic and eutectic systems. Equiaxed grains were assumed to have nucleated heterogeneously and the subsequent growth and interaction with the columnar front was examined using an approximated analytical solution and a more accurate numerical integration of the heat flow equation. A simple expression predicting when fully equiaxed structures should occur was developed, a full derivation of which can be found in Appendix A.

The critical gradient condition for fully equiaxed growth is given approximately by

$$G < 0.617 \cdot N_0^{1/3} \cdot \left[1 - \frac{(\Delta T_N)^3}{(\Delta T_c)^3} \right] \cdot \Delta T_c \quad [3.19]$$

where G is the temperature gradient, N_0 the total number of heterogeneous substrate particles originally available per unit volume, ΔT_N is the supercooling at the heterogeneous nucleation temperature, and ΔT_c is a supercooling equal to that of the columnar growth front temperature. Similarly, assuming that a fully columnar structure results when the volume fraction ahead of the front is less than 1 % of the value required for a fully equiaxed one, leads to the condition for fully columnar growth being derived as

$$G > 0.617 \cdot (100 \cdot N_0)^{1/3} \cdot \left\{ 1 - \frac{(\Delta T_N)^3}{(\Delta T_c)^3} \right\} \cdot \Delta T_c \quad [3.20]$$

Calculations were performed for an Al-Cu system using Equation 3.19 from which Figure 3.17 was drawn ^[Hun84]. Also from these calculations the following observations were made;

- i) at low temperature gradients it is the size of the critical supercooling for nucleation, ΔT_N , which determines the nature of the structure, and
- ii) at high temperature gradients, the number of heterogeneous nuclei is critical.

Figure 3.17 a) shows the predicted results for Al-3 wt. % Cu where the solid lines illustrate the columnar and equiaxed regions calculated using the approximate analysis, and the dashed lines represent calculated results using the more accurate analysis. Only the transition from a fully equiaxed structure is shown. The value of A , used in equation A7, is taken from experimental results ^[Bur74] as $300 \mu\text{m s}^{-1} (\text{wt. \%})^{-1} \text{K}^{-2}$. The number of sites, N_0 , is assumed to be one per cubic millimetre ($N = 1000 \text{ cm}^{-3}$) and ΔT_N is taken to be 0.75 K. Figure 3.17 b) demonstrates the effect of four different alloy compositions using the same parameters for the approximate analysis. Of particular interest are results ^[Hun84] for an Al-3 wt. % Cu alloy showing the effect of changing the alloy composition (increasing Cu content), where a quantity of $-m(1-k_0)C_0$ was found to give the temperature difference between the liquidus and solidus at composition k_0C_0 . m is the liquidus slope, k_0 the partition coefficient, and C_0 the alloy composition.

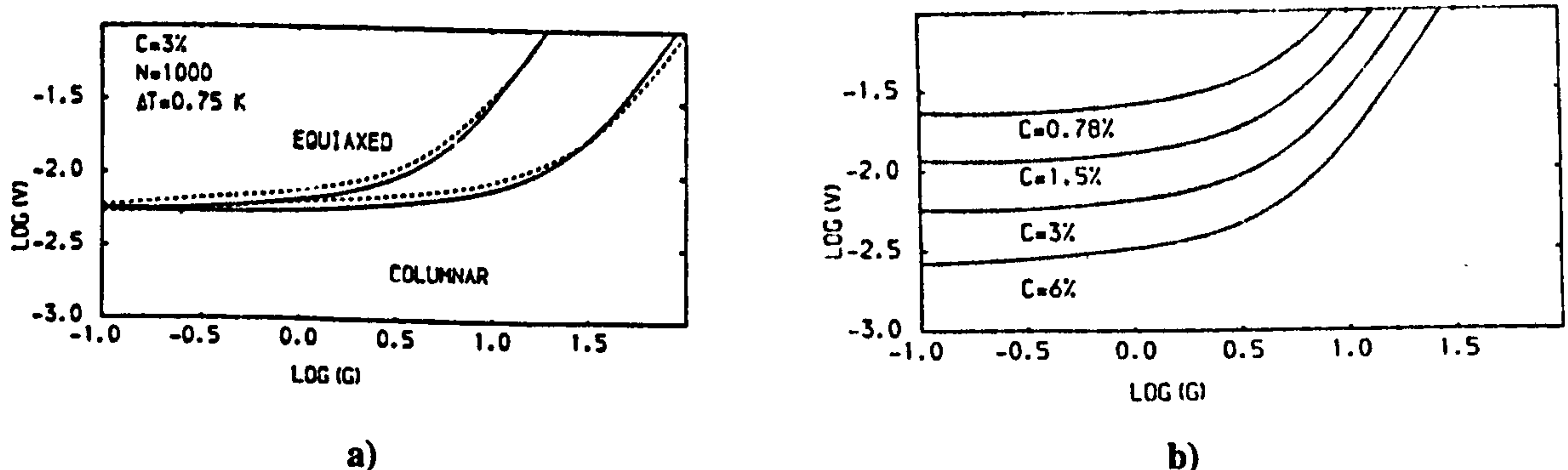


Figure 3.17 Plot of growth velocity V (cm s⁻¹) against temperature gradient G (K cm⁻¹) a) for Al-3 wt. % Cu, and b) for four different compositions C (wt. % Cu), after Hunt ^[Hun84]

Flood and Hunt ^[Flo86] went on to compare these results with a numerical study of the CET under unsteady state conditions using mathematical models that included a non-equilibrium supercooling at the columnar front and described the simultaneous evolution of both columnar and equiaxed zones. Although latent heat liberated ahead of the columnar front had been considered qualitatively it had not, so far, been included in any calculations. It was understood that the latent heat liberated by equiaxed grains in the bulk, could create a thermal interaction between the columnar and equiaxed growth and should be considered quantitatively. They found that considering only the growth of the equiaxed grains in castings can reproduce a reduction in the columnar range with increasing alloy composition, increasing convection and decreasing cooling rate, but it cannot explain the dramatic effect of superheat found in practice. Thus, it was concluded to be the result of the 'big bang' mechanism for nuclei production. The equiaxed zone develops when grains exist ahead of the front because of the favourable conditions for their growth; the temperature gradient in the bulk is low and consequently all the grains grow at supercoolings comparable to that of the front. The equiaxed zone can only be suppressed by preventing the nucleation of the grains when the temperature gradient is low. This is supported by an approximate steady state analysis of the problem, which also points to the number of nuclei present being critical at high gradients. The thermal interaction between columnar and equiaxed grains, which it had been thought could be important, does not appear to influence the CET.

3.5 Grain Refinement

Grain size is an important, readily observed feature of aluminium alloys and a uniform, fine grain size is sought in most instances to obtain optimum properties in the cast product. Several methods are used to achieve this 'grain refinement' including rapid cooling, growth hindering, and addition of nucleating agents. The first of these, rapid cooling, works by reducing nuclei sizes and hence increasing the number of nucleation sites, thus restricting grain growth and homogeneous nucleation. However, as can be seen from Figure 3.18 refinement by rapid cooling is generally not as effective as that attained by deliberate grain refiner additions. Growth-hindering additions are usually alloying elements added to an alloy system to enable supercooling to take place during solidification. It is in the supercooled zone that solute enrichment facilitates nucleation and therefore a greater number of smaller grains. This process is, however, most effective in copper alloys and additional methods of grain

refinement are employed commercially for aluminium alloys, through which the growth is controlled.

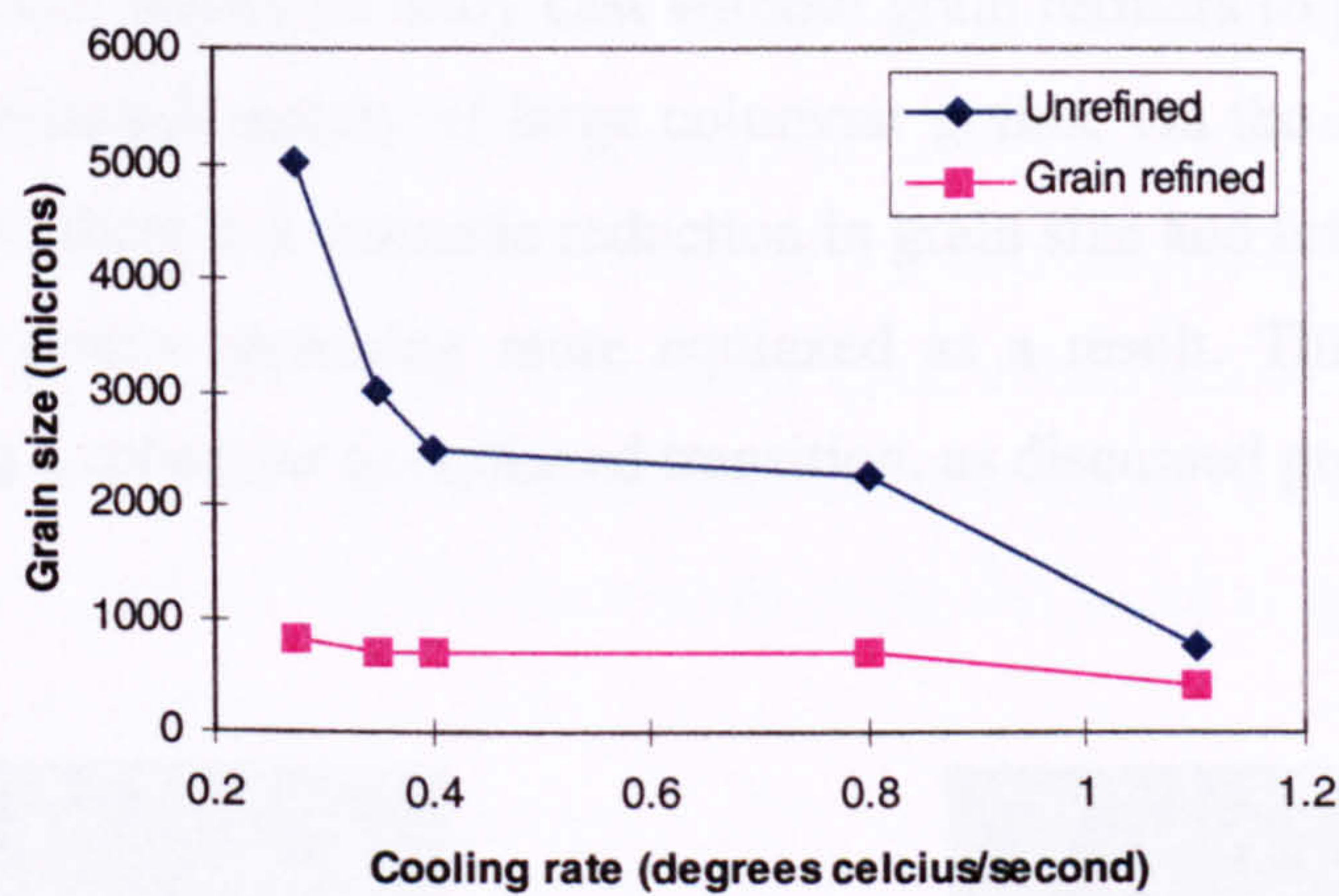


Figure 3.18 Effect of cooling rate and grain refinement on grain size of an Al-Si casting, based on data by Boone ^[Boo98]

Grain refinement by the controlled addition of certain elements dispersed into the melt to serve as sites for heterogeneous nucleation is the most common method of achieving finer grains in aluminium alloys. Small quantities of grain refining agents such as titanium and boron are added singly or in combination without greatly altering the base composition of the melt. The nucleation is kept as close as possible to the liquidus temperature and supercooling is minimised ensuring that as many grains as possible are formed during initial solidification, and that they all grow at the same rate. It is this grain refinement by inoculation that is most commonly used in casting practice and shall be considered here.

Although extensive theoretical and experimental studies have been carried out to explain the operating mechanism of grain refinement, most of these studies are limited to pure aluminium or wrought alloys. Information on grain refinement of aluminium-silicon alloys is scarce despite the commercial importance of this practice being the most important of the aluminium casting alloys. Indeed, the commercial procedure for grain refinement in Al-Si alloys seems to be borrowed wholly from grain refining practice in wrought aluminium alloys without a consideration of the influence of silicon content. The grain refining inoculants commonly used in the aluminium industry are master alloys containing titanium or titanium plus boron, and as a result Al-Ti-B master alloys form the standard grain refiner in the foundry industry.

In the alloys used in this research Ti is the main grain refining addition. B is not used in these casting alloys as the borides cause problems during feeding of the intricate piston moulds. The effects of the addition of grain refiners to an Al-Si casting alloy are shown in Figure 3.19 a) and b). Figure 3.19 a) shows an alloy cast without grain refiners to produce a coarse, non-uniform structure consisting mainly of large columnar grains. On the addition of refiners, in this case Ti, Zr and V, there is a dramatic reduction in grain size and improvement in structure uniformity with the grains appearing more equiaxed as a result. Thus, the effect of grain refiners in promoting a columnar to equiaxed transition, as discussed previously, is evident.

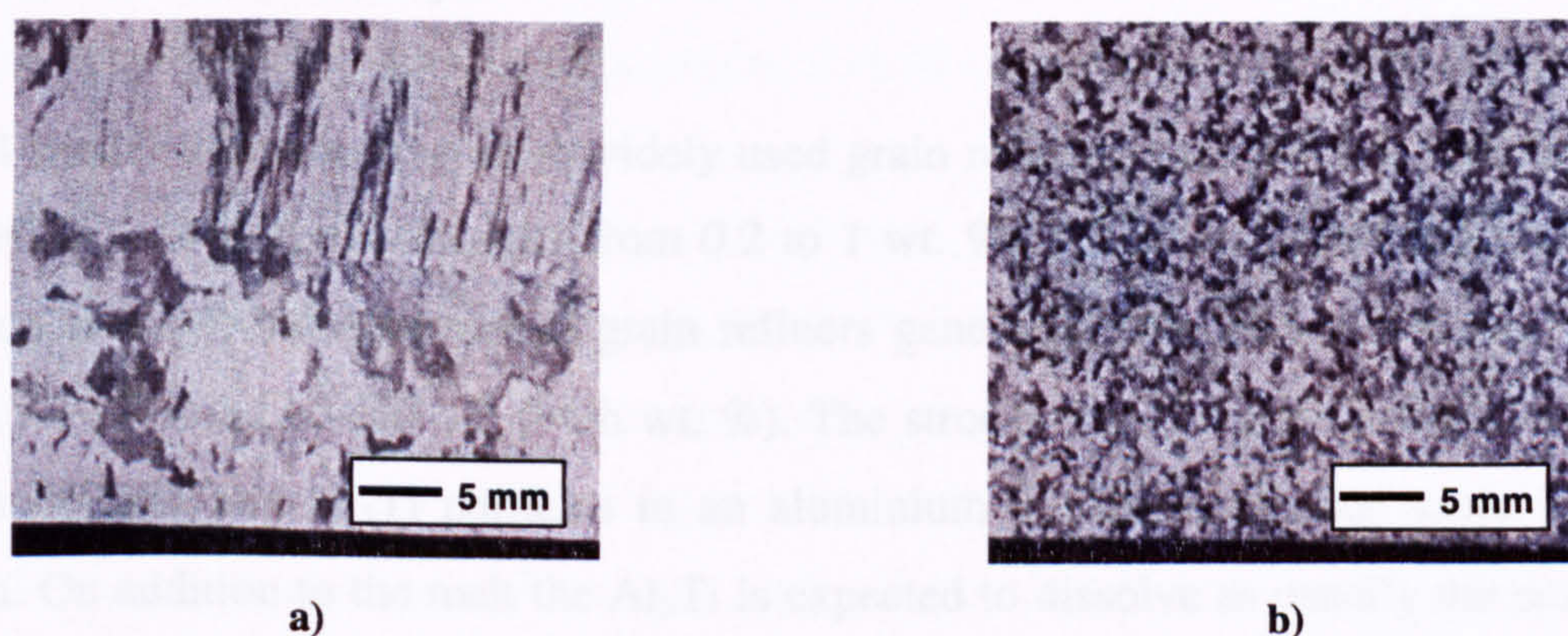


Figure 3.19 Structure of an Al-Si casting a) without refiners and b) with Ti, Zr and V additions

A grain refiner is typically an alloy containing inoculant particles embedded in an Al matrix. The refiner is added to the melt of the alloy to be refined and dissolves completely apart from the inoculant particles, which are dispersed in the melt. The inoculated melt is poured into the mould and is cooled. During cooling several important stages occur which can be summarised as nucleation (controlling the number of grains that are initiated) and growth (the speed of which determines the size of the particles), both of which depend on the temperature of the melt and its solute content. Although the two stages are not independent of each other, it is necessary to consider them separately in order to gain a better understanding of the individual mechanisms.

Titanium, particularly in association with boron, in the form of Al-Ti or Al-Ti-B master alloys has a powerful nucleating effect when added to an Al melt and is the most common method applied for grain refining the castings of Al and its alloys. An efficient heterogeneous nucleus

for α -aluminium is one that will provide a surface for growth near the liquidus temperature of the alloy. It is generally acknowledged that the Al_3Ti constituent meets all the necessary criteria, with direct experimental evidence and thermodynamic data suggesting that Al_3Ti is a very stable compound in Al melts. The Al-Ti binary system contains Al_3Ti , but because Al_3Ti is so soluble in molten aluminium it is necessary to add titanium to levels greater than 0.15 wt. % in order to retain grain refining effectiveness. At this concentration, the peritectic point is exceeded and the first phase formed in the alloy upon solidification is the Al_3Ti . However, this high level of Ti can give rise to coarse intermetallic particles which are detrimental to mechanical properties. Moreover, the reduction in grain size is not as great as can be achieved with the Al-Ti-B master alloys.

Al-Ti-B master alloys are the most widely used grain refiners, with Ti concentrations from 3 to 10 wt. %, and B concentrations from 0.2 to 1 wt. %. The weight ratio required for TiB_2 formation is 2.2:1, but commercial grain refiners generally have Ti levels higher than this, such as Al-10Ti and Al-5Ti-1B (both wt. %). The structure of the grain refiner master alloy consists of TiB_2 and Al_3Ti particles in an aluminium matrix containing some Ti in solid solution. On addition to the melt the Al_3Ti is expected to dissolve as usually the composition of the melt is below the peritectic composition for Al_3Ti , leaving the insoluble TiB_2 particles in suspension suggesting that the boride particles play a dominant role in nucleation. The chemical composition, and particularly the Ti:B ratio is an important factor. The optimum value of this ratio depends on the alloy being refined ^[Sig84]. The exception arises in the case of high silicon casting alloys where sub-stoichiometric refiners, i.e. with excess B beyond that needed for TiB_2 particles, may be used. Although the exact mechanism by which this occurs is not well understood, Sigworth and Guzowski ^[Sig84] believe that the Si interferes with the Ti and B leading to different optimum ratios of these two elements in the grain refiner.

3.5.1 Mechanisms of Grain Refinement

The average grain size of a casting depends on the nucleation rate of the crystals inside the melt and on the growth rate of these crystals. Therefore, the contribution of any added element in the grain refinement of Al is determined by its control over the nucleation rate and/or the rate of crystal growth of the α -Al solid solution. According to Bunn ^[Bun98], the inoculant responsible for the nucleation stage of grain refinement must fulfil several criteria:

- thermodynamic stability over a reasonable time period;
- low lattice disregistry between the substrate and the nucleating crystal;
- wetting, i.e. a suitable balance of interfacial energies;
- suitable size and distribution; and
- suitable density to eliminate excessive or rapid sedimentation or flotation in the melt.

In general, nucleation takes place when the driving force for solidification becomes large enough to overcome the interfacial energy barrier (refer to Section 3.2.1). The driving force is approximately proportional to the undercooling in the liquid and during solidification nucleation can occur over a range of supercoolings. It is desirable to have nucleants with a low nucleation undercooling and hence a high potency for nucleation, since the higher the nucleation temperature the lower the subsequent growth rate of the nucleated grains. However, if the nucleating efficiency of the added inoculants varies greatly then the most potent inoculants will become active first, and the resultant latent heat released into the melt from the growth of the grains may prevent nucleation on the remaining, less potent inoculants.

In the past much controversy has surrounded the exact mechanism by which Al-Ti-B refiners nucleate aluminium. The TiB_2 particles were known to be essential for effective grain refinement, but without excess Ti to tie up all the B in TiB_2 , their grain refining performance was found to be almost negligible. Most theories surrounding grain refinement involved a mechanism for prolonging the stability of Al_3Ti by TiB_2 particles. Grain refinement theories has been reviewed in detail by McCartney ^[McC89] and more recently by Easton and St. John ^[Eas99], the most common of which are examined here.

Phase Diagram Theories

These theories were first developed by Crossley and Mondolfo ^[Cro51] who attributed grain refinement to the peritectic reaction



at 3°C above the melting point of pure aluminium, which is believed to be a very powerful nucleating mechanism for α -Al. However, at typical addition levels, the TiAl_3 is not expected to survive since this is well below the peritectic composition of TiAl_3 at 0.15 wt. % Ti. In the peritectic model it is suggested that the composition of the Al-Ti peritectic point is depressed by the presence of B, so that the TiAl_3 is able to survive for longer at low Ti concentrations in the melt, and nucleate the α -Al ^[Bac90]. This is illustrated in Figure 3.20. Other authors ^[Mon87, Mar71] suggest that there is a metastable high boron content in the melt, which causes depression of the peritectic point so that the peritectic reaction can occur at lower temperatures. However, experimental investigations into this explanation ^[Sig84] determined that a ternary peritectic does not exist and therefore changes in the Al-Ti phase diagram due to B additions could not be used to explain the grain refinement mechanism of Al-Ti-B additions.

Alternatively, Al_3Ti particles may remain undissolved from the master alloy addition. The Al_3Ti particles that are added to aluminium are able to nucleate α -aluminium until they have dissolved. Hence, for hypoperitectic compositions the kinetics of dissolution is as important as the equilibrium phase diagram in understanding the role of Al_3Ti in grain refinement, because if Al_3Ti can exist in non-equilibrium conditions for a long time, it can still be the nucleant particle.

The main problem with phase diagram theories is that, at hypoperitectic compositions, Al_3Ti is not stable and therefore not present as nucleation sites except at very short holding times. This means that the phase diagram theories cannot explain grain refinement at hypoperitectic titanium concentrations. Grain refinement must therefore be due to non-equilibrium conditions. In the late 1980's and early 1990's one of the most popular theories was the peritectic hulk theory ^[Bac91]. This accepted that Al_3Ti is a more powerful nucleant than TiB_2 , and tried to explain how the borides could slow down the rate of dissolution of the Al_3Ti so

that these nuclei remained active longer. The theory suggested that the borides formed a shell around the aluminides, slowing down the rate of dissolution as diffusion needed to proceed through the boride shell. The Al_3Ti eventually diffuses through the boride covering producing a Ti-rich layer around the outside termed the 'peritectic hulk', from which α -aluminium nucleates upon cooling. The evidence to the contrary of this theory, however, suggests that other mechanisms are more dominant as more often boride particles have been found in the grain centre rather than as a shell.

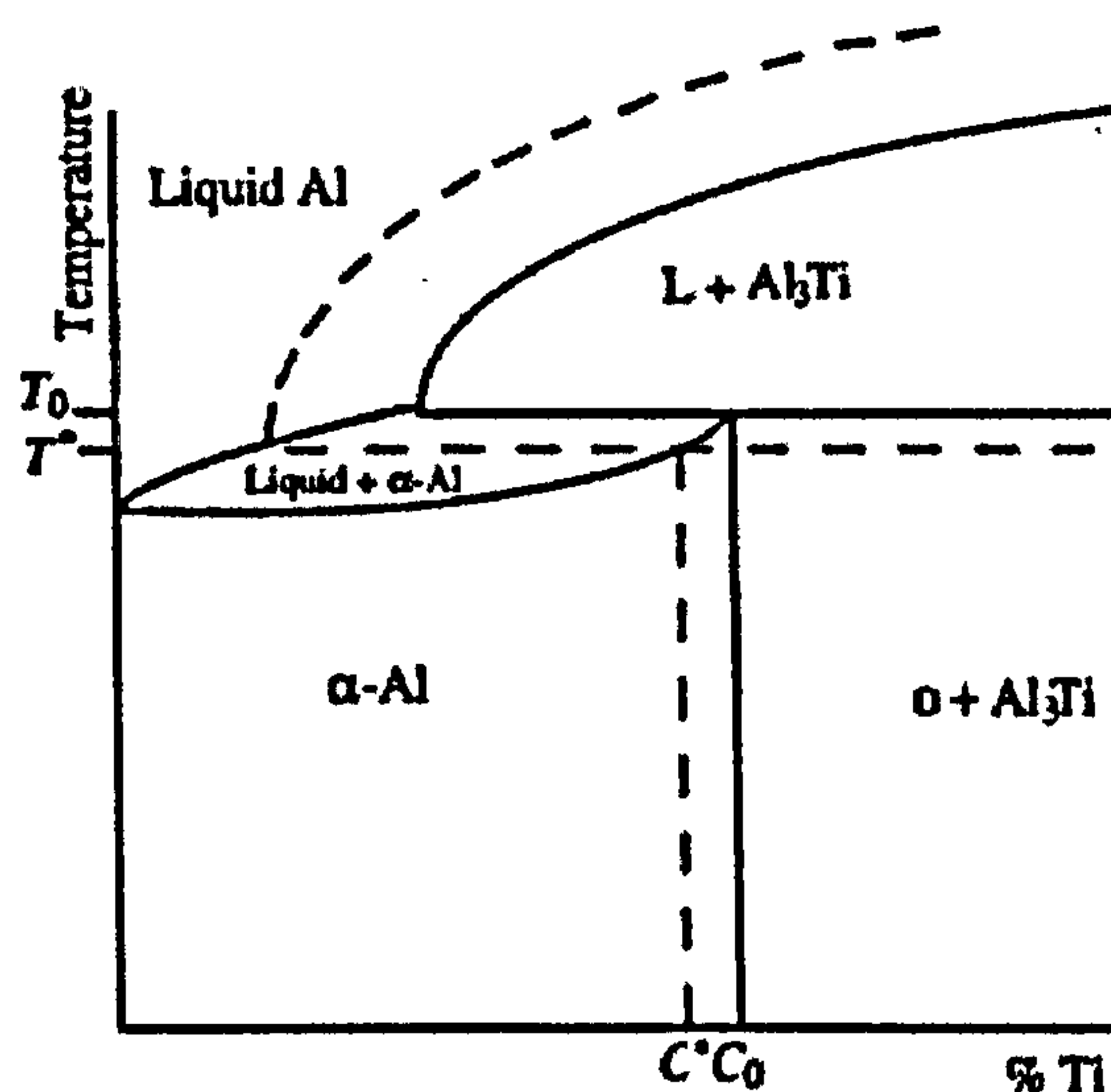


Figure 3.20 Peritectic reaction in the aluminium-rich end of the Al-Ti phase diagram. Dashed line represents where the stability field of Al_3Ti is predicted to be increased by addition of B, after Bunn ^[Bun98]

Nucleant Particle Theories

The carbide-boride theory was first proposed by Cibula in 1949 ^[Cib49] suggesting a nominal addition of Al-Ti master alloy promotes the formation of TiC or TiB particles. Borides are added by way of a master alloy, whilst carbides are formed even when no deliberate additions of carbon are made by the residual carbon content (several hundred ppm being sufficient) reacting to promote TiC formation. With the addition of a Ti-Al-B master alloy, TiB_2 particles are dispersed in the melt and TiB_2 and TiC , being virtually insoluble in molten aluminium, act as heterogeneous nucleation sites. However, Mohanty and Gruzleski ^[Moh95] experimentally demonstrated that TiC particles are unstable in aluminium melts rendering the carbide theory invalid, and so the rest of the section will concentrate on borides as nucleants.

It was believed that a complex metastable phase $(\text{Al,Ti})\text{B}_2$ aided grain refinement either by acting as the nucleant itself or by nucleating Al_3Ti crystals during cooling. However, Marcantonio and Mondolfo ^[Mar71] concluded that $(\text{Al,Ti})\text{B}_2$ is a stable compound due to a continuous range of solid solubility of AlB_2 and TiB_2 . The addition of Ti and B together produces greater refinement than either element alone and this suggests that crystals of TiB_2 are produced and are in some way key to grain refinement. It was concluded that $(\text{Al,Ti})\text{B}_2$ may nucleate grains but only in the absence of Al_3Ti since nucleation occurs at 1 to 2° below the temperature at which Al_3Ti would become active. However, analysis of the phase diagram by Sigworth ^[Sig84] for this system does not support these proposals.

Thus, a hypernucleation theory was proposed by Jones ^[Jon80], who suggested that since the TiAl_3 particles are unstable while the TiB_2 particles remain chemically and physically stable during holding, it is the TiB_2 particles which behave as the inoculants during grain refinement. By calculating the presence of Ti both in the melt and in TiB_2 , he speculated that the Ti in solution from the dissolution of the Al_3Ti phase segregates to the surface of the borides. This ‘plating’ of the surface of the boride with a semi-solid layer of aluminium creates a condition where solidification of $\alpha\text{-Al}$ is possible even above the liquidus temperature, and growth can occur with virtually no nucleation supercooling. Experimental work following these observations ^[Moh95, Sch95, Moh96] confirmed that the TiB_2 crystals were to play an indirect role in the grain nucleation. In the presence of dissolved Ti, even below the peritectic composition, TiB_2 introduces a concentration gradient with respect to Ti leading to segregation of Ti atoms to the TiB_2 -melt interface. Thus, precipitation of a thin layer of Al_3Ti occurs on the boride, which undergoes a peritectic reaction and thereby nucleates the solid.

Schumacher and Greer ^[Sch95, Sch98] have produced the most convincing evidence for their version of the ‘hypernucleation theory’, referred to as the ‘duplex nucleation theory’. They confirmed through experimental analysis that the grain refining action is due to the preservation of Al_3Ti in association with stable TiB_2 particles in the melt, and found that the TiAl_3 is stabilised as a layer on the $\{0001\}$ basal faces of the borides. Nucleation of aluminium then occurs on the Al_3Ti layers. Well defined orientation relationships were determined, with the close packed planes in the three phases being parallel: $\{0001\}_{\text{TiB}_2} \parallel \{112\}_{\text{Al}_3\text{Ti}} \parallel \{111\}_{\text{Al}}$. Thus, this is now the accepted mechanism of grain refinement whereby boride particles are stable in nearly pure Al melts, but their action as nucleants relies on the presence of excess Ti (beyond that of TiB_2 stoichiometry) forming Al_3Ti .

3.5.2 Effect of Additions on the Grain Refining Ability of Ti and Ti+B

The grain refinement of aluminium castings produced by the addition of Ti or Ti+B is generally attributed to the nucleation of α -Al by a combination of Al_3Ti and TiB_2 . The presence of any other element in the melt, either as residual impurities in Al or as alloying additions, may affect the efficiency of the grain refiners. Some elements enhance or improve the efficiency while others can deteriorate or 'poison' it ^[Abd89].

Elements which Enhance Grain Refiner Performance

The reaction of a third element with the dissolved Ti in the Al melt can form a new and more efficient nucleant for α -Al. Only a very small amount of the third element with a much lower amount of Ti is necessary to produce good grain refinement in Al castings. The well known examples of such elements are boron and carbon which form good nucleants with the Ti as TiB_2 or $(\text{Ti,Al})\text{B}_2$ and TiC , respectively. These particles can nucleate α -Al directly or after being covered by a thin layer of Al_3Ti , and are also able to nucleate Al_3Ti leading to an increase in its number and a decrease in its size. The presence of a very small amount of carbon in an Al melt containing Ti leads to the formation of TiC , which has a very low solubility in liquid Al. TiC was expected to be a very good nucleant for α -Al, and therefore expected to enhance the grain refining efficiency of Ti in Al castings due to the good epitaxial matching of their lattice parameters. However, it is reported that small additions of C enhance the Ti efficiency while large amounts reduce or destroy it. The addition of large amounts of carbon leads to the formation of Al_4C_3 and Ti_3AlC around TiC which results in the poisoning of the TiC particles.

It has been shown that the grain refinement of Al by Ti is improved by the addition of small amounts of the alkaline earth metals, for example Ca, Mg, Be or Sr ^[Abd89]. The mechanism of enhanced grain refining efficiency for these metals is believed to be through the formation of a ternary compound $\text{Ti}(\text{Al,Me})_3$ (Me representing metal) having the same crystal structure but a lower formation or nucleation entropy than Al_3Ti . Here the third element replaces some of the Al in TiAl_3 leading to the improvement of its grain refining efficiency or the ternary compound nucleates TiAl_3 in the Al-Ti-Me master alloy.

Some elements, however, have a little or no solubility in solid aluminium, such as Bi, In, Pb, Sn, Sb, Co, and Fe. In this case the third element results in the presence of a concentration

gradient around the solid/liquid interface and leads to the restriction of the grain growth of α -Al, and thereby an improvement in the grain refining of the solidified castings. The enhancement is relatively small (less than 50%) and varies with the Ti level in the melt. Since this enhancement is attributed to the contribution of the crystal growth restriction to grain refinement, it will be lost when the insoluble element exceeds the eutectic level for the corresponding binary Al system and an intermediate compound nucleates as the primary phase.

The addition of V up to 0.1 wt. % in the Al melt produces no or very little enhancement in the grain refining efficiency of the two commercial master alloys (Al-Ti and Al-Ti-B). The grain refining enhancement is only found when the V content is 0.1 wt. % or more, i.e. above the peritectic limit in the Al-V phase diagram. The effect of V may be due to the presence of VAl_{10} particles in Al melts containing more than 0.1 % V. VAl_{10} can nucleate α -Al but its nucleation power is much lower than that of Al_3Ti and TiB_2 . Therefore, it nucleates α -Al only after the consumption of these active nucleants presented in the master alloys ^[Bun98].

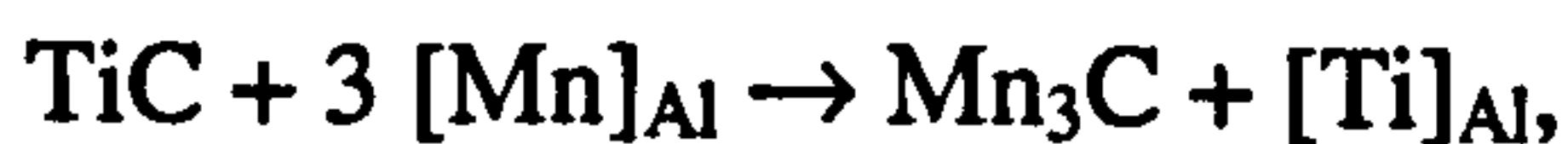
Poisoning Effects of Other Elements on Ti or Ti+B grain refiners

The term 'poisoning' is generally used in the literature when an Al alloy is difficult to grain refine due to the presence of certain elements. This means that the poisoning element adversely affects the grain refining efficiency of the grain refiner. Ti and Ti+B grain refiners are susceptible to poisoning by certain transition metals, in particular Zr, Cr and Ta. The poisoning of grain refiners is troublesome in industrial practice since it can occur very quickly and can not generally be reversed. At present is best dealt with by adding the Al-Ti-B master alloys of the rod type just before casting.

Although Zr has been proven to be a strong grain refiner for Al through the formation of ZrAl_3 ^[Arj97], the effect of Ti and Zr additions together in the Al melt element is less clear. Work by Johnsson ^[Joh94] investigated the effect of hypo- and hyperperitectic additions of Zr on the grain refining ability of Ti or Ti + B, concluding that hypoperitectic concentrations of Zr cooperate with Ti in promoting a fine-grained structure and the combined effect can be described by the sum of their ability to restrict the growth. However, he observed that hyperperitectic Zr concentrations in combination with a low Ti concentration results in a coarser grain size than an equivalent Ti addition without Zr present.

Both chromium and tantalum have little or no grain refining effect when added alone in the Al melts, but cause grain coarsening in the Al castings which are grain refined by Ti or TiB. Several authors ^[Abd89, Arj97] have investigated the poisoning mechanism in detail, concluding that the Zr, Cr and Ta additions replace the Ti in Al_3Ti and TiB_2 to form the ternary solid solutions $\text{Al}_3(\text{Ti}_{1-x}\text{Zr}_x)$, $\text{Al}_3(\text{Ti}_{1-x}\text{Cr}_x)$, $\text{Al}_3(\text{Ti}_{1-x}\text{Ta}_x)$ and $(\text{Ti}_{1-x}\text{Zr}_x)\text{B}_2$, $(\text{Ti}_{1-x}\text{Cr}_x)\text{B}_2$, $(\text{Ti}_{1-x}\text{Ta})\text{B}_2$ respectively. This is accompanied by a change in the lattice parameters and therefore the nucleation properties of the original Al_3Ti and TiB_2 crystals, resulting in the deterioration of their grain refining efficiency. Bunn ^[Bun99] substantiated these findings and deduced that the Zr interferes with the nucleation of the aluminium by substituting into the boride phase consequently changing its lattice parameter in the basal plane. This inhibits the formation of the Al_3Ti coating known to be essential for effective nucleation, and thus poisoning of the grain refiner results.

A similar effect was found by Cibula ^[Cib49] who reported that the presence of a high concentration of Mn, relative to that of Ti, might cause grain coarsening of such castings as in the case of Al-1 % Mn- 0.002 % Ti. He attributed this grain coarsening to the suppression of the grain refining action of the good nucleant TiC (having simple structure) by the formation of the poor nucleant Mn_3C (having a complex structure) according to the reaction:



although more work is needed to explain this mechanism.

3.5.3 Additional Effects on Grain Refinement Ability

Stirring

For optimum grain refinement, growth rates should be as low as possible. Aside from imposed cooling rates, growth is controlled by solute redistribution at the solid/liquid interface. The solute usually has a different solubility in the solid than liquid resulting in either solute depletion or build-up. This lowers the temperature locally at the interface, which in turn reduces the growth rate. Stirring homogenises the melt temperature enabling slightly deeper supercoolings to be reached prior to recalescence, resulting in enhanced nucleation rates and finer grain sizes.

Fade

Figure 3.21 shows grain size as a function of time after a grain refiner addition. The curve is characterised by a rapid initial decline in grain size to the ultimate grain size (UGS) at a critical contact time, t_c . This is followed by an increase in the grain size at longer holding times. This prolonged holding resulting in a gradual loss of grain refining effectiveness is commonly referred to as 'fade' [Kear96]. Fade can be ameliorated in part by stirring the melt, though the degree of recovery depends on the melt composition. The two main causes of fade are settling and agglomeration. Settling is a common problem in unstirred melts due to the higher density of insoluble TiB_2 relative to the liquid aluminium (4.5 g/cm^3 against 2.3 g/cm^3). Stirring the molten alloy that has been previously grain refined re-suspends and disperses the particles that have settled from the melt. Agglomeration of borides can also occur, leading to reduced performance and the formation of large clusters which can settle faster. Partial reactivation may be achieved through brief stirring of the melt, though in some instances this may be undesirable or impractical. If very large agglomerates are allowed to form these will be brought back into suspension and can cause filter blockages or inclusion problems in the casting. Titanium alone, added at the rate of 0.02-0.15%, as a master alloy can be used but the effect fades within 40 minutes. The addition of boron together with titanium produces finer grains and reduces fade.

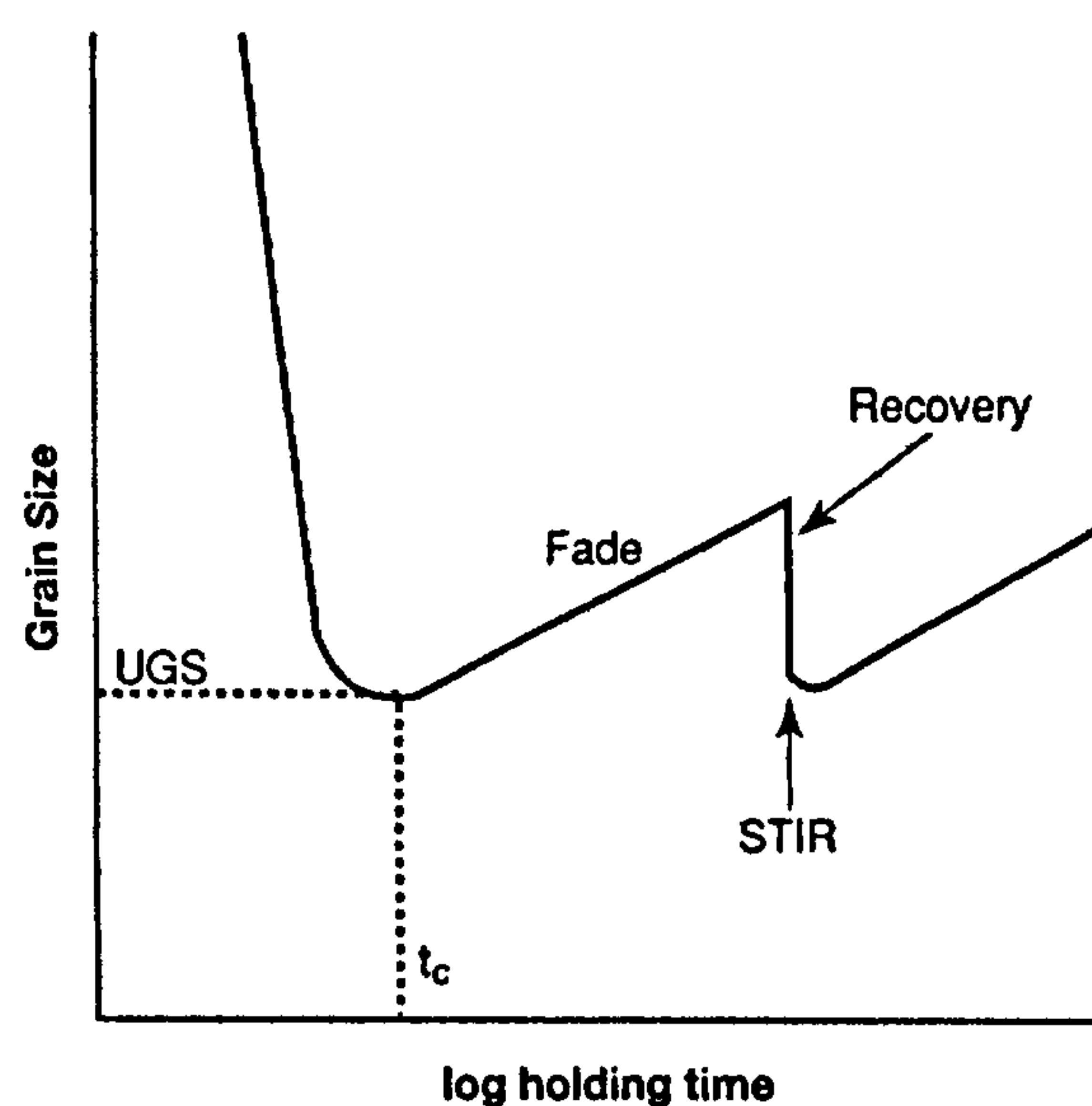


Figure 3.21 Grain size as a function of holding time after the addition of a grain refiner to an aluminium melt, after Kearns et al [Kear96]

3.5.4 Quantification of Grain Refining Ability

Much experimental work has been carried out attempting to quantify the effect of grain refiners on grain size [Kea97, Spi97, Kar98]. Based on early work [Tar71] on the constitutional supercooling parameter, P (K), where the degree of growth restriction was described as

$$P = \frac{m(k-1)C_0}{k} \quad [3.21]$$

where m (K wt.%⁻¹) is the liquidus slope, k is the equilibrium partition coefficient (defined in Equation 3.17), and C_0 (wt. %) is the solute content in the alloy melt. In the absence of solute interactions, the overall constitutional supercooling parameter for a multicomponent alloy can be estimated by summing the P values for each element [Joh94, Kea97]. However, as P is the supercooling of a planar solidification front it is not the best measure of growth restriction [Max75].

Thus, a growth restriction parameter was developed where it is assumed that the final grain size is strongly influenced by how rapid the growth of the first nucleated grains is. Therefore, for optimum grain refinement the growth rate should be as slow as possible. For a spherical crystal growing into the melt at a rate controlled by solute diffusion in the melt, the rate of growth at a given diameter is inversely proportional to a quantity Q , defined as:

$$Q = m(k-1)C_0 = kP \quad [3.22]$$

where Q (K) is termed the growth restriction parameter. Values of Q are assumed to be additive for various solutes in the melt, provided they remain as solutes and do not interact to form complexes or precipitates effectively reducing the overall solute content.

3.6 Controlling the Microstructure

The properties of cast aluminium alloys are very strongly influenced by the microstructure, i.e. the primary aluminium, and the interdendritic microconstituents such as secondary phases, intermetallics, inclusions and porosity. The final microstructure is also modified by the crystal growth, fluid flow, and structural coarsening processes that are important in the later stages of

ingot freezing. The cooling rate of the alloy greatly influences the microstructure, particularly silicon morphology. Slow solidification of a pure Al-Si alloy produces a very coarse microstructure in which the eutectic comprises large plates or needles of silicon in a continuous aluminium matrix. The eutectic itself is composed of individual cells within which the silicon particles appear to be interconnected. Alloys having this coarse eutectic exhibit low ductility because of the brittle nature of the large silicon plates. Rapid cooling, as occurs during permanent mould casting, greatly refines the microstructure and the eutectic silicon phase assumes a fibrous form with the result that both ductility and tensile strength are much improved. The eutectic may also be refined by the process known as modification.

3.6.1 Modification

Irrespective of the composition of an Al-Si alloy it is the morphology of the eutectic Si phase that gives rise to the practice of modification. By the nature of eutectic growth, as described in Section 3.3, near-eutectic silicon forms coarse polyhedral structures such as plates and cuboids. These angular morphologies are believed to be detrimental to the structural integrity of most aluminium-silicon alloys causing a reduction in mechanical properties. Modifiers are a group of elements that are deliberately added to aluminium-silicon alloy melts before casting, affecting the silicon nucleation and growth to change its morphology from a coarse acicular form to one which is finer and more fibrous, as can be seen in Figures 3.22 a) and b) respectively. This is called the flake-fibre transition. Since the constituents are smaller and more uniformly dispersed filling and feeding characteristics of castings are improved. There is also an increase in some mechanical properties, such as tensile strength, ductility, and machinability, whilst the variability of results is reduced. This change in morphology is often referred to as the flake-fibre transition, and results in a shift from a faceted to a more isotropic growth morphology.

Until 1900 the addition of silicon to aluminium was considered to be detrimental and hence the aluminium-silicon alloys were not used. However, in 1920 an investigation of Al-Si casting alloys by Pacz^[Pac21] revealed that a modification of the microstructure, similar to that achieved by rapid cooling, occurred when a small quantity of a powder consisting essentially of an alkaline fluoride (NaF) was added to the melt prior to casting. The mechanical properties of aluminium-silicon alloys could be substantially improved and the commercial potential of these alloys was realised. This process subsequently became known as 'modification'. Further developments in modification took place in 1923 and 1924 with the

introduction of the use of alkali metals by Edwards *et. al.* [Edw23] and of the alkaline earth metals and their oxides and hydroxides by Gwyer and Phillips [Gwy24]. Up until the 1960's much research was carried out concentrating on sodium as a modifier, with early work centred around investigating the Al-Si-Na ternary phase diagram [Ota26] as well as the structure and properties of the modified alloys [Ema93, Fat89, Gwy26, Hag83, Par94, Tel88]. Similar work has been done for strontium [Ema93, Hag83, Par94, Par95].

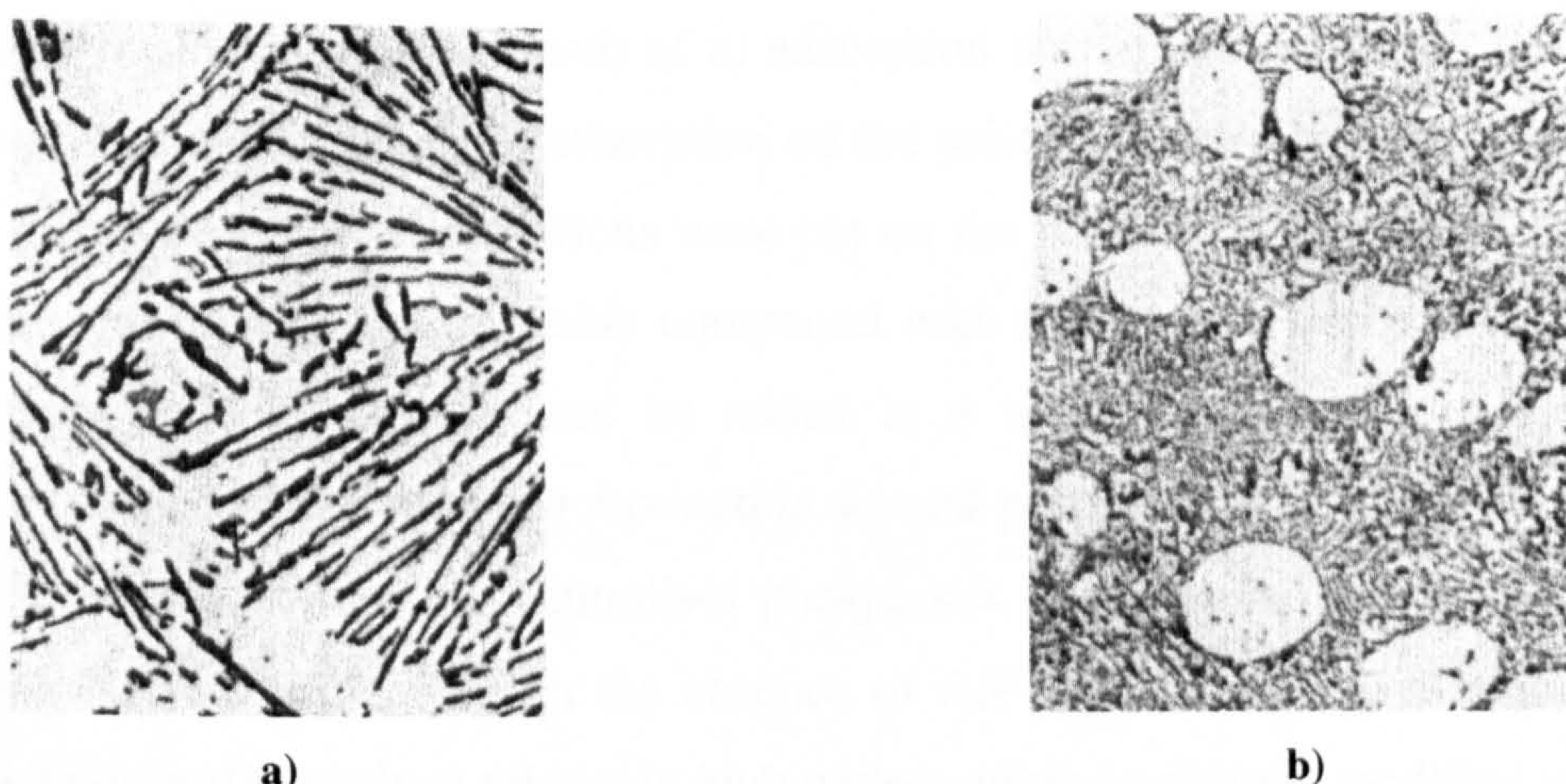


Figure 3.22 Structure of silicon in **a)** an unmodified alloy, and **b)** in a sodium modified alloy, after Polmear [Pol89]

The most common modifiers used today are sodium and strontium, with other elements including calcium, arsenic, lithium and sulphur also known to have modification or refinement properties. However, these latter elements are not used generally either because they, along with antimony, a) poison the effect of sodium and/or strontium, b) have deleterious effects on other properties, c) efficient methods of addition have not been developed, or d) have significant health and safety implications.

Many explanations for the modification process have been put forward although none of the theories proposed has obtained universal acceptance and is still the subject of much research in the present day. These theories can be generally grouped under either nucleation or growth of the silicon phase, however, as the transition of the morphology of eutectic Si from plate-like to fibrous may result from the alteration of the conditions for nucleation and/or growth, many researchers consider both mechanisms.

There are two main theories behind the nucleation mechanism and its effect on eutectic modification. The first theory considers the effect of modification on the stability of silicon nuclei, normally AlP. Several authors ^[Kim63, Plu57] have investigated a theory proposed by Edwards and Archer in 1924 ^[Edw24] where sodium was believed to retard the nucleation of silicon crystals during eutectic solidification by preventing the formation of stable nuclei at the normal eutectic temperature. Solidification would occur at a steady-state temperature considerably below the freezing point, where slower diffusion inhibits the individual silicon crystals from attaining such a large size. Plumb and Lewis's study ^[Plu57] explained this retardation of nucleation to be a result of a) adsorption on the nuclei making it difficult for them to grow to a stable size or b) adsorption on the solid surfaces where the silicon crystals form. For this to be achieved conditions were put on the modifier stating that the modifying element must potentially form a stable compound with silicon over the proper temperature range, but not with aluminium, and be added at a temperature where it is adequately dispersed. A second theory has been reported in several papers ^[Cro66, Ho95] where it is believed that the addition of sodium neutralises phosphorus thus eliminating nucleation by AlP and forming Na_3P in preference. In the absence of AlP the surrounding aluminium matrix nucleates silicon inefficiently at relatively high undercooling to give the modified structure.

Early theories on modified growth mechanisms include the ternary phase theory, where a second liquid phase consisting mainly of Na was believed to mechanically interfere with the growth of Si crystals ^[Ota26], and the protective colloid theory, where the adsorption of Na was thought to hinder the growth of the Si crystals ^[Gwy26]. These and other speculative explanations for modification were soon disproved, many by Plumb and Lewis ^[Plu57], or forgotten as a few choice theories became favoured. In 1966 Crosley ^[Cro66] proposed that the change of lead in eutectic crystallisation changes the structure of the eutectic from a mixture of two interpenetrating phases to that of a discontinuous brittle silicon phase embedded in a soft aluminium matrix. In non-modified alloys the eutectic grows with the silicon leading the crystallisation, forming continuous skeletons, as seen in Figure 3.23 a). In modified alloys aluminium precedes the silicon and tends to envelop it. This enveloping action breaks up the silicon in to many small crystals imbedded in the aluminium matrix (Figure 3.23 b). This change of structure produces the improvement of mechanical properties which is characteristic of modification. The change of lead is believed to be due to either to a change of relative interfacial energies or to a decrease of diffusion rate of silicon in the liquid, with most probably a change in the growth mechanism of aluminium as a contributing factor.

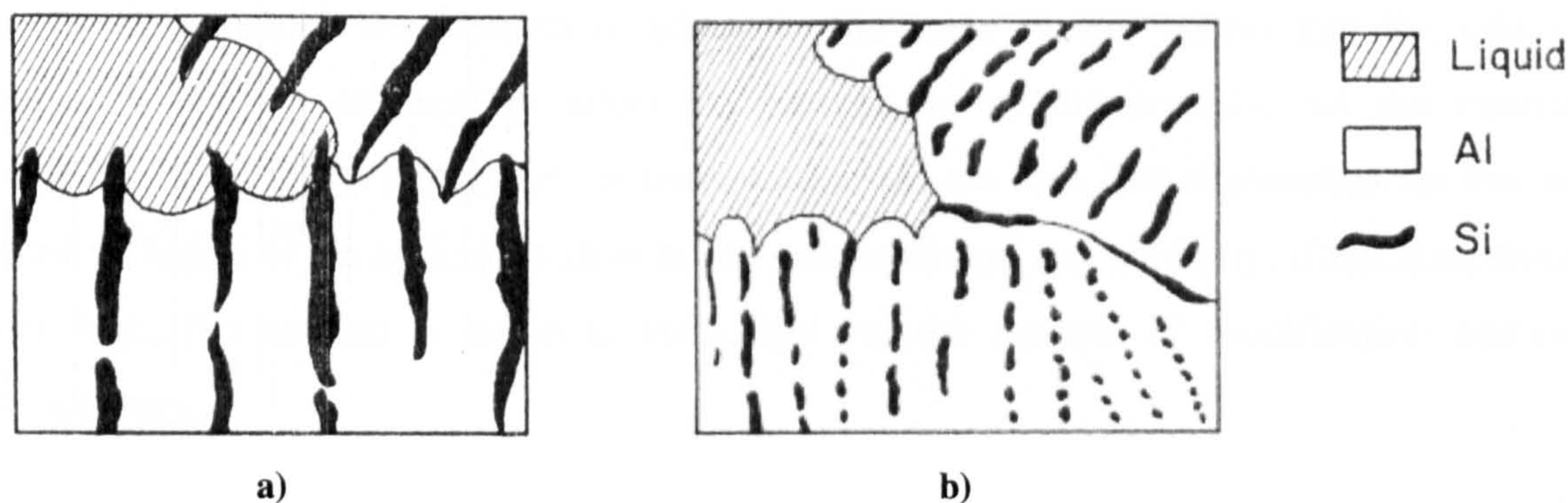


Figure 3.23 Silicon growth in **a)** unmodified alloy, and **b)** a modified alloy, after Crosley ^[Cro66]

In early work on the Al-Si eutectic microstructure ^[Day68, Ste72] it was proposed that the flake-fibre transition of silicon be related to an increase in the number of {111} twins in the phase with modification. It has since been established that in fact fibrous silicon contains very few twins, and that modification probably occurs by the twin plane re-entrant edge (TPRE) mechanism. This has been widely investigated by a number of authors ^[Cla89, Dav63, Flo81, Fre73, Kob85, Maj89, Sha86, Sha89] and was discussed fully in Section 3.3. In impurity modification, such as sodium or strontium additions, it is proposed that the modifying agent removes the growth advantage of the TPRE mechanism by concentrating at the re-entrant edges. It has been said that the most dominant facets in the unmodified silicon are associated with the {111} planes. This suggests that the {111} planes have the lowest surface energy and therefore grow the most slowly, eventually bounding the crystal. Positive adsorption of an impurity should reduce the surface tension of other planes relative to the {111} type, allowing these other planes to ‘compete’ as bounding planes on the external surface and therefore change the growth model to non-faceted.

Thus, the growth of flake-fibre transition is now considered to depend on one or both of two events: a) a reduction of the lead distance of silicon at the eutectic-liquid interface which leads to strongly coupled growth with a smooth solid-liquid interface; b) a partial transition of the silicon phase from faceted to non-faceted growth (TPRE mechanism).

3.6.2 Effect of Cooling Rate

Many works have investigated the effect of cooling rate on the effectiveness of the modifying additions and as a modification process in its own right with several theories having been suggested ^[Day68, Fat89, Kim 63, Kob85, Ota26]. An early study ^[Ota26] looked at the effect of the

temperature at which the sodium is added to the melt. It was found that the addition temperature did not appreciably affect the size of the silicon crystals, but the structure appeared to be seriously affected if the temperature was too low. The explanation for this was that the diffusion of the sodium is slow at low temperatures, and similarly, if the temperature is too high, the sodium is liable to evaporate and the process of modification becomes unsatisfactory.

Rate of diffusion as a function of temperature was also considered in a 'change in lead distance' mechanism similar to that suggested earlier for growth of modified silicon ^[Kob85]. In chill modification the most probable cause of the reduction in lead distance is a differential reduction in diffusion rate of the two species in the eutectic melt, so that the potential growth rate of the aluminium phase decreases less rapidly with falling temperature than that of the silicon phase. At the same time the faceting tendency of silicon is reduced with increasing undercooling so that semi-isotropic fibrous growth is possible when the critical transition temperature range is reached. Day and Hellawell ^[Day68] again related modification to rate of diffusion. High temperature gradients and slow freezing rates were seen to produce a planar aluminium front where large silicon particles grew by a relatively long-range diffusion process, whereas lower temperature gradients and more rapid freezing rates formed duplex solid-liquid fronts where growth occurred by short-range diffusion. At low rates silicon developed a $\langle 100 \rangle$ texture and had a morphology that developed from close packed fibres and at higher freezing rates the $\langle 100 \rangle$ texture of silicon disappeared and particles contained a high density of $\langle 111 \rangle$ twins. This theory could also be linked to the TPPE mechanism described earlier with regards to silicon modification by additions.

In 1963, Kim and Heine ^[Kim63] developed a theory of crystal-growth habit in relation to temperature of growth that was already well documented in the field of physical chemistry. They claimed that the silicon phase shape was temperature dependant, with one shape being grown at one temperature and by changing the temperatures, growth is continued in a shape characteristic of the second temperature. This hypothesis explained the role of addition elements in eutectic modification as depressants of the nucleation temperature, therefore decreasing the growth temperature and changing the growth shape from coarse plate to globular silicon.

Fast cooling rates produce Si particles of the same shape as in slowly cooled alloys but scaled down to much smaller dimensions. This modification of the structure is accompanied by the appearance of primary Al dendrites. Work carried out on the fine lamellar structure obtained under rapid cooling conditions found the material to exhibit microstructures and properties, which are not only better than those of slowly cooled alloys, but also comparable to the modified eutectic alloys ^[Fat89].

3.7 Summary

In this chapter the issues of solidification by nucleation and growth have been discussed with respect to both generic thermodynamics and the solidification of the Al-Si system in particular. Nucleation of a crystal occurs when the temperature of the melt supercools below the freezing temperature, although nucleation at a reduced supercooling is promoted by the presence of impurities which act as heterogeneous nucleation sites. Al_3Ti and AlP act as nucleants for the aluminium and silicon phases respectively. Growth of the crystals is then advanced as atoms attach themselves to the solid in a variety of structures depending on the composition of the alloy and thermal conditions. The latter sections of this chapter considered various casting practices developed to control the solidification of Al-Si alloys. Grain refinement was described as the addition of a grain refining addition, such as Ti, which serves to act as a nucleant for the aluminium phase, hence promoting a change in growth mechanisms from columnar to equiaxed. In modification, on the other hand, certain elements are added to hinder the growth of the silicon and produce fine, non-acicular particles less detrimental to the material properties. Thus, the final microstructure in a multicomponent Al-Si alloy is a complex function of alloy composition and casting conditions.

Chapter 4

Experimental Procedure

4.1 Introduction

This chapter introduces the various practical techniques used in the analysis of piston alloys in this research. Both commercial and model alloys were analysed in this work in order to build up an understanding of the effect of alloying additions and cooling rates on the microstructures of multicomponent near-eutectic Al-Si alloys. Due to the large number of complex intermetallic phases present in most commercial Al-Si alloys, a number of simpler model alloys were designed and cast to aid both in identification of phases, and to gain an understanding into the development of the complex microstructure.

4.2 Alloy Compositions, Casting Methods, and Heat treatments

The exact compositions of all the alloys (model and commercial) investigated in this work are given in Table 4.1, all of which were determined by spark analysis at Federal-Mogul. The various groups of alloys are discussed in the following sections.

4.2.1 Cylindrical Mould: Model Alloys 5, 7 to 11

The base alloy used in these castings was that of the eutectic Al-Si alloy, LM6 (BS 1490), composition given in Table 4.2. The effects of three alloying additions were studied: copper, nickel and manganese, both individually and in combination. The quantity of each element to be added was determined through study of commercial alloy compositions and the observation of the relevant binary phase diagrams ^[Day98]. In general, additions were made as follows (exact compositions are given in Table 4.1);

Alloys 5 and 11 have additions of Mn, and Mn and low Ni respectively.

Alloys 7 and 8 have low and high additions of Ni respectively.

Alloys 9 and 10 have low and high Cu additions respectively.

Table 4.1 Compositions of all alloys (commercial and model) investigated in this research

Alloy	Wt. % Element												ppm
	Si	Mg	Cu	Ni	Mn	Fe	Sn	Pb	Zn	Ti	Zr	V	P
Cylindrical Mould: Model Alloys 5, 7 to 11													
5	10.37	0.06	0.08	0.05	0.47	0.44		0.01	0.02	0.04			
7	10.83	0.07	0.08	1.19	0.09	0.47		0.02	0.02	0.04			
8	9.58	0.07	0.08	4.37	0.07	0.51		0.01	0.02	0.03			
9	10.47	0.06	1.10	0.06	0.08	0.47		0.01	0.02	0.04			
10	9.57	0.06	5.10	0.05	0.07	0.46		0.01	0.02	0.03			
11	10.24	0.07	0.08	1.04	0.49	0.48		0.01	0.02	0.03			
Keel Bars													
1/1	11.8	0.88	3.08	0.91	-	0.23				-	-	-	11
1/4	11.4	0.87	2.95	0.87	-	0.23				0.10	-	-	12
3/1	11.8	0.92	3.15	0.93	-	0.23				-	-	-	12
3/4	11.8	0.89	3.16	0.93	-	0.25				0.04	-	-	11
4/1	11.5	0.92	3.09	0.93	-	0.23				0.10	-	0.01	69
4/2	11.5	0.91	3.01	0.89	-	0.22				0.16	-	-	11
4/3	11.2	0.90	3.05	0.90	-	0.23				0.19	-	-	11
5/1	11.3	0.89	2.98	0.89	-	0.22				-	0.08	0.01	10
5/2	10.8	0.83	2.89	0.87	-	0.21				-	0.15	0.01	9
5/3	10.6	0.79	2.76	0.84	-	0.20				-	0.22	0.01	11
10/1	12.1	0.91	3.23	0.85	0.03	0.20				0.17	0.01	-	154
10/2	11.8	0.90	3.25	0.87	0.03	0.20				0.16	0.08	-	51
10/3	11.3	0.82	3.10	0.83	0.03	0.19				0.16	0.14	-	141
17/3	11.6	0.78	3.18	0.84	0.03	0.20				0.18	0.08	0.09	98
Model Alloys 24, 25 and 38													
24	11.6	0.99	3.50	2.40		0.31				0.18	0.11	0.05	80
25	11.6	0.99	3.80	2.73		0.31				0.16	0.12	0.065	59
38	11.94	0.76	3.49	2.28		0.28				0.13	0.12	0.12	66
Stepped Mould: Model Alloys 83 to 90													
83	12.5	0.63	3.62	2.53	0.19	0.50				0.01	0.01	0.01	48
84	12.3	0.65	3.605	2.38	0.18	0.49				0.01	0.01	0.09	42
85	12.2	0.62	3.52	2.36	0.18	0.48				0.01	0.14	0.085	40
86	12.1	0.68	3.48	2.4	0.18	0.48				0.15	0.15	0.09	40
87	14.1	0.68	5.02	2.94	0.2	0.47				0.015	0.01	0.01	48
88	14.2	0.70	5.09	2.92	0.2	0.47				0.01	0.01	0.08	43
89	14.1	0.63	5.01	2.8	0.19	0.48				0.01	0.14	0.09	48
90	14.2	0.68	4.91	2.82	0.19	0.48				0.15	0.13	0.09	53
Stepped Mould: Model Alloys 3													
3/1	12.45		0.17	0.12		0.30				0.008	-	-	18
3/2	12.49		0.17	0.13		0.31				0.051	-	-	16
3/3	12.34		0.16	0.12		0.30				0.148	-	-	16
3/4	12.20		0.09	0.10		0.38				0.007	0.221	-	12
3/5	12.15		0.07	0.03		0.20				0.009	0.005	0.063	15
3/6	12.11		0.12	0.08		0.22				0.009	0.142	0.020	10
Commercial Alloys													
AE113	10.5-12.5	0.8-1.2	2.5-3.5	0.7-1.3	0.15	0.4	0.1	0.1	0.1	0.2			30
AE413	12.3	1.0	1.2	0.82	0.22	0.6	0.01	0.03	0.1	0.07			15
AE135	12.5-14.0	0.8-1.3	4.5-5.5	0.8-1.3	0.1	0.5	0.1	0.1	0.2	0.2			30
AE160	11.2	1.05	3.1	2.27	0.08	0.3				0.17	0.15	0.06	53
Nüral S2	12.0	1.1	3.4	2.3	0.1	0.4			0.05	0.01			
Mahle 142	12.0	0.75	3.5	2.5		0.3				0.15	0.15	0.1	0.02
FMS2N	12.3	1.0	3.6	2.5	0.2	0.5				0.05	0.16	0.08	
FMB2	14.5	1.0	4.2	3.1	0.15	0.5				0.05	0.07	0.07	

Table 4.2 Standard composition of LM6 (wt. %)

Si	Mn	Ni	Cu	Mg	Fe	Zn	Pb
10 - 13	< 0.5	< 0.1	< 0.1	< 0.1	< 0.6	< 0.1	< 0.1

Balance is Al, all other elements unspecified

The casting was carried out at Loughborough University[†] using a process designed to be as close to that used in industry as possible. The LM6 base alloy was accurately weighed, melted in a furnace at between 850 °C and 900 °C where the required alloying additions were introduced via master alloys of the appropriate weight. After all the additions had dissolved, the melt was stirred and the crucible removed from the furnace; flux and degasser were then added and the melt mixed well. Finally the resulting slag produced by the fluxing was skimmed from the surface, and the liquid metal poured into a metal mould. A two piece cylindrical metal mould was used with a cross-section of 2.5 cm diameter and approximately 9-10 cm in length, see Figure 4.1.

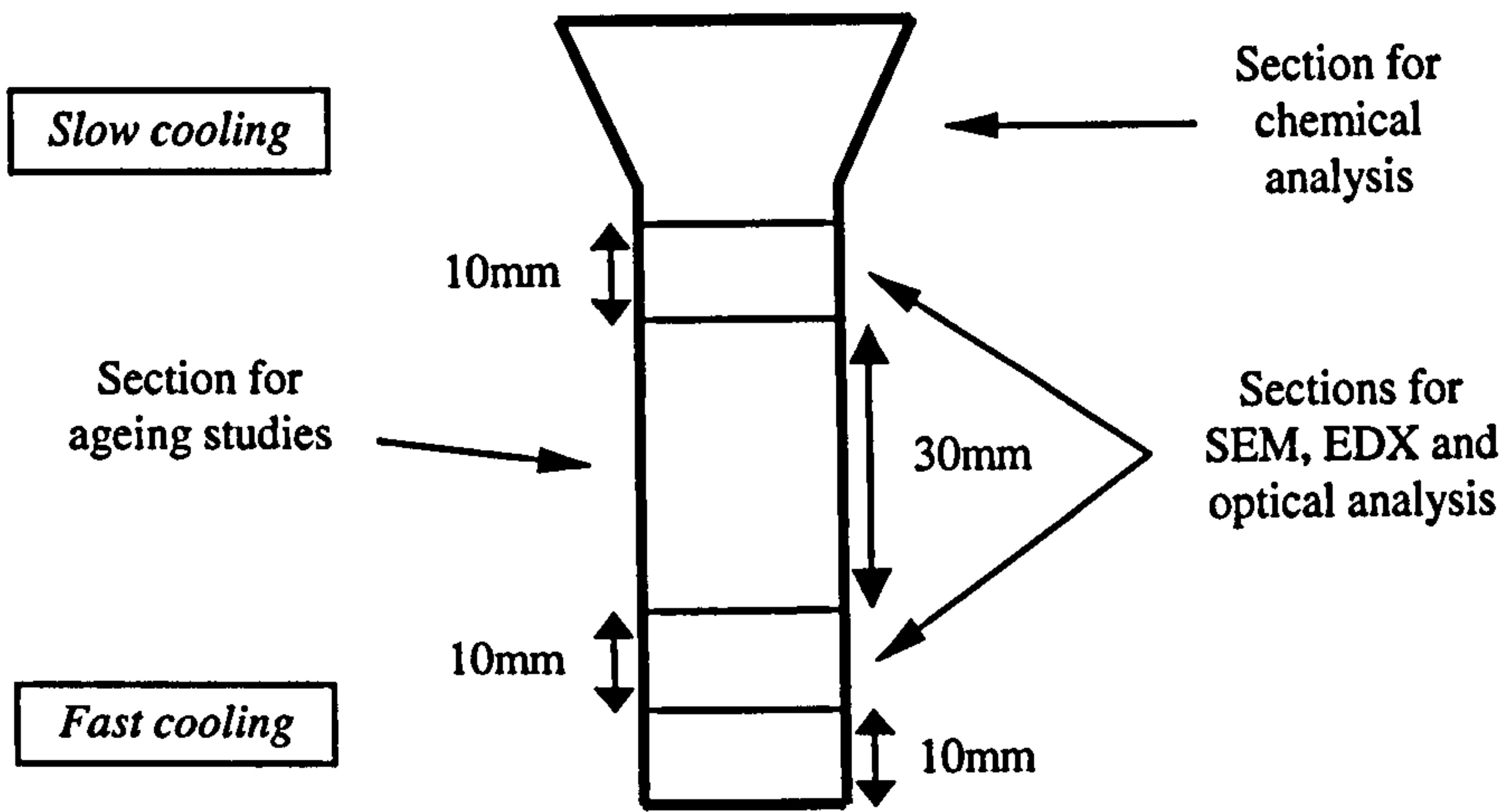


Figure 4.1 Cross-section of cylindrical mould casting, model alloys 5, 7 to 11

Once the castings had solidified they were removed from the mould and allowed to air-cool to room temperature. A section from the lower end of the casting where the fastest cooling rate was seen was chosen for analysis as it was thought to best represent the cooling rate seen in

[†] The casting was carried out by C. R. S. Daykin and T. Atkinson

the commercial piston casting process. The cooling curve of a typical air-cooled pure LM6 casting is shown in Figure 4.2 and is thought to be representative of the air-cooled model alloys 5, 7-11.

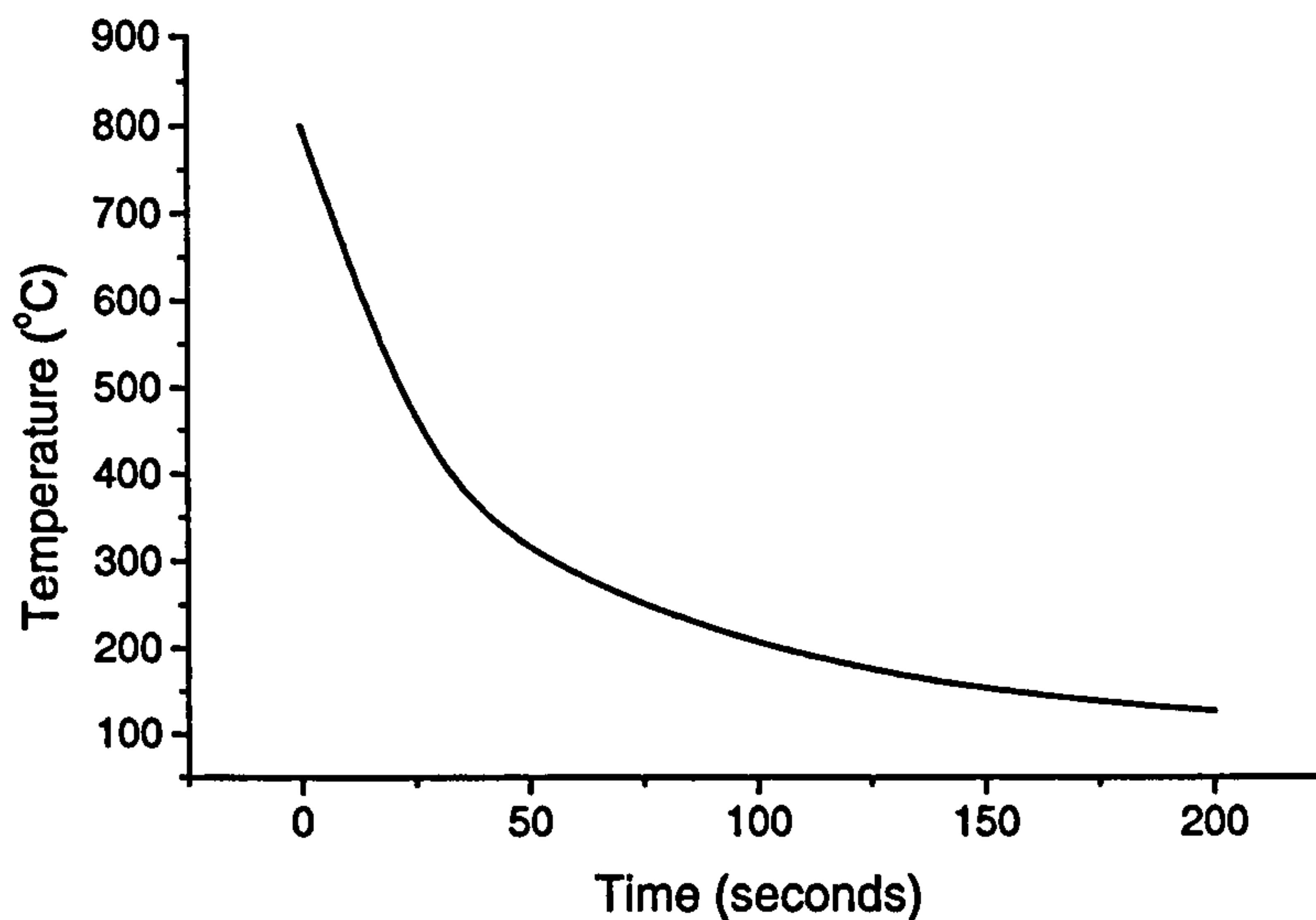


Figure 4.2 Cooling curve for a pure LM6 casting

Two different heat treatments were carried out on samples of model alloys 5, 7-11, both aimed at producing a microstructure close to equilibrium and therefore representative of a piston microstructure after ageing. Temperature profiles for both heat treatments can be seen in Figure 4.3. The time is on a log scale in order to represent the long times at which the alloys were held at the appropriate heat treatment temperatures. The first treatment involved pieces of each of the six alloys being heated to 748 K whilst sealed in a partial pressure of argon in quartz tubes. 748 K was chosen as it was sufficiently high to allow rapid diffusion but presented no risk of remelting. The samples were held for 50 days before being rapidly cooled and the phases present re-analysed. The second heat treatment was executed in muffle furnaces, with samples of each of the alloys placed in alumina crucibles set in a mild steel block. The process involved heating the samples to a temperature of 903 K, above the liquidus, and holding for 1 – 2 hours to ensure complete melting before cooling to 838 K, just below the liquidus, where it was held for 7 days. This was aimed at enabling an isothermal transformation within the ‘mushy’ zone (both liquid and solid phases present). The sample

was then ‘splat’ quenched[†] in order to freeze the microstructure for analysis. ‘Splat’ quenching involved pouring the molten sample out of the crucible onto a thick steel plate, and once the ‘blob’ had definitely solidified, quenching in water[‡].

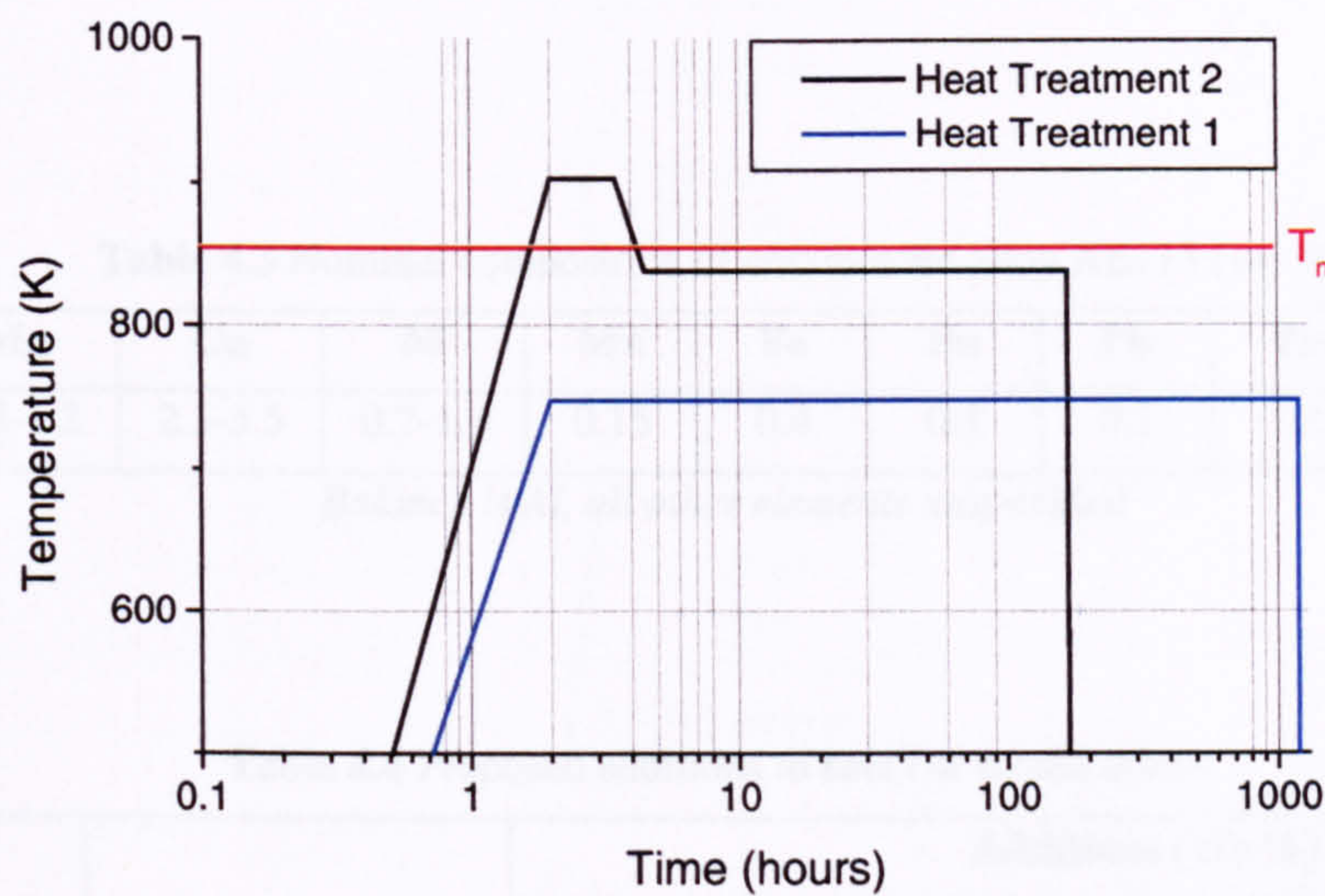


Figure 4.3 Heat treatment profiles for model alloys 5, 7 to 11

4.2.2 Keel Bars

Following work carried out by Daykin [Day98], a brief experimental program was set up to investigate the effects of titanium, zirconium and vanadium additions on the grain size of cast Al-Si piston alloys. 14 alloys were designed based on the commercial alloy AE113 (proposed compositions below in Table 4.3, and actual compositions given in Table 4.1), and two investigations were carried out.

The first set of castings were based on the AE113 composition but with no Ti or P additions (Base alloy #1). To this additions of titanium were introduced using several different types of Ti-containing master alloy. In alloy 1/4 the titanium was added with a TiBA1 - TiB₂ grain refiner, in alloy 3/4 the titanium was added as Nucleant 70, a Foseco grain refining agent, and in alloys 4/1 to 4/3, an AlTi₆ master alloy was used to supply the titanium. Using the AlTi₆ master alloy, model alloys 4/1 to 4/3 were cast to investigate the effect of different amounts of Ti according to Table 4.4. A similar practice was carried out with comparable amounts of

[†] Private communication with H. Cama, AlCan, Banbury
[‡] These heat treatments were carried out with the help of Mr. P. Fossati who visited Loughborough University under funding by the European Commission through the provision of a Leonardo Fellowship.

Ti according to Table 4.4. A similar practice was carried out with comparable amounts of zirconium added via an AlZr₅ master alloy. Commercial AE113 stock nominally contains 0.15 wt. % Ti and 30 ppm phosphorus (Base alloy #2), and so the second part of the casting investigated the effect of titanium, zirconium and vanadium additions to the commercial alloy.

Table 4.3 Nominal composition of commercial alloy AE113 (wt. %)

Si	Mg	Cu	Ni	Mn	Fe	Sn	Pb	Zn	Ti	P (ppm)
10.5-12.5	0.8-1.2	2.5-3.5	0.7-1.3	0.15	0.4	0.1	0.1	0.1	0.2	30

Balance is Al, all other elements unspecified

Table 4.4 Proposed additions to keel bar model alloys

Alloy Designation	Base alloy	Additions (Wt.%)		
		Ti	Zr	V
1/1	1	-	-	-
1/4	1	0.15	-	-
3/1	1	-	-	-
3/4	1	0.15	-	-
4/1	1	0.10	-	-
4/2	1	0.15	-	-
4/3	1	0.20	-	-
5/1	1	-	0.10	-
5/2	1	-	0.20	-
5/3	1	-	0.30	-
10/1	2	0.15	-	-
10/2	2	0.15	0.10	-
10/3	2	0.15	0.20	-
17/3	2	0.15	0.10	0.10

The alloys were cast at Federal-Mogul into a keel bar mould with cross section dimensions as given in Figure 4.4. From these bars transverse slices were cut, approximately 10 mm in thickness, ground, polished and macroetched for optical analysis. The samples were then sectioned as shown, the circular top being sent for accurate spark analysis at FMT, and the middle section being mounted in Bakelite, reground and polished to 1 µm, as before. A third

slice was also cut from selected alloys for heat treatment at 350 °C for 100 hours before mounting, grinding and polishing for further investigation[†].

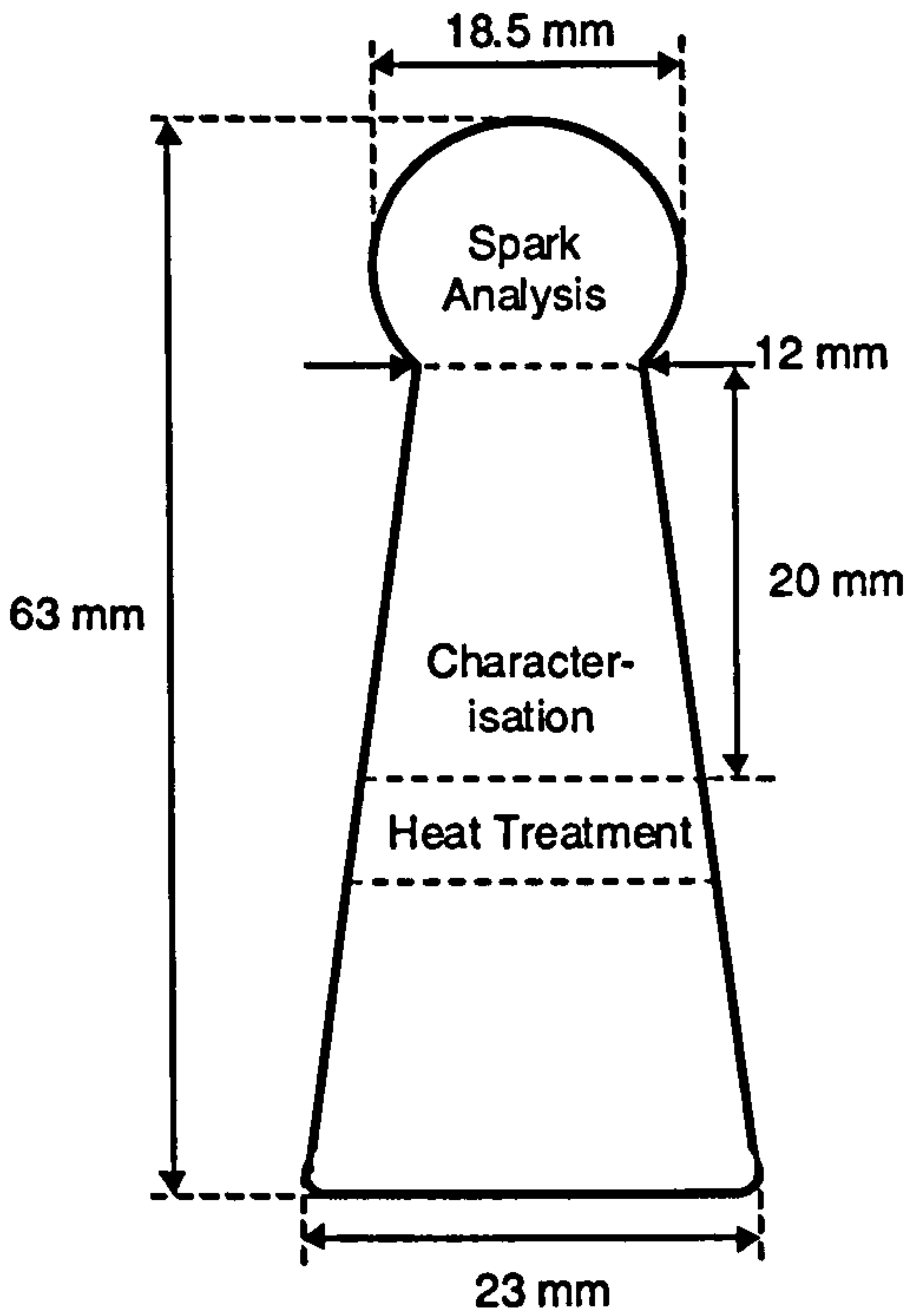


Figure 4.4 Schematic diagram of the cross section of a keel bar casting

4.2.3 Commercial Alloy AE160 and Model Alloys 24, 25 and 38

Alloy AE160 is a commercial piston alloy with additions of Ti, Zr and V, elements previously not used in Federal-Mogul piston alloys. The additions were made following an investigation of competitor piston materials which were found to have improved properties as a result of the grain refining elements. This was discussed in Section 2.6. Although in production, to date, very little analysis has been carried out on AE160 (composition in Table 4.1 and below in Table 4.5) to understand the mechanism behind the improvement in properties, particularly high temperature fatigue strength, in relation to the microstructure. Thus, a thorough analysis of this alloy was executed in this research, particular interest being paid to characterisation of the secondary, or intermetallic, phases.

[†] This work was carried out with the help of project student, S. Needham.

Table 4.5 Nominal composition of commercial alloy AE160 (wt. %)

Si	Mg	Cu	Ni	Mn	Fe	Ti	Zr	V	P (ppm)
11.2	1.05	3.1	2.27	0.08	0.3	0.17	0.15	0.06	53

Balance is Al, all other elements unspecified

The material used for analysis was taken from the centre of the crown of a 75 mm diameter piston cast on the production line at Federal-Mogul Piston Technology, Bradford. The production conditions under which the casting took place are with the mould temperature being the residual temperature of the previous casting (~ 100 °C), and the pistons being air-cooled. Model alloys 24, 25 and 38 were cast in small (75 mm diameter) piston moulds in the foundry at Federal-Mogul Technology, Cawston, in the same way as they would have been cast in production. The composition is based on alloy AE160, but with controlled additions of vanadium at 0.05, 0.065 and 0.12 wt. % V in addition to the Ti and Zr. The exact compositions are given in Table 4.1.

4.2.4 Stepped Mould: Model Alloys 83 to 90

Following the grouping of Federal-Mogul and Nüral there was a need to standardise and produce a common specification for the composition and manufacture of piston alloys. This was achieved by the design of alloys FMS2N and FMB2. As discussed in Section 6.2, FMS2N has a very similar composition to both AE160 and Nüral S2, the major difference being the addition of Ti, Zr and V not previously used by Nüral. As a large amount (~ 0.15 wt. %) of Ti causes problems in casting by Nüral, the Ti, Zr and V contents were reduced for FMS2N as seen in Tables 4.1 and 4.6. A higher silicon and copper version of FMS2N was also conceived and designated FMB2.

Table 4.6 Nominal composition of commercial alloys FMS2N and FMB2 (wt. %)

	Si	Mg	Cu	Ni	Mn	Fe	Ti	Zr	V
FMS2N	12.3	1.0	3.6	2.5	0.2	0.5	0.05	0.16	0.08
FMB2	14.5	1.0	4.2	3.1	0.15	0.5	0.05	0.07	0.07

Balance is Al, all other elements unspecified

Based on the commercial alloys FMS2N and FMB2 two sets of model alloys were designed not only to investigate additions of titanium, zirconium, and vanadium, but also cooling rate effects. Model alloys 83 to 86 were based on FMS2N and additions of Ti, Zr, and V were made by master alloys to investigate the grain refining effect of these elements individually (V) and in combination (V + Zr and V + Zr + Ti), as found in Table 4.1. Alloys 87 to 90 contained the same additions, but to a FMB2 base alloy.

The alloys were cast in the foundry at Federal-Mogul, Cawston, into stepped moulds of shape and dimensions as in Figure 4.5, the mould being filled from step 5. The moulds were used at two temperatures; pre-heated to 440 °C, and at the residual temperature of the previous casting around 100 °C. In each of the castings thermocouples were placed in the first, third and fifth steps of the mould to monitor the cooling rate of that step. The average cooling rates for steps 3 and 5 are given in Figure 4.5, however, step 1 cooled too quickly for any measurement to be taken. Large pistons (120 mm diameter) were also cast from each of the alloys. Thermal analysis was carried out on samples from the same melt of these alloys using an Ideco machine at Federal-Mogul. This equipment measures the cooling curve for a slowly cooled sample of the alloy, and values of liquidus and solidus are determined from discontinuities in the curve. However, this machine is not particularly sensitive and therefore results should be treated with caution.

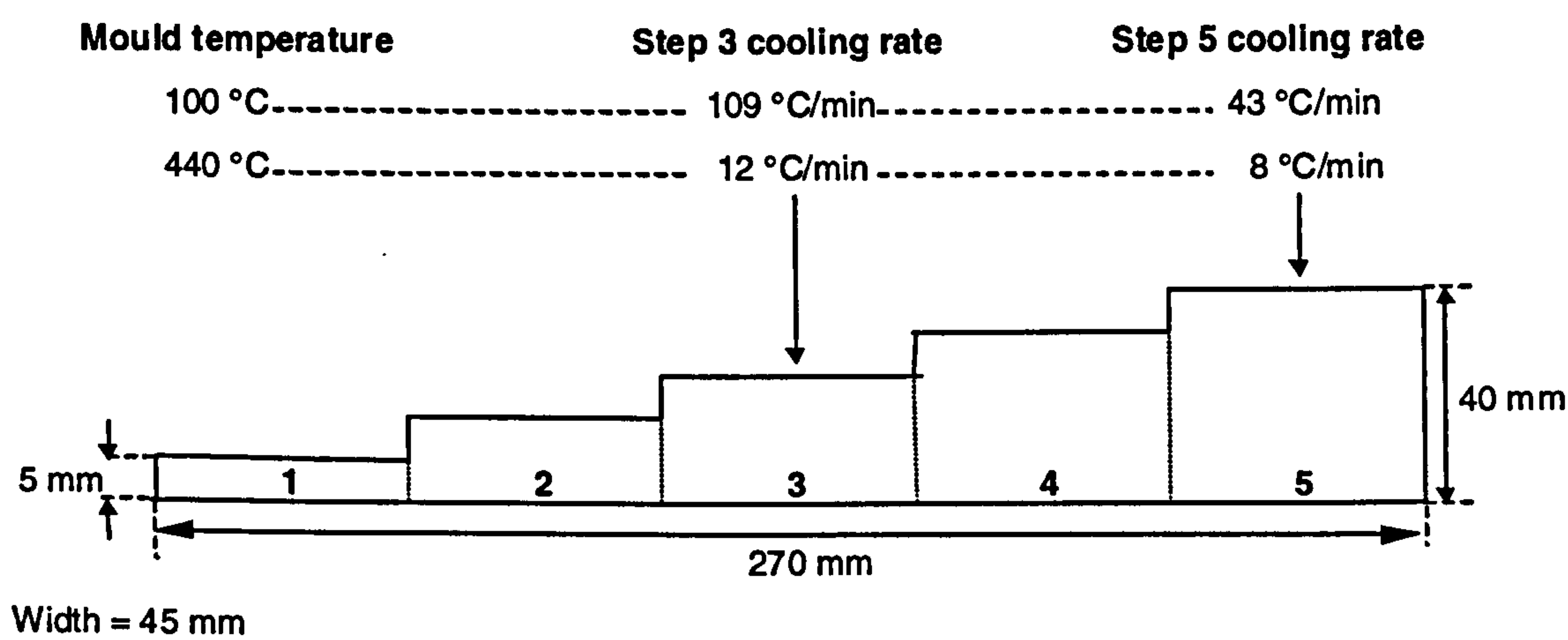


Figure 4.5 Cross-section of a stepped mould, model alloys 83 to 90 (and subsequently model alloys 3)

The stepped castings were sectioned lengthways and prepared for macroscopic analysis to expose the grain structure across each of the steps, and similarly, the pistons were cut in half to reveal the structure in both the crown (slow cooling rate) and skirt (fast cooling rate). From the photomacrographs, step 4 from the 100 °C mould was established to be most representative of a piston crown. To obtain an overview of both cooling and compositional effects further analysis was focused on samples from the centres of the first, third and fifth steps of each alloy. In addition to the as-cast samples, pieces of alloys 83 and 85 were aged by heating in a furnace at 350 °C for 100 hours in accordance with the commercial process, to investigate any microstructural changes as a result of ageing.

4.2.5 Stepped Mould: Model Alloys 3

Despite controlling the Ti, Zr, and V additions in model alloys 83 to 90, the effect of these elements appears to be complicated by the presence of the numerous other components. Therefore, model alloys 3, a series of simple ternary Al-Si-X (X = Ti, Zr, V) alloys were formulated to isolate the effect of the grain refiners. Designed with the use of growth restriction parameter calculations (introduced in Section 3.5.4), these model alloys were based on the simple Al-12 wt.% Si system with systematic additions of increasing Ti (3/1 to 3/3), and Zr and V both individually and in combination (3/4 to 3/6). The proposed compositions are given in Table 4.7, and exact compositions in Table 4.1. The final compositions contain small amounts of Cu, Ni, and Fe, as these elements are present as impurities in the melt stock, although these minor additions should have little effect on the final microstructure.

Using the stepped moulds at both 100 and 440 °C temperatures (as seen previously in Figure 4.5) model alloys 3 were cast using master alloys to make the appropriate additions. The solidified castings were then sectioned lengthways and prepared for macroscopic analysis to expose the grain structure across each of the steps. Once photographed, fairly large samples (12 × 20 × 10 mm) were cut from the step 4 (thought to be most representative of a piston casting) for mounting and preparation for optical and electron microscopy.

Table 4.7 Proposed compositions of stepped mould model alloys 3

	Al	Si	Ti	Zr	V
3/1	Bal.	12	0.01	-	-
3/2	Bal.	12	0.05	-	-
3/3	Bal.	12	0.15	-	-
3/4	Bal.	12	-	0.26	-
3/5	Bal.	12	-	-	0.05
3/6	Bal.	12	-	0.12	0.03

4.3 Analysis Techniques

4.3.1 Sample Preparation

For macrostructural analysis the castings were sectioned using a rotary saw with liquid coolant before grinding on SiC paper to 1200 grit and polishing to 1 µm diamond. For all other analyses pieces of material, approximately 1 cm³ in size, were cut from the centres of the castings (centre of the crown for pistons, centre of the step for stepped moulds) in order to avoid any surface effects. These cubes were mounted in conducting Bakelite, ground on SiC paper to 1200 grit and polished at 6 µm diamond on an un-napped cloth and 1 µm diamond on a napped cloth. The polishing time was kept as short as possible to avoid any relief of the phases. For electron backscatter diffraction in the scanning electron microscope and image analysis an additional polish of 0.06 µm colloidal silica was required and carried out using a Bhueler Vibromet, for approximately 1 hour with a weighted holder of 500 g.

For transmission electron microscopy (TEM) sections approximately 200 µm in thickness were cut using a Struers Accutom-5, from which 3 mm diameter discs were then removed using a spark erosion machine. These discs were then ground down to between 50 and 100 µm thickness and polished to a 6 µm finish on a diamond cloth. Thin foil samples were prepared in an Ion Tech ion beam thinning instrument using argon ions at an energy of 5-6 kV. The bombardment angle was first set at 30 °, and reduced to a small angle of ~ 5 ° to finish until penetration was visible.

4.3.2 Optical Microscopy

Macrographs of cross sections of both the stepped moulds and piston sections were taken both at Federal-Mogul and at Loughborough University. At Federal-Mogul a version of Keller's macro-etch (1 % HF, 2.5 % HNO₃, 1.5 % HCl, 95 % H₂O (% vol)) was applied to the polished sections (after ultrasonically cleaning to remove debris from the pores) by swabbing with cotton wool soaked in etchant until the structure appeared, then washed very thoroughly with water and dried with the aid of isopropanol. The photographs were taken using a Nikon Coolpix 990 camera. The aforementioned etch did not work, however, for the model alloys with very low alloying additions (i.e. the Al-Si binaries). It is believed that this is because the etch relies on attacking the intermetallics, of which very few were present in model alloys 3. An alternative etch, Tuckers reagent (45 ml HCl, 15 ml HNO₃, 15 ml HF, 50 ml H₂O), was made up at Loughborough University, in which the samples were immersed for 5 seconds before rinsing in warm water and drying with the aid of alcohol. The macrographs were taken using a Pentax single lens reflector camera with a macro lens using Ilford 35 mm monochrome film, 100 ASA.

To view the microstructures optically the samples were etched in a 0.5 % vol. HF in water aluminium etch for 15 seconds before thoroughly rinsing with alcohol and drying. The colour micrographs were taken on a Reichart MEF3 microscope, usually in bright field mode. Differential interference contrast mode was also used to reveal features by their refractive index inhomogeneities, such as growth traces, often not seen in standard light microscopy. Pictures were taken on the attached camera with Fujifilm 35 mm colour film, 200 ASA.

4.3.3 Image Analysis

Two different types of image analysis were carried out. The first type of image analysis investigated the macroscopic grain structure, and was used solely for the keel bar model alloys. The aluminium grains visible on enlarged optical macrographs (taken after etching) were traced onto acetate by hand, before the acetate was scanned into the system by an Oscar CCD Camera with Vivitar macro lens. A Foster Findlay Associates C_IMAGES Image Analysis and Processing Library system software was then used to determine grain sizes which could be accessed by hand to remove any anomalies.

The second type of image analysis was carried out at Federal-Mogul using a ProgRes 3008 High Resolution Colour Camera for Light Microscopy, and KS 400 and 300 software

programs for the data collection and analysis respectively. A beam scanned over a selected area of a sample to capture and store images of the microstructure according to the data collection macro. Subsequent analysis used another macro, whereby the user had to input variables such as minimum and maximum particle sizes, and decide the margins by which primary and secondary silicon, and intermetallics were separated. The sequence was repeated four times to reduce the variation produced by user-set thresholds. The two software macros used, one for data collection and one for data analysis, are given in Appendices B and C.

In processing the data, some statistical analysis was used consistent with basic statistics [Lar01]. The 90% maximum length of phases was calculated by;

$$\text{Total number of maximum length measurements} \times 0.9 \quad [4.1]$$

This number corresponded to a measurement when all the values had been sorted in ascending order. A confidence interval (CI) was calculated for the sample mean to indicate a range within which it is believed the population mean lies. It is calculated by the following formula;

$$CI = X \pm \frac{ts}{\sqrt{n}} \quad [4.2]$$

where X is the sample mean, s is the sample standard deviation, and n is the number of observations. The value of t is obtained using mathematical theory and can be read from tables such as that presented in Appendix D. A confidence interval of 95% was used and as there are 3 degrees of freedom (degrees of freedom = number of tests – 1) the value of t is defined as 3.18.

4.3.4 Transmission Electron Microscopy

Transmission electron microscopy (TEM) was carried out using a Jeol 2000FX at 200 kV and fitted with an Oxford Instruments/Link Analytical AN 10/25S energy dispersive X-ray (EDX) detector.

4.3.5 Scanning Electron Microscopy

Scanning electron microscopy (SEM) was carried out on two machines. First, a Cambridge Instruments Stereoscan 360 with an Oxford Instruments AN10000 EDX instrument with a standard beryllium window detector, using an accelerating voltage of 20 kV and working distance of 25 mm. Both backscattered and secondary electron techniques were used for spot chemical analysis of phases pre-marked with a microhardness indenter of which optical micrographs had been taken. This enabled chemical compositions to be accurately coupled with phase morphology and colour.

The second SEM used was a Leo 1530 VP field emission gun (FEG) SEM with an EDAX Pegasus system comprising EDX equipped with an ultra-thin window and electron backscatter diffraction (EBSD). The operating voltage used was 20 kV at working distances ranging from 12 to 16 mm. The EBSD enabled simultaneous chemical analysis and crystallographic data to be collected for large areas of the sample. This was analysed by one of two commercial packages produced by TexSEM Laboratories: Orientation Imaging Microscopy (OIM) and Delphi phase identification. Delphi was used to produce material files containing both the crystallographic and chemical data of each phase, which could then be used in OIM for mapping the orientation of selected areas of the microstructure. OIM was also used for low magnification mapping to reveal the true crystallographic macrostructure of the material. As EBSD was used extensively in this work and is a relatively new analysis technique, it will be discussed further now with particular attention to the interpretation of data.

Electron Backscatter Diffraction (EBSD)

The EBSD technique relies on the positioning of a prepared specimen within the SEM sample chamber to form an inclined surface of ~70 degrees so that a small angle (~20 degrees) is made between the incident electron beam and the specimen surface. When an electron of narrowly defined energy (such as that formed in a SEM) strikes a crystal, the electrons disperse beneath its surface and subsequently diffract in a systematic manner. These diffracted electrons are detected by a phosphor screen placed close to the sample in the SEM sample chamber. A pattern composed of intersecting bands, termed Kikuchi bands, is formed by the diffracted electrons on the phosphor screen and these bands are representative of lattice planes in the diffracting crystal. The width and intensity of the bands are directly related to the spacing of atoms in the crystal planes, and the symmetry of the crystal lattice is reflected in

the pattern. The diffraction pattern is averaged and background corrected and then digitised into the computer memory where it is automatically or manually indexed. The following data are calculated and stored: three Euler angles defining the orientation of the crystal (ϕ_1 , Φ , ϕ_2); (x , y) coordinates giving the position where the data was obtained on the specimen; an image quality (IQ) factor defining the sharpness of the diffraction pattern; a confidence index (CI) indicating the degree of confidence that the indexing is correct; and an integer defining the phase of the material.

It is not the intention of this section to provide a complete introduction to crystallography and orientation analysis, however, some of the essential concepts as they relate to OIM will be reviewed. In particular it is necessary to describe the relationship between the specimen co-ordinate system and the crystal co-ordinate system, as in order to specify an orientation it is necessary to have defined both sets of reference axes. A schematic diagram of the geometry for imaging EBSD patterns is shown in Figure 4.6 with both systems Cartesian and right-handed.

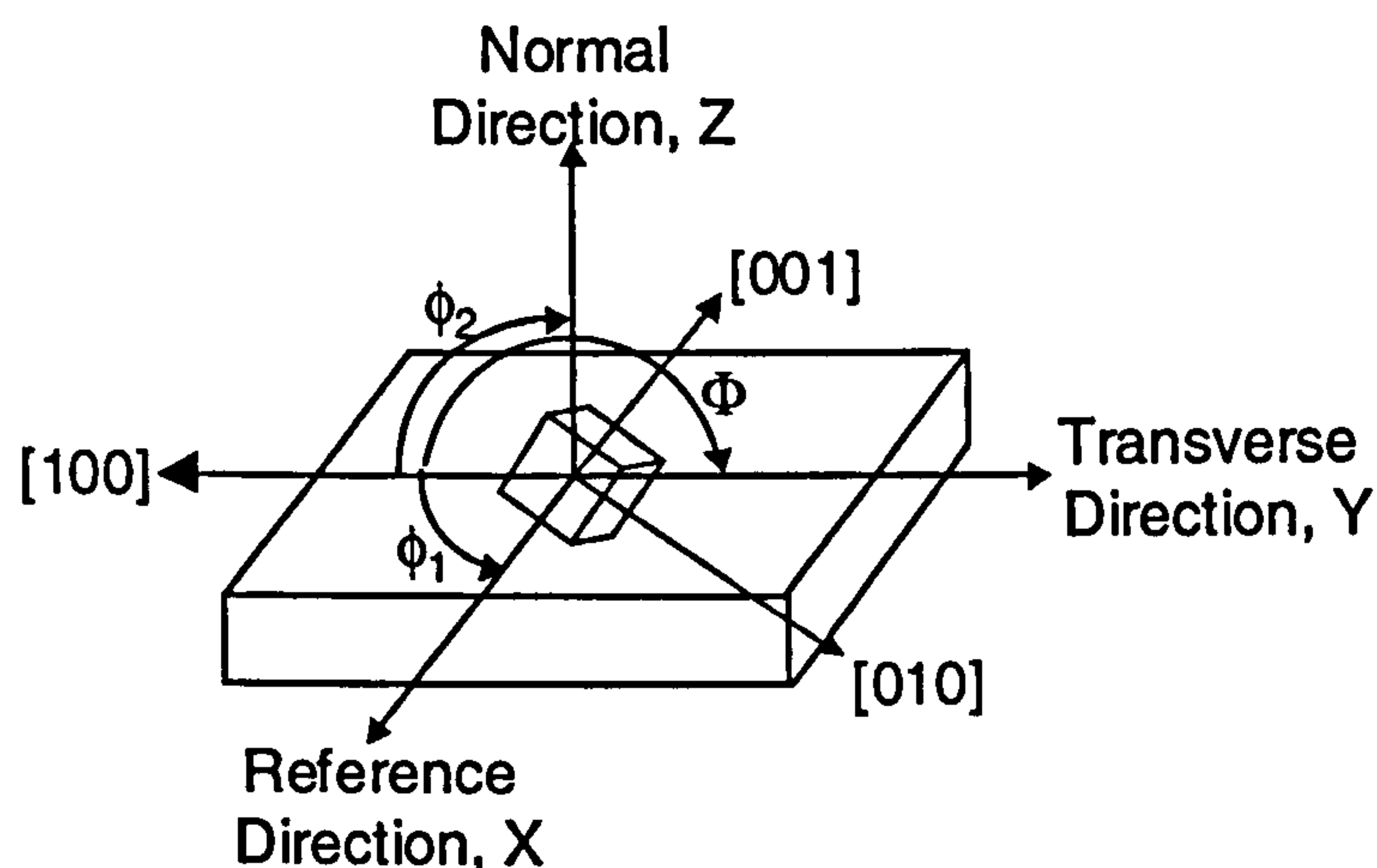


Figure 4.6 Schematic diagram showing the sample and crystal (in blue) geometries for imaging EBSD patterns, with corresponding Euler angles

The axes of the sample or specimen co-ordinate system are chosen according to important surfaces or directions associated with the external shape of the specimen. The important thing to note here is the definition of sample reference frame, shown in Figure 4.6, as this is used throughout the OIM software. The axes defining the sample co-ordinate system are the

reference direction, RD, for the 'X' axis (often called rolling direction in texture studies), the transverse direction, TD, for the 'Y' axis, and the normal direction, ND, for the 'Z' axis. ND is a direction normal to the sample surface and RD is parallel to the direction of tilt of the sample. In scans generated by OIM the horizontal or x direction is from left to right and corresponds to the horizontal direction or TD on the sample. The vertical direction in these maps is from top to bottom and corresponds to the tilt direction of the sample in the microscope or RD.

A direction in a crystal can be specified using the principal axes of the unit cell of the crystal structure, namely u , v and w , where the unit distance along these axes are equal to the lattice parameters. Because of symmetry in the crystal lattice, there may be several symmetrical equivalent directions for any given direction. For example, in the case of a cubic crystal, a rotation of 90 degrees about one of the principle axes of the cube would produce a structure that is crystallographically equivalent to the original structure prior to the rotation. The notation $[uvw]$ is used to denote a single direction and $\langle uvw \rangle$ denotes the family of symmetrically equivalent directions.

Planes in a crystal can be defined in a similar manner to the crystal directions. In this case, the indices are termed Miller indices. A given plane is denoted as (hkl) and a family of crystallographically symmetric planes as $\{hkl\}$. For a cubic crystal, the normal to a plane (hkl) , also termed a pole, is the direction $[hkl]$ as shown in Figure 4.6. Thus, the precise definition of the indices used to describe planes and directions is sometimes loosely used. However, in non-cubic crystal systems, one must be precise in distinguishing between the indices used to define directions and those used to define planes.

Having specified the specimen and crystal co-ordinate systems, an orientation is then defined as the position of the crystal with respect to the specimen co-ordinate system, thus describing the orientation of the principal axes of the crystal ($[100]$, $[010]$ and $[001]$) relative to the principal axes of the sample (RD, TD and ND). The Euler angles are a set of three angles about the principal axes of the crystal that can be used to describe the rotations necessary to bring the axes of a crystal lattice into coincidence with the axes of the sample. Bunge's form of the Euler angles (ϕ_1 , Φ , ϕ_2) are shown in Figure 4.6 and are defined as follows. It is assumed that the crystal frame of reference is parallel to the specimen co-ordinate system. It is then rotated successively through three sets of rotations: ϕ_1 about the Z-axis, Φ about the new

X-axis, and ϕ_2 about the new Z-axis. The angles ϕ_1 and ϕ_2 range from 0 to 2π and Φ ranges from 0 to π . These limits form a bounded space referred to as Euler space.

While the concept of a grain in conventional metallography is commonly understood, the definition of a grain in an OIM scan is slightly different. Grains in OIM are formed by an algorithm that groups sets of connected and similarly oriented points into 'grains'. For each point in the OIM scan, the neighbours of that point are checked to see if they are within the grain tolerance angle of the given point. If a neighbouring point is found then the neighbours of this point are checked to see if they are within the tolerance angle. The procedure is repeated over and over again until the set of connected grains is bounded by points which exceed the tolerance angle. Using this approach, the point to point misorientation in a 'grain' will be quite small but the spread of orientation among all the points in the 'grain' can be relatively large. The number of points required to decide whether a given group of points should be considered a 'grain' group (the minimum grain size) can be specified by the user along with the grain tolerance angle. Thus, the definition of a grain in OIM can vary depending on user-specified values.

Once this crystallographic information has been collected, it can be represented in a number of graphical approaches. The most commonly used forms, will be briefly reviewed here with respect to sample and/or lattice plane orientation, namely; pole figures and inverse pole figures represented in terms of stereographic projections, and orientation distribution functions projected in Euler space.

Pole figures provide a means of plotting orientations as two-dimensional projections. Such figures can be useful for simplifying the analysis of the orientation distribution. Figure 4.7 shows how a cubic crystal is considered to sit at the centre of the stereographic sphere with the orthogonal reference directions as X, Y and Z-axes. The orientation of this crystal can be represented by plotting its three {100} poles at the appropriate angular positions relative to the sample reference directions as defined by ND, TD and RD. In practice, all poles concerned are projected on to the equatorial projection plane to produce a stereographic projection as shown. For a polycrystalline material, all the grains must be considered and the three {100} poles must be plotted for each to give the pole figure shown in Figure 4.7. If we consider a sample with sheet geometry and a cubic crystal symmetry, the orientation data from ten grains can be presented together by plotting the positions of their {100} poles on a

single stereographic projection plane parallel to the sheet surface. Since each grain has three $\{100\}$ poles there will be 30 (3×10) poles plotted on the projection. If the resulting poles are distributed uniformly over the area of the projection there is no preferred orientation and the specimen is said to have a random texture. If a preferred orientation does exist however, the poles will tend to cluster together into certain areas of the projection, leaving other areas virtually unoccupied.

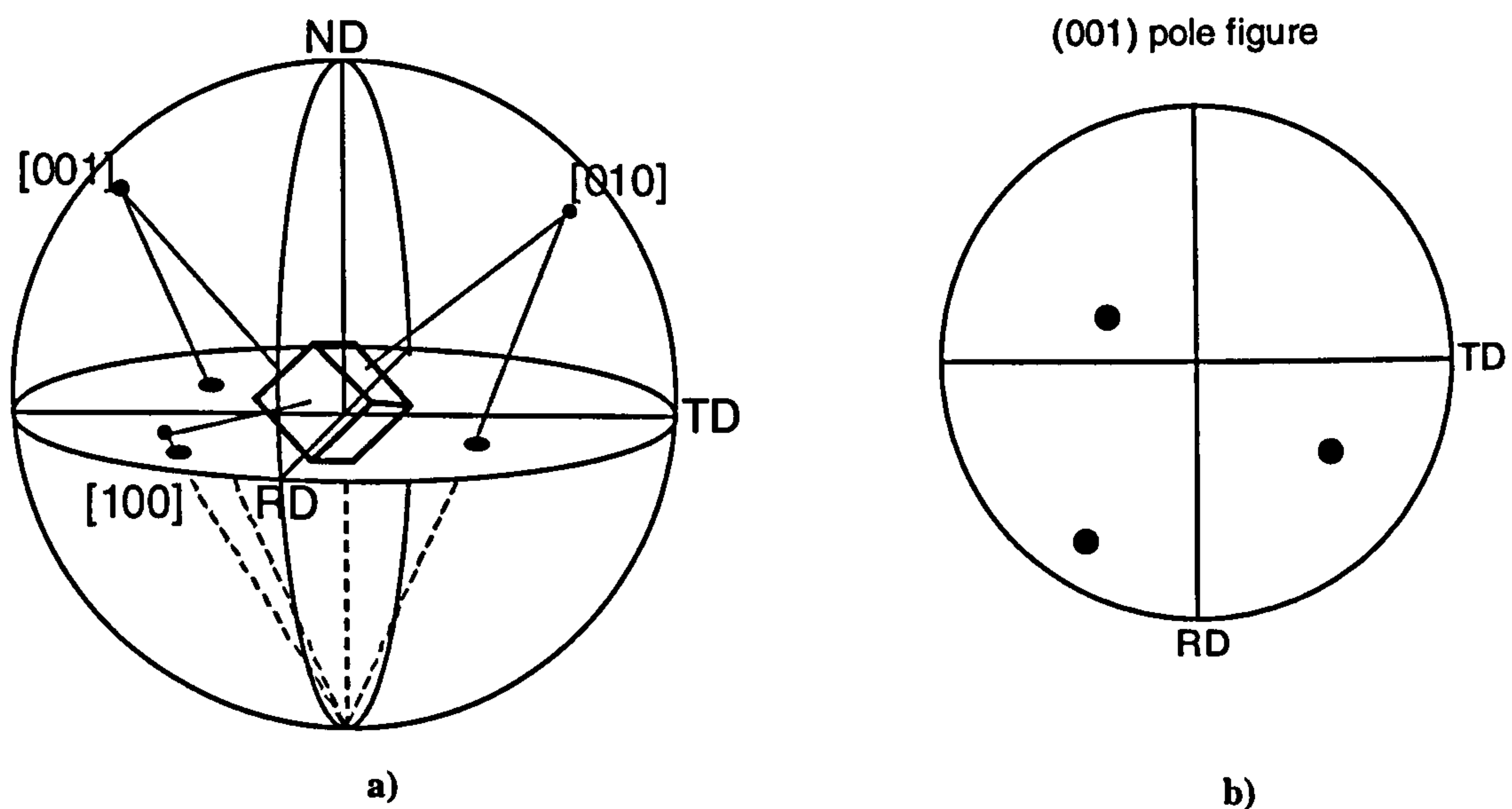


Figure 4.7 a) Stereographic sphere showing crystal reference axis, and b) corresponding (001) pole figure where the normal direction (Z-axis) is perpendicular to the page

The requirements of cubic crystal symmetry are such that a particular orientation can be described by three $\{100\}$ poles, four $\{111\}$ poles, six $\{110\}$ poles, twelve $\{hk0\}$ poles or twenty-four $\{hkl\}$ poles. The simplest pole figures will be those depicting the distribution of poles of planes with the lowest multiplicity, usually the $\{100\}$. The plots in Figure 4.8 depict three pole figures for identically oriented cubic crystals, each showing the pattern formed by plotting different poles i.e. the $\{100\}$, $\{111\}$ and $\{011\}$.

From the pole figure in Figure 4.8 a), the three $\{100\}$ poles can be seen; one as a full point in the centre and four half points lying around the circumference of the projection between the RD and TD axes. Consider first the (100) pole in the centre of the pole figure. This lies perpendicular to both the RD and TD axes but parallel to the ND. The other two poles (halved

on opposite sides of the circle) must lie perpendicular to the ND, and are placed symmetrically between the RD and TD axes. This symmetry means that they must be at 45 degrees to both the RD and TD directions. Thus, in this example, one face of the cubic crystal is lying in the plane of the projection oriented as is suggested by the dotted lines in Figure 4.8, and the crystal direction parallel to the RD and TD is the $[011]$. The orientation of the grain can thus be described by crystallographic directions parallel to any two of the reference directions, conventionally the ND and RD, and defined in the form $\{hkl\}\langle uvw\rangle$. This states that the plane of the form $\{hkl\}$ is parallel to the RD (i.e. its pole is parallel to ND), and that a direction of the form $\langle uvw\rangle$ is parallel to RD.

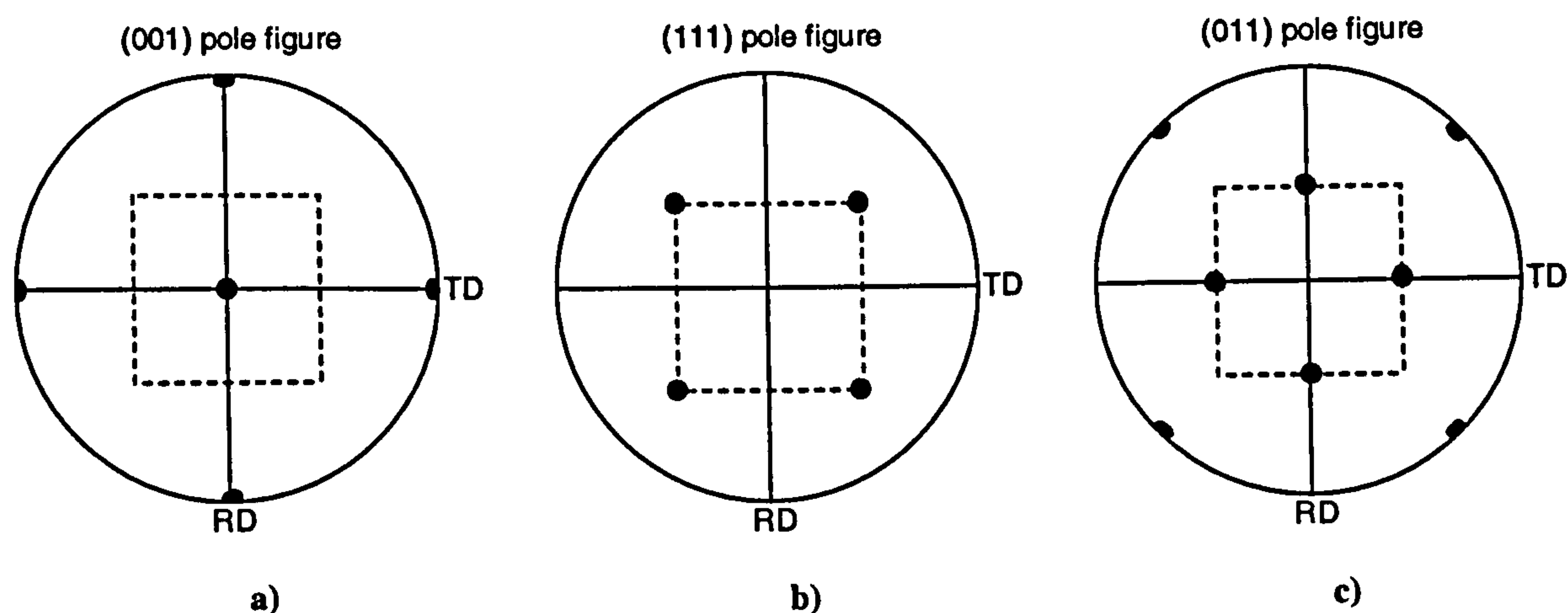


Figure 4.8 a) (100), b) (111) and c) (011) pole figures showing a $\{100\}\langle 001\rangle$ crystal orientation

It is important at this stage to recognise that while pole figures provide a description of the texture, they still have to be interpreted by the user. In the simple cases given (Figure 4.8) the description of texture by the indices, $\{100\}\langle 001\rangle$ is rather incomplete and oversimplified. Indeed, a major source of difficulty in the study of textures associated with the problem of relating the relatively simple 'ideal' orientations that have been discussed so far, to the complex multicomponent textures that are common in practice. A more complete description of the texture can be provided by a function that describes the orientation of all the crystals in the metal – an orientation distribution function - which is discussed later.

Conventional pole figures, as previously reviewed, are the most common method of presenting textural data for materials where the description of the product requires the

specification of two directions. For deformation processes of higher symmetry that require only one axis to be specified, a satisfactory description of the texture can be given by an inverse pole figure. An inverse pole figure shows the position of a sample direction relative to the crystal reference frame. The user enters the sample direction to consider by entering indices defining a vector by components of the sample axes (ND, TD, and RD). Thus, a [001] inverse pole figure shows which direction in the crystal lattice is aligned with the normal direction (ND) in the sample reference frame, and similarly the RD and TD directions are defined [100] and [010] respectively. Since no distinction is made between families of directions, an inverse pole figure is plotted as a portion of the stereographic projection in a unit triangle in such a manner that only one pole from a family of poles will occur within each area, as seen in Figure 4.9 a and b.

One method in which inverse pole figures are particularly useful is when drawing an inverse pole figure map. In this method the grains on the map are shaded according to a colour coded unit triangle which uses a colour gradient (red for (001), green for (101) and blue for (111) for a cubic material) according to the alignment of the crystal directions to the user specified sample direction (Figure 4.9 c). Thus, if a point in the scan is oriented such that the crystal direction aligned with the specified sample direction is somewhere between a [001] and [101] the point would be shaded in purple.

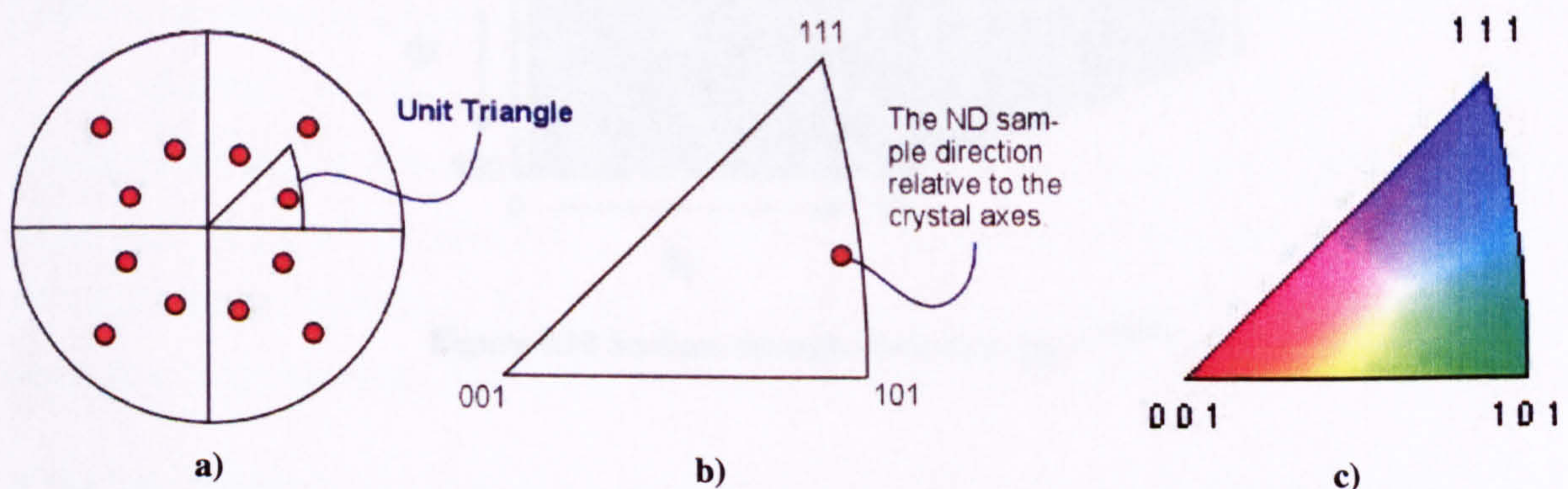


Figure 4.9 a) Inverse pole figure and b) corresponding unit triangle. c) is a colour coded unit triangle^[OIM02]

Some time spent trying to solve textures using pole figures or inverse pole figures by the standard trial and error methods soon leads to an appreciation of their limitations. Often it is difficult even to obtain good qualitative solutions. The fundamental reason for this is that a

general orientation has three degrees of freedom whereas a pole figure (or inverse pole figure) specifies only two independent variables. Such figures are, therefore, only 'projections' of the three dimensional orientation distribution function (ODF) which is the full description of a texture.

Orientation distribution functions (ODF's) provide a quantitative means of assessing structure-property relationships in materials. The Euler angles (ϕ_1 , Φ , ϕ_2 as defined earlier) essentially describe the orientation of a crystal (or texture component) rather than the plane as in the case of a pole figure, and hence require a three dimensional representation. Since three independent parameters are involved here it is usual to consider these representing three orthogonal axes which define a volume of orientation space. Any point in this space therefore corresponds to a single orientation (hkl)[uvw] and the density at that point is the strength of the texture component in x-random units. The volume of orientation space is divided by contour surfaces which separate regions of higher and lower orientation density. Since it is difficult to handle such a three-dimensional plot, the final presentation is usually made as a series of parallel sections through this space as is shown in Figure 4.10.

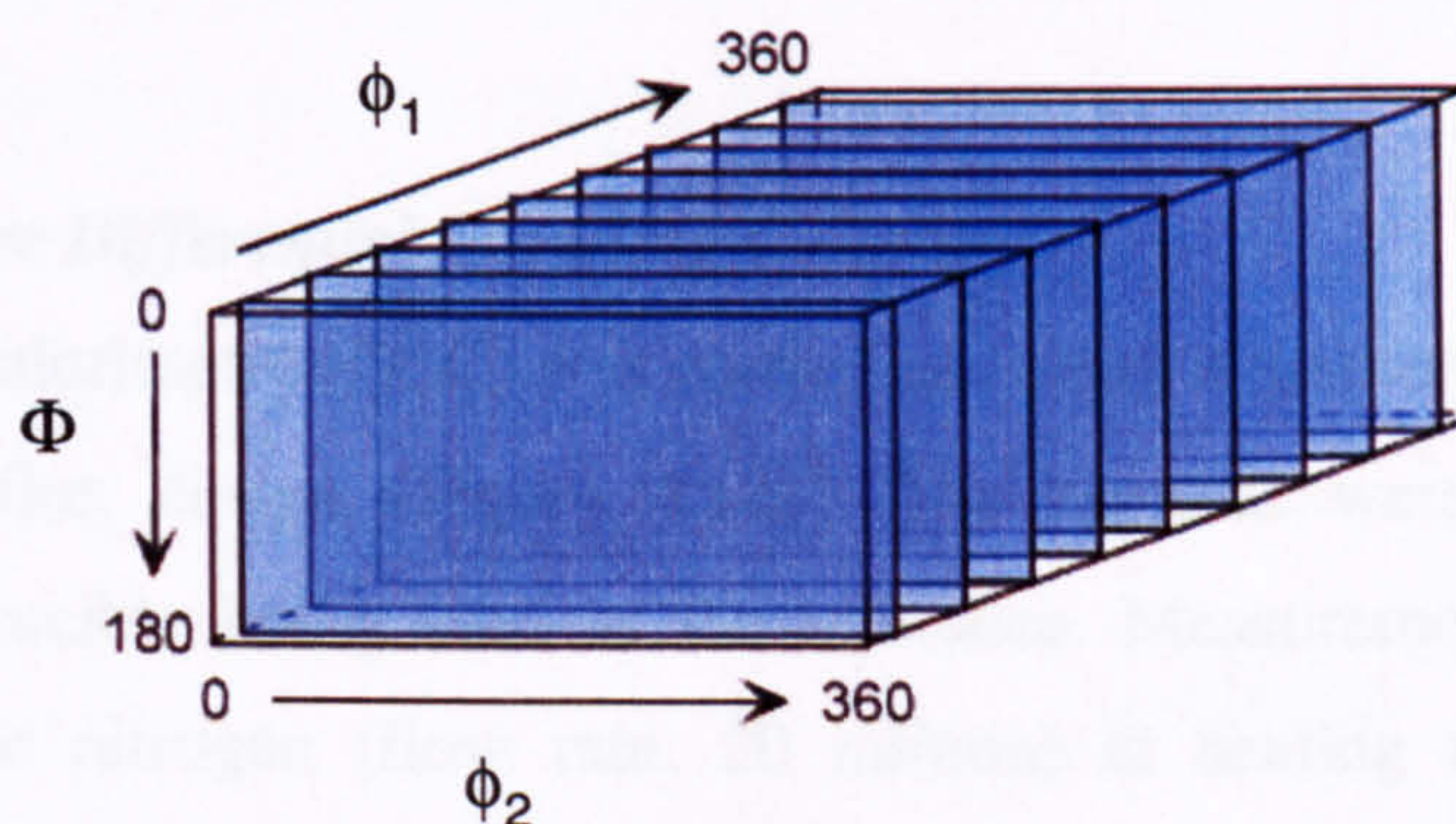


Figure 4.10 Sections through orientation space ^[OIM02]

The output of this method is the ODF, which is used to plot contours of orientation density and permits one to calculate the texture from a limited set of pole figures. Such a plot is shown in the Figure 4.11, where the space has been sectioned at constant angles along ϕ_1 . At first sight ODF's in this form seem much more formidable than the corresponding pole figures, but they are, in fact, much easier to use. There is no question of interpretation since this has already been done by the computer. It is only necessary to read off the density value

corresponding to any orientation of interest. Two charts which can be used to relate orientations in the form (hkl)[uvw] to their positions in orientation space are given in Appendix E.

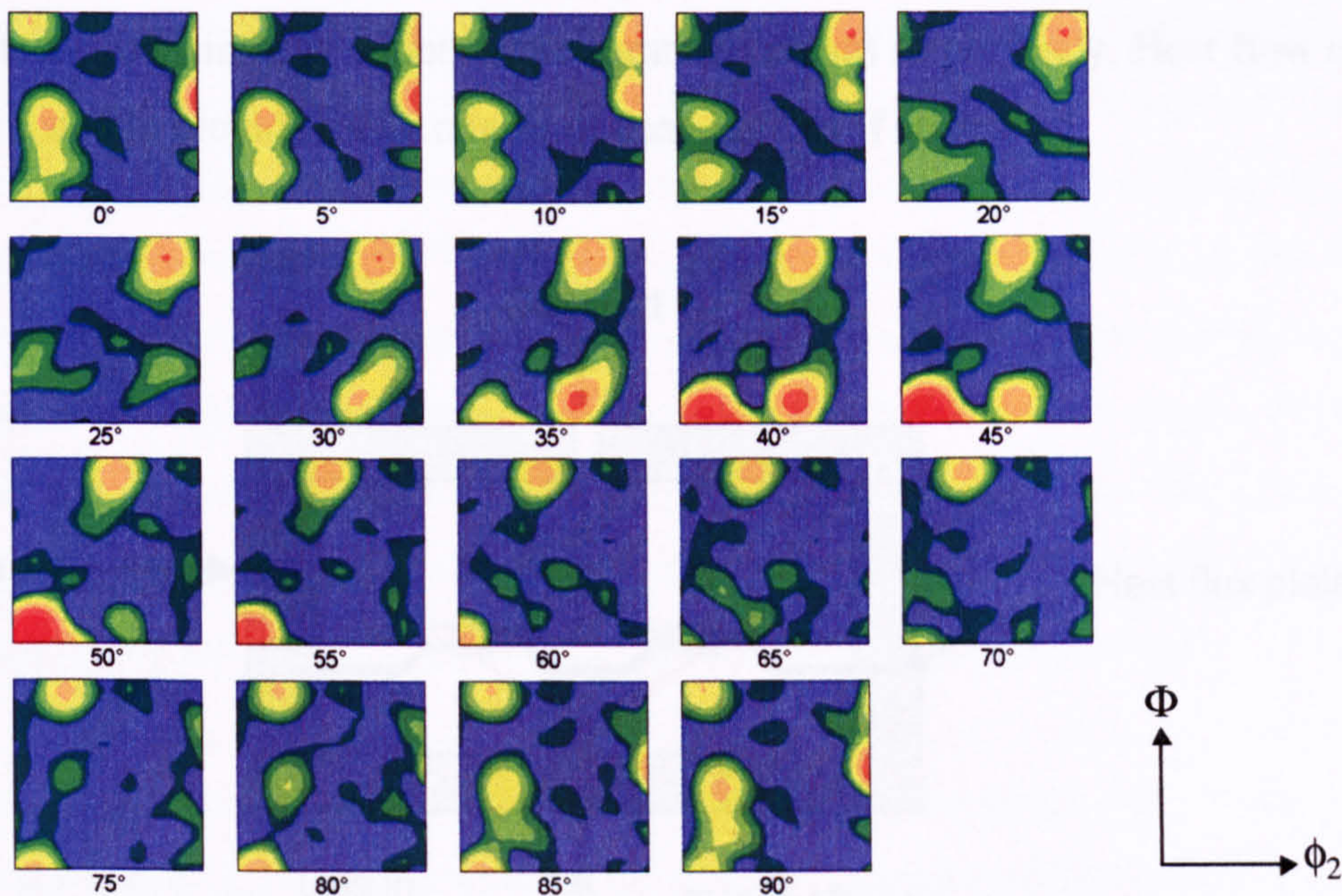


Figure 4.11 Series of ODF plots at angles of $\phi_1^{[OIM02]}$

4.3.6 High Temperature Differential Scanning Calorimetry

Differential scanning calorimetry (DSC) was carried out using a Stanton Redcroft DSC 1500 of the classical heat-flux design (Figure 4.12)[‡]. The samples were placed in alumina crucibles, an empty crucible being used as the reference. Measurements were carried out under dry, oxygen-free nitrogen (flow rate: 20 ml/min) at heating and cooling rates of 1°C/min, unless specified. The DSC was calibrated for temperature and heat flow rate according to the melting temperature and heat of fusion of pure aluminium.

If the two materials, S and R, are heated at the same rate their temperatures will rise. As the temperature increases, the temperature of the inert reference material will rise steadily as it is chosen to have no physical or chemical transitions. The temperature of the sample material also increases, steadily in the absence of any transitions, but at a different rate during transitions. For example, as the sample material melts, the temperature will lag behind that of

[‡] This work was carried out in collaboration with Mr. D. Price

the reference material as the sample absorbs the heat energy necessary for melting. When melting is complete, steady heating is resumed. The temperature difference is converted to differential heat flow by means of calibration against a substance with known heats of fusion and/or heat capacity (i.e. pure aluminium). A typical DSC curve is shown in Figure 4.13, and exhibits positive and negative peaks depending on whether the reaction of the material is exothermic (heat-producing), or endothermic (heat absorbing) respectively. Heat flow can be further manipulated to provide measurement of heat capacity if so desired.

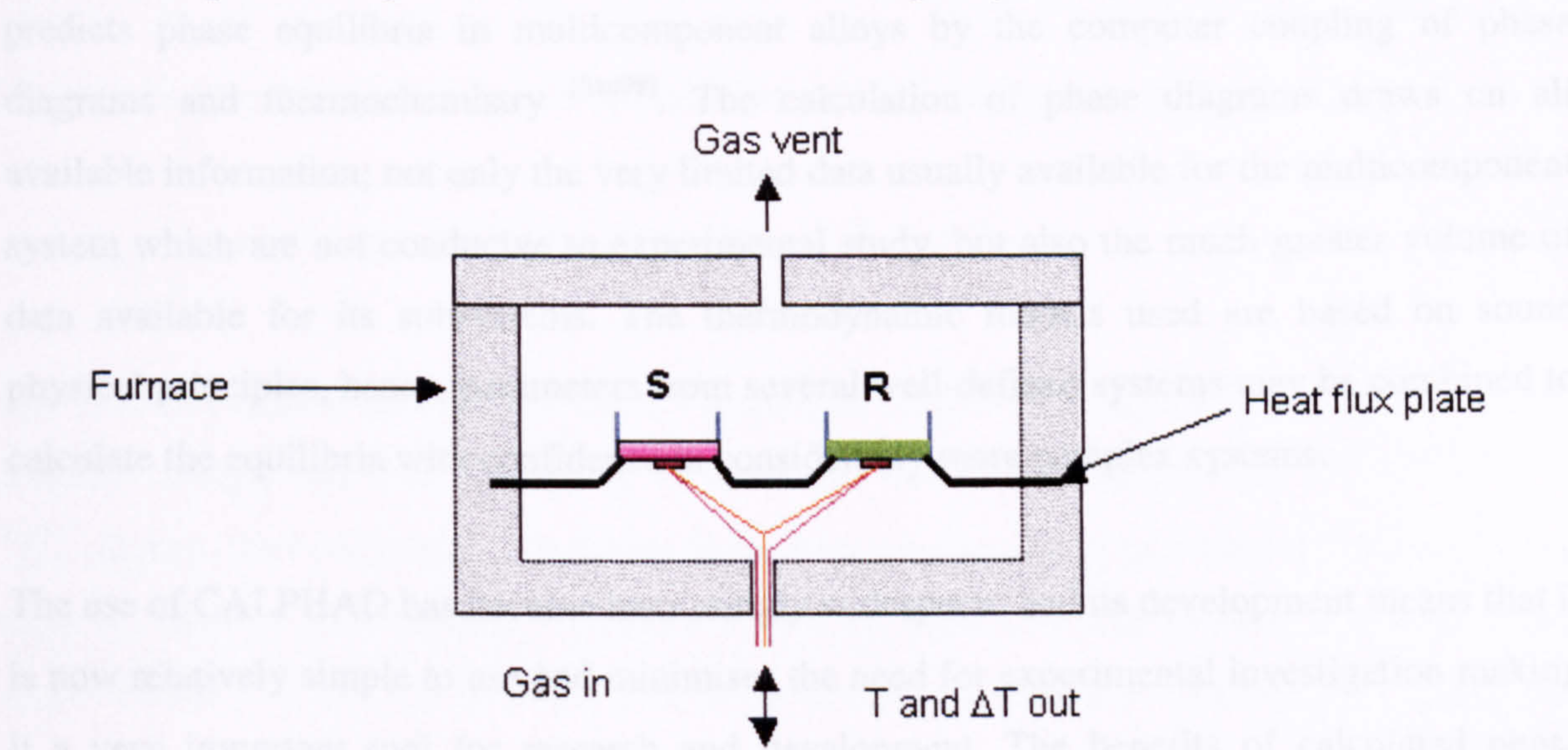


Figure 4.12 Schematic of a heat-flux DSC arrangement, where S and R are the sample and inert reference materials respectively ^[Ana02]

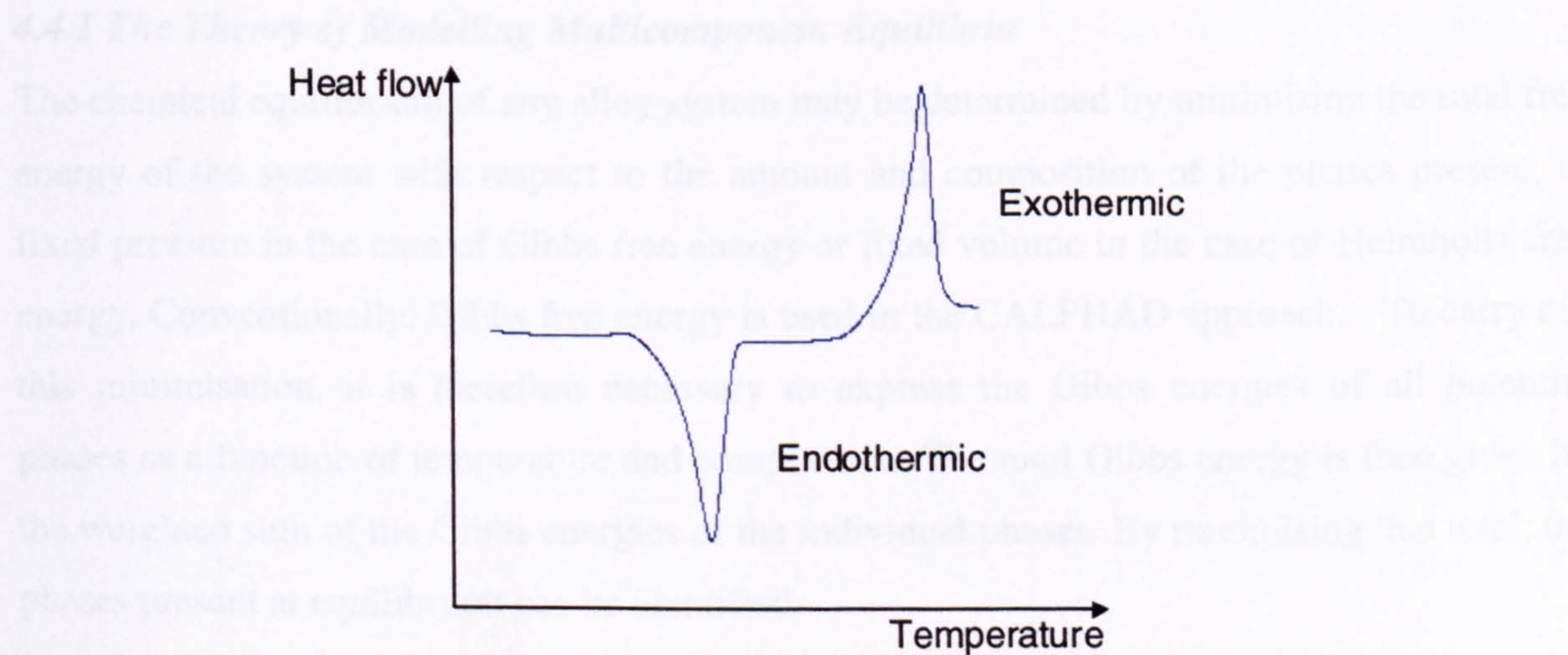


Figure 4.13 DSC curve showing examples of endothermic and exothermic reactions of the sample material

4.4 Thermodynamic Calculations

For many years, phase diagrams have been used to predict the equilibrium structure of binary, ternary, and occasionally higher order systems. However, problems in metallurgy generally involve many components, and to perform an experimental investigation of the potential range of compositions and conditions for such a multicomponent system would be both time-consuming and expensive. The CALPHAD (CALculation of PHase Diagrams) method predicts phase equilibria in multicomponent alloys by the computer coupling of phase diagrams and thermochemistry [Sau98]. The calculation of phase diagrams draws on all available information; not only the very limited data usually available for the multicomponent system which are not conducive to experimental study, but also the much greater volume of data available for its subsystems. The thermodynamic models used are based on sound physical principles, hence, parameters from several well-defined systems may be combined to calculate the equilibria with confidence in considerably more complex systems.

The use of CALPHAD has become increasingly widespread and its development means that it is now relatively simple to use and minimises the need for experimental investigation making it a very important tool for research and development. The benefits of calculated phase diagrams include cost and time savings, process prediction, assessment of materials compatibility, improved control of processes, and pollution and corrosion control.

4.4.1 *The Theory of Modelling Multicomponent Equilibria*

The chemical equilibrium of any alloy system may be determined by minimising the total free energy of the system with respect to the amount and composition of the phases present, at fixed pressure in the case of Gibbs free energy or fixed volume in the case of Helmholtz free energy. Conventionally, Gibbs free energy is used in the CALPHAD approach. To carry out this minimisation, it is therefore necessary to express the Gibbs energies of all potential phases as a function of temperature and composition. The total Gibbs energy is then given by the weighted sum of the Gibbs energies of the individual phases. By minimising this total, the phases present at equilibrium can be identified.

Pure Elements

By convention the Gibbs energy of a pure element, i , in its standard state, ${}^0G_i^\phi(T)$, is referred to the enthalpy for its stable state ϕ at 298.15K, ${}^0H_i^\phi(298.15K)$ [Ans94, Bal93, Bar93, COS94]. This is the standard element reference (SER) and the Gibbs energy is thus denoted $G - H_{SER}$ where:

$$G - H_{SER_i} = {}^0G_i^\phi(T) - {}^0H_i^\phi(298.15K) \quad [4.3]$$

This can be described as a function of temperature, T , by an equation of the form:

$$G - H_{SER_i} = a + bT + cT \ln T + dT^2 + eT^3 + fT^{-1} + gT^7 + hT^{-9} \quad [4.4]$$

The first and second differentials of $G - H_{SER}$ with respect to temperature are related to the absolute entropy and heat capacity of the element i at the same temperature [Bal93, Bar93, COS94, Tay93]. Hence, the coefficients a to h may be determined directly from measured values of heat capacity, entropy and enthalpy. The same functional form may also be used to represent the same element in a solution in which it takes the structure ϕ which is different from that of the pure stable element, since the expression ${}^0G_i^\phi(T) - {}^0H_i^\phi(298.15K)$ is equivalent to ${}^0G_i^\phi(T) - {}^0G_i^\phi(T) + G - H_{SER_i}$ [Ans94].

For elements that display magnetic ordering (Cr, Fe, Ni and Mn) an additional term $G_{magnetic}$ must be added to the Gibbs energy equation (Equation 4.4 refers to the paramagnetic state of the material). That is:

$$G_{magnetic} = R \cdot T \cdot \ln(1 + \beta) \cdot g(\tau) \quad [4.5]$$

where R is the universal gas constant, β is the average magnetic moment per atom of the alloy, expressed in Bohr magnetons and $\tau = T/T_c$, where T_c is the critical temperature for magnetic ordering [COS94, Din97]; a detailed description of the function $g(\tau)$ is provided by Dinsdale [Din97].

Binary Compounds

The Gibbs energy of formation of a compound A_aB_b may be expressed as:

$$G_{A_aB_b} - a^0 \cdot H_A^\phi \cdot (298.15K) - b^0 \cdot H_B^\phi \cdot (298.15K) = f(T) \quad [4.6]$$

where a and b are constants, different from those in Equation 4.4, and the function $f(T)$ is identical to that given in Equation 4.4 [Ans94, COS94]. Thus, applying Equation 4.3 to each component of the compound in turn, Equation 4.6 becomes:

$$f(T) = G_{A_aB_b}^T - a^0 \cdot G_A^{\phi,T} - b^0 \cdot G_B^{\phi,T} + a \cdot (G - H_{SER_A}) + b \cdot (G - H_{SER_B}) \quad [4.7]$$

$$f(T) = \Delta_f \cdot G_{A_aB_b}^T + a \cdot (G - H_{SER_A}) + b \cdot (G - H_{SER_B}) \quad [4.8]$$

The term $\Delta_f \cdot G_{A_aB_b}^T$ is the Gibbs energy of formation of the compound at a given temperature, T , referred to the stable elements at the same temperature.

Solid and Liquid Solutions

The Gibbs energy of each solution phase is slightly more complex. It is made up of three distinct terms such that:

$$G = G^{ref} + G^{id} + G^{ex} \quad [4.9]$$

Here the first term, G^{ref} , is simply a weighted sum of the data for the pure elements, the second term, G^{id} , is the sum of the contributions from the configurational entropy to the Gibbs energy of mixing, and the third term, G^{ex} , represents the excess Gibbs energy of mixing. More explicitly, this takes the general form:

$$G = \sum_i x_i \cdot G_i^0 + R \cdot T \cdot \sum_i x_i \cdot \ln x_i + \Delta G^{ex} \quad [4.10]$$

where x_i is the mole fraction of component i , and ΔG^{ex} is the excess Gibbs energy of mixing; for an ideal solution this last term is equal to zero [Bar93]. The modelling of multicomponent

systems is concerned mainly with deriving suitable expressions for the excess Gibbs energy, and in general two models are used: the Redlich-Kister model, and the sub-lattice model.

The Redlich-Kister model [Ans94, Bal93, Bar93, COS94] is used for solutions where the interactions between components are small, and takes the form of a polynomial in composition. For example, the binary interactions for an m component system, to s terms, takes the form:

$$\Delta G^{ex} = \sum_{i=1}^{m-1} \sum_{j=i+1}^m \sum_{r=0}^s A_{ij} \cdot x_i \cdot x_j \cdot (x_i - x_j)^r \quad [4.11]$$

where x_i and x_j are the mole fractions of components i and j respectively, and A_{ij} is a model parameter which can be temperature dependent [Bal93, COS94]. The ternary and higher order interactions may be added to this and take a similar form [Bal93, Bar93]. Phases modelled using the Redlich-Kister model include fcc (Al-Cu), fcc (Al-Ti), and hcp (Mg-Al) [COS94].

The sub-lattice model [Bal93, COS94] is generally used for solid solutions where the interactions between components are large, or some ordering within the phases exists. Examples of phases modelled using the sub-lattice model include CuAl_2 , Mg_2Si , and Al_8Mn_5 [COS94]. One or more sub-lattices with one or more types of atoms on each sub-lattice may be used to describe a structure, so that stoichiometric, non-stoichiometric and substitutional phases may all be described. In the case of a non-stoichiometric phase, several sub-lattices are used with different species (atoms, ions, or vacancies) coexisting on the same sub-lattice. Stoichiometric phases are also modelled using more than one sub-lattice, but each sub-lattice contains only one type of atom or ion. This contrasts with substitutional phases which may be modelled on a single sub-lattice containing two or more species.

Gaseous Species

Gaseous species [Ans94, COS94] may be represented by an expression identical to that given in Equation 4.6 with an additional term, $RT \ln P$, where P is the total pressure; the reference state is taken as the pure component at atmospheric pressure. The gas phase is assumed to form an ideal solution.

4.4.2 Prediction of Phase Equilibria

Given an expression for the free energy of the system, it is then possible to predict equilibrium in two ways. In order to understand this, it is recalled that when the Gibbs energy of the system is at a minimum, the chemical potentials of the components are equalised throughout the system. Equilibrium can therefore be computed either by minimising the Gibbs energy of the system, or by equalisation of the chemical potentials.

Due to an increasing interest in thermochemical modelling and in particular the calculation of phase diagrams, a number of commercial computer software packages are available which carry out the Gibbs energy minimisation process. A comprehensive review of eight such packages is given by Bale & Eriksson [Bal90]. Of the packages available, the two most often cited are MTDATA[†] [Dav89, Dav90, Din88, Din95, Gis93] and ThermoCalc[‡] [Jan93, Sun85, Sun88]. Both of these packages provide facilities for the manipulation of thermodynamic data, allowing equilibrium in binary, ternary and higher order systems to be explored using the Gibbs energy models for phases previously discussed. The method by which the Gibbs energy minimisation is performed however differs between the two programs.

MTDATA has two different minimisation algorithms, and operates using either or both for determining equilibria. The first algorithm, usually termed stage 1, is a true Gibbs energy minimisation of the integral Gibbs energy of the system. This method is compatible with all models, and thus all phases; it ensures a lower Gibbs energy is obtained at each iteration; it requires no 'initial guess' of the equilibrium point, and it is inherently highly reliable. Within MTDATA, this method has a system mass limit of 10^{-6} moles. The second algorithm, termed stage 2, equalises the chemical potentials of the components between phases. This process is faster than the true Gibbs energy minimisation, and as the stage 2 algorithm determines the speciation to a tolerance on a logarithmic scale, the absolute accuracy is higher, reducing the system mass limit to 10^{-8} moles. Unfortunately, this method does not actually work with all models. For example, the sub-lattice model [Gis97] requires an 'initial guess' of the equilibrium point for which the results of a stage 1 or previous stage 2 calculation are used [Din88, Gis93], and

[†] MTDATA is developed and maintained by the Materials Thermochemistry Group at the National Physical Laboratory, Teddington, Middlesex, TW11 0LW, U.K.

[‡] ThermoCalc is developed and maintained by the Department of Materials Science and Engineering, The Royal Institute of Technology, Stockholm, S-100 44, Sweden

thus within MTDATA it is only invoked when a detailed knowledge of the speciation or distribution of components present in very small amounts is required.

ThermoCalc, on the other hand, uses only the equalisation of chemical potentials. This results in a fast calculation algorithm but, due to the requirements for an ‘initial guess’ of the equilibrium point, it can have convergence problems leading to the prediction of local minima rather than global equilibrium, or possible failure to produce any results at all ^[Gis97]. For these reasons, MTDATA has been chosen as the package to be used in this investigation. A long-standing collaboration with the National Physical Laboratory involving the provision of data for complex metallurgical systems also exists. MTDATA is discussed further later in this section.

4.4.3 Solidification Simulations

Equilibrium Calculations

At equilibrium, the composition of solidifying phases can be obtained from the lever rule assuming complete diffusion of solute in both the solid and liquid phases at all temperatures during cooling. For a binary alloy, assuming linear solidus and liquidus lines, the composition of the solidifying solid, C_s , as a function of the fraction of solid, f_s , is then given by:

$$C_s = \frac{k \cdot C_0}{f_s \cdot (k - 1) + 1} \quad [4.12]$$

where C_0 is the bulk composition of the alloy and k is the partition coefficient, defined as $k = C_s/C_l$ where C_l and C_s are the compositions of the liquid and solid that are in equilibrium at temperature T . If the solidus and liquidus temperatures are given by T_s and T_l respectively, this can then be rearranged to give ^[Kur86]:

$$f_s = \left(\frac{1}{1 - k} \right) \cdot \left(\frac{T_l - T}{T_s - T} \right) \quad [4.13]$$

This is the basis of calculations performed by MTDATA. The information obtained from such calculations is valuable, however, as we know, the cooling rates observed in piston structures

rarely result in the formation of equilibrium structures. To complement this approach the Scheil equation can thus be used ^[Kur86, Por92].

Non-Equilibrium Scheil Calculations

As described in Section 3.2.2, the Scheil model assumes complete mixing in the liquid ($D_l = \infty$) but no solid state diffusion ($D_s = 0$). In this case, Equation 4.12 becomes:

$$C_s = k \cdot C_0 \cdot (1 - f_s)^{(k-1)} \quad [4.14]$$

and Equation 4.13:

$$f_s = 1 - \left(\frac{T_s - T}{T_s - T_l} \right)^{\left(\frac{1}{k-1} \right)} \quad [4.15]$$

This is explained in more detail by Figure 4.14.

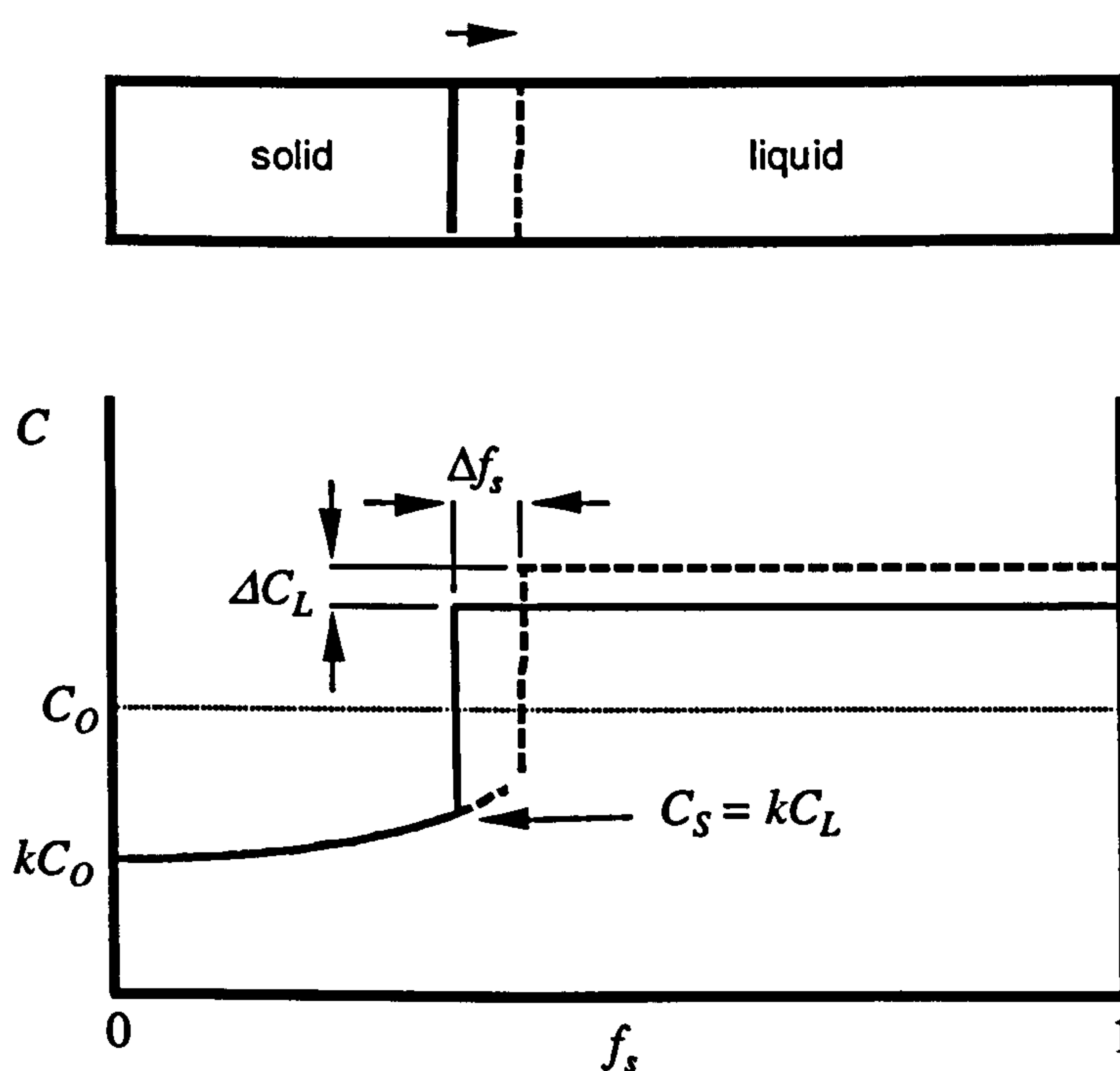


Figure 4.14 The Scheil model

Ignoring the change in molar volume on solidification, the variation of the fraction of solid, f_s , along a solidifying bar can be obtained by conserving solute when a small amount of solid, Δf_s , is formed:

$$(C_L - k \cdot C_L)df_s = (1 - f_s)dC_L \quad [4.16]$$

where C_s and C_L are the mole fractions of solute in the solid and liquid in equilibrium at a given temperature, and k is the partition coefficient, defined as $k = C_s/C_L$. Integrating, we then see:

$$\int_0^{f_s} \frac{df_s}{(1 - f_s)} = \int_0^{f_s} \frac{dC_L}{C_L \cdot (1 - k)} \quad [4.17]$$

and so:

$$C_L = C_0 \cdot (1 - f_s)^{(k-1)} \quad \text{and} \quad C_s = k \cdot C_0 \cdot (1 - f_s)^{(k-1)} \quad [4.18]$$

The Scheil approach assumes equilibrium exists only at the solid - liquid interface but, since no diffusion data are required, it can be modelled using thermodynamic data alone and thus can be implemented using packages such as MTDATA and ThermoCalc. In fact, many modified versions of the Scheil equation exist, allowing for effects such as backdiffusion (diffusion in the solid state). However, since such approaches require more than just thermodynamic data, they will not be considered here.

Implementation of the Scheil Equation

There are currently two possible methods for performing Scheil type simulations within thermodynamic modelling packages [Din96]. These are described below and illustrated schematically in Figure 4.15.

Method 1: Stepping the fraction of solid

Consider a liquid of composition C_0 ; this is first cooled until the liquidus is reached ($T = T_l$). Cooling is then allowed to continue until a chosen fraction of liquid, in this case 5%, has

solidified ($T = T_2$). From the lever rule, this solid will have a composition $C_{s,1}'$, the remaining liquid having a new composition, $C_{l,1}'$. Cooling then continues to freeze 5% of the remaining liquid, which this time results in the formation of solid of composition $C_{s,2}'$ and liquid $C_{l,2}'$ ($T = T_3$). This process is then repeated until the desired fraction of solid is obtained, usually $f_s = 0.99$. Since it is assumed that there is negligible diffusion in the solid formed, that is $D_s = 0$, a composition gradient is then set up in the solid, as observed in experiment.

Method 2: Stepping in temperature

Here again the liquid of composition C_0 is cooled until the liquidus is reached ($T = T_1$). Cooling ΔT below this to T_2 results in the formation of solid of composition $C_{s,1}^2$, leaving liquid of composition $C_{l,1}^2$. Cooling by a further ΔT produces more solid, this time, however, the initial liquid takes the composition $C_{l,1}^2$, resulting in the formation of solid of composition $C_{s,2}^2$ leaving liquid of composition $C_{l,2}^2$.

Both the above procedures are simple to implement and have a number of benefits over the basic Scheil equation [Sau96-1].

- The Scheil equation is applicable only to binary alloys, and can not easily be derived with multiple k values, necessary for a multicomponent alloy; the calculations described above can easily be carried out for multiple elements.
- The partition coefficients need not be linear; this is, however, a necessity for the basic Scheil equation.
- The Scheil equation only allows for solidification of a single solid phase; the CALPHAD approach described can deal with multiple solid phases.

Comparing the two methods, stepping in temperature has the advantages that it is faster, requiring fewer steps, and it allows for complete solidification ($f_s = 0$), although the resolution is assumed to be less good, particularly for eutectic systems where a large fraction of solid is formed over a small temperature range [Din96]. However, Saunders has in fact shown excellent agreement between a temperature stepping Scheil simulation with ThermoCalc and the Al-Data database, and experimental data from Backerud et al. [Bac86]. Hence, the stepping in temperature method will be employed in this work.

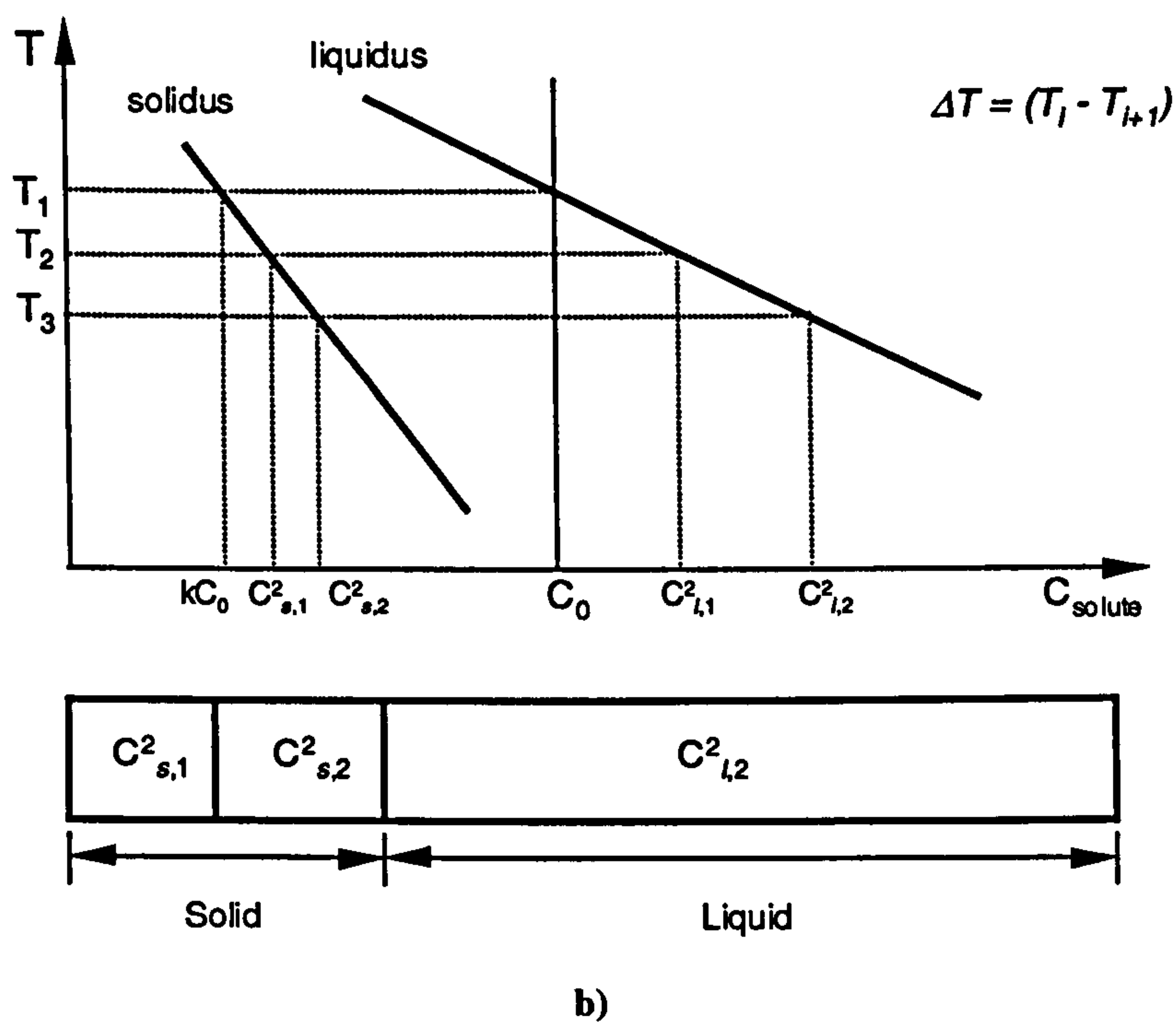
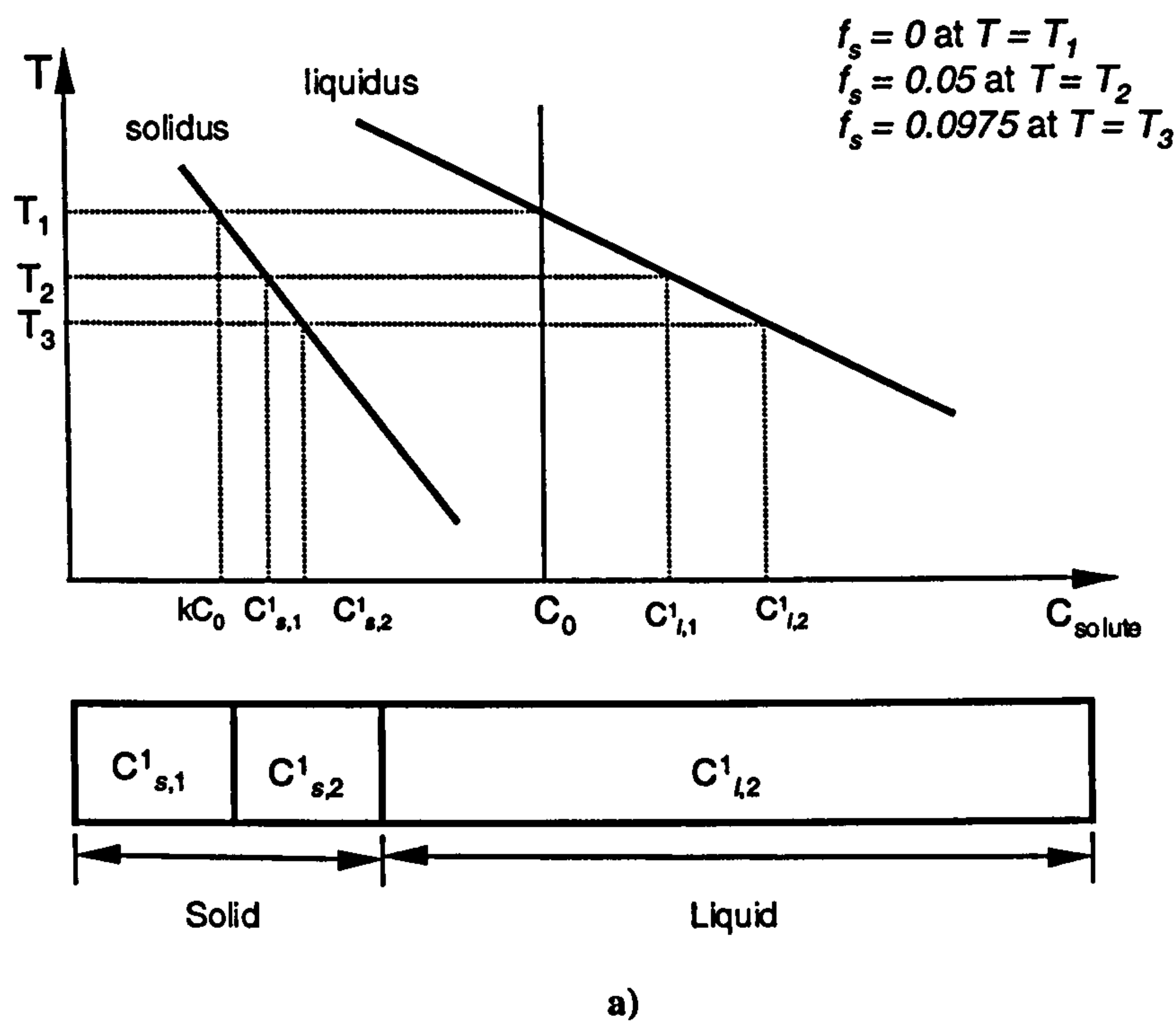


Figure 4.15 Implementation of the Scheil equation a) Method 1; Stepping the fraction of solid, and b) Method 2; Stepping the temperature

4.4.4 Thermodynamic Modelling Software: MTDATA

The MTDATA software provides a facility for retrieving thermodynamic data from databases, compiling data sets for the elements of interest, and assessing these data; calculating binary and ternary equilibrium phase diagrams, as well as equilibria in higher order multicomponent, multiphase systems; and also a facility for linking the minimisation algorithms to external software or user code ^[Dav90, Gis93] enabling, among others, the investigation of non-equilibrium processes. A number of modules are incorporated for manipulating and retrieving the data, making various types of calculation, and plotting binary, ternary, multicomponent, and predominance area diagrams ^[Dav89].

ACCESS Module

The ACCESS module is designed as a tool for the preparation of data for the calculation modules by retrieving data for multicomponent systems from one or more databases. The database can be a specialist or private database or one provided with MTDATA. Data for a wide variety of system types can be handled and systems can be specified by elemental or compound components and preference can be given to data arising from a particular model. A datafile of system data is created which can then be used by the other MTDATA modules for thermodynamic calculations. The types of substance and phase/model for which data can be stored and retrieved include stoichiometric compounds, gases, aqueous species, other associates, non-ideal situations, and phases with solution on fixed or variable sublattices. It is important to note that MTDATA cannot predict the existence of an 'unknown' species or phase for which it has no thermodynamic data.

MULTIPHASE Module

The MULTIPHASE module of MTDATA is used for making calculations of chemical equilibria in multi-component, multi-phase systems. Calculations can be made individually or as a function of a single variable, and the results can be plotted in a variety of ways. MULTIPHASE also acts as a service to most of the other calculation modes. The command protocol of MULTIPHASE allows composition, temperature, pressure or volume, partial pressures and activities to be set and one variable stepped. Amounts can be specified in terms of mass or moles and depending on the nature of the problem, either or both of the two calculation stages described earlier can be used. It is possible to make the calculations more efficient by using results or the program variables from previous calculations as a starting point for the next calculation.

The calculation of equilibria in a system of many components generates an enormous quantity of information that can rarely be displayed on a single graph and would be difficult to assimilate in tabular form. For this reason MULTIPHASE incorporates flexible procedures to control what is to be plotted from the graph files calculated previously. Amounts of phases or substances (individually, in a phase, compounds of a particular compound, or all), component distribution between phases or within a phase, component and compound activities, partial pressure, and Gibbs energy can all be plotted. The axis scales can be varied and made logarithmic, and amounts can be expressed in moles or mass terms irrespective of the way the problem was formulated. Moreover, the abscissa of the graph can be changed from the originally stepped variable to one of the calculated variables. Alternatively, the data can be saved in tabulated format for post-processing in a spreadsheet.

APPLICATION Module

The APPLICATION interface takes the form of a series of FORTRAN functions and subroutines with a number of 'built-in' applications supplied with MTDATA. It is designed to allow users to write software of their own, this software being specific to particular applications, which make use of the existing functionality of MTDATA. It also allows users to link MTDATA with third party software, such as kinetics, fluid flow or plant simulation and management packages. A relationship between MTDATA and a user's own application software can be created in one of two ways. Either MTDATA can act as the executing process hosting the user application (MASTER or Level 1 mode) or MTDATA can be called upon by the user application which is itself part of another main program (SLAVE or Level 2 mode). It is through the APPLICATION module that Scheil simulations are run, the Scheil calculation being a 'built-in' macro where MTDATA acts as the MASTER.

ASSESSMENT Module

The ASSESSMENT module provides tools to help in the task of deriving values for thermodynamic model parameters, which, when used as a basis for phase equilibrium calculations, give the best possible representation of a collection of experimental data. This is referred to as data assessment as it involves comparing data of many different types, from many different sources, obtained using many different experimental techniques. The specific task of generating model parameters appropriate to a set of experimental data is called optimisation.

Any property or combination of properties that can be calculated using MTDATA can feature in an experimental data file, which takes the form of a macro giving instructions for the calculation of each property and associating each calculation with an experimental value and uncertainty. Properties typically considered in experimental files include activities, heats of mixing, equilibrium phase compositions, and phase boundary temperatures. The values of parameters can be stepped to observe their effect or optimised automatically using a choice of algorithms. It is possible to 'flag' a parameter for change during an optimisation run, and also link sets of parameters together to mirror any changes, therefore ensuring that the data remain constant across temperature boundaries. During an optimisation run it is the weighted sum of squared errors that is minimised, where an error is defined as the difference between calculated and experimental values of a property divided by the stated experimental uncertainty.

$$\text{Weighted sum of squares of errors} = \sum_{i=1}^n W_i \cdot \left(\frac{C_i - E_i}{U_i} \right)^2 \quad [4.19]$$

where n is the number of properties considered in the optimisation run, C_i is the calculated value of the property i , E_i is the experimental value of property i , U_i is the uncertainty associated with E_i , and W_i is the weight assigned to property i .

4.4.5 Thermochemical Databases

The essential principle underlying MTDATA is that the mathematical models incorporated in the software allow equilibria in multicomponent systems to be calculated on the basis of critically assessed thermodynamic data from simpler subsystems [Bal93, Dav90, Din95]. In theory, it is therefore possible to explore with confidence alloy compositions and temperature regimes for which no direct experimental data exist. In the published literature studied, the reliability of predictions for higher order systems using lower order data is rarely considered, although where it is discussed it is usually taken as acceptable [Bal93, Din95]. It would appear that through thermodynamic modelling it should be possible to predict the volume fraction and composition of phases occurring in commercial Al-Si alloys as a function of alloy composition and temperature. However, in order to do this successfully, accurate thermodynamic data for all the phases of interest are necessary, and MTDATA also requires a thermodynamic interaction between every element in every phase, some of which data may be

unavailable. In the absence of certain data the interaction is assumed to be 'ideal'. The reliability of predictions is therefore dependent on the quality of data of the system under discussion, and thus some care is required in the interpretation of any predictions made.

At present, four commercial data sets exist for aluminium alloys. These are:

SGTE Solution Plus Database ^[Din91]

This data set is a version of the standard Scientific Group Thermodata Europe solution database, modified by the Materials Thermochemistry Group at the National Physical Laboratory. It contains at least unary and binary interaction data for most elements.

Al-Data ^[Sau96-3]

Developed by ThermoTech Ltd., Al-Data is a database for commercial aluminium alloys of all major types containing data for the following elements; Al, Cr, Cu, Fe, Mg, Mn, Ni, Si, Ti, V, Zn, Zr. Results presented by Saunders ^[Sau96-1, Sau96-2] for non-equilibrium Scheil simulations using Al-Data with ThermoCalc, show good agreement with experimental work of Backerud. Al-Data is reported ^[Sau96-2] to contain interaction data of all the phases of interest in commercial Al alloys. Two versions of Al-Data were used in this work and are referred to as Al-Data¹ and Al-Data³,

COST 507 Thermochemical Database for Light Alloys ^[COS94]

This project was established within the framework of European Co-operation in the Field of Scientific and Technical Research as COST 507 for light alloy systems based on Al, Mg, and Ti. There are 14 signatory countries to the action, which had an official commencement date on January 1 1990, running initially for three years to address the problem of a lack of accurate thermodynamic data for these systems. The alloy systems towards which work was directed were defined by the industrial partners involved in the project, and include: Al-Mg-Mn-Fe-Si, Al-Mg-Si-Cu (-Fe), Al-Zn-Cu-Mg (-Zr, Cr, rare earth metals), and Al-Li-Cu-Mg-Zr (-H).

EurAl ^[Cha99]

The EurAl project follows and builds upon data provided by the COST 507 Action involving a limited number of its participants with the aim of providing an advanced database for a wide range of applications concerned with the development and usage of wrought and cast

aluminium alloys. This work is still ongoing and part of the work discussed in Chapter 6 was carried out in order to provide data for the development of this database.

4.4.6 Calculation Methodology

All the calculations were carried out using MTDATA. The ACCESS module was used to compile datafiles for the different alloys, drawing on data from 3 commercial databases, namely Al-Data versions 1 (1996) and 3 (2000), COST 507, and EurAl. During the compilation it was possible to specify which database was used as the source for the data, enabling predictions for the same alloy composition to be calculated and compared for each of the three databases. Following validation of the databases (Chapter 5), Al-Data was deemed to contain the most accurate and complete data and was therefore used for further work as referenced.

Equilibrium calculations were done through the MULTIPHASE module of MTDATA. A temperature range of 400 – 1200 K with a 20 K step between calculations was used initially to be consistent with the work by Daykin^[Day98]. Further work used similar temperature ranges and a range of step sizes dependant on the system under investigation and the data required. In order to speed up the calculation the ‘compute print graphics initial last’ command was used to provide an ‘initial guess’ for each step of the calculation, as determined by the result from the previous step. Scheil calculations were carried out through the APPLICATION module using the stepping temperature macro, ‘mt-tscheil.mac’. The parameters used were as prompted by MTDATA. For both equilibrium and Scheil type calculations it was necessary for certain classifications to be made, depending on the database used. When using a database compiled from AlData, classifying all phases normal was required to stop those that had been classified as absent being omitted from the calculation. From previous work^[Day98], it was suggested that miscibility gaps be classified in certain phases dependent on the database: Al_3Ni_2 in AlData¹ (not required in Al-Data³), and DIAMOND_A4 (silicon phase) in COST 507. These were classified in the current work where appropriate. As yet, no similar classifications have been made for calculations using EURAL.

The results of the thermodynamic calculations are presented in Chapter 5 with respect to verification of thermodynamic modelling for predicting phase stability in comparison with experimental results, and in Chapters 6 and 8 as a tool for predicting the effect on phase stability of various elemental additions.

Chapter 5

Phase Analysis

5.1 Introduction

This chapter aims to provide an understanding of the phases present in multicomponent, near-eutectic Al-Si alloys used for commercial piston applications, through microstructural characterisation and thermodynamic modelling. In the first instance, the thermodynamic calculations are tested to determine the accuracy of the predictions with respect to different thermodynamic databases, equilibrium and Scheil simulations, and phase compositions. The thermodynamic predictions are then used in combination with optical and electron microscopy to produce a detailed analysis of typical phases in a multicomponent Al-Si alloy. Through simultaneous electron backscatter diffraction (EBSD) and energy dispersive X-ray (EDX) analysis, a database of materials files containing diffraction and composition data for individual phases is generated.

5.2 Verification of Thermodynamic Modelling

As explained in Chapter 4, the use of CALPHAD techniques has become increasingly popular, using the Gibbs energy of a system to predict phases present in multicomponent alloys at thermal equilibrium. Thermodynamic data are retrieved from commercial databases consisting of critically assessed thermodynamic data of simpler systems (e.g. unary and binary) which is extrapolated for the higher order systems. The accuracy of such calculations is, therefore, highly dependent on the extent and quality of the data available. In order to verify how valid the predicted phases were in comparison to the observed phases in 'real' alloys, a series of investigations were carried out. The first investigation looked at how equilibrium thermodynamic predictions of phase stability, using data from three commercial databases, compared qualitatively to the microstructure of a multicomponent alloy analysed by optical and electron microscopy. The second investigation was a qualitative assessment of both Scheil and equilibrium predictions to determine which simulation was the most

representative of observed phases in as-cast alloys. Finally, model alloys were heat-treated to attain an ‘equilibrium’ microstructure for a quantitative evaluation of predicted phases and their compositions with those observed.

5.2.1 Comparison of Databases

This study was aimed at qualitatively comparing a number of commercially available thermodynamic databases with experimental results, to determine the quality of thermodynamic data and accuracy of the extrapolation method for multicomponent systems. To do this three databases, namely Al-Data¹, COST 507 and EurAl (discussed in Section 4.4) were used to predict equilibrium phase stability for commercial alloy AE160, composition in Table 5.1. The elements for which thermodynamic data is included in each of the databases are given in Table 5.2.

Table 5.1 Nominal composition of commercial alloy AE160 (wt. %)

Si	Mg	Cu	Ni	Mn	Fe	Ti	Zr	V	P (ppm)
11.2	1.05	3.1	2.27	0.08	0.3	0.17	0.15	0.06	53

Balance is Al, all other elements unspecified

Table 5.2 Elemental data included in each of the databases

	Al	Cr	Cu	Fe	Mg	Mn	Ni	Si	Ti	V	Zn	Zr
Al-Data ¹	√	√	√	√	√	√	√	√	√	√	√	√
COST 507	√		√	√	√	√		√	√		√	√
EurAl	√		√	√	√	√		√				

From the two tables, it can be seen that whilst Al-Data¹ contains all the elemental data for the components of AE160, several additions have yet to be incorporated into the COST 507 and EurAl databases. Indeed, most noticeable is the lack of data for Ni in the COST 507 and EurAl databases, as this element, typically added at 1 - 3 wt. %, interacts to form many different intermetallics as will be discussed in Section 5.3. Thus, the first impression of how accomplished the data from each of the databases is indicates Al-Data¹ will be most accurate as the compositional data is most complete.

For comparison, equilibrium predictions for alloy AE160 were made using data from each of the Al-Data¹, COST 507, and EurAl databases, independently, with data produced in tabulated form (Table 5.3), and as phase stability plots (Figures 5.1 a) to c). Phase analysis on AE160 and alloys of similar compositions from previous work (AE135, Nür al S2 and Mahle 142) [Day98], provided an qualitative indication of the phases forming in piston castings of these alloys. The predicted phases in Table 5.3 are shown in comparison with the phases that have been observed experimentally, and the phase stability plots in Figures 5.1 a) to c) show mass fraction of phases as a function of temperature and illustrate the stability of the phases during solidification of the alloy.

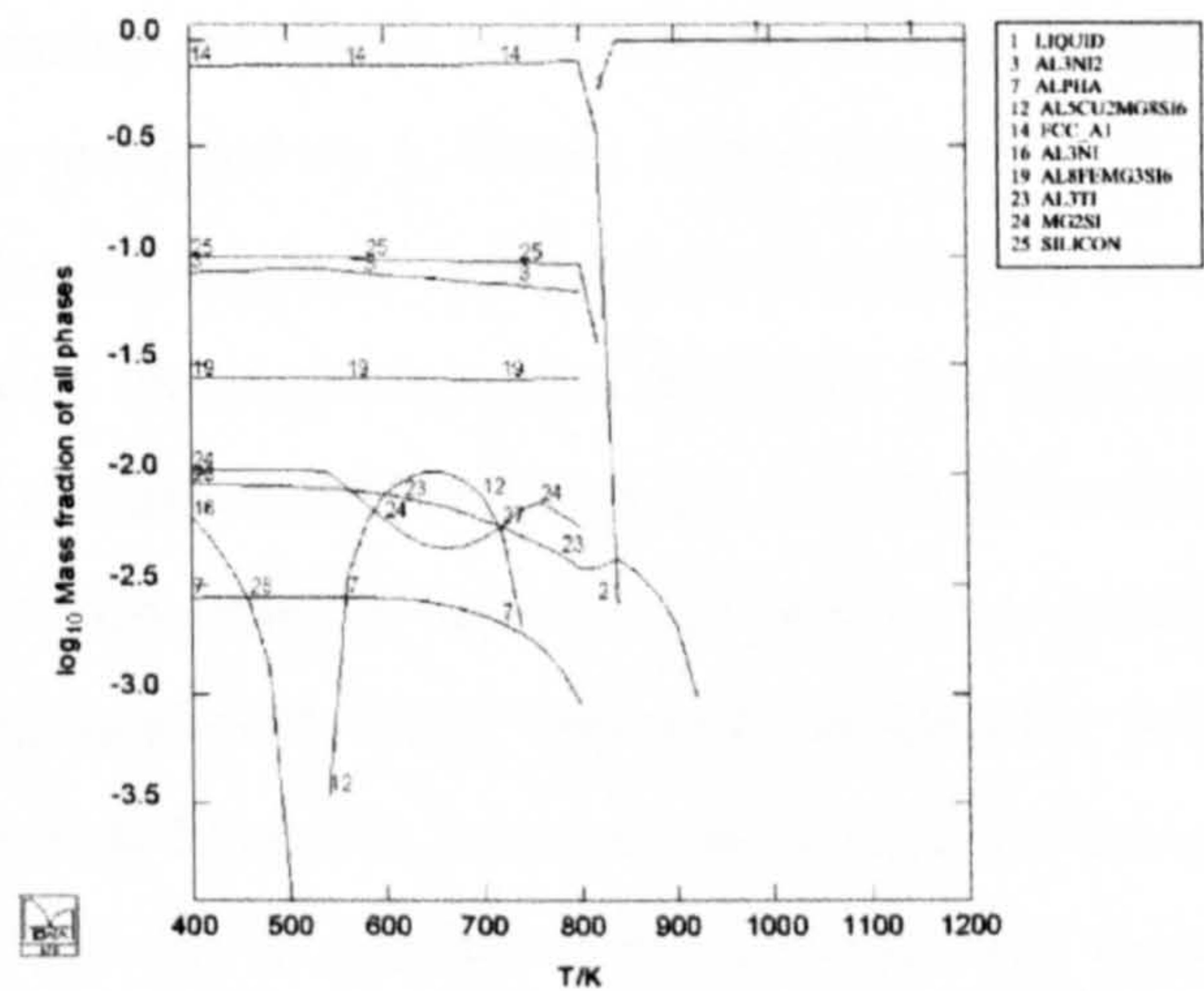
Initially, the fractions of phases for Table 5.3 were taken at a temperature of 400 K, however, the data appeared to be quite inaccurate at these lower temperatures particularly in the COST 507 database. For example, from the stability plot in Figure 5.1 b) it can be seen that COST 507 predicts a BCC_B2 phase at 400 K instead of the expected silicon (DIAMOND_A4) phase, which is not calculated to evolve until a slightly higher temperature of 440 K. This is inconsistent with the other databases and experimental findings, and believed to be a result of low temperature inaccuracy in COST 507. By extracting data at 480 K it is anticipated that the predictions were realistic for the phases present in the alloy casting.

It can be seen that the prediction of phases in AE160, as calculated using Al-Data¹, compares favourably to those observed in the alloy. Eight phases, namely Al, Si, Al₃Ni₂, π (Al₈FeMg₃Si₆), Mg₂Si, Al₃Ni, α (AlMnFeSi) and Al₃Ti, were predicted at the highest mass fractions and agree with those observed. However, calculations using the COST 507 and EurAl databases were less accurate in their predictions. With the exception of the Al and Si phases, which form 90 % of the microstructure, only one or two intermetallics which correspond to the phases observed were predicted by these databases, although several additional phases were predicted but not observed. The calculations by the COST 507 database predicted several phases to form which were not found in the microstructural characterisation; Al₆Mn, Si₂Ti, α (AlFeSi), and Si₂Zr. The Al₆Mn and α (AlFeSi) phases were most probably calculated to form in preference to the α (AlMnFeSi) phase predicted by the other two databases and observed in the alloy. Similarly, it is likely that the Si₂Ti, and Si₂Zr phases were predicted to form as a substitute for the Al₃Ti. These discrepancies are almost definitely a result of the lack of interaction data for the missing elements, particularly Ni.

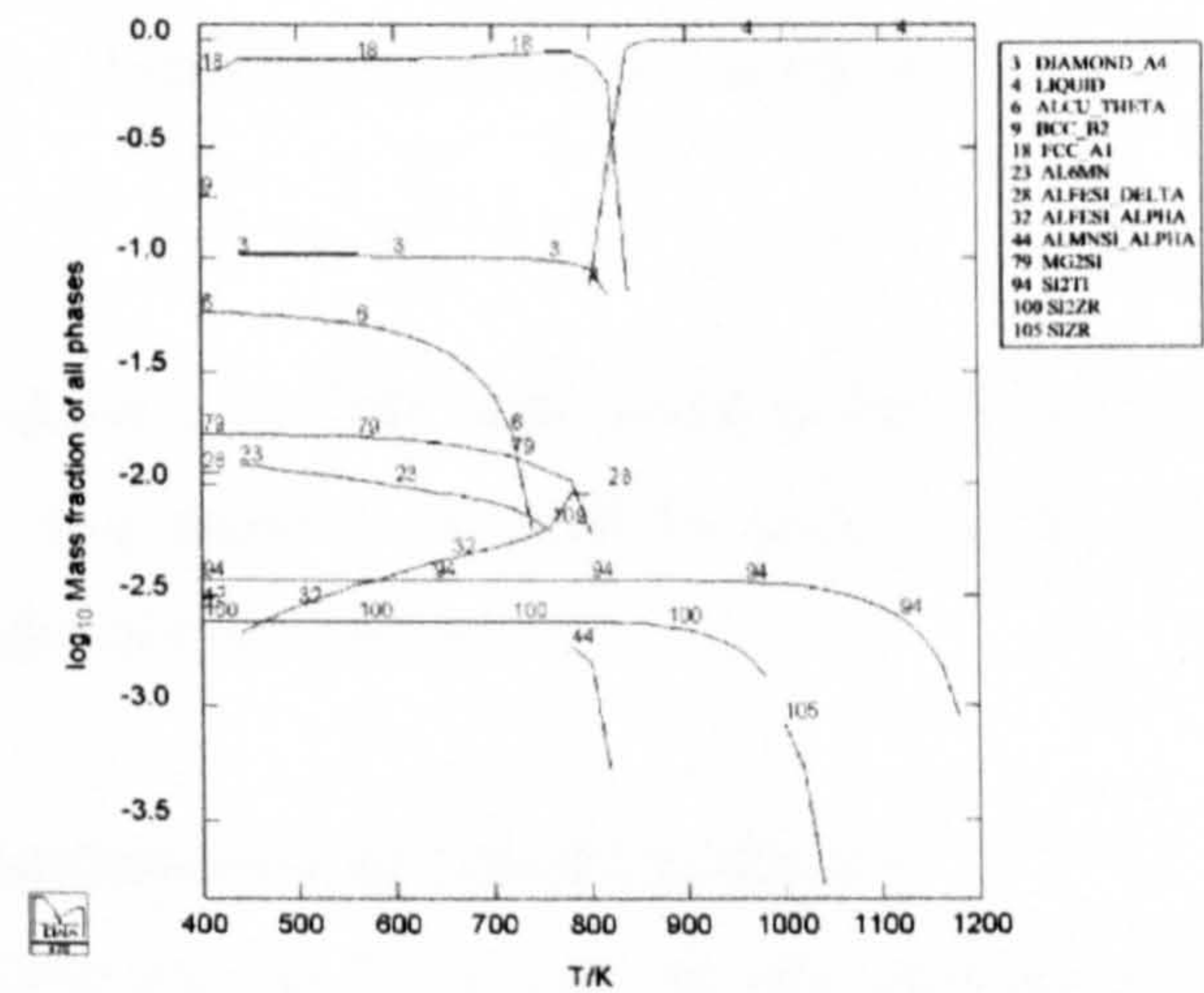
Table 5.3 Comparison of calculated and observed fraction of phases in AE160

Phase	Amount of phase predicted (%) at 480 K			Observed
	Al-Data ¹	COST 507	EurAl	
Aluminium (FCC_A1)	76	80	81	√
Silicon (DIAMOND_A4)	9.9	10	10	√
Al ₃ Ni ₂	8.7			√
π (Al ₈ FeMg ₃ Si ₆)	2.7		3.4	√
Mg ₂ Si	1.0	1.6		√
Al ₃ Ni	0.1			√
α (AlMnFeSi)	0.3		1.3	√
Al ₃ Ti	0.9			√
θ (Al ₂ Cu)		5.6	4.3	√
Al ₆ Mn		1.2		
Si ₂ Ti		0.4		
α (AlFeSi)		0.3		
Si ₂ Zr		0.2		
λ (Al ₅ Cu ₂ Mg ₆ Si ₅)				√
β (AlFeSi)				√
Al ₉ FeNi				√

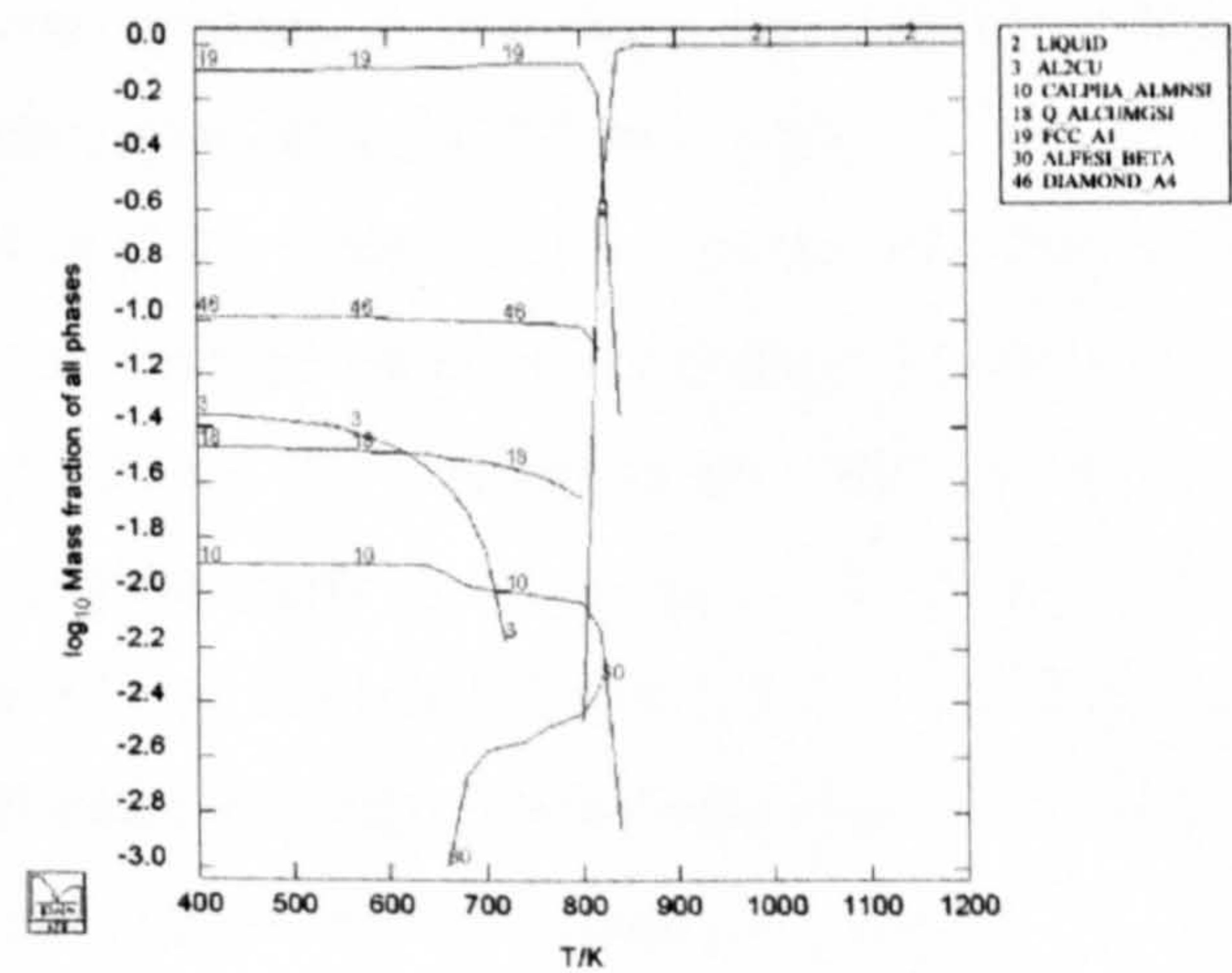
In addition to the main eight phases observed and subsequently predicted by Al-Data¹, four phases were analysed; θ (Al₂Cu), λ (Al₅Cu₂Mg₆Si₅), β (AlFeSi), and Al₉FeNi. Both COST 507 and EurAl predict the θ (Al₂Cu) phase to form in reasonably large fractions (4 - 6 %), and although this phase was identified in AE160, it was only observed in trace amounts such as in segregated regions of the casting. It is most likely that the θ (Al₂Cu) phase is being predicted in the absence of Ni data, as Ni forms several major intermetallics, for example Al₃Ni₂, into which Cu is modelled and found to substitute extensively (see Section 5.3). The other three observed phases, λ (Al₅Cu₂Mg₆Si₅), β (AlFeSi), and Al₉FeNi, none of which were predicted by any database, could be the result of constitutional effects as the local composition of the alloy changes during solidification enough to initiate their formation.



a)



b)



c)

Figure 5.1 Plots of phases stability in AE160 as a function of temperature predicted using **a)** Al-Data¹, **b)** COST 507, and **c)** Eural databases

Also of interest is the missing data for V in COST 507, and Ti, Zr and V in EURAL. The Ti is known to form Al_3Ti , as predicted by Al-Data¹, within which the Zr and V are soluble. These $\text{Al}_3(\text{Ti}, \text{Zr}, \text{V})$ precipitates are stable at high temperatures and act as nuclei for the aluminium, affecting the solidification characteristics and therefore the microstructure of Al-Si alloys. This grain refinement is described fully in Chapter 3, and shall be discussed further in Chapter 6. It is also important, at this time, to mention the addition of phosphorus to alloys such as AE160 to form the compound AlP, which acts as a nucleant for primary Si, as explained in Chapter 3. It is not unexpected that P is not in any of the databases as it is not commonly used in commercial Al-Si alloys due to conflict with strontium and sodium which are added for modification of the eutectic. It is also very difficult to analyse as it is usually washed or pulled out during sample preparation. However, it clearly plays an important role in nucleating silicon, thus changing the thermodynamics of a system, and will therefore be considered further in Chapter 7.

From this initial investigation, Al-Data¹ was found to be, without doubt, the most complete and accurate database, and therefore it shall be used for the predictive modelling work discussed in the remainder of this Chapter.

5.2.2 Comparison of Equilibrium and Scheil Simulations

In this work both equilibrium and Scheil calculations were carried out and compared with experimental analysis of the as-cast (air-cooled) cylindrical mould, model alloys 5, 7 to 11, in order to determine which simulation was most representative of the as-cast state and to establish any major differences between the two models. Compositions for the model alloys are given in Table 5.4 and the effect of the various alloying additions will be discussed briefly. Results of the calculations were saved in tabulated format from which the charts in Figures 5.2 to 5.7 were drawn. In addition to the FCC_{Al} matrix and the silicon phase calculated to form the highest mass fractions in all the model alloys, several intermetallic phases were also predicted and observed. Figures 5.2 to 5.7 show the log fraction of phases predicted by both equilibrium and Scheil calculations with ☆ markers indicating whether the phase was observed in bulk (B) or trace (T) amounts in the alloys.

Table 5.4 Composition of cylindrical mould model alloys (wt. %)

Alloy	Si	Mg	Cu	Ni	Mn	Fe	Pb	Zn	Ti
5	10.37	0.06	0.08	0.05	0.47	0.44	0.01	0.02	0.04
7	10.83	0.07	0.08	1.19	0.09	0.47	0.02	0.02	0.04
8	9.58	0.07	0.08	4.37	0.07	0.51	0.01	0.02	0.03
9	10.47	0.06	1.10	0.06	0.08	0.47	0.01	0.02	0.04
10	9.57	0.06	5.10	0.05	0.07	0.46	0.01	0.02	0.03
11	10.24	0.07	0.08	1.04	0.49	0.48	0.01	0.02	0.03

Balance is Al, all other elements unspecified

Cylindrical Mould: Model Alloys 5 and 11 (Figures 5.2 and 5.3)

Only two intermetallic phases were observed in model alloy 5: α (AlFeMnSi) and β (AlFeSi). The α phase was seen in bulk throughout the microstructure, corresponding with both equilibrium and Scheil calculations, which predicted α to form in the highest mass fraction of the intermetallic phases. The β phase was only seen in trace amounts in this alloy which is in agreement with the Scheil calculation, which predicted the β phase to form with the next highest fraction of intermetallics at less than 1 % mass fraction. However, β was not predicted to form at all in this alloy by the equilibrium simulation.

Four phases; α (AlFeMnSi), Al₉FeNi, Al₃Ni and β (AlFeSi), were observed in model alloy 11. The first two, α and Al₉FeNi, were both seen in bulk quantities and were predicted to form the highest mass fractions of intermetallic phases by both equilibrium and Scheil simulations. Al₃Ni was seen in trace amounts, again corresponding to the calculations which predict this phase to form ~ 1 % mass fraction. The β phase was not predicted by the equilibrium calculation, and was predicted only in small amounts by Scheil. These predictions were represented by the β phase only being seen in trace quantities, most likely as a result of segregation during solidification.

The effect of increasing Ni additions (0.05 to 1.04 wt. % Ni) to an alloy with a reasonably high Mn content (~ 0.48 wt. % Mn) appears to be to increase the stability of the Ni containing phases, Al₉FeNi and Al₃Ni, as would be expected. The α phase remains the most stable and is seen in bulk in both alloys, and the β phase, predicted only by Scheil, becomes less stable with increasing Ni and is only observed in trace quantities.

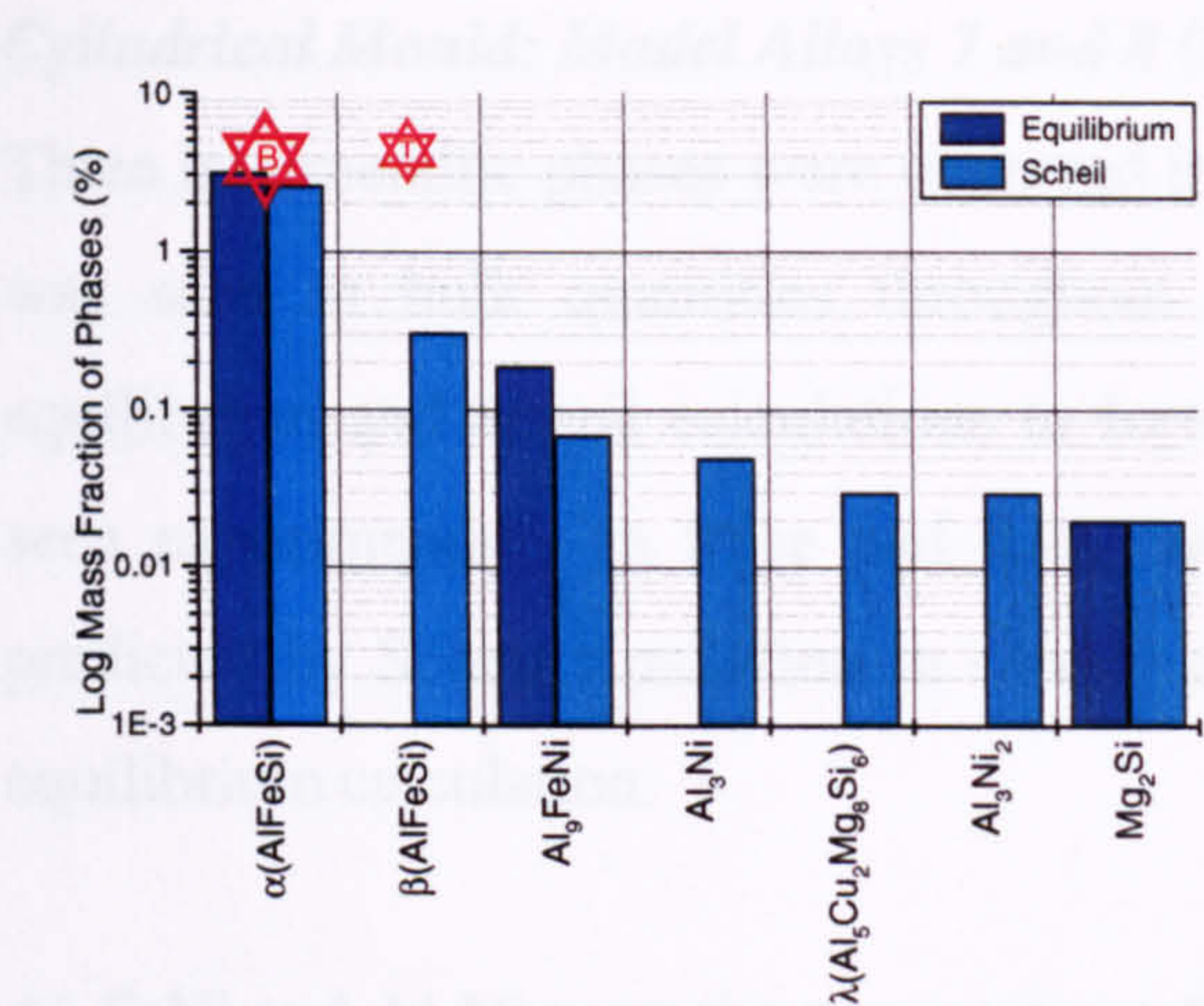


Figure 5.2 Predicted and observed phases for as-cast model alloy 5

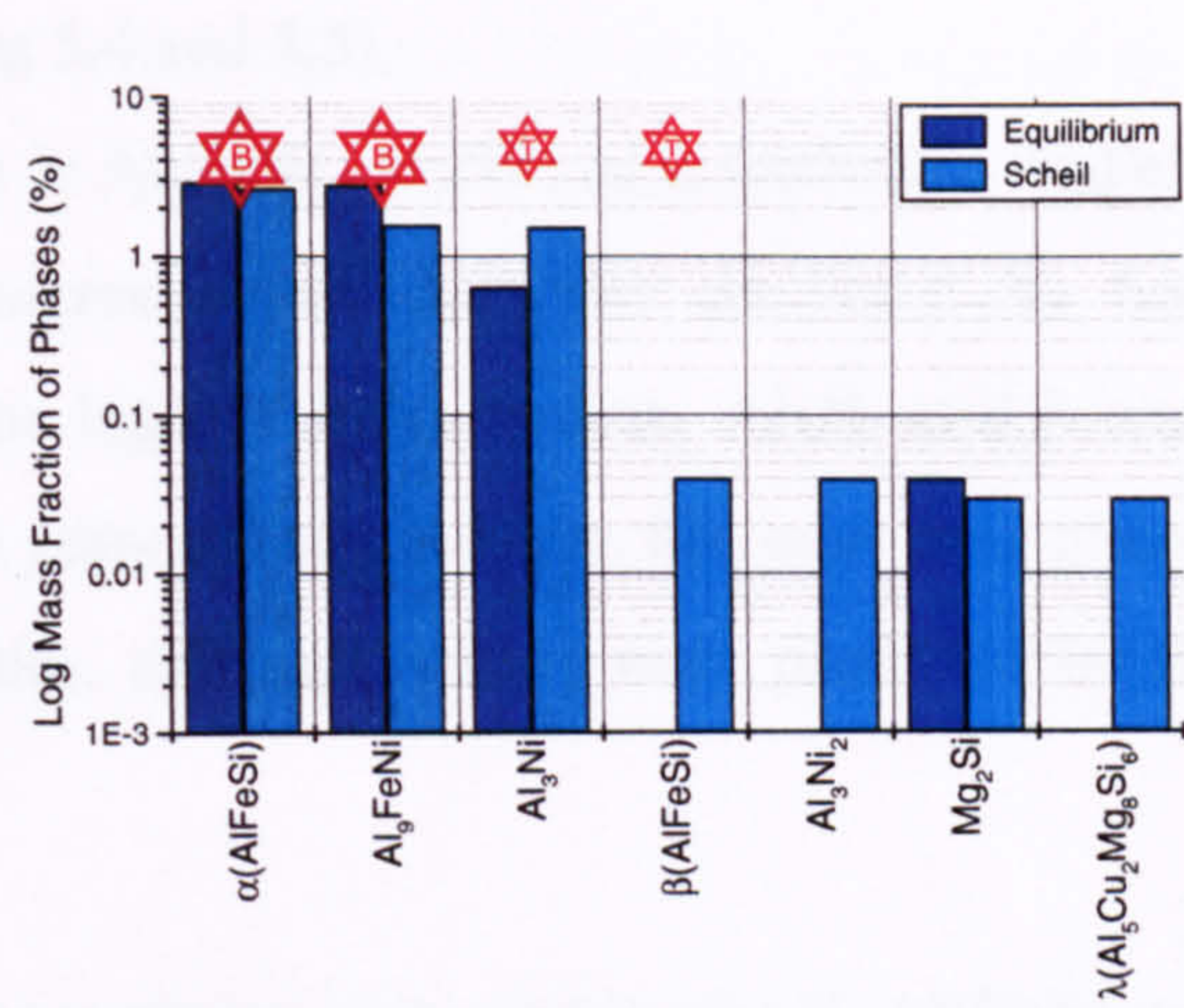


Figure 5.3 Predicted and observed phases for as-cast model alloy 11

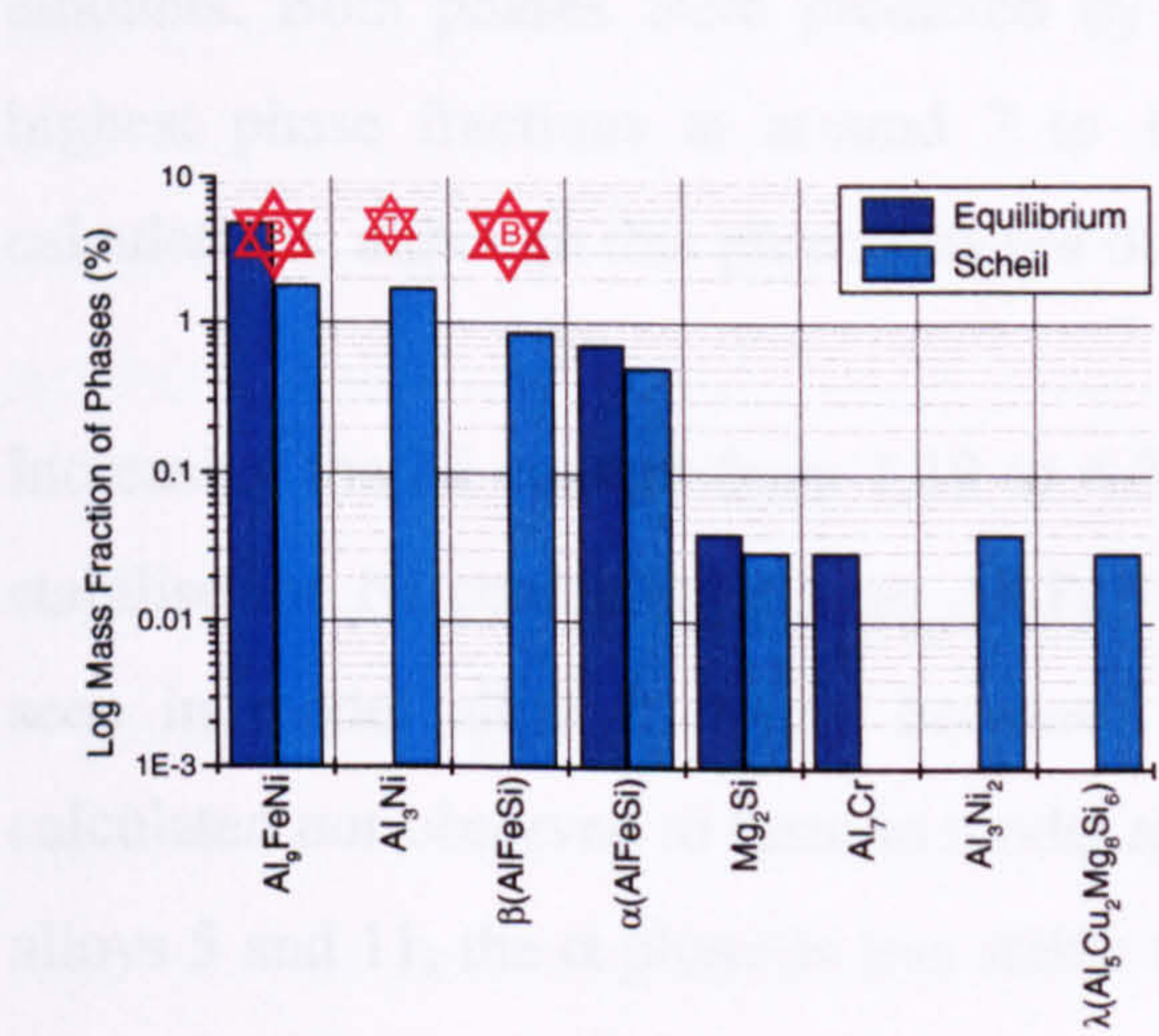


Figure 5.4 Predicted and observed phases for as-cast model alloy 7

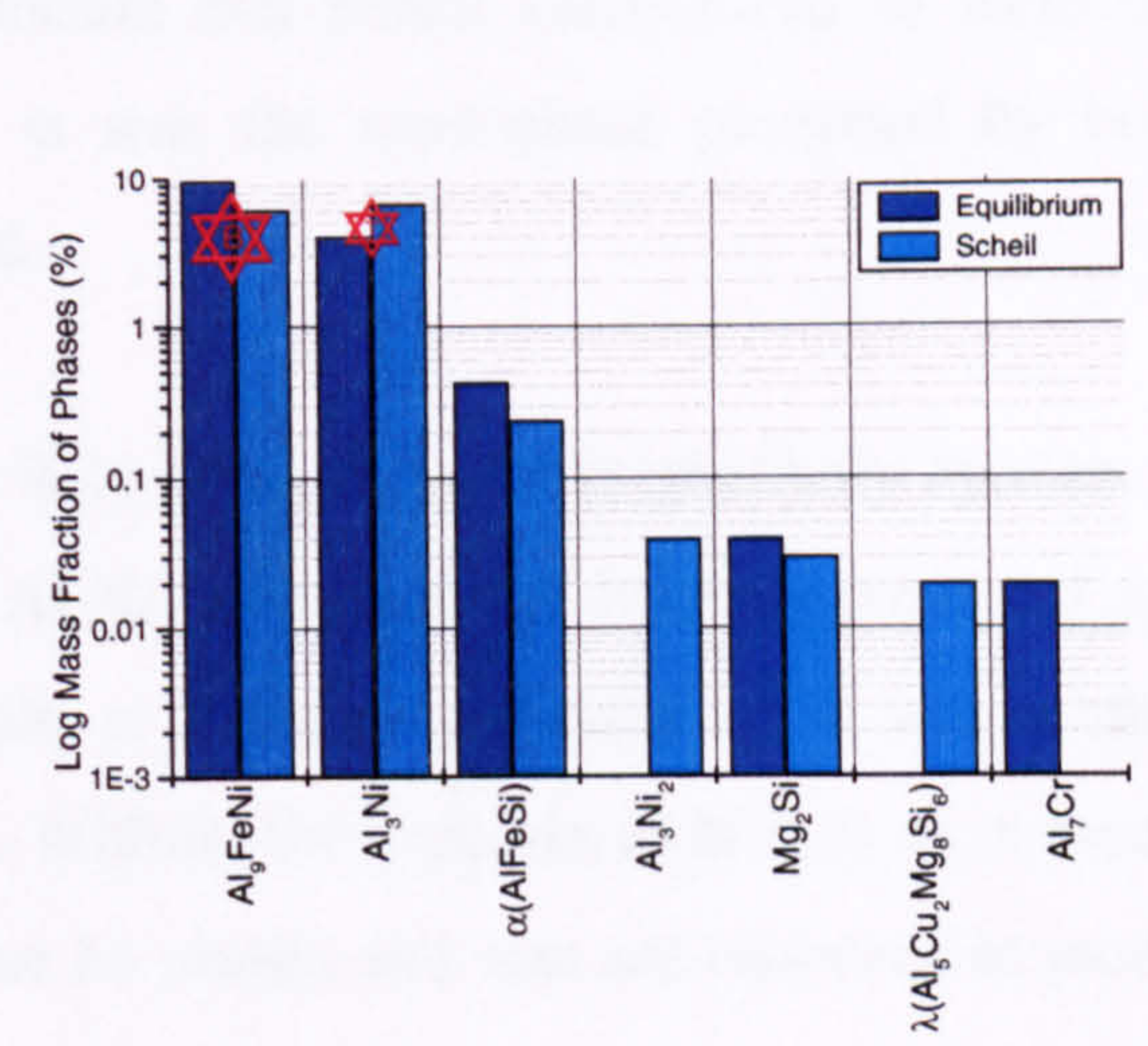


Figure 5.5 Predicted and observed phases for as-cast model alloy 8

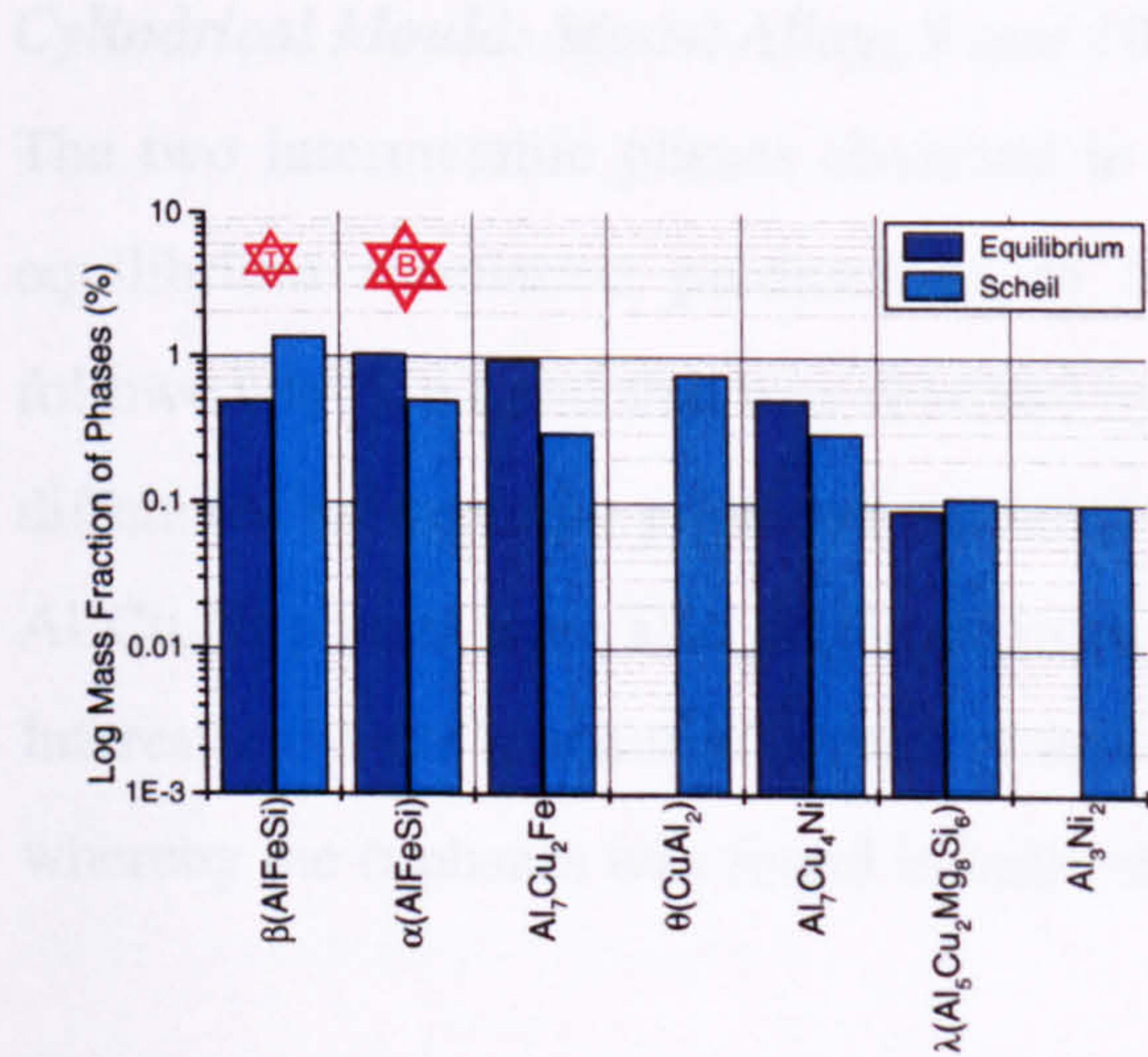


Figure 5.6 Predicted and observed phases for as-cast model alloy 9

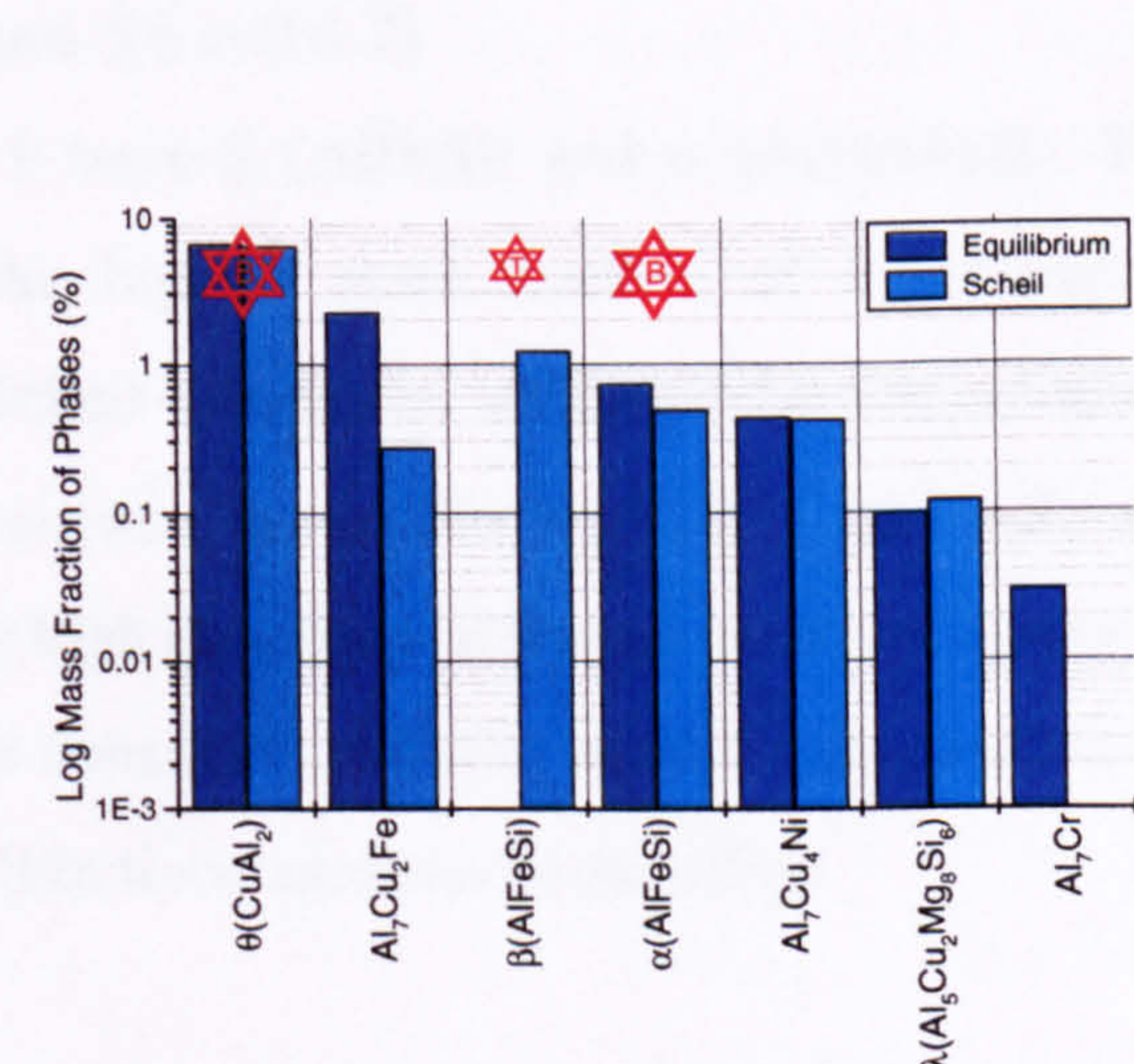


Figure 5.7 Predicted and observed phases for as-cast model alloy 10

Cylindrical Mould: Model Alloys 7 and 8 (Figures 5.4 and 5.5)

Three intermetallic phases were observed in alloy 7: Al_9FeNi , Al_3Ni and β (AlFeSi). Al_9FeNi was seen in bulk quantities throughout the microstructure and was predicted by both equilibrium and Scheil calculations to form in the highest mass fraction. Al_3Ni and β were seen experimentally in trace and bulk amounts respectively and are the next two phases predicted by Scheil simulation in similar quantities, although neither were predicted by the equilibrium calculation.

Al_9FeNi and Al_3Ni were the two intermetallic phases observed in model alloy 8. Al_9FeNi was observed in large quantities in the microstructure whereas Al_3Ni was only seen in small amounts. Both phases were predicted by equilibrium and Scheil calculations to form the highest phase fractions at around 7 to 10 %. α was the next phase predicted by both calculations, although this phase was not observed.

Increasing the Ni content from 1.19 to 4.37 wt. % in alloys 7 and 8 respectively appears to stabilise the Ni containing phases Al_9FeNi and Al_3Ni . However, the β phase predicted and seen in model alloy 7 clearly becomes unstable at high Ni additions as it was neither calculated nor observed to form in model alloy 8. Without the high Mn additions, as in model alloys 5 and 11, the α phase is less stable than the Ni phases and was not observed in model alloys 7 or 8.

Cylindrical Mould: Model Alloys 9 and 10 (Figures 5.6 and 5.7)

The two intermetallic phases observed in alloy 9 were β (AlFeSi) and α (AlFeMnSi). The equilibrium simulation predicted α to form the highest mass fraction of intermetallics followed by β , a trend that was reversed by the Scheil calculation, although there is not much difference between the predicted amounts of these two phases. The θ (Al_2Cu), $\text{Al}_7\text{Cu}_2\text{Fe}$ and $\text{Al}_7\text{Cu}_4\text{Ni}$ phases were also predicted in similarly high quantities although were not observed. Interestingly, the amount of phases observed was consistent with the equilibrium predictions, whereby the α phases was found in bulk and the β in trace amounts in the alloy.

Three phases were observed in this alloy: θ (Al_2Cu), β (AlFeSi) and α (AlFeMnSi). θ (Al_2Cu) was seen in bulk throughout the microstructure, corresponding with both the equilibrium and Scheil simulations which predict this phase to be present in the highest mass fraction of

intermetallic phases. β and α are, in turn, the next phases predicted by Scheil, although they were seen in trace and bulk amounts respectively. β is not predicted to form by equilibrium calculation. Of particular interest is the phase $\text{Al}_7\text{Cu}_2\text{Fe}$, which was predicted to form by both simulations at the second highest fraction, and yet was not observed at all. This could be due to the preferential formation of the α phase which was predicted to be more stable than $\text{Al}_7\text{Cu}_2\text{Fe}$ in model alloy 9, or alternatively that this phase, being present in small quantities, was not found.

Increasing the Cu content from 1.10 to 5.10 wt. % Cu in model alloys 9 and 10 can be seen to increase the predicted stability of the θ (Al_2Cu) and $\text{Al}_7\text{Cu}_2\text{Fe}$ phases, as expected. The θ (Al_2Cu) was observed in bulk in model alloy 10 and not in alloy 9 as predicted, however, the $\text{Al}_7\text{Cu}_2\text{Fe}$ was not found in either alloy despite it being predicted by both equilibrium and Scheil in both alloys. The α and β phases were both predicted and observed in bulk and trace amounts respectively, in both model alloys 9 and 10.

Thus, it can be summarised that both types of simulation, equilibrium and Scheil, are capable of predicting phases representative of an as-cast alloy. Scheil also has the potential to predict minor phases that are likely to form in segregated regions of the microstructure as a result of constitutional effects during solidification.

5.2.3 Comparison of Observed Phases and Equilibrium Predictions

Equilibrium calculations have been proven (Section 5.2.2) to be able to qualitatively predict phases representative of an as-cast alloy, with Scheil having the added capability of predicted phases occurring in segregated regions. This final stage of the verification goes on to quantitatively compare the equilibrium predictions of phase compositions, with EDX analysis of phases precipitated in heat-treated alloys designed to produce microstructures characteristic of equilibrium conditions. The heat treatments were carried out on cylindrical mould model alloys 5, 7 to 11 as described in Chapter 4, and as shown in Figure 5.8 by the heat treatment 2 line. The long holding times above and below the liquidus temperature allowed some very large intermetallic particles to grow, as can be seen in Figure 5.9, enabling precise EDX analysis which is not often possible when particles are very small. The accurate EDX analysis thus facilitated a comparison with equilibrium thermodynamic calculations of phase compositions.

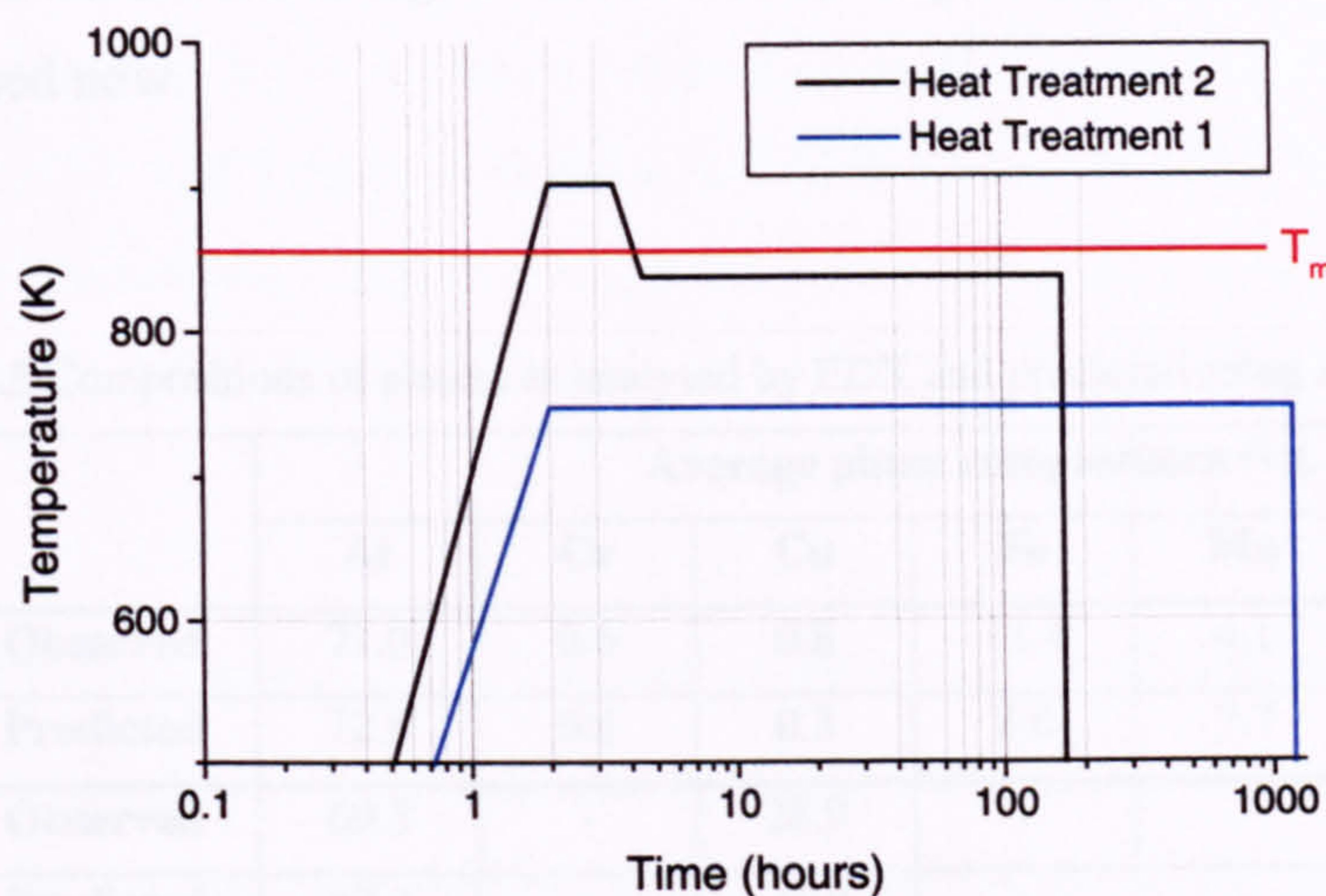


Figure 5.8 Heat treatment profiles for cylindrical mould model alloys 5, 7 to 11

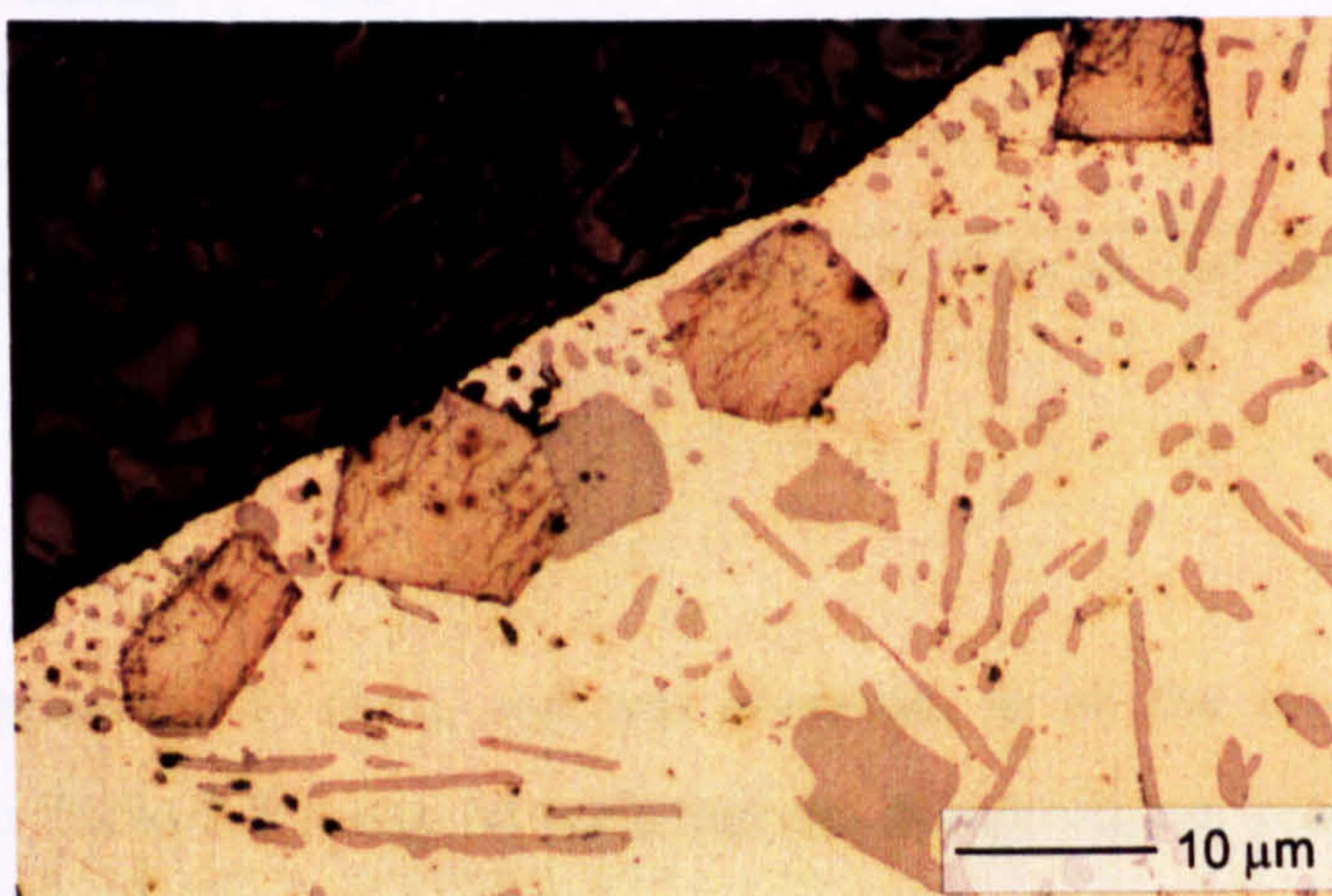


Figure 5.9 Optical micrograph of model alloy 5 after heat treatment

From the equilibrium calculations, 903 K was confirmed to be a high enough temperature for complete melting, and liquid was predicted to be present at 838 K during the second stage of heat treatment 2, establishing that the alloy was indeed in the ‘mushy zone’. several intermetallic phases were predicted in addition to the FCC_A1 matrix and the silicon phase seen to form the highest mass fractions in all the model alloys. In general the same 5 intermetallic phases were observed and predicted after both heat treatments, namely Al_3Ni , α (AlFeMnSi), Al_9FeNi , β (AlFeSi) and θ (Al_2Cu). These are the same intermetallics previously observed in the as-cast alloys. Average compositions of the five intermetallic phases observed in the heat-treated alloys, as determined by EDX, were compared with those predicted at 600

K in an equilibrium simulation using Al-Data¹. The average compositions are given in Table 5.5 and are discussed now.

Table 5.5 Compositions of phases as analysed by EDX and predicted using Al-Data¹

Phase		Average phase compositions (wt. %)						
		Al	Cr	Cu	Fe	Mn	Ni	Si
$\alpha(\text{AlFeMnSi})$	Observed	71.0	0.6	0.8	11.4	4.1	1.0	11.3
	Predicted	72.8	0.8	0.3	8.6	7.7	-	9.8
$\theta(\text{Al}_2\text{Cu})$	Observed	69.3	-	28.9	-	-	0.8	1.0
	Predicted	67.3	-	31.9	-	-	-	0.7
$\beta(\text{AlFeSi})$	Observed	64.1	-	-	15.6	1.5	1.1	17.9
	Predicted	69.2	-	-	15.4	-	-	15.4
Al_9FeNi	Observed	80.6	0.1	-	4.2	0.4	11.5	3.0
	Predicted	81.8	-	-	4.0	-	14.2	-
Al_3Ni	Observed	75.4	-	0.8	0.5	-	22.6	0.8
	Predicted	75.0	-	-	-	-	25.0	-

(Errors approximately ± 5 wt.% for Al, and ± 1 wt. % for all other elements)

$\alpha(\text{AlFeMnSi})$

The α phase was predicted to form, and was observed, in all the model alloys after heat treatment, and from Table 5.3 it can be seen that the compositions, predicted and observed, compare well. Slight discrepancies can be explained by the way in which this non-stoichiometric phase is modelled in Al-Data¹, where Al and Si are modelled to mix extensively, with Fe, Cr, Cu and V all being able to substitute for Mn.

$\theta(\text{Al}_2\text{Cu})$

The θ phase was observed and predicted to form in model alloy 10 which has the highest Cu content of all the model alloys at 5.1 wt. % Cu. The predicted and observed compositions again match well, with an indication that there is some limited solubility of Ni, which is not allowed for in the non-stoichiometric model of this phase. However, Cu and Ni are often found to substitute with each other, and therefore provides an explanation for the Ni content.

β (AlFeSi)

β was observed in just one alloy, 9, and predicted in both 7 and 9. It is modelled as a stoichiometric compound, and although observations indicate that the Al, Si and Fe contents match well with the predictions, there is clearly also some solubility of Mn and Ni in this phase, again not accounted for in the calculations

 Al_9FeNi

The intermetallic Al_9FeNi was observed in model alloys 7, 8 and 11, these having the higher Ni content of greater than 1 wt. % Ni. This non-stoichiometric phase was predicted in alloys 5, 8, 9 and 11 with the Fe and Ni modelled to mix in Al_9FeNi as can be seen in Table 5.5. From observations there also appears to be some solubility of Si, Mn, and Cr in very small amounts, although the Si could be a result of beam overlap with silicon crystals.

 Al_3Ni

The Al_3Ni phase was observed and predicted in the alloy with highest Ni content, model alloy 8. The phase is modelled as stoichiometric and the Al and Ni contents compare favourably, however, observations also show traces of Si and Cu solubility in this phase. The Si could again be a result of beam overlap with silicon crystals, and it has been discussed already that Cu and Ni are known to substitute for each other.

5.2.4 Summary

Three commercial thermodynamic databases were investigated and it was established that Al-Data¹ contained the most accurate and complete data, and would therefore be used in further work. Phases predicted by both equilibrium and Scheil calculations were found to be representative of the castings, with Scheil having the potential to predict phases that only occur in segregated regions. Discrepancies between the observed and predicted compositions can generally be explained by the way in which the phase has been modelled [Sau99], with the solubility and substitution of certain elements in some of the phases often not taken into account.

5.3 Phase Analysis of AE160

It has been shown (Chapter 2) that commercial aluminium-silicon piston alloys contain many elements in the form of both deliberate additions and impurities. These additions can interact to form many different phases, the majority of which are non-stoichiometric containing three or more elements as shown in Table 5.6. The phases that make up the microstructure of a casting are of particular importance in determining the properties of the alloy, as discussed in Chapter 2. A detailed knowledge of these phases is therefore critical in being able to develop and model such alloys.

Table 5.6 Phases likely to occur in multicomponent aluminium-silicon piston alloys

Elemental	Binary	Ternary	Quaternary
Al	Al ₃ Ti	Al ₃ (Cu,Ni) ₂	λ (Al ₅ Cu ₂ Mg ₈ Si ₆)
Si	AlP	Al ₇ Cu ₄ Ni	π (Al ₈ FeMg ₃ Si ₆)
	θ (Al ₂ Cu)	β (AlFeSi)	α (AlFeMnSi)
	Mg ₂ Si	Al ₉ FeNi	
	Al ₃ Ni		

Although the properties of the commercial alloy AE160, previously discussed in Section 2.6, are known to be better than its predecessors, to date no detailed characterisation of the alloys has been carried out. In this section, AE160 and three model alloys based on AE160, are thoroughly investigated using optical and electron microscopy, and thermodynamic modelling using the Al-Data³ database. The compositions of the four alloys used are given in Table 5.7, and it can be seen that model alloys 24, 25 and 38 have compositions close to that of AE160 but with slightly different additions of V. An equilibrium phase stability plot of AE160 is given in Figure 5.10 and shows that 6 intermetallic phases are predicted in addition to the aluminium and silicon; Al₃Ni₂ (referred to in this work as Al₃(Cu,Ni)₂), λ (Al₅Cu₂Mg₈Si₂), Al₉FeNi, Al₃Ti, and α (AlFeMnSi). EBSD and EDX were also used for phase identification, and in this work three materials databases were used; the Powder Diffraction File produced by the International Centre for Diffraction Data (ICDD), the TexSEM Laboratories (TSL) database constructed from experimental findings, and the user generated database consisting of material files created during this work.

Table 5.7 Compositions of commercial alloy AE160 and model alloys 24, 25 and 38

Alloy	Wt. % Element									ppm
	Si	Mg	Cu	Ni	Mn	Fe	Ti	Zr	V	P
AE160	11.2	1.05	3.1	2.27	0.08	0.3	0.17	0.15	0.06	53
24	11.6	0.99	3.50	2.40	-	0.31	0.18	0.11	0.05	80
25	11.6	0.99	3.80	2.73	-	0.31	0.16	0.12	0.065	59
38	11.94	0.76	3.49	2.28	-	0.28	0.13	0.12	0.12	66

Balance is Al, all other elements unspecified

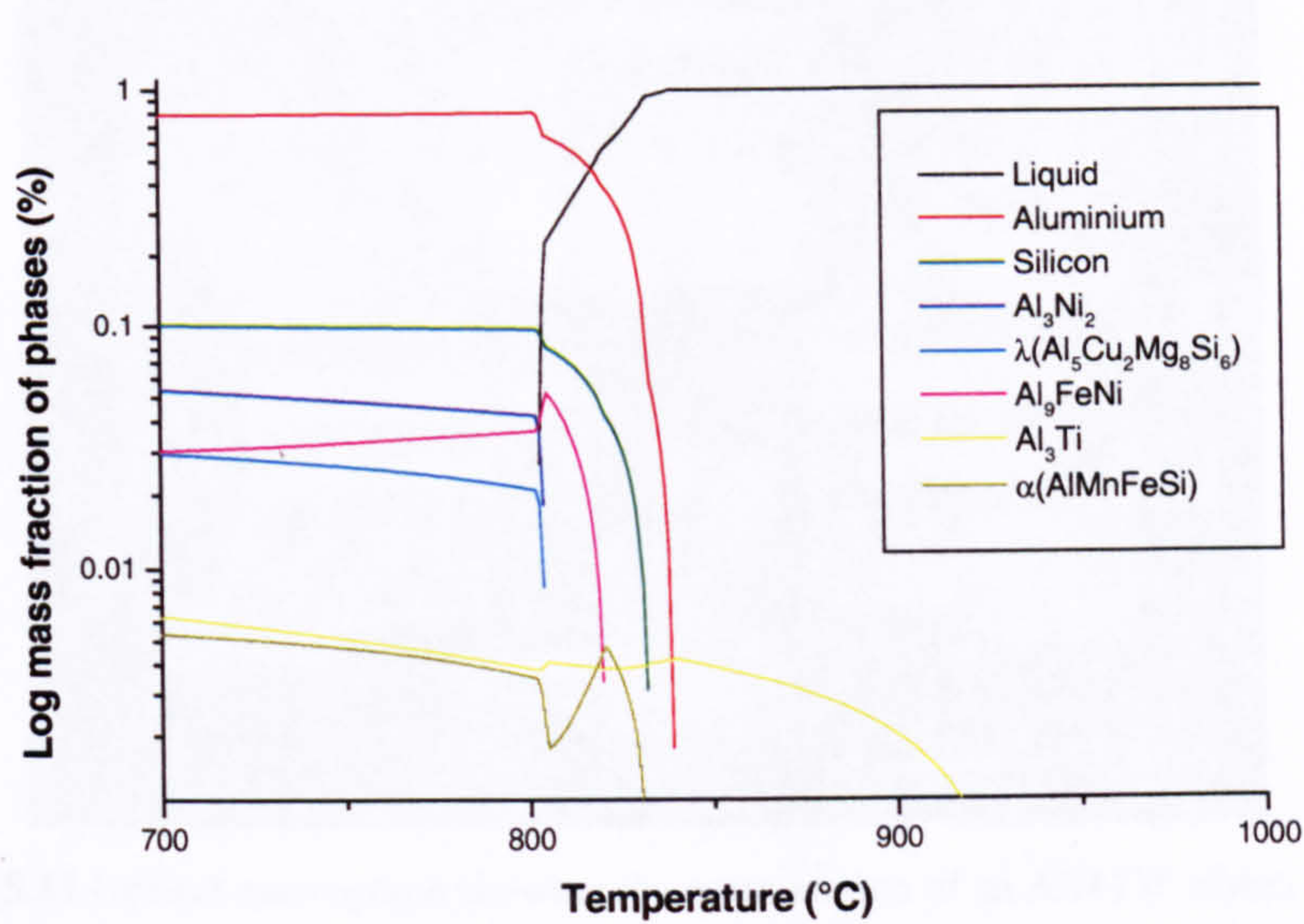


Figure 5.10 Phase stability as a function of temperature for AE160

5.3.1 Aluminium Matrix

The Al phase, also referred to as FCC_A1 in respect to its sublattice, forms the matrix of the microstructure in all the alloys of interest, aluminium being the main constituent with small concentrations of impurities present in solid solution. The aluminium matrix is known to grow with a well-defined dendritic structure forming both columnar and equiaxed grains, as seen in the macrograph in Figure 5.11. The large columnar grains are a result of dendritic growth along the direction of heat flow, for example in thin sections and at the edges of the casting where there are large temperature gradients. The more equiaxed grains occur in thicker sections of a casting where cooling rates are generally slower and temperature gradients are negligible. Nucleation is achieved by supercooling and can be enhanced by addition of certain elements which act as grain refiners and lower the supercooling necessary for nucleation (see

Chapter 3), thus promoting equiaxed growth. Equiaxed growth is preferential in castings as large aluminium dendrites have been found to initiate and promote fatigue failure, as seen in Figure 5.12. Figure 5.12 a) shows an Al dendrite initiated fracture, and Figure 5.12 b) shows a slant fracture along a number of Al dendrites.

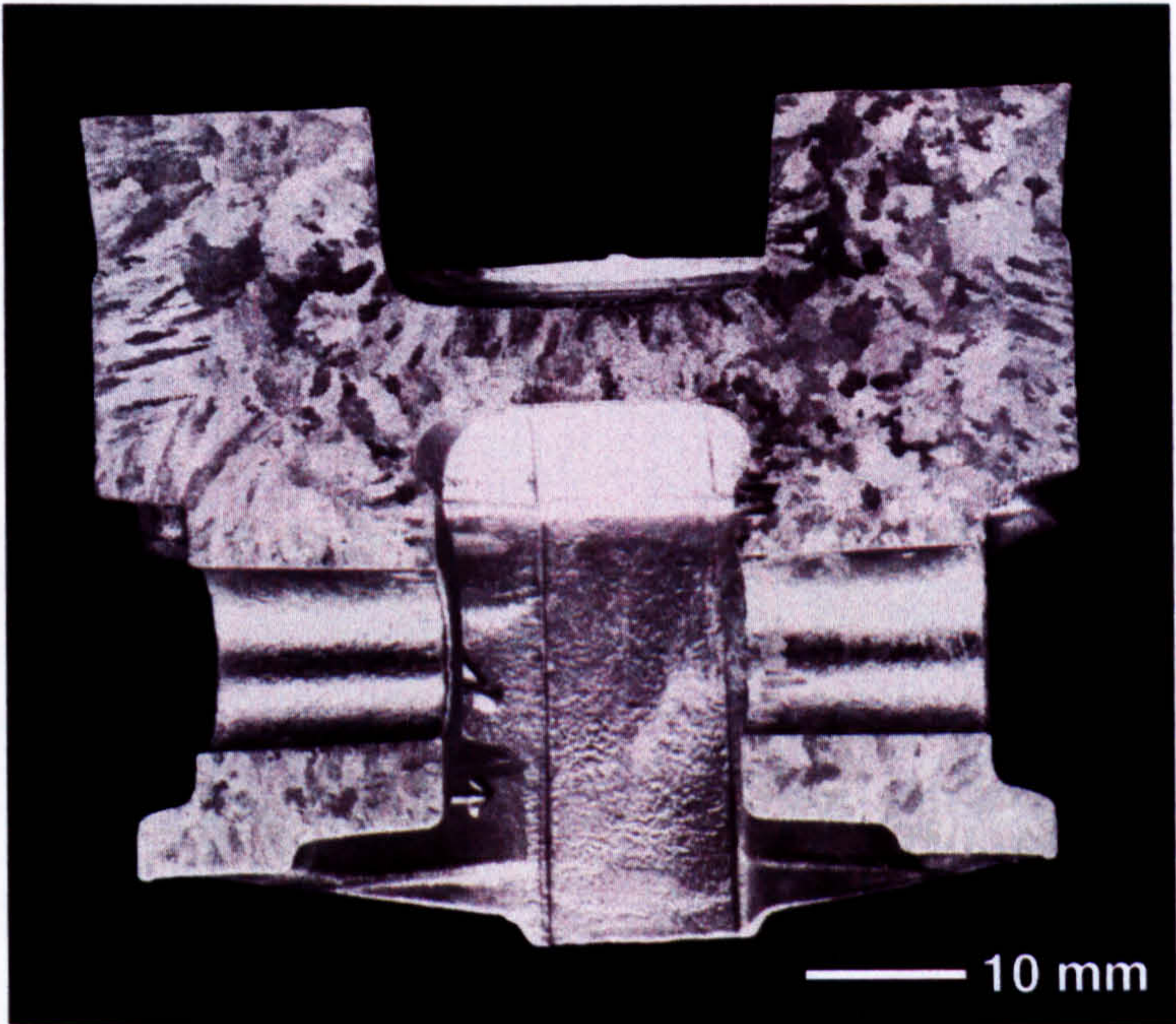


Figure 5.11 Optical macrograph showing the cross section of an AE413P piston casting, etched (3 % HCl, 1 % HF and 1 % HNO₃) to reveal the aluminium grain structure

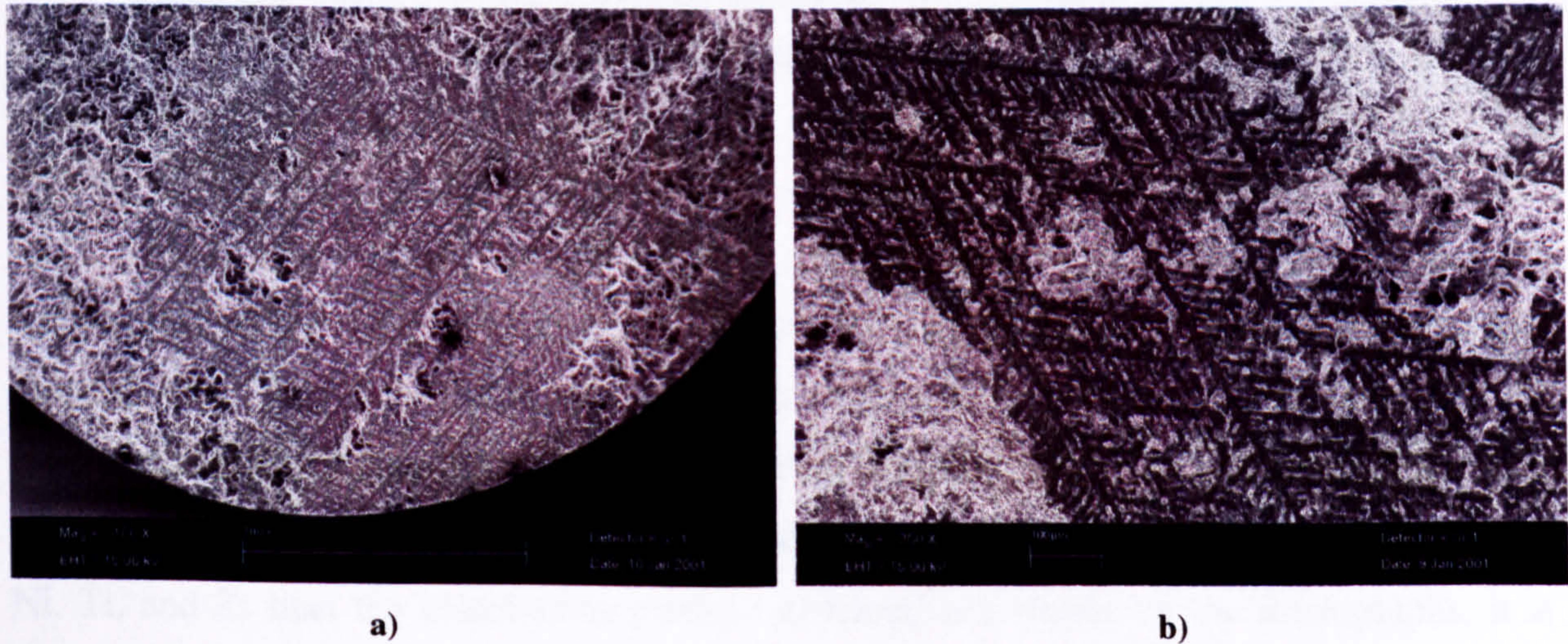


Figure 5.12 SEM micrographs of **a)** dendrite initiated failure, and **b)** slant fracture along Al dendrites during a fatigue test at 200 °C, courtesy of S. Barnes, Federal-Mogul, Cawston

On micro-etching with 0.5 % HF in water, the aluminium phase appears a pale yellow colour. At low magnifications the dendritic structure is often clearly visible, such as in the microstructure representative of the columnar region shown in Figure 5 13 a), where the large aluminium dendrites form the columnar grains seen in Figure 5.11. Constitutional effects appear to have lead to the formation of secondary phases between the dendrite arms and ahead of dendrite tips due to segregation at the solidifying front. In particular clustering of primary Si particles can be seen ahead of the dendrite tips. The dendritic structure is not as evident in the equiaxed zone (Figure 5.13 b) with secondary phases evenly distributed throughout the matrix. The intermetallics appear to be slightly larger in this region, which is to be expected as a result of longer solidification times enabling further growth and coarsening.

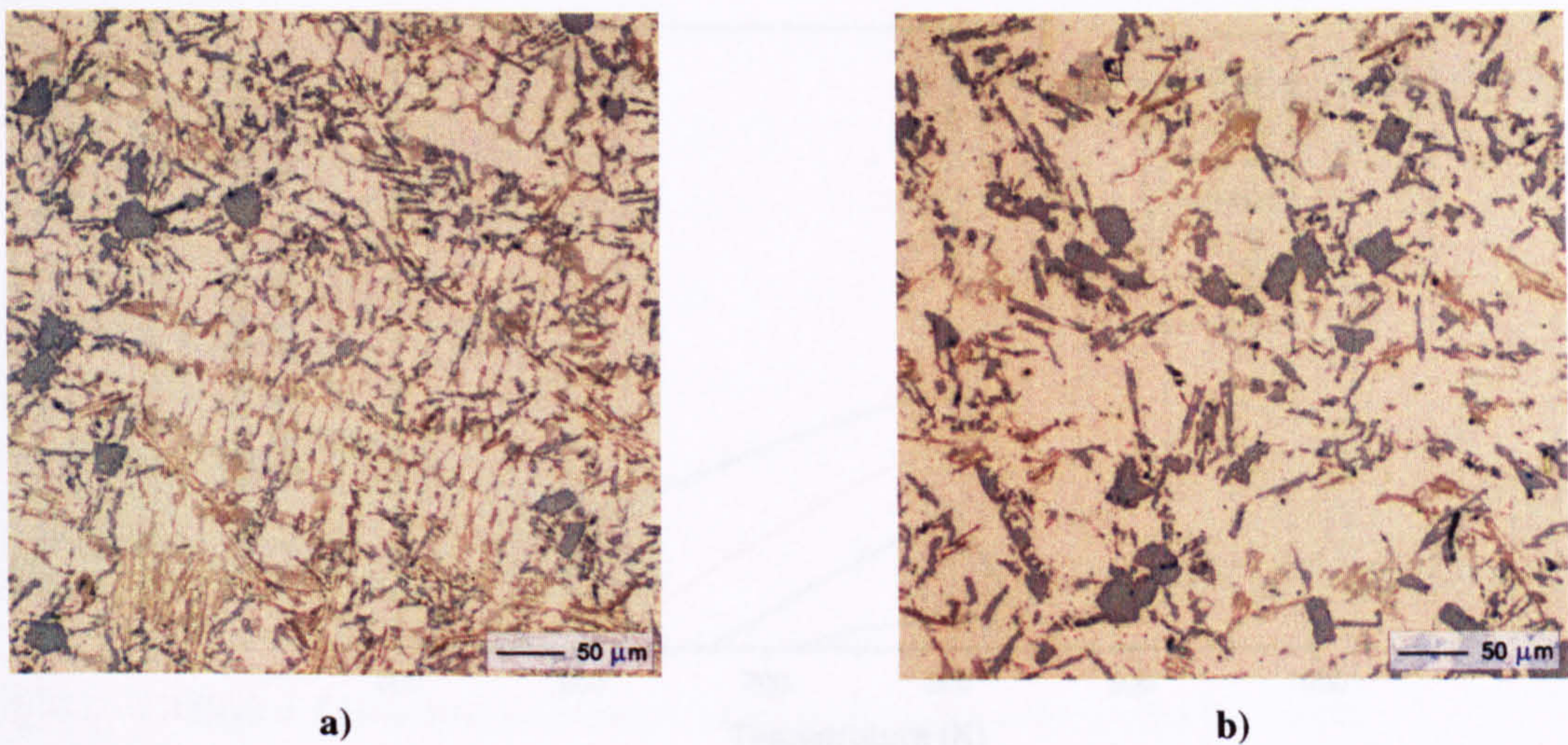


Figure 5.13 Optical micrographs showing microstructures representative of the **a)** the columnar, and **b)** the equiaxed regions of a piston casting

EDX analysis was carried out on all four alloys (AE160 and model alloys), and the composition of the FCC_{Al} phase was found to be predominantly aluminium with very small amounts (less than 1 wt.% in most cases) of other elements. Table 5.8 shows how the predicted composition compares with the observed compositions. The sets of data are very similar, with the observed values indicating that there is more solubility in aluminium of Cu, Ni, Ti, and Zr than the calculations predict. Although not visible on the micrographs, it is known that precipitates, such as $\theta(\text{Al}_2\text{Cu})$, often form in the matrix which could account for the presence of these elements. These are investigated further in Chapter 6. The predicted values in the table are taken from the calculation at a temperature of 500 K, whilst the plot in

Figure 5.14 shows solubility as a function of temperature. The level of solubility of all the minor elements is predicted to increase with temperature, and therefore variation in the solubility of these elements is to be expected.

Table 5.8 Composition of the FCC_A1 phase (aluminium matrix)

	Fraction of component in phase									
	Al	Cu	Fe	Mg	Mn	Ni	Si	Ti	V	Zr
Observed (At.%)	99.0	0.4	-	-	-	0.2	-	0.2	-	0.4
Observed (Wt.%)	97.4	1.0	-	-	-	0.1	-	0.3	0.1	1.2
Predicted (Wt.%)	99.85	< 0.1	< 0.1	< 0.1	< 0.1	< 0.1	< 0.1	< 0.1	< 0.1	< 0.1

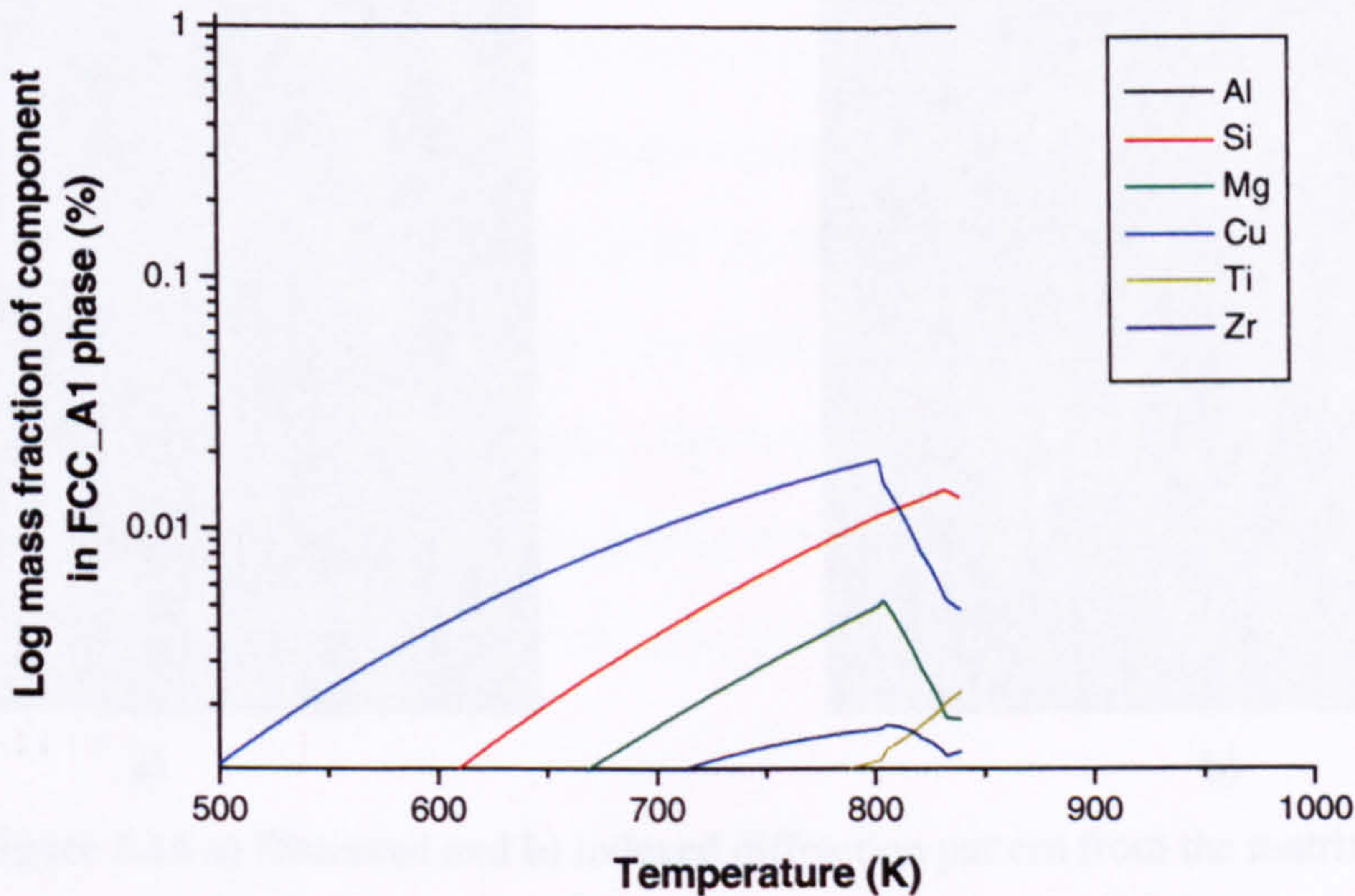


Figure 5.14 Plot of log mass fraction of components in the FCC_A1phase as a function of temperature

EBSD and corresponding EDX were carried out on the matrix. The EDX spectrum from a spot analysis is given in Figure 5.15, showing energy, eV (x-axis) against intensity (y-axis), and confirming the matrix to be predominantly Al. A Kikuchi diffraction pattern was collected and is shown in Figure 5.16 a). The ICDD database contains 7 aluminium phases, all of which are cubic and have similar diffraction data, however, the pattern was indexed automatically as card number 85-1327. The indexed pattern is given in Figure 5.16 b) and can be seen to fit reasonably well with a few slight discrepancies between the observed and indexed images. Out of the 5 x-ray reflectors given in the ICDD database, the first four (111,

200, 220, and 311) correspond almost exactly with the powder diffraction, as shown in Table 5.9.

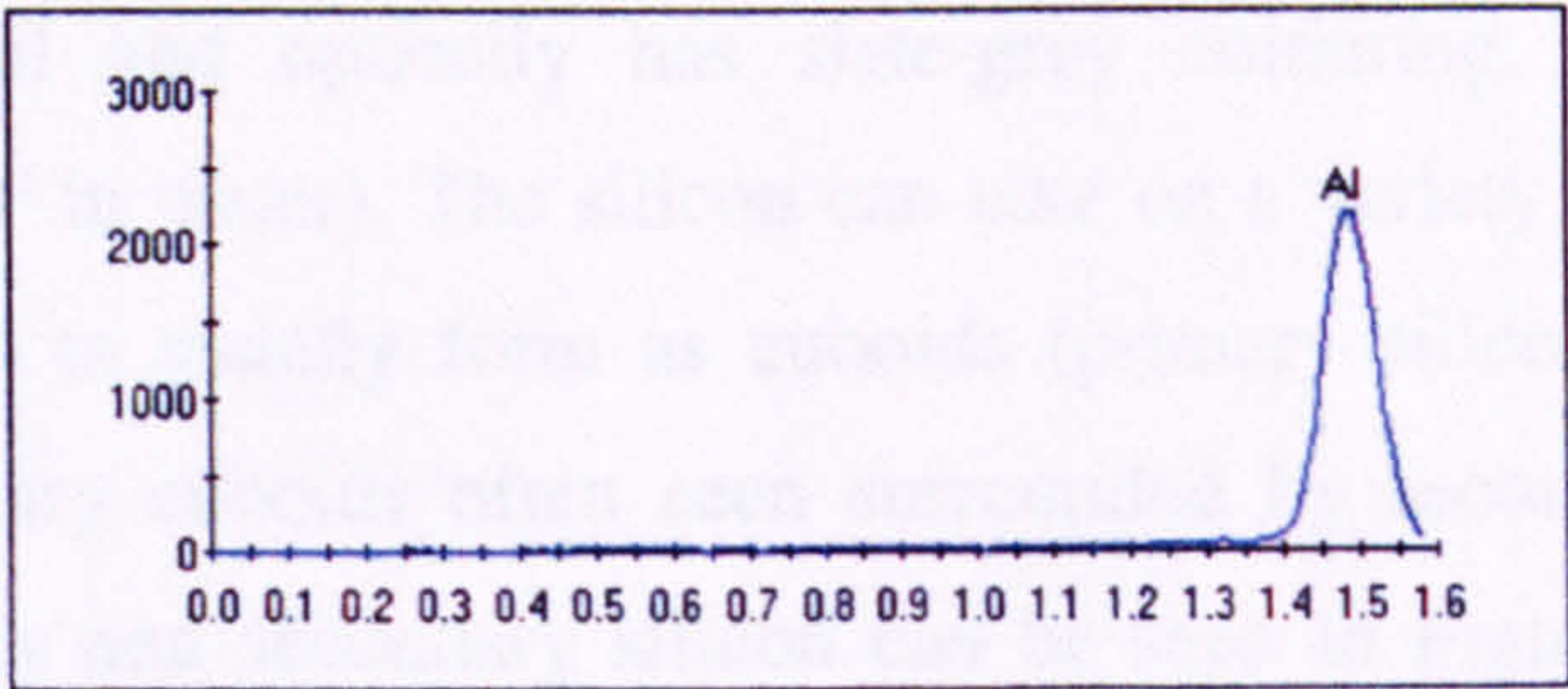


Figure 5.15 EDX spectrum of the matrix (x-axis is energy (eV), and the y-axis is intensity)

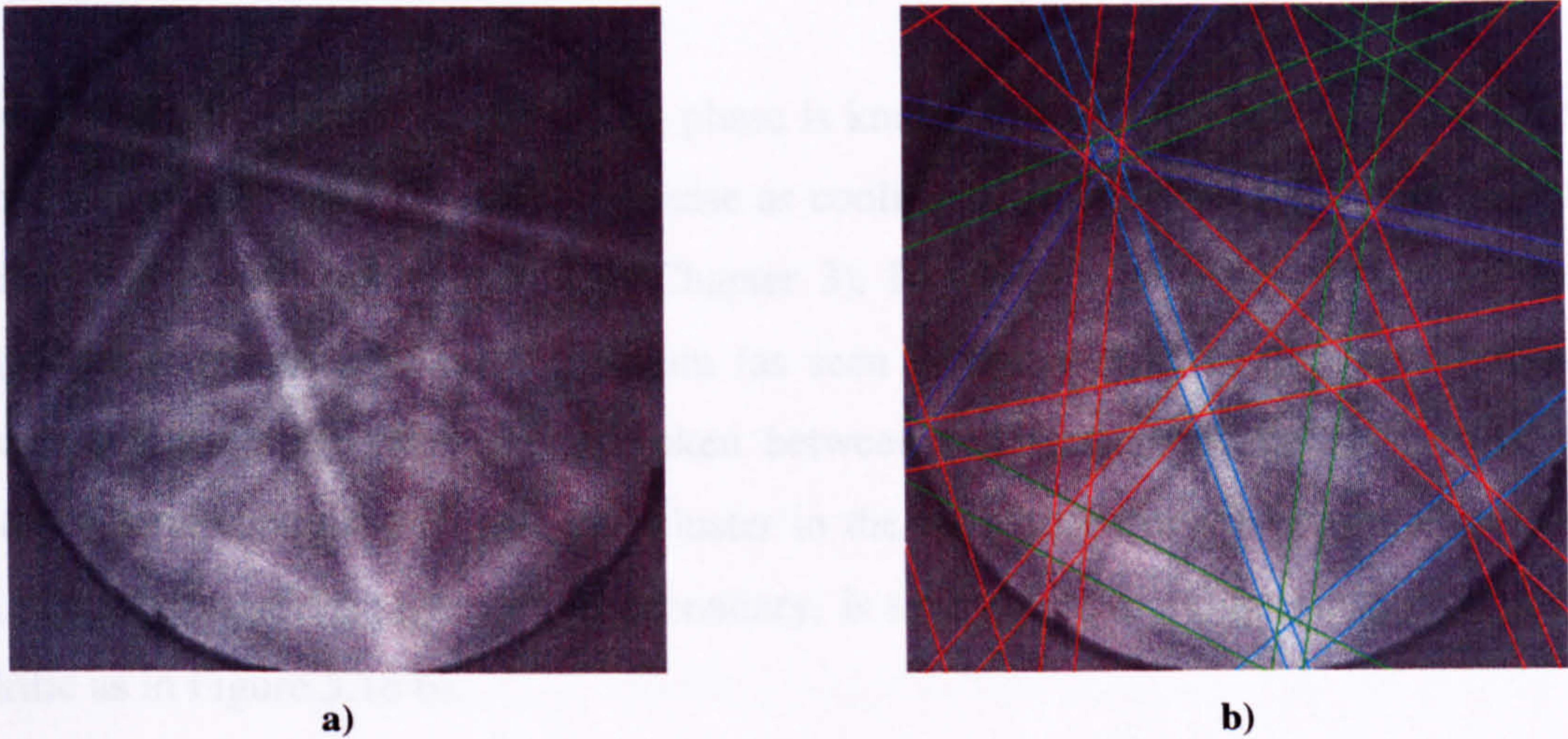


Figure 5.16 a) Observed and b) indexed diffraction pattern from the matrix

Table 5.9 Crystallographic and diffraction data for the matrix

Crystal System		Cubic F		
Space Group		Fm3m		
Lattice Parameter (Å)		a=4.0494		

hkl	ICDD (85-1327)		EBSD	
	Interplanar spacing, d (Å)	Intensity	Interplanar spacing, d (Å)	Intensity
111	2.3379	999	2.332	-
200	2.0247	455	2.020	-
220	1.4316	233	1.428	-
311	1.2209	228	1.218	-
222	1.1689	63	-	-

5.3.2 Silicon

The bulk silicon content in the alloys studied in this work is near-eutectic, that is it ranges from 10-14 wt.% silicon. The silicon, or DIAMOND_A4, phase is present throughout all regions of the material and optically has slate-grey colouring, both before and after microetching (0.5 % HF in water). The silicon can take on a variety of morphologies, but in this work it was found to usually form as cuboids (primary silicon) or plates (secondary silicon), with the primary cuboids often seen surrounded by secondary flakes in a radial formation. Both primary and secondary silicon can be seen in Figure 5.17, although many silicon particles have a less defined shape than the more common cuboids and plates. Silicon particles are studied at in greater detail with respect to nucleation, growth, and resultant morphology in Chapter 7.

The shape and distribution of the silicon phase is known to be dependent on the cooling rate, and the size of the phase is seen to increase as cooling rates decrease due to the longer time available for growth (as discussed in Chapter 3). In addition, it seems that when there is strong dendritic growth of the aluminium (as seen in Figure 5.18 a) the secondary silicon particles become more fibrous and broken between and around the dendrite arms, whilst primary silicon cuboids segregate and cluster in the bulk ahead of the dendrite tip. A fairly even distribution of Si, primary and secondary, is seen when the aluminium growth is less dendritic as in Figure 5.18 b).

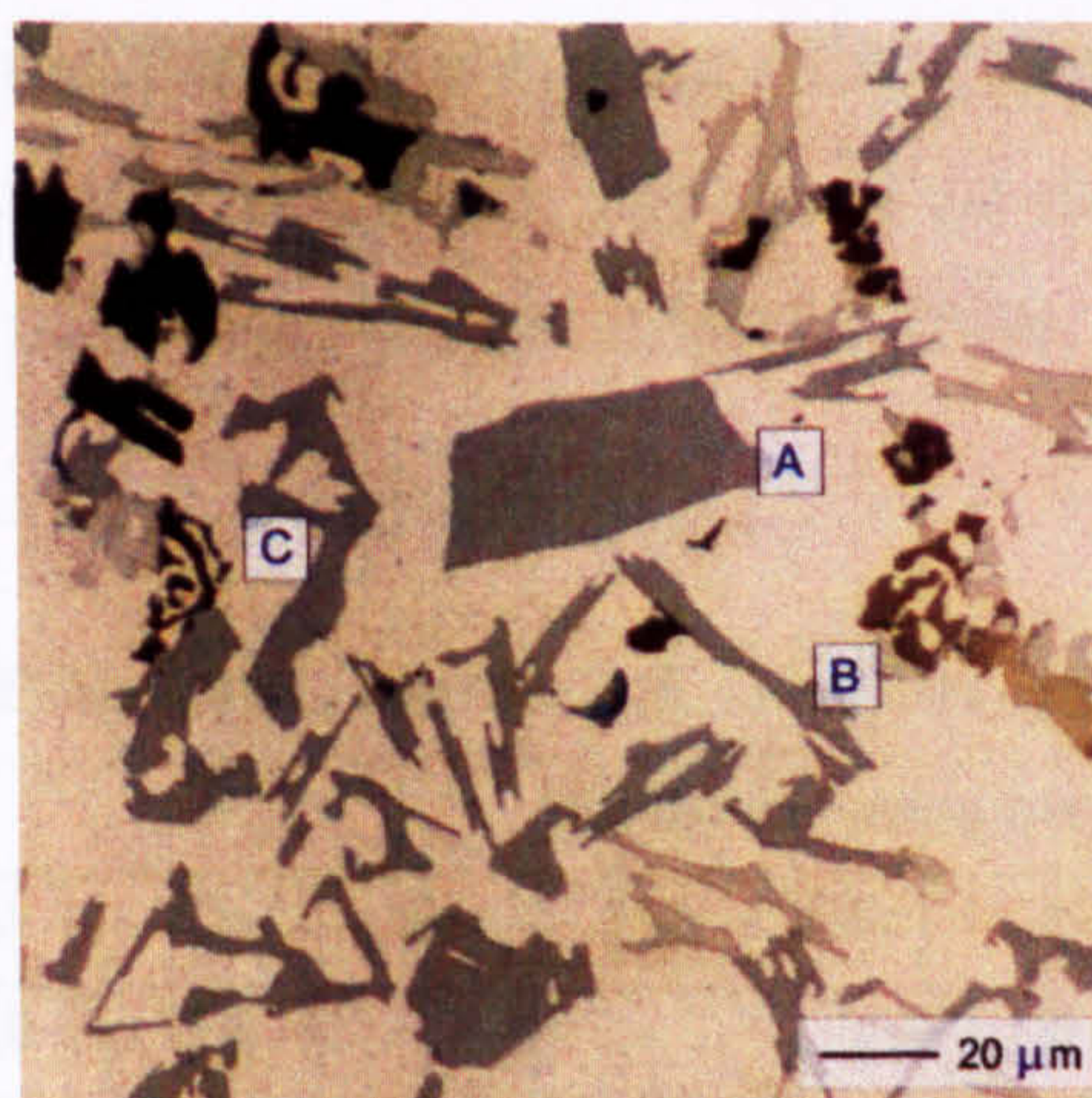


Figure 5.17 Optical micrograph showing (A) primary silicon, (B) secondary silicon, and (C) less defined silicon particles

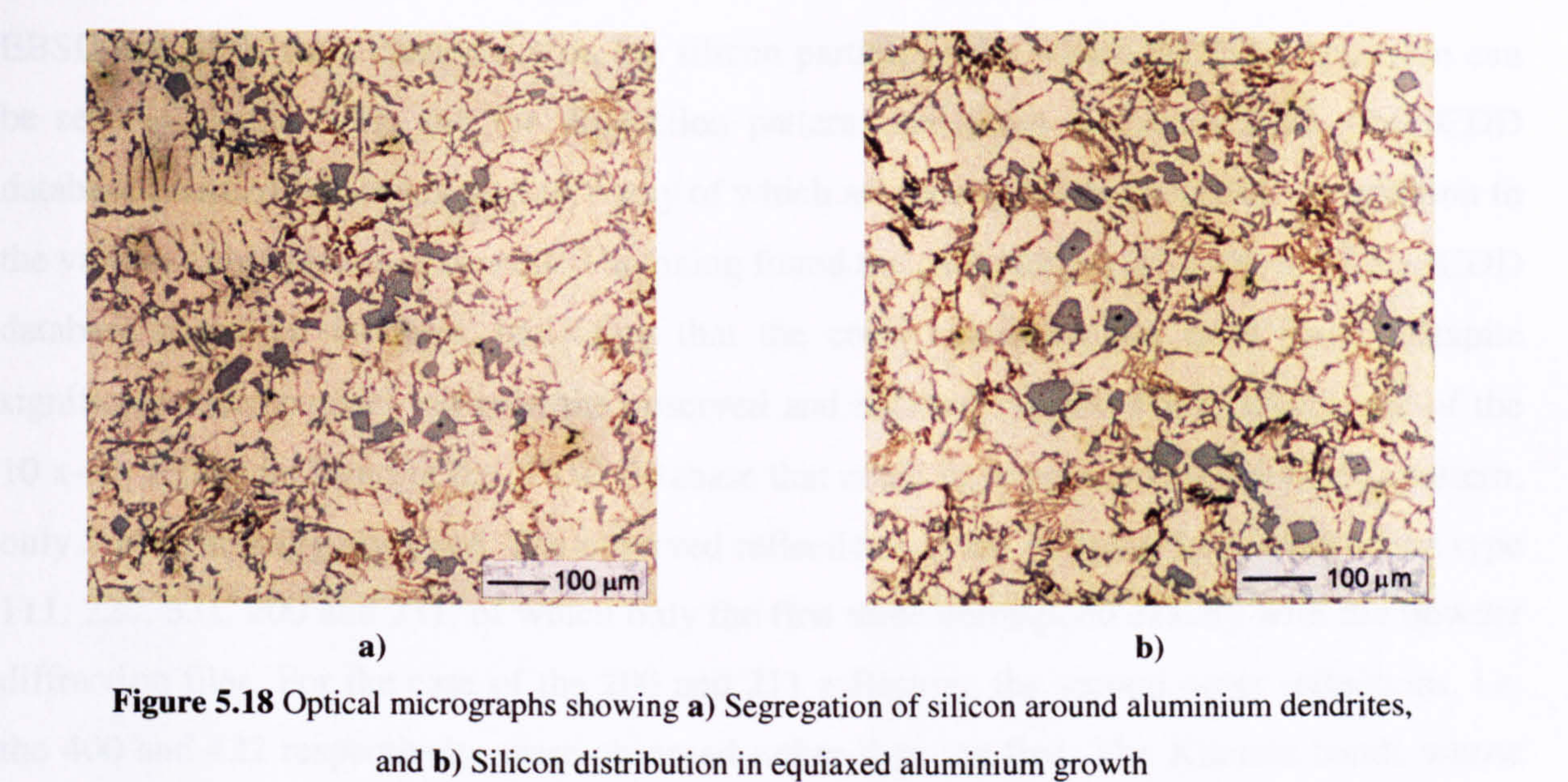


Table 5.10 shows the observed compositions together with those predicted. Through SEM analysis the silicon phases were found to have two distinct compositions, one containing a substantial content of Al. The Si composition with low Al (> 95 wt.% Si) and insignificant amounts of Al, Cu and Ni, is in close agreement with the predicted silicon phase which is modelled as being stoichiometric at 100 wt.% Si with no solubility of any other elements. The second group of silicon analyses, however, contain around 25 wt.% Al, a large deviation from both the predicted and previously observed compositions. According to the binary Al-Si diagram (Figure 3.9) there is no formation of a binary Al-Si phase. Although it is impossible to determine the thickness of the Si crystals in the z-direction, the particles appear to be large enough to preclude pick-up from the surrounding Al matrix. Moreover, the composition of the Al-Si phase is recurrent, occurring in a large proportion ($\sim 40\%$) of the crystals analysed. Thus, this is believed to be a true, but as yet unexplained, effect.

Table 5.10 Composition of the silicon phase

		Fraction of component in phase									
		Al	Cu	Fe	Mg	Mn	Ni	Si	Ti	V	Zr
Observed (At. %)	Low Al	4.0	0.2	-	-	-	0.4	95.7	-	-	-
	High Al	27.3	0.4	-	-	-	0.2	72.0	-	-	-
Observed (Wt. %)	Low Al	3.9	0.3	-	-	-	0.1	95.6	-	-	-
	High Al	26.3	1.0	0.1	-	-	0.4	72.1	-	-	-
Predicted at 500 K (Wt.%)		-	-	-	-	-	-	100	-	-	-

EBSD and EDX were carried out on the silicon particles from which the EDX spectrum can be seen in Figure 5.19, and the diffraction patterns are given in Figure 5.20. The ICDD database contains 30 silicon phases, many of which are hexagonal or tetragonal, in addition to the various cubic phases. Automated indexing found the card number 27-1402 from the ICDD database to match the best, indicating that the correct solution has been found, despite significant discrepancies between the observed and indexed images. For example, out of the 10 x-ray reflectors listed in the ICDD database that could have appeared in the EBSD pattern, only 5 were actually observed. The observed reflections, given in Table 5.11, were of the type 111, 220, 331, 200 and 211, of which only the first three correspond exactly with the powder diffraction files. For the case of the 200 and 211 reflectors, the second order reflections, i.e. the 400 and 422 respectively, were observed rather than the first. The Kikuchi bands whose lines were un-indexed, were subsequently identified by tracing the centreline of the band onto the screen enabling automatic calculation of the plane normal, and hence Miller indices. Two additional reflectors were indexed in this way, namely the 331 and 511 reflections.

Despite having good quality material files for the silicon phase, when using the orientation imaging mapping (OIM) the EBSD patterns alone were found to be insufficient in differentiating between the aluminium and silicon phases. This is because aluminium and silicon are both cubic systems, with FCC_A1 and DIAMOND-A4 sublattices respectively. The silicon diffraction pattern has additional reflectors to the aluminium, however, the automatic indexing discriminates using reflectors which are present rather than taking into account those which are absent. This was overcome through simultaneous EBSD and EDX whereby crystallographic and chemical information were collected at each point, enabling discrimination by composition during post processing of the data. It is understood that, as a result of these analyses, modifications have now been made to a future software release to overcome this problem.

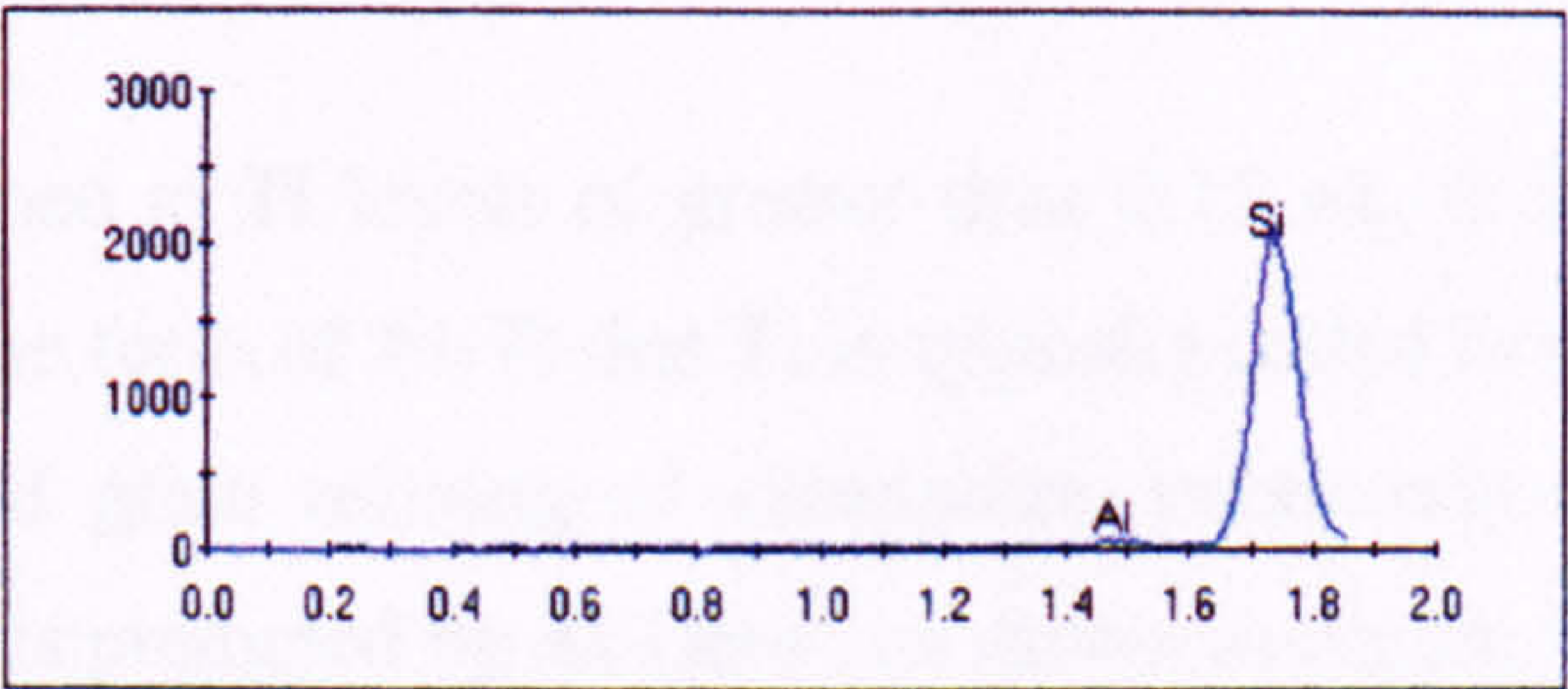
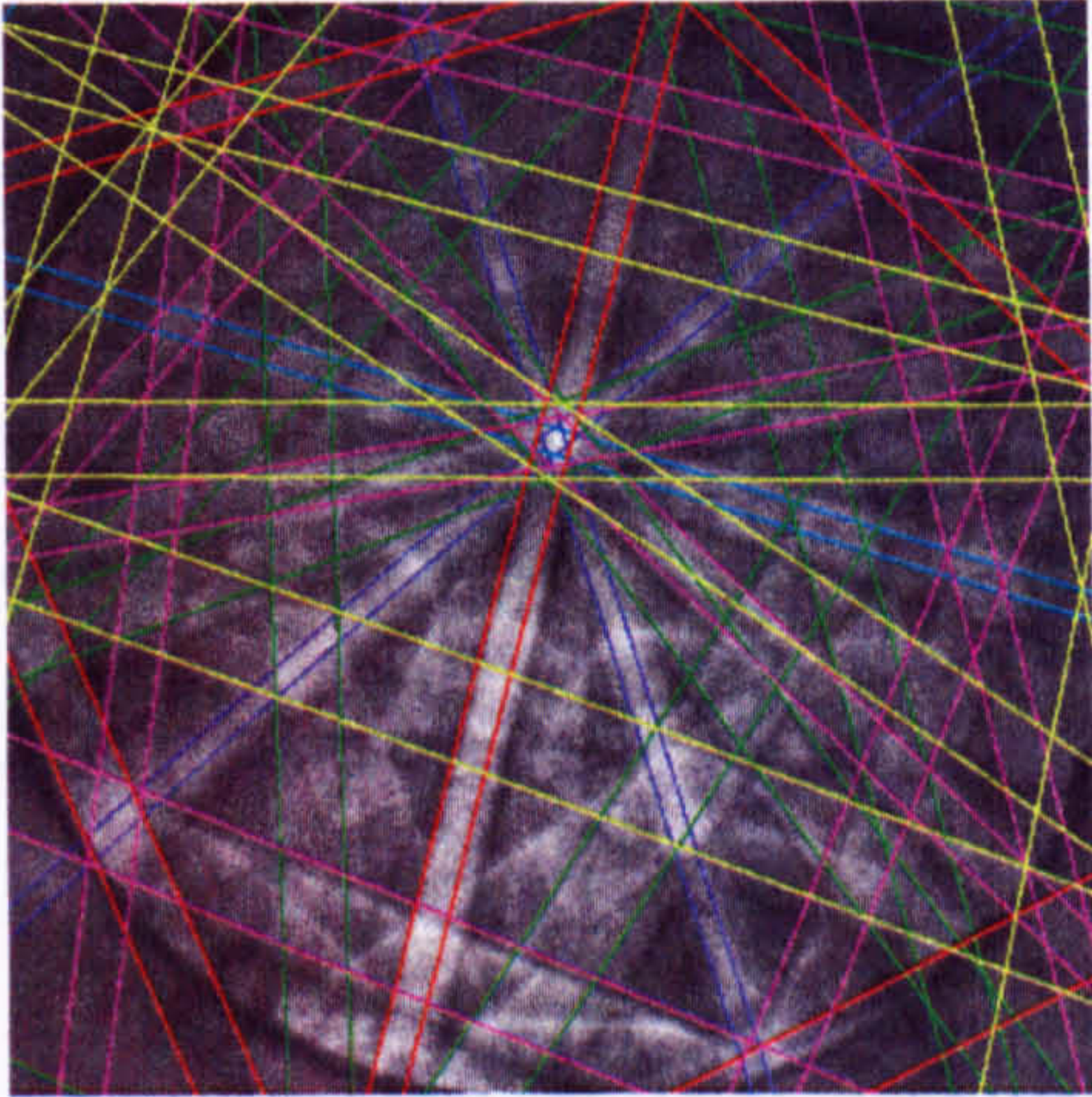


Figure 5.19 EDX spectrum of a silicon particle



a)



b)

Figure 5.20 a) Observed and b) indexed diffraction pattern from a silicon particle

Table 5.11 Crystallographic and diffraction data for the silicon phase

Crystal System	Cubic F
Space Group	Fd3m
Lattice Parameter (Å)	a=5.43088

hkl	ICDD (27-1402)		EBSD	
	Interplanar spacing, d (Å)	Intensity	Interplanar spacing, d (Å)	Intensity
111	3.13552	100	3.135	-
220	1.92011	55	1.920	-
311	1.63747	30	1.637	-
400	1.35772	6	1.357	-
422	1.10857	12	1.108	-

5.3.3 Al₃Ti

The Al₃Ti phase is formed at Ti levels of greater than 0.15 wt. % in a simple Al-Ti binary phase diagram. It is in the form of Al₃Ti that Ti is typically added to molten metal as a master alloy for nucleation and grain refining of aluminium, previously discussed in Chapter 3. Indeed, the Al₃Ti phase is predicted by Al-Data³, as shown in Figure 5.10, to be the first phase to form at the highest temperature, 933 K (660 °C), in alloy AE160. In alloys with more than 0.15 wt. % Ti the Al₃Ti phase should be stable, although it is possible to find Al₃Ti particles remnant from the master alloy additions in alloys with less than 0.15 wt. % Ti. Al₃Ti, as shown in Figure 5.21, is quite distinct from other phases and is of particular interest due to its very long, plate-like shape. After etching (0.5 % HF in water), Al₃Ti takes on a pale yellow-grey colour with a clear dark outline and is often seen to have other phases, including silicon, nucleating from its edges. The geometric morphology and large size of these particles is thought to be undesirable from a mechanical properties perspective, potentially providing an easy path for crack propagation, although work on fatigue of these alloys^[Joy02] has yet to find this to be the case.

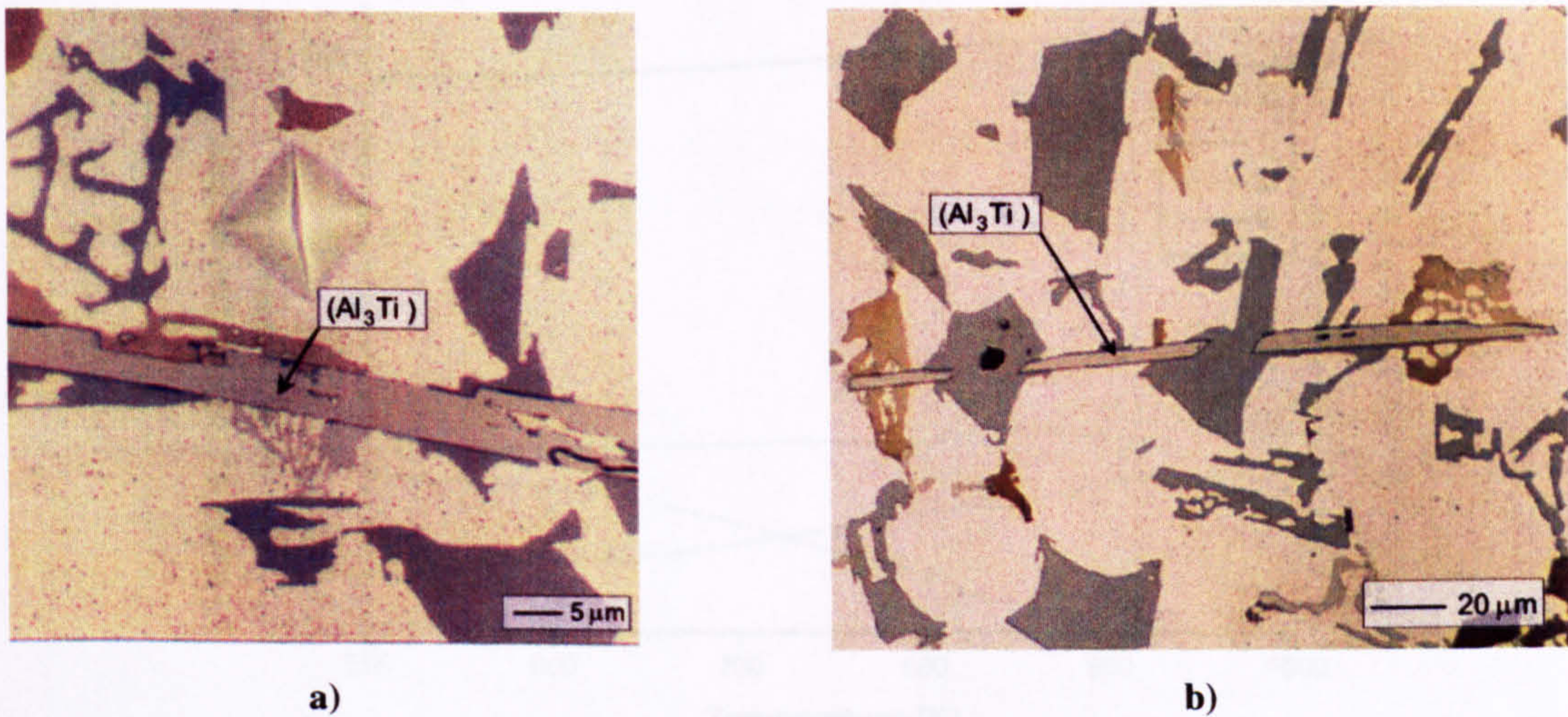


Figure 5.21 a) and b) Optical micrographs of Al₃Ti particles

The composition of the Al₃Ti phase is distinct from other phases as it contains large amounts of Ti, Zr, and V as is shown in Table 5.12. These alloying additions are only found in insignificant quantities, if at all, in most other phases. No phases of a similar composition were observed previously in work on commercial piston alloys^[Day98], unsurprisingly so as the alloys investigated generally contained less than 0.05 wt. % Ti which is below the solubility

for Al₃Ti as stated earlier. The Al₃Ti phase was, however, predicted at equilibrium with a composition that fits closely to that observed. The major discrepancy is the substantial amount of Si detected in the Al₃Ti by EDX which is not predicted, but is most likely due to pick up from the silicon particles frequently found nucleating from the needles. Differences in the predicted and observed Ti, Zr and V contents can be accounted for by the non-stoichiometry of the phase. This is illustrated as a phase stability plot in Figure 5.22, where it can be seen that the solubility of Ti, Zr and V are predicted to change significantly with temperature.

Table 5.12 Composition of Al₃Ti phase

	Fraction of component in phase									
	Al	Cu	Fe	Mg	Mn	Ni	Si	Ti	V	Zr
Observed (At.%)	52.7	0.2	0.1	-	-	0.2	14.8	20.5	1.9	9.7
Observed (Wt.%)	37.1	0.4	0.1	-	-	0.3	10.8	25.6	2.5	23.1
Predicted (Wt.%)	57.7	-	-	-	-	-	-	19.1	6.8	16.5

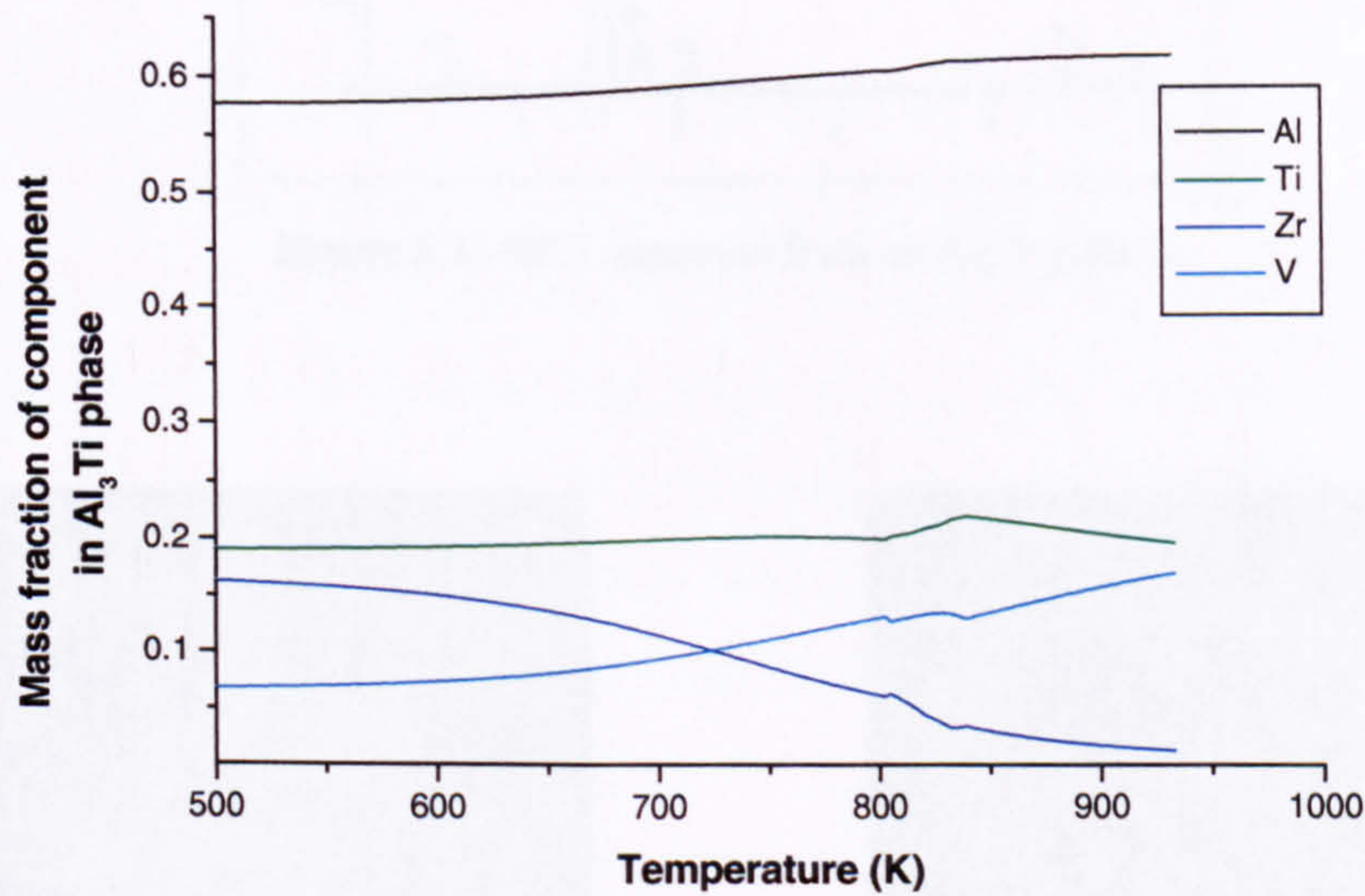


Figure 5.22 Mass fraction of components in the Al₃Ti phase as a function of temperature

EBSD and EDX were carried out simultaneously on Al₃Ti particles. An EDX trace is given in Figure 5.23 and shows peaks for Al, Si, Ti and V, as expected, but also for Pt. This is because the Pt and Zr peaks overlap, a problem that can be overcome in Delphi Phase ID by selecting

the most probable elements in the periodic table to re-identify the peak as Zr. The diffraction patterns for Al_3Ti are given in Figure 5.24. The ICDD database contains 19 Al-Ti phases of varying stoichiometry and crystal structure. Automatic indexing found the best match to be that of the card number 18-0069, $\text{Al}_{23}\text{Ti}_9$, despite significant differences between the observed and indexed images. Of the first 14 x-ray reflectors from the ICDD database, only 5 of those observed correspond with the powder diffraction files; 118, 200, 20 16, 11 24, and 318. These are listed in Table 5.13 with those from the ICDD database excluding the first 4 lines (008, 103, 01 10, and 110). For the case of the 100 and 108 reflectors, the second order reflections, i.e. the 200 and 20 16 respectively, were observed rather than the first. Only one un-indexed Kikuchi band was identified by tracing the centreline of the band onto the screen for automatic indexing of the plane normal. This was the second order reflection of the 10 16, the 20 32 reflector, with an interplanar spacing of 0.991 Å.

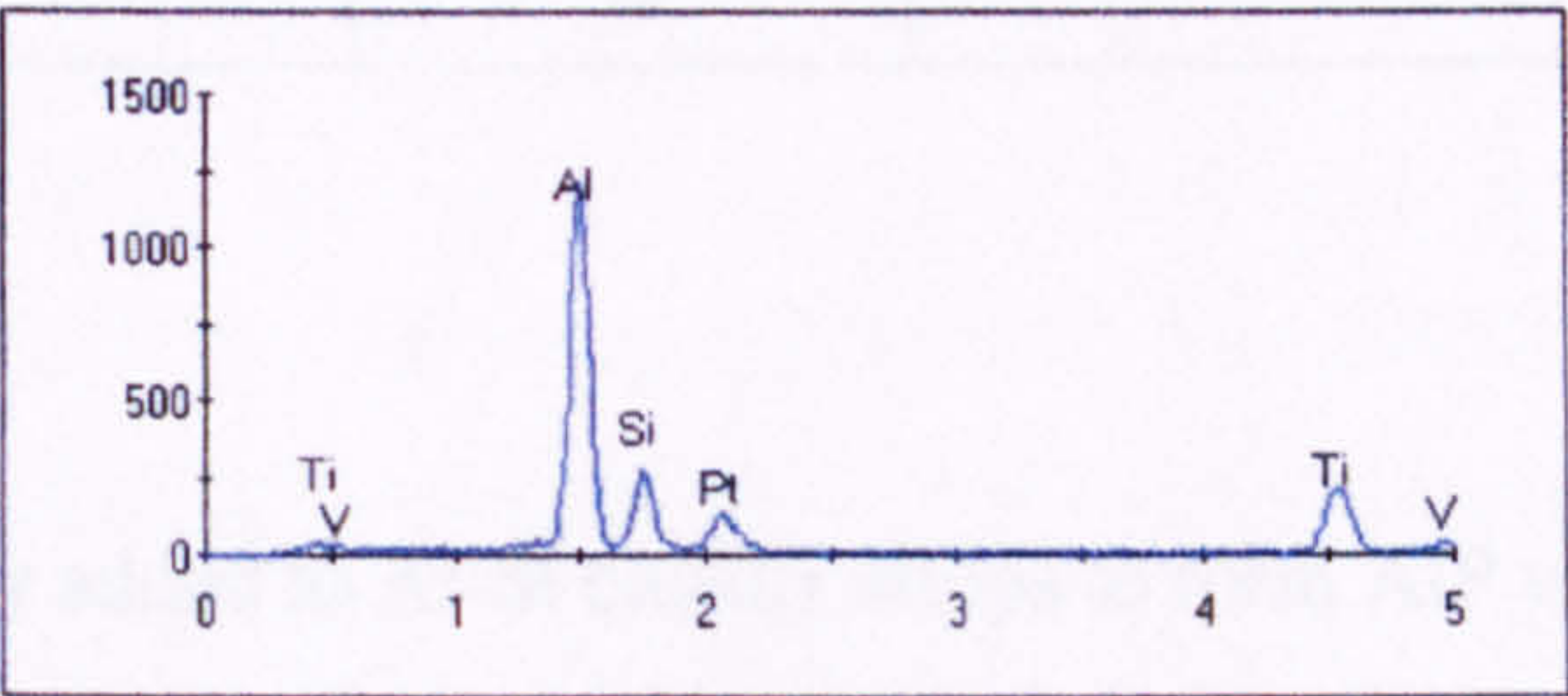
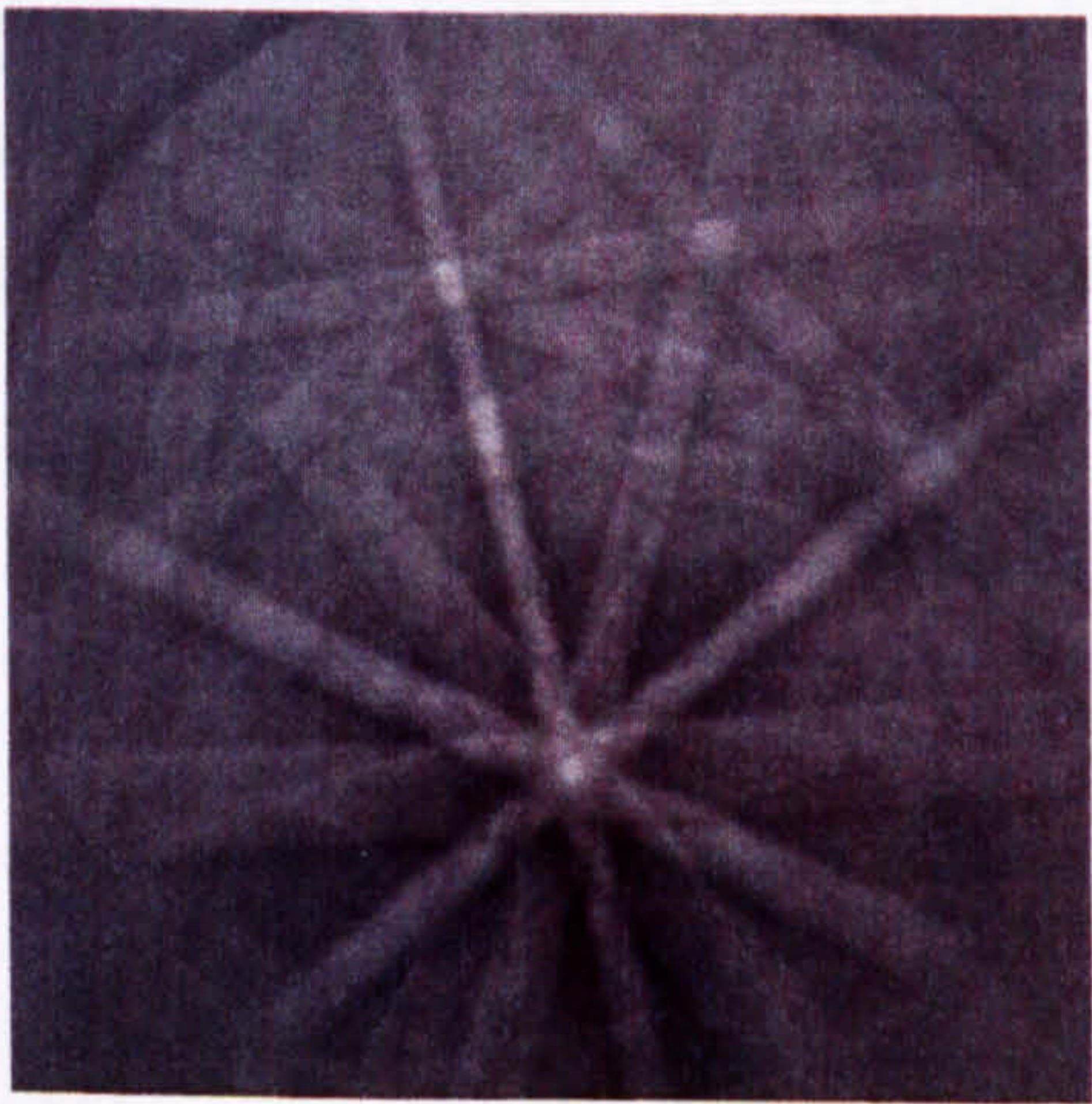
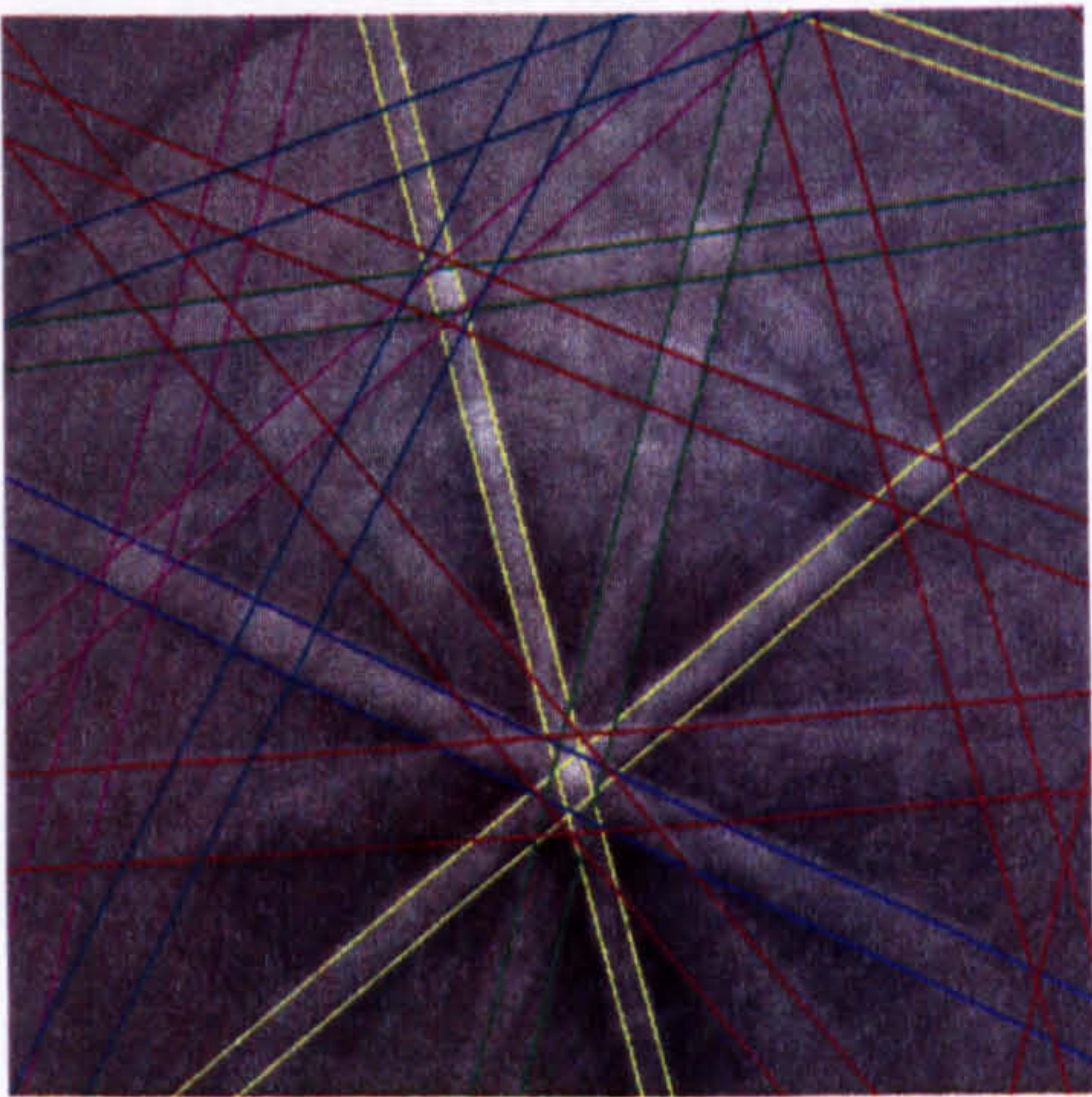


Figure 5.23 EDX spectrum from an Al_3Ti particle



a)



b)

Figure 5.24 a) Observed and b) indexed diffraction patterns from an Al_3Ti particle

Table 5.13 Crystallographic and diffraction data for Al₃Ti

Crystal System	Tetragonal
Space Group	I
Lattice Parameter (Å)	a=3.84, c=33.46, C=8.7135

hkl	ICDD (18-0069)		EBSD	
	Interplanar spacing, d (Å)	Intensity	Interplanar spacing, d (Å)	Intensity
114	2.566	5	-	-
10 11	2.384	5	-	-
118	2.279	100	2.342	100
00 16	2.092	80	-	-
200	1.921	80	1.920	80
20 16	1.414	80	1.477	80
220	1.358	70	-	-
11 24	1.240	70	1.341	70
318	1.165	70	1.175	70
22 16	1.138	70	-	-

5.3.4 AlP

Phosphorous is deliberately added to Al-Si casting alloys to form AlP which acts as a nucleant for primary silicon, as discussed previously in Chapter 3. AlP is believed to be the source of the cavity in the centre of most Si particles, as seen in Figure 5.25, because the particles tend to be washed or pulled out during specimen preparation or react with air making them very difficult to analyse. Indeed, no standard SEM analysis was achieved on the AlP, and as P is not currently in any of the thermodynamic databases no predictions were made either, although this latter issue will be considered further in Chapter 7.

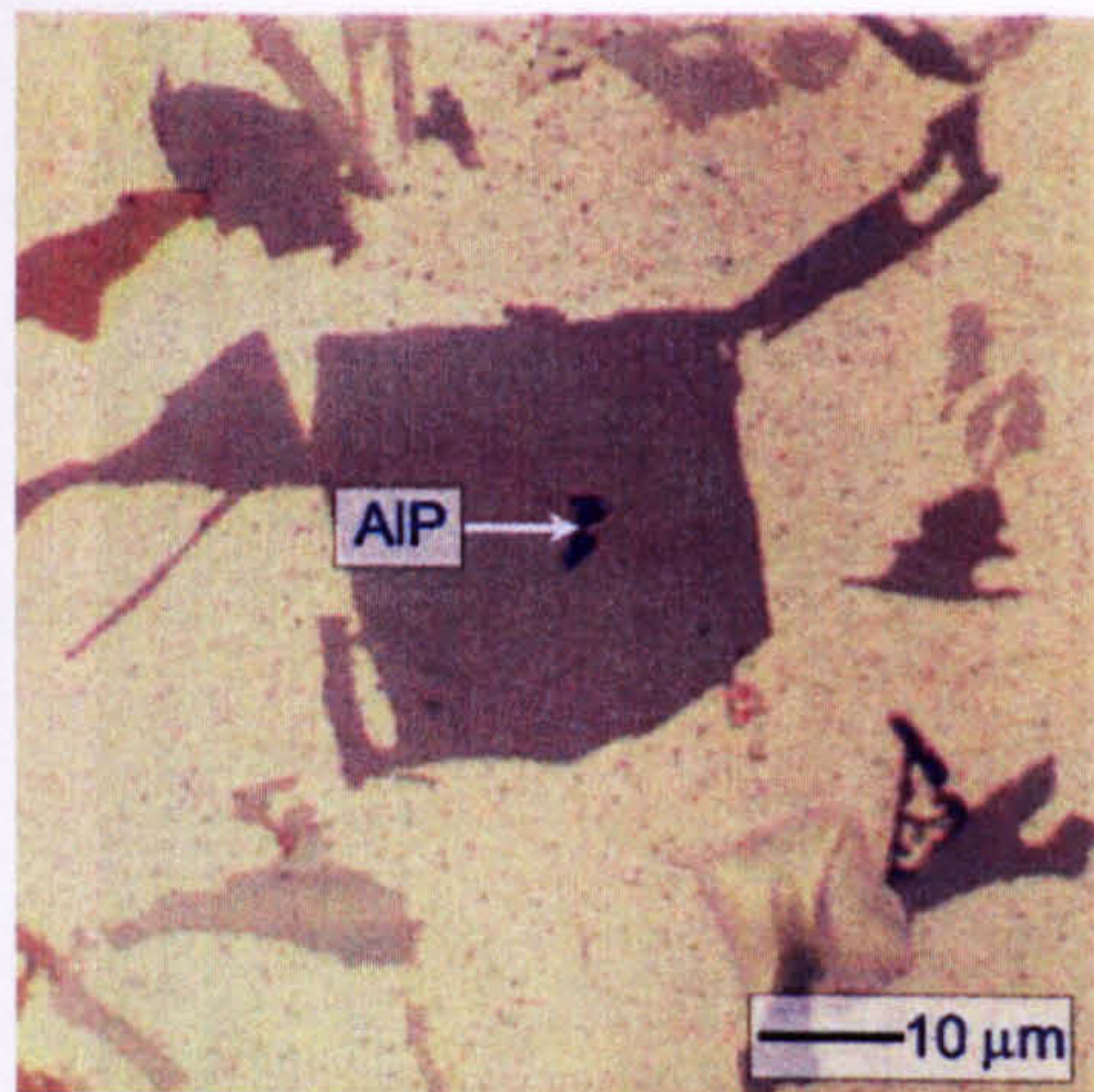


Figure 5.25 Optical micrograph of an AlP ‘void’ in the centre of a primary silicon particle

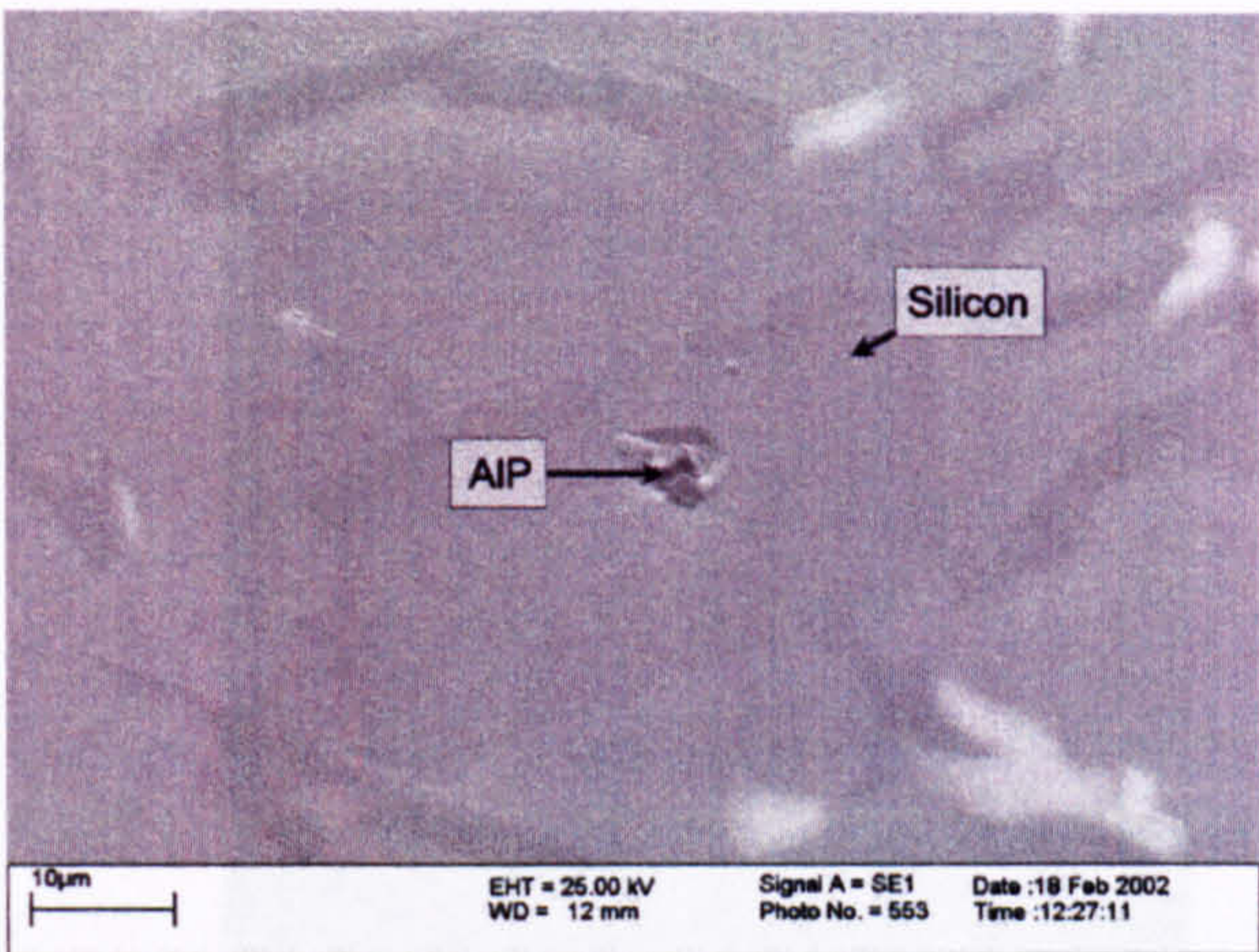


Figure 5.26 SEM image of silicon particle with AlP centre

EBSD and EDX, however, were able to detect a trace of AlP remaining in a void in the silicon particle shown in Figure 5.26. The EDX spectrum in Figure 5.27 shows a large Si peak, which is pickup from the surrounding particle, and also significant Al, O and P peaks. The presence of O is reasonable if the AlP has reacted with the atmosphere, as might be expected. A diffraction pattern from the AlP is given in Figure 5.28. The ICDD database was found to contain seven AlP phases of which card number 73-1957 automatically fitted the best and was taken as the correct solution. The nine x-ray reflectors listed in the database are given in Table 5.14, of which only 4 were observed: 111, 220, 311, and 422. For the case of the 110 and 211 reflectors, the second order reflections, i.e. the 220 and 422 respectively, were observed rather than the first. No un-indexed bands required manual identification. The relationship between the silicon and AlP nucleant is explored further in Chapter 7.

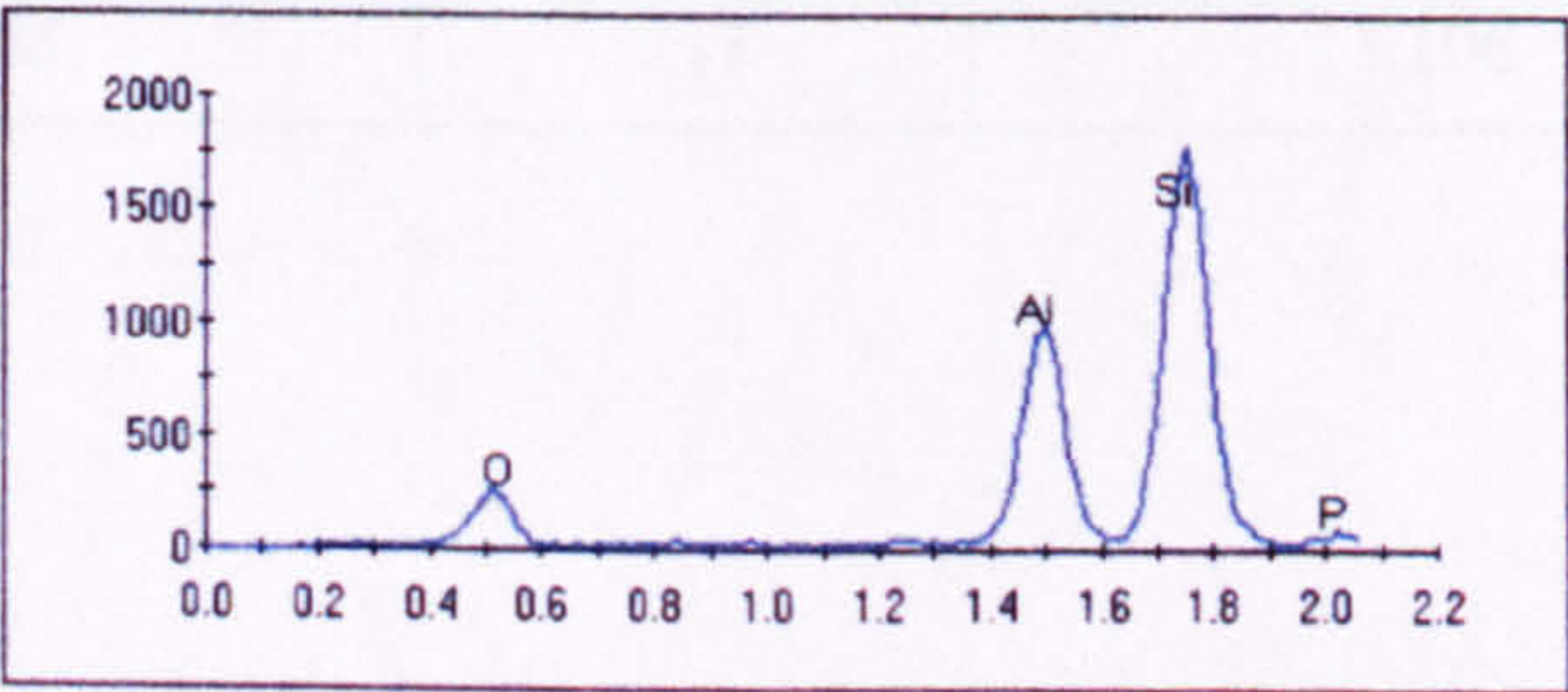


Figure 5.27 EDX spectrum of an AlP particle

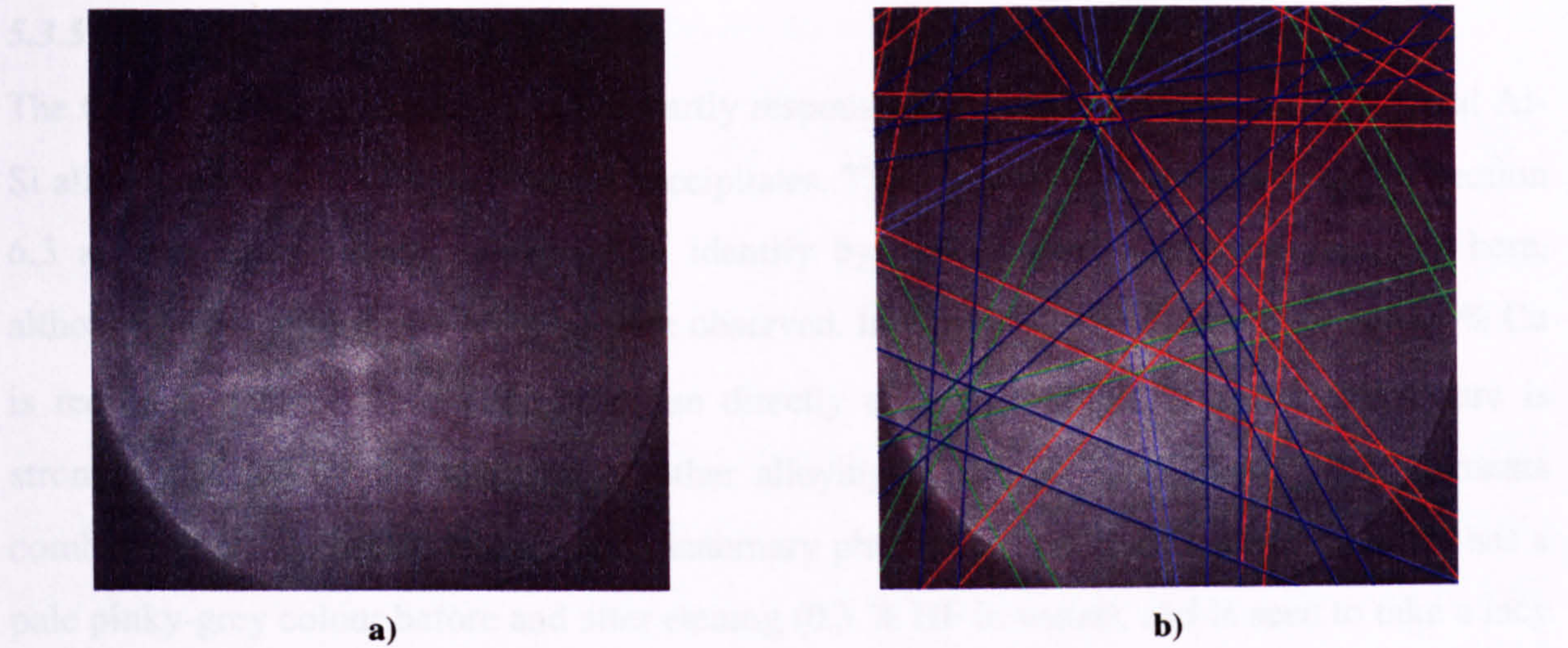


Figure 5.28 a) Observed and b) indexed diffraction patterns from an AlP particle

Table 5.14 Crystallographic and diffraction data for AlP

Crystal System		Cubic		
Space Group		F43m		
Lattice Parameter (Å)		a=5.42		

hkl	ICDD (73-1957)		EBSD	
	Interplanar spacing, d (Å)	Intensity	Interplanar spacing, d (Å)	Intensity
111	3.129	999	3.129	999
200	2.7100	4	-	-
220	1.9162	543	1.961	543
311	1.6341	294	1.634	294
222	1.5646	1	-	-
400	1.3550	67	-	-
331	1.2434	93	-	-
420	1.2119	1	-	-
422	1.1063	111	1.106	111

5.3.5 $\theta(\text{Al}_2\text{Cu})$

The $\theta(\text{Al}_2\text{Cu})$ phase is believed to be partly responsible for strengthening in commercial Al-Si alloys by forming very fine matrix precipitates. These precipitates are discussed in Section 6.3 as they are generally too small to identify by the standard analysis techniques here, although larger phases of $\theta(\text{Al}_2\text{Cu})$ were observed. In a pure Al-Cu alloy at least 5.7 wt.% Cu is required to form the $\theta(\text{Al}_2\text{Cu})$ phase directly on solidification, however this figure is strongly affected by the presence of other alloying elements. When these other elements combine with the copper, ternary and quaternary phases form in preference. $\theta(\text{Al}_2\text{Cu})$ has a pale pinky-grey colour before and after etching (0.5 % HF in water), and is seen to take a lacy morphology that can be either fine or coarse. These characteristics are very similar to the ternary AlCuNi phases and are difficult to distinguish optically.

The $\theta(\text{Al}_2\text{Cu})$ was found in trace amounts in the alloys studied, usually nucleating from another phase as seen in Figure 5.29. Due to its small size and sparse distribution it was difficult to obtain a multiple SEM analyses of this phase, however an accurate chemical analysis of several particles was achieved, the compositional data of which are given in Table 5.15. It can be seen that the Al:Cu ratio in At. % is 1.8:1 confirming that the phase is θ , with slight solubility for the other elements, in particular Ni. This phase is not predicted to form in AE160 probably as the Cu content is lower (~ 3 wt.%) than required for $\theta(\text{Al}_2\text{Cu})$ formation according to the binary phase diagram, and the higher order phases are more calculated to be more stable in the presence of alloying additions. It is possible that this phase may form in segregated regions and therefore a Scheil approach may be more appropriate.

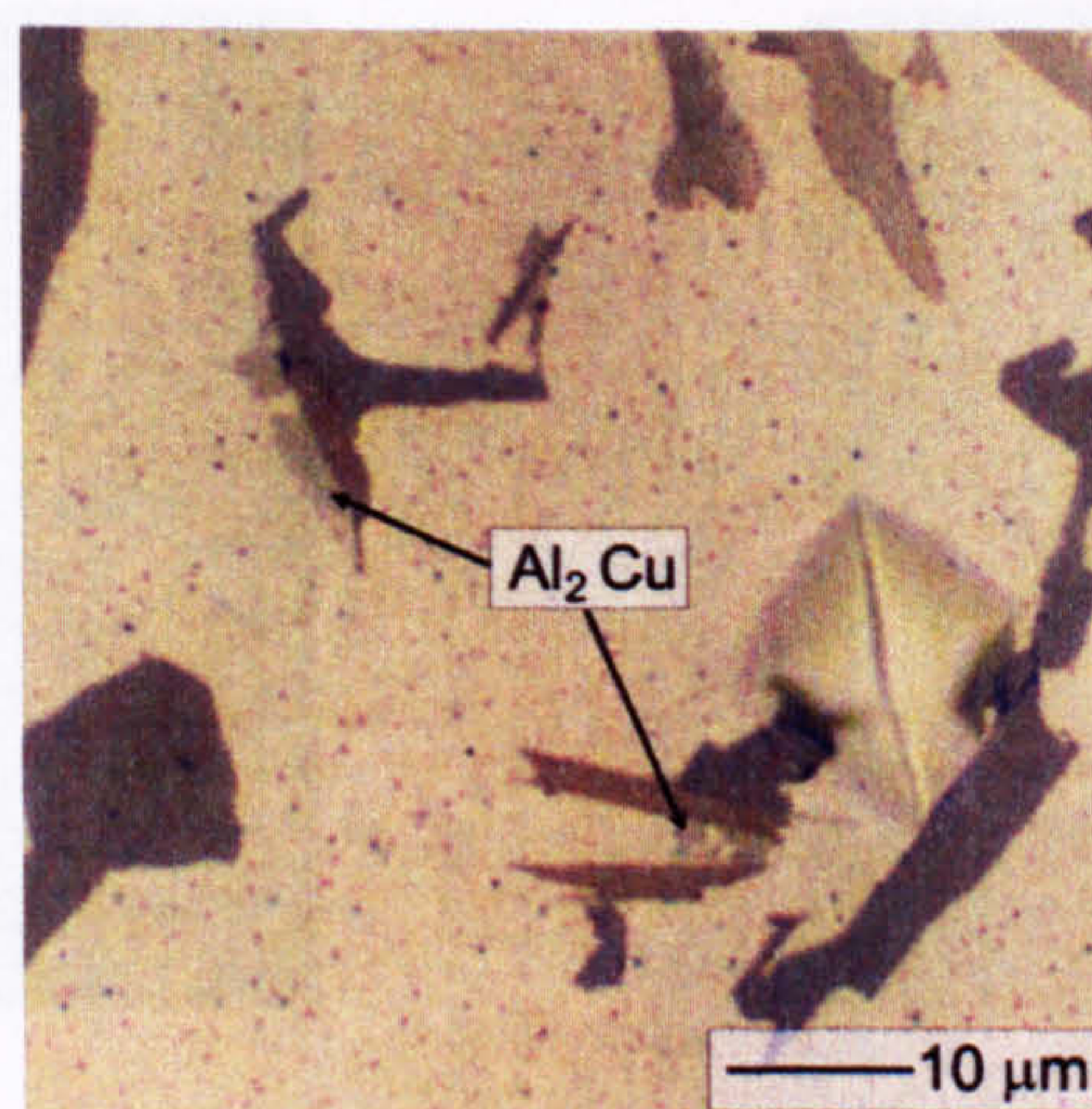


Figure 5.29 Optical micrograph of the $\theta(\text{Al}_2\text{Cu})$ phase

Table 5.15 Composition $\theta(\text{Al}_2\text{Cu})$ phase

	Fraction of component in phase									
	Al	Cu	Fe	Mg	Mn	Ni	Si	Ti	V	Zr
Observed (At. %)	60.70	34.35	0.82	-	0.11	2.87	0.69	-	0.08	0.41
Observed (Wt. %)	39.95	53.23	1.11	-	0.15	4.11	0.48	-	0.09	0.90

The EDX trace in Figure 5.30 confirms the composition of the phase as Al and Cu. The ICDD database contains 13 Al-Cu phases, of which 3 are Al_2Cu and of tetragonal structure. From the EBSD diffraction pattern in Figure 5.31 a) the phase was automatically indexed as card number 25-0012 with a reasonable fit to indicate this to be the correct solution. Out of the 18 x-ray reflectors that could have appeared, only 7 were actually observed, and these are given in Table 5.16. These were of the type 220, 112, 202, 400, 402, 332, and 422 and all correspond with the powder diffraction files. For the case of the 310 reflector, the second order reflection, the 620, was observed rather than the first. The fully indexed pattern can be seen in Figure 5.31 b).

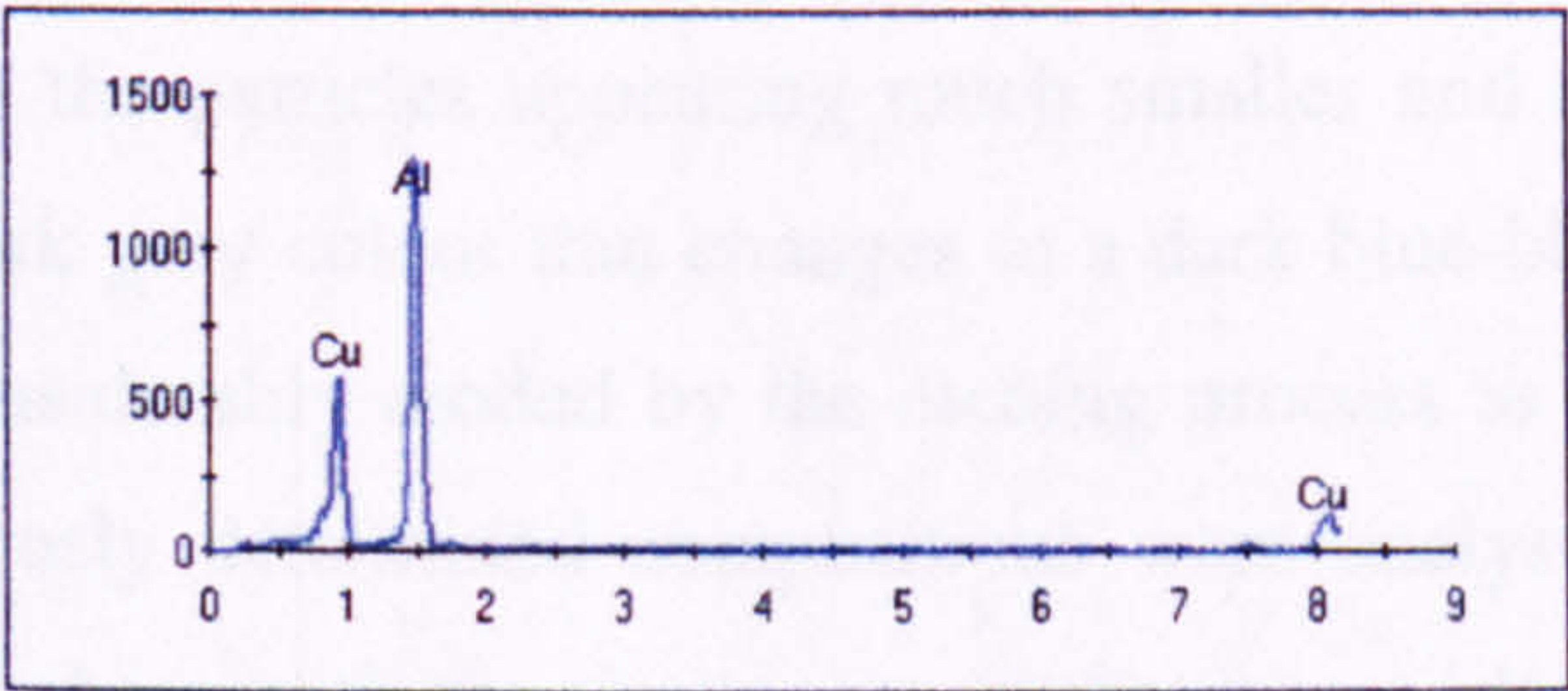


Figure 5.30 EDX spectrum for $\theta (\text{Al}_2\text{Cu})$

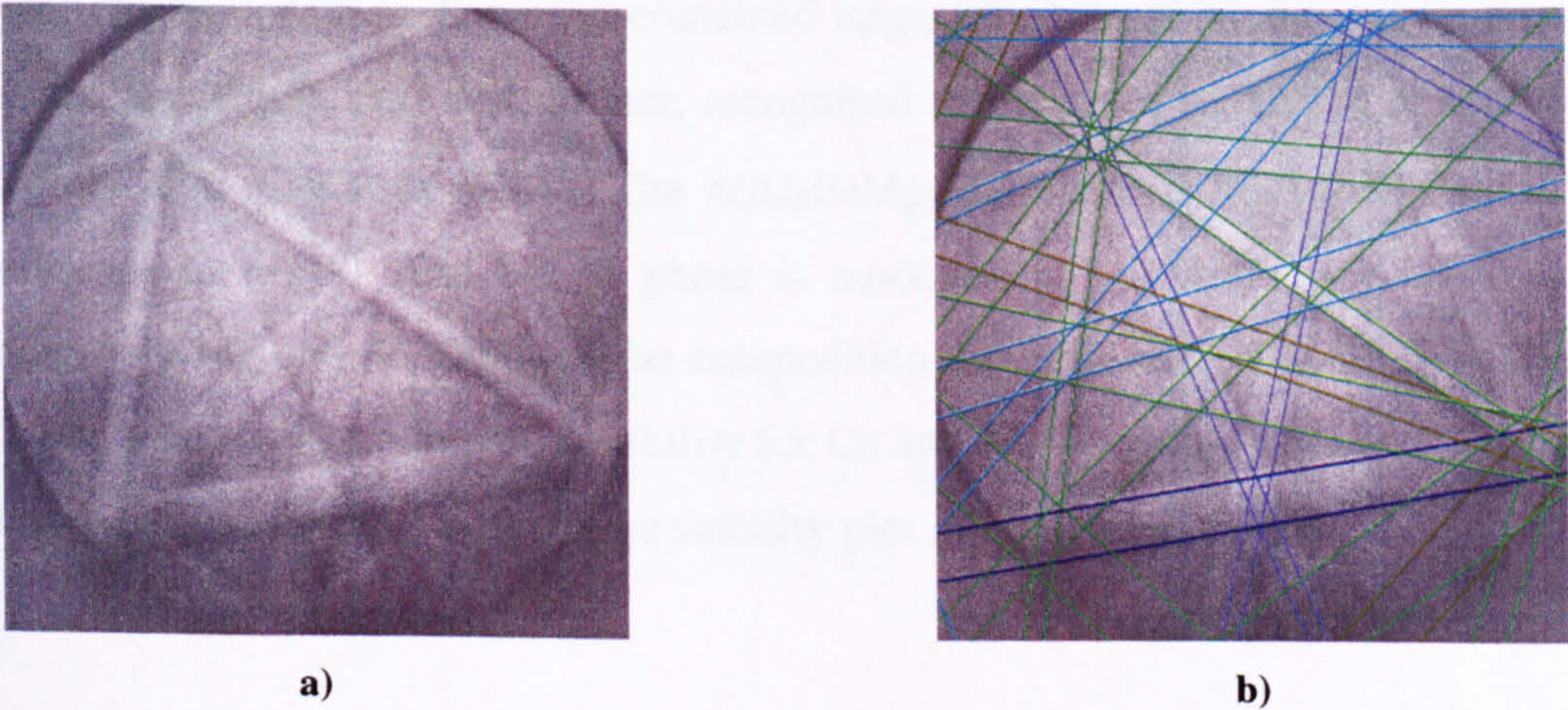


Figure 5.31 a) Observed and b) indexed diffraction patterns from a $\theta (\text{Al}_2\text{Cu})$ particle

.Table 5.16 Crystallographic and diffraction data for θ (Al_2Cu)

Crystal System		Tetragonal	
Space Group		14/mcm	
Lattice Parameter (Å)		a=6.0654, c=4.8732, C=0.8034	

hkl	ICDD (25-0012)		EBSD	
	Interplanar spacing, d (Å)	Intensity	Interplanar spacing, d (Å)	Intensity
220	2.146	35	2.144	100
112	2.121	90	2.458	90
202	1.901	60	2.133	60
400	1.517	2	1.516	35
402	1.288	21	1.353	21
332	1.234	20	1.291	20
422	1.186	-	1.236	70

Not shown are the 110, 200, 211, 310, 222, 312, 411, 213, 420, 332, and 510 reflectors

5.3.6 Mg_2Si

The Mg_2Si phase has been observed in previous work [Day98] to adopt a very fine Chinese script morphology, with the particles appearing much smaller and sparsely distributed than other phases. It has a dark grey colour that changes to a dark blue-black colour after etching, also appearing to be considerably eroded by the etching process as seen in Figure 5.32. No phases matching previously determined compositions were analysed by standard SEM in these alloys, although a phase with the similar morphology was identified. This phase had a fine script morphology as seen in Figure 5.33, with colouring ranging from a paler grey colour in the centre of the particle, to the dark, blue-black colour associated with the Mg_2Si around the edges. The composition, however, contained larger amounts of Al, Ni and Fe than would be expected for Mg_2Si , and was, in fact, recognised to be closer to that of $\pi(\text{Al}_8\text{FeMg}_3\text{Si}_6)$ with slightly high quantities of Mg. The $\pi(\text{Al}_8\text{FeMg}_3\text{Si}_6)$ phase is discussed later in 5.3.13 with reference to Mg_2Si . The Mg_2Si phase is modelled by Al-Data³ to be stoichiometric containing only Mg and Si, although the composition determined by Daykin, given in Table 5.17, can be seen to have a limited solubility for Cu and Ni. The Mg_2Si phase is not predicted to form in AE160 according to the phase stability plot in Figure 5.10.

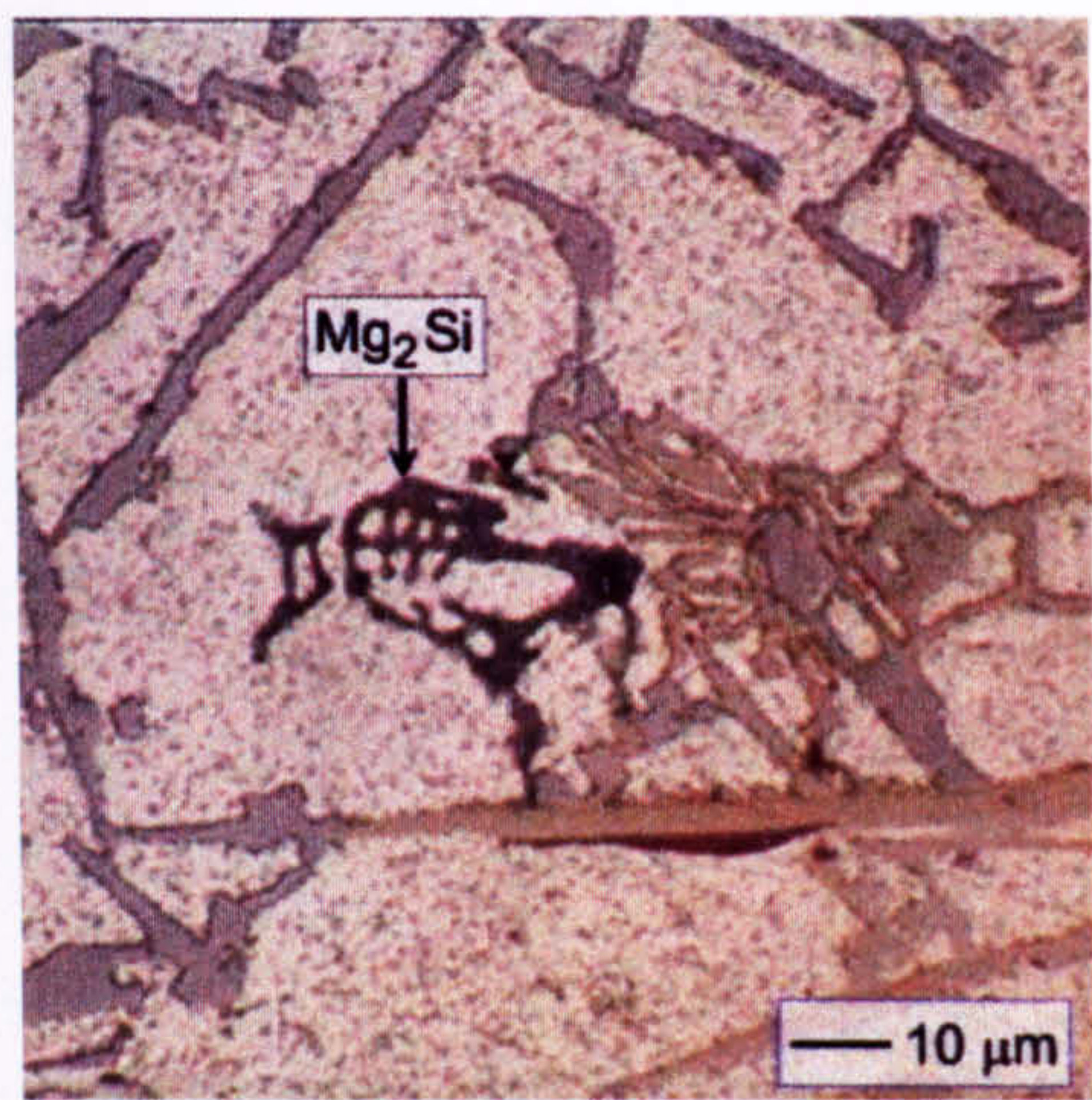


Figure 5.32 Optical micrograph of Mg_2Si as observed by Daykin [Day98]

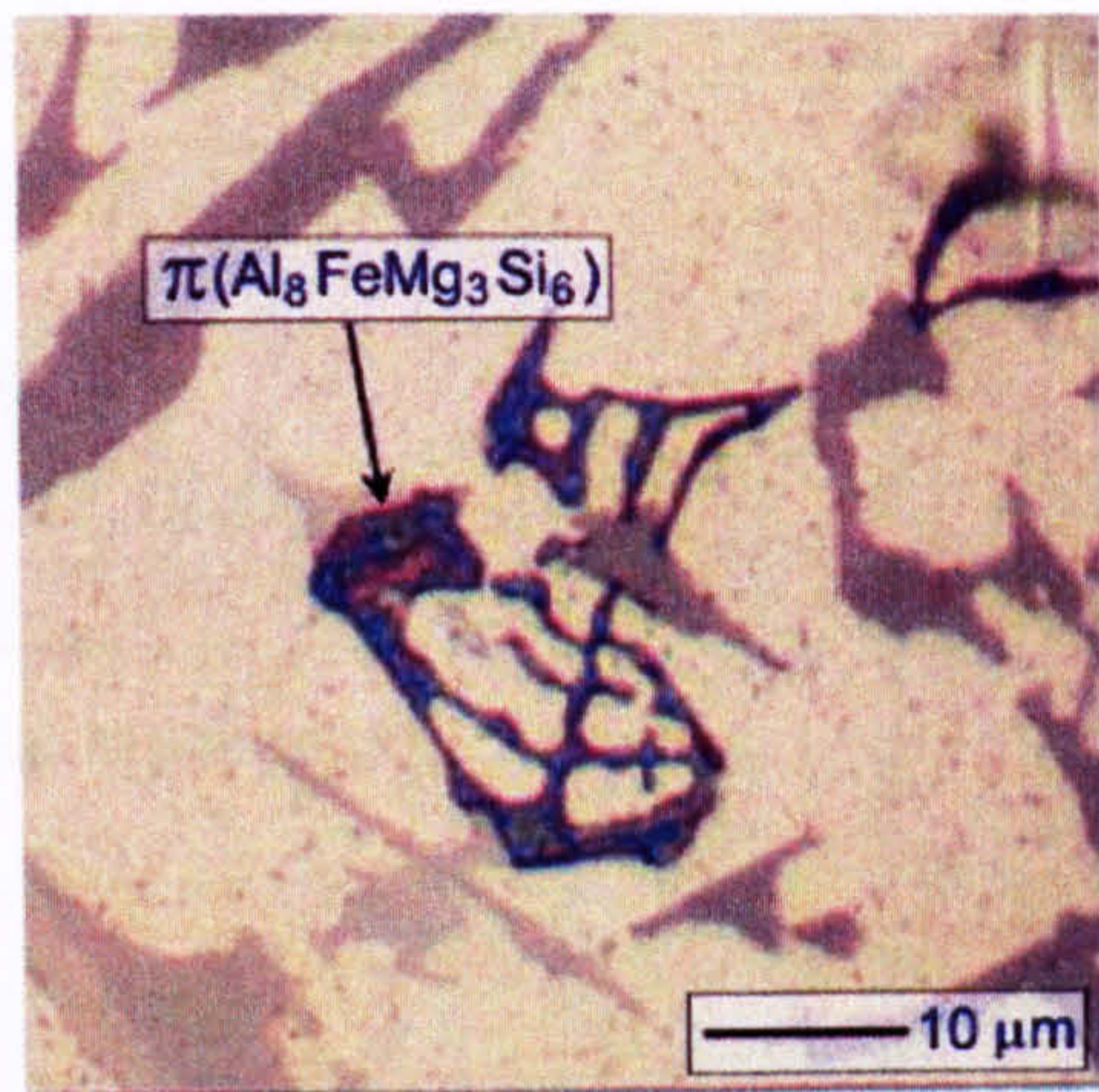


Figure 5.33 Optical micrograph of $\pi(\text{Al}_8\text{FeMg}_3\text{Si}_6)$

Table 5.17 Compositions of the Mg_2Si phase, after Daykin [Day98]

	Fraction of components in phase									
	Al	Cu	Fe	Mg	Mn	Ni	Si	Ti	V	Zr
Observed (Wt. %)	-	1.45	-	56.3	-	0.38	41.7	-	-	-
Observed (At. %)	-	0.59	-	63.7	-	0.17	35.4	-	-	-

Despite being unable to distinguish Mg_2Si by standard SEM techniques, simultaneous EBSD and EDX analysis identified a Mg-Si phase, the EDX spectrum for which is given in Figure 5.34. In addition to the Mg and Si peaks, it can be seen that there is a large aluminium peak, most likely a result of overlap of the electron beam with the surrounding matrix due to the small dimensions of the particle. There is also an indication of a very small Cu/Ni/Fe peak at around 0.95 keV which, together with the large Al peak, could again suggest some overlap with the π phase. Nonetheless, the diffraction pattern in Figure 5.35 a) was indexed automatically as Mg_2Si , card number 73-2246, from the 9 Mg-Si phases contained in the ICDD database. Out of the 11 x-ray reflectors listed in Table 5.18 (the first two reflectors, 111 and 200, have been left out of the table) that could have appeared in the EBSD pattern, only 3 were actually observed. The observed reflectors correspond exactly with the powder diffraction files and were of the type 222, 400, and 440. For the case of the 311 reflector, the second order reflection, the 622, was observed rather than the first.

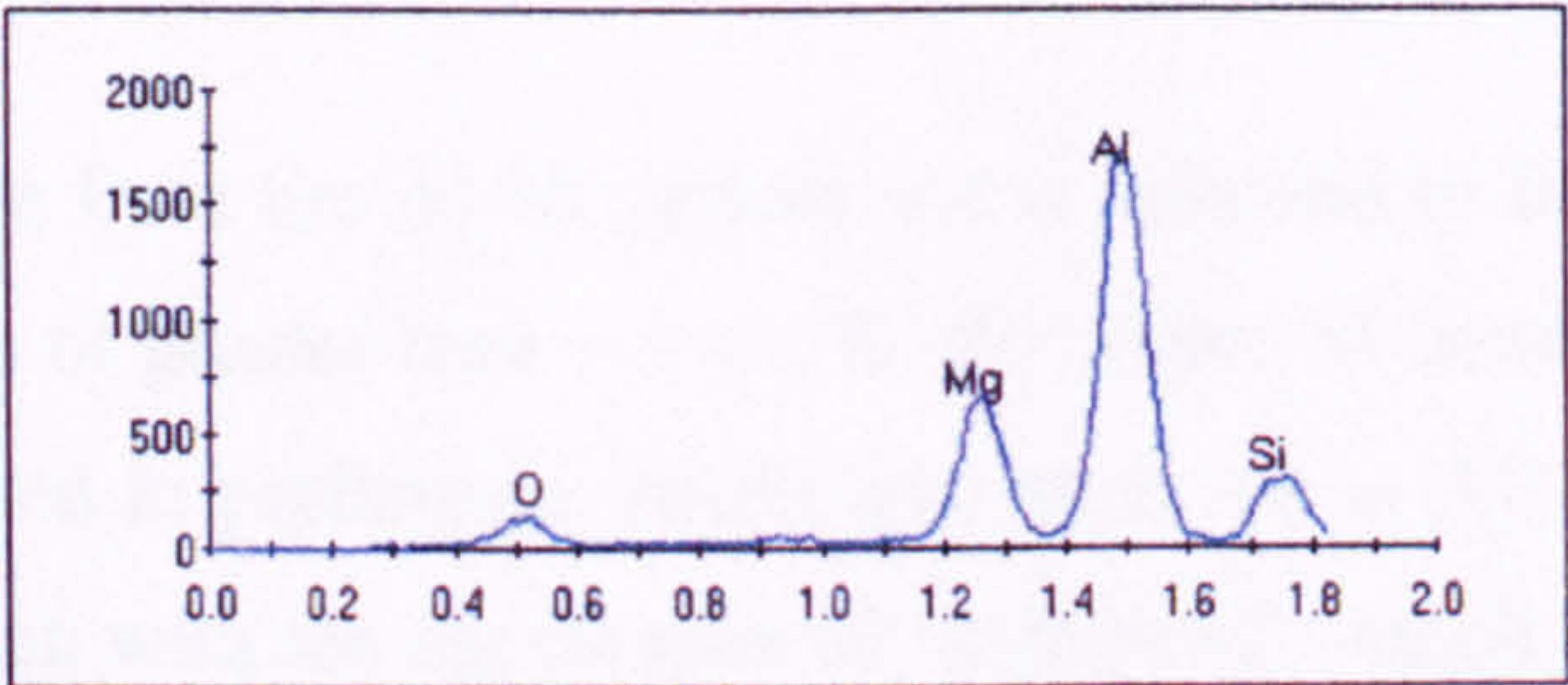
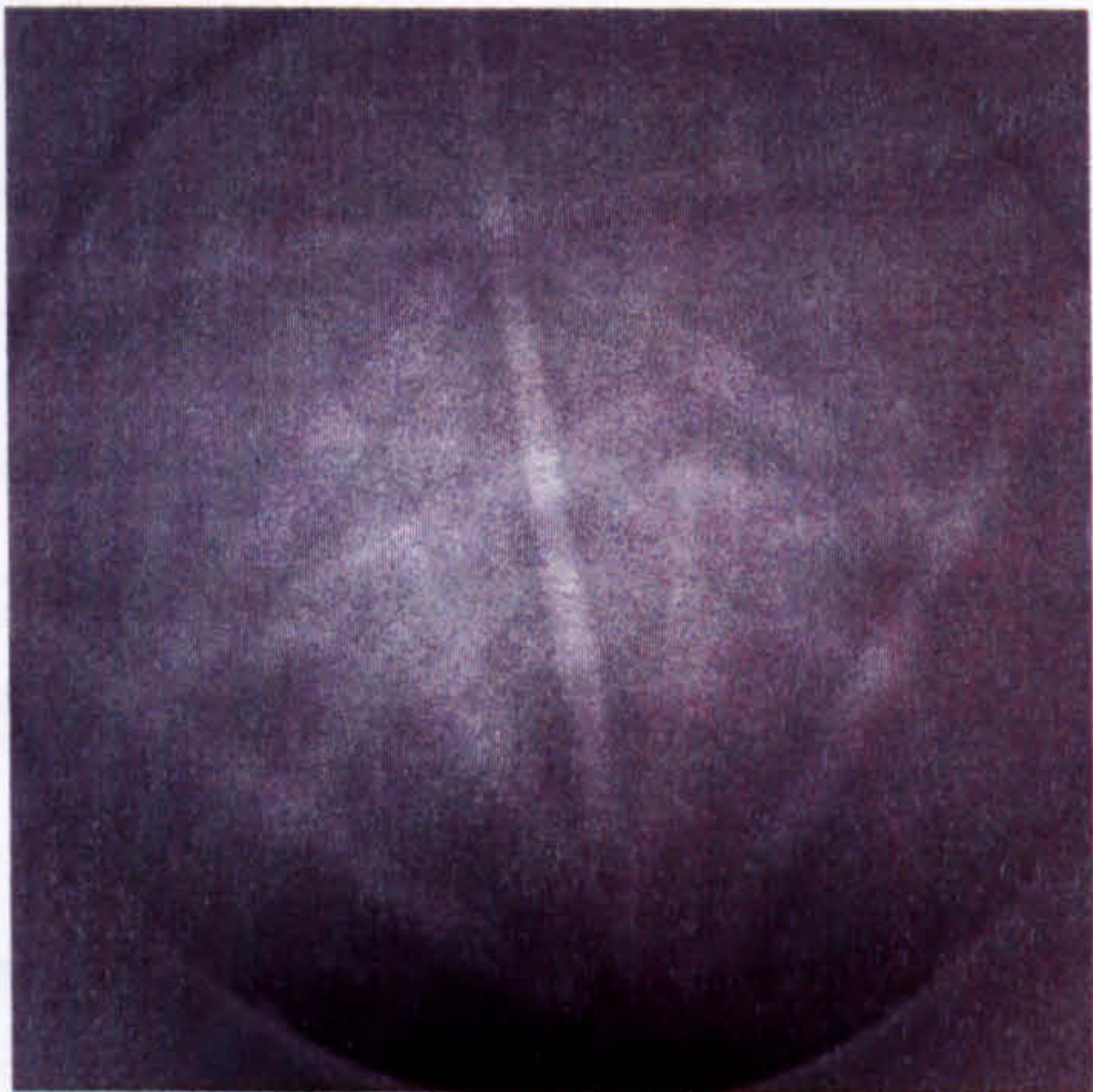
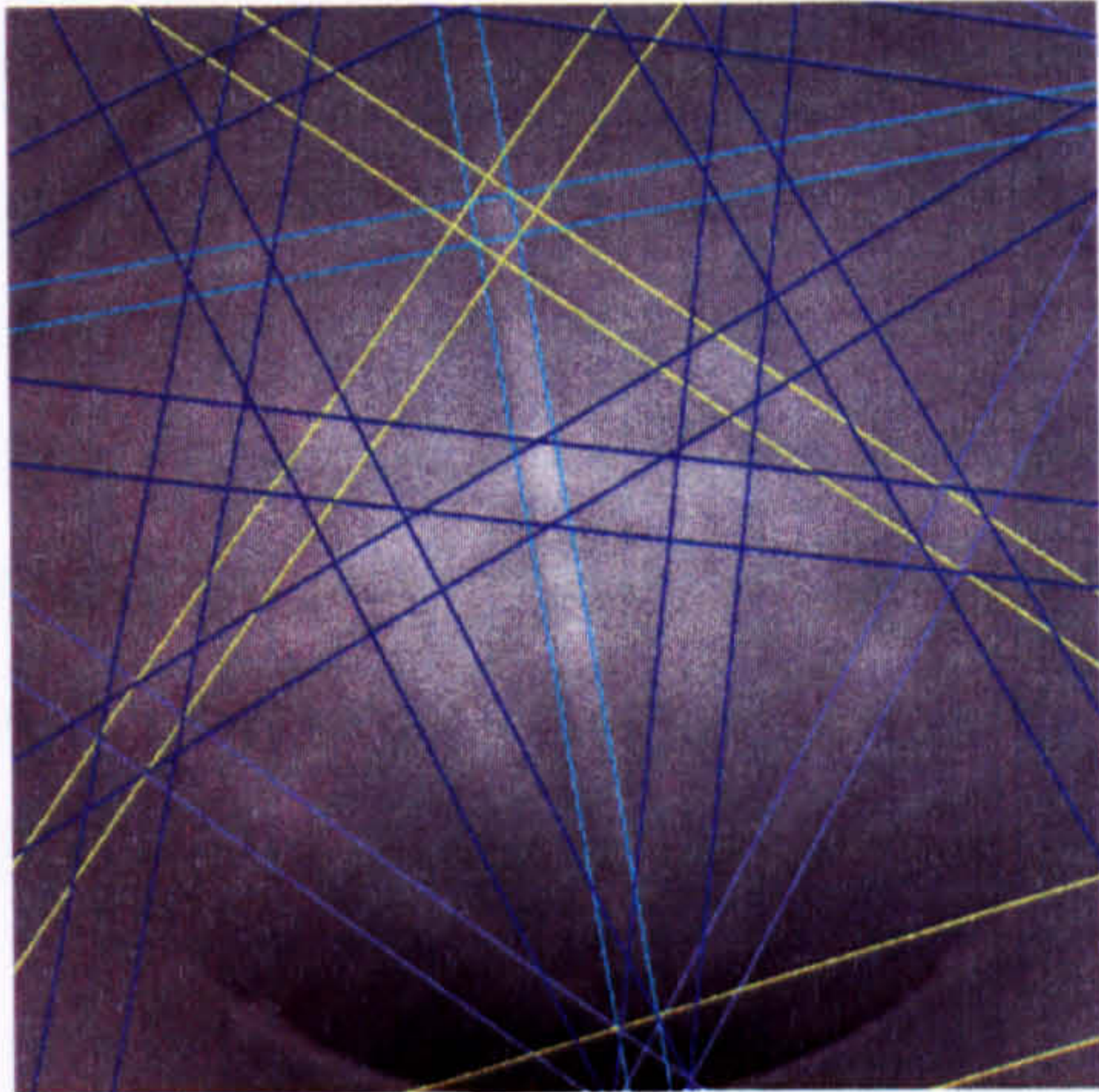


Figure 5.34 EDX spectrum for an Mg-Si particle



a)



b)

Figure 5.35 a) Observed and b) indexed diffraction patterns from a Mg₂Si particle

Table 5.18 Crystallographic and diffraction data for Mg₂Si

Crystal System		Cubic		
Space Group		Fm3m		
Lattice Parameter (Å)		a=6.391		

hkl	ICDD (73-2246)		EBSD	
	Interplanar spacing, d (Å)	Intensity	Interplanar spacing, d (Å)	Intensity
220	2.2595	999	-	-
311	1.9269	142	-	-
222	1.8449	27	1.845	429
400	1.5977	136	1.598	400
331	1.4662	49	-	-
420	1.4290	25	-	-
422	1.3045	222	-	-
333	1.2299	31	-	-
440	1.1297	57	1.130	999

5.3.7 Al_3Ni

Al_3Ni is the binary phase from the Al-Ni system and is believed to form when there is a high enough Ni concentration of greater than ~ 1 wt. %. For lower Ni contents ternary $AlCuNi$ and $AlFeNi$ phases are formed in preference. Al_3Ni was observed in AE160 to adopt a plate like morphology, often broken with the appearance of 'vertebrae', which upon etching (0.5 % HF in water) acquires a brown colour as seen in Figure 5.36. Multiple analyses were carried out by standard EDX resulting in a range of compositions falling between those expected for Al_3Ni and Al_9FeNi . The Al_9FeNi phase will be discussed further in 5.3.11. The differentiation was made more difficult by the fact that all the phases analysed had similar morphology and colouring, the Al_9FeNi being slightly darker and more script like. Furthermore, Figure 5.37 shows an individual crystal appearing to consist of two phases linked together with different colouring and morphology. By calculating the stoichiometry (ratio of At. %) of Al:Ni(+Fe) it was possible to distinguish between the two phases, Al_3Ni having a ratio of 1.8 in comparison to 4.5 for Al_9FeNi . The final composition observed and identified as Al_3Ni is given in Table 5.19, and through EDX the single particle in Figure 5.37 was found to be Al_9FeNi at one end and Al_3Ni at the other.

The Al_3Ni phase is not predicted to form in the thermodynamic equilibrium simulation shown in Figure 5.10. The phase is modelled as non-stoichiometric with a limited solubility of Cu, Fe, and Si at higher temperatures, although from the observed compositions in Table 5.19 there appears to be more solubility of these elements than might be predicted. Given that the Al_3Ni phase was observed but not predicted in these alloys, it is possible that during non-equilibrium solidification, the local composition has changed sufficiently to promote its formation. This could explain how a range of compositions between Al_3Ni and Al_9FeNi exist, as Al_9FeNi is formed preferentially at high temperatures, but as the temperature decreases and the local solute concentration changes, Al_3Ni becomes stable.

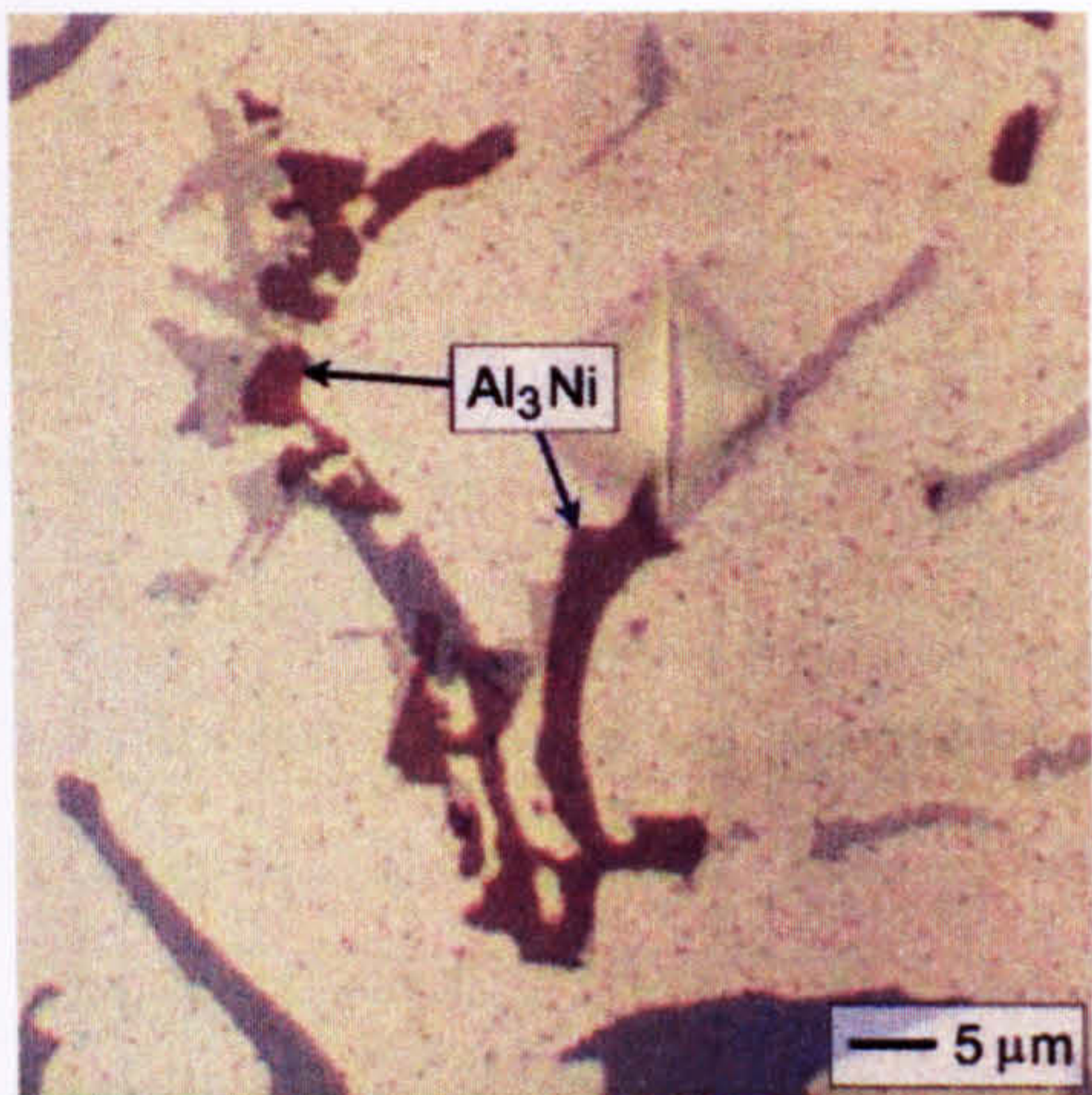


Figure 5.36 Optical micrograph of Al₃Ni

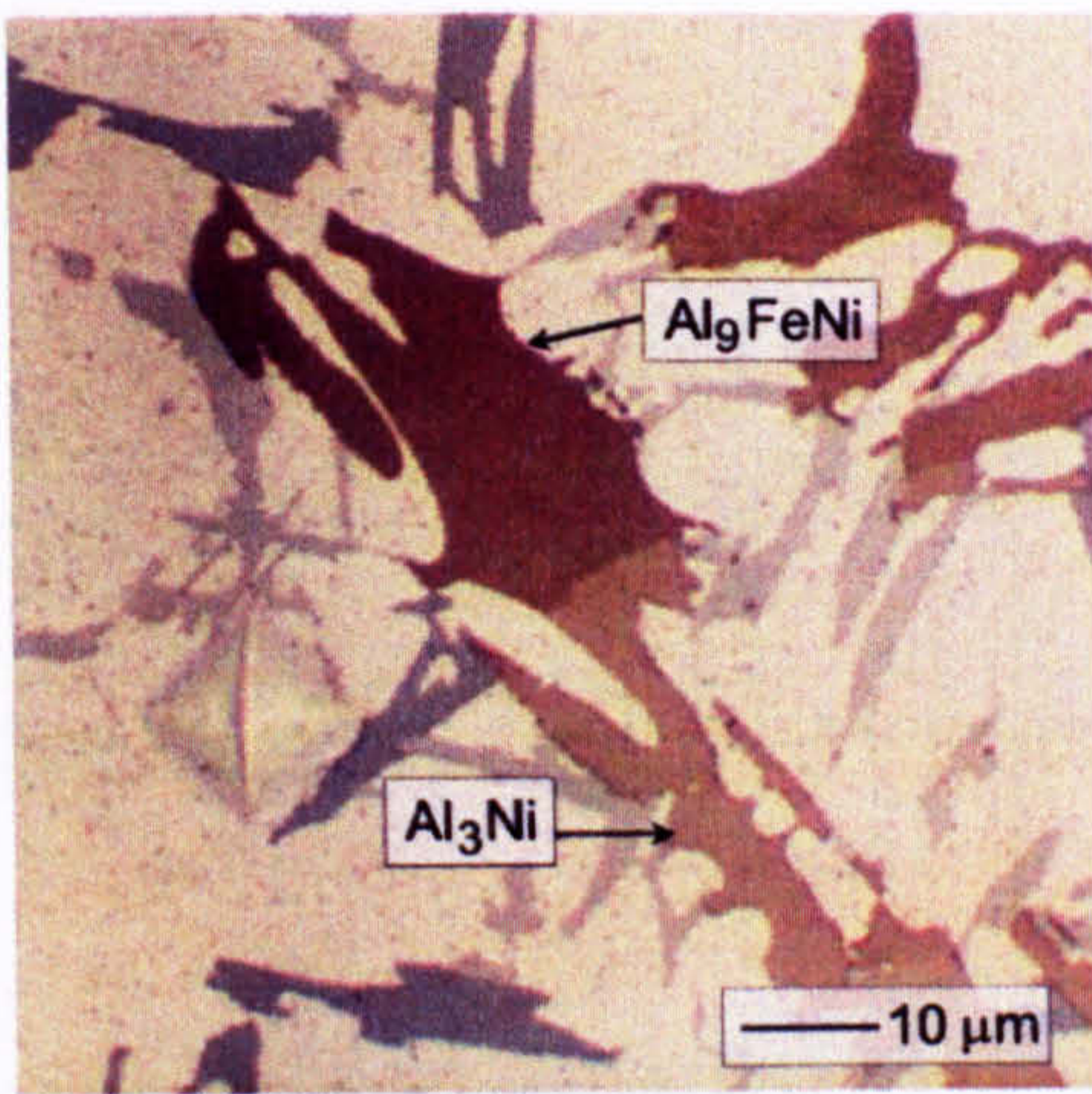


Figure 5.37 Optical micrograph showing single particle consisting of two separate phase compositions

Table 5.19 Composition of Al₃Ni

	Fraction of component in phase									
	Al	Cu	Fe	Mg	Mn	Ni	Si	Ti	V	Zr
Observed (At.%)	64.70	5.60	4.40	-	1.21	18.30	5.36	0.01	0.05	0.37
Observed (Wt.%)	47.51	9.63	6.70	-	1.81	29.24	4.10	0.02	0.07	0.92

EBSD and EDX were carried out on a number of Al₃Ni particles from which a representative EDX spectrum can be seen in Figure 5.38, and the diffraction patterns are given in Figure 5.39. The ICDD database was found to contain 18 Al-Ni phases of which only one was Al₃Ni. Automatic indexing found the card number 02-0416 from the ICDD database to match the best, although significant discrepancies between the observed and indexed images were clear. For example, of the 12 x-ray reflectors listed in the ICDD database that could have appeared in the EBSD pattern, only 3 were actually seen and are given in Table 5.20. The observed reflectors were of the type 011, 002 and 112, none of which correspond exactly with the powder diffraction files. One un-indexed Kikuchi band was subsequently identified manually as the 013. An explanation for inconsistency between the powder diffraction file data and observed diffraction patterns can be established by considering that substitution of Cu, Fe, and Si (as detected by EDX), will alter the crystal structure, and hence the lattice parameters of the phase.

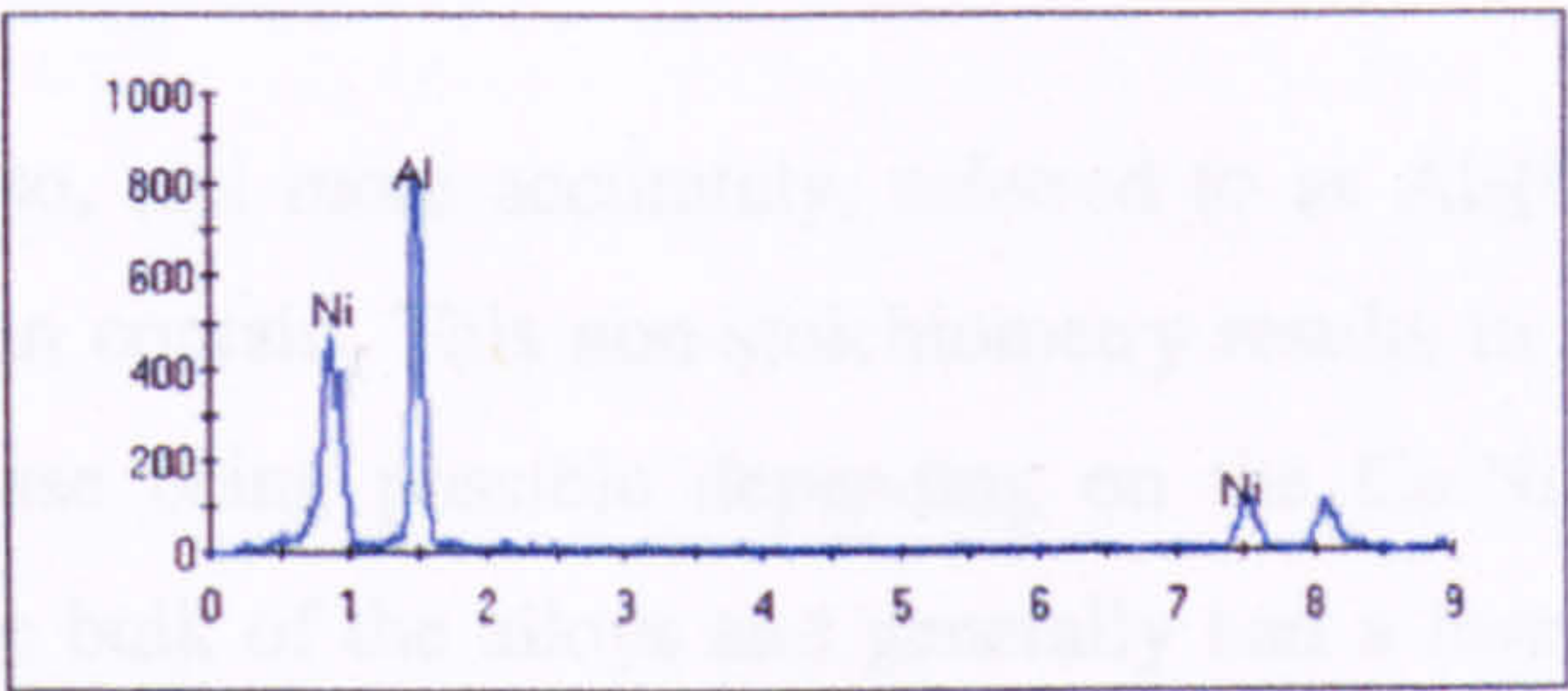


Figure 5.38 EDX spectrum for an Al₃Ni particle

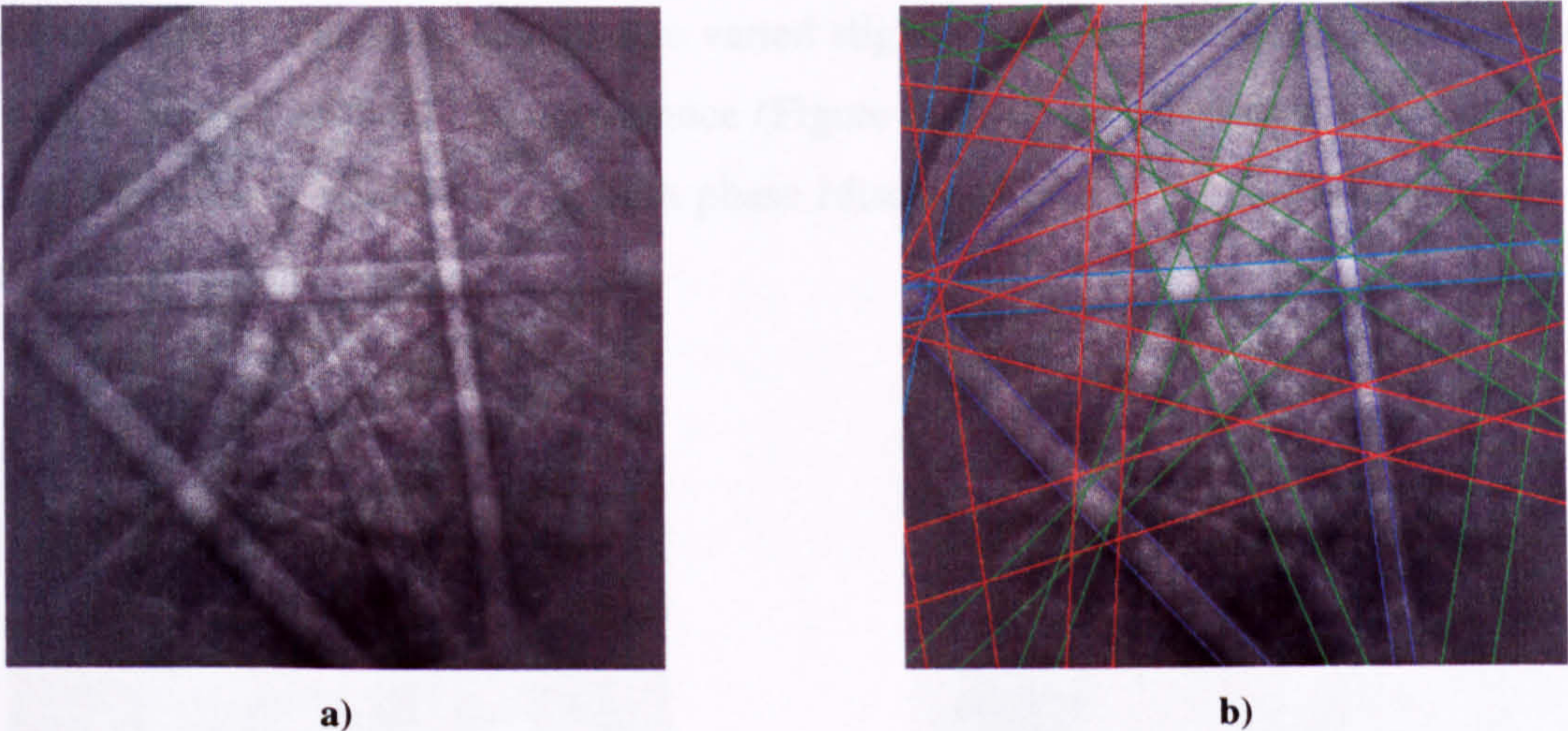


Figure 5.39 a) Observed and b) indexed diffraction patterns from an Al₃Ni particle

Table 5.20 Crystallographic and diffraction data for Al₃Ni

Crystal System	Orthorhombic
Space Group	Pmna
Lattice Parameters (Å)	a=6.598, b=7.352, c=4.802, A=0.8974, C=0.6532

hkl	ICDD (02-0416)		EBSD	
	Interplanar spacing, d (Å)	Intensity	Interplanar spacing, d (Å)	Intensity
011	4.02	40	2.036	4.7
101	3.89	70	-	-
220	2.46	40	-	-
002	2.40	20	1.440	3.3
102	2.26	5	-	-
031	2.18	70	-	-
112	2.16	80	1.176	2.6

Not shown are the 020, 111, 210, 201, and 211 reflectors

5.3.8 $\text{Al}_3(\text{Cu},\text{Ni})_2$

The Al_3Ni_2 phase is also, and more accurately, referred to as $\text{Al}_3(\text{Cu},\text{Ni})_2$ due to the large amounts of copper it can contain. This non-stoichiometry results in several variations of the composition of the phase being possible depending on the Cu:Ni ratio. $\text{Al}_3(\text{Cu},\text{Ni})_2$ was observed throughout the bulk of the alloys and generally had a form similar to the particles shown in Figure 5.40, taking on a pale brown-grey colouring after etching which was found to lighten slightly as the Cu:Ni ratio increased. This colour is very similar to that of the $\pi(\text{Al}_8\text{FeMg}_3\text{Si}_6)$ phase, with $\theta(\text{CuAl}_2)$ being lighter and more pink, and $\lambda(\text{Al}_5\text{Cu}_2\text{Mg}_6\text{Si}_5)$ being more yellow. The morphology also varied slightly with composition; high Cu:Ni ratios taking on a 'lakey', globule like appearance (Figure 5.40 a), whilst phases with a low Cu:Ni ratio are often found adjoining a Zr-rich phase (discussed in 3.3.15) and are therefore more linear in shape (Figure 5.40 b).

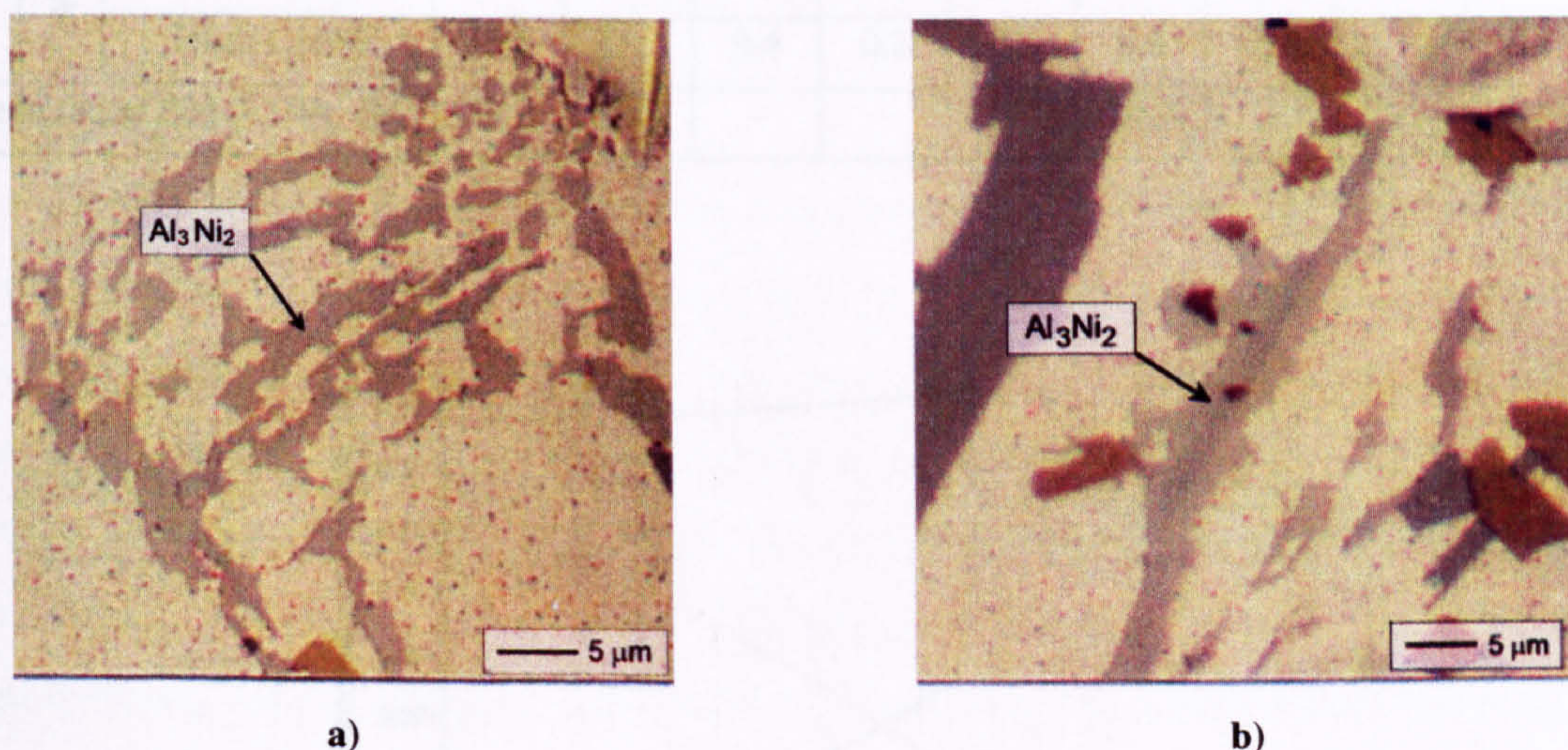


Figure 5.40 Optical micrographs of $\text{Al}_3(\text{Cu},\text{Ni})_2$ **a)** with high (< 3) Cu:Ni ratio, and **b)** with low (< 1) Cu:Ni ratio adjoining a high Zr particle

The $\text{Al}_3(\text{Cu},\text{Ni})_2$ phases observed were found to have a similar composition to Al_3Ni and Al_9FeNi , but were easy to distinguish because of the high copper content. Three distinct variations of the $\text{Al}_3(\text{Cu},\text{Ni})_2$ composition were classified: low Cu:Ni ratio of < 1 ; medium Cu:Ni ratio of 2-3; and a high Cu:Ni ratio of > 4 . The plot in Figure 5.41 shows how the composition of the $\text{Al}_3(\text{Cu},\text{Ni})_2$ phase is non-stoichiometric and highly temperature dependent; the nickel content increasing and copper decreasing with increasing temperature. This confirms that depending at which stage of solidification the phase has formed, a range of

compositions are to be expected. The medium Cu:Ni ratio is of particular interest, however, as the composition matches that for $\text{Al}_7\text{Cu}_4\text{Ni}$, highlighted in blue in Table 5.21, and discussed in section 5.3.9. Indeed, by comparing the $\text{Al}:(\text{Cu}+\text{Ni})$ ratios of both $\text{Al}_3(\text{Cu,Ni})_2$ and $\text{Al}_7\text{Cu}_4\text{Ni}$ phases, they can be seen to be very similar at 1.5 and 1.4 respectively, making them very difficult to differentiate.

Table 5.21 Range of compositions for the $\text{Al}_3(\text{Cu,Ni})_2$ phase

			Fraction of component in phase									
			Al	Cu	Fe	Mg	Mn	Ni	Si	Ti	V	Zr
Observed	At. %	Low Cu:Ni	61.3	16.2	0.5	-	-	19.7	1.6	0.1	0.1	0.6
		Med. Cu:Ni	63.3	23.5	0.5	0.3	0.1	11.9	0.3	0.1	-	0.2
		High Cu:Ni	65.5	26.0	0.3	0.4	0.2	6.5	0.8	-	0.1	0.2
	Wt. %	Low Cu:Ni	41.8	25.8	0.6	-	-	29.0	1.2	0.1	0.1	1.4
		Med. Cu:Ni	43.7	37.0	0.6	0.2	0.1	17.5	0.2	-	-	0.6
		High Cu:Ni	46.1	42.1	0.4	0.2	0.3	9.6	0.7	-	0.2	0.6
Predicted at 500 K (Wt. %)			39.7	36.3	-	-	-	24.0	-	-	-	-

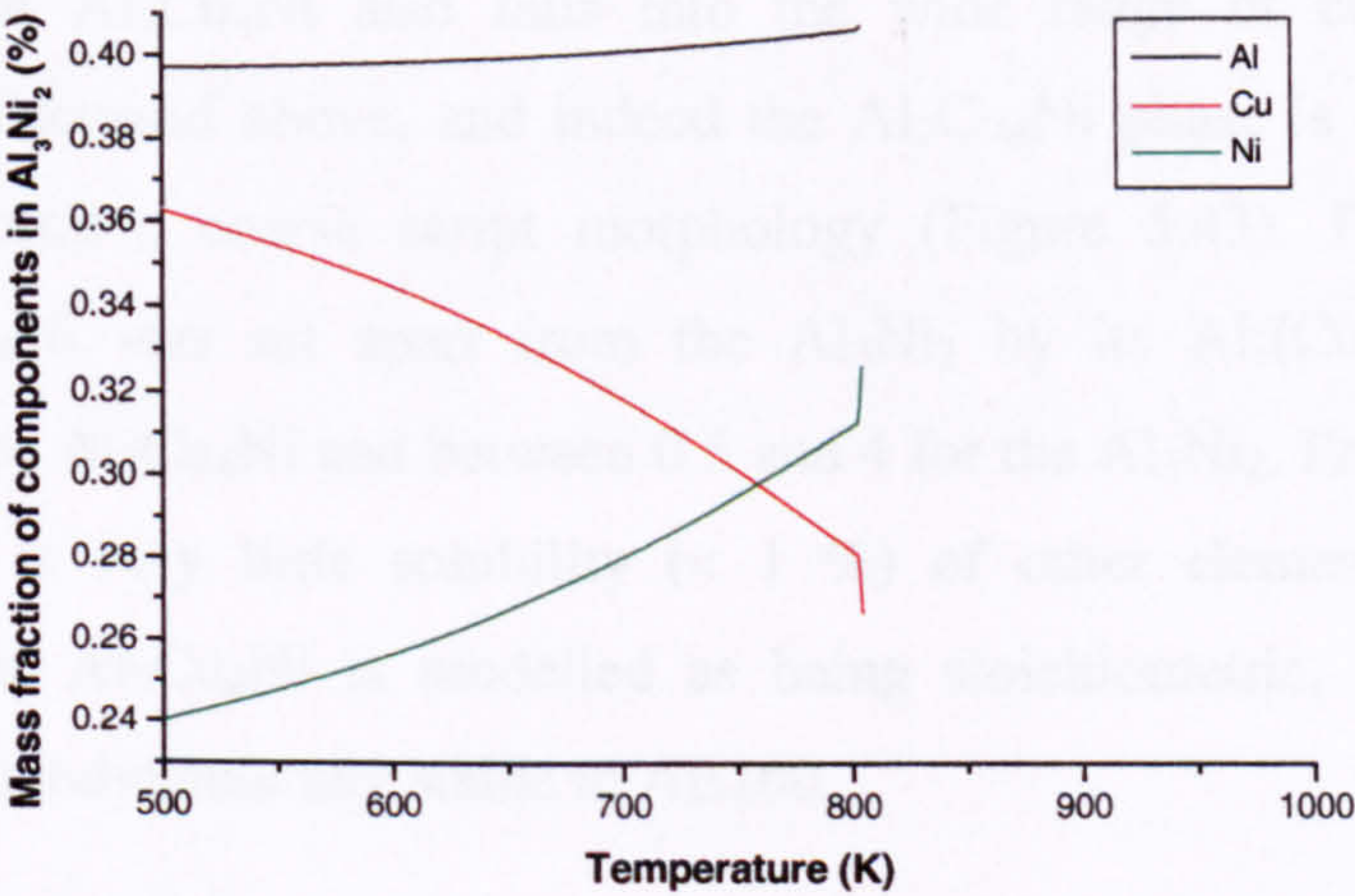


Figure 5.41 Mass fraction of components in $\text{Al}_3(\text{Cu,Ni})_2$ as a function of temperature

EBSD and EDX were carried out on particles believed to be $\text{Al}_3(\text{Cu,Ni})_2$. The EDX trace is given in Figure 5.42, where Al, Cu, and Ni peaks can all be seen. However, on automatic indexing of the pattern in Figure 5.45 a), from a particle believed to be $\text{Al}_3(\text{Cu,Ni})_2$, the phase was identified as card number 28-0016, $\text{Al}_7\text{Cu}_4\text{Ni}$, despite there being 3 Al_3Ni_2 phases in the ICDD database. This is covered in more detail with respect to $\text{Al}_7\text{Cu}_4\text{Ni}$ in section 5.3.9.

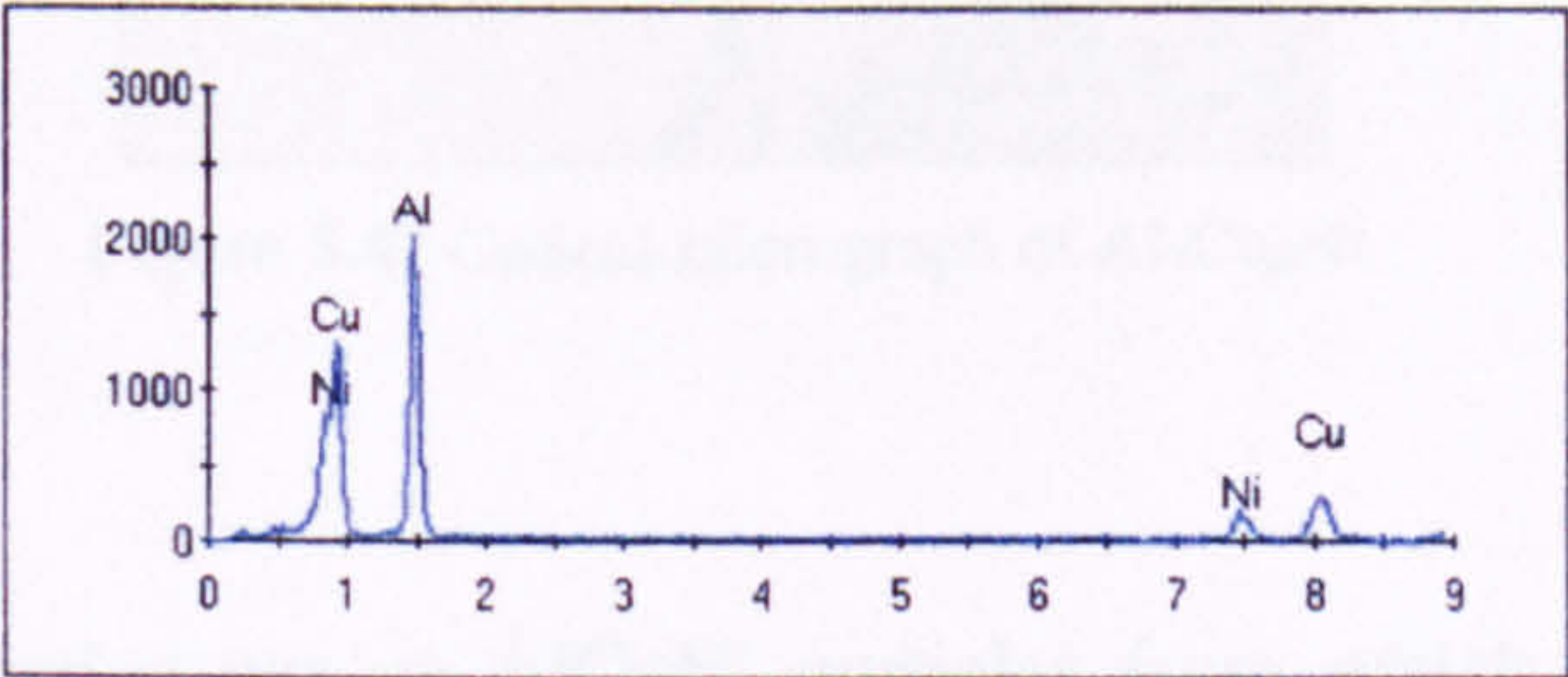


Figure 5.42 EDX spectrum for AlCuNi phase

5.3.9 $\text{Al}_7\text{Cu}_4\text{Ni}$

Also referred to as τ , $\text{Al}_7\text{Cu}_4\text{Ni}$ has been reported to have a broad composition range often incorporated as $\text{Al}_7(\text{CuNi})_5$ and is understood to form in alloys with high Cu, low Ni contents. This composition of $\text{Al}_7\text{Cu}_4\text{Ni}$ also falls into the wide range of compositions for the $\text{Al}_3(\text{Cu,Ni})_2$ phase discussed above, and indeed the $\text{Al}_7\text{Cu}_4\text{Ni}$ phase is seen to have a very similar, pale grey-brown, coarse script morphology (Figure 5.43). From standard SEM analysis the $\text{Al}_7\text{Cu}_4\text{Ni}$ was set apart from the Al_3Ni_2 by its Al:(Cu,Ni) ratio which is approximately 1.4 for $\text{Al}_7\text{Cu}_4\text{Ni}$ and between 0.5 and 4 for the Al_3Ni_2 . From Table 5.22 it can be seen that there is very little solubility ($< 1\%$) of other elements in the phase. In thermodynamic data, $\text{Al}_7\text{Cu}_4\text{Ni}$ is modelled as being stoichiometric, although it was not calculated to be thermodynamically stable in AE160.

Table 5.22 Composition of $\text{Al}_7\text{Cu}_4\text{Ni}$ phase

	Fraction of component in phase									
	Al	Cu	Fe	Mg	Mn	Ni	Si	Ti	V	Zr
Observed (At.%)	63.3	23.5	0.5	0.3	0.1	11.9	0.3	0.1	-	0.2
Observed (Wt.%)	43.7	37.0	0.6	0.2	0.1	17.5	0.2	-	-	0.6

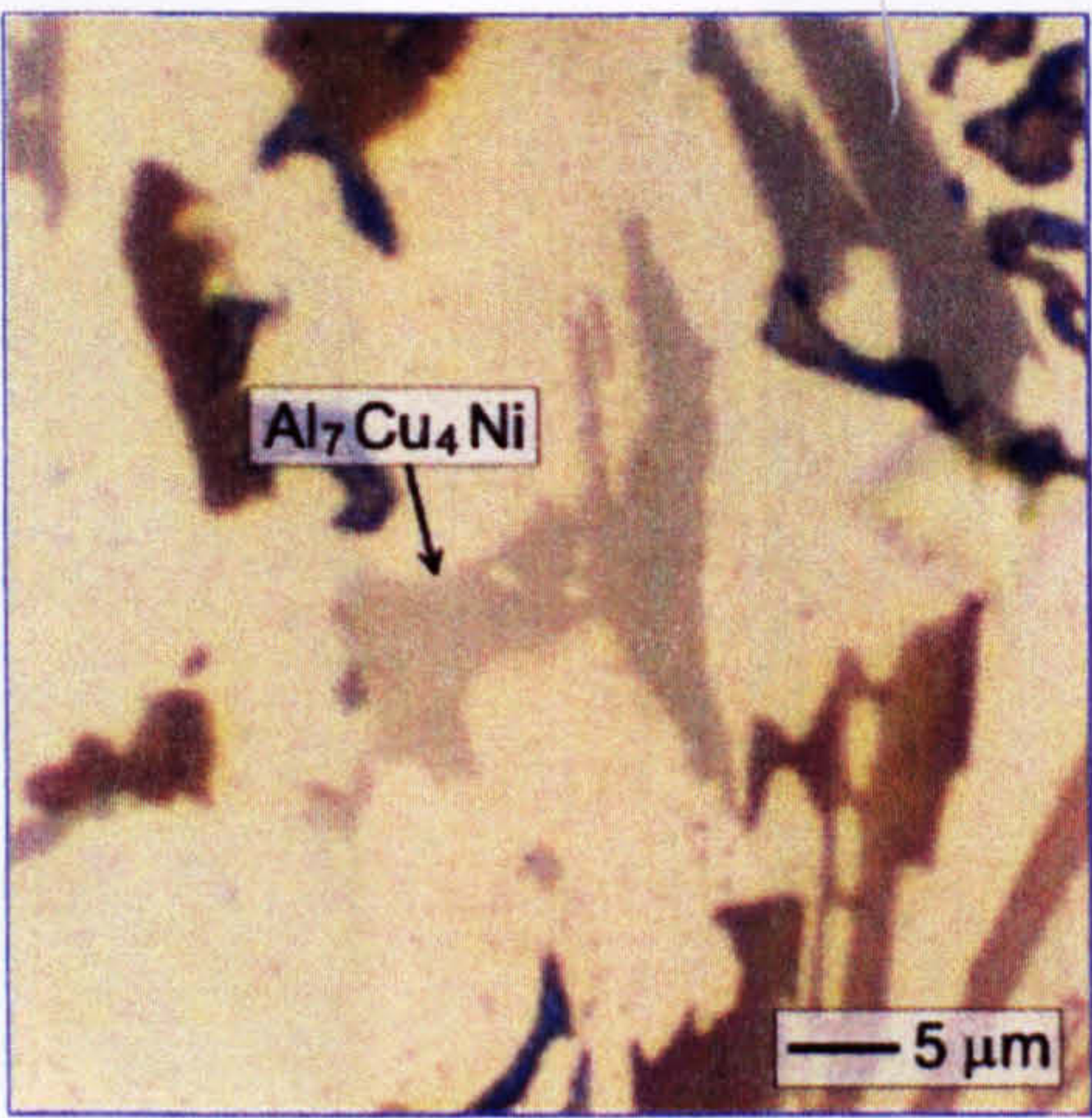


Figure 5.43 Optical micrograph of Al₇Cu₄Ni

EBSD and EDX were carried out on AlCuNi particles from which the EDX spectrum in Figure 5.44, and the diffraction patterns in Figure 5.45, were taken. The ICDD database contains 4 AlCuNi phases from which automatic indexing found card number 28-0016 to fit the best, indicating Al₇Cu₄Ni to be the correct solution despite discrepancy between the observed and indexed images. The number of x-ray reflectors listed in the ICDD database is extensive and so only the 5 observed reflectors, $11\bar{2}0$, $10\bar{1}16$, $01\bar{1}17$, $21\bar{3}16$, and $01\bar{1}32$, are given in Table 5.23 with the corresponding powder diffraction data. For the case of the $01\bar{1}8$ reflector, the second order reflection, i.e. the $02\bar{2}16$, was observed rather than the first. Lines which remained un-indexed were subsequently identified through the use of the computer software by tracing the centreline of the bands enabling calculation of the plane normal, and hence the Miller indices. Two additional reflectors were indexed in this way; the $13\bar{4}16$ and $12\bar{3}33$.

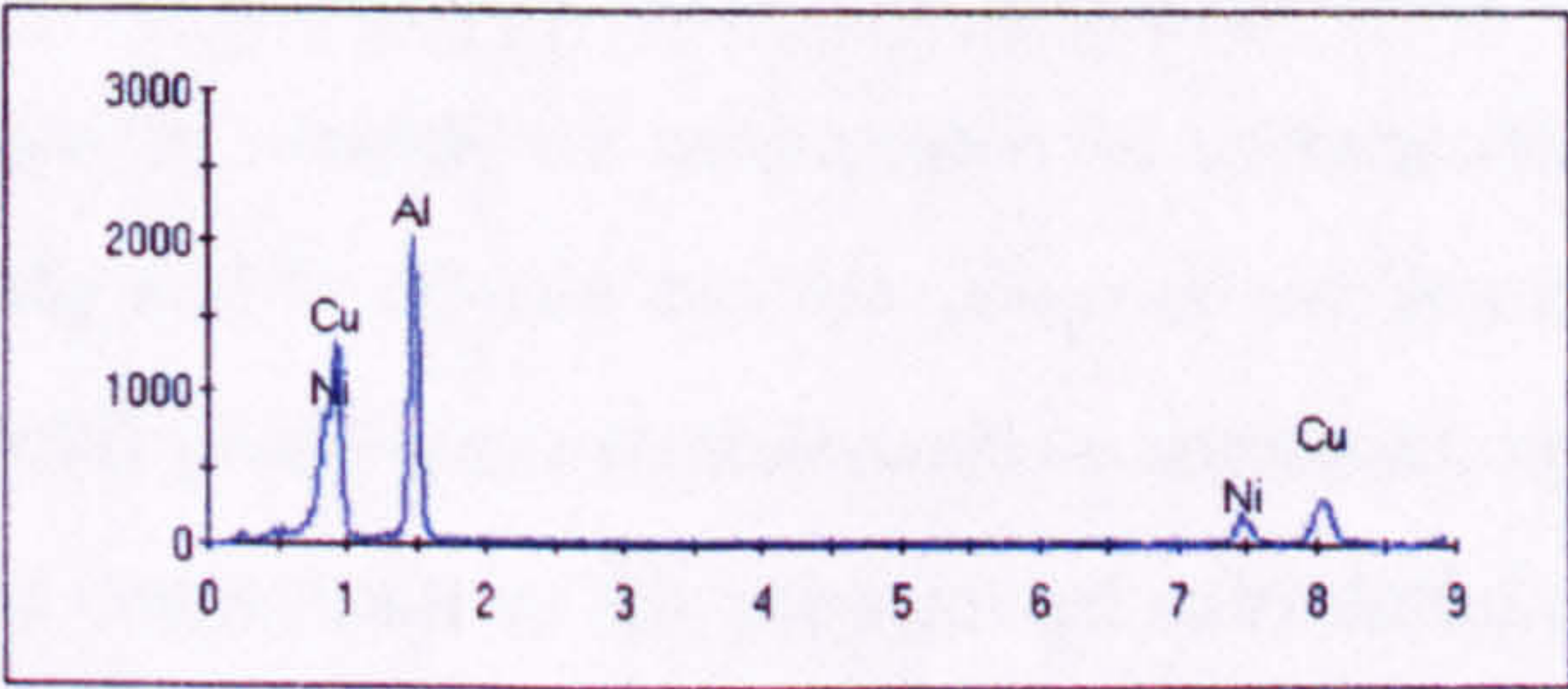


Figure 5.44 EDX spectrum for Al₇Cu₄Ni

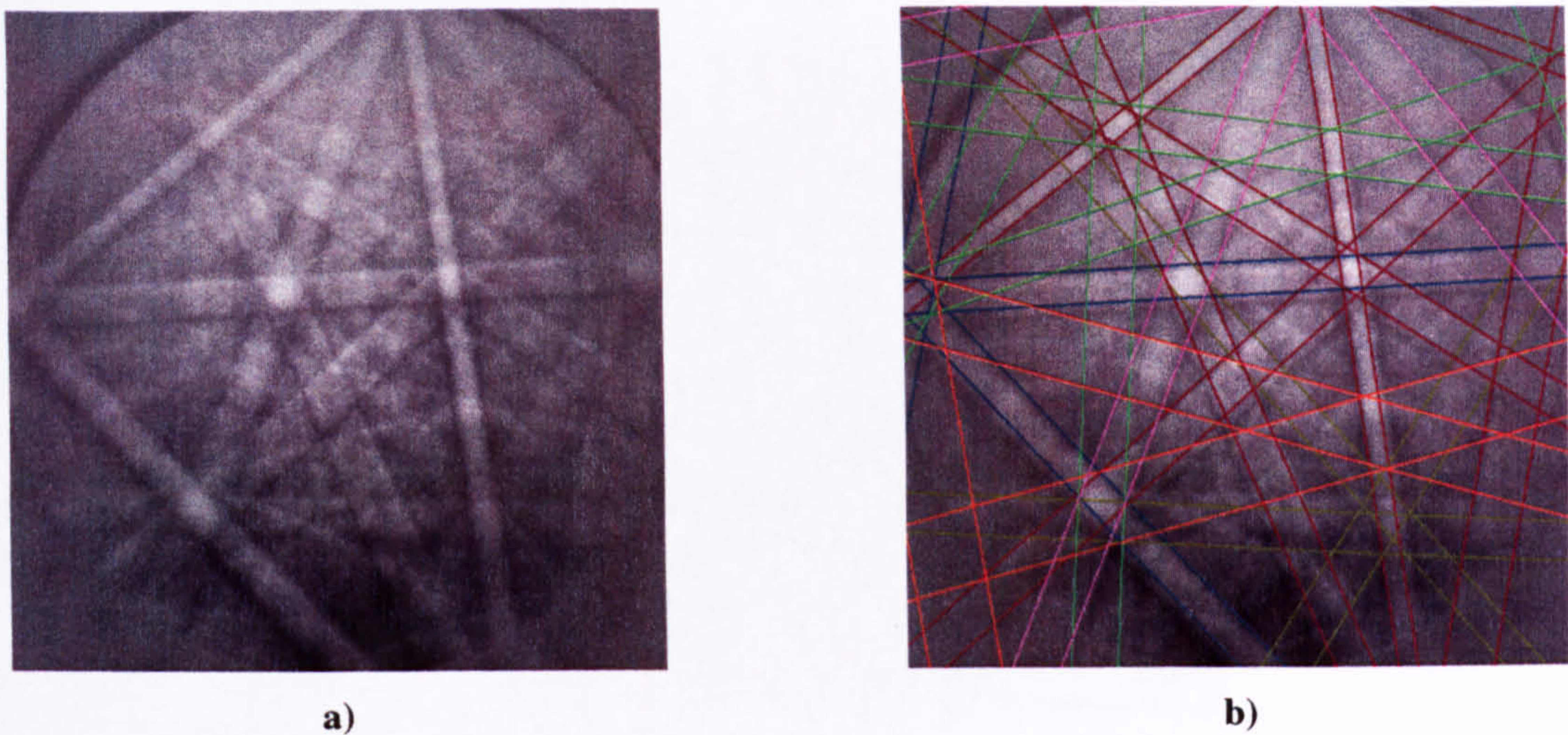


Figure 5.45 a) Observed and b) indexed diffraction patterns from an Al₇Cu₄Ni particle

Table 5.23 Crystallographic and diffraction data for Al₇Cu₄Ni

Crystal System	Rhombohedral			
Space Group	R3m			
Lattice Parameters (Å)	a=4.105, c=39.970			

hkl	ICDD (28-0016)		EBSD	
	Interplanar spacing, d (Å)	Intensity	Interplanar spacing, d (Å)	Intensity
11-20	2.052	98	2.053	98
10-1 16	2.044	100	2.044	100
01-1 17	1.961	12	1.961	12
21-3 16	1.183	21	1.183	21
01-1 32	1.178	9	1.178	9

5.3.10 β (AlFeSi)

This phase is also referred to as Al₅FeSi, Al₉Fe₂Si₂ and Al₁₄Fe₃Si₃. It forms in long plates of up to 100 μm and hence is considered undesirable in commercial piston alloys. Certain additions, Mn, Cr, Co, Mg and Ni hinder this formation of needles by the formation of other compounds. The β (AlFeSi) phase was not observed, or predicted, in AE160, most likely due to the formation of other compounds in the presence of substantial quantities of Mg and Ni. However, this phase was observed in a previous work [Day98] where it was found to take on a light grey-brown colour after etching (0.5 % HF in water) as seen in Figure 5.46, and have a composition as in Table 5.24.

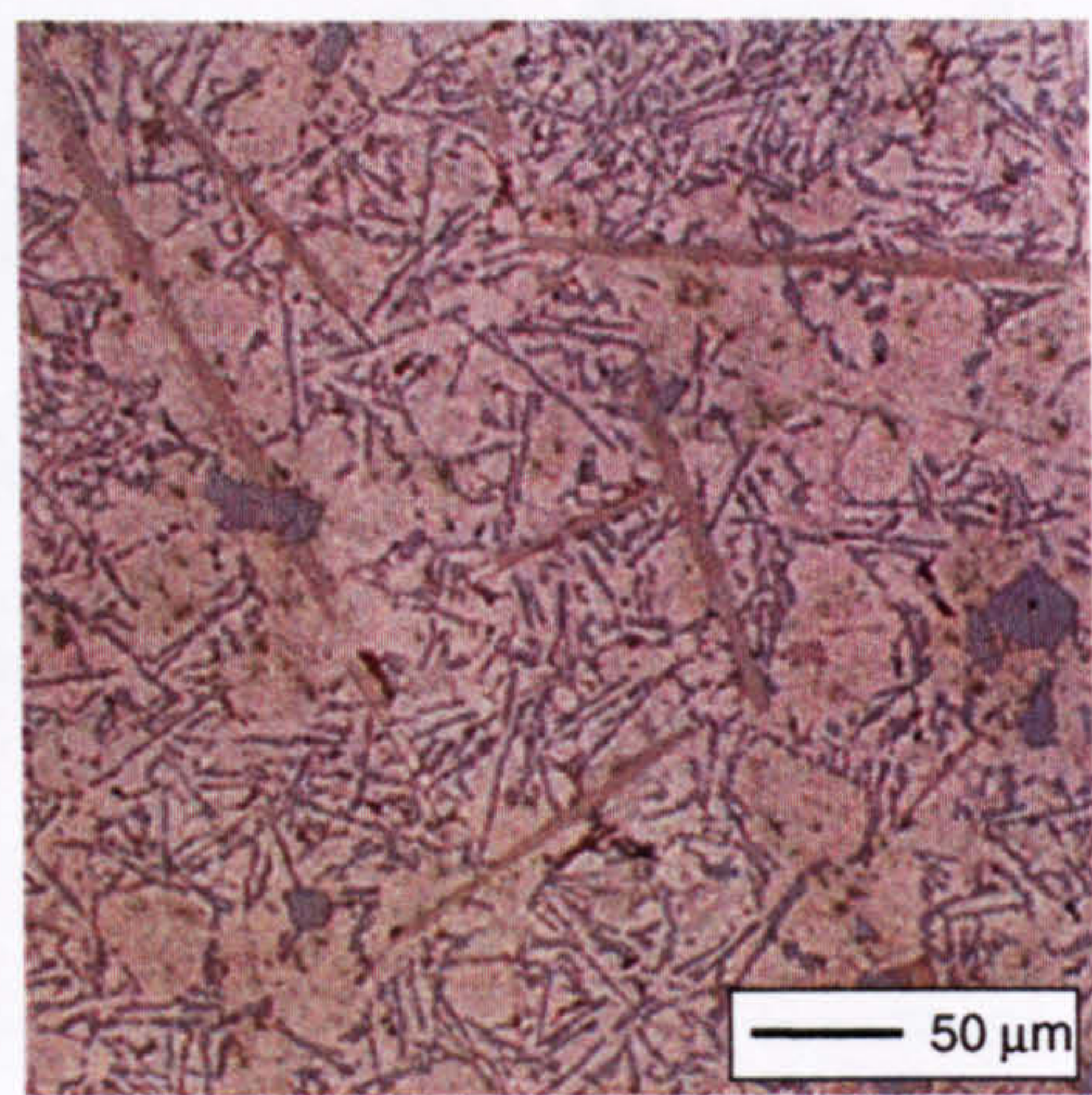


Figure 5.46 Optical micrograph of the β (AlFeSi) phase [Day98]

Table 5.24 Composition of β (AlFeSi) phase [Day98]

	Fraction of component in phase									
	Al	Cu	Fe	Mg	Mn	Ni	Si	Ti	V	Zr
Observed (At.%)	64.1	-	15.6	-	1.46	1.09	17.9	-	-	-
Observed (Wt.%)	53.4	-	26.9	-	2.47	1.43	15.6	-	-	-

5.3.11 *Al₉FeNi*

Al₉FeNi is a non-stoichiometric phase and is often referred to as *Al₉(Fe,Ni)₂* because of the range of solubility of Cu and Ni. *Al₉FeNi* forms in varying quantities depending on the Ni content of the alloy, and takes on a brown colouring, darker than that seen previously for *Al₃Ni*. The morphology of the phase varies slightly from lake-like to a coarse script, shown in Figure 5.47, most likely as a result of cooling rate and/or composition. The composition of the *Al₉FeNi* phase, given in Table 5.25, contains higher aluminium and lower nickel than *Al₃Ni*, with some limited solubility of Cu and Ni, and matches well with the calculated composition. *Al₉FeNi* was predicted by equilibrium calculations to form at around 820 K (547 °C), and although the phase is not modelled as stoichiometric, the composition is not predicted to vary much with temperature (Figure 5.48).

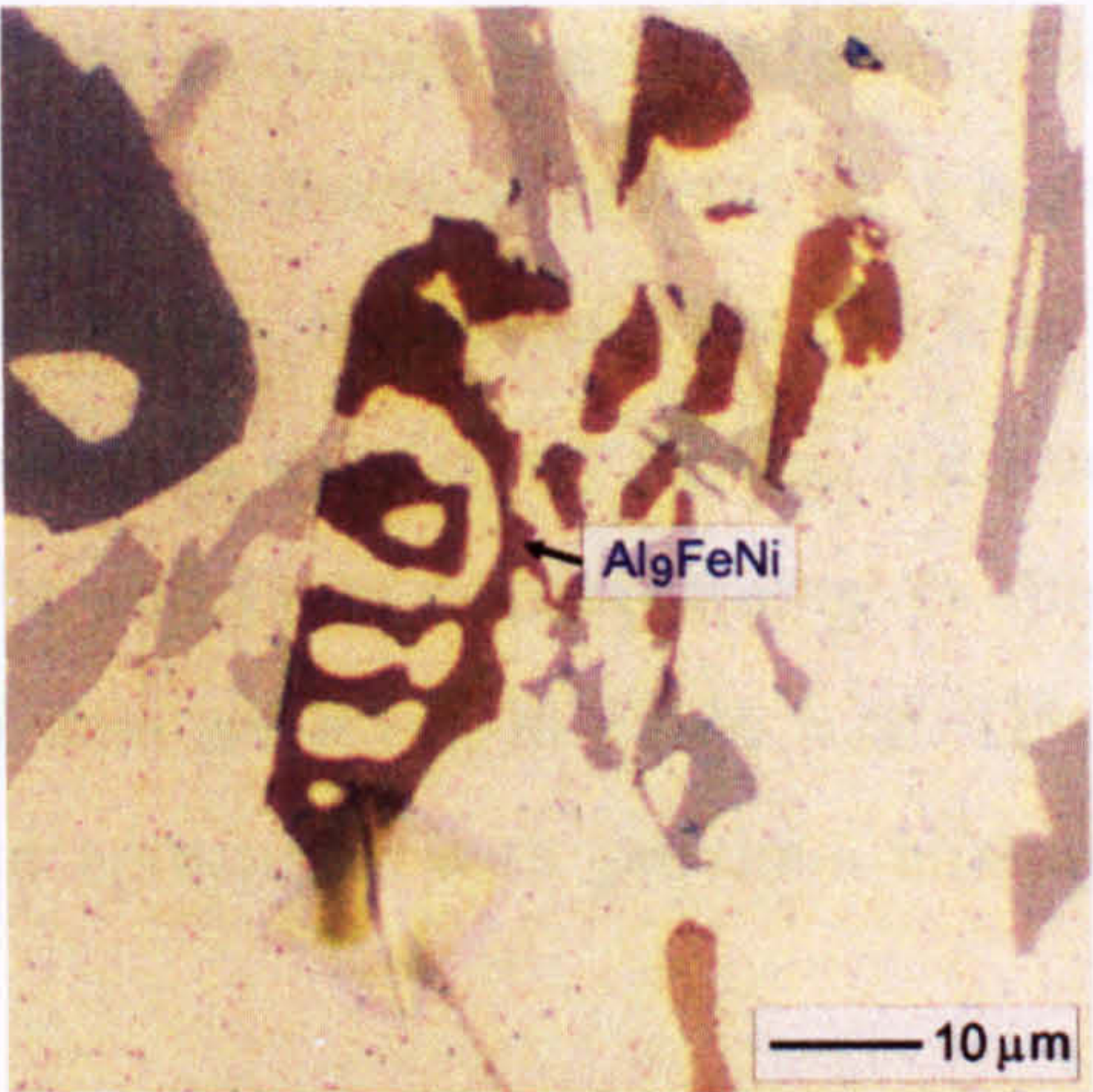


Figure 5.47 Optical micrograph of Al₉FeNi

Table 5.25 Composition of the Al₉FeNi phase

	Fraction of component in phase									
	Al	Cu	Fe	Mg	Mn	Ni	Si	Ti	V	Zr
Observed (At.%)	79.7	1.72	2.86	0.56	0.18	14.4	0.22	0.04	0.02	0.32
Observed (Wt.%)	64.6	3.29	4.83	0.43	0.30	25.6	0.19	0.04	0.03	0.72
Predicted at 500 K (Wt.%)	67.7	-	7.10	-	-	25.3	-	-	-	-

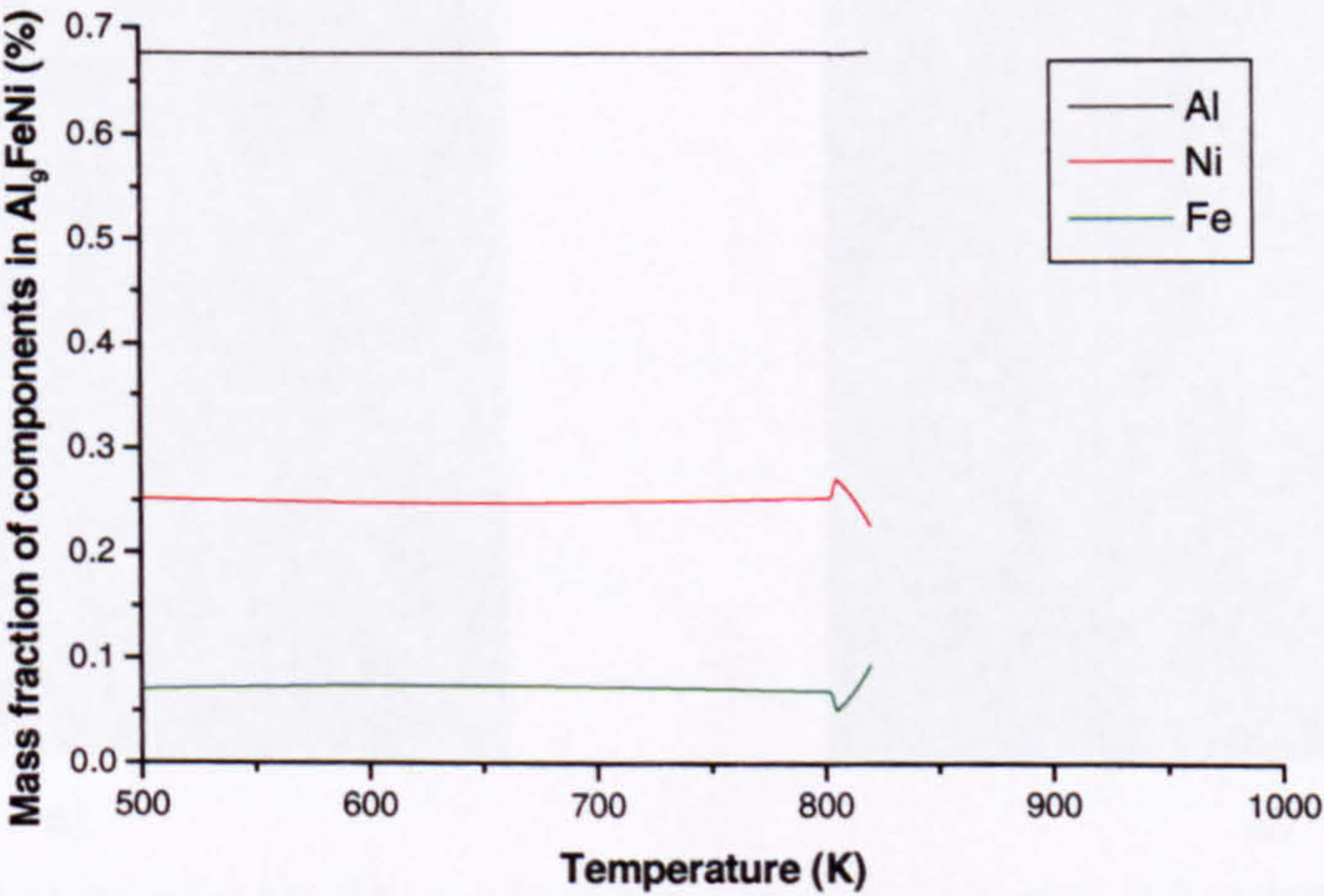


Figure 5.48 Mass fraction of components in the Al₉FeNi phase as a function of temperature

Simultaneous EBSD and EDX were carried out on Al_9FeNi , from which the EDX spectrum can be seen in Figure 5.49, and diffraction patterns in Figure 5.50. Although the ICDD database contains four AlFeNi phases, incidentally none of which are Al_9FeNi , the diffraction pattern in Figure 5.50 automatically indexed as Al_9Co_2 , card number 30-0007. The solution matched well with all of the reflectors corresponding to those contained in the powder diffraction files. Both sets of data are given in Table 5.26. This suggests that the Al_9FeNi is isomorphous with Al_9Co_2 , in agreement with previous analysis of the crystal structure of Al_9FeNi [Day98].

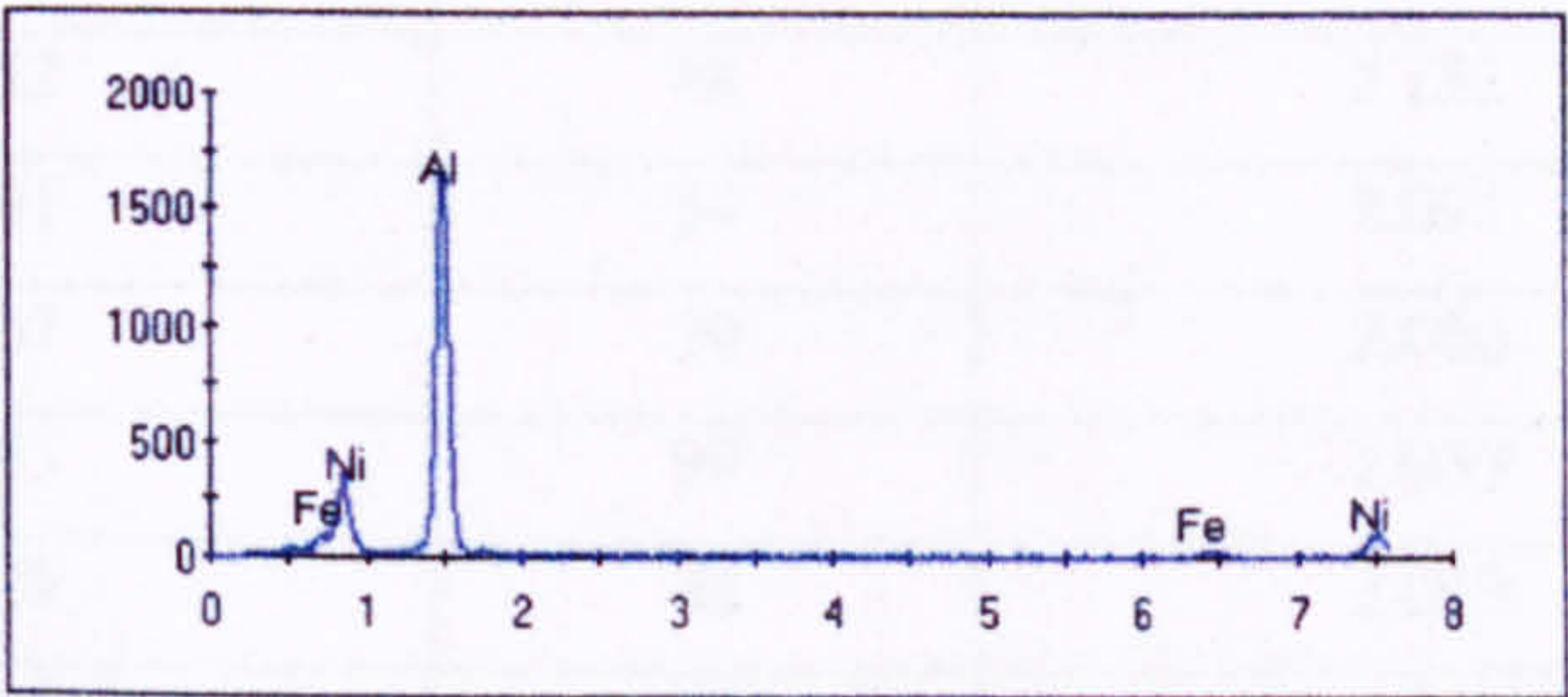
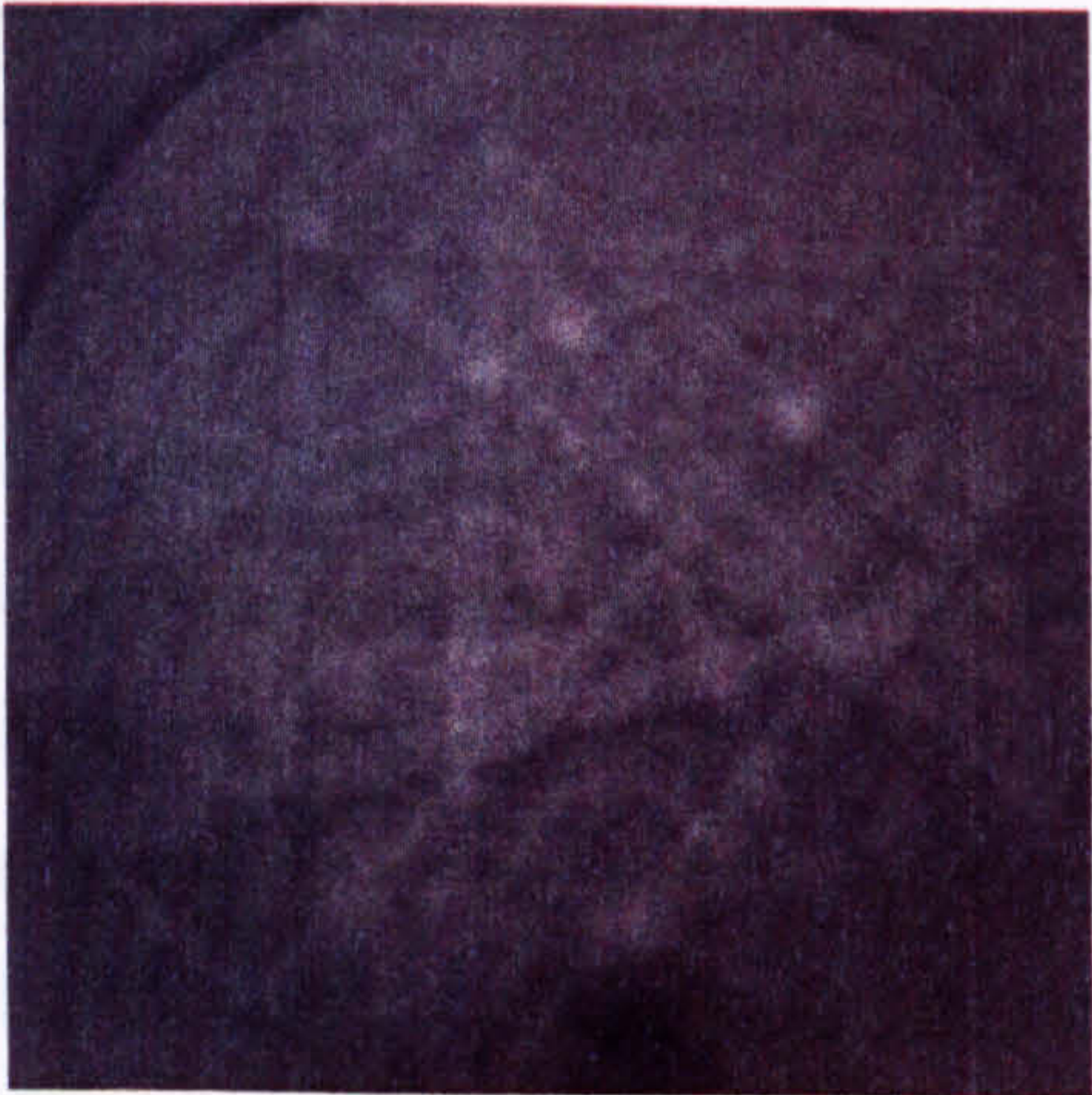
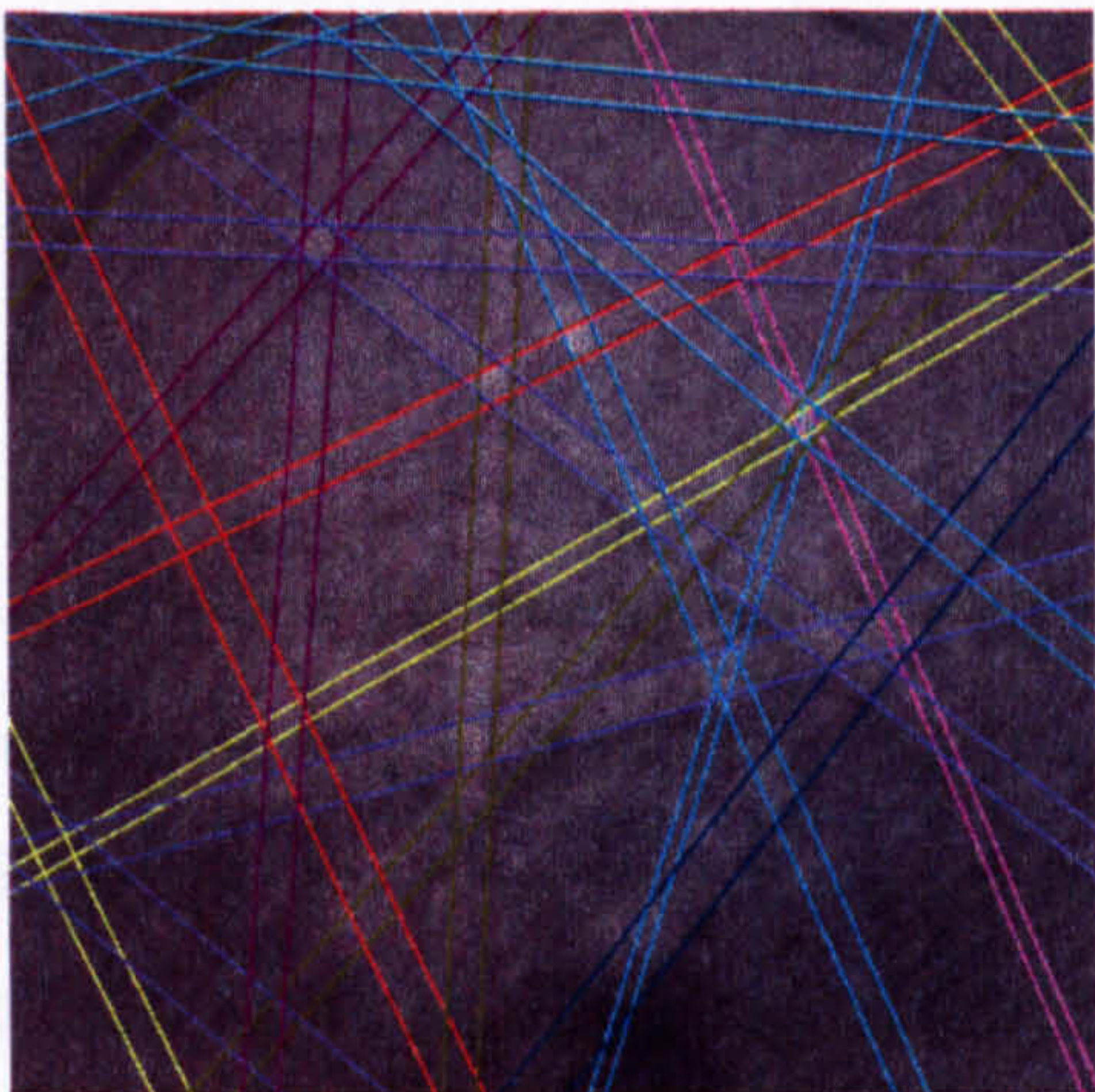


Figure 5.49 EDX spectrum of Al_9FeNi



a)



b)

Figure 5.50 a) Observed and b) indexed diffraction patterns from an Al_9FeNi particle

Table 5.26 Crystallographic and diffraction data for Al₉FeNi (Al₉Co₂)

Crystal System	Monoclinic
Space Group	P2 ₁ /a
Lattice Parameters (Å)	a=8.556, b=6.290, c=6.123, C=0.9734, β=94.76

Hkl	ICDD (30-0007)		EBSD	
	Interplanar spacing, d (Å)	Intensity	Interplanar spacing, d (Å)	Intensity
110	5.062	74	4.380	100
-111	3.994	80	3.994	80
111	3.805	87	3.805	87
221	2.298	88	2.298	88
212	2.233	93	2.233	93
-122	2.152	48	2.152	48
122	2.091	54	2.091	54
-401	2.067	29	2.066	29
-312	2.053	99	2.053	99
410	2.019	42	2.019	42
031	1.982	87	1.983	87
321	1.956	85	1.956	85
-131	1.942	74	1.943	74
013	1.935	81	1.935	81
-113	1.920	73	1.920	73

5.3.12 λ (Al₅Cu₂Mg₈Si₆)

λ (Al₅Cu₂Mg₈Si₆) is a quaternary phase from the AlCuMgSi system. In characterisation of AE160, λ was found throughout the bulk of the material, adopting a ‘cloud-like’ morphology and a pale yellow-grey colour after etching (0.5 % HF in water), very similar to that of Al₃Ni₂. An example of this phase is shown in Figure 5.51. Through SEM analysis the phase composition was determined, as given in Table 5.27, and can be seen to contain large quantities of Al, Si and Mg, with a substantial amount of Cu. There is also some limited solubility of other elements, but at less than 0.5 %. λ (Al₅Cu₂Mg₈Si₆) is modelled as stoichiometric by Al-Data³, and the predicted composition is in good agreement with the observed (Table 5.27). The phase stability plot in Figure 5.10 shows λ to form at around 804 K (531 °C) and increase in stability slightly as the temperature decreases.

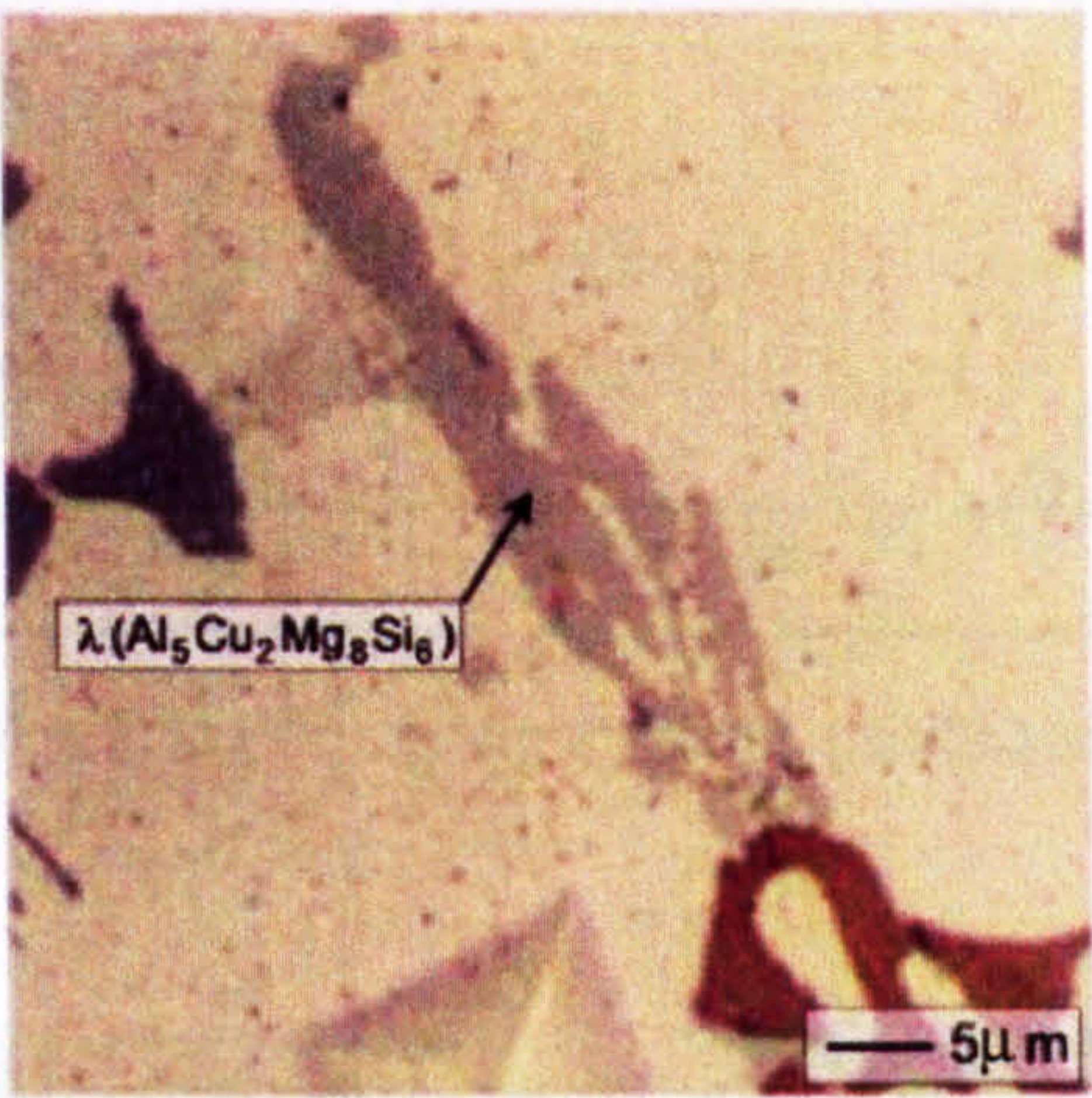


Figure 5.51 Optical micrograph of λ ($\text{Al}_5\text{Cu}_2\text{Mg}_8\text{Si}_6$)

Table 5.27 Composition of λ ($\text{Al}_5\text{CuMg}_8\text{Si}_6$) phase

	Fraction of elements in phase									
	Al	Cu	Fe	Mg	Mn	Ni	Si	Ti	V	Zr
Observed (At. %)	38.0	7.61	0.05	30.2	0.02	1.23	23.5	0.02	0.02	0.06
Observed (Wt. %)	35.0	16.3	0.11	24.9	0.03	1.23	22.2	0.04	0.03	0.19
Predicted at 500 K (Wt. %)	21.6	20.3	-	31.1	-	-	27.0	-	-	-

Through simultaneous EBSD and EDX, an EDX spectrum identified Al, Cu, Mg, and Si peaks, as shown in Figure 5.52. There is just one AlCuMgSi phase in the ICDD database, that of the hexagonal $\text{Al}_{1.9}\text{CuMg}_{4.1}\text{Si}_{3.3}$, card number 41-1068. Automatic indexing of the diffraction pattern in Figure 5.53 found this phase to match best, although significant discrepancies existed between the indexed and observed images. For example, out of the 26 x-ray reflectors listed in the ICDD database that could have appeared in the EBSD pattern, only 5 were actually observed. These are given in Table 5.28 and can be seen to relate well to the powder diffraction data. In addition to the reflectors in Table 5.28, three un-indexed bands were subsequently identified using the computer software to determine the Miller indices. These extra bands were the $\bar{4}131$, $14\bar{5}0$, and $5\bar{1}\bar{5}\bar{2}$.

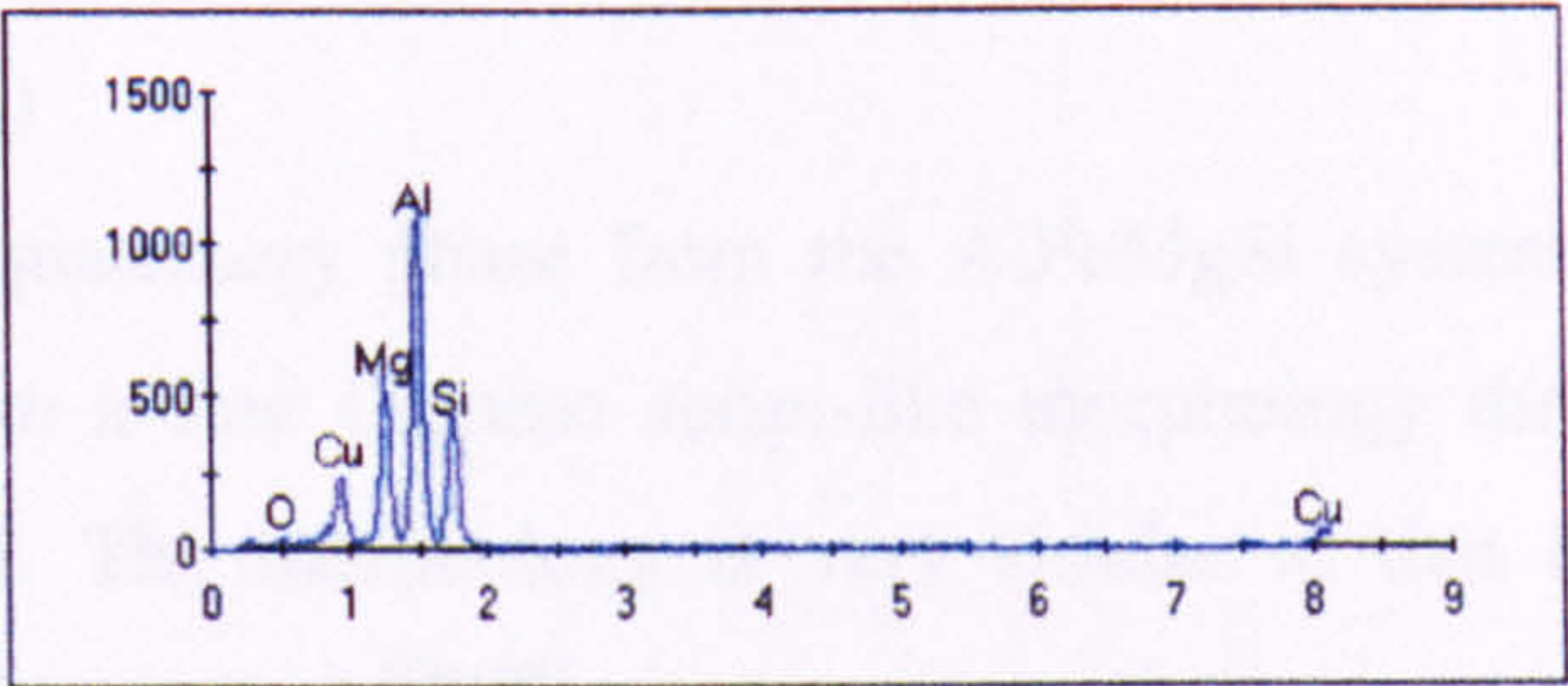
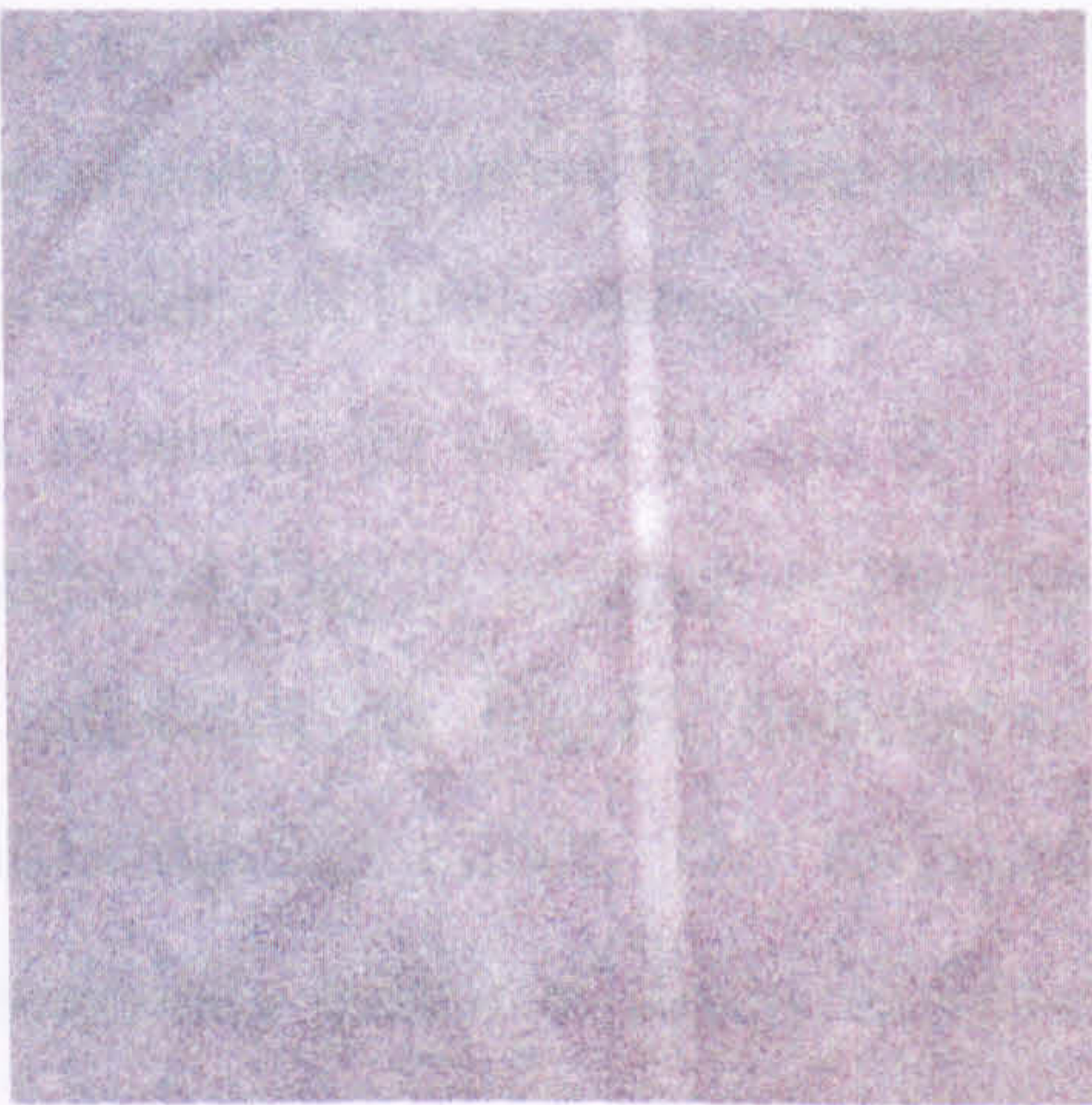
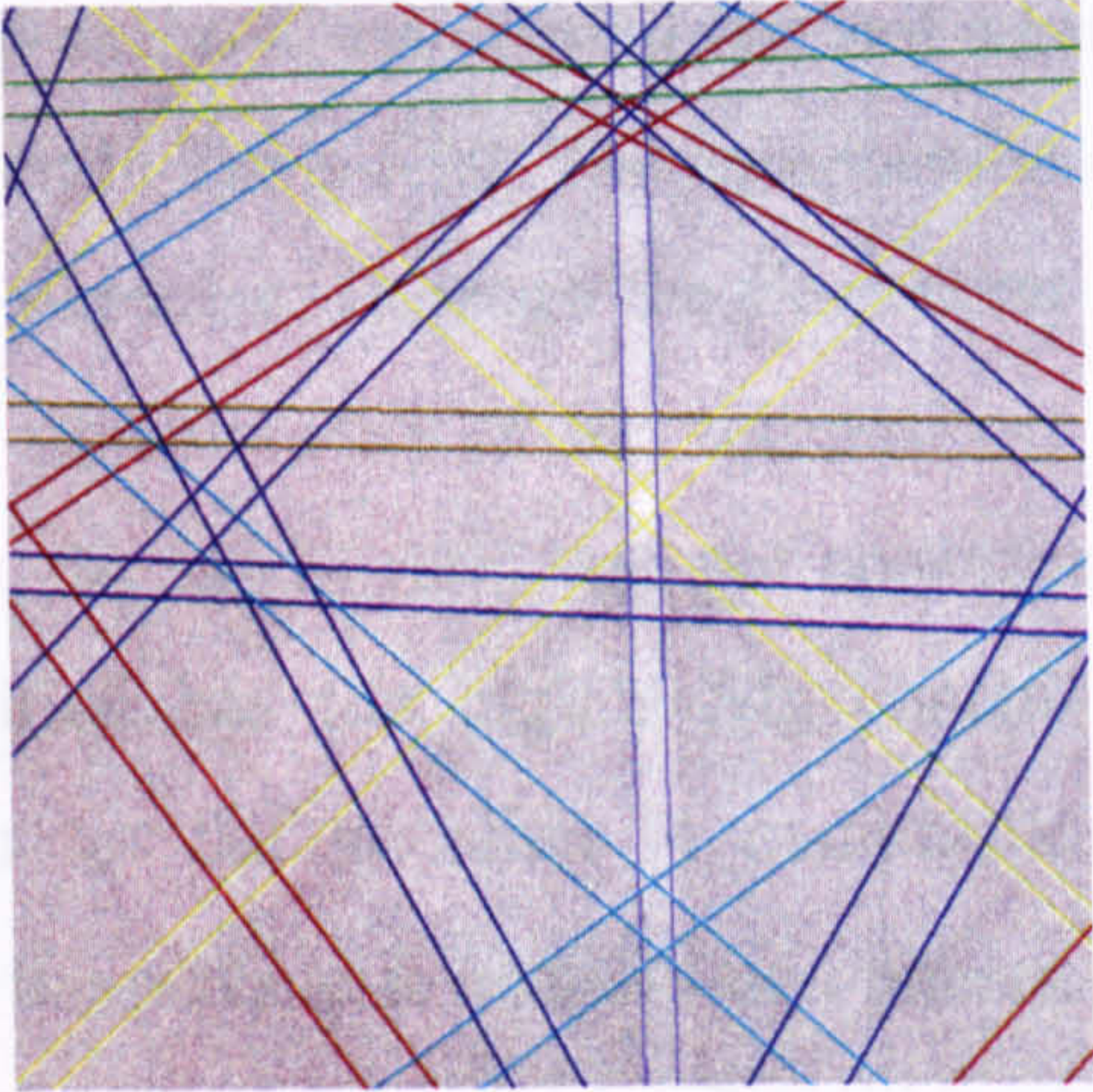


Figure 5.52 EDX spectrum from λ (Al₅CuMg₈Si₆)



a)



b)

Figure 5.53 a) Observed and b) indexed diffraction patterns from an λ (Al₅CuMg₈Si₆) particle

Table 5.28 Crystallographic and diffraction data for λ (Al₅CuMg₈Si₆)

Crystal System	Hexagonal P
Space Group	P6 ₃ /m
Lattice Parameter (Å)	a=10.36, c=4.04

hkl	ICDD (41-1068)		EBSD	
	Interplanar spacing, d (Å)	Intensity	Interplanar spacing, d (Å)	Intensity
21-31	2.593	100	2.597	100
31-40	2.485	75	2.488	75
32-50	2.065	75	2.058	75
0002	2.010	80	2.020	80
40-41	1.961	100	1.961	100

5.3.13 $\pi(\text{Al}_8\text{FeMg}_3\text{Si}_6)$

$\pi(\text{Al}_8\text{FeMg}_3\text{Si}_6)$ is a quaternary phase from the AlFeMgSi system. Small amounts of this phase are seen to form a fine Chinese script-like morphology throughout the material, as shown in Figure 5.54. The morphology is very similar to that of Mg_2Si (section 5.3.6) although the π phase is reported [Day98] to take on a pale grey watery colouring after etching (0.5 % HF in water) rather than the dark blue-black colour of the Mg_2Si . However, in this work a phase of composition best matching that of $\pi(\text{Al}_8\text{FeMg}_3\text{Si}_6)$ was observed as being pearly grey with a dark blue edging. Standard SEM analysis was carried out and a range of compositions measured, the average of which is given in Table 5.29. The composition can be seen to contain large amounts of Al, Mg and Si as expected, although the Fe content is less than expected for the π phase. By calculating the stoichiometry of the composition it was established that, in addition to the high Al content, the Mg:Si ratio was not consistent with that expected for Mg_2Si . Moreover, the composition has too high a Mg content to be $\pi(\text{Al}_8\text{FeMg}_3\text{Si}_6)$ either. The favoured explanation for the variation in composition, and consequently colour of the phase observed, is that the particle is actually two phases. The π phase is presumed to be stable during the initial stages of solidification until a point where the local composition changes to promote the growth of Mg_2Si on the existing π .

Thermodynamic data models $\pi(\text{Al}_8\text{FeMg}_3\text{Si}_6)$ as stoichiometric, and calculations do not predict this phase to be stable in AE160. It is most likely that formation of the $\lambda(\text{Al}_5\text{Cu}_2\text{Mg}_8\text{Si}_6)$ phase, previously shown (Section 5.3.12) to contain large amounts of Al, Mg and Si, is preferred. However, as both the λ and π phases were observed in AE160 and its model alloys, it is likely that solidification conditions in a casting promote the growth of both phases.

Although extensive EBSD and EDX were carried out on AE160, no particles were identified as $\pi(\text{Al}_8\text{FeMg}_3\text{Si}_6)$. However, the ICDD database does contain data for 2 AlFeMgSi phases, both $\text{Al}_8\text{FeMg}_3\text{Si}_6$, the diffraction data for which are given in Table 5.30. If compared with the data for Mg_2Si (Table 5.18), it can be seen that the two π phases have very different x-ray reflectors to those of Mg_2Si , indicating that, despite having overlapping compositions and similar morphologies, the phases should be distinguishable by their EBSD patterns.

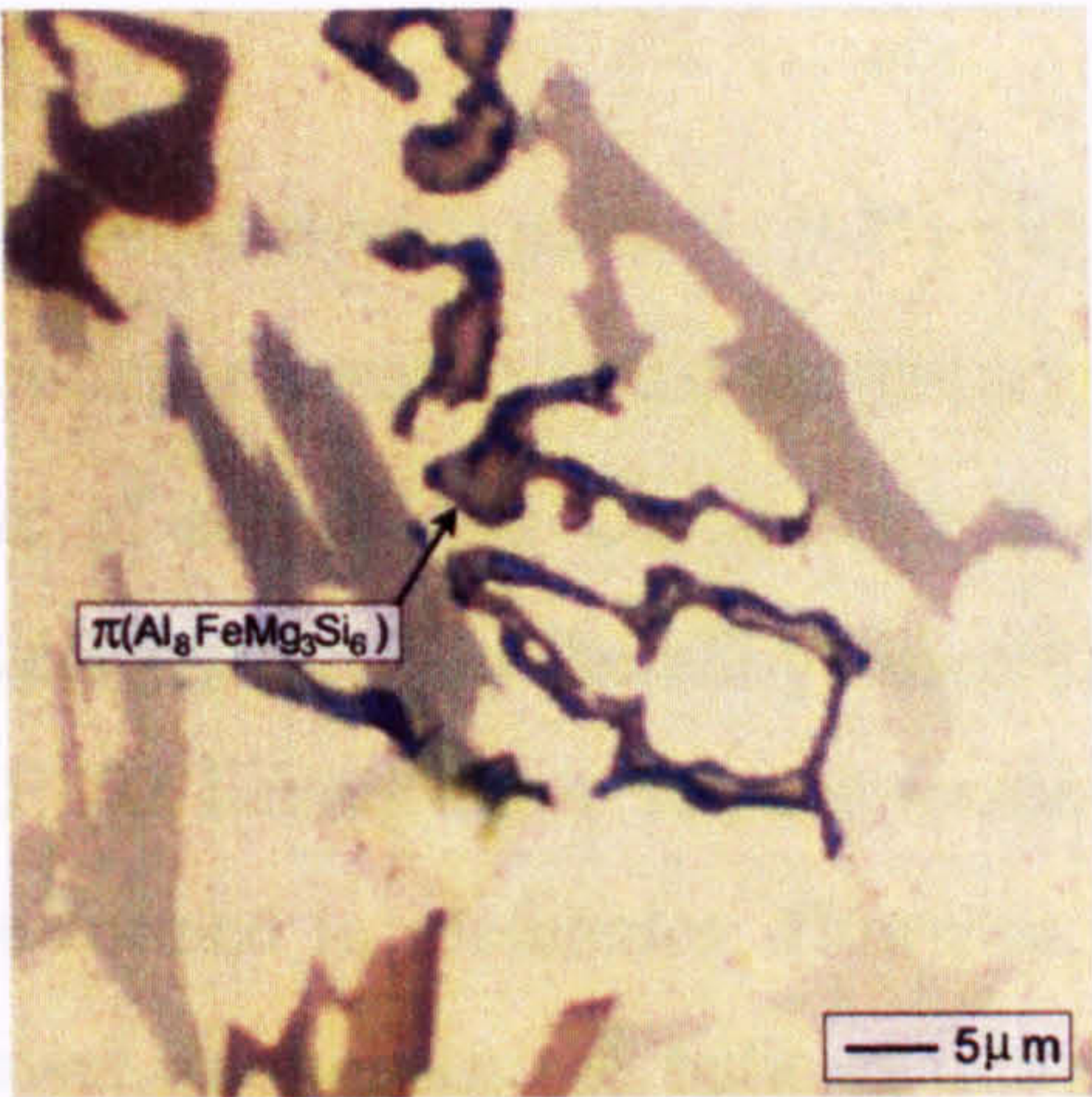


Figure 5.54 Optical micrograph of the π ($\text{Al}_8\text{FeMg}_3\text{Si}_6$) phase

Table 5.29 Composition of the π ($\text{Al}_8\text{FeMg}_3\text{Si}_6$) phase

	Observed fraction of element in phase									
	Al	Cu	Fe	Mg	Mn	Ni	Si	Ti	V	Zr
At. %	30.72	0.57	0.13	39.70	0.02	0.40	28.27	0.02	0.03	0.17
Wt. %	30.90	1.35	0.27	36.23	0.03	0.87	29.72	0.03	0.03	0.56

Table 5.30 Crystallographic and diffraction data for π ($\text{Al}_8\text{FeMg}_3\text{Si}_6$)

Crystal System	Hexagonal
Space Group	P62m
Lattice Parameter (Å)	a=6.62, c=7.92, C=1.1964

hkl	ICDD (25-1085)		ICDD (74-1372)	
	Interplanar spacing, d (Å)	Intensity	Interplanar spacing, d (Å)	Intensity
001	7.92	45	7.92	383
100	5.733	23	5.7330	184
101	4.644	17	4.6440	125
002	-	-	3.9600	10
110	3.310	11	3.3100	94
102	3.258	7	3.2582	56
111	3.054	2	3.0540	17
200	2.867	9	2.8665	73
201	-	-	2.6954	2
003	2.640	2	2.6400	25

5.3.14 α (AlFeMnSi)

α (AlFeMnSi) is based on the cubic ternary phase α (AlMnSi), however since Fe substitutes extensively for Mn it is most often referred to as the quaternary α (AlFeMnSi). α (AlFeMnSi) is also known to be capable of substituting Cu, Cr and V for Mn. No α phases, either (AlMnSi) or (AlFeMnSi), were observed in the alloys investigated for this work, the most likely reason being that in AE160, having a low Mn and reasonably high Cu and Ni contents, the λ and π quaternaries are formed in preference. However, in previous work by Daykin [Day98], this phase was observed throughout the bulk of alloys based on commercial alloy AE413P, and seen to adopt a coarse script morphology which took on a light brown colour on etching as seen in Figure 5.55. The composition is given in Table 5.31.

The α (AlFeMnSi) phase was, however, predicted to form at 832 K (559 °C) in AE160 by thermodynamic calculations. It is modelled as a non-stoichiometric AlFeMnSi phase with a slight solubility for Cu, although the composition is not predicted to vary much with temperature as seen in Figure 5.56. The observed composition [Day98] compares well with that predicted by Al-Data³, with a slight solubility of Ni not accounted for in the modelling of the α phase. Furthermore, α (AlFeMnSi) is only predicted to form as a very small fraction during the lower temperatures of solidification, and it is therefore possible that although this phase was not observed in AE160, it is present in areas other than that analysed.

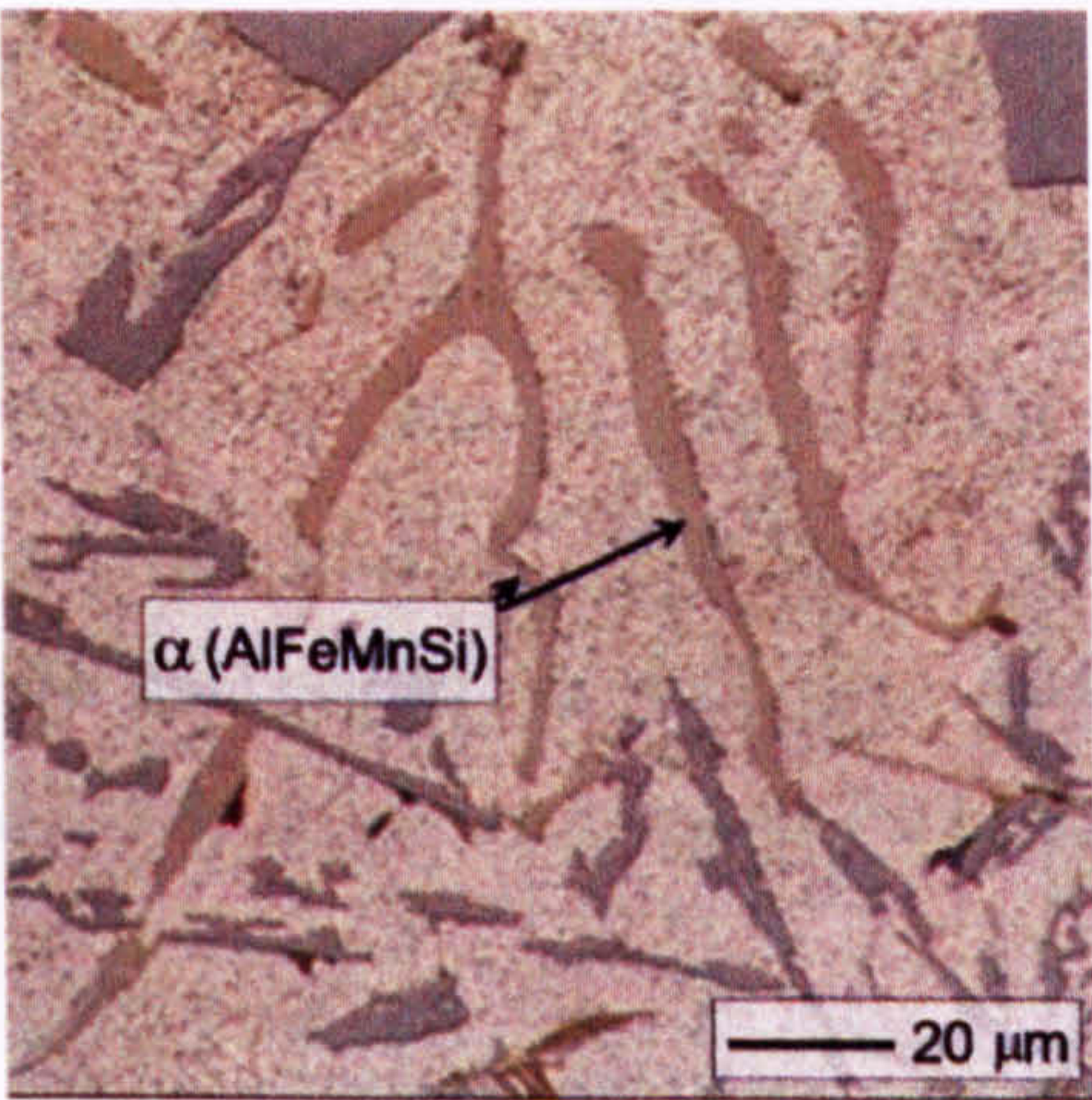


Figure 5.55 Optical micrograph of the α (AlFeMnSi) phase,
as seen in alloy AE413P [Day98]

Table 5.31 Composition of α (AlFeMnSi) phase

	Fraction of component in phase									
	Al	Cu	Fe	Mg	Mn	Ni	Si	Ti	V	Zr
Observed ^[Day98] (At. %)	70.9	0.81	11.4	-	4.05	0.96	11.3	-	-	-
Observed ^[Day98] (Wt. %)	59.3	1.59	19.7	-	6.90	1.75	9.8	-	-	-
Predicted at 500 K (Wt. %)	61.3	0.3	16.2	-	13.6	-	8.6	-	-	-

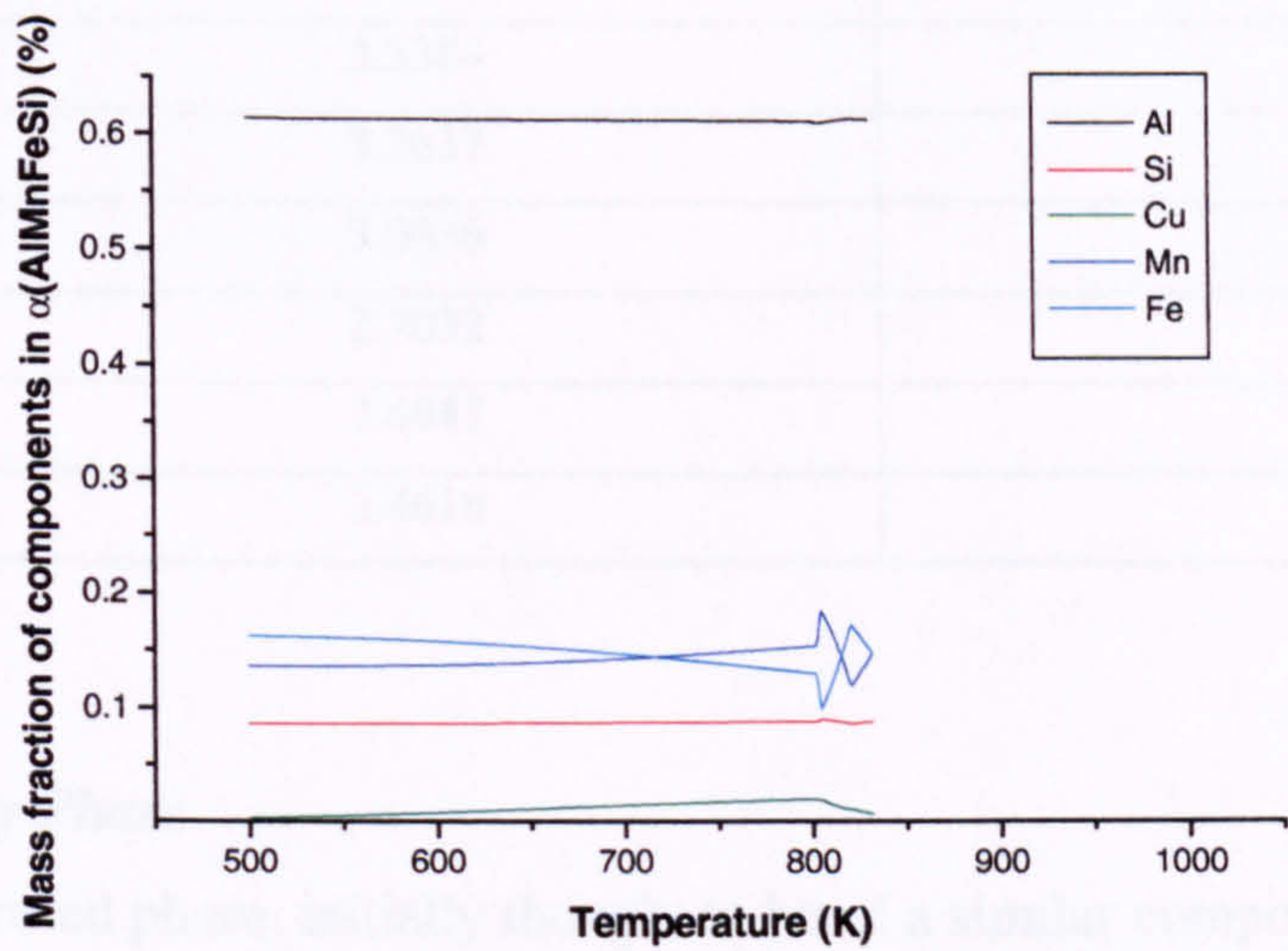


Figure 5.56 Mass fraction of components in the α (AlFeMnSi) phase as a function of temperature

Although extensive EBSD and EDX were carried out on AE160, no particles were identified as α (AlFeMnSi). However, the ICDD database does contain data for just one AlFeMnSi phase, card number 42-1206 ($\text{Al}_9\text{Fe}_{0.84}\text{Mn}_{2.16}\text{Si}$). This stoichiometry does not quite match that of the phases identified by SEM analysis as $\text{Al}_{6.5}\text{FeSiMn}_{0.4}$, however, being similar, the first 10 x-ray reflectors from the ICDD database are given in Table 5.32 for future reference.

Table 5.32 Crystallographic data for $\text{Al}_9\text{Fe}_{0.84}\text{Mn}_{2.16}\text{Si}$

Crystal System	Hexagonal
Space Group	$\text{P6}_3/\text{mmc}$
Lattice Parameter (Å)	$a=7.5198, c=7.7688$

hkl	ICDD (42-1206)	
	Interplanar spacing, d (Å)	Intensity
100	6.5243	47
101	4.9912	16
002	3.8854	23
110	3.7606	13
102	3.3384	14
200	3.2637	10
201	3.0036	17
112	2.7032	8
202	2.4947	8
210	2.4618	9

5.3.15 New Quinary Phase

A previously unreported phase, initially thought to be of a similar composition to $\text{Al}_3(\text{Cu},\text{Ni})_2$ due to its high Al, Cu, and Ni content, was found to contain unusually large amounts of Zr. Such quantities of Zr have been observed in the Al_3Ti phase reported in section 5.3.3, however, this new phase had neither the composition nor the morphology to be Al_3Ti . The new phase was found to have the same grey-brown colour as $\text{Al}_3(\text{Cu},\text{Ni})_2$, but tended to be slightly more plate-like in morphology and often adjoining $\text{Al}_3(\text{Cu},\text{Ni})_2$ as can be seen in Figure 5.57. The composition of the Zr phase, as determined by standard EDX, is shown in Table 5.33, where large quantities of Al and Ni are seen together with substantial amounts of Cu, Si and Zr, and a small amount of Fe. There is also some limited solubility of Mg, Mn and Ti at less than 1 %. One explanation for the large range, and substantial quantities of components in the new phase could be that there is pickup from the adjoining $\text{Al}_3(\text{Cu},\text{Ni})_2$, although this is not believed to be the case in this instance as several phases were analysed in isolation with the same composition. Thus, from the elemental analysis, the composition can be seen to be less like the aforementioned $\text{Al}_3(\text{Cu},\text{Ni})_2$, and more likely to be a previously unreported higher order phase. Calculation of the stoichiometry of the high Zr phase reveals a

phase of the order $\text{Al}_2\text{Ni}(\text{Cu},\text{Si},\text{Fe},\text{Zr})$. The new quinary phase was not predicted by the thermodynamic calculations.

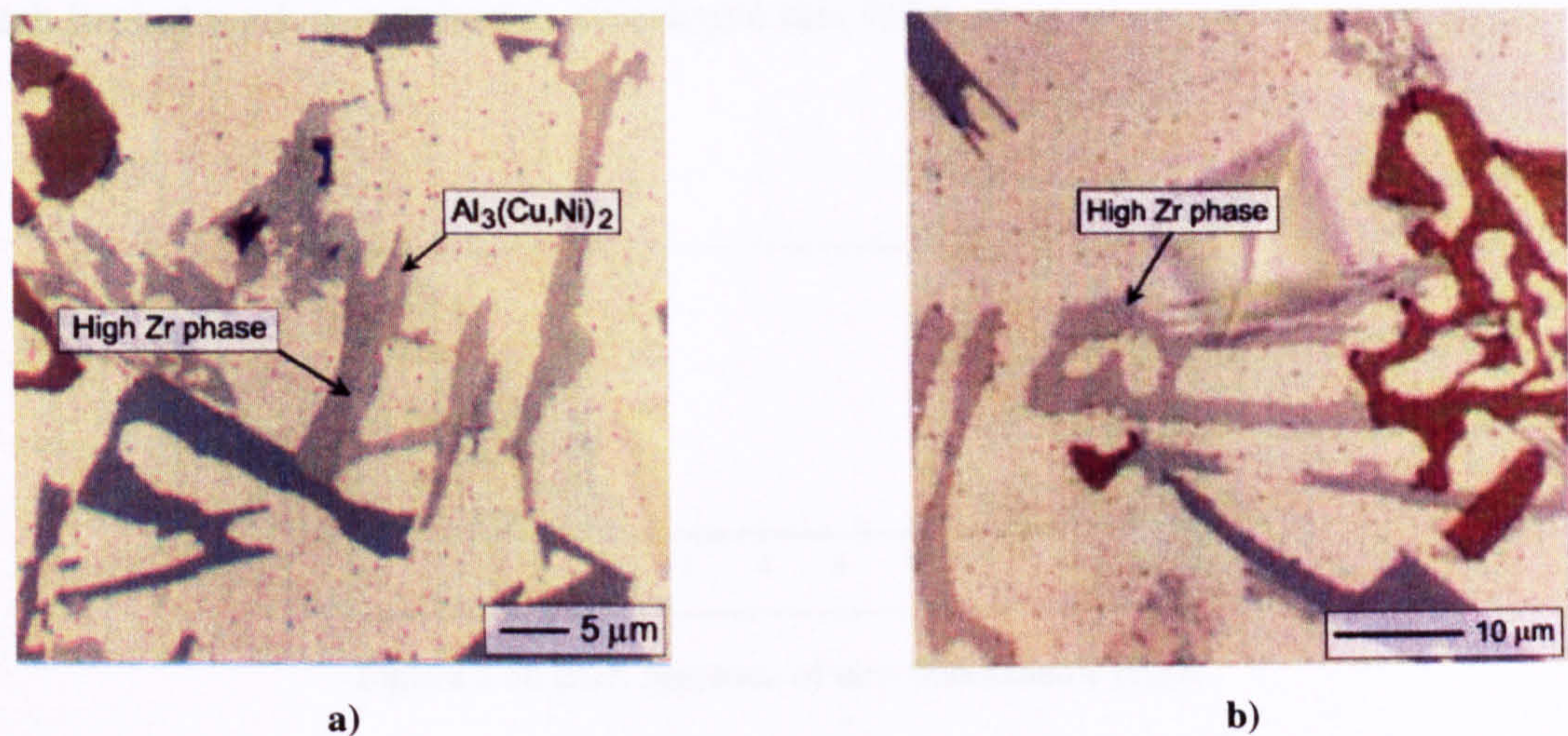


Figure 5.57 Optical micrographs of the new quinary, where **a)** it can be seen adjoining an $\text{Al}_3(\text{Cu},\text{Ni})_2$ particle, and **b)** the phase is independant

Table 5.33 Composition of new quinary phase

	% of component in phase									
	Al	Cu	Fe	Mg	Mn	Ni	Si	Ti	V	Zr
At. %	53.2	3.8	2.5	0.1	0.1	22.8	13.2	0.5	-	3.8
Wt. %	37.0	6.2	3.6	-	0.1	34.1	9.5	0.6	-	8.9

EBSD and EDX were carried out on the new intermetallic phase from which the EDX spectrum can be seen in Figure 5.58, and the diffraction patterns in Figure 5.59. The ICDD database does not contain any phases which match the composition of the new phase, and thus found no solution when automatically indexing. The whole pattern had to be indexed manually, using the computer software to identify Kikuchi bands by tracing the centrelines of the bands for automatic calculation of the Miller indices. 7 reflectors were indexed in this way and are given in Table 5.34. In the case of the 0001 and $10\bar{1}0$, higher order reflections, i.e. the 0002 and $30\bar{3}0$ respectively, were observed rather than the first.

This analysis resulted in the indication that the new phase was hexagonal, with lattice parameters $a = 4.14$, $c = 3.9 \text{ \AA}$. It is interesting to note that the ‘a’ parameter is similar to that of $\text{Al}_7\text{Cu}_4\text{Ni}$ (Table 5.23), with the ‘c’ parameter being a factor of 10 different. It is possible that this is a result of different stacking sequences due to the substitution of Si and Zr, although further work is required to investigate this fully.

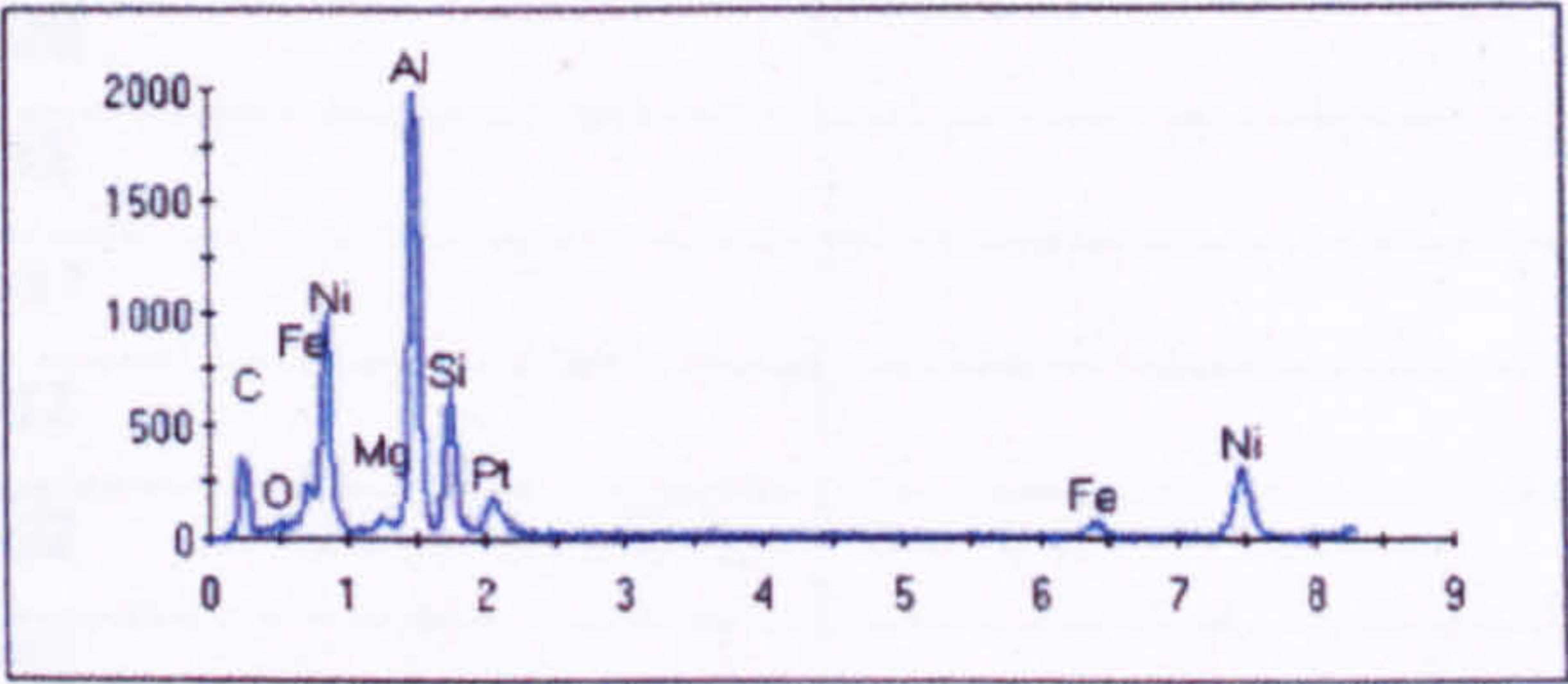
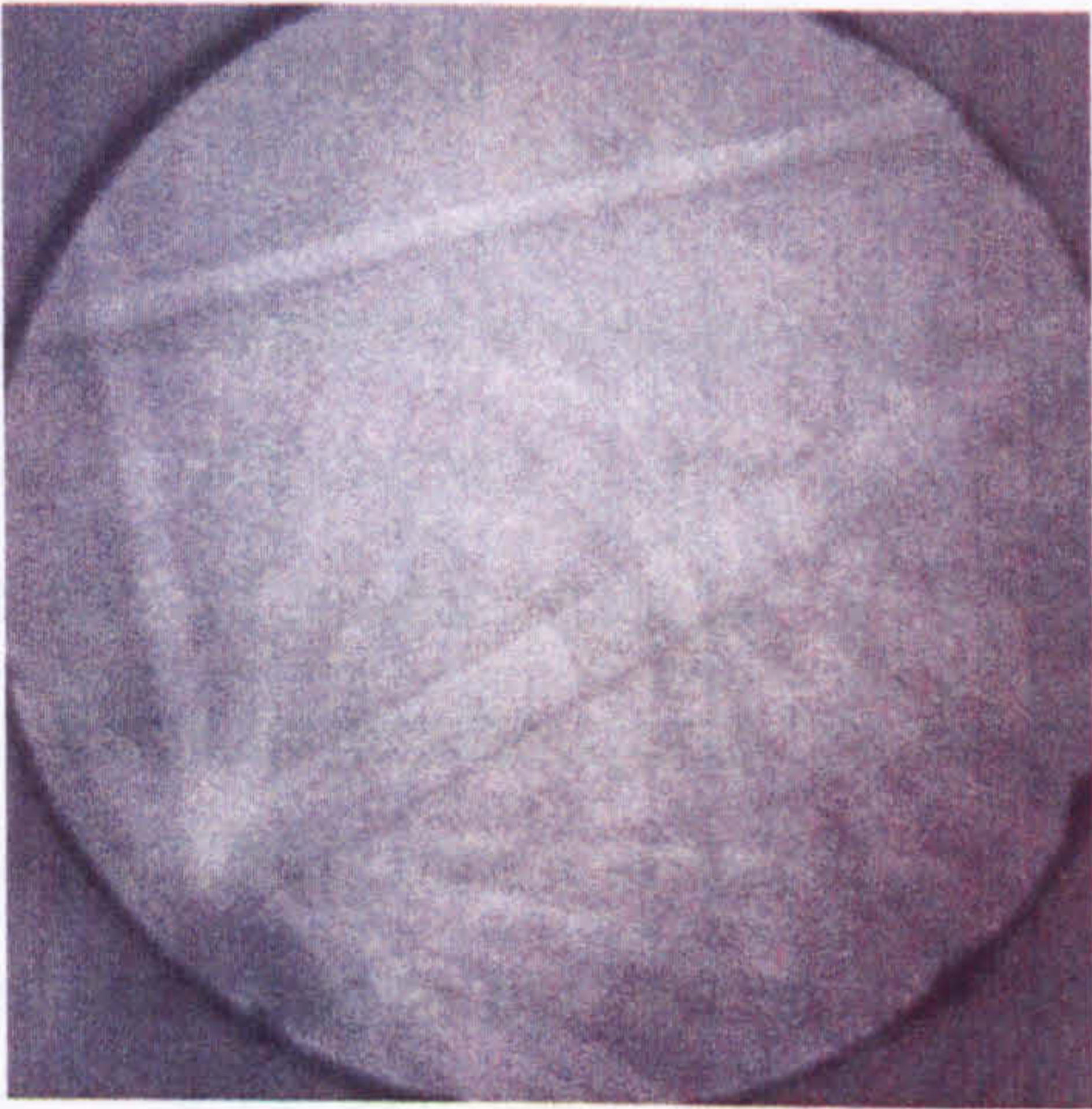
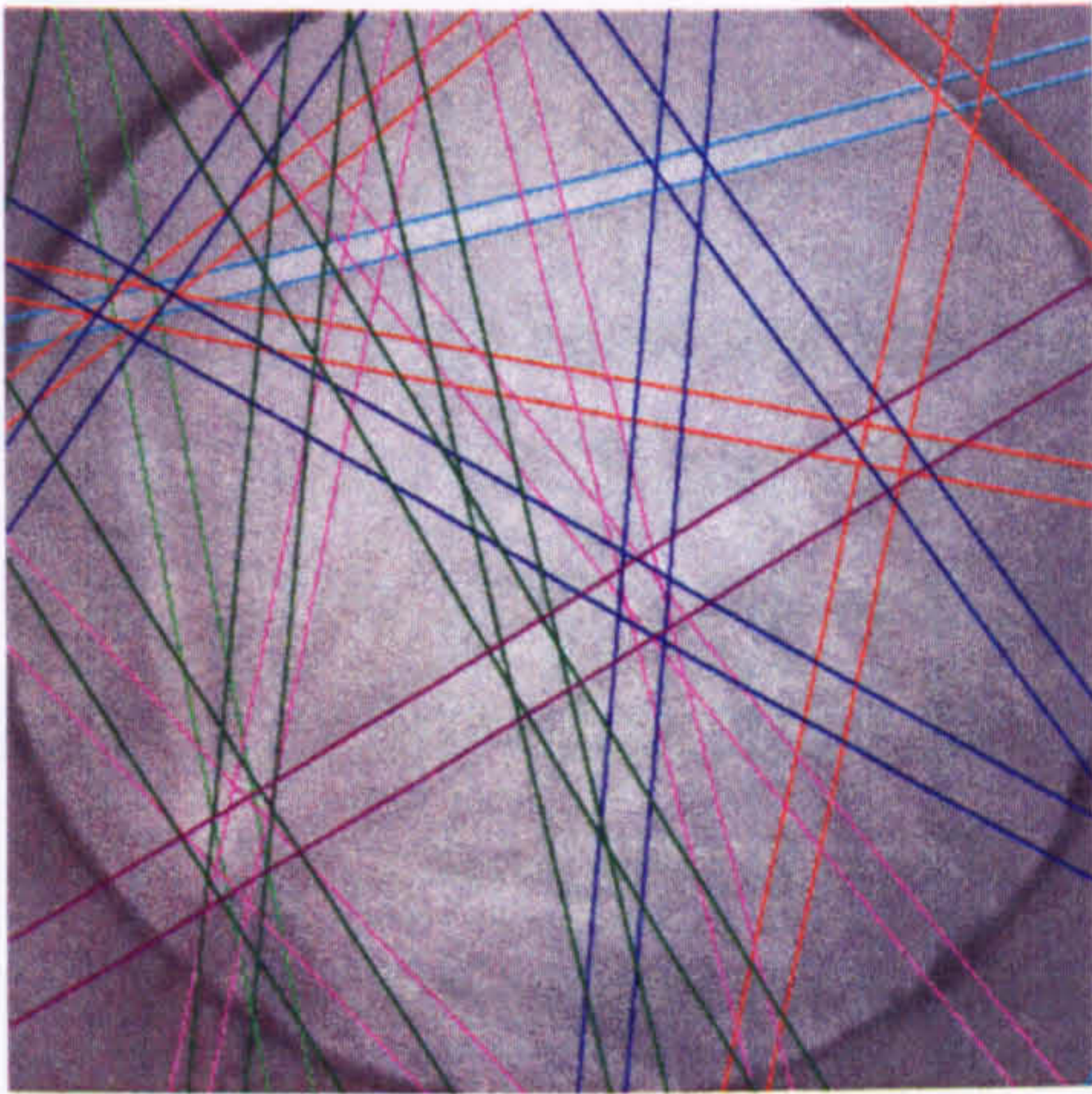


Figure 5.58 EDX spectrum of new intermetallic phase



a)



b)

Figure 5.59 a) Observed and b) indexed diffraction patterns from the new quinary phase

Table 5.34 Diffraction data for the new quinary phase

Crystal System	Hexagonal
Space Group	D6h 6/mm
Lattice Parameter (Å)	a=4.14, c=3.9

EBSD	
hkl	Interplanar spacing, d (Å)
11-20	2.070
0002	1.950
2-1-11	1.828
10-12	1.713
11-22	1.419
10-13	1.222
30-30	1.195

5.4 Phase Mapping

Having constructed a complete database of materials files during the phase analysis discussed earlier in this chapter, a scan was set up to collect simultaneous EBSD and EDX data of a large area of model alloy 24. An SEM image of the area of the scan can be seen in Figure 5.60, where large silicon cuboids and intermetallic phases are visible in the aluminium matrix. From the EBSD data an inverse pole figure (IPF) map was generated, with the points colour coded according to the unit triangle. Both the map and corresponding unit triangle are given in Figure 5.61. From the colouring of the matrix it appears that the scan covers four separate aluminium grains, and interestingly there appears to be some segregation of the smaller particles (silicon and intermetallics) between the dendritic grains and along the dendrite arms. Figure 5.62 is a phase map of the scanned area, generated by automatic indexing of the diffraction pattern from each pixel of the scan, using the user database containing the material files created and discussed in Section 5.3. The legend next to the map shows that 5 phases were identified, namely aluminium, silicon, AlCuNi, Al₉FeNi and Al₃Ti. The AlCuNi phase is so-called as the indexing was unable to differentiate between Al₃(Cu,Ni)₂ and Al₇Cu₄Ni, identifying all the intermetallics as Al₇Cu₄Ni. From the phase analysis it is known that both phases are present, justifying the use of the generic AlCuNi label.

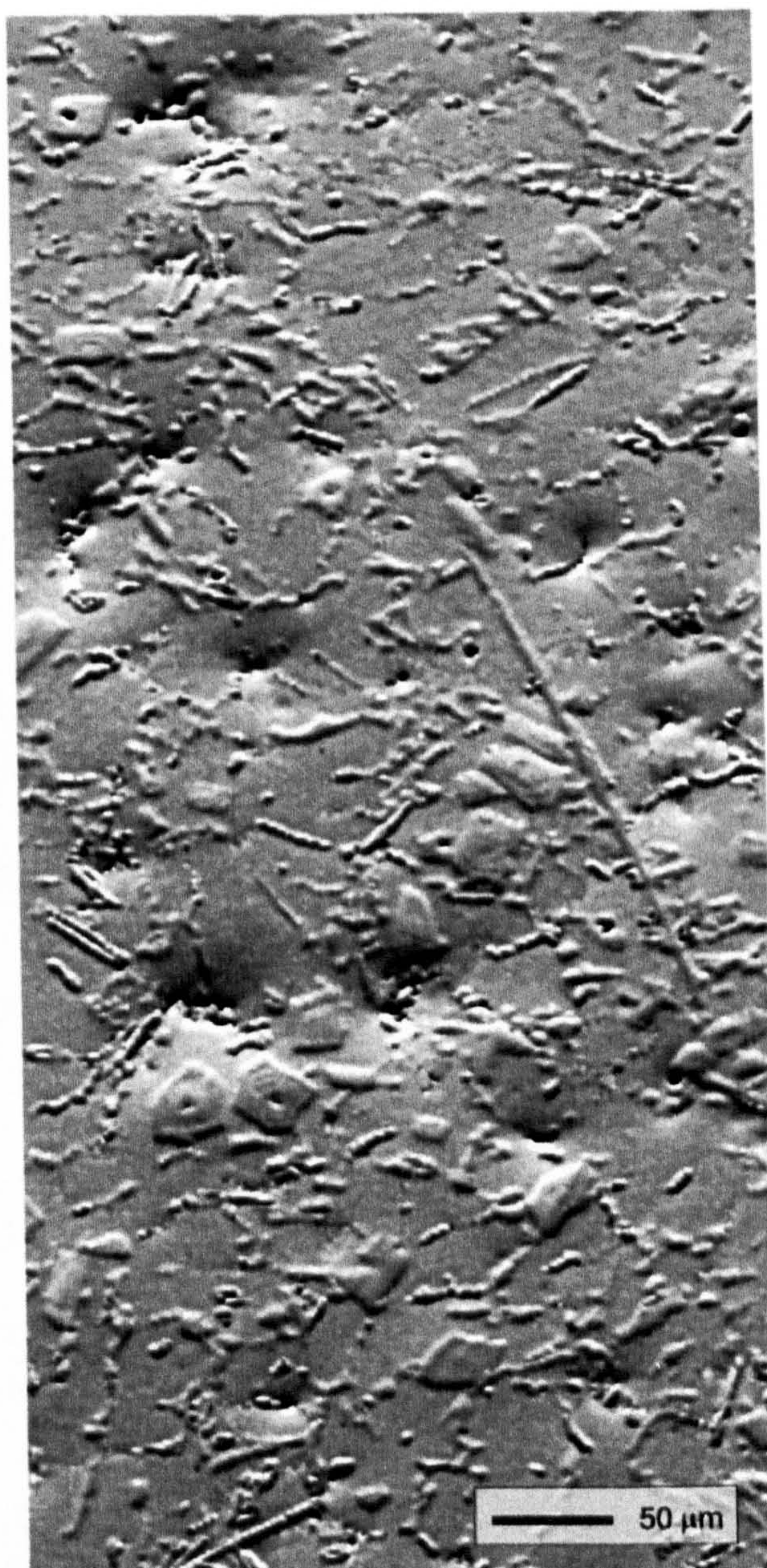


Figure 5.60 SEM image of scan area

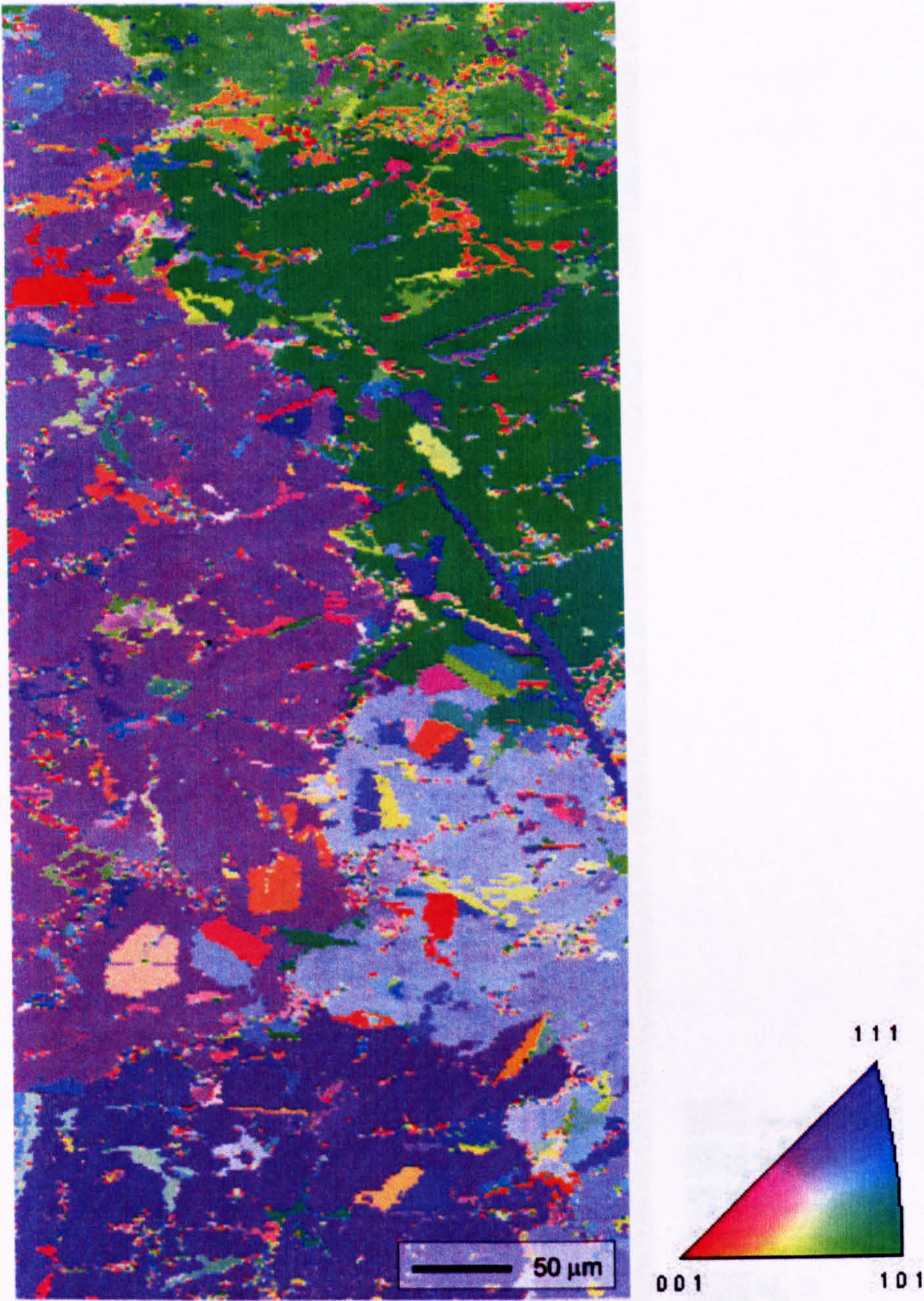


Figure 5.61 EBSD inverse pole figure map of scan area

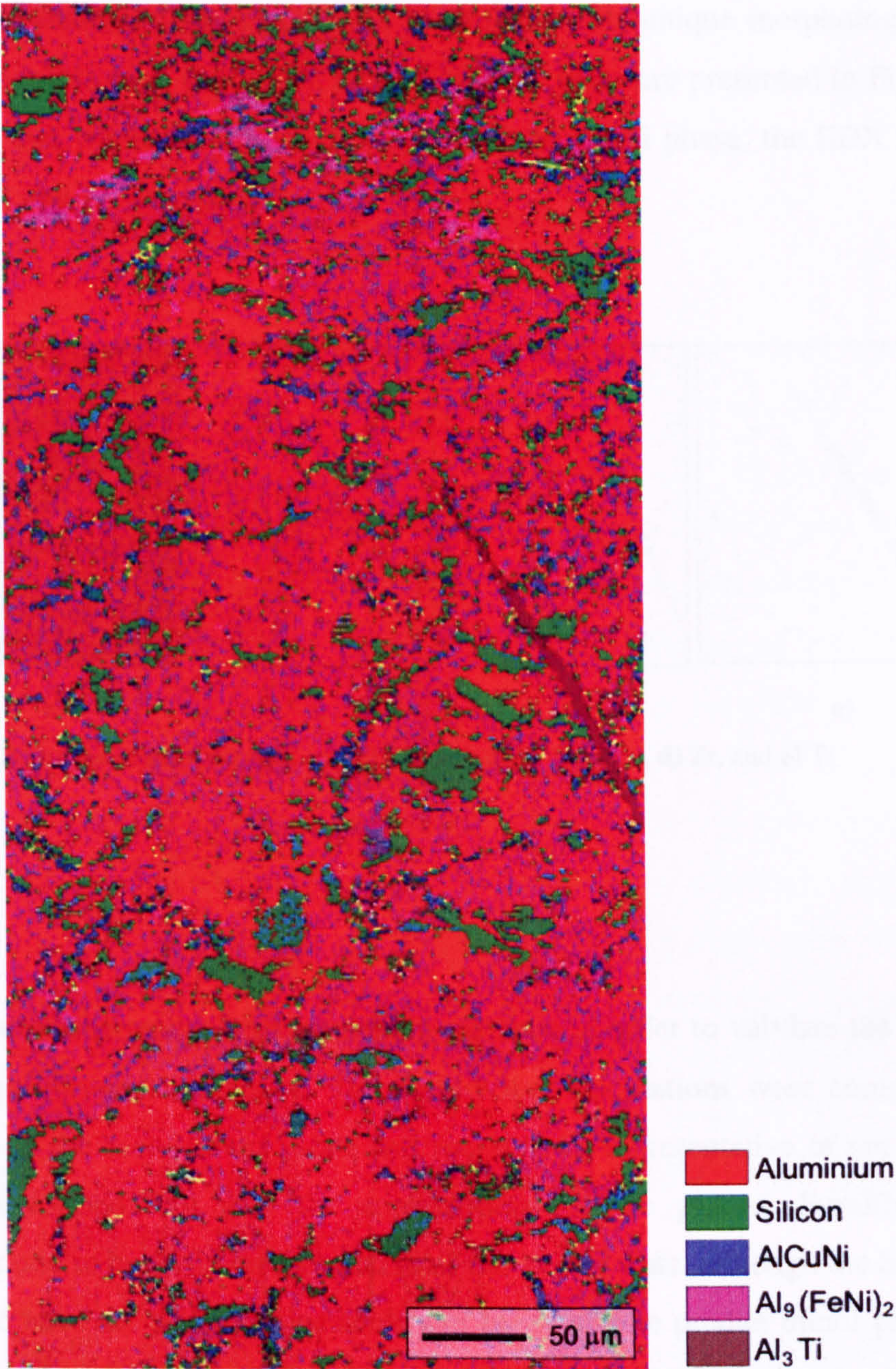


Figure 5.62 Phase map of the scan area

Also collected were EDX data for each pixel of the scan. These data can be presented as maps showing the concentration of elements over the whole scan. A small area of the scan was selected for illustration, containing the Al_3Ti phase identified by its unique morphology as seen in Figure 5.63 a). For this area, the Al, Si, Zr and Ti EDX maps are presented in Figure 5.63 b) to e). It is clear that where the EBSD had identified the Al_3Ti phase, the EDX map showed it to be rich in Ti and Zr, as expected.

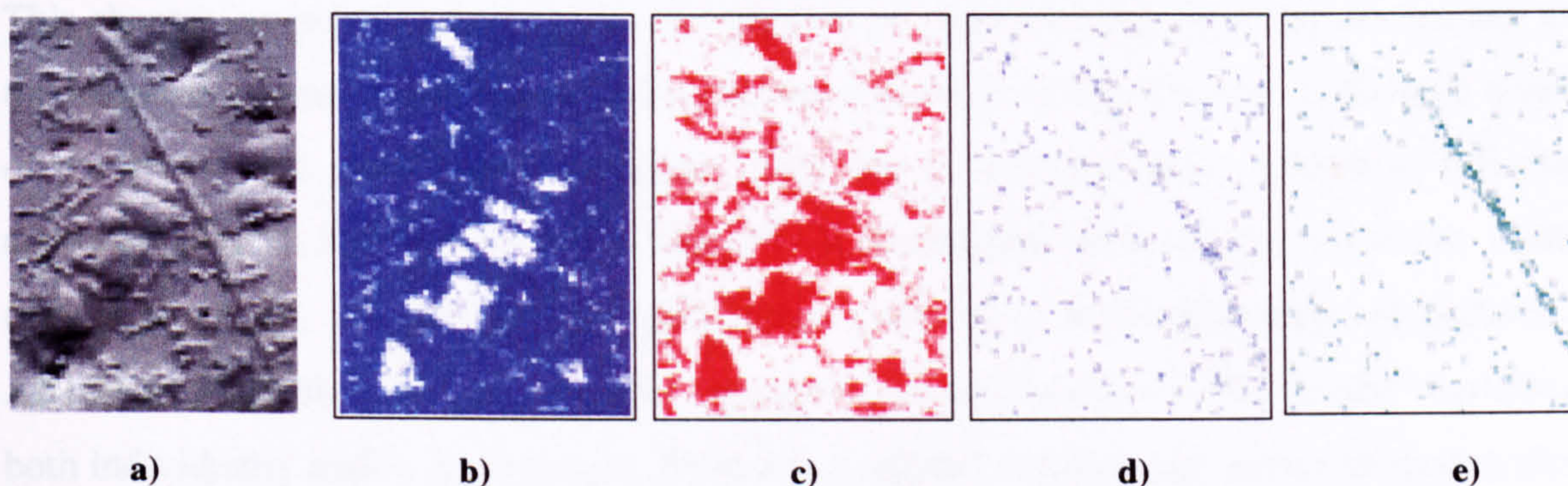


Figure 5.63 a) SEM image of the scan area, and EDX maps of b) Al, c) Si, d) Zr, and e) Ti

5.5 Summary

This chapter has scrutinised thermodynamic modelling methods in order to validate the both equilibrium and non-equilibrium simulations. The equilibrium calculations were compared with heat treated alloys in the ‘equilibrium’ state and found to be representative of not only the fraction of phases formed, but also the compositions of the phases. Equilibrium calculations were also found to be fairly representative of the as-cast state, although the Scheil simulation was found to have the additional capability of being able to predict minor phases characteristic of segregated regions of a casting. Thermodynamic calculations were then used, in conjunction with thorough analysis by optical and electron microscopy, to establish a detailed study of phases in commercial and model alloy systems. Information on phase morphology, composition, stability over temperature, and crystallographic data were collated to provide a comprehensive understanding of all the phases present in multicomponent Al-Si casting alloys. Finally, a scan was carried out over a large area of microstructure, and using both diffraction and chemical data, maps were generated illustrating crystal orientation and identifying individual phases. This now has the potential to be a very powerful analysis tool in the future.

Chapter 6

Grain Refinement

6.1 Introduction

This chapter investigates the commercial practice of grain refining, typically carried out with the intention of improving mechanical properties, as discussed in Chapter 3, through a series of theoretical and experimental analyses. First, the commercial alloy AE160 (a full phase analysis of which was presented in Chapter 5) is investigated with varying vanadium content (model alloys 24, 25 and 38). The predictive capability of thermodynamic calculations on AE160, as verified in Chapter 5, is then utilised to predict the effect of Ti, Zr and V additions, both individually and in combination. From the predicted results a new series of model alloys, denoted 83 to 90, were cast in stepped moulds to investigate the effect of Ti, Zr and V additions and cooling rate on the structure of the castings. The concept of quantifying the effect of a grain refiner is then explored using a growth restriction parameter. Keel bar castings from earlier work were also analysed with respect to the effect of the grain refining additions, and compared to calculations of the growth restriction parameters. Using the growth restriction parameter calculations, a set of simple ternary alloys (model alloys 3) were designed and cast, again in stepped moulds, to isolate the effect of Ti, Zr and V. These were then examined in detail using electron backscatter diffraction (EBSD) with particular reference to the columnar to equiaxed transition.

At this point it is important to note that there is a small, but significant, quantity of P in these alloys which combines with aluminium to form AlP, as discussed in Chapter 3, and is then efficient at nucleating silicon. This is not taken into account in the thermodynamic calculations in this chapter due to the lack of P data in the thermodynamic databases; a problem that is considered further in Chapter 7. The AlP will almost certainly be acting in competition with the grain refiners in nucleating their respective phases, however, a quantitative comparison of the effects of Ti, Z and V is still believed to be valid because similar amounts of P are present in all the alloys.

6.2 Commercial Alloy AE160 and Model Alloys 24, 25 and 38

The first investigation examined the commercial alloy AE160, and model alloys 24, 25 and 38 which have similar compositions to AE160 but with varying vanadium contents. A full phase analysis of these alloys was presented in Chapter 5. The V additions were made to the model alloys at levels close to that of AE160 to determine the effect of small increases in V content on the microstructure. The compositions of all four alloys can be found in Table 6.1, but in summary AE160 contains 0.06 wt. % V, and additions of 0.05, 0.065 and 0.12 wt. % V were made resulting in alloys 24, 25 and 38 respectively. There is also a constant amount of Ti and Zr in these alloys. AE160 was cast on the production line at Federal-Mogul, Bradford as a small piston, and model alloys 24, 25 and 38 were also cast as small pistons under production line conditions at Federal-Mogul, Cawston.

Table 6.1 Compositions of commercial alloy AE160 and model alloys 24, 25 and 38

	Wt. % Element									ppm
Alloy	Si	Mg	Cu	Ni	Mn	Fe	Ti	Zr	V	P
AE160	11.2	1.05	3.1	2.27	0.08	0.3	0.17	0.15	0.06	53
24	11.6	0.99	3.50	2.40	-	0.31	0.18	0.11	0.05	80
25	11.6	0.99	3.80	2.73	-	0.31	0.16	0.12	0.065	59
38	11.94	0.76	3.49	2.28	-	0.28	0.13	0.12	0.12	66

Balance is Al, all other elements unspecified

6.2.1 Microstructural Characterisation

Figures 6.1 a) to d) are optical pictures taken of the microstructures of the alloys after etching (0.5 % HF in water). All four alloys can be seen to have very similar microstructures: the dendritic growth of the aluminium matrix is clear, with primary and secondary silicon and intermetallics segregated to the dendrite tips and between the arms. Alloy 38 (Figure 6.1 d), with the highest V content, appears to have a slightly finer and less dendritic microstructure than the other alloys, with secondary particles appearing more uniformly distributed. Of particular interest in alloy 25 (Figure 6.1 c), is the Al₃Ti phase that is recognisable from its distinct morphology of very large ‘needles’, as previously discussed in Section 5.3.3, an example of which is given in Figure 6.2. Although present in the other alloys, this phase appears much coarser in alloy 25.

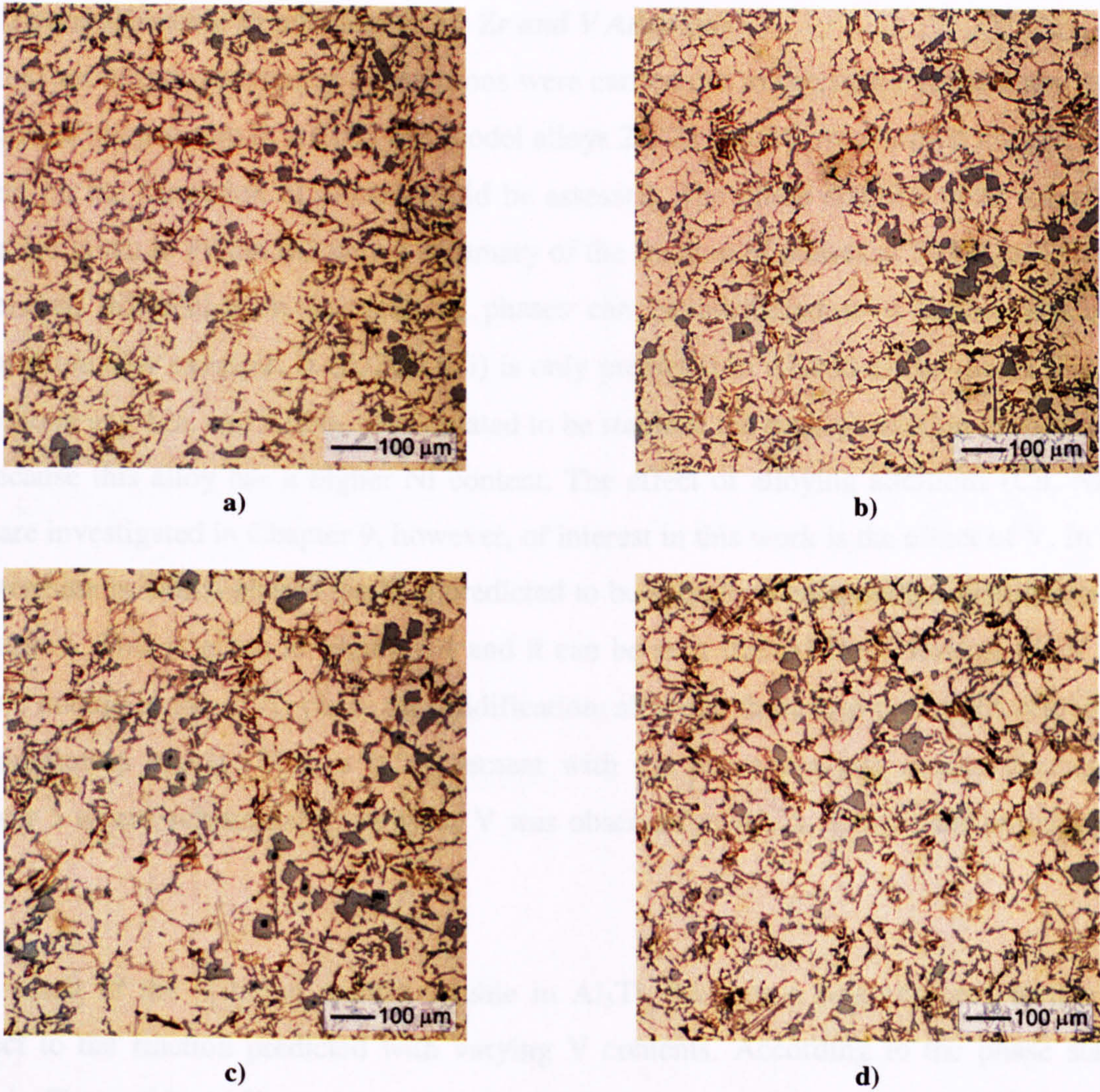


Figure 6.1 Optical micrographs of **a)** commercial alloy AE160, **b)** model alloy 24, **c)** model alloy 25, and **d)** model alloy 38

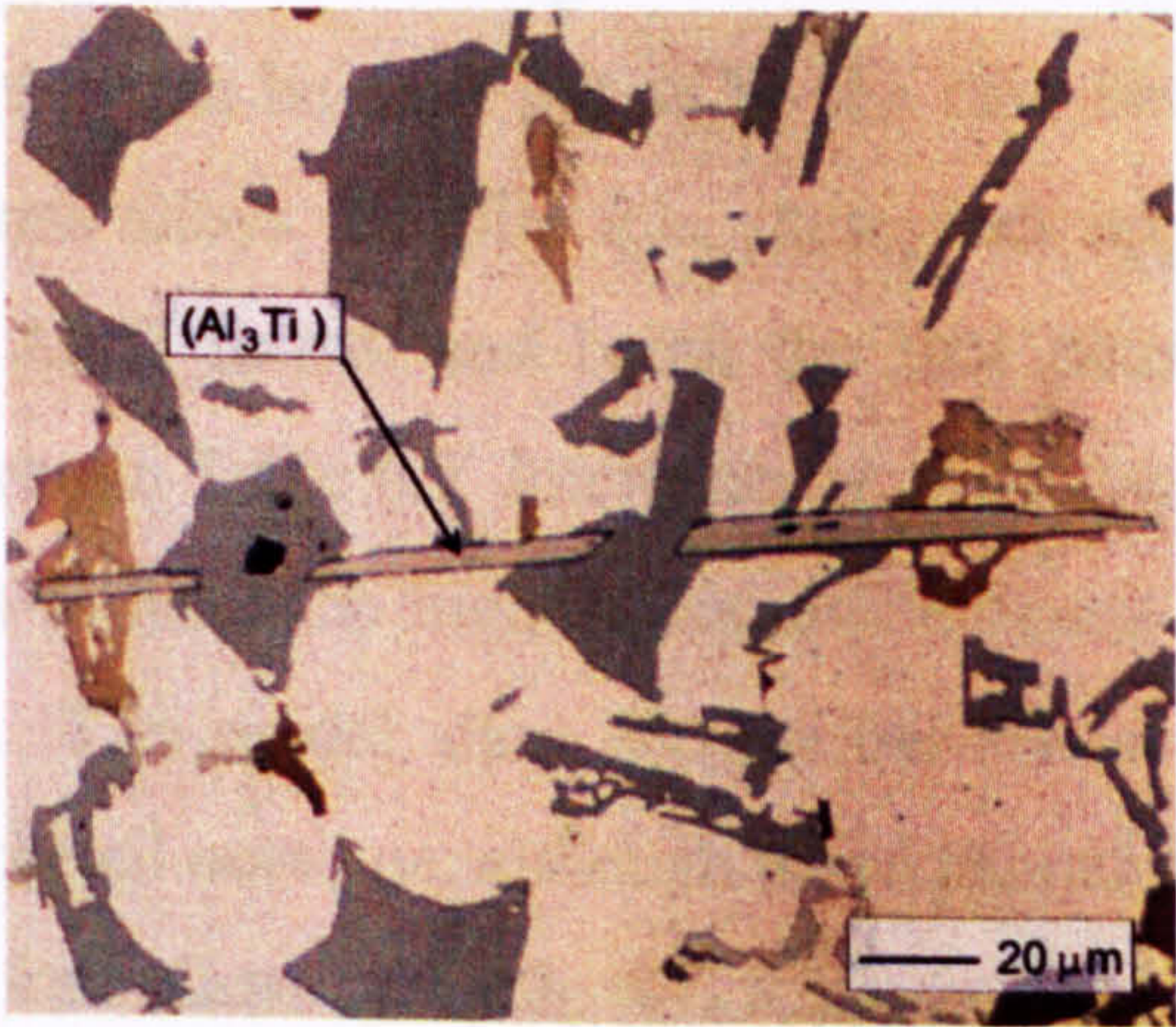


Figure 6.2 Optical micrograph of an Al₃Ti particle in model alloy 25

6.2.2 Thermodynamic Predictions of Ti, Zr and V Additions

The first set of thermodynamic calculations were carried out to determine phase stability as a function of temperature in AE160 and model alloys 24, 25 and 38, from which the effect of V content on the formation of phases could be assessed. The phase stability plots for all four alloys are given in Figure 6.3 with a summary of the fraction of phases at 500 K in Table 6.2. In general, differences in fractions of phases can be attributed to a slight variation in composition. For example, α (AlFeMnSi) is only predicted in AE160 as the model alloys do not contain any Mn, and Al_3Ni_2 is calculated to be stable at the highest fraction in model alloy 25 because this alloy has a higher Ni content. The effect of alloying additions (Cu, Ni, Mg etc.) are investigated in Chapter 9, however, of interest in this work is the effect of V. In order to determine in which phases the V is predicted to be soluble, a composition distribution plot was drawn. This is given in Figure 6.4 and it can be seen that Al-Data³ models the V to be soluble mainly in the Al_3Ti phase on solidification, although there also is a slight solubility in the aluminium matrix. This is in agreement with the phase analysis results discussed in Chapter 5 where substantial quantity of V was observed in Al_3Ti , and a trace amount in the matrix.

As a result of the V being mainly soluble in Al_3Ti , this phase was explored further with respect to the fraction predicted with varying V contents. According to the phase stability plots in Figure 6.3, Al_3Ti can be seen to be the first phase to form during solidification, at a temperature much higher than the next phase to solidify, in this case the aluminium. It was discussed in Chapter 3 that Al_3Ti is added to the melt as a master alloy, and remains stable at reasonably high temperatures to act as a nucleant for aluminium. As V is mainly soluble in Al_3Ti it might be expected that with increasing V content, the fraction of Al_3Ti also increases. However, from Table 6.2 this can be seen not to be the case because the fraction of Al_3Ti remains at 0.9 % for all four alloys. Despite this, there does appear to be an effect on the temperature at which the Al_3Ti forms, and being the first phase to form this is also the liquidus temperature, as given in Table 6.2. Interestingly, the lowest addition of V, 0.05 wt. % in model alloy 24, appears to have the highest liquidus temperature, and the alloy with the highest additions, 0.12 wt. % in model alloy 38, has the lowest liquidus temperature. This effect is opposite to the expected outcome, although the explanation is a simple one. Referring to the compositions of the four alloys in Table 6.1, it can be seen that model alloy 24 has the highest amount of Ti additions (0.18 wt. %), and model alloy 38 the lowest (0.13 wt. %).

Thus, it can be concluded that Ti has a much more profound effect on the stability of the Al₃Ti phase than V does.

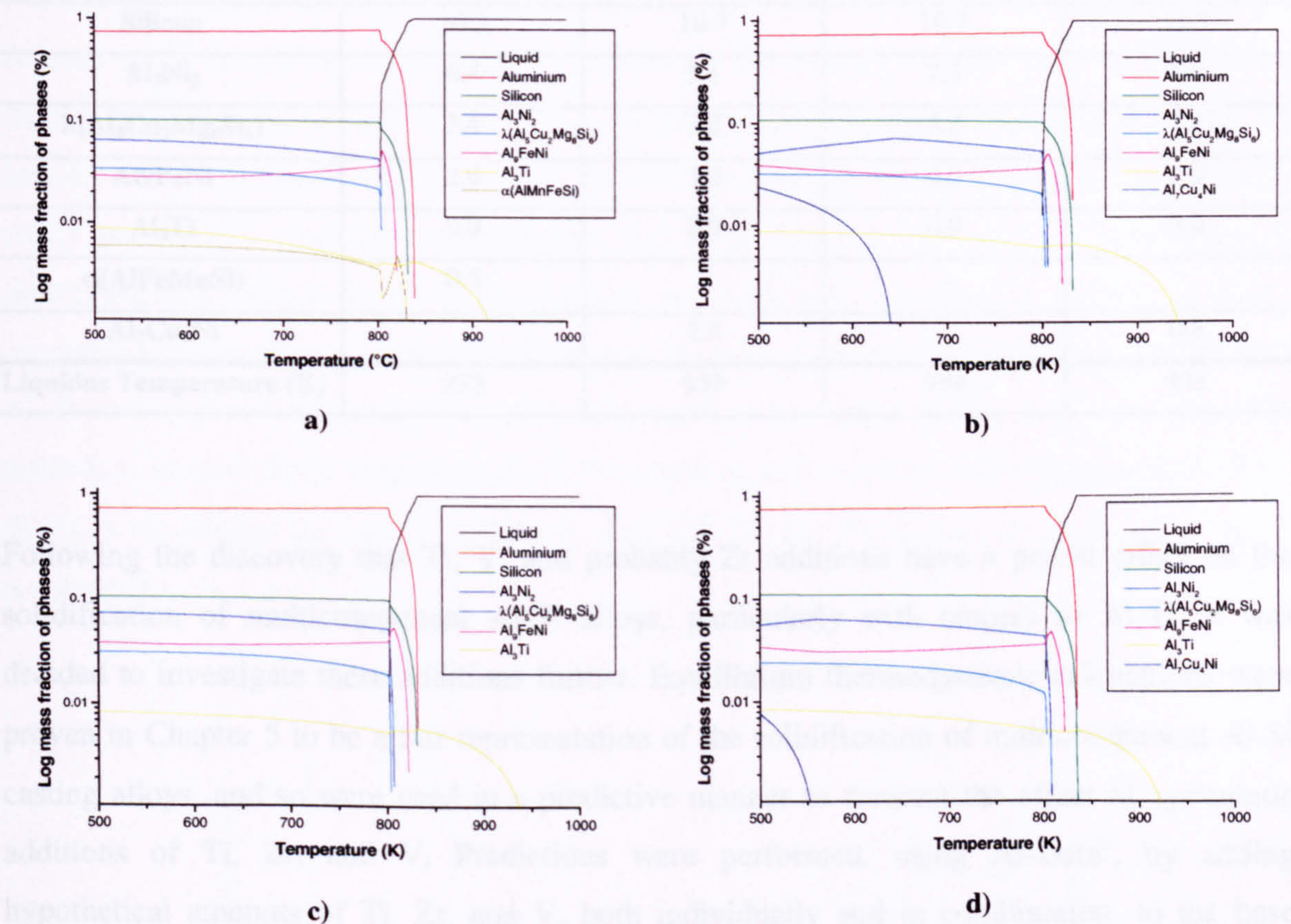


Figure 6.3 Phase stability plots of **a)** commercial alloy AE160, **b)** model alloy 24, **c)** model alloy 25, and **d)** model alloy 38

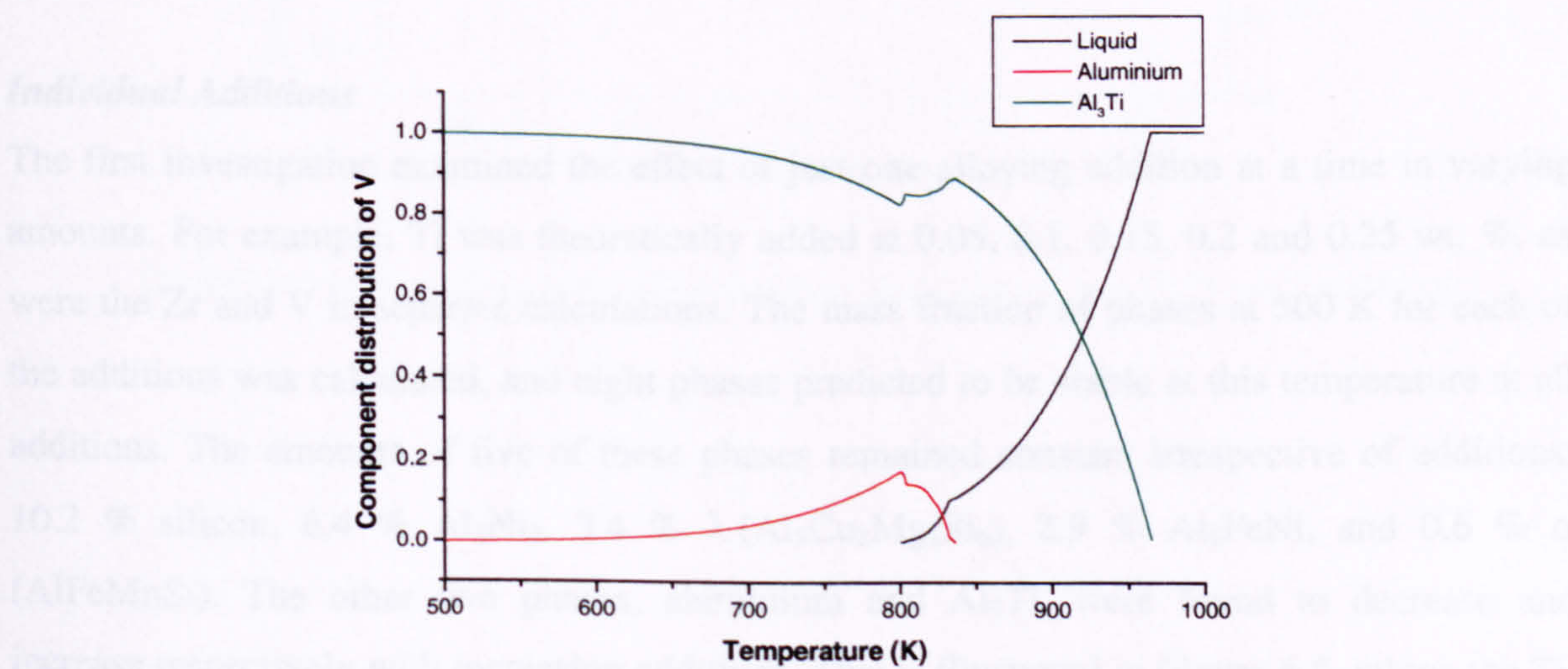


Figure 6.4 Distribution of V as a function of temperature

Table 6.2 Fraction of phases predicted in AE160 and model alloys 24, 25, and 38 at 500 K

Phase	% fraction of phase			
	AE160	24	25	38
Aluminium	75.6	73.9	73.8	75.5
Silicon	10.2	10.7	10.7	11.2
Al ₃ Ni ₂	6.4	5.1	7.5	5.7
λ(Al ₅ Cu ₂ Mg ₈ Si ₆)	3.4	3.2	3.2	2.4
Al ₉ FeNi	2.9	3.9	4.0	3.5
Al ₃ Ti	0.9	0.9	0.9	0.9
α(AlFeMnSi)	0.6	-	-	-
Al ₇ Cu ₄ Ni	-	2.4	-	0.8
Liquidus Temperature (K)	933	953	949	933

Following the discovery that Ti, V, and probably Zr additions have a potent effect on the solidification of multicomponent Al-Si alloys, particularly with respect to Al₃Ti, it was decided to investigate these additions further. Equilibrium thermodynamic calculations were proven in Chapter 5 to be a fair representation of the solidification of multicomponent Al-Si casting alloys, and so were used in a predictive manner to forecast the effect of systematic additions of Ti, Zr, and V. Predictions were performed, using Al-Data³, by adding hypothetical amounts of Ti, Zr, and V, both individually and in combination, to the base composition of AE160 (without Ti, Zr or V). These additions, known for their grain refining abilities (Chapter 3), should not only have an effect on the phases formed, but also on the solidification temperatures of the alloy.

Individual Additions

The first investigation examined the effect of just one alloying addition at a time in varying amounts. For example, Ti was theoretically added at 0.05, 0.1, 0.15, 0.2 and 0.25 wt. %, as were the Zr and V in separate calculations. The mass fraction of phases at 500 K for each of the additions was calculated, and eight phases predicted to be stable at this temperature at all additions. The amounts of five of these phases remained constant irrespective of additions; 10.2 % silicon, 6.4 % Al₃Ni₂, 3.4 % λ (Al₅Cu₂Mg₈Si₆), 2.9 % Al₉FeNi, and 0.6 % α (AlFeMnSi). The other two phases, aluminium and Al₃Ti, were found to decrease and increase respectively with increasing additions. This is illustrated in Figure 6.5, where the Ti,

Zr and V additions can be seen to stabilise the Al_3Ti phase at the expense of the aluminium (the single Al curve represents all three additions).

The compositions of these two phases are given in Table 6.3, from which it can understood that the Al_3Ti should more correctly be referred to as $\text{Al}_3(\text{Ti,Zr,V})$. The relevant section for the binary diagrams for each of the Al-Ti, Al-Zr, and Al-V systems are given in Figure 6.6 and show that individual additions of Ti, Zr, and V should, in theory, form the phases Al_3Ti , Al_3Zr and Al_{10}V , respectively. However, this is clearly not the case in predictions of multicomponent alloys as all three elements are modelled as primarily soluble in Al_3Ti , despite the binary phases being included in the database. Also of interest is the prediction that Al_3Ti forms at concentrations less than that required according to the phase diagram. The minimum Ti content for formation of Al_3Ti according to the binary phase diagram is 0.15 wt. % Ti, with similar Zr and V additions required for the formation of Al_3Zr and Al_{10}V , respectively.

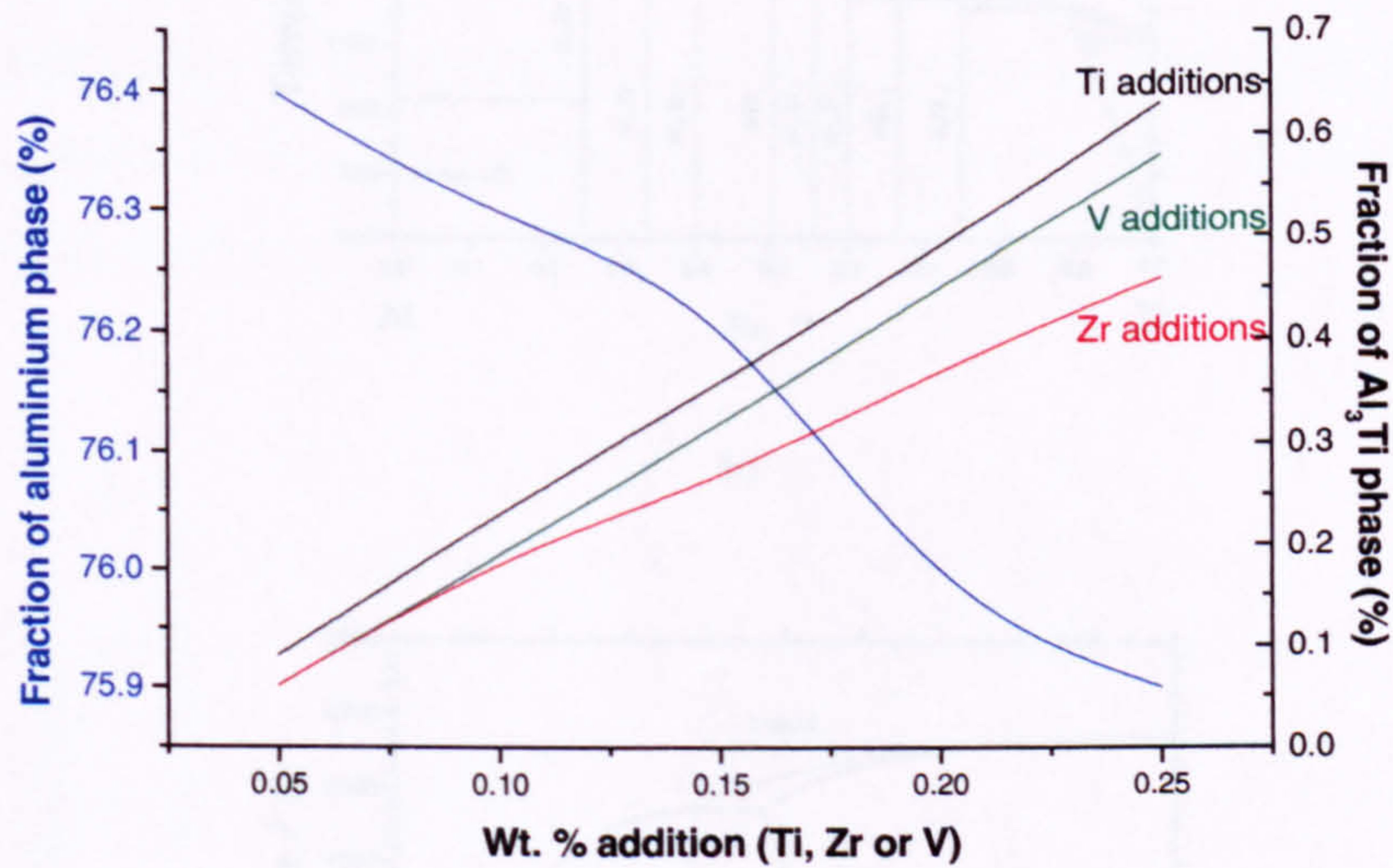


Figure 6.5 Fraction of aluminium and Al_3Ti phases predicted at various Ti, Zr and V additions

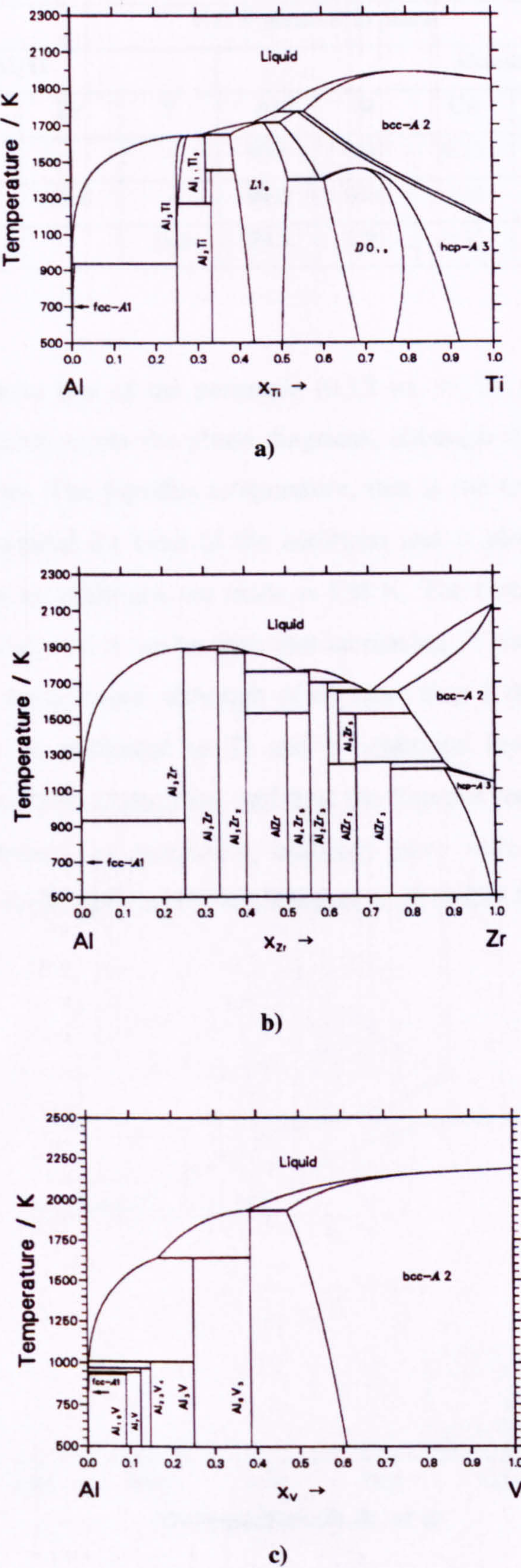


Figure 6.6 Binary phase diagrams for the a) Al-Ti, b) Al-Zr, and c) Al-V systems, after COST 507 [COS94]

Table 6.3 Composition of phases in which Ti, Zr and V are soluble

	Wt. % element in phase									
	Al ₃ Ti				Aluminium					
Additions	Al	Ti	Zr	V	Al	Si	Cu	Ti	Zr	V
Ti	62.8	37.2	-	-	99.8	0.01	0.11	0.02	-	-
Zr	47.0	-	53.0	-	99.6	0.01	0.11	-	0.01	-
V	61.4	-	-	38.6	99.8	0.01	0.11	-	-	0.03

Moreover, at additions above that of the peritectic (0.15 wt. % Ti) the Al₃Ti phase should solidify before the aluminium as per the phase diagrams, although this appears not to be so according to the predictions. The liquidus temperature, that is the temperature at which the first solid forms, was measured for each of the additions and is plotted in Figure 6.7. The liquidus temperature when no additions are made is 838 K. The first phase to solidify at all additions was the aluminium, and it can be seen that increasing Ti and V additions produce a slight rise in the liquidus temperature, although of no more than 2 degrees. This increase in liquidus temperature can be attributed to Ti and V additions lowering the supercooling required for solidification of the aluminium, and thus the liquidus temperature. The effect of the Zr is less clear, however, as increasing additions have little effect on the liquidus temperature, which remains the same as for no additions at all at 838 K.

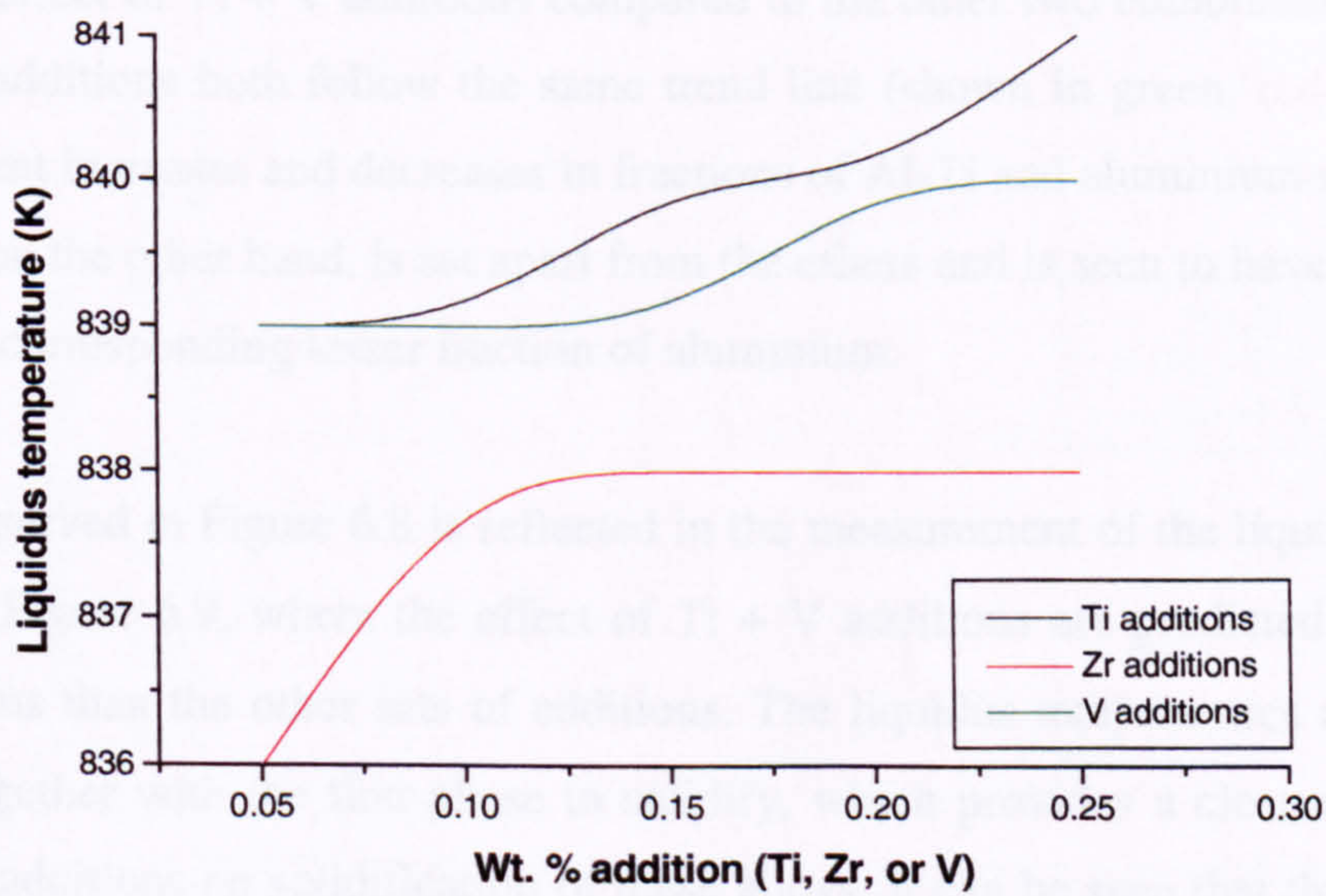


Figure 6.7 Liquidus temperature as a function of Ti, Zr, or V additions

Combinations of Additions

The second part of the investigation considered the predicted effect on AE160 of systematic additions of the grain refiners in combination with each other. Calculations were carried out for Ti + Zr, Ti + V and V + Zr additions with each of the elements being added at 0.1, 0.2, and 0.3 wt. %. This resulted in 27 combinations of which the most extreme examples, i.e. 0.1 A + 0.1 B, 0.1 A + 0.3 B, 0.3 A + 0.1 B, and 0.3 A + 0.3 B (where A and B represent the additions, all in wt. %), were selected for comparison. As for the individual additions eight phases were predicted to be stable at 500 K at all additions. The fractions of five of these phase remained constant irrespective of additions; 10.2 % silicon, 6.4 % Al_3Ni_2 , 3.4 % $\lambda(\text{Al}_5\text{Cu}_2\text{Mg}_8\text{Si}_6)$, 2.9 % Al_9FeNi , and 0.6 % $\alpha(\text{AlFeMnSi})$. However, with increasing additions the Al_3Ti and aluminium were found to increase and decrease respectively, as illustrated in Figure 6.8. where the Ti, Zr and V additions can be seen to stabilise the Al_3Ti phase at the expense of the aluminium.

All four sets of additions can be seen to behave in approximately the same way for the three elemental combinations. For example, if the alloying additions are taken as A and B then, as expected, the largest difference in the fraction of phases predicted is between 0.1 A + 0.1 B and 0.3 A + 0.3 B (wt. %), as phases Al_3Ti and aluminium increase and decrease respectively when the additions are made. There is little difference in the effect of 0.1 A + 0.3 B and 0.3 A, 0.1 B (wt. %) for any of the combinations of additions. However, there is a clear difference between the effect of Ti + V additions compared to the other two combinations. The Ti + Zr and V + Zr additions both follow the same trend line (shown in green, red line not shown) with equivalent increases and decreases in fractions of Al_3Ti and aluminium respectively. The Ti + V line, on the other hand, is set apart from the others and is seen to have a larger fraction of Al_3Ti and corresponding lesser fraction of aluminium.

The trend observed in Figure 6.8 is reflected in the measurement of the liquidus temperature, as shown in Figure 6.9, where the effect of Ti + V additions are predicted to have a much higher liquidus than the other sets of additions. The liquidus temperatures are also given in Table 6.4 together with the first phase to solidify, which provides a clearer insight into the effect of the additions on solidification of these alloys. It can be seen that the higher liquidus temperatures correspond to Al_3Ti being the first phase to form during solidification. For the Ti + V combination, the additions are predicted to form a large fraction of Al_3Ti which is stable at high temperatures. Although the Al_3Ti phase is also predicted for certain levels of Ti

+ Zr and V + Zr additions, the temperature at which the phase solidifies is much lower than the Ti + V. This indicates that either V has a stabilising effect on the Ti and solidification of Al_3Ti , or more likely, that the Zr is predicted to have a detrimental effect on the Ti and V additions, thus inhibiting the formation of Al_3Ti . This is particularly important when studying the grain refining ability of Ti, Zr, and V, as in practice, the formation of Al_3Ti would undoubtedly act as a nucleant for the aluminium. In the calculations the Al phase is always predicted to form at around 839 K.

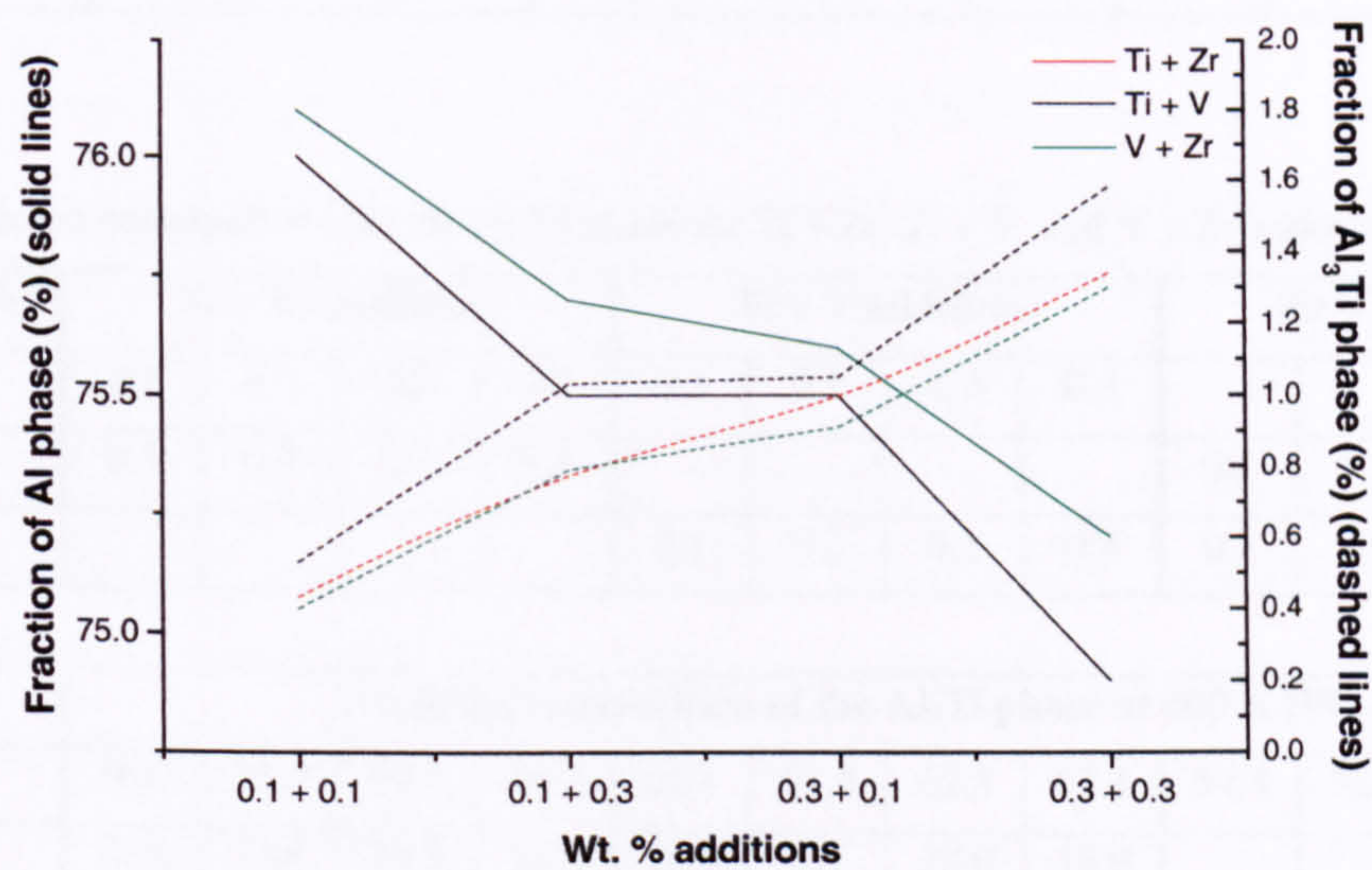


Figure 6.8 Fraction of aluminium and Al_3Ti phases predicted for Ti + Zr, Ti + V, and V+ Zr additions

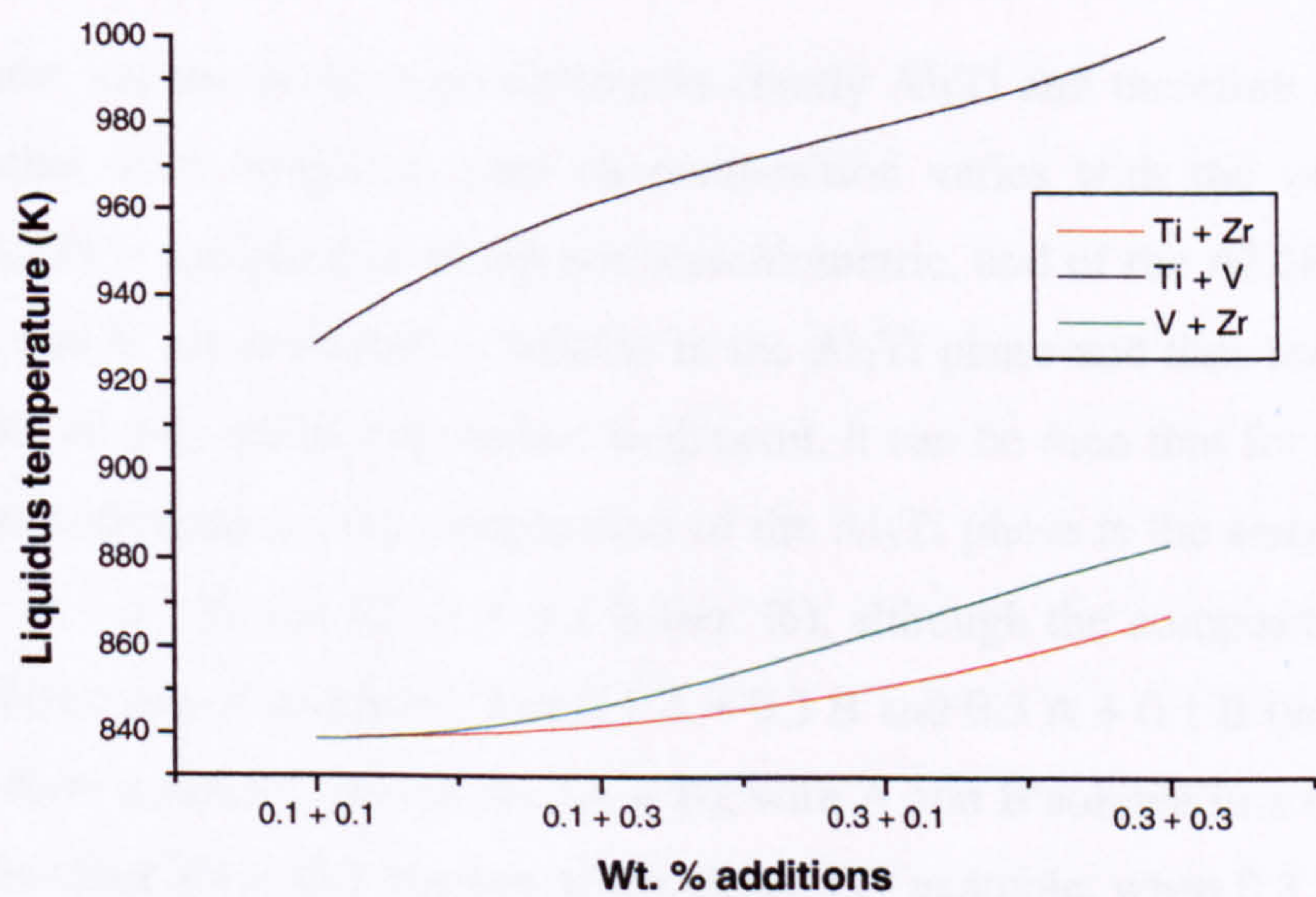


Figure 6.9 Liquidus temperature as a function of Ti + Zr, Ti + V, and V + Zr additions

Table 6.4 Predicted liquidus temperatures for Ti + Zr, Ti + V, and V + Zr addition combinations

	Ti + Zr additions (wt. %)				Ti + V additions (wt. %)				V + Zr additions (wt. %)			
Ti	0.1	0.1	0.3	0.3	0.1	0.1	0.3	0.3	-	-	-	-
Zr	0.1	0.3	0.1	0.3	-	-	-	-	0.1	0.3	0.1	0.3
V	-	-	-	-	0.1	0.3	0.1	0.3	0.1	0.1	0.3	0.3

Liquidus temp. (K)	839	839	847	867	929	975	972	>1000	839	839	866	883
First phase to solidify	Al	Al	Al ₃ Ti	Al ₃ Ti	Al ₃ Ti	Al ₃ Ti	Al ₃ Ti	Al ₃ Ti	Al	Al	Al ₃ Ti	Al ₃ Ti

Table 6.5 Predicted compositions for the Al₃Ti phase for Ti + Zr, Ti + V, and V + Zr addition combinations

Additions (Wt. %)	Ti + Zr additions				Ti + V additions				Zr + V additions			
Ti	0.1	0.1	0.3	0.3	0.1	0.1	0.3	0.3				
Zr	0.1	0.3	0.1	0.3					0.1	0.3	0.1	0.3
V					0.1	0.3	0.1	0.3	0.1	0.1	0.3	0.3

Element	Predicted composition of the Al ₃ Ti phase at 500 K (Wt. %)											
Al	56.0	51.9	59.7	56.2	62.1	61.8	62.5	62.1	54.8	51.3	58.4	55.2
Ti	21.1	11.6	29.9	21.6	18.9	9.7	28.0	18.9	-	-	-	-
Zr	23.0	36.5	10.4	22.2	-	-	-	-	24.3	37.3	10.7	23.0
V	-	-	-	-	18.9	28.5	9.5	18.9	20.9	11.4	30.4	21.9

The phase of most interest in these predictions is clearly Al₃Ti and therefore this phase was investigated further with respect to how its composition varies with the various addition combinations. Al₃Ti is modelled as being non-stoichiometric, and of the AE160 composition only Al, Ti, Zr, and V are predicted as soluble in the Al₃Ti phase and thus the data given in Table 6.5 consists of only these 4 elements. In general, it can be seen that for predictions for all three addition combinations the composition of the Al₃Ti phase is the same at both equal additions of 0.1 A + 0.1 B and 0.3 A + 0.3 B (wt. %), although the compositions obviously vary for the different sets of additions. The 0.1 A + 0.3 B and 0.3 A + 0.1 B (wt. %) additions are predicted to have a similar ratio of Al: (A + B), with A and B soluble in a ratio of 1:3, the larger addition forming the larger fraction of the phase. For example, when 0.3 Ti + 0.1 V (wt. %) additions are calculated, the Al₃Ti phase is predicted to contain 3 times more Ti than V. Also of interest is that the composition of the Al₃Ti phase, when formed on addition of Ti +

V, is predicted to contain a substantial amount more Al than in the other two systems. This is the same addition combination that was seen in Table 6.4 to have the highest liquidus temperature, and calculated to form Al_3Ti at all addition levels.

In order to understand the effect the elemental additions are predicted to have on the Al_3Ti phase, stability plots were drawn to show the temperature dependence of the composition of the phase. The plots are given in Figures 6.10, 6.11 and 6.12 for Ti + V, Ti + Zr and V + Zr additions respectively. The composition of Al_3Ti with Ti + V additions (Figure 6.10) can be seen to vary little with temperature, with 0.1 A + 0.1 B and 0.3 A + 0.3 B (wt. %) combinations having the same fraction of components. Similarly the component stability of Ti and V at 0.1 A + 0.3 B and 0.3 A + 0.1 B (wt. %) additions remain fairly stable varying very little as the temperature changes. In general terms the plots for the Ti + Zr (Figure 6.11) and V + Zr (Figure 6.12) are very similar for equivalent additions, although there is clearly a wide range of compositions for the Al_3Ti phase depending on the amount of additions. The composition of the Al_3Ti phase is predicted to become less variable with decreasing temperature, and illustrate how the composition of Al_3Ti will vary greatly depending on at which temperature it has solidified.

6.2.3 Summary

Thermodynamic calculations have been carried out to predict the effect of theoretical additions of Ti, Zr, and V, known for their grain refining ability, on commercial alloy AE160. Whether the additions were individual or in combination they were found to increase the stability of the Al_3Ti phase at the expense of the aluminium matrix. This in turn leads to a change in the liquidus temperature of the alloy when Al_3Ti solidifies first at higher temperatures than the aluminium. Individual additions of Ti and V were predicted to have a greater effect on the stability of Al_3Ti , and therefore the liquidus temperature, than the Zr. In Chapter 5 it was discussed how Zr has been observed by EDX analysis to be soluble in an intermetallic other than Al_3Ti , although no such phase is accounted for in the thermodynamic modelling. It is concluded, therefore, that the solubility of Zr in an alternative phase reduces the amount available for the formation of Al_3Ti . These findings were consistent with those of subsequent calculations predicting the effect of Ti, Zr and V in combination. Ti + Zr and Zr + V were found to have a lesser effect on the fraction of Al_3Ti than Ti + V which was calculated to form Al_3Ti at all levels of addition and to be stable at much higher temperatures. This would, in theory, make the Ti + V combination desirable for grain refining purposes.

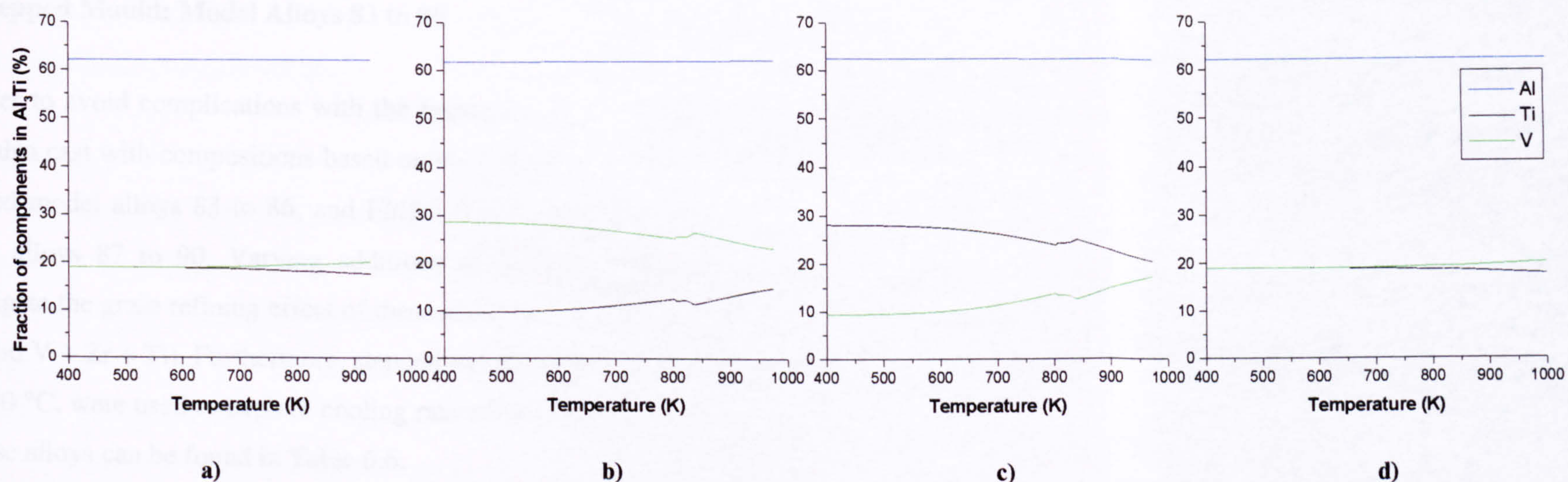


Figure 6.10 Component distribution plots for the Al_3Ti phase in AE160 with **a)** 0.1 Ti + 0.1 V, **b)** 0.1 Ti + 0.3 V, **c)** 0.3 Ti + 0.1 V, and **d)** 0.3 Ti + 0.3 V (all wt. %)

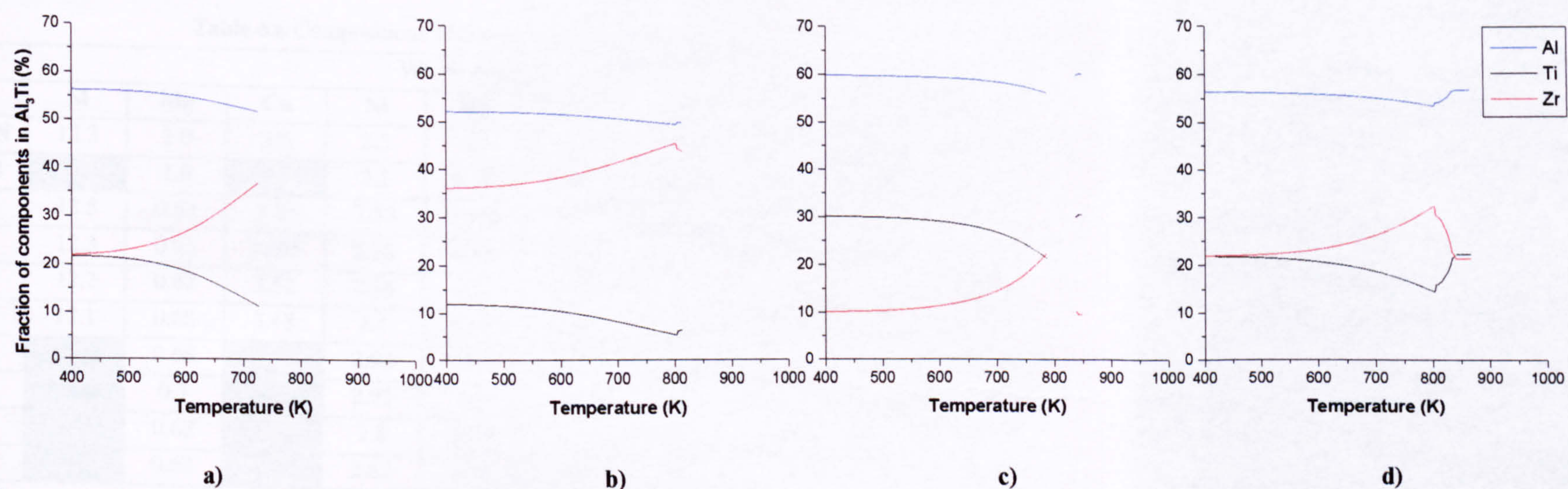


Figure 6.11 Component distribution plots for the Al_3Ti phase in AE160 with **a)** 0.1 Ti + 0.1 Zr, **b)** 0.1 Ti + 0.3 Zr, **c)** 0.3 Ti + 0.1 Zr, and **d)** 0.3 Ti + 0.3 Zr (all wt. %)

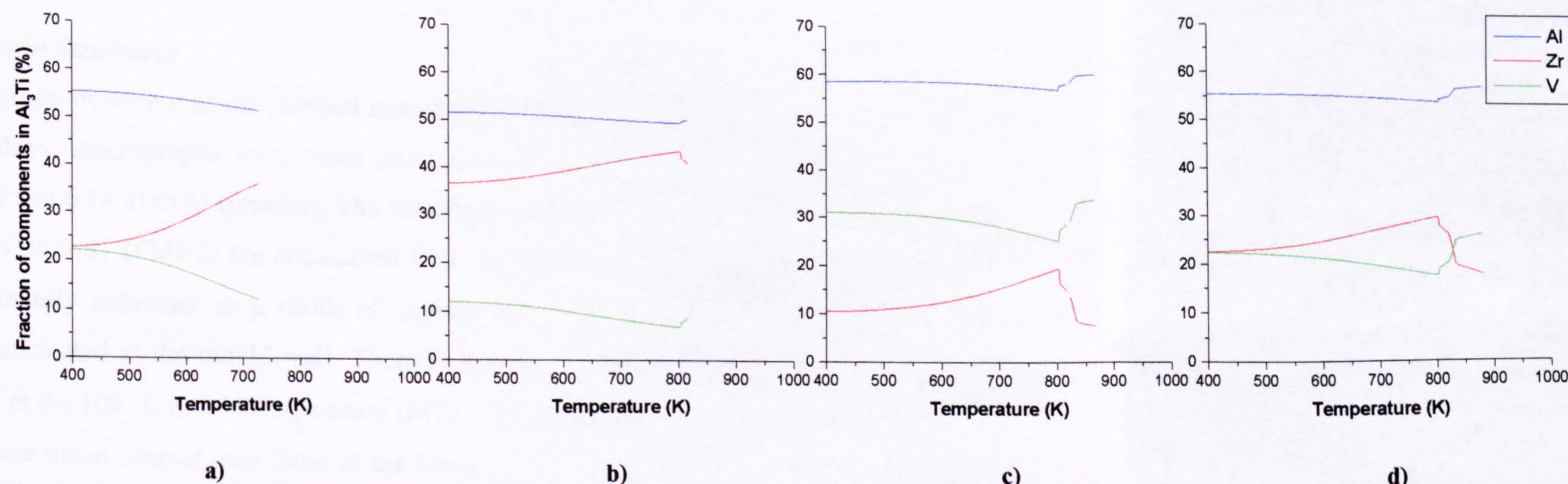


Figure 6.12 Component distribution plots for the Al_3Ti phase in AE160 with **a)** 0.1 V + 0.1 Zr, **b)** 0.1 V + 0.3 Zr, **c)** 0.3 V + 0.1 Zr, and **d)** 0.3 V + 0.3 Zr (all wt. %)

6.3 Stepped Mould: Model Alloys 83 to 90

In order to avoid complications with the presence of intermetallics, a range of model alloys were also cast with compositions based on the commercial alloys FMS2N (formally AE160), denoted model alloys 83 to 86, and FMB2 (higher silicon and copper version of FMS2N), model alloys 87 to 90. Varying additions of Ti, Zr and V were made to the alloys to investigate the grain refining effect of these elements individually (V), and in combination (V + Zr and V + Zr + Ti). Furthermore, stepped moulds at two different mould temperatures, 100 and 440 °C, were used to explore cooling rate effects on the microstructure. Compositions for all these alloys can be found in Table 6.6.

Table 6.6 Compositions of commercial and model alloys

	Wt. % element									ppm
Alloy	Si	Mg	Cu	Ni	Mn	Fe	Ti	Zr	V	P
FMS2N	12.3	1.0	3.6	2.5	0.2	0.5	0.05	0.16	0.08	-
FMB2	14.5	1.0	4.2	3.1	0.15	0.5	0.05	0.07	0.07	-
83	12.5	0.63	3.62	2.53	0.185	0.5	0.01	0.01	0.01	48
84	12.3	0.65	3.605	2.38	0.18	0.49	0.01	0.01	0.09	42
85	12.2	0.62	3.52	2.36	0.18	0.48	0.01	0.14	0.085	40
86	12.1	0.68	3.48	2.4	0.18	0.48	0.15	0.15	0.09	40
87	14.1	0.68	5.02	2.94	0.2	0.47	0.015	0.01	0.01	48
88	14.15	0.7	5.09	2.92	0.2	0.47	0.01	0.01	0.08	43
89	14.1	0.63	5.01	2.8	0.19	0.48	0.01	0.14	0.09	48
90	14.2	0.68	4.91	2.82	0.19	0.48	0.15	0.13	0.09	53

Balance is Al, all other elements unspecified

6.3.1 Grain Structures

To obtain an overview of the stepped mould grain structures and those of the pistons of the same alloys, macrographs were taken and can be found in Figures 6.13 a) to p) (stepped moulds) and 6.14 a) to h) (pistons). The structures of the alloys without additions, namely 83 (FMS2N) and 87 (FMB2) are considered first. At both mould temperatures the castings are predominantly columnar as a result of growth along the temperature gradient, the grains having nucleated at the mould wall. There is some evidence of an equiaxed zone in model alloy 83 at the 100 °C mould temperature (MT). The columnar grains in the castings at 440 °C MT appear much coarser than those at the lower mould temperature, as a result of the lower

temperature gradients and slower cooling rates due to the longer solidification times associated with a pre-heated mould.

It appears that at 100 °C MT the V and V + Zr additions (84, 85, 88 and 89) have little effect on the macrostructure with it remaining largely columnar. At 440 °C MT, however, the V + Zr produces a more equiaxed structure consisting of coarse equiaxed grains in alloy 89 and a finer structure in 85. From this it can be postulated that when small amounts of V and Zr + V are added, the cooling rate of the relatively small castings plays a more critical role in determining the macrostructure of the casting than the grain refining additions do. This is most likely because the liquid cools too rapidly for the nucleants to become active, except in the case of model alloys 85 and 89 where the solidification rate is slow and nucleation sites arise in the bulk of the casting, not just at the mould wall. On addition of Ti in combination with the V and Zr there is a large reduction in grain size and a change from columnar to equiaxed growth at both mould temperatures. This is most evident in model alloy 86 at the 100 °C MT where a very fine grain structure is visible. In section 6.2 it was shown that the addition of Ti (Zr and V) instigates the formation of the Al_3Ti phase which is stable at high temperatures. This phase acts as a nucleant for the aluminium and therefore the aluminium will grow at a lesser supercooling than usual. It can be assumed that on addition of the Ti (Zr and V) in model alloys 86 and 90 the Al_3Ti phase becomes stable and nucleates many aluminium grains throughout the casting to produce the structures seen in Figures 6.13 g), h), o) and p).

The effect of different step sizes along the stepped mould produces varying cooling rates and consequently a change in grain structure along the length of the mould. This can be seen in Figures 6.13 a) to p). The structure of the larger steps (4 and 5) depends more obviously on the alloy composition as discussed above. Model alloys 83 to 85 have an essentially columnar structure with some equiaxed in the centre, whereas 87 to 89 are completely columnar. The smallest step (1) is always columnar due to the extremely fast cooling rates, whilst the intermediate steps (2 and 3) graduate between the extremes of steps 1 and 5. On addition of Ti (model alloys 86 and 90) the whole casting is equiaxed irrespective of step size. If the stepped moulds are compared with the cross sections of pistons cast from the same model alloys (Figures 6.14 a) to h)) it can be seen that the stepped moulds cast at 100°C MT are most representative of a piston structure, steps 4 and 5 relating to the crown area, and the smaller steps corresponding to the skirt.

6.3.2 Microstructural Analysis

It has been shown that the addition of Ti, Zr and V has a grain refining effect on the aluminium, however, as a result of controlling the macrostructure, it is assumed that there must be a residual effect on the microstructure also. Samples from the first, third and fifth steps of all the model alloys (83 to 90) at both mould temperatures (100 and 440 °C) were prepared and etched according to details presented in Chapter 4, and the microstructures analysed. The optical micrographs in Figures 6.15, 6.16 and 6.17 show both the effects of additions (left to right) and cooling rate (top to bottom) on the microstructure. It is also possible to compare the variation in microstructure caused by different mould temperatures (Figures 6.15 and 6.16) and the effect of increased silicon and copper content in the alloy (Figures 6.15 and 6.17).

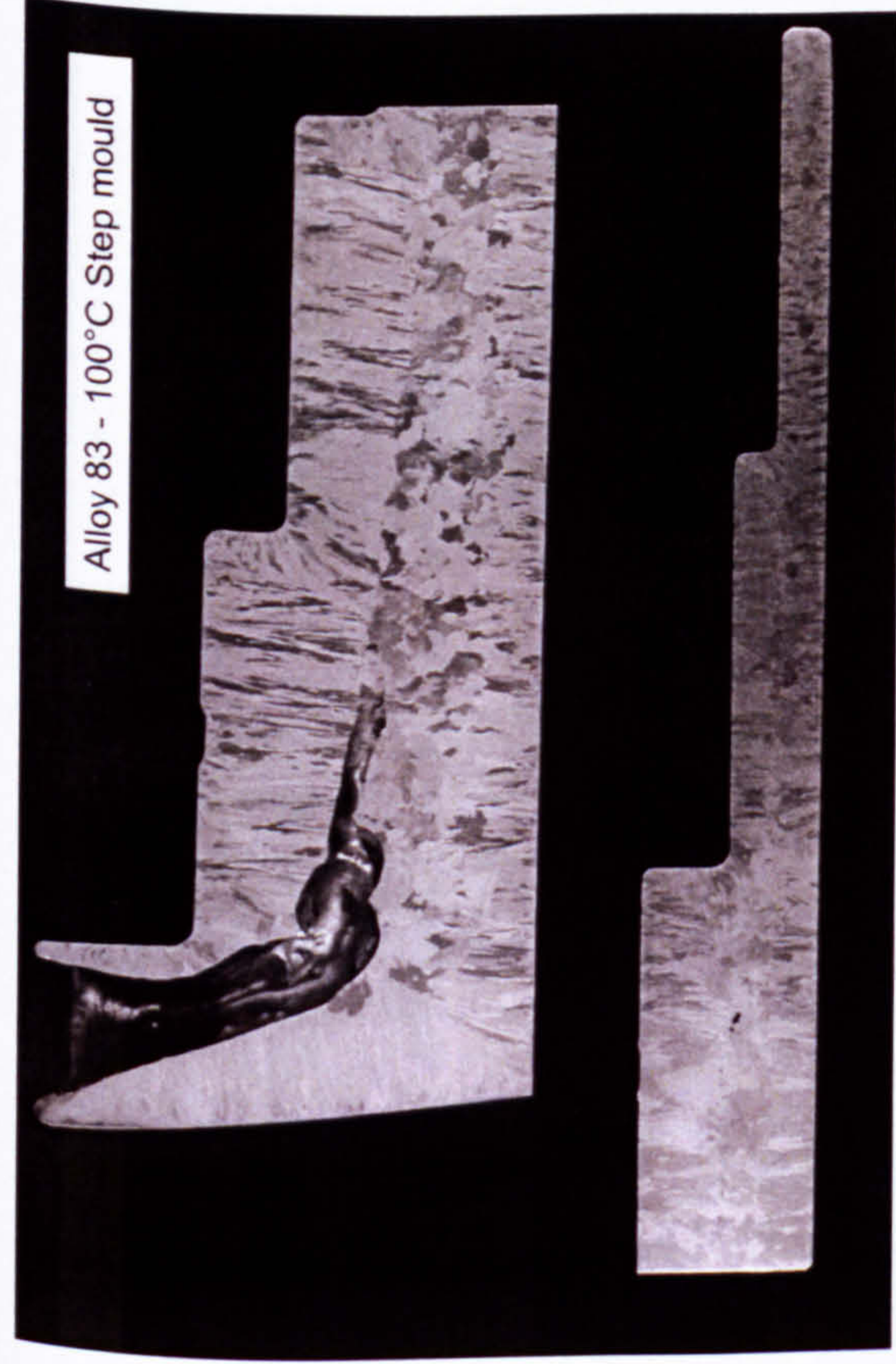
The difference in mould temperatures produces very different microstructures in alloys 83 to 86 as can be seen in Figures 6.15 and 6.16. The most prominent contrast is that at the 440 °C mould temperature the microstructure is much coarser with silicon particles, in particular, often being twice the size of those in the 100 °C MT casting. This effect is most pronounced in step 5 of the stepped moulds where the cooling rate was slowest in each the individual castings at both mould temperatures, but was slowest in the pre-heated mould (440 °C). Here (Figure 6.16), the silicon particles, and indeed the intermetallics also, have grown to extremely large sizes in comparison with the particles in the microstructure of the 100 °C mould.

It is also clear that within the stepped moulds, the change in cooling rate as a result of different step sizes has a significant effect of the microstructure. The alloy structures in step 1, the thinnest section, have a very clear dendritic formation and small phases as a result of the alloy being cooled very rapidly. It was shown in Chapter 4 that in fact step 1 cooled too rapidly for the thermocouple to measure the cooling rate. In comparison, step 5 consists of much larger phases, particularly silicon, where the slower cooling rate has allowed time to grow. The largest phases are seen in step 5 of the moulds pre-heated to 440°C, the cooling rate being the slowest here as previously discussed. Thus, as expected, the slower the cooling rate, whether as a result of thicker sections or pre-heated moulds, the larger and more equiaxed the grain structures are.

Consider next the difference in microstructures of the FMS2N (83 to 86) and FMB2 (87 to 90) alloys, from the 100 °C MT castings, optical micrographs of which are given in Figures 6.15 and 6.17 respectively. It is not surprising that the most distinct difference is that there is considerably more silicon phase in model alloys 87 to 90 and the silicon particles are much larger than those seen in alloys 83 to 86 at the 100 °C MT. The effect of the increased copper content is less defined as there does not appear to be an increase in the amount of intermetallic phases in which copper would be soluble. However, as previously mentioned in Chapter 5, copper is known to form Al_2Cu precipitates in the matrix which are difficult to see on a standard optical microscope. These precipitates are investigated later in Section 6.3.3.

Looking at all three sets of micrographs in Figures 6.15 to 6.17 it is possible to see the effect of increasing additions from left to right across the page. The addition of V (84 and 88) appears to have little effect on the microstructure with the secondary phases being evenly distributed within the aluminium matrix. The Zr + V additions (85 and 89) again have little effect on the microstructure although it does appear that the silicon particles are larger than the previous alloys. This could be a result of the alloys solidifying at a slightly slower rate thus enabling the silicon to grow to a larger size. On addition of Ti there is a definite change in the microstructure to show segregated regions where silicon and intermetallics are clustered together, the silicon in particular appearing to form large agglomerates. Referring back to section 6.3.1 it was discussed that the addition of Ti stabilises the formation Al_3Ti which acts as a nucleant for the aluminium enabling its solidification at higher temperatures. If this is so then as the aluminium grows there is probably a constitutional effect whereby solute in the melt is expelled to the liquid around the solidifying front. The silicon and intermetallic phases then form in these segregated regions when the solidification conditions are suitable, creating the microstructures seen in alloys 86 and 90.

From the observations above it was concluded that in this alloy series the greatest grain refining effect was that of V + Zr + Ti additions, and so further research was concentrated on the differences between none and all three additions. Model alloys 83, 86, 87 and 90, step 3, at both mould temperatures were considered with micrographs of these 8 conditions shown in Figure 6.18 to clearly illustrate the effects described above. Samples were then analysed by scanning electron microscopy (SEM), and image analysis, both of which were described in full in Chapter 4.



a)



b)



c)



d)



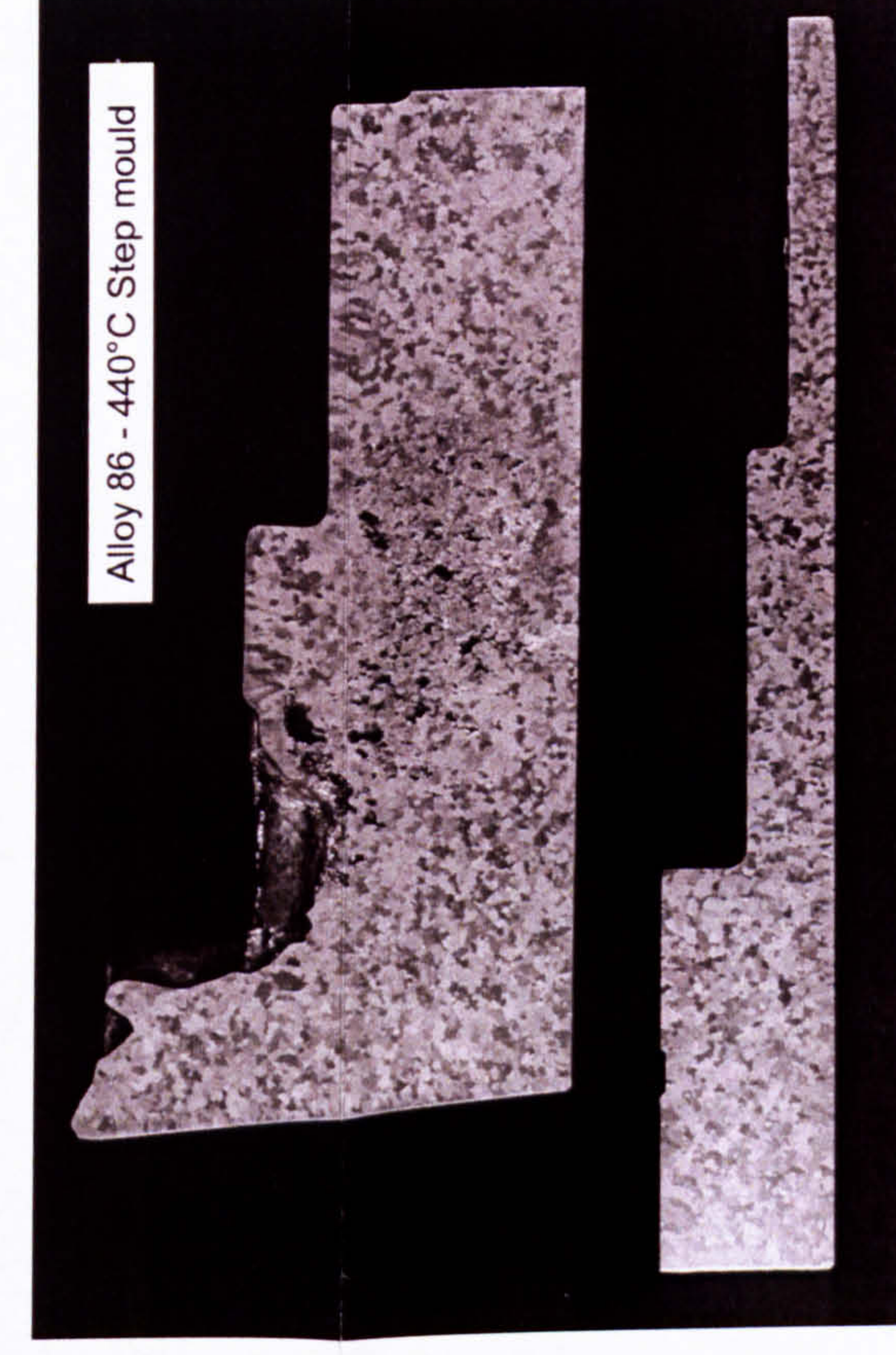
e)



f)



g)



h)

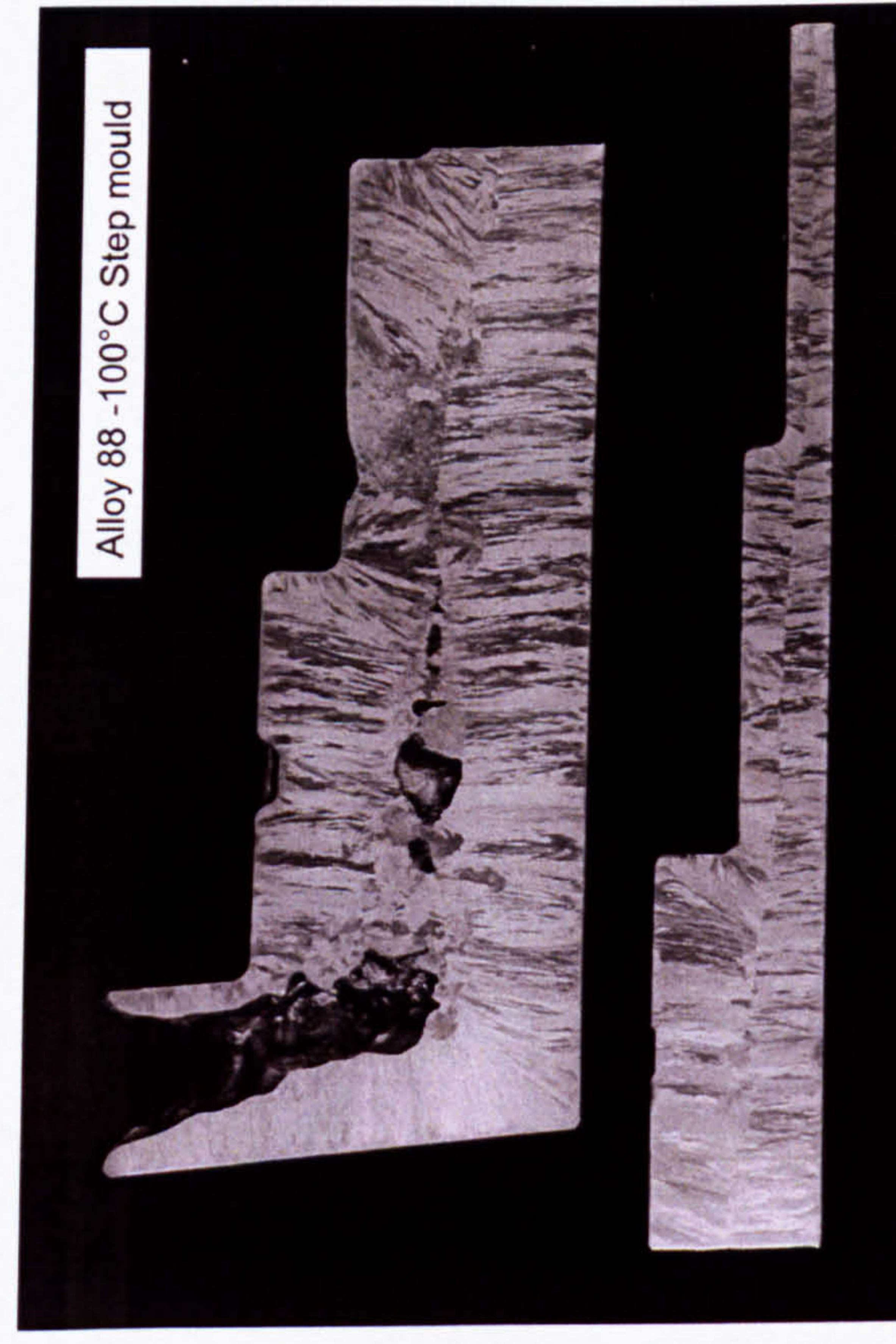
Figure 6.13 a) to h) Stepped mould model alloys 83 to 86 cast at 100 and 440 °C mould temperature



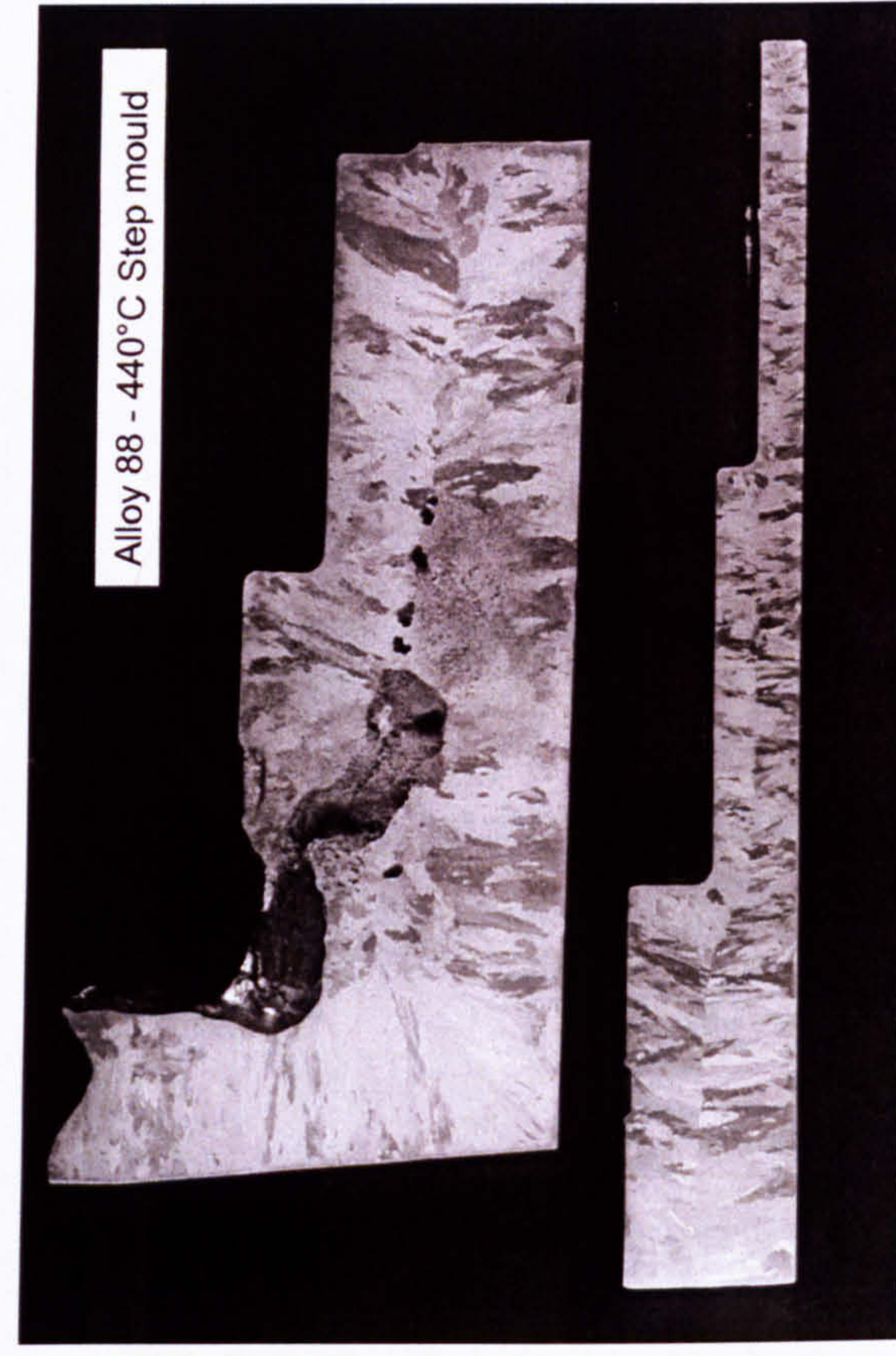
i)



j)



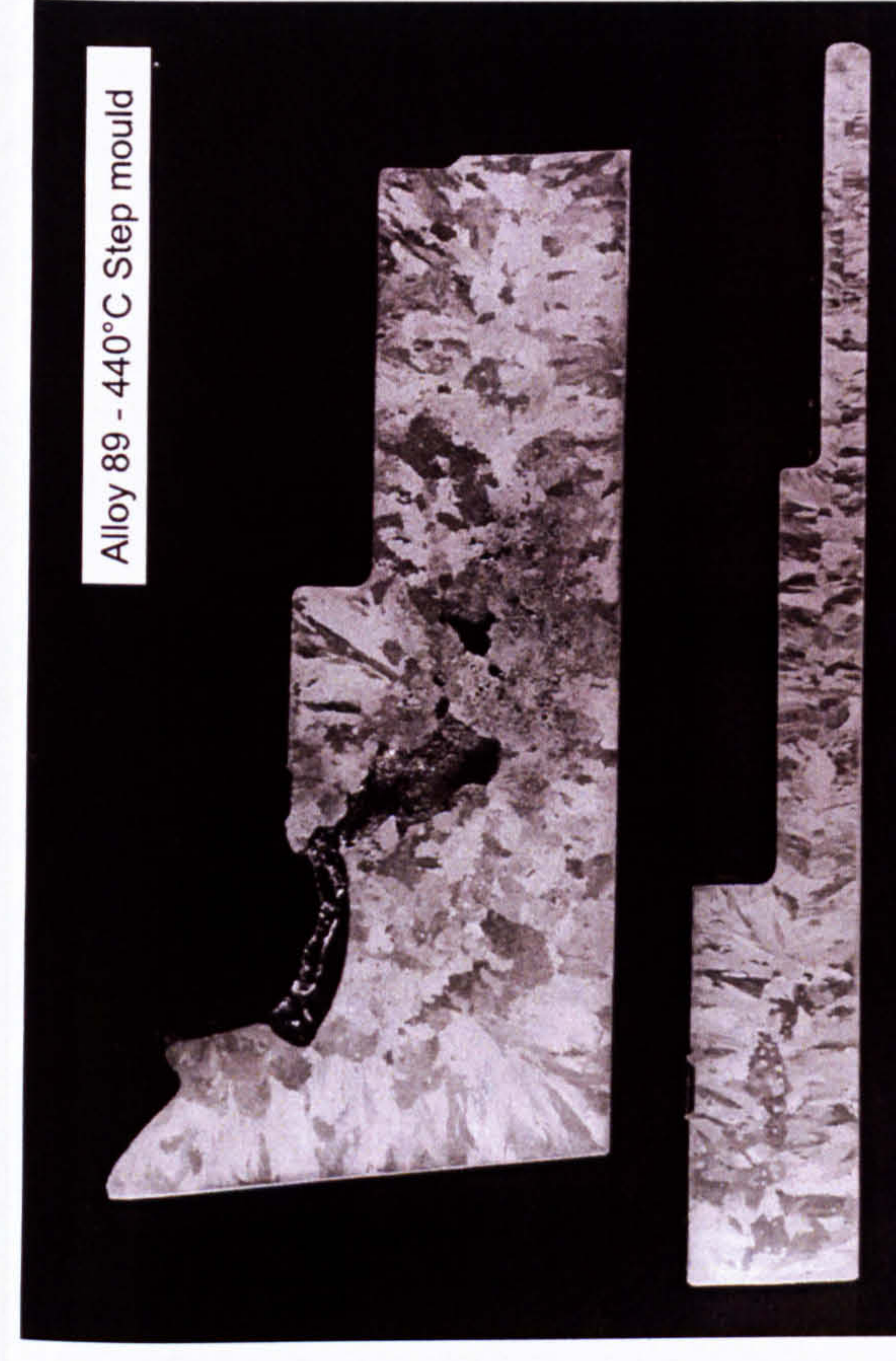
k)



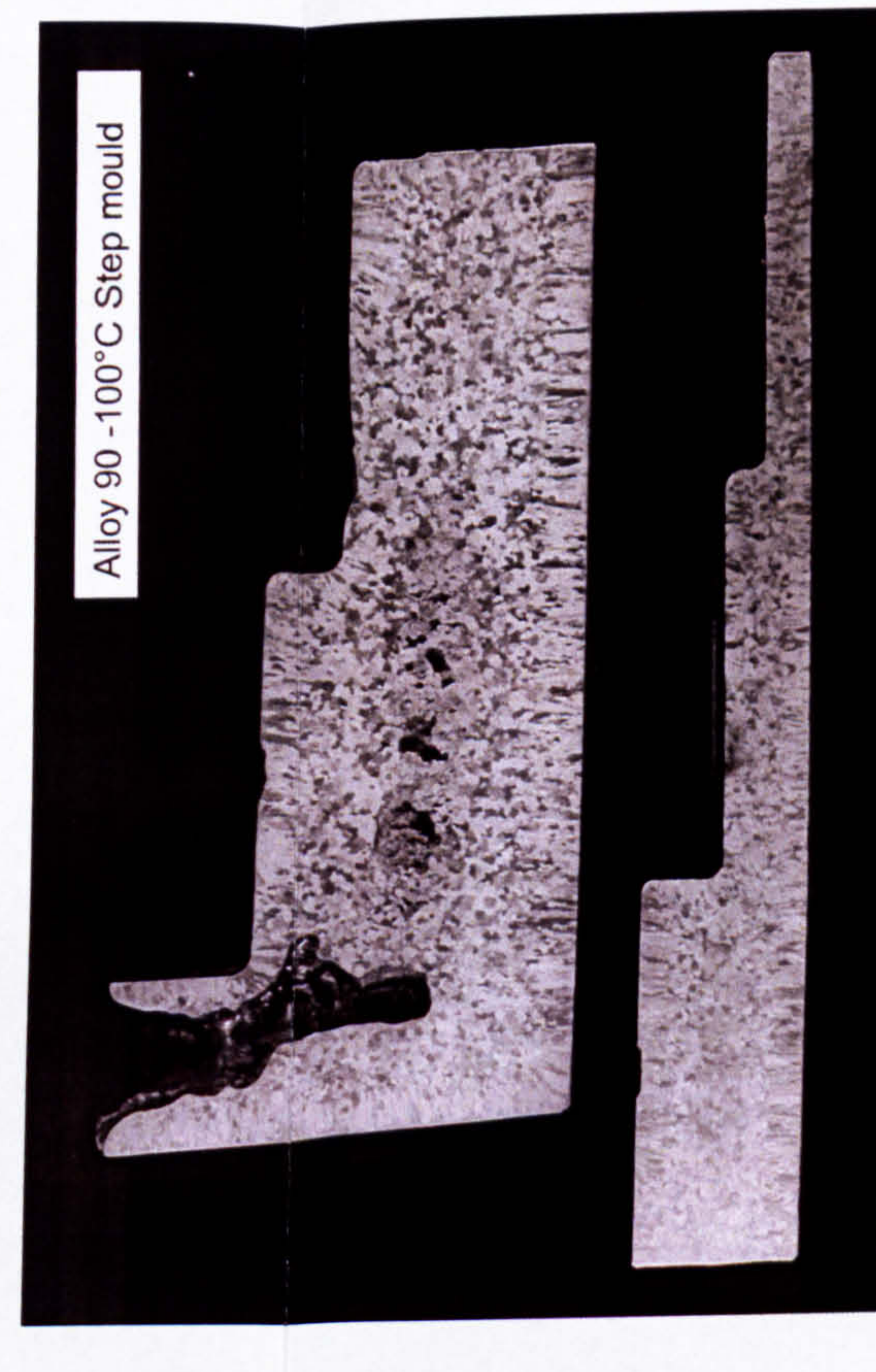
l)



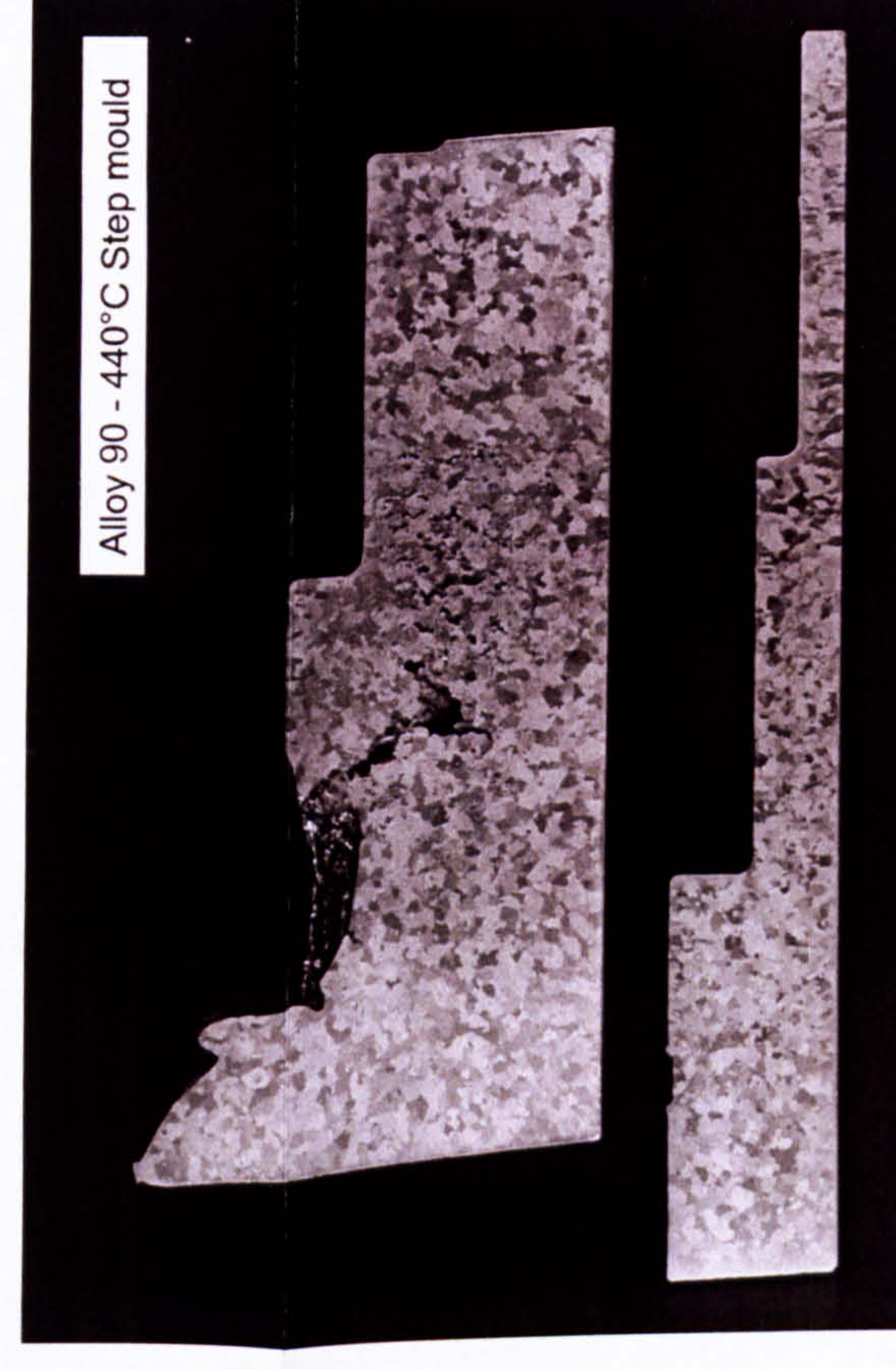
m)



n)



o)

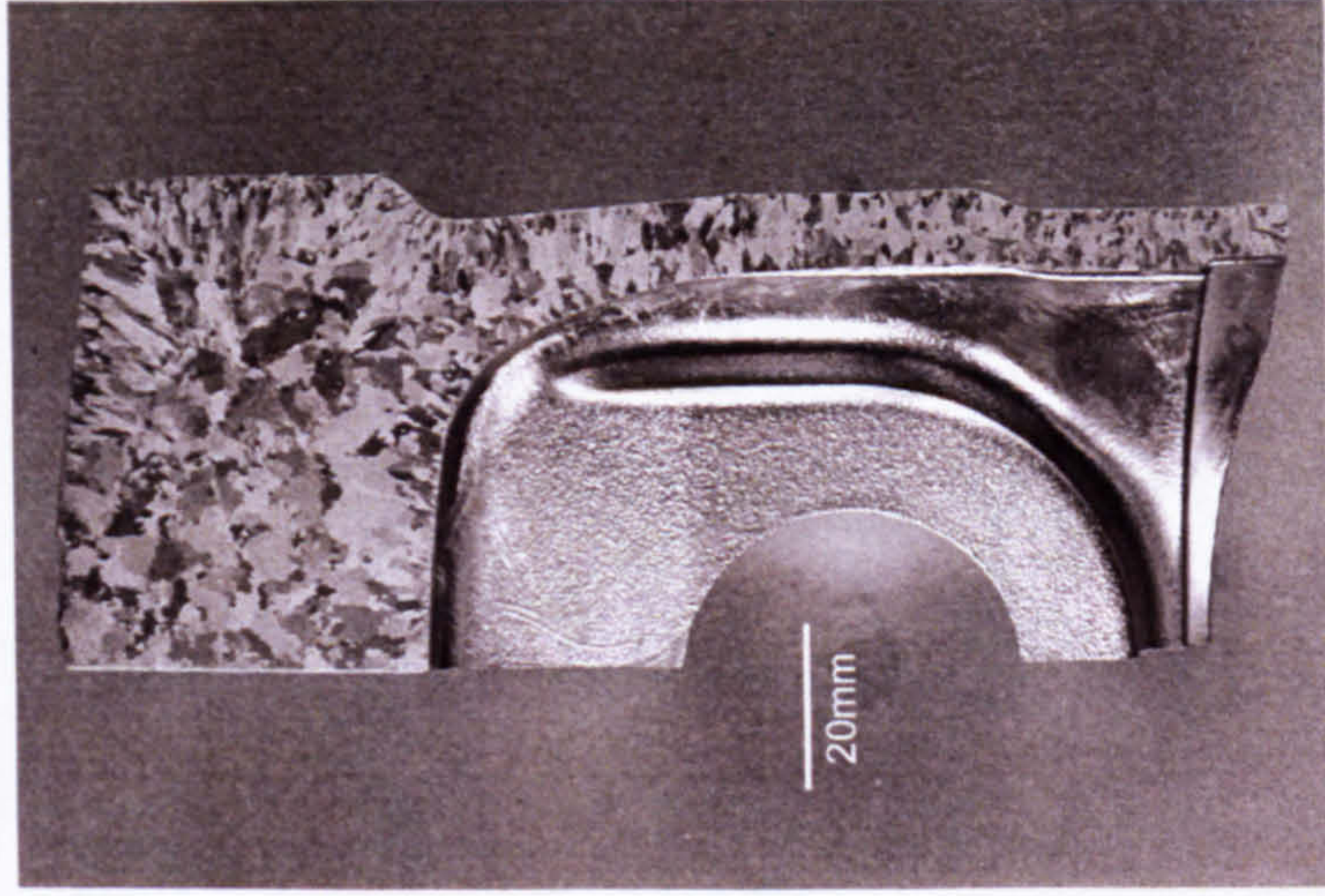


p)

Figure 6.13 i) to p) Stepped mould model alloys 87 to 90 cast at 100 and 440 °C mould temperature



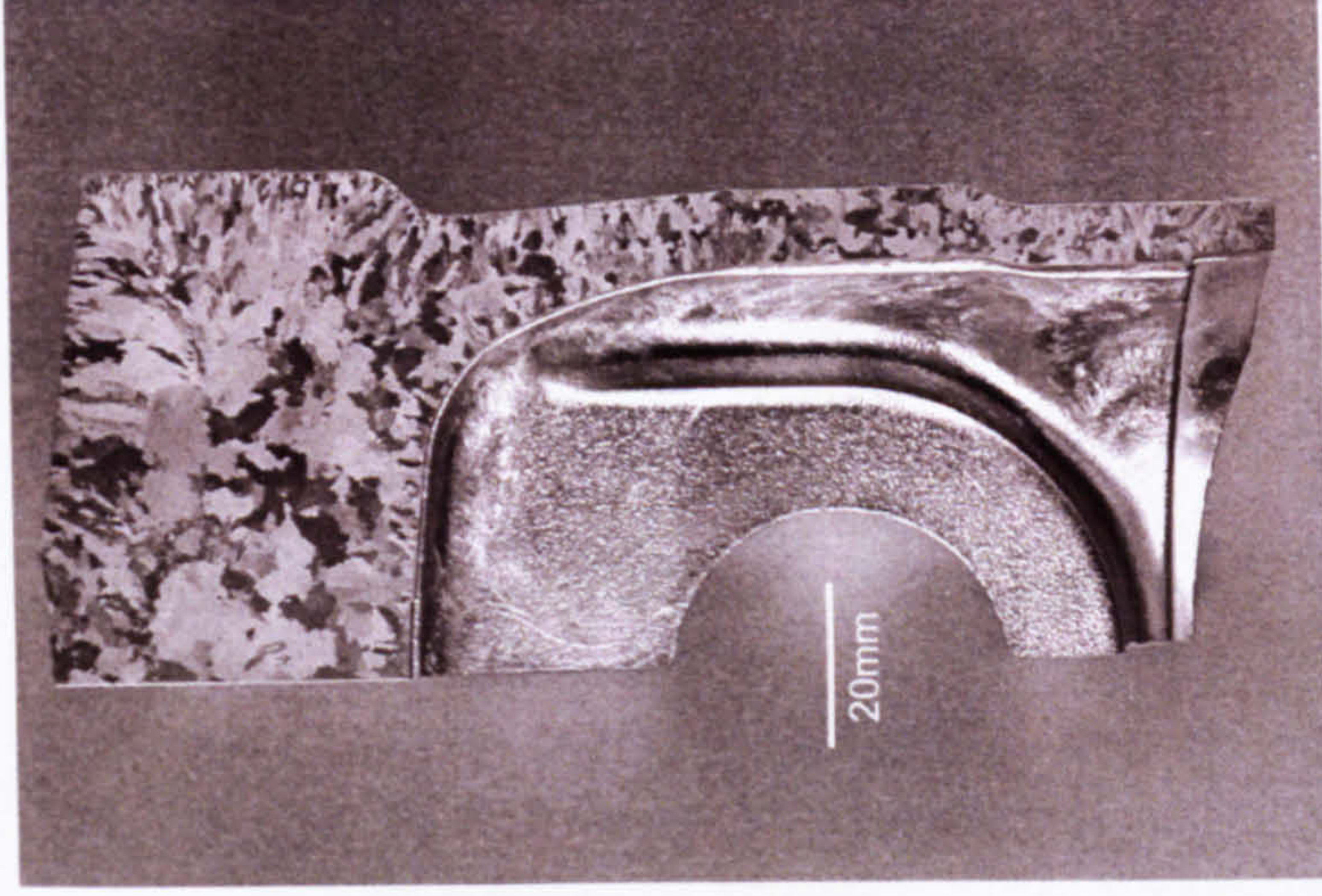
Alloy 83 -
Scania



a)



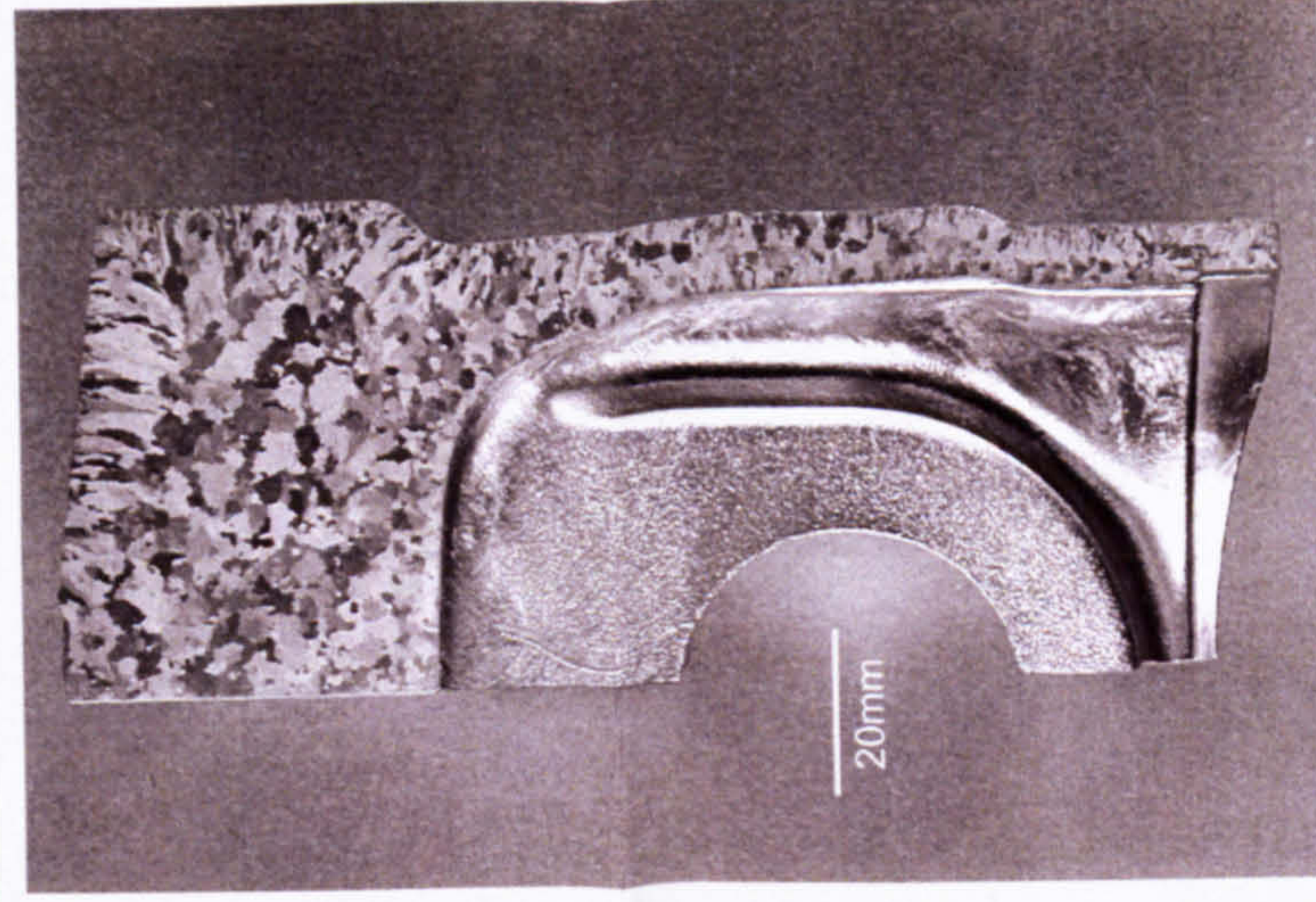
Alloy 84 -
Scania



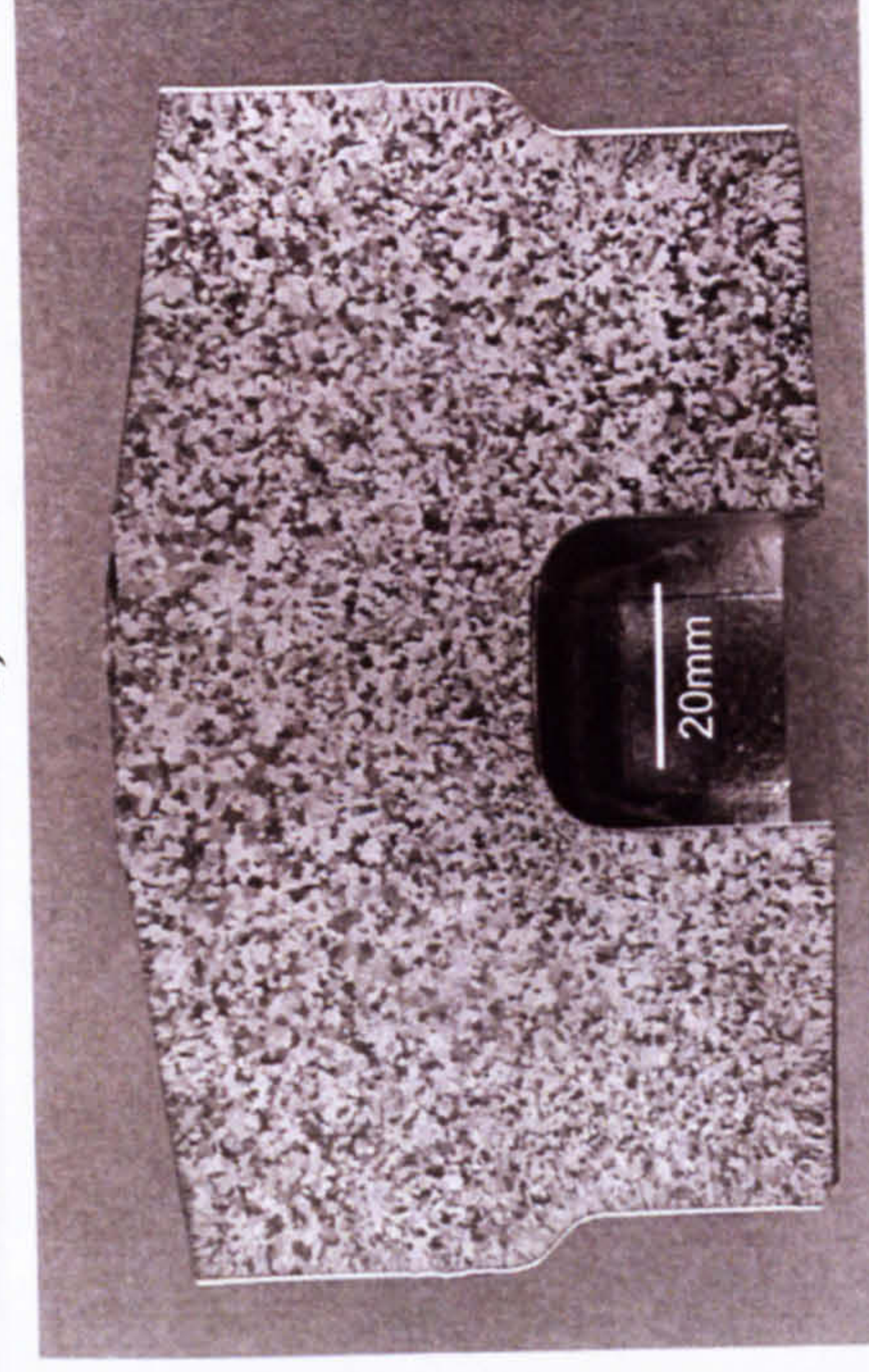
b)



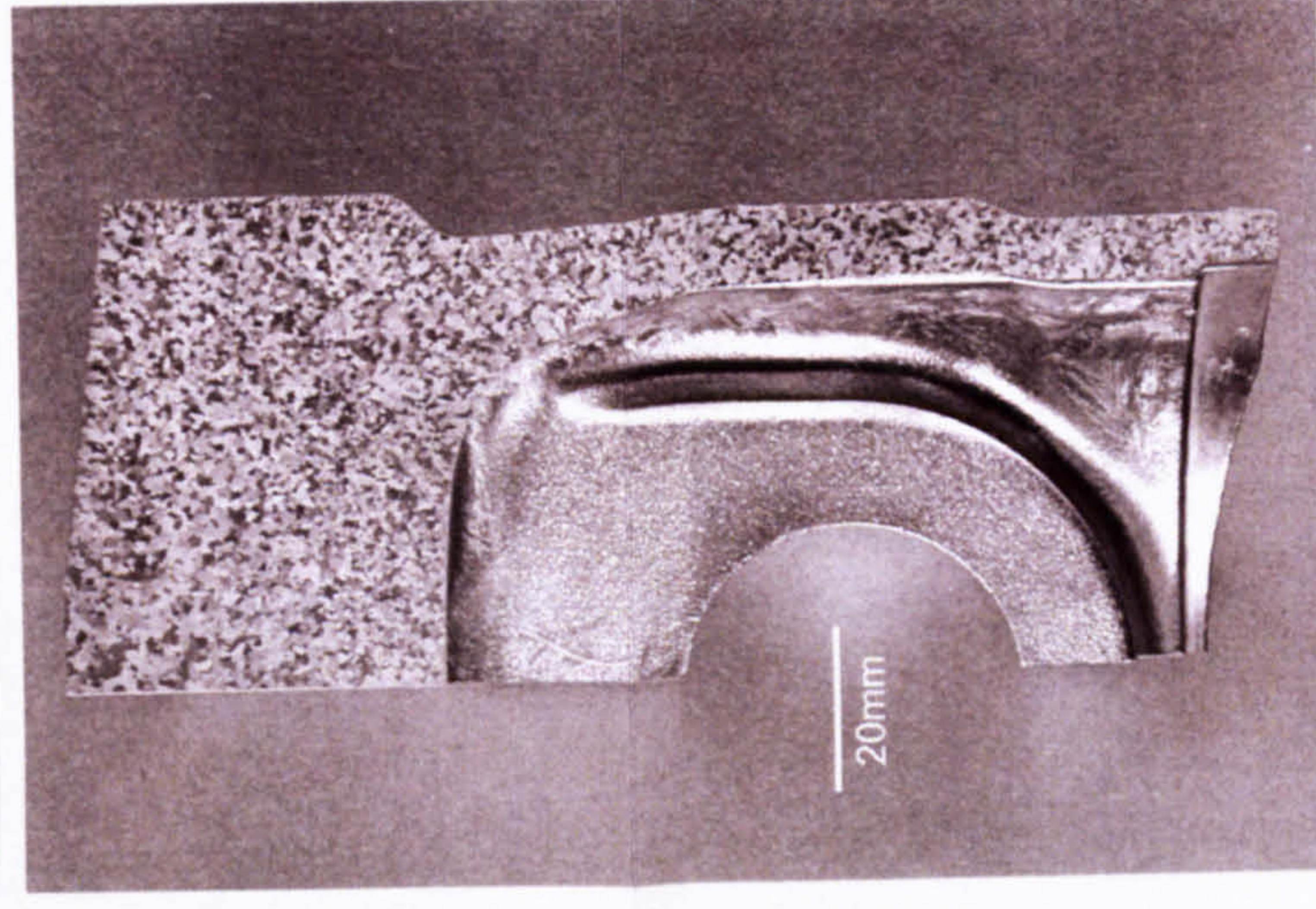
Alloy 85 -
Scania



c)



Alloy 86
Scania



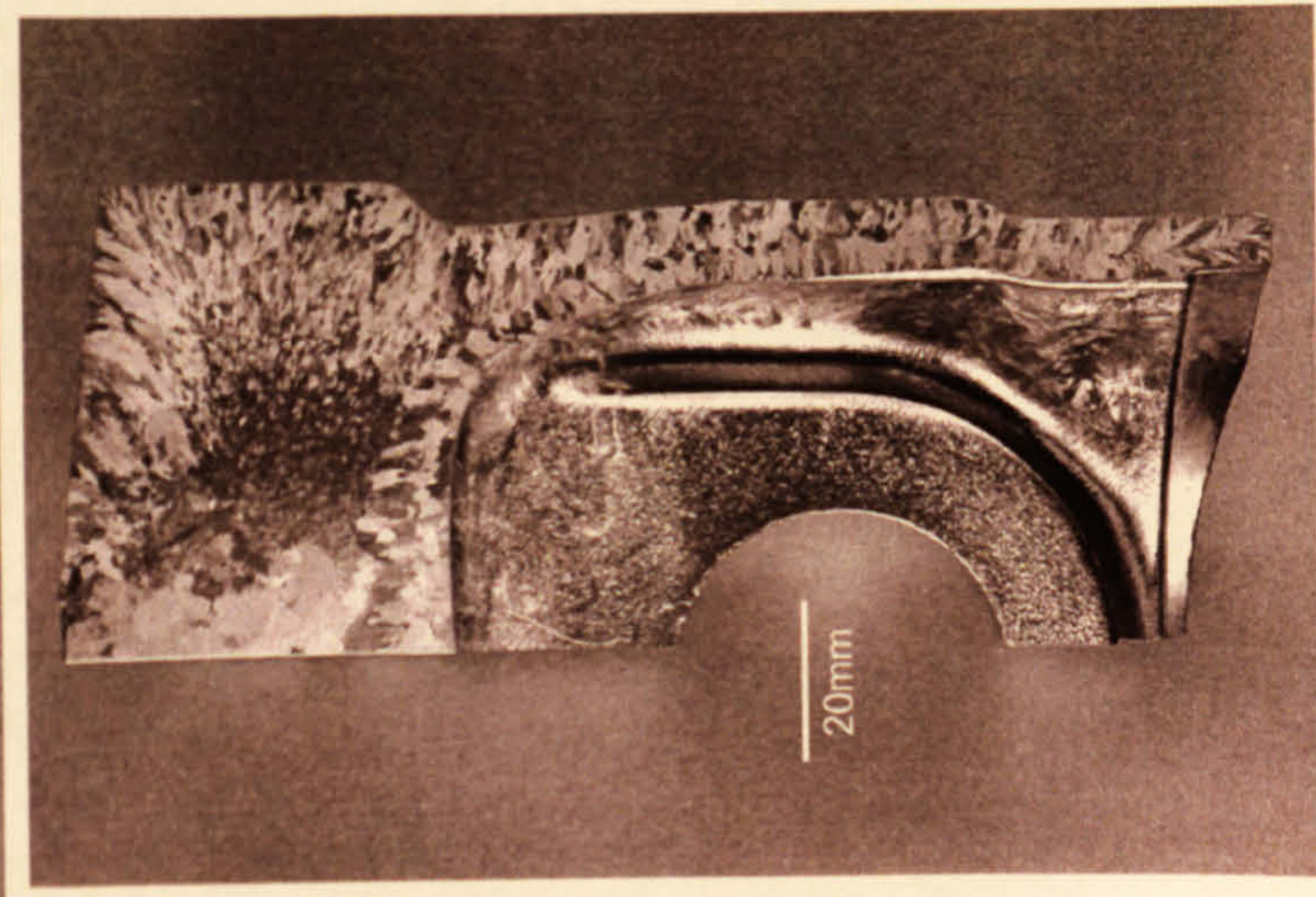
d)

Figure 6.14 a) to d) Stepped mould model alloys 83 to 86 cast in a piston mould

Step No.



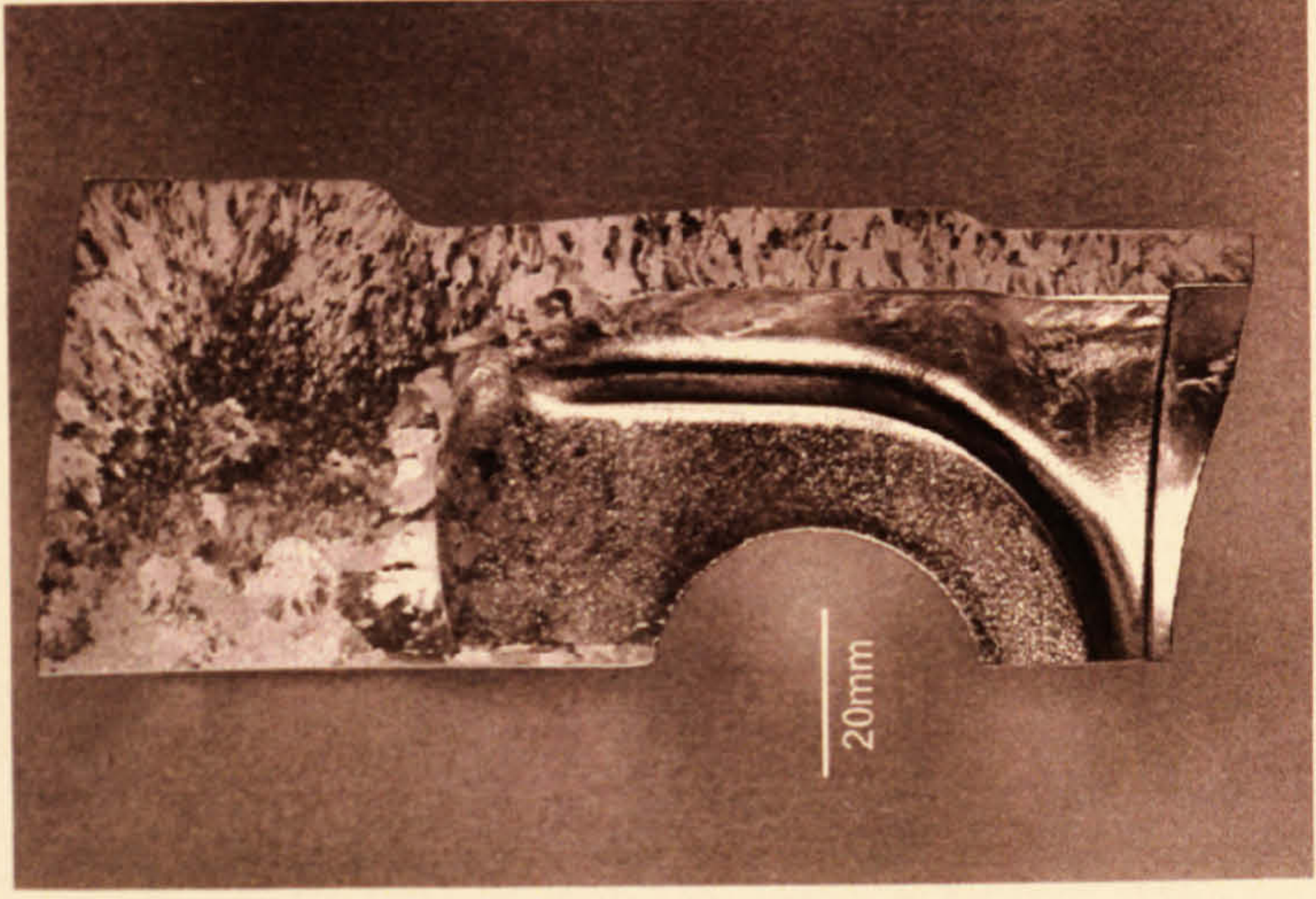
Alloy 87 -
Scania



e)



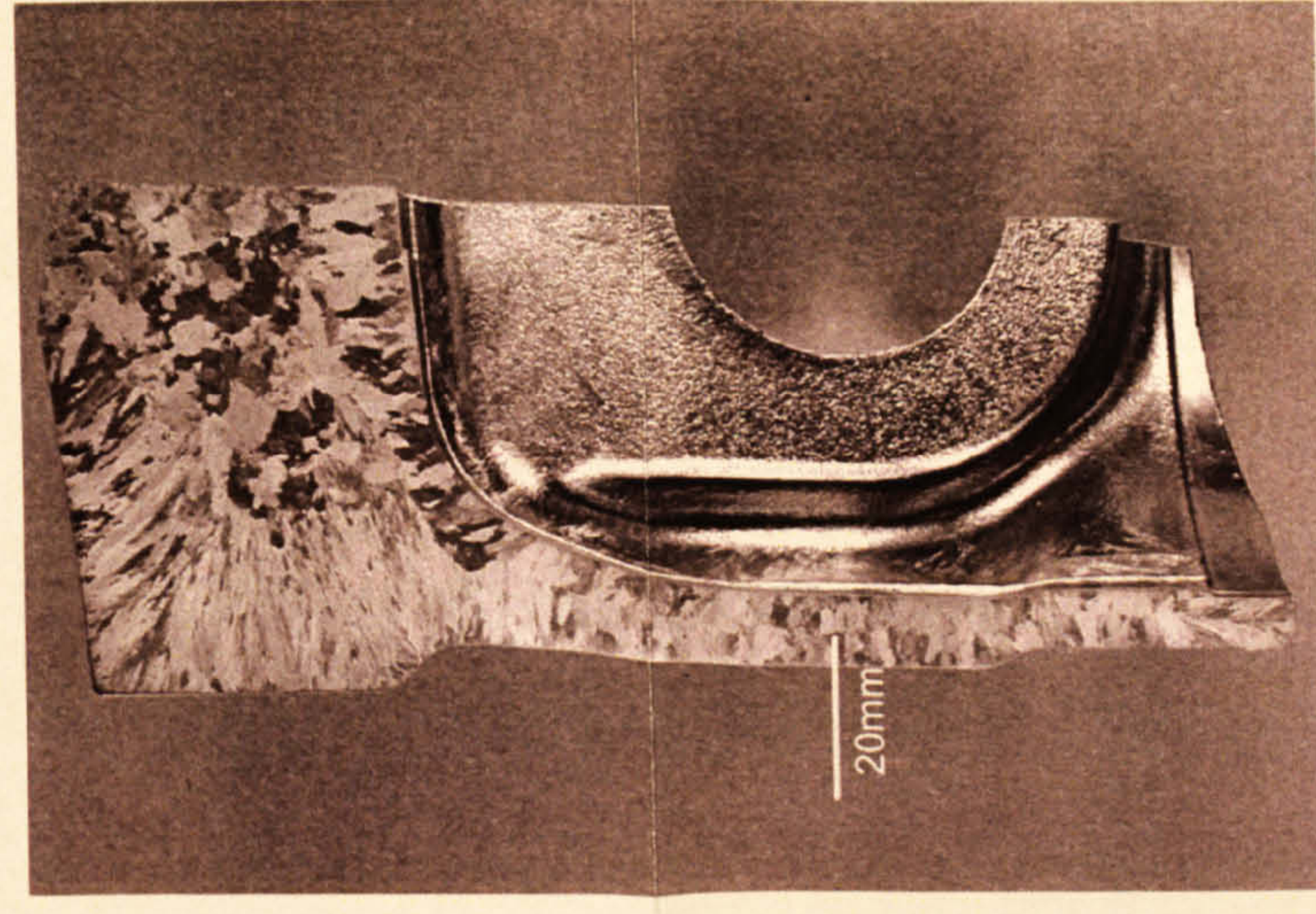
Alloy 88
Scania



f)



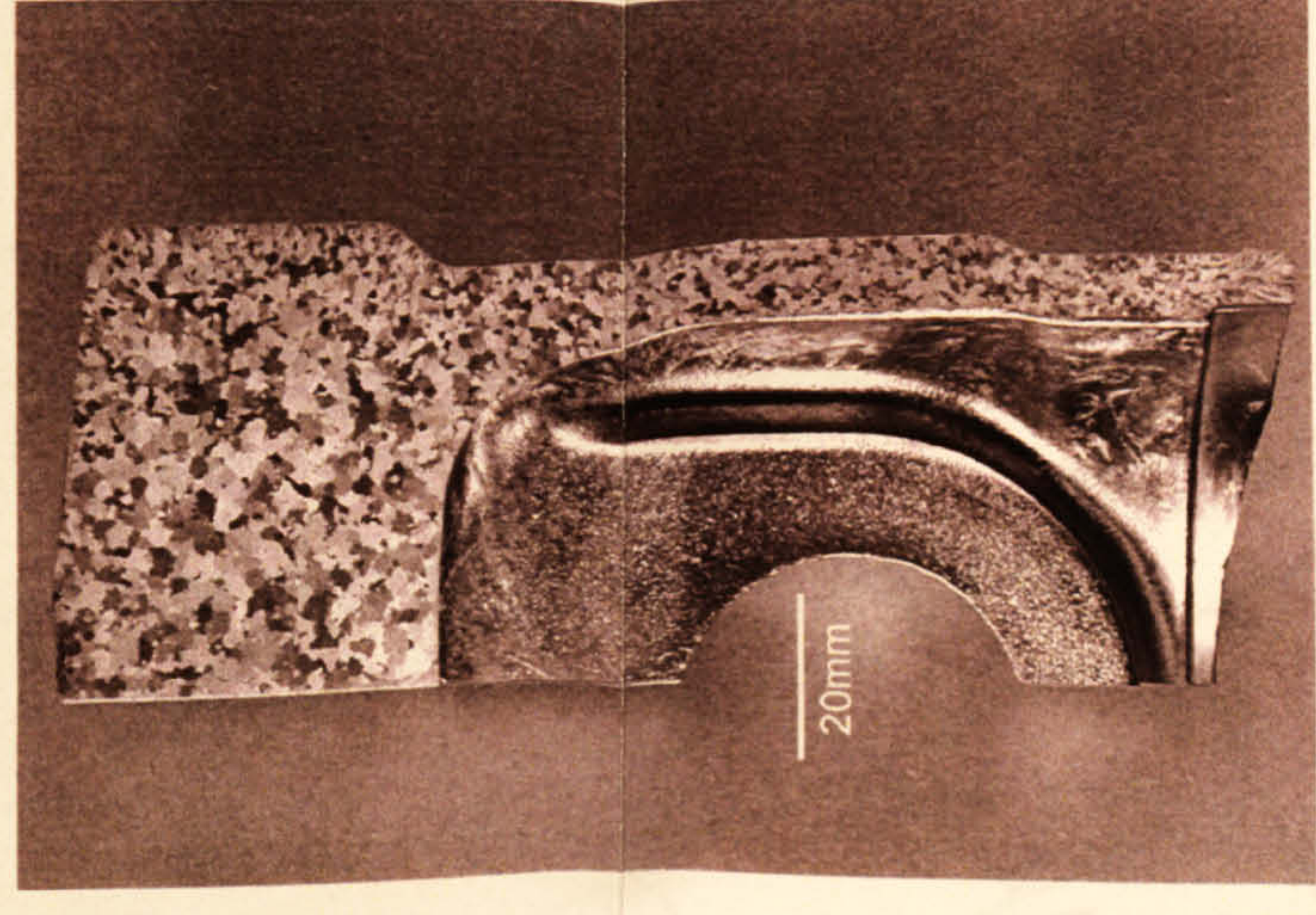
Alloy 89
Scania



g)



Alloy 90
Scania



h)

Figure 6.14 e) to h) Stepped mould model alloys 87 to 90 cast in a piston mould

Figure 6.15 Micrographs of stepped mould model alloys 83 to 86, cast at 100 °C mould temperature

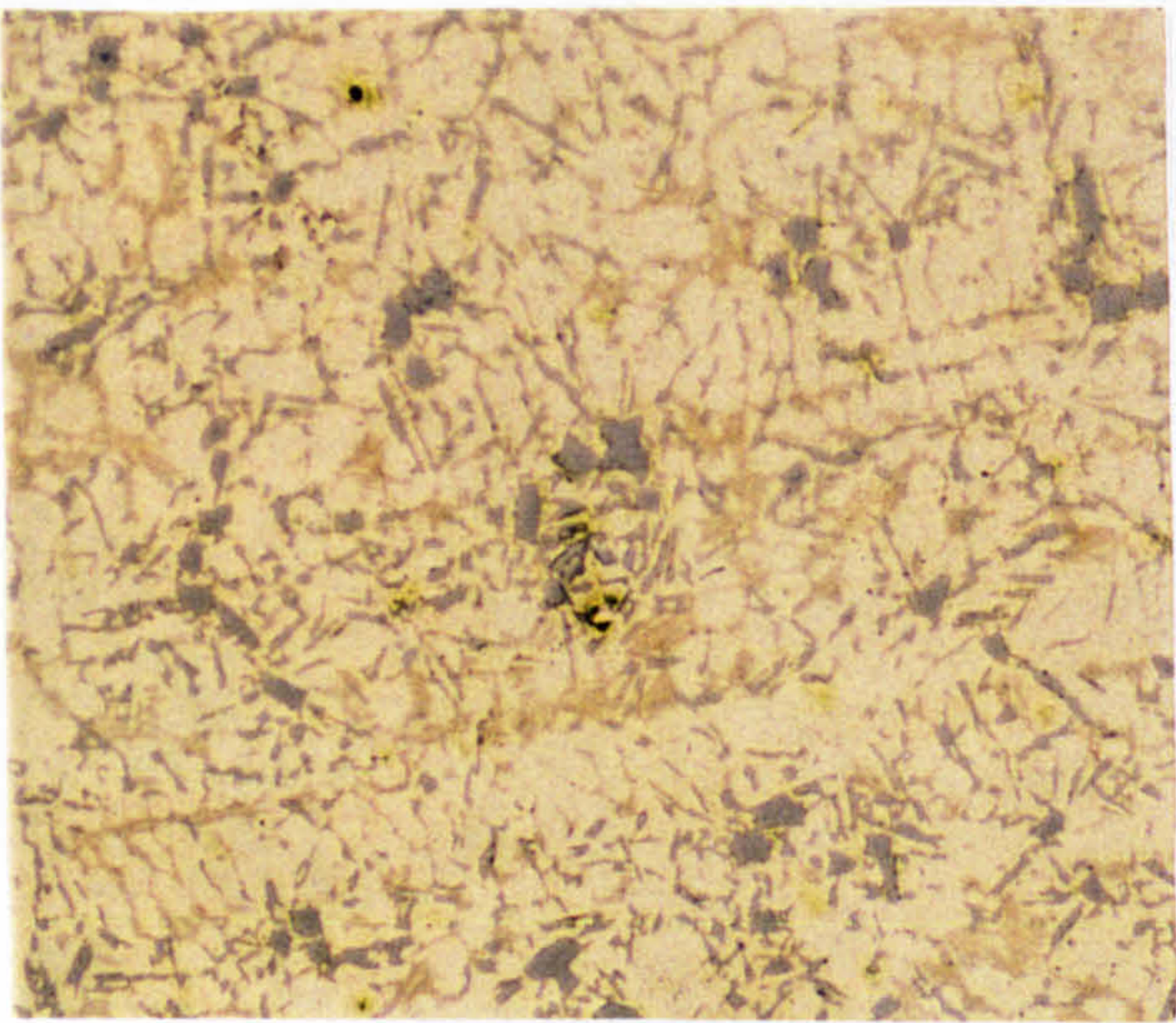
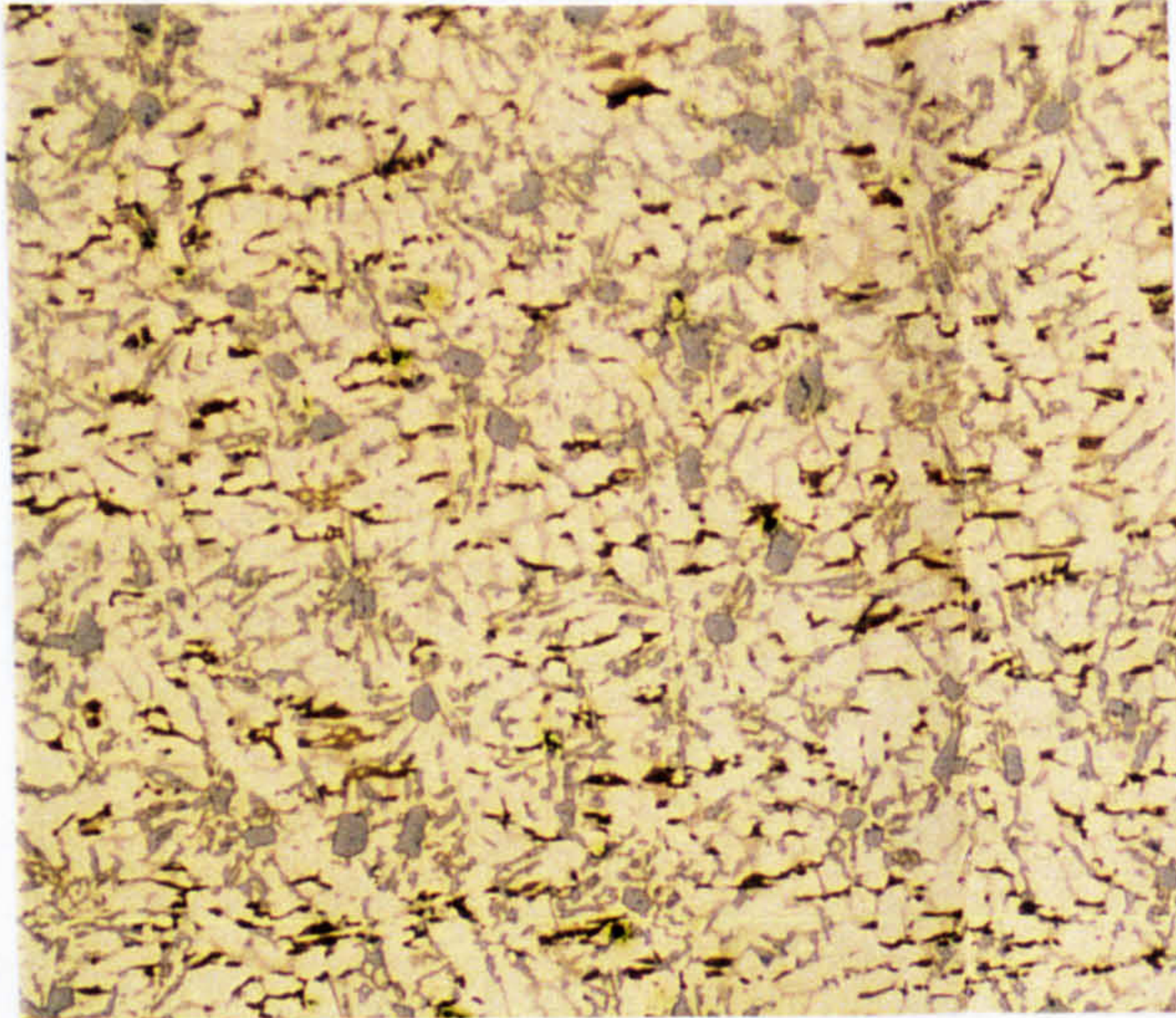
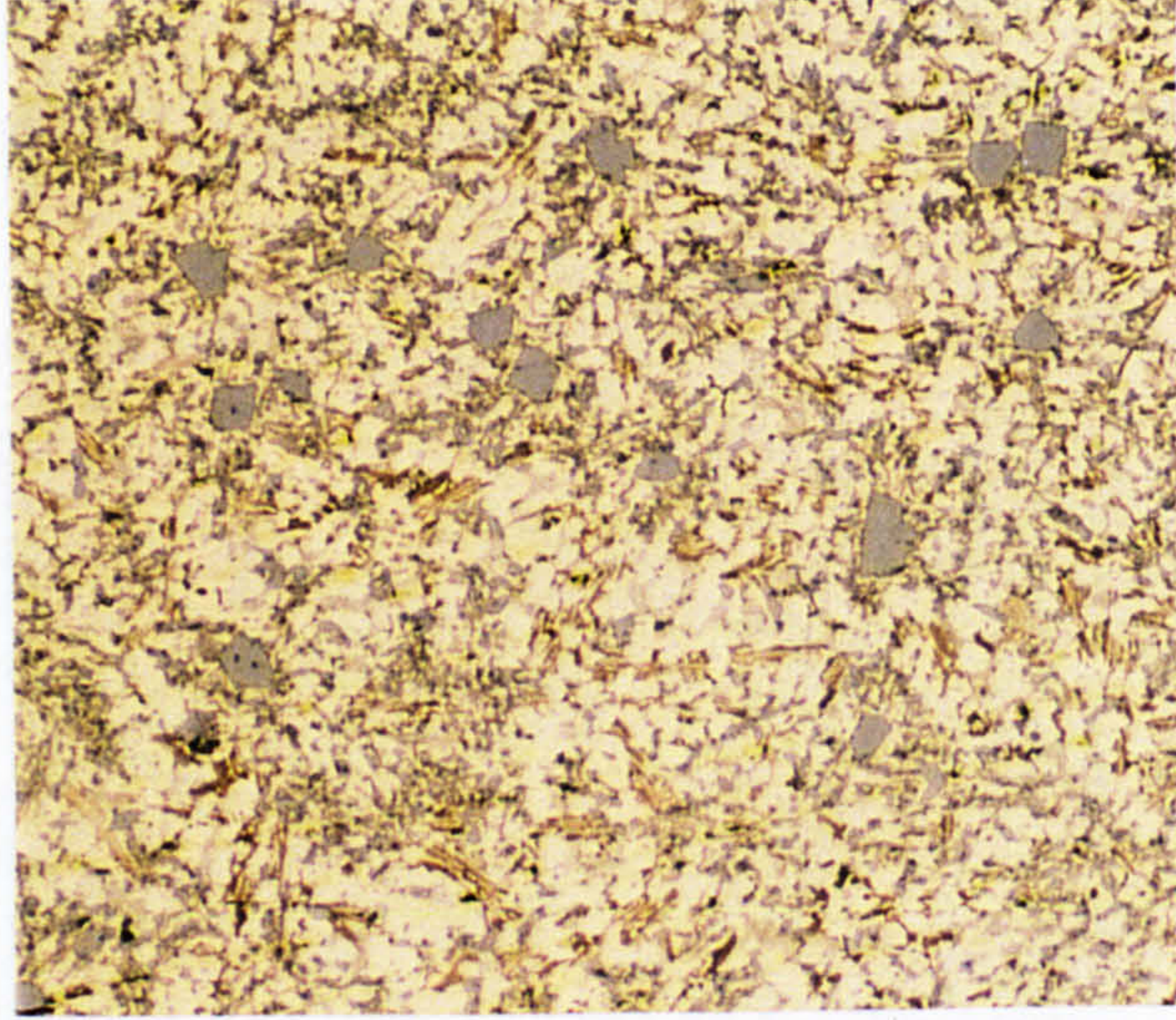
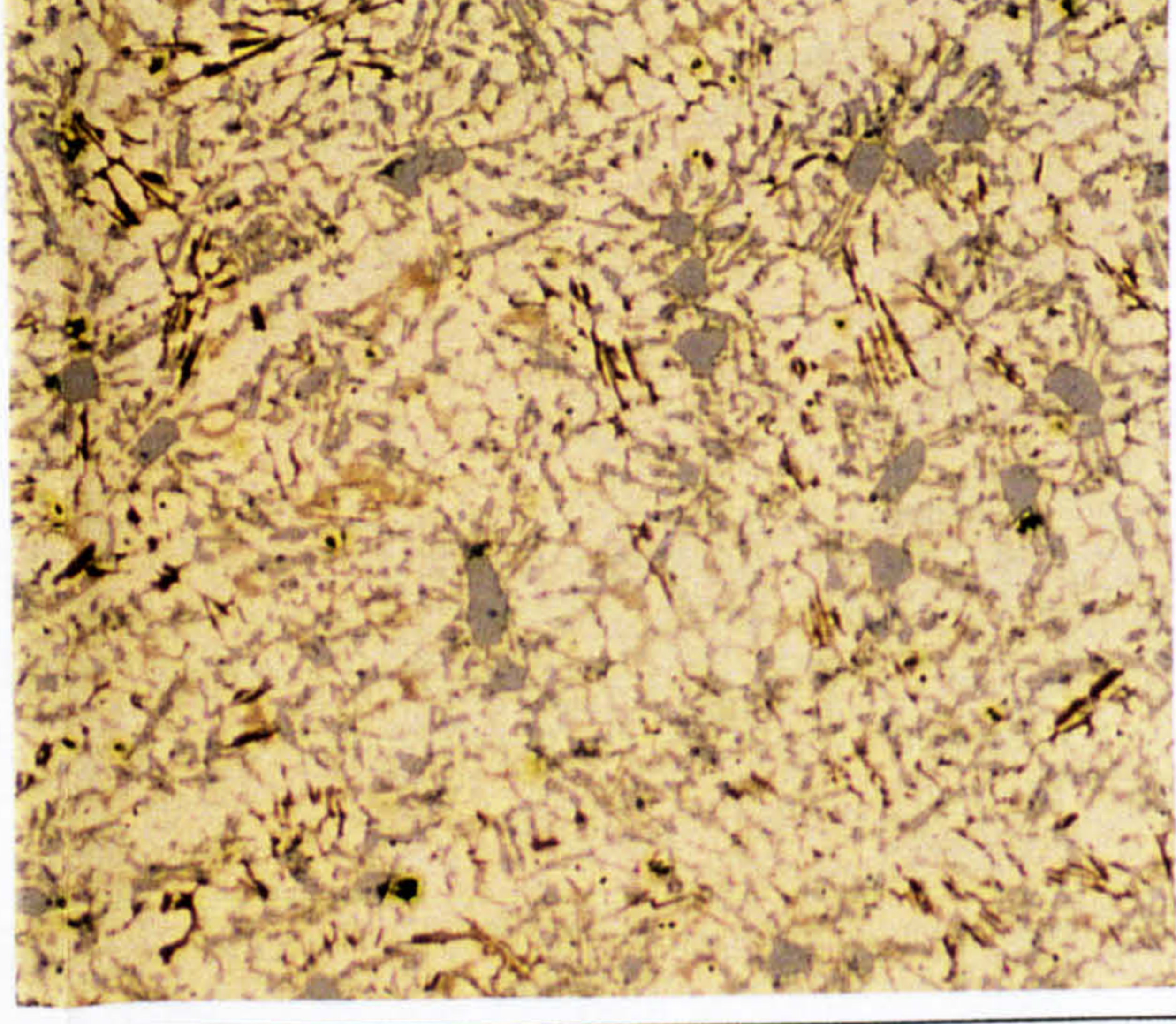
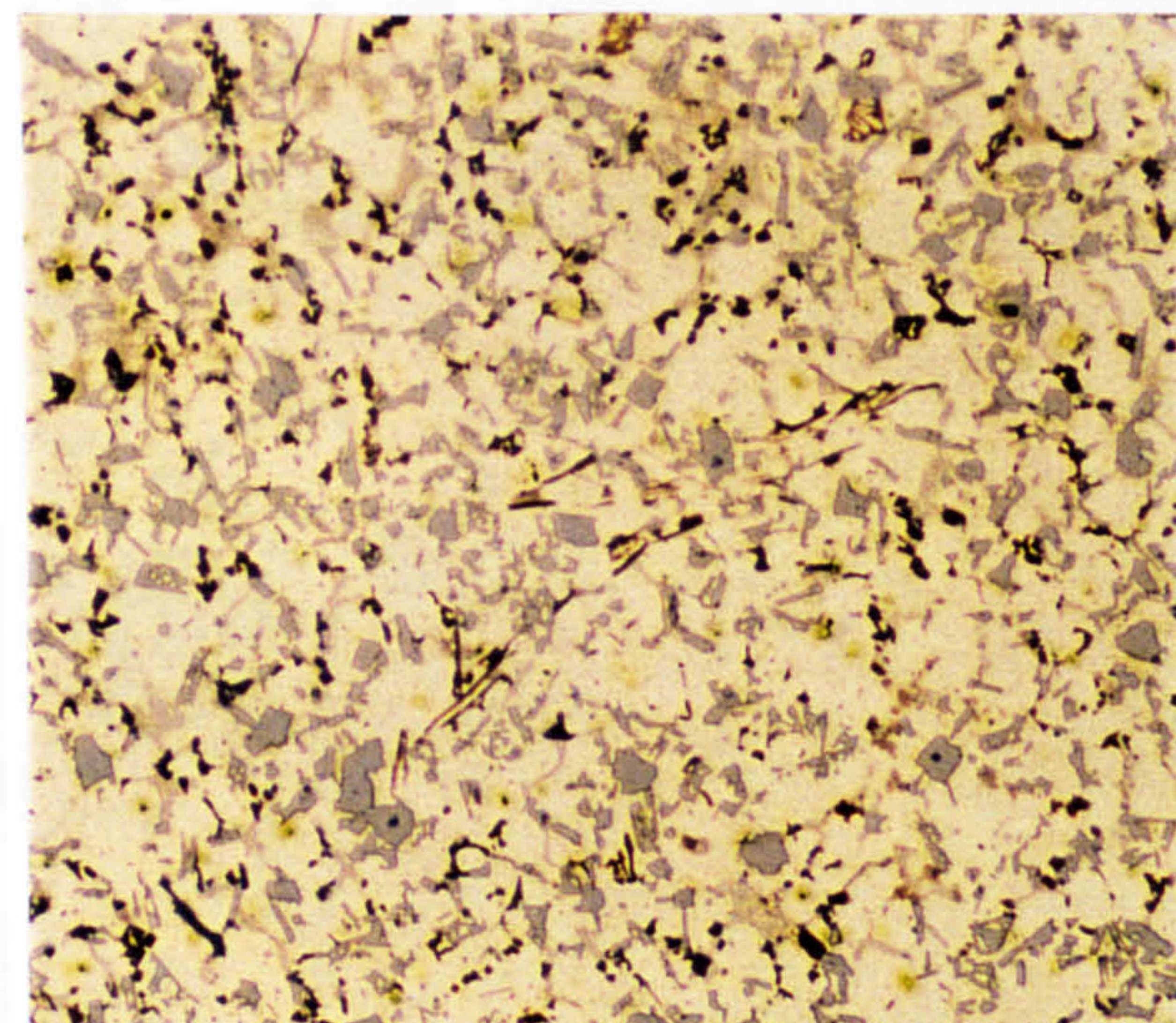
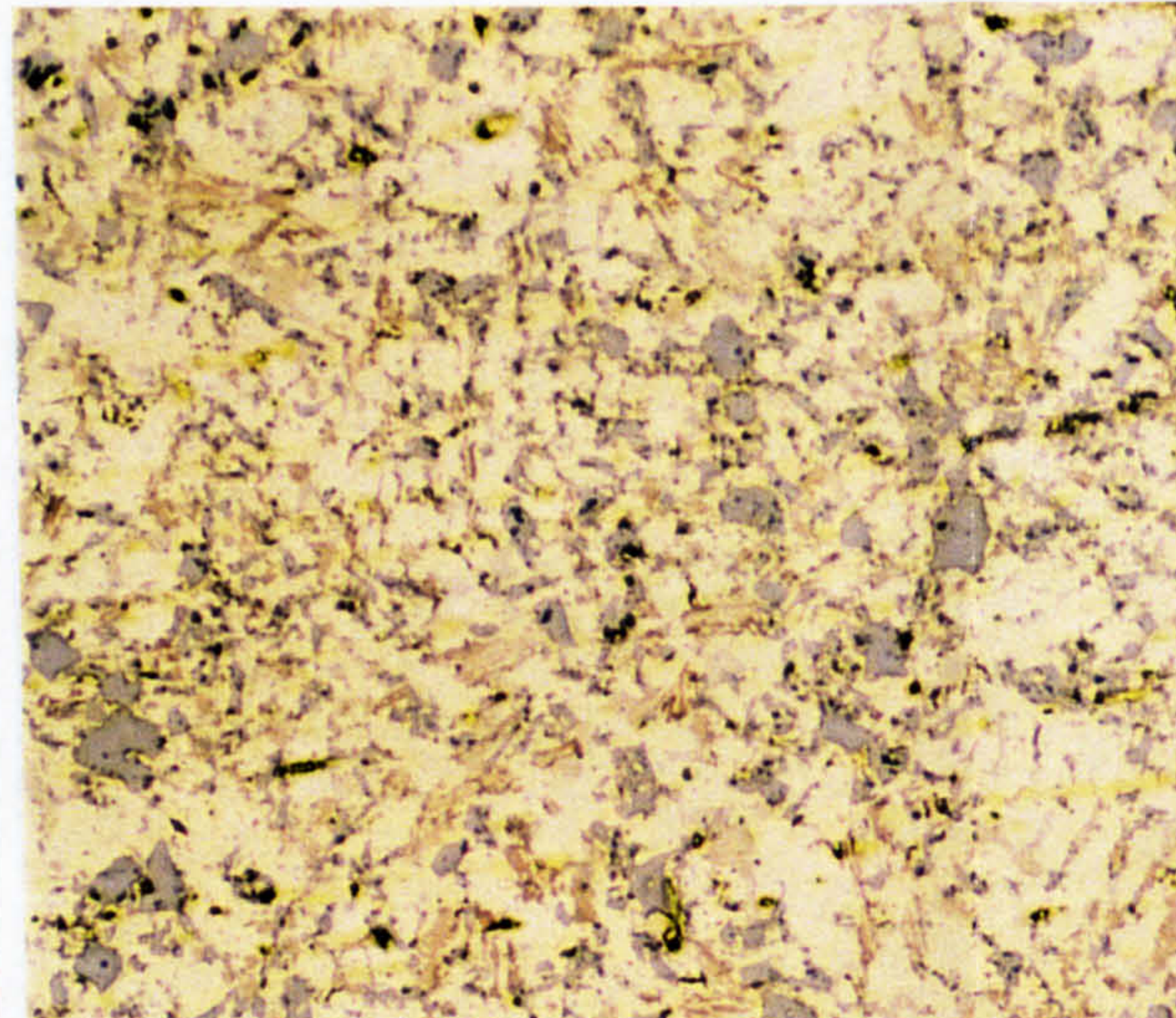
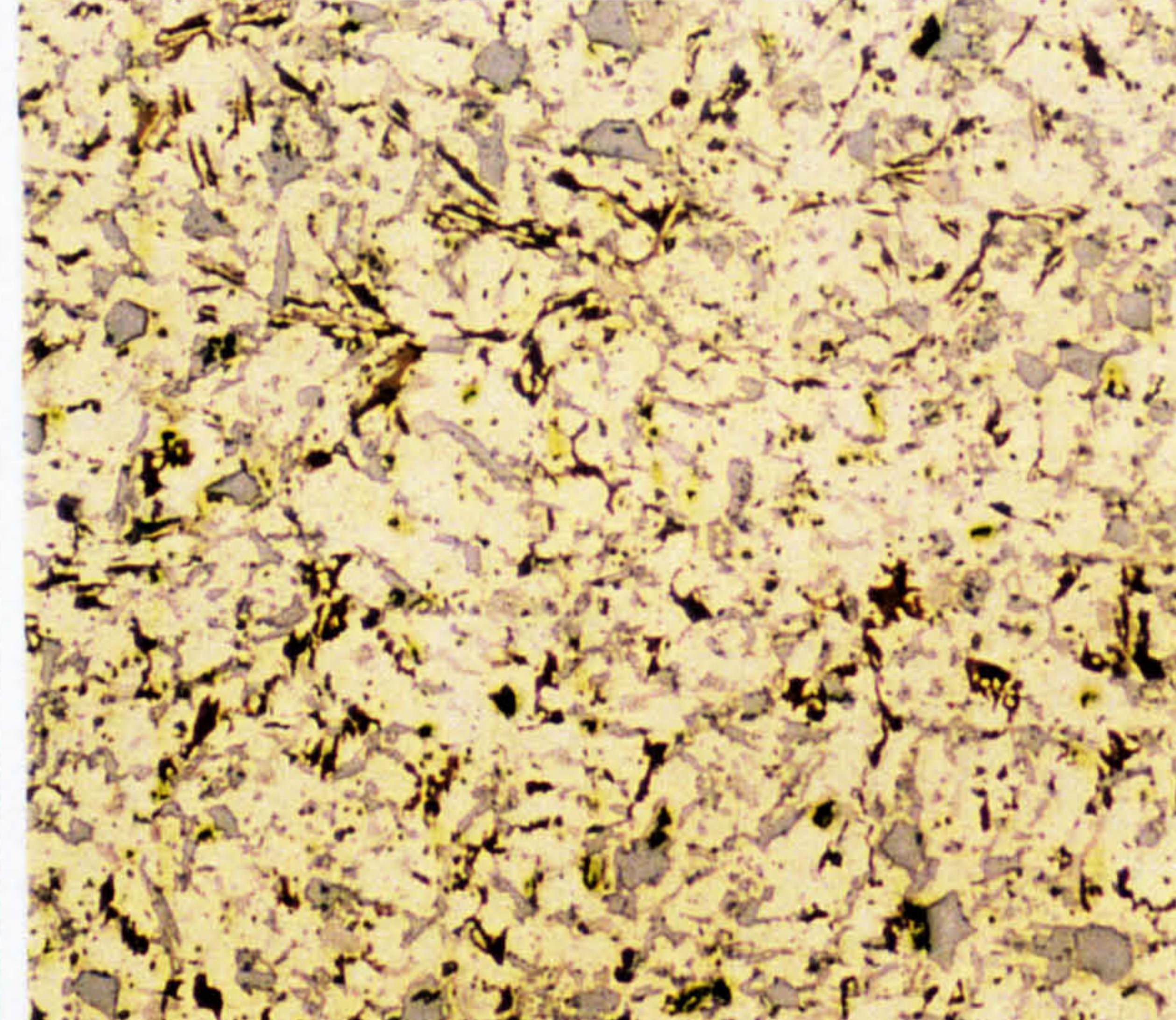
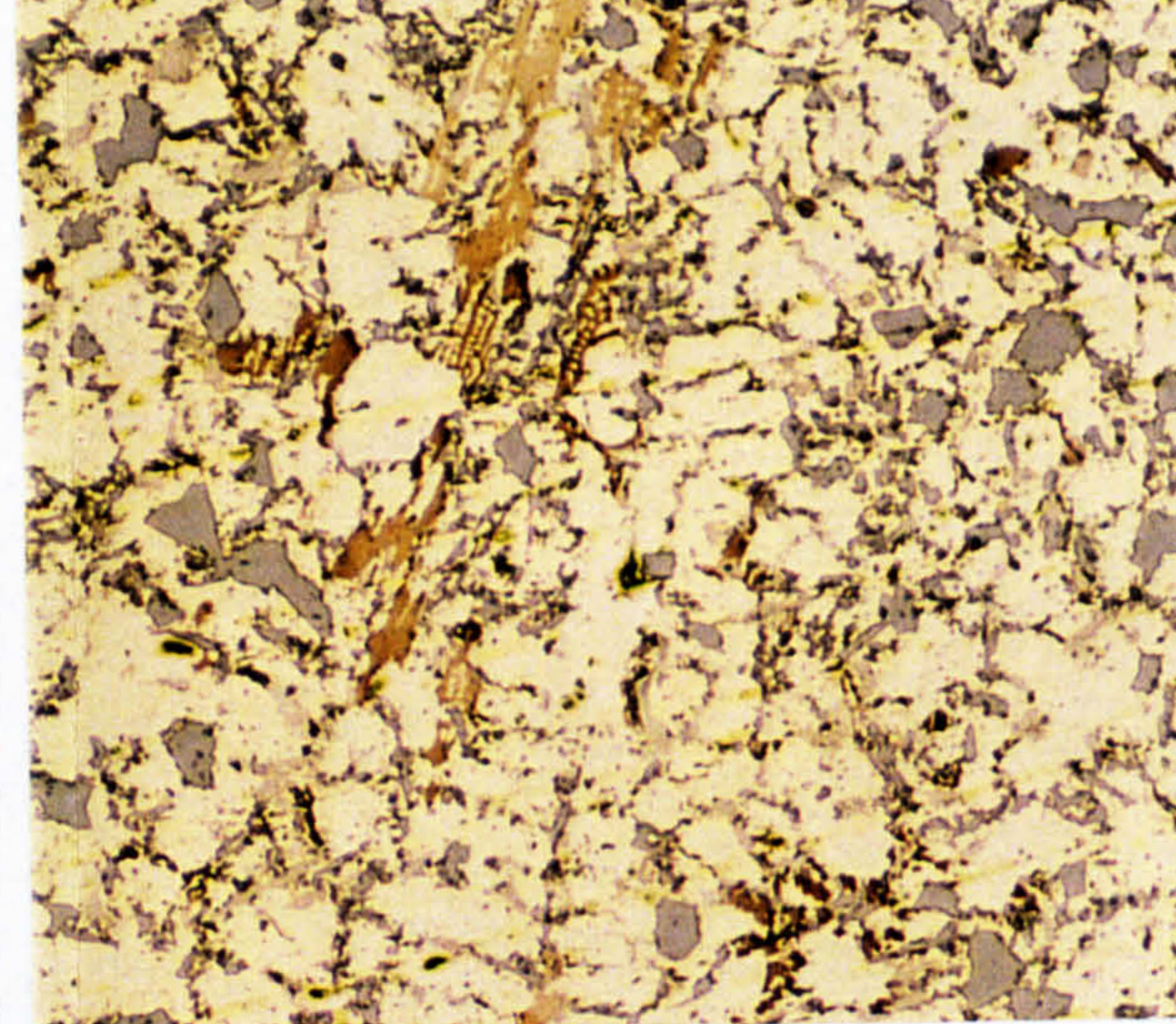
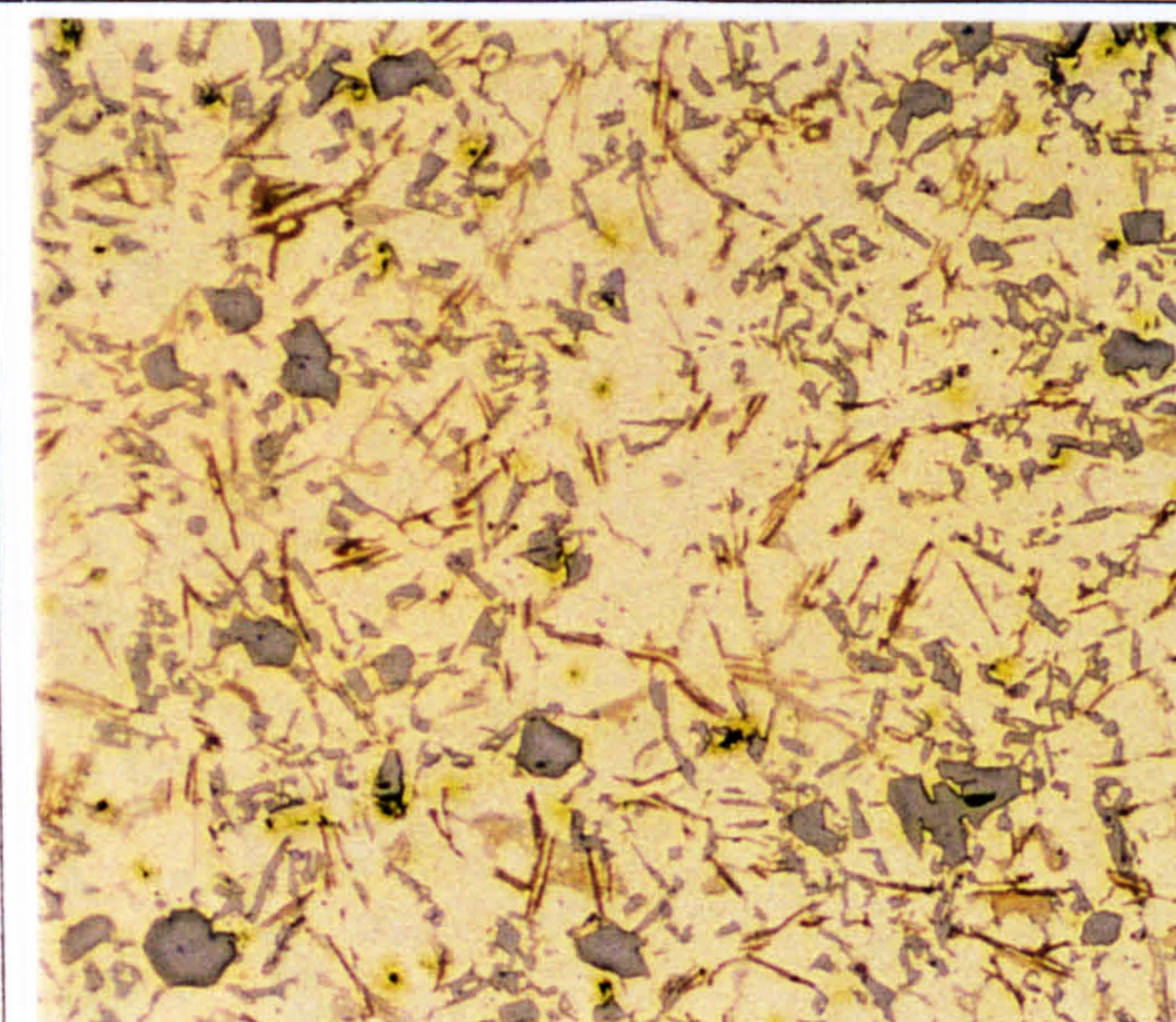
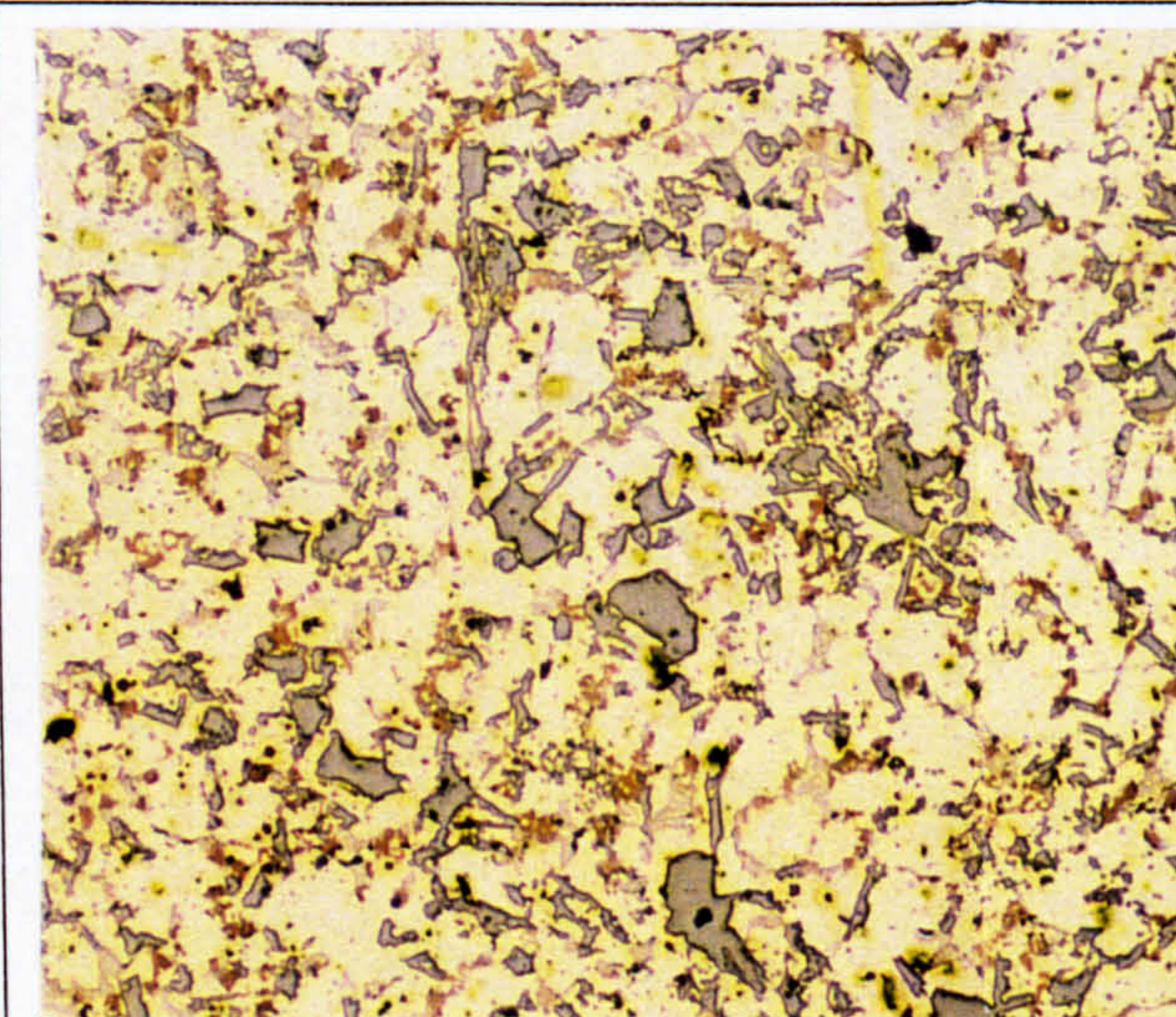
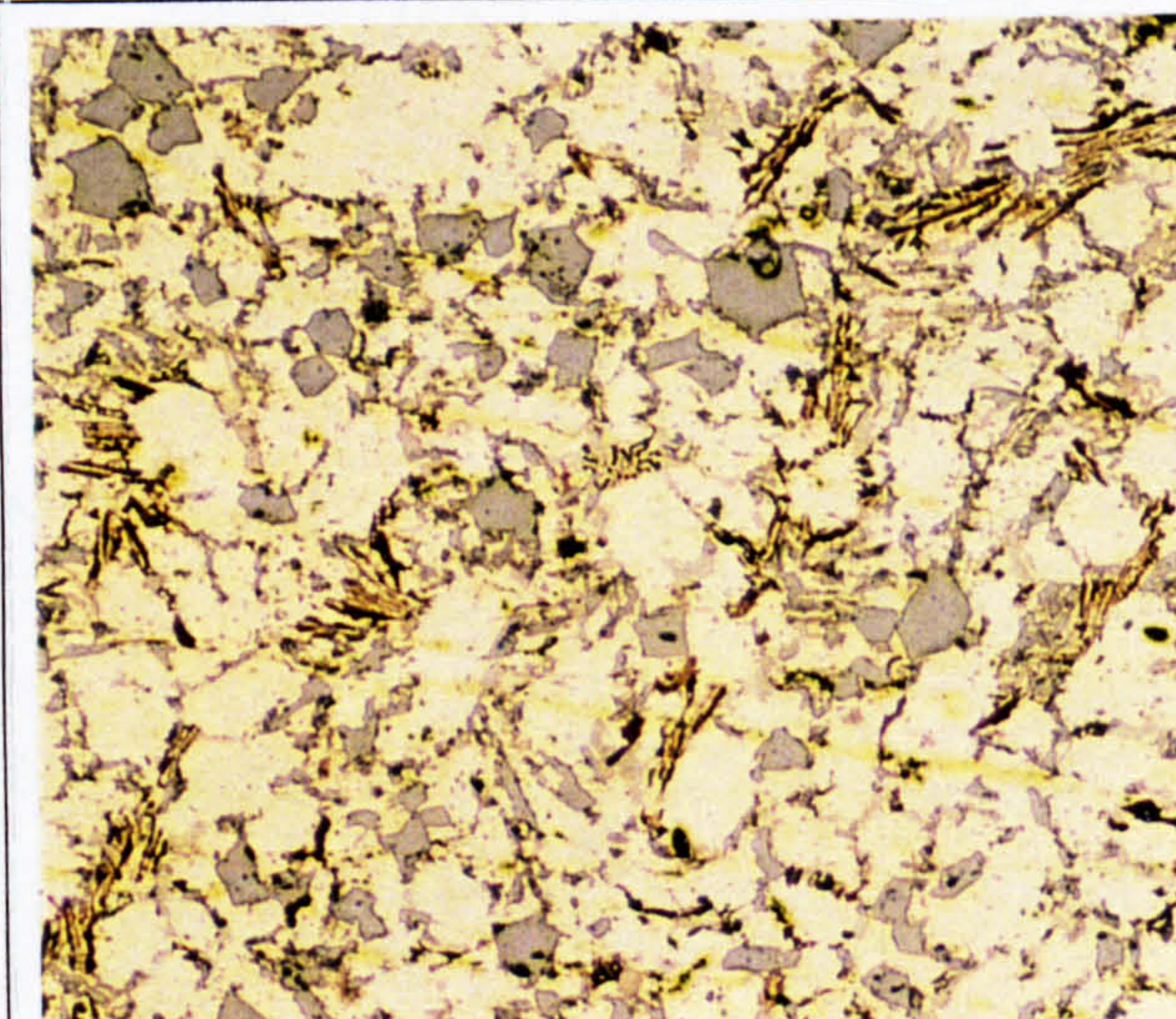
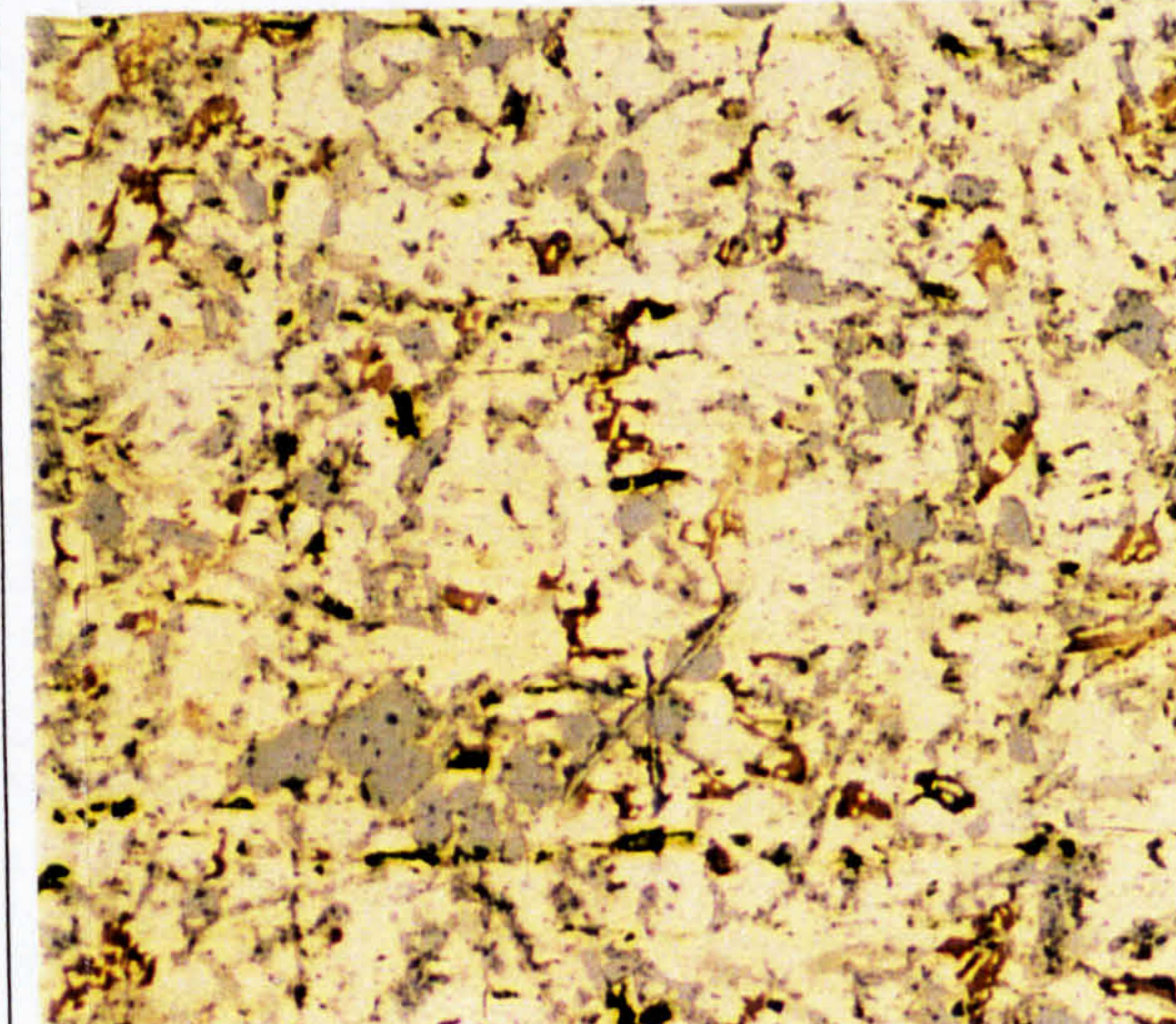
Step No.		Alloy 83	Alloy 84	Alloy 85	Alloy 86
1					
					
					

Figure 6.16 Micrographs of stepped mould model alloys 83 to 86, cast at 440 °C mould temperature

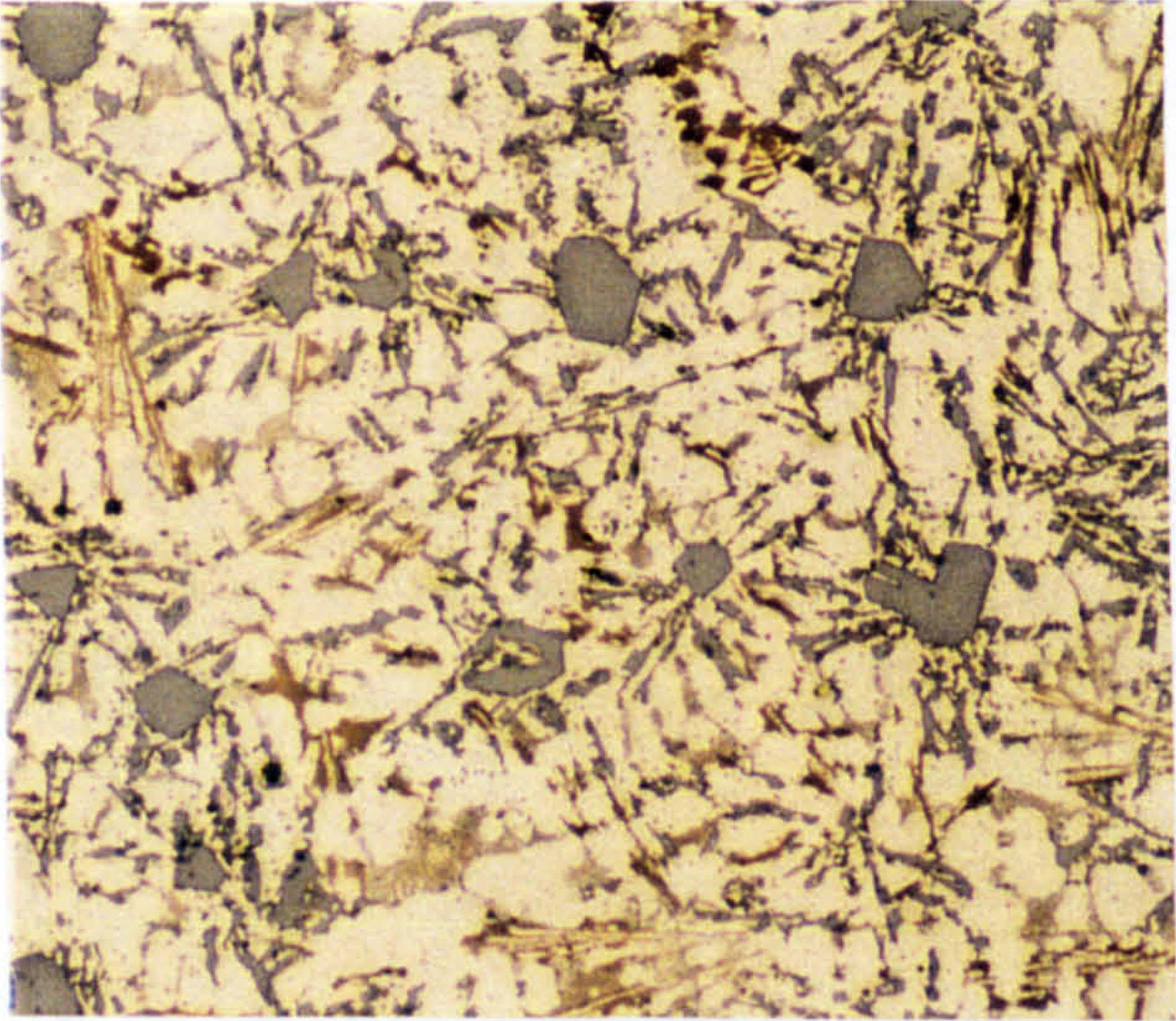
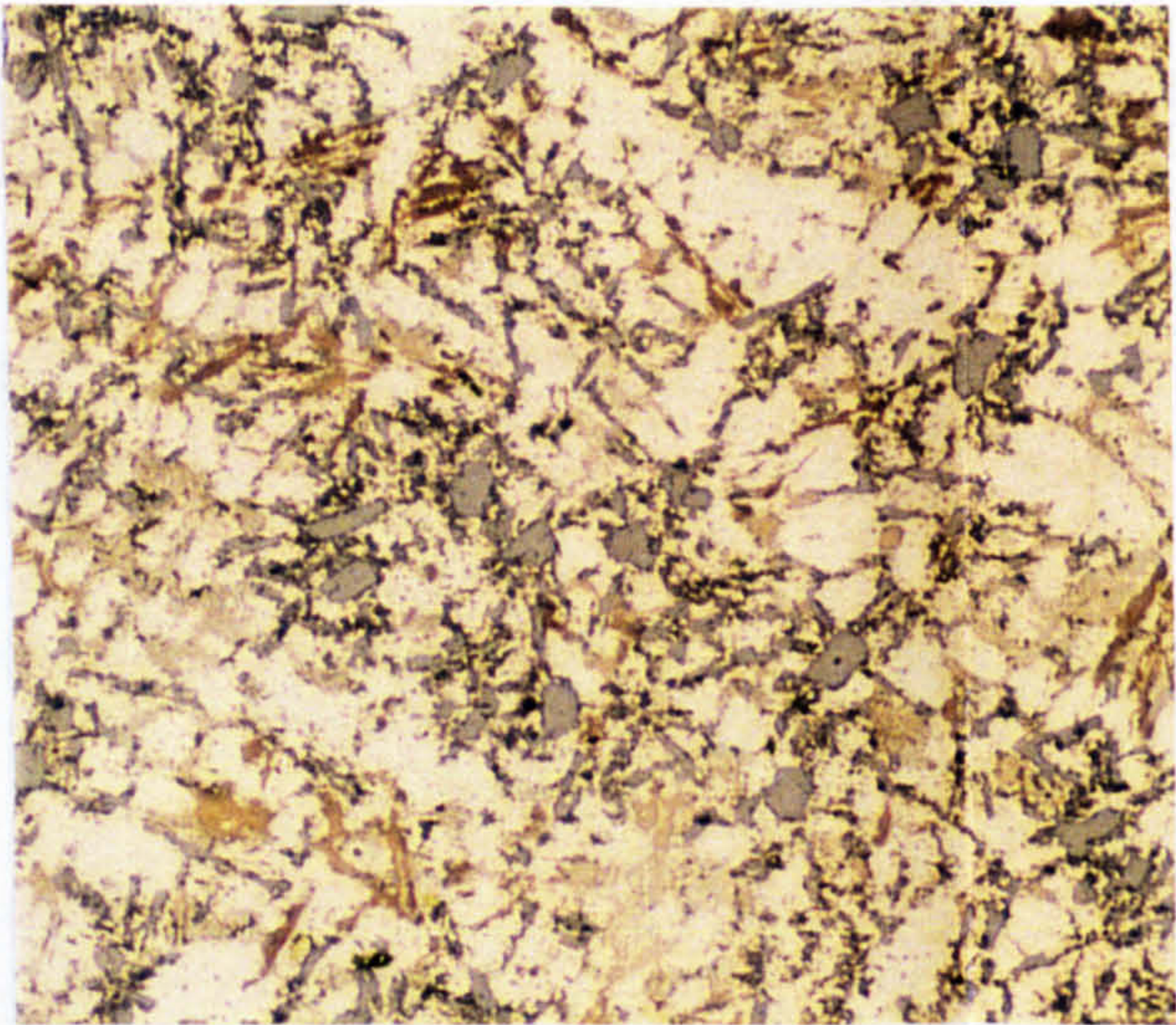
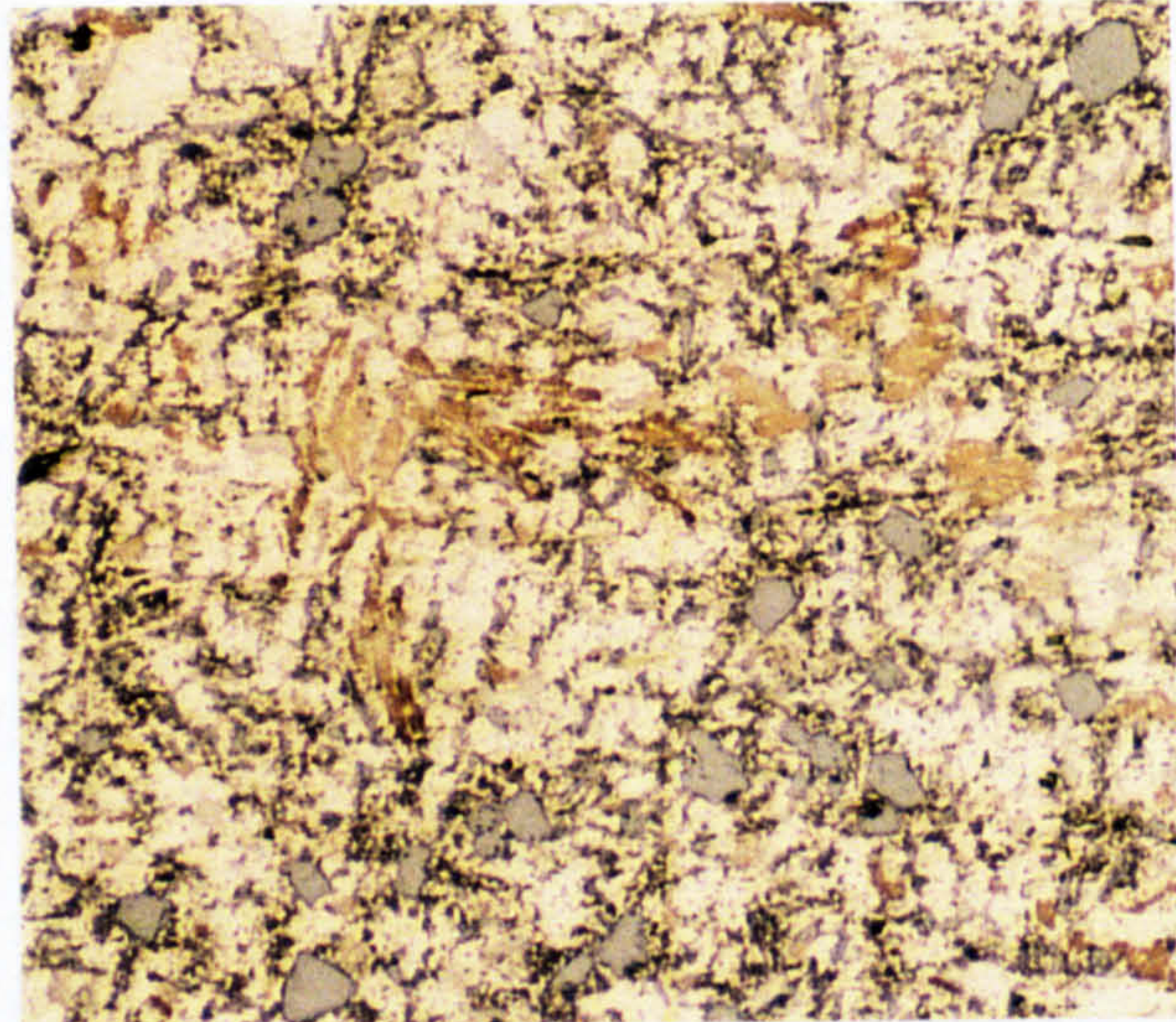
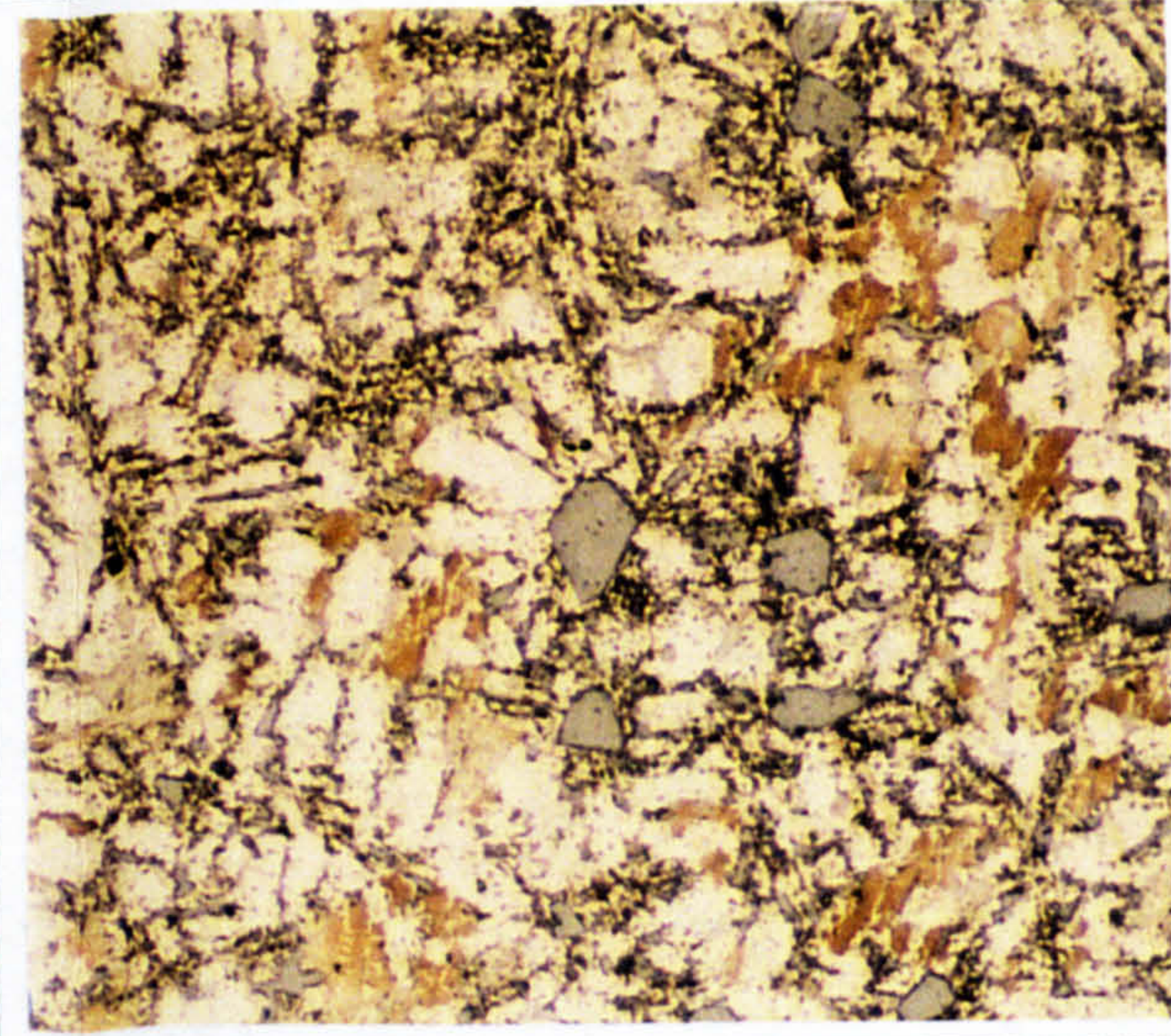
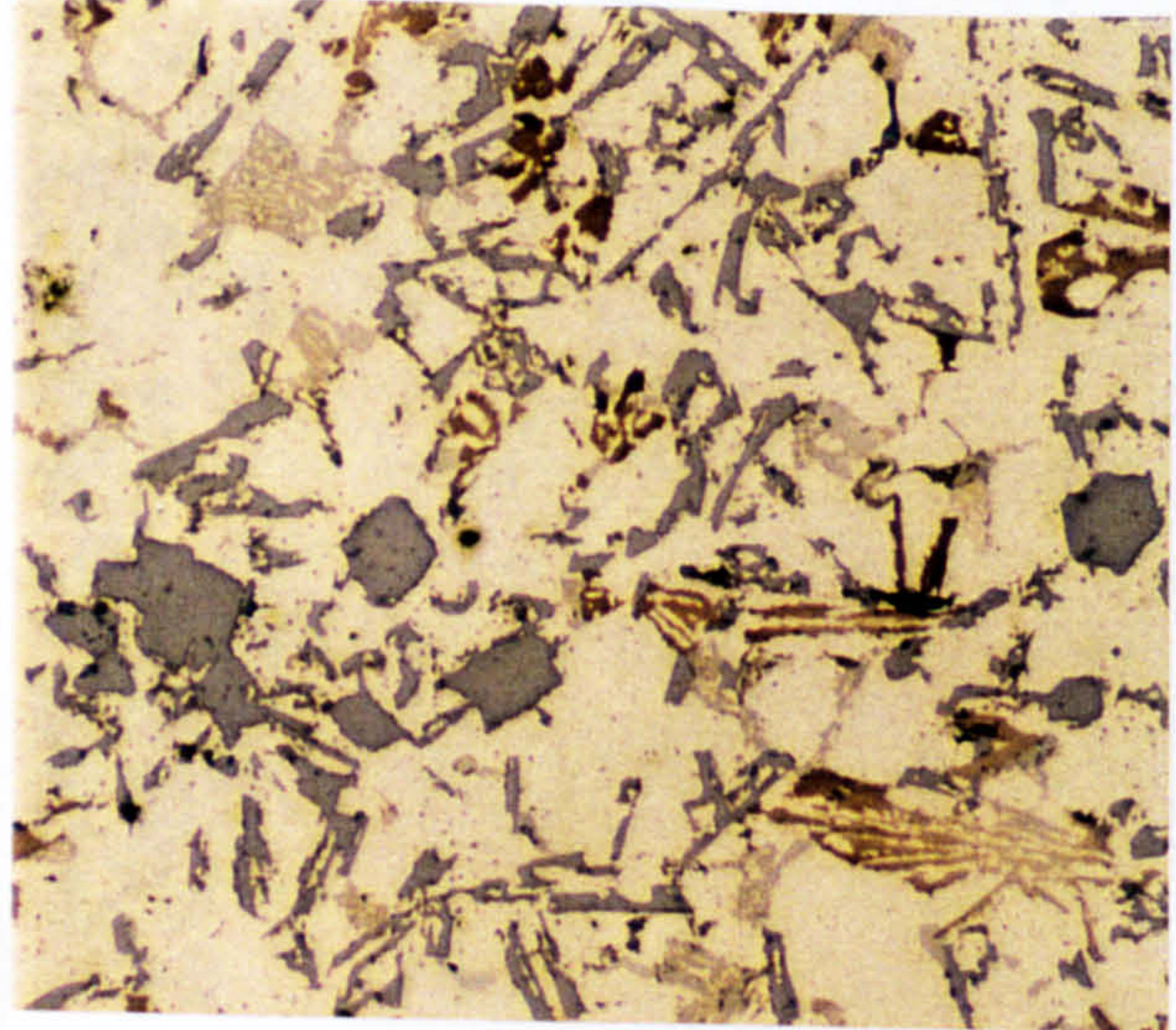
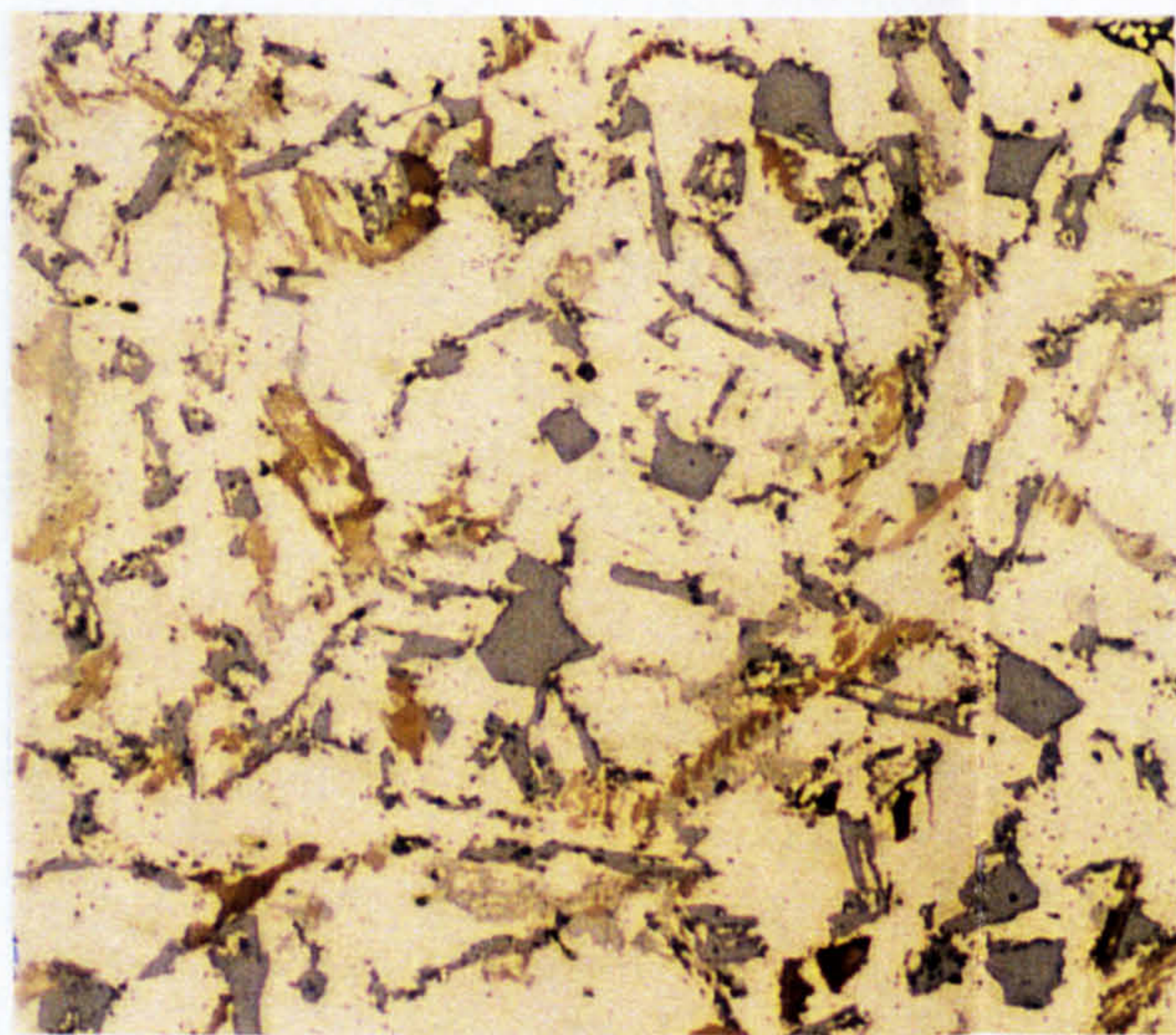
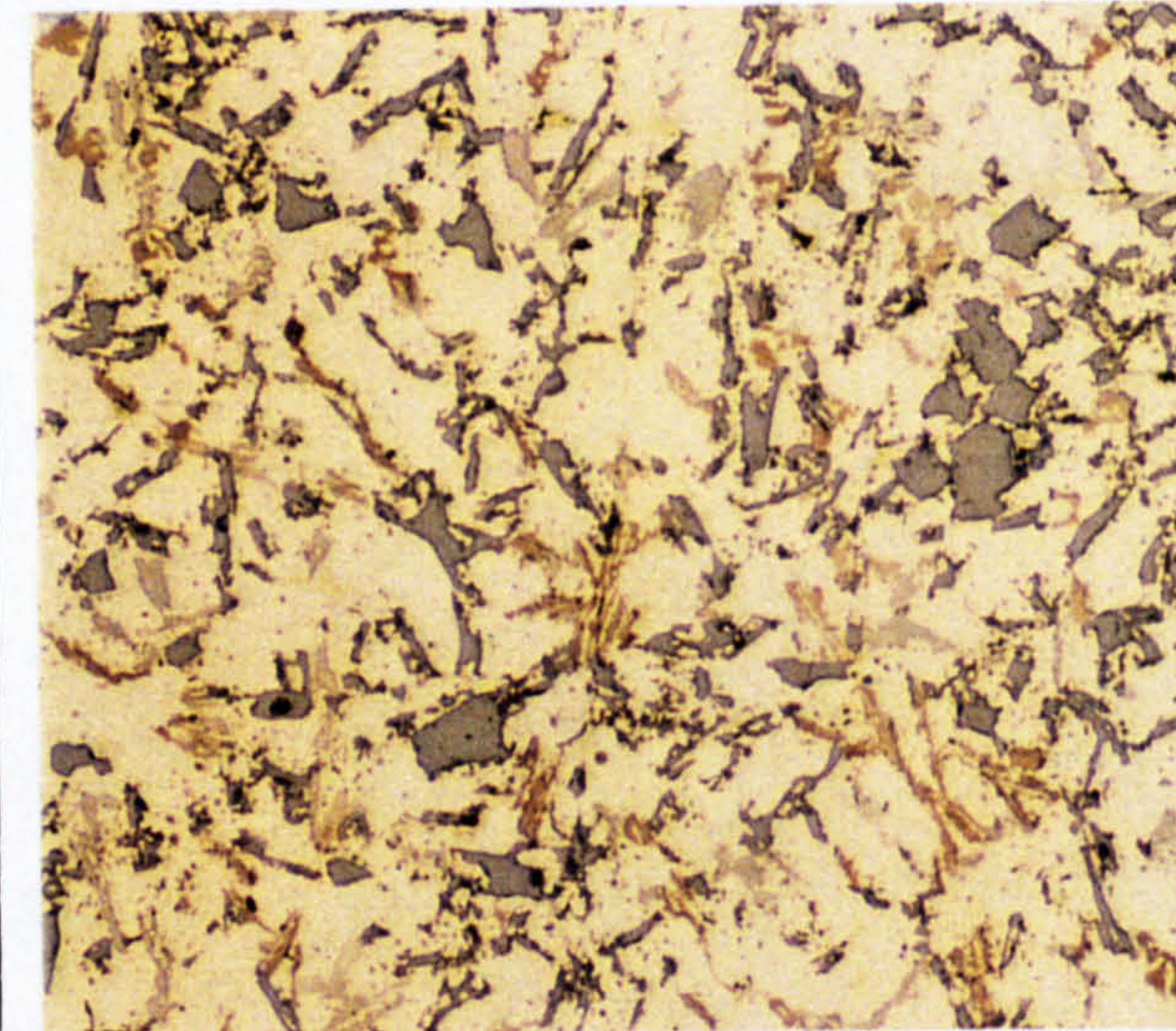
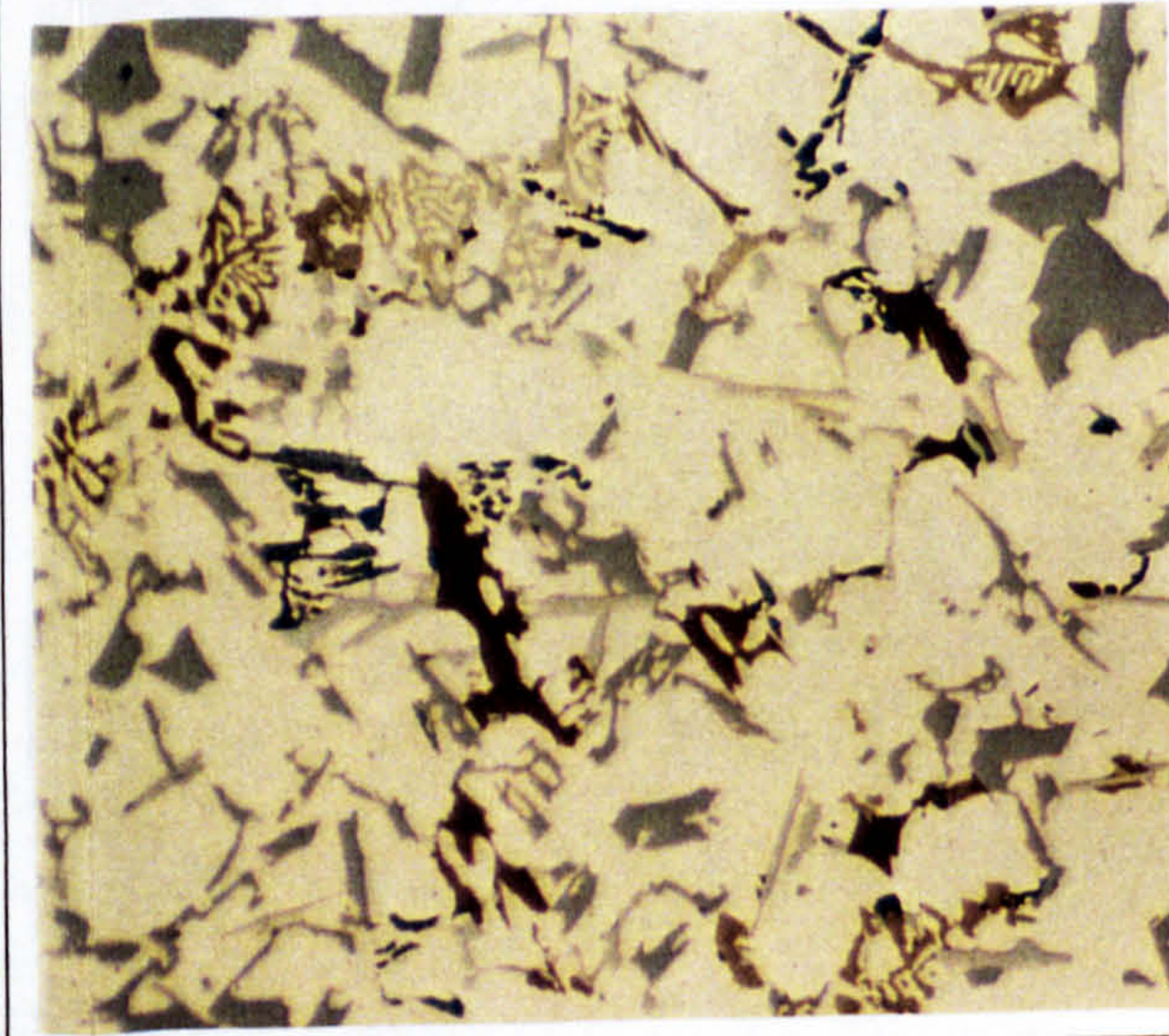
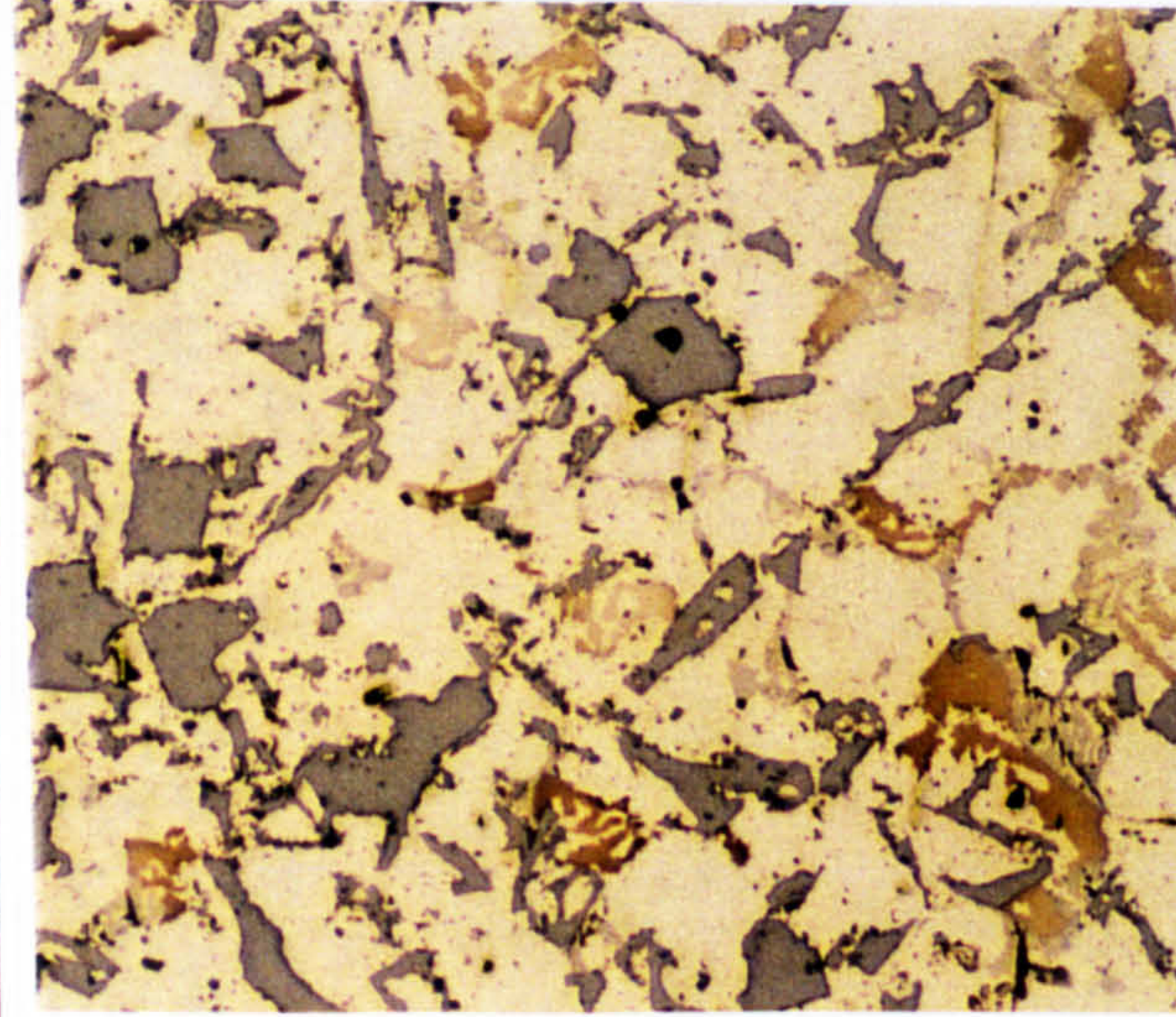
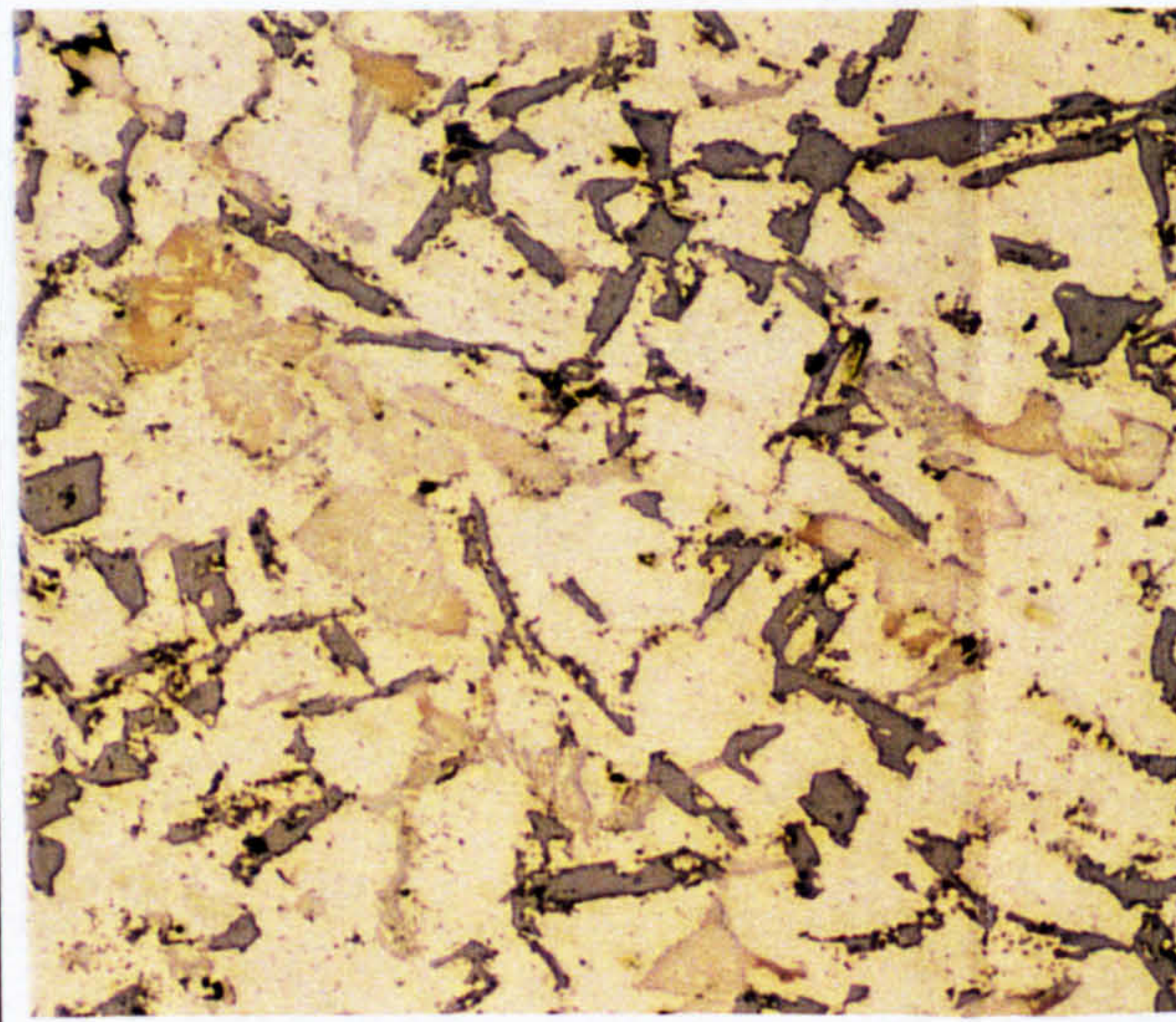
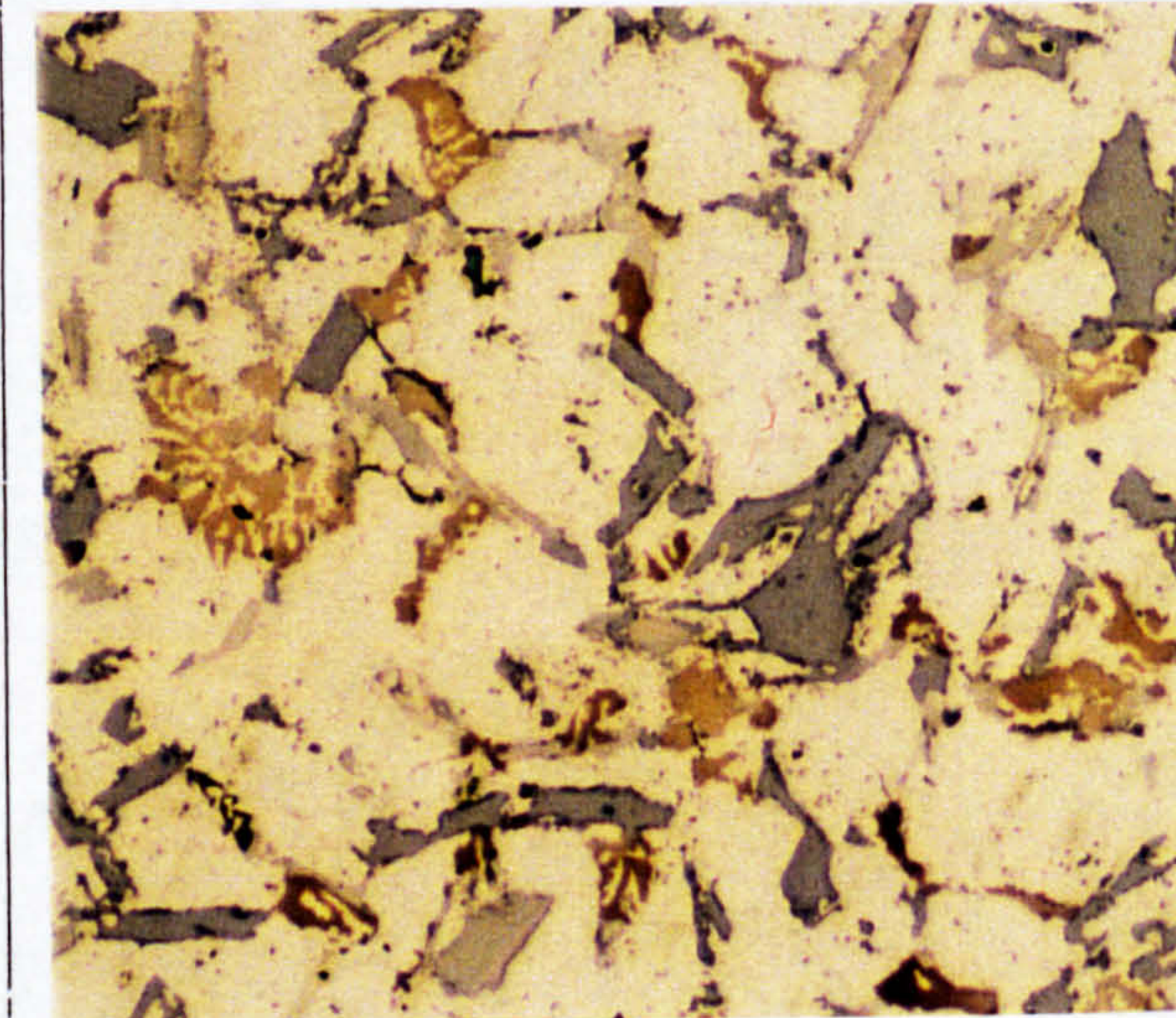
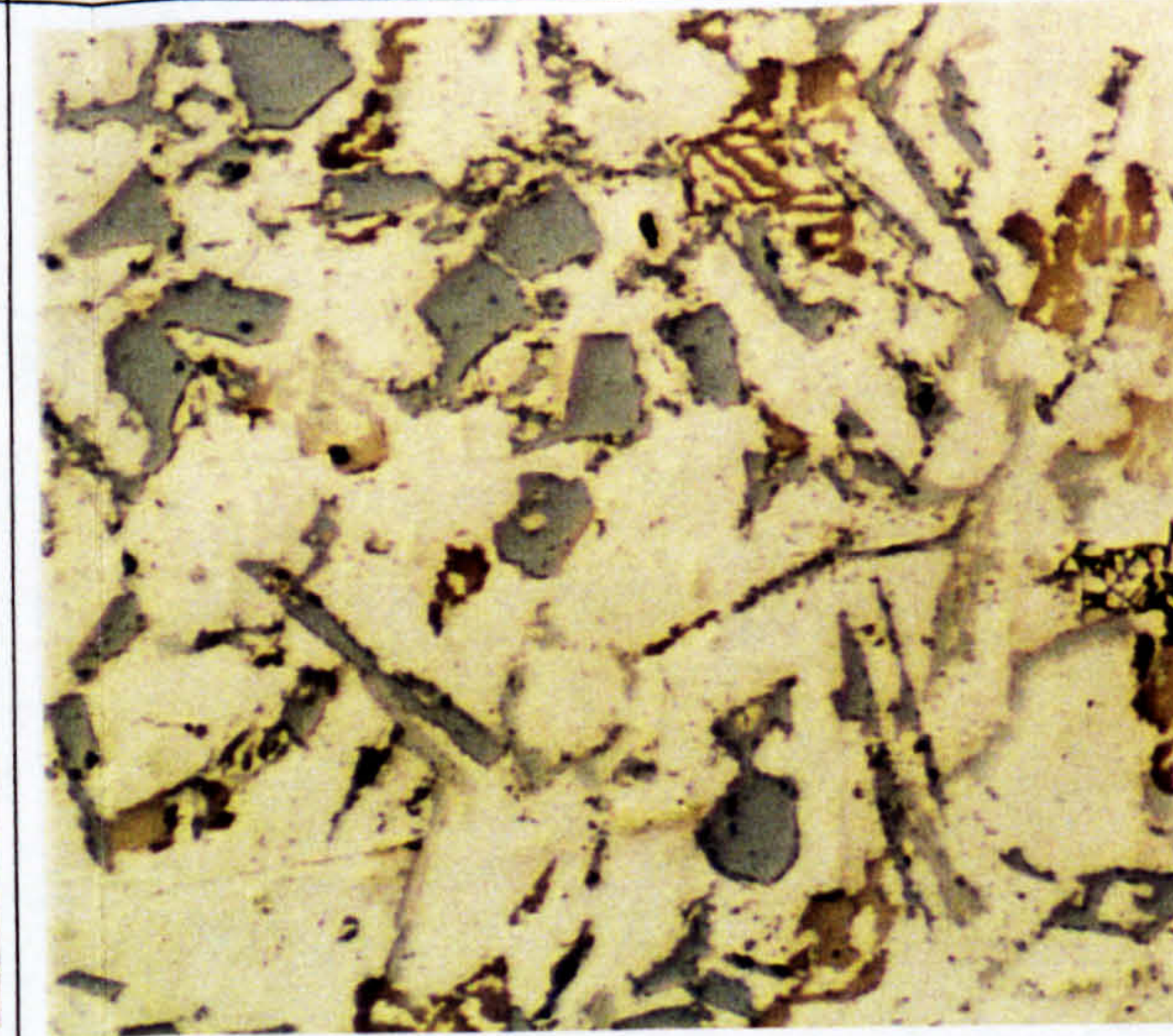
Step No.		Alloy 83	Alloy 84	Alloy 85	Alloy 86
1					
					
					

Figure 6.17 Micrographs of stepped mould model alloys 87 to 90, cast at 100 °C mould temperature

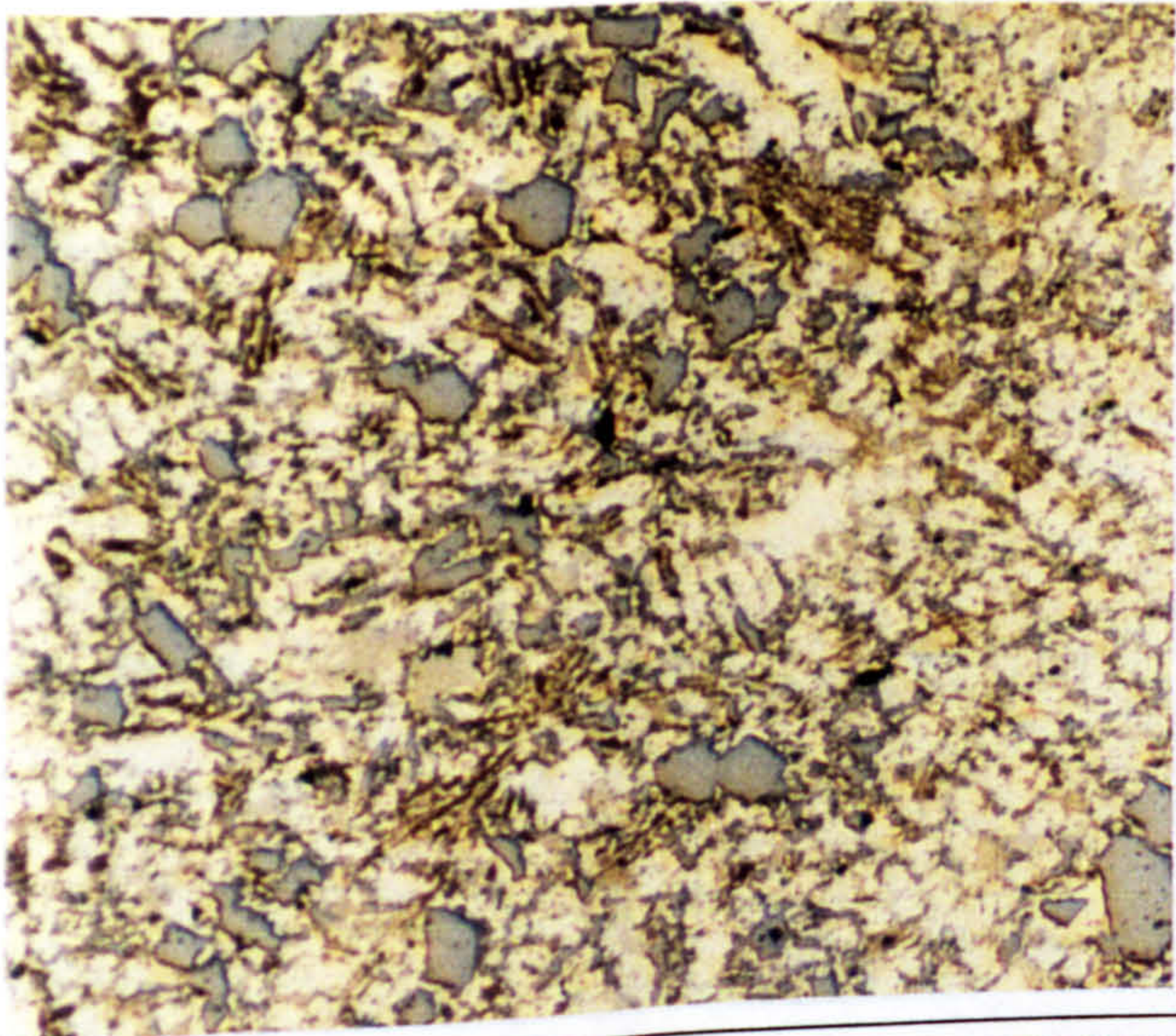
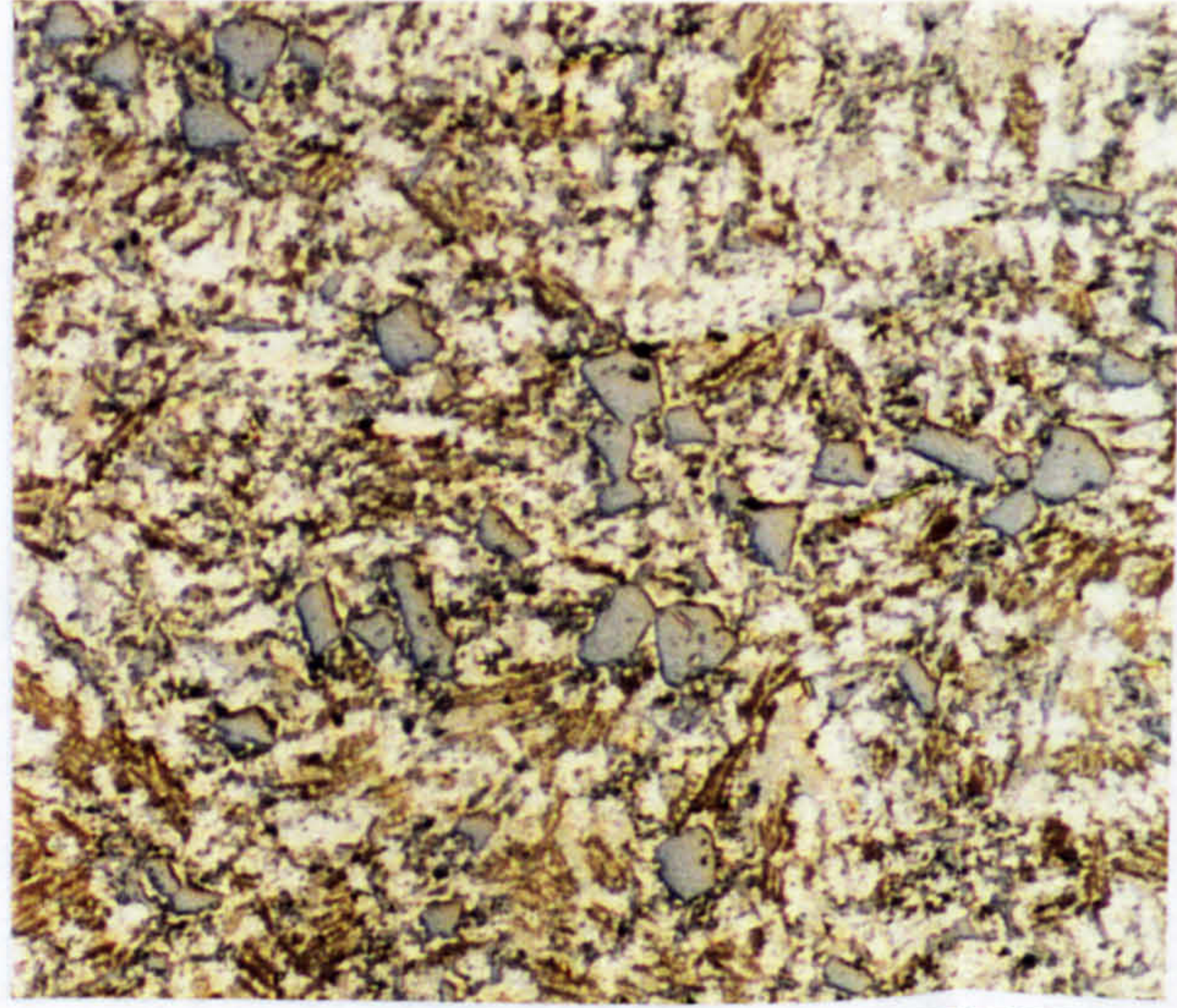

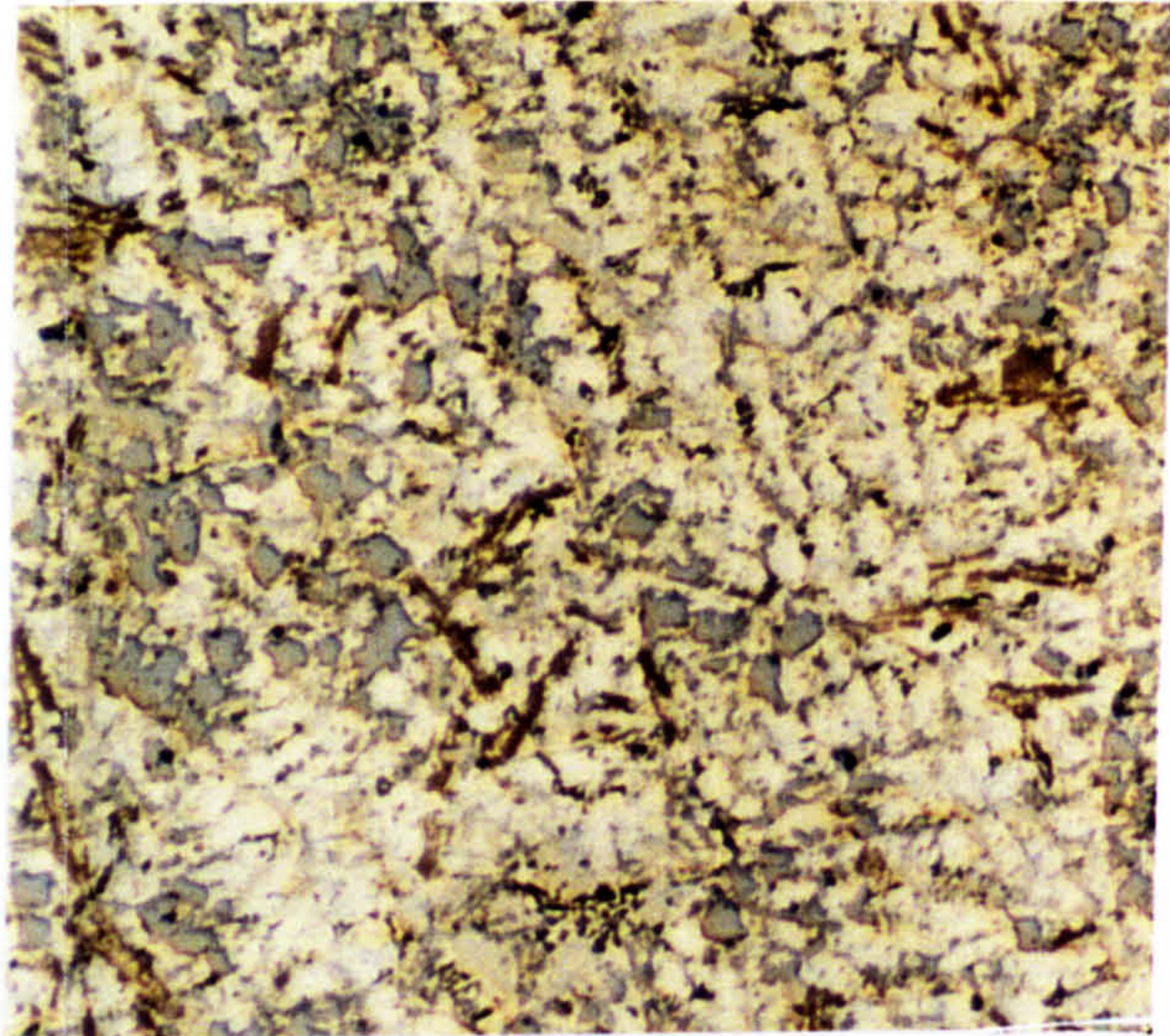
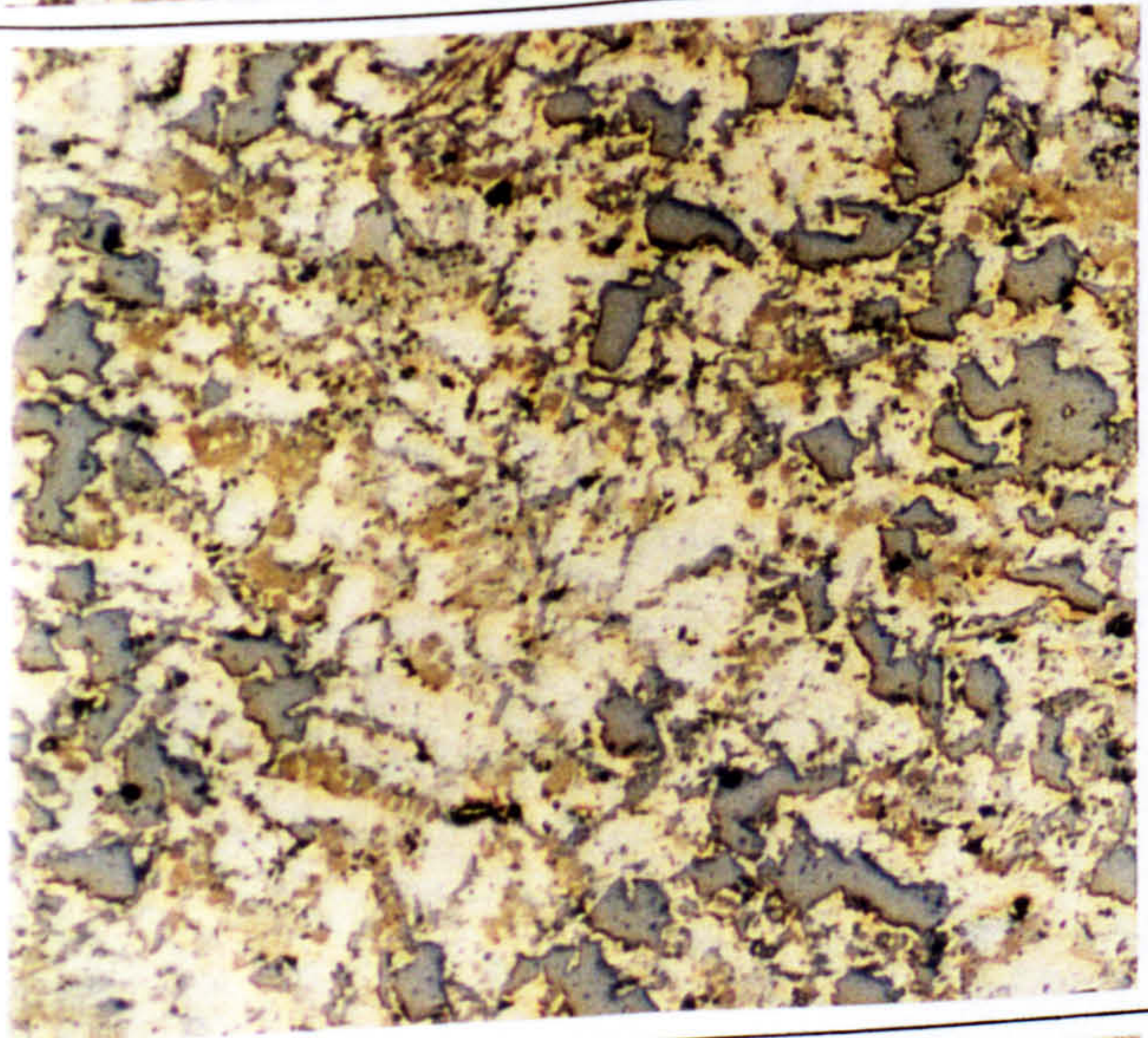
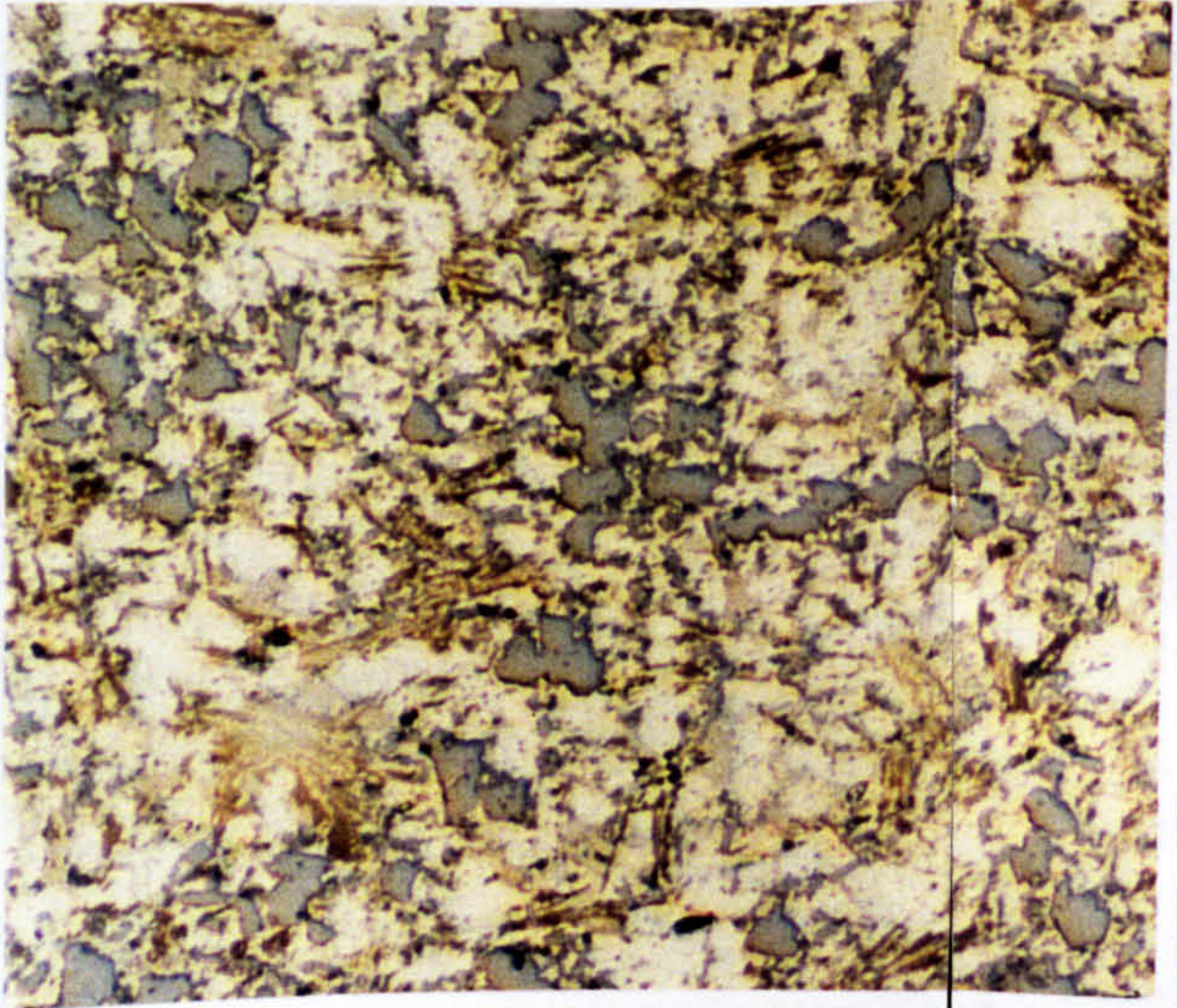
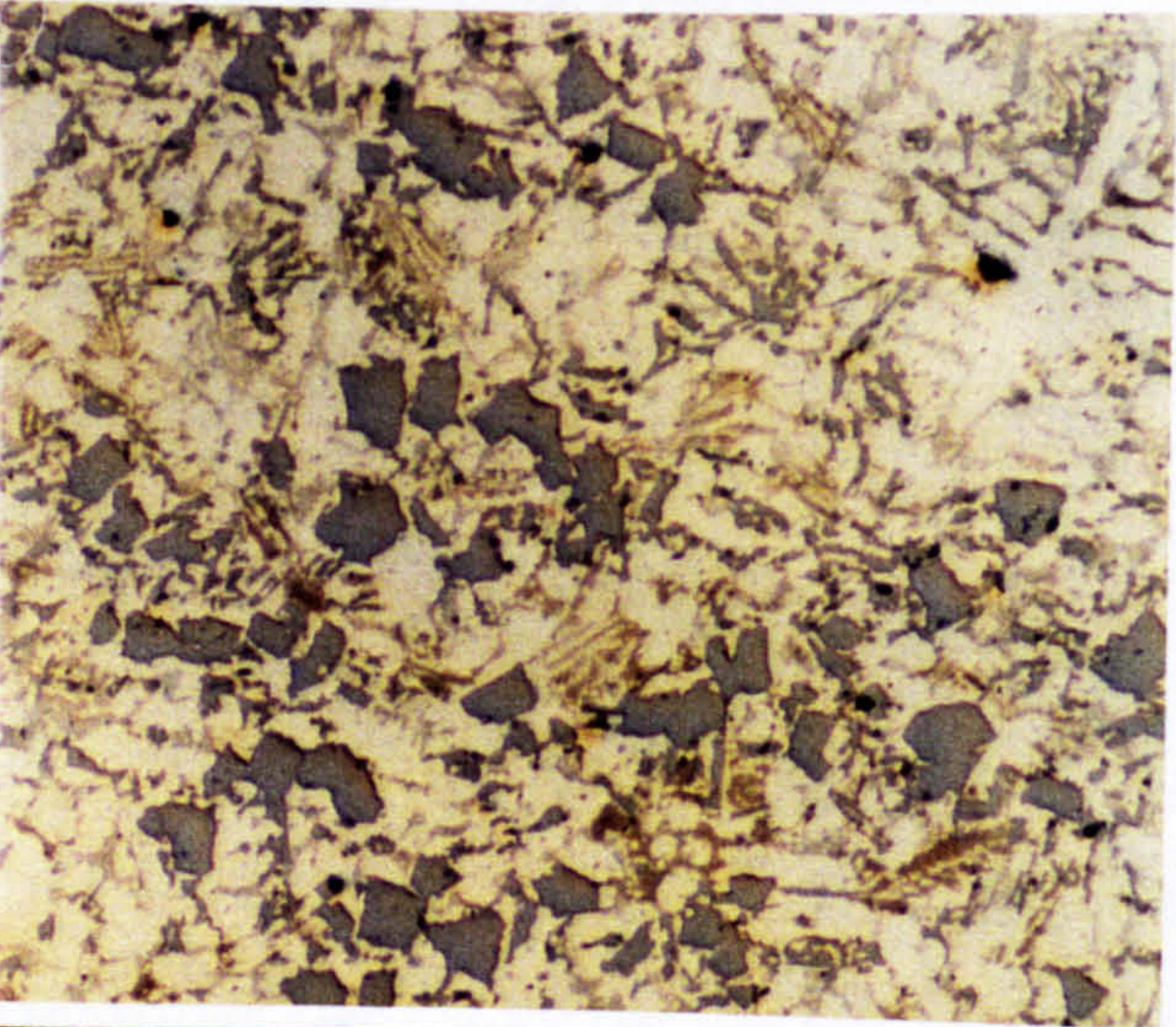
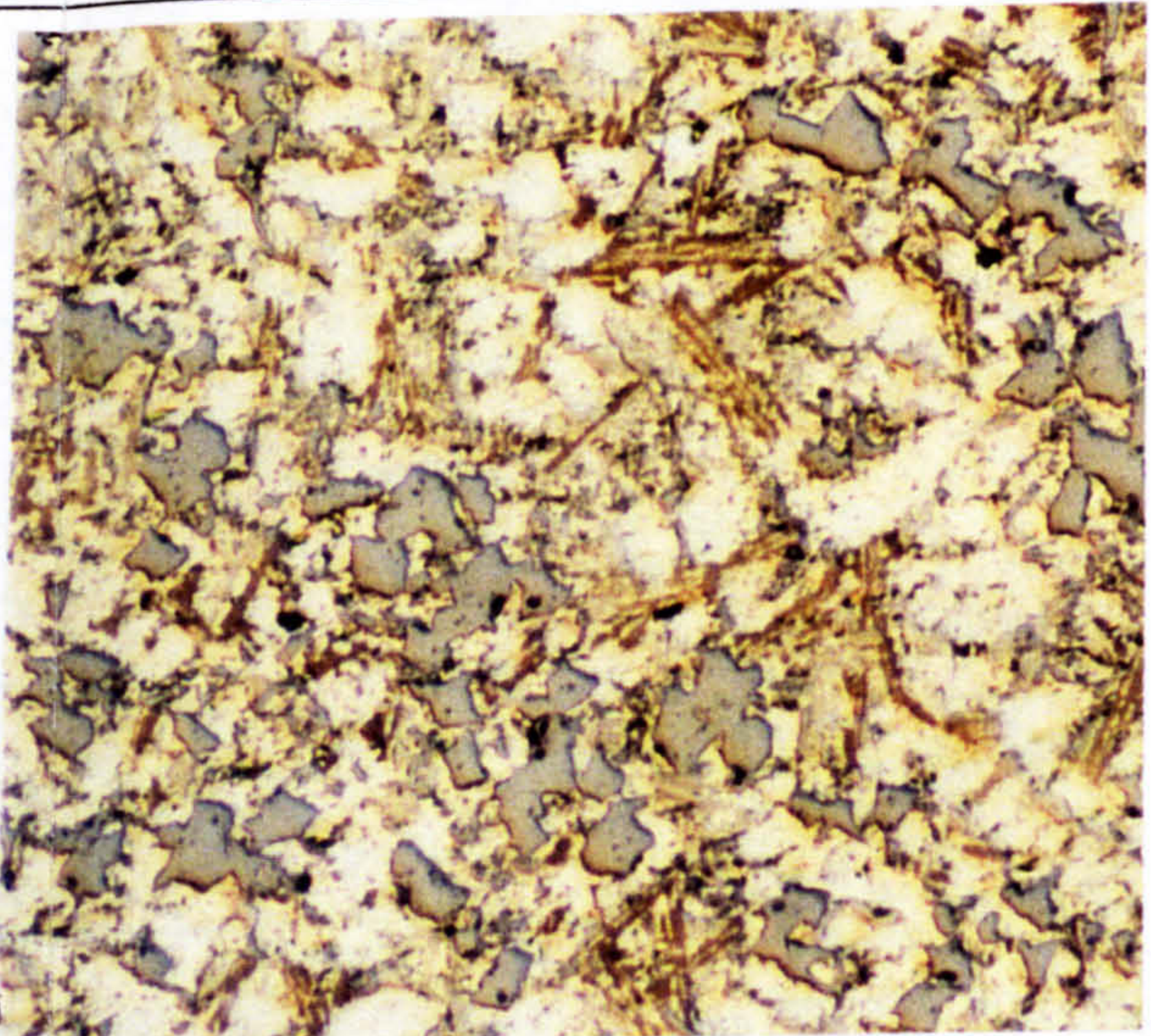
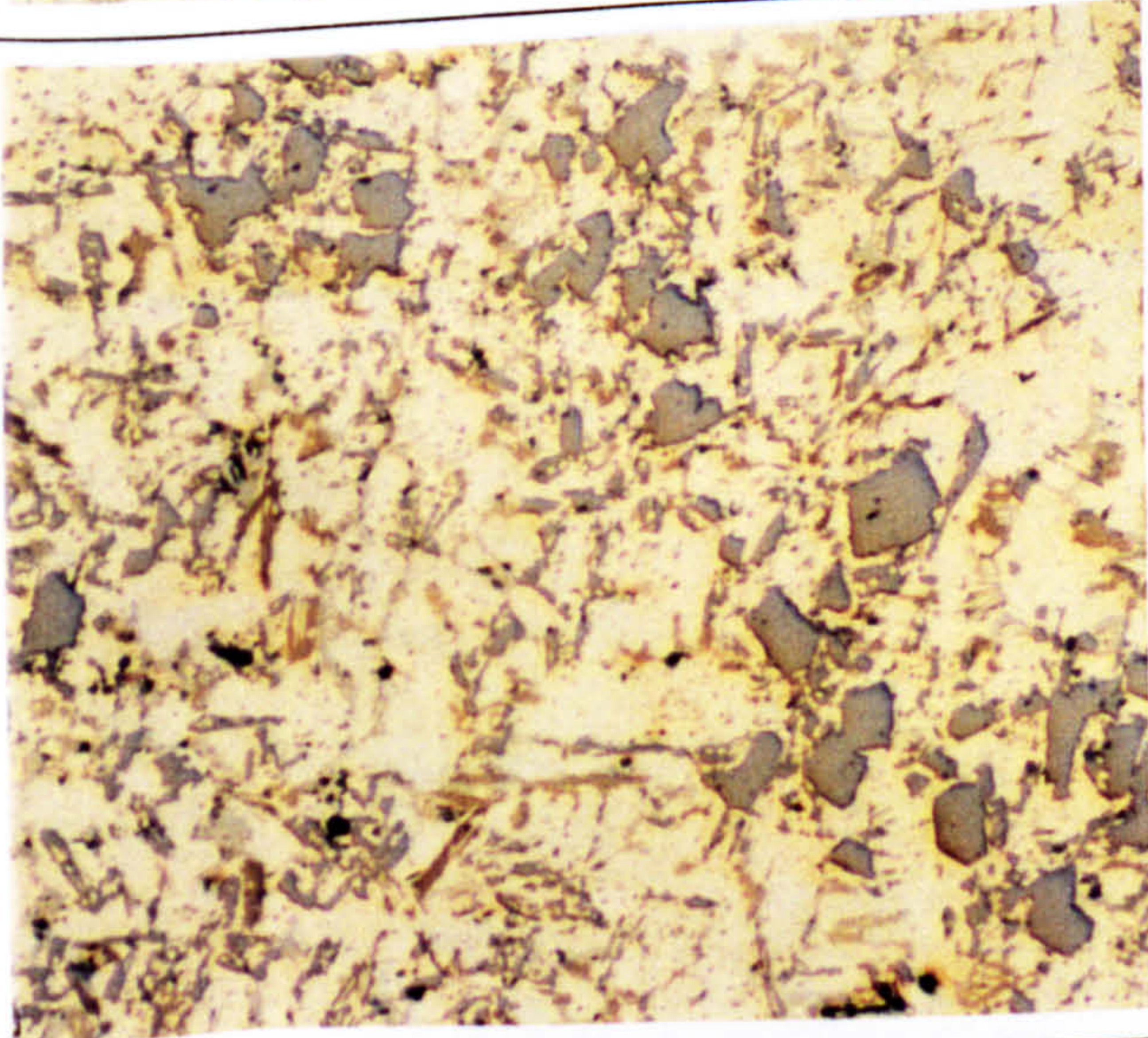
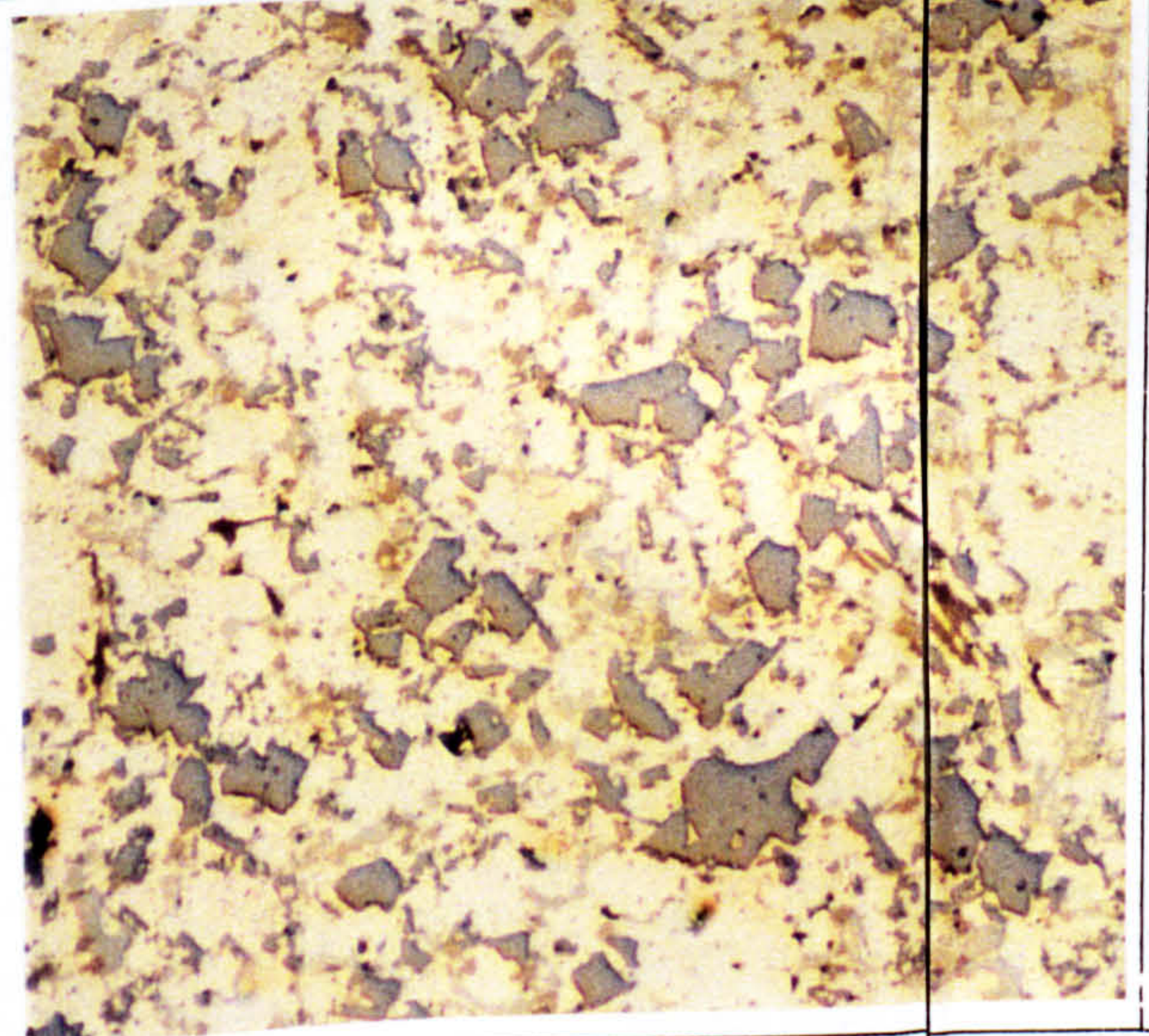
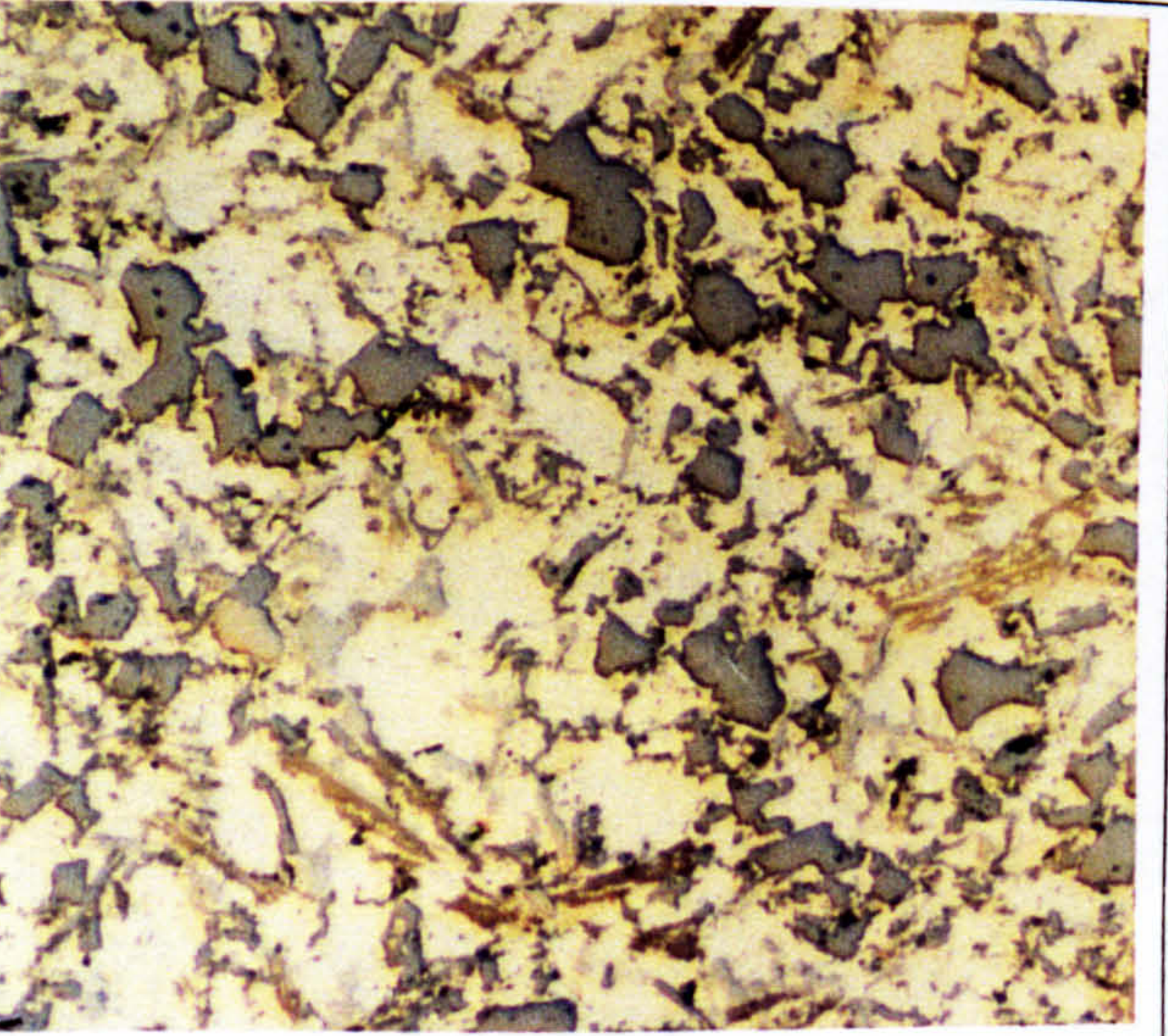
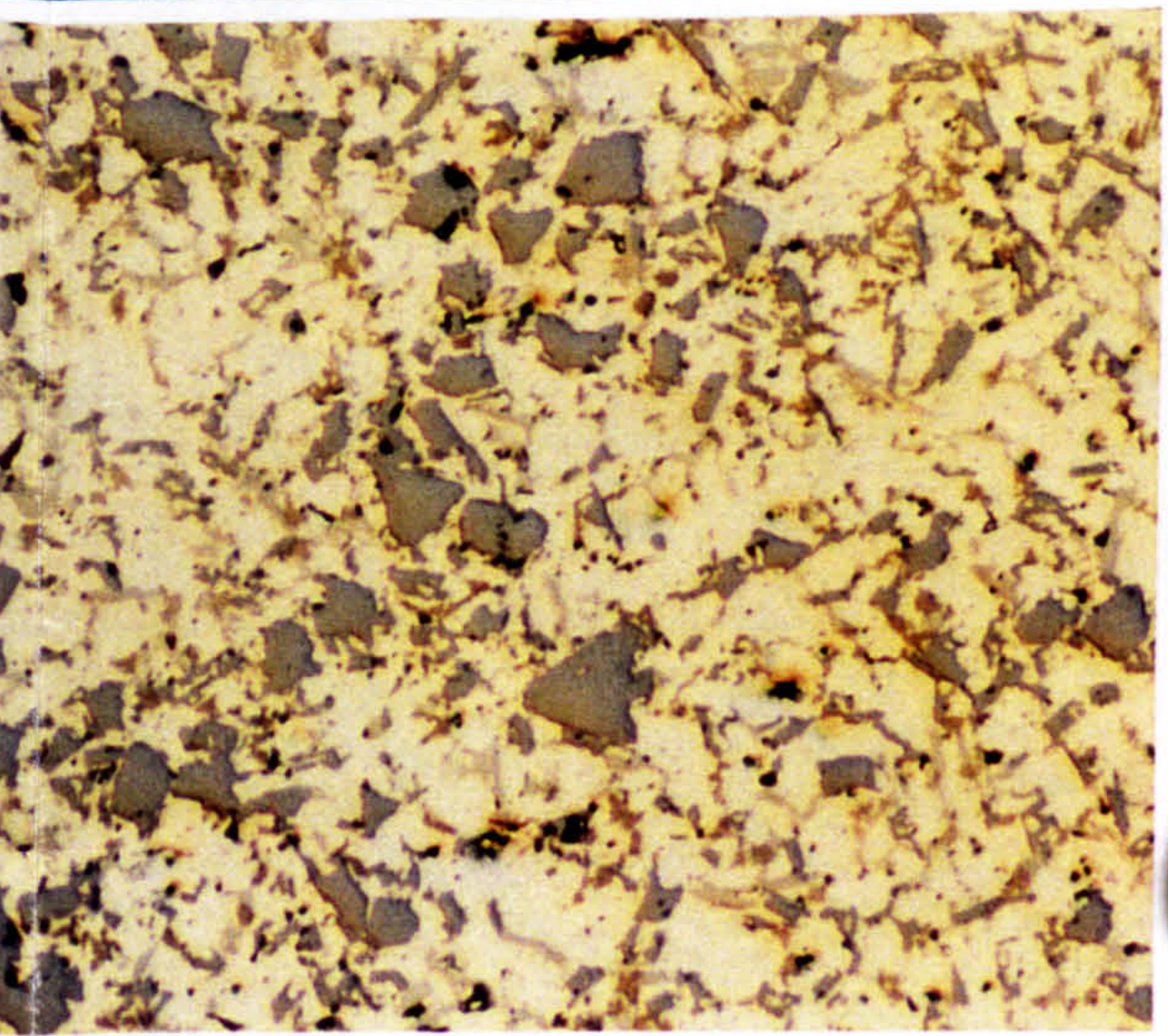
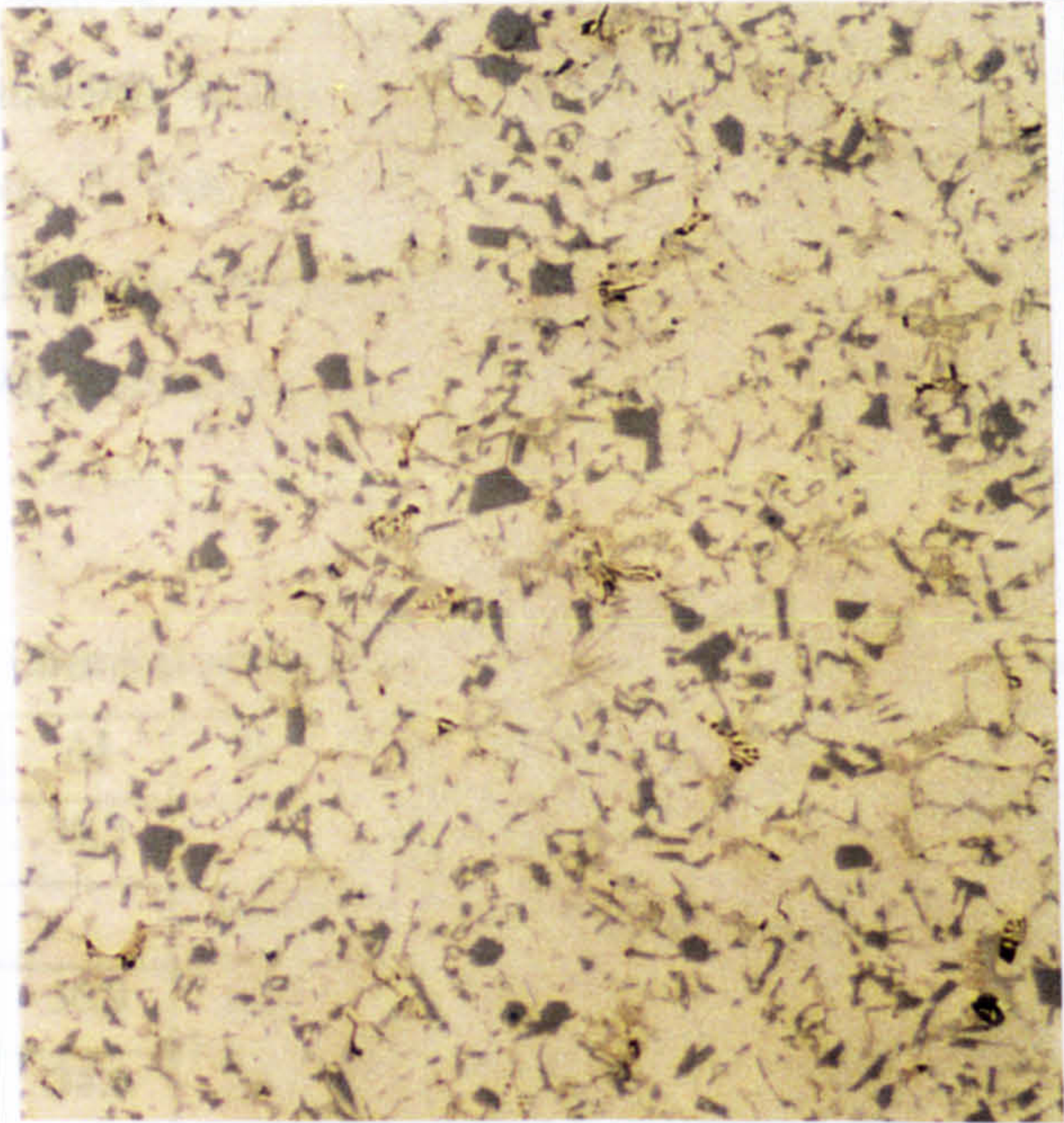
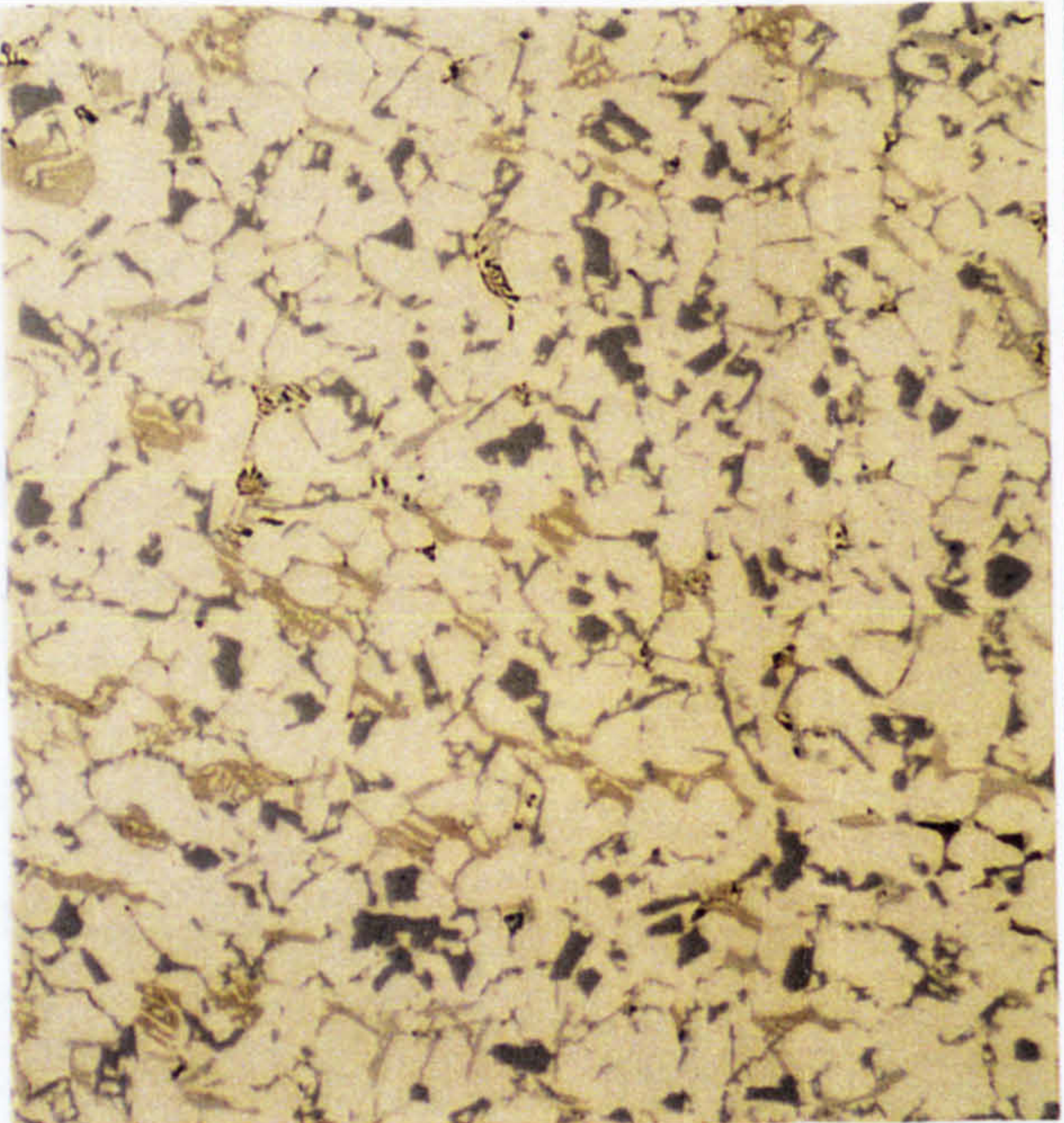
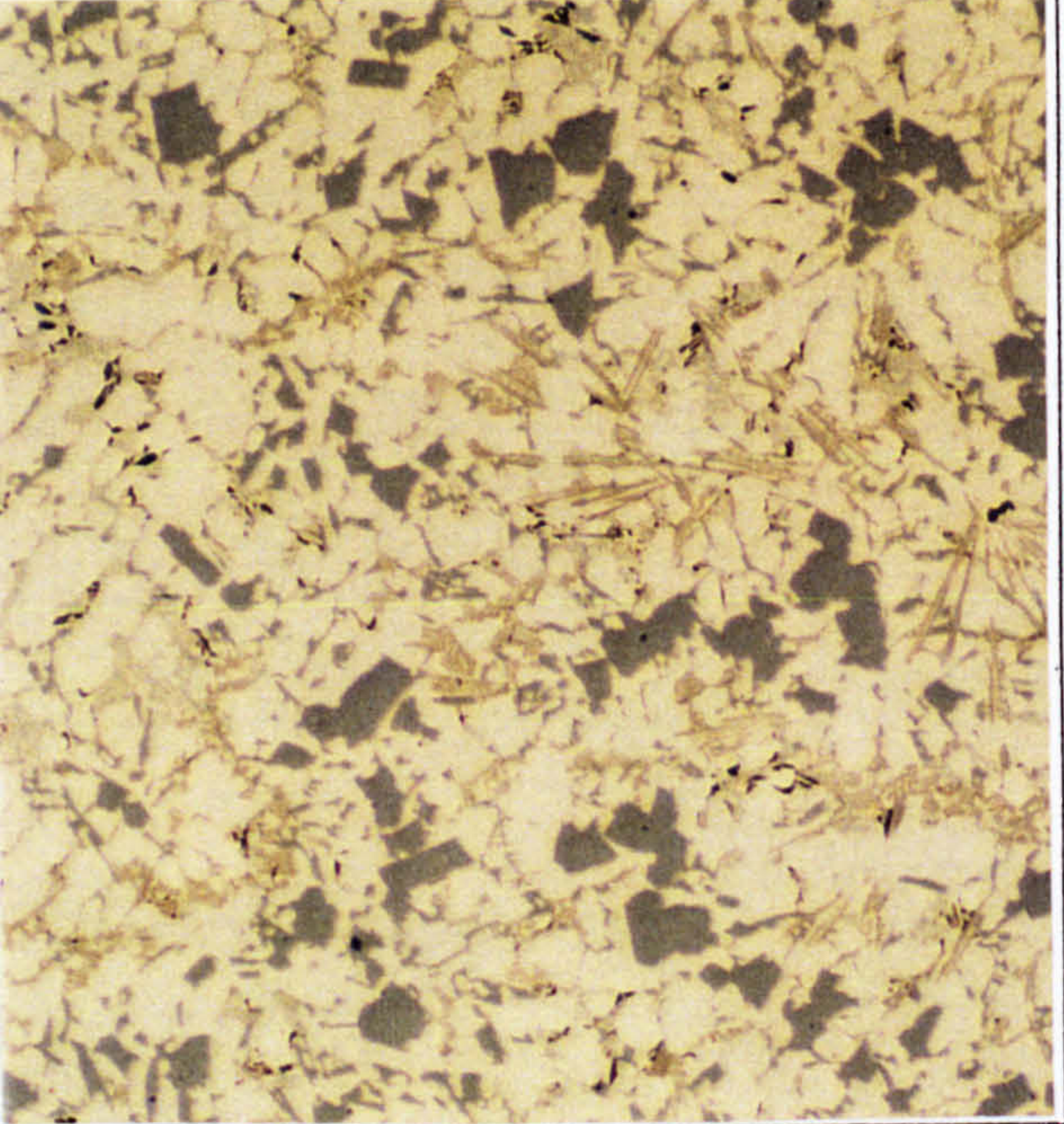
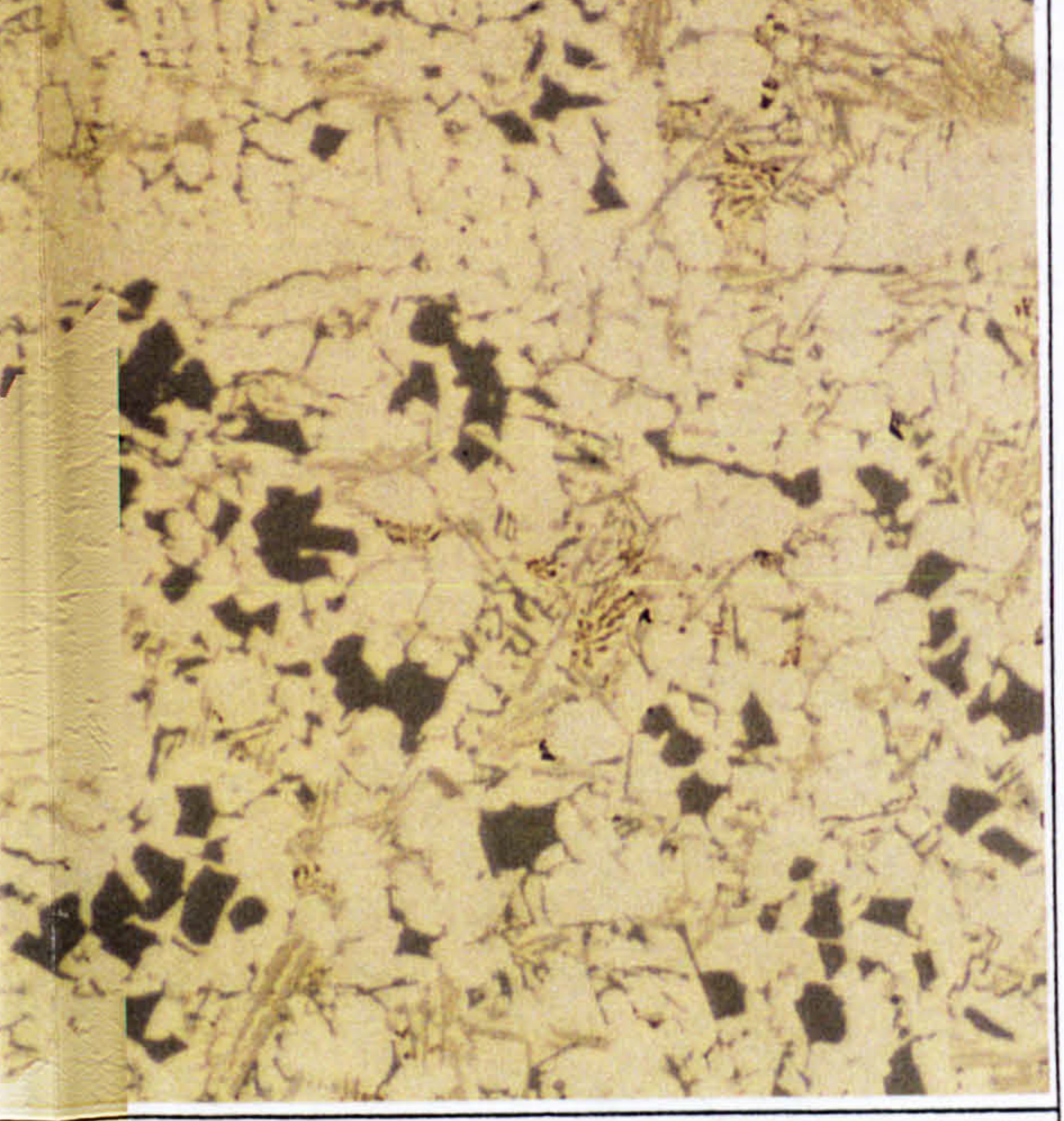
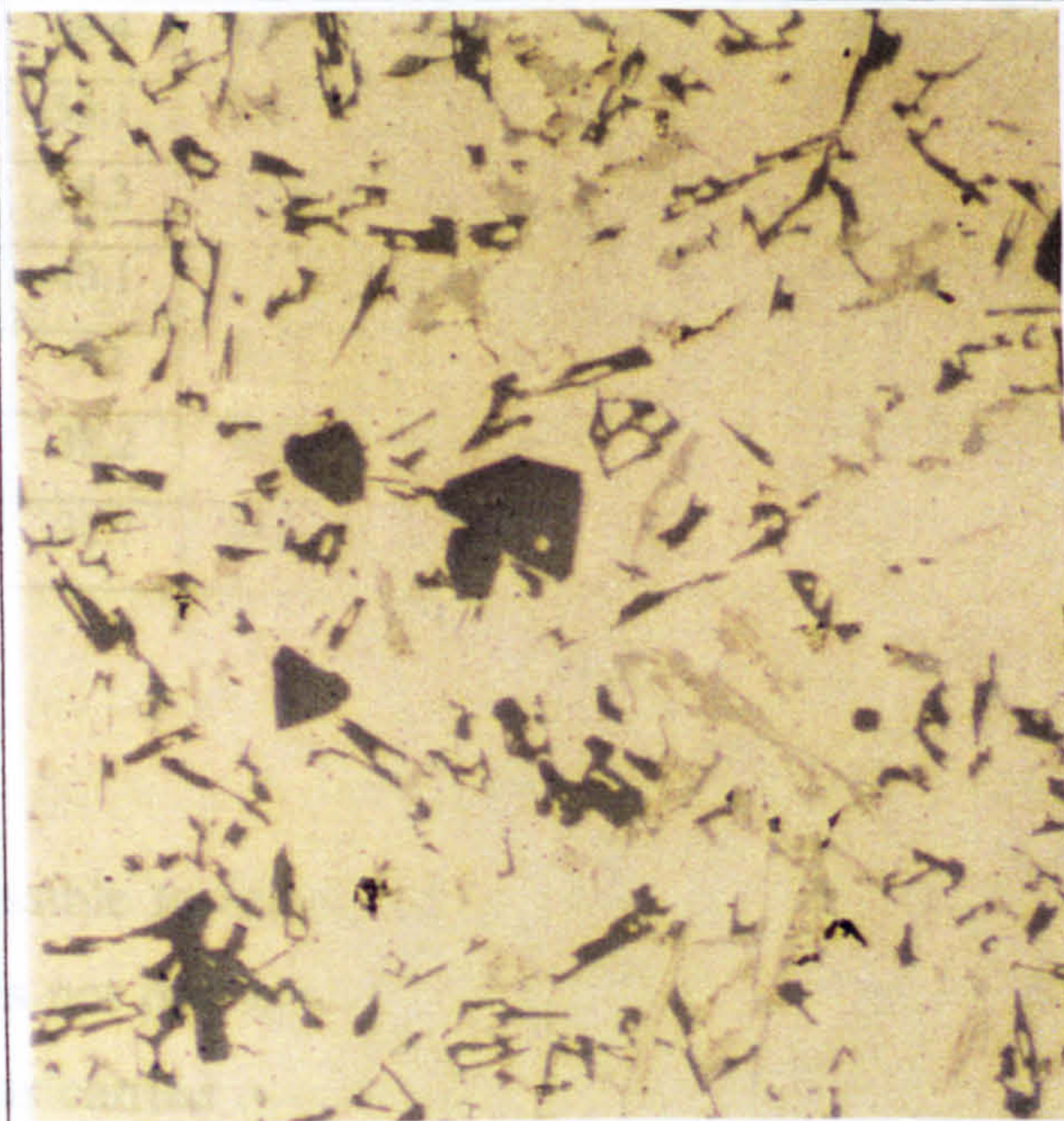
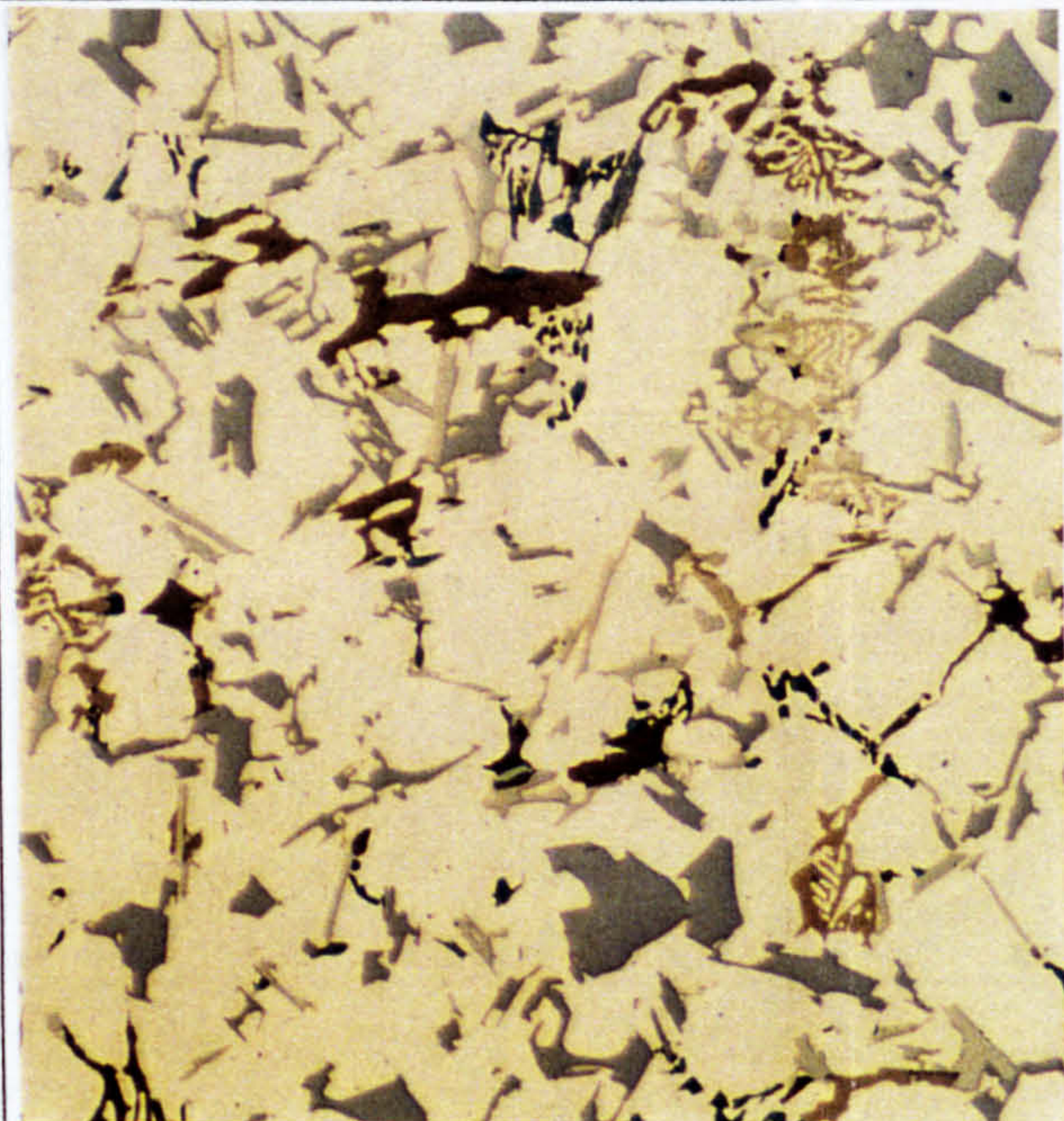
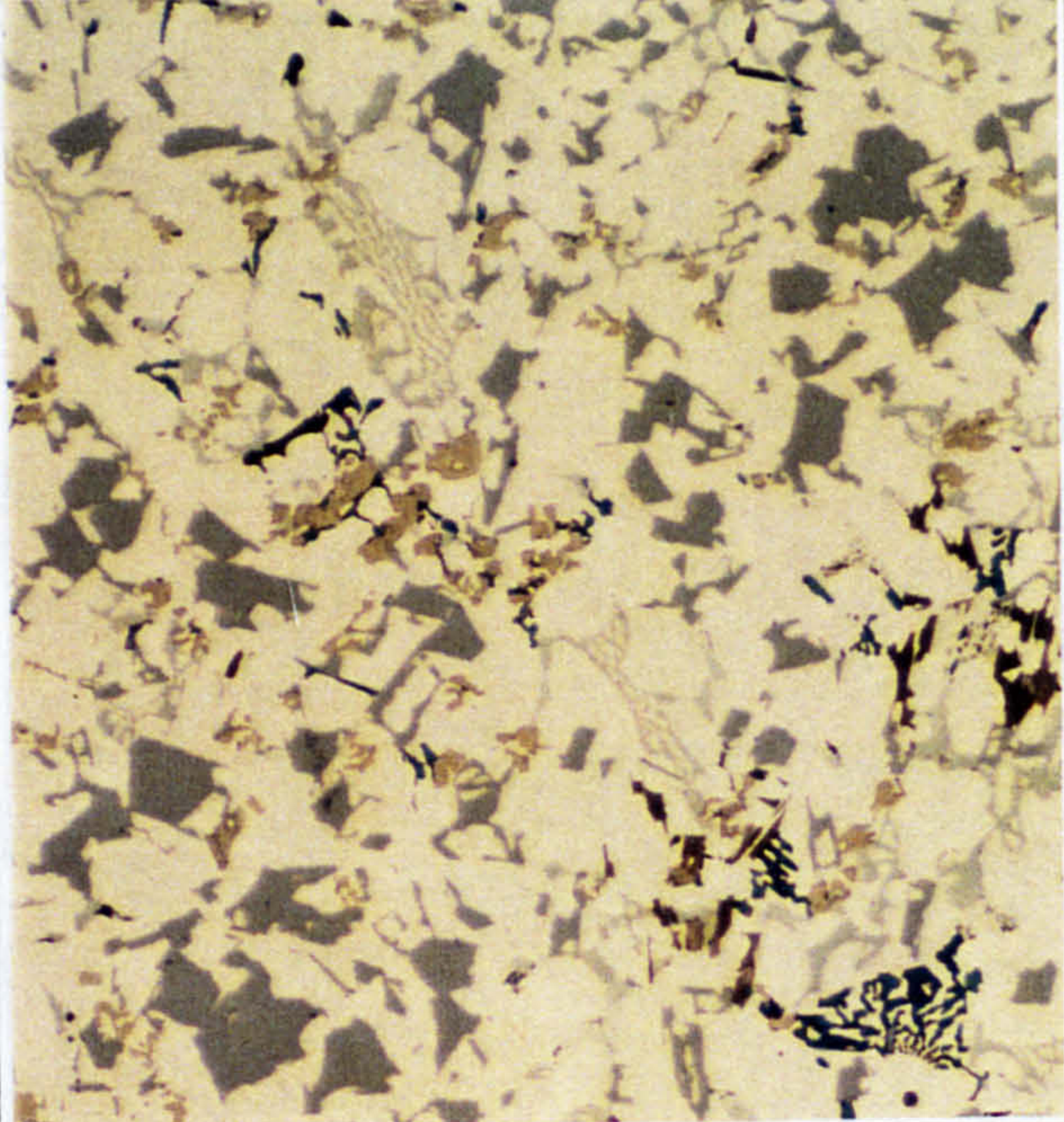
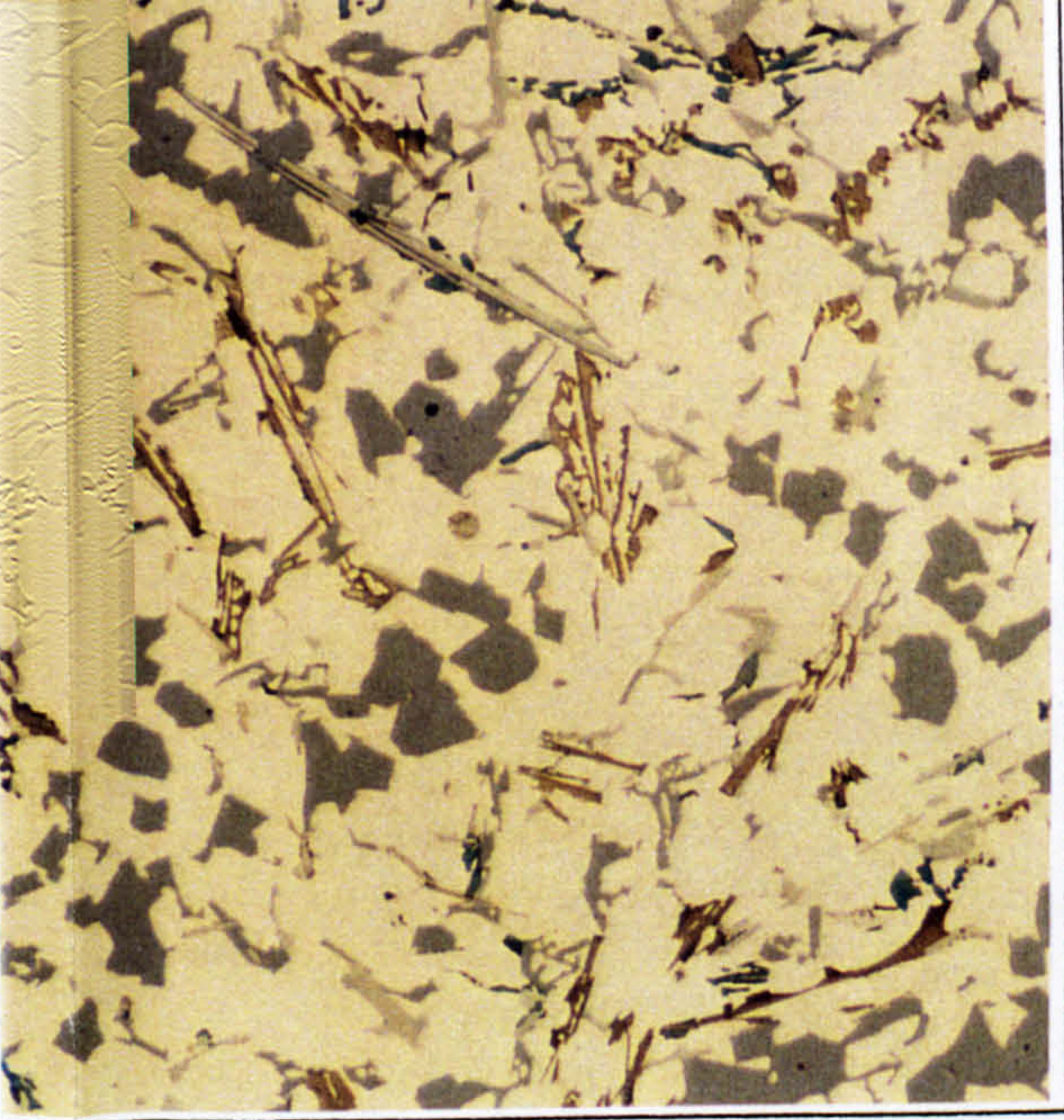
Step No.		Alloy 87	Alloy 88	Alloy 89	Alloy 90
1					
3					
5					

Figure 6.18 Micrographs of stepped mould model alloys 83, 86, 87 and 90, cast at 100 and 440 °C mould temperature , Sep 4-.

	Model Alloy 83 (FMS2N)	Model Alloy 86 (FMS2N with Ti, Zr and V)	Model Alloy 87 (FMB2)	Model Alloy 90 (FMB2 with Ti, Zr and V)
100°C MT				
440°C MT				

100 μm

Standard EDX analysis in the SEM was carried out on the model alloys, and 9 intermetallics were identified in addition to the aluminium and silicon phases, the chemical compositions of which are all given in Table 6.7 below. The phase compositions are the averages determined by grouping analyses from all the model alloys by both chemical composition and morphology. All of these phases are expected to form in all the model alloys, with the exception of Al_3Ti and $\text{Al}_3(\text{Ni}, \text{Cu})_2 + \text{Zr}$, which only form in the presence of V, Zr and Ti (model alloys 86 and 90). Some phases are difficult to distinguish from each other, as was discussed in Chapter 5. For example, the composition ranges of Al_9FeNi and Al_3Ni , and $\text{Al}_7\text{Cu}_4\text{Ni}$ and $\text{Al}_3(\text{Ni},\text{Cu})_2$, overlap making phase identification non trivial. In this case it can be assumed that both phases are present over the composition range.

Table 6.7 Chemical compositions of phases identified in model alloys by SEM (wt. %)

Phase	Al	Si	Cu	Ni	Mg	Fe	Mn	Ti	Zr	V
Aluminium	96.3	-	2.2	-	-	-	-	-	1.2	-
Silicon	-	99.1	-	-	-	-	-	-	-	-
Al_3Ti	36.9	13.2	-	-	-	-	-	22.0	23.7	2.8
$\text{Al}_3(\text{Ni},\text{Cu})_2 + \text{Zr}$	34.6	10.4	4.3	33.5	5.2	-	-	-	10.8	-
$\text{Al}_9\text{FeNi} / \text{Al}_3\text{Ni}$	58.4	1.0	4.2	27.4	6.6	-	1.7	-	-	-
$\text{Al}_3(\text{Ni},\text{Cu})_2$	53.1	1.8	9.8	26.3	4.4	-	2.4	-	-	-
Al_2Cu	54.3	1.2	38.6	4.2	-	-	0.4	-	-	-
$\text{Al}_7\text{Cu}_4\text{Ni} / \text{Al}_3\text{Ni}_2$	43.1	-	36.7	19.1	-	-	-	-	-	-
Mg_2Si	5.2	40.5	-	-	52.8	-	-	-	-	-
$\pi(\text{Al}_8\text{FeMg}_3\text{Si}_6)$	38.2	35.4	2.3	-	-	23.3	-	-	-	-
$\lambda(\text{Al}_5\text{Cu}_2\text{Mg}_6\text{Si}_5)$	32.7	18.9	24.2	-	-	23.2	-	-	-	-

All other elements < 1 wt. %

Although it is possible to identify the various intermetallic phases and their compositions through SEM, it is not possible to determine the mass fractions of these phases. To do this image analysis was carried out on the microstructures of model alloys 83, 86, 87 and 90 at both mould temperatures. The image analysis software enabled differentiation between the aluminium matrix, total and primary silicon, and total intermetallics, and was able to measure the area fractions of the phases and particle lengths as an indication of their size. The data gathered are summarised in Table 6.8 (full results in Appendix F). It is important to note at this stage that the measurements of primary silicon are to be looked at sceptically as there is a

problem with the conditions under which primary and secondary silicon particles are differentiated during analysis. As described in Chapter 4, from a collected image the analysis program automatically highlights all the silicon based on grey scale, which can then be adjusted by the user to ensure differentiation between the silicon and intermetallics. Based on pre-set conditions for size within the macro, the program then selects all silicon particles which match the criteria for primary silicon. However, if the primary silicon particles fall outside the pre-set range then the program will discount them as being secondary phases. This means that although the total silicon measurements are reasonably precise, care should be taken in interpretation of the primary silicon analyses.

Figure 6.19 shows the area fraction of silicon and intermetallic phases (%) for each of the 8 alloys. It can be seen that alloys 87 and 90, irrespective of mould temperature, have a larger fraction of total silicon than 83 and 86, as would be expected from the higher silicon content. It is also shown that despite the fraction of total silicon being larger in 87 and 90, the fraction of secondary silicon is less than in 83 and 86 whilst the primary silicon is substantially greater. This is in agreement with observations of the microstructures previously in Figures 6.15 to 6.17. There is also an increase in the fraction of intermetallics analysed in alloys 87 and 90 which would again be expected from the higher copper content in these alloys, although this finding was not evident in the micrographs. The effect of a pre-heated mould (440 °C) appears to be that more primary silicon is able to grow whilst a lesser fraction of intermetallics were seen.

In order to determine whether increases in area fraction are a result of an increased number of particles, or the same number, but larger crystals, a plot was drawn of the mean length of phases for each of the alloys. This can be seen in Figure 6.20. Overall the particles are found to be larger in the 440 °C MT casting than that of 100 °C MT as one would expect from the longer growth times that result from slower cooling. Between the alloys there is a slight trend towards an increase in particle size in alloys 87 and 90 particularly for the primary silicon. This fits with the observations that large primary silicon are seen in the micrographs, often clustered, and a higher fraction of primary silicon was measured in the image analysis results plotted in Figure 6.19. It must be noted, however, that at 440 °C MT the intermetallics and secondary silicon in alloys 87 and 90 are smaller than those in 83 and 86 at this mould temperature.

Having measured the fraction of phases in a number of castings it was decided to perform thermodynamic calculations for comparison. Equilibrium calculations were carried out for each of the four model alloys under consideration, namely 83, 86, 87 and 90. In addition to the aluminium matrix and silicon, five intermetallic phases were predicted to form during solidification in all four of the model alloys. These are Al_3Ni_2 , λ ($\text{Al}_5\text{Cu}_2\text{Mg}_8\text{Si}_6$), Al_9FeNi , $\text{Al}_7\text{Cu}_4\text{Ni}$, and α (AlFeMnSi), and their mass fractions (log scale) are shown in Figures 6.21 a) to d). There are two points of interest in these figures. The first is that the $\text{Al}_7\text{Cu}_4\text{Ni}$ phase is predicted to stabilise at a higher temperature and greater fraction in alloys 87 and 90 presumably as a result of the higher Cu content in the alloy. The second issue is that of the Al_3Ti phase, discussed in detail earlier with respect to whether it stabilises on addition of Ti to the melt, thus acting as a nucleant for the aluminium.

Considering first model alloy 83 (no Ti) it can be seen that the Al_3Ti is not predicted at all and the first major phases to solidify are the silicon and aluminium at around the same temperature. In alloy 87, again with no Ti additions, there is no Al_3Ti and due to the high silicon content it is the silicon phase which forms first on solidification. When Ti is added to both alloys to create model alloys 86 and 90, the Al_3Ti phase becomes stable at high temperatures and is the first to solidify. Although the effect of the presence of this phase appears negligible according to the thermodynamic predictions, it almost certainly nucleates the aluminium at a higher temperature as a consequence.

From the predictions it was also possible to determine liquidus and solidus temperatures to compare with measurements of the alloys from a thermal analysis machine at Federal-Mogul. From the data in Table 6.9 it can be seen that there is a considerable difference between the measured and calculated values and although the predicted transition temperatures are not assured of being accurate, the most likely reason for the dissimilarity are the thermal analysis readings, which were measured by a very basic technique (see Chapter 4). Considering the predicted values for the liquidus it appears that the addition of Ti increases this temperature dramatically by formation of Al_3Ti which is stable at high temperatures and is the first phase to freeze during cooling. Thermal analysis traces from a DTA would be unlikely to detect this phase due to the trace quantities in which it forms, and consequently the liquidus would be a measure of when the first bulk phase solidifies, aluminium in this case.

Table 6.8 Image analysis results from stepped mould: model alloys 83, 86, 87 and 90

Model Alloy		Mould Temp. (°C)	% Silicon			% Primary Silicon			% Intermetallics				
			Mean Si Length (µm)	Max. Si Length (µm)	90% Si Length		Mean Prim. Si length (µm)	Max. prim. Si Length (µm)	90% Prim. Si Length		Mean Ints. Length (µm)	Max. Ints Length (µm)	90% Ints. Length
83	83	100	9.74	10.21	18.22	0.92	27.93	69.48	35.49	9.87	19.54	163.79	34.41
	83	440	10.08	18.79	38.66	2.82	36.81	105.66	49.80	8.57	27.06	356.29	54.27
	83	Scania Crown	-	-	-	5.06	40.02	202.77	59.27	9.42	25.56	316.6	49.73
86	86	100	9.24	10.86	20.73	2.20	29.87	86.18	39.02	10.31	21.11	251.11	37.49
	86	400	12.30	21.00	43.83	6.06	38.72	159.90	55.31	8.06	27.60	349.03	53.67
	86	Scania Crown	-	-	-	5.67	40.08	182.29	60.76	10.61	25.21	394.87	48.96
87	87	100	12.93	12.32	24.41	6.09	34.20	104.70	48.44	13.69	23.96	302.62	45.86
	87	440	14.85	18.33	37.06	8.04	37.85	143.85	55.54	10.02	25.07	281.07	49.86
	87	Scania Crown	-	-	-	6.71	42.79	193.01	68.68	11.61	26.78	273.47	52.5
90	90	100	11.07	11.44	22.40	5.96	34.77	172.44	49.99	10.59	21.86	377.00	38.33
	90	440	15.41	19.12	40.09	9.20	39.84	150.06	60.35	9.46	27.16	308.80	52.54
	90	Scania Crown	-	-	-	8.41	45.31	208.57	74.73	13.35	28.20	413.11	57.08

(Errors all < ± 0.1)

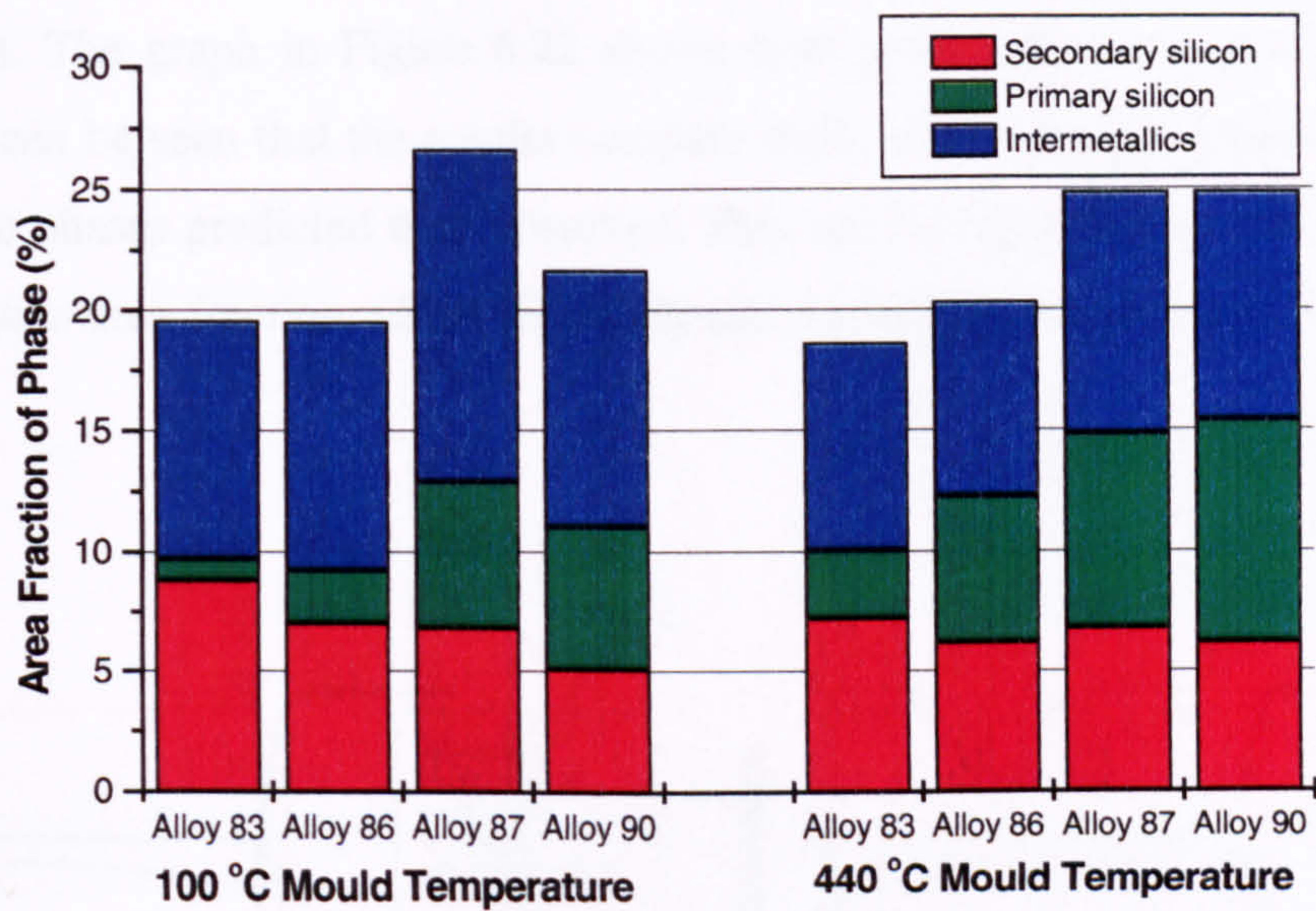


Figure 6.19 Area fraction of phases in model alloys measured by image analysis

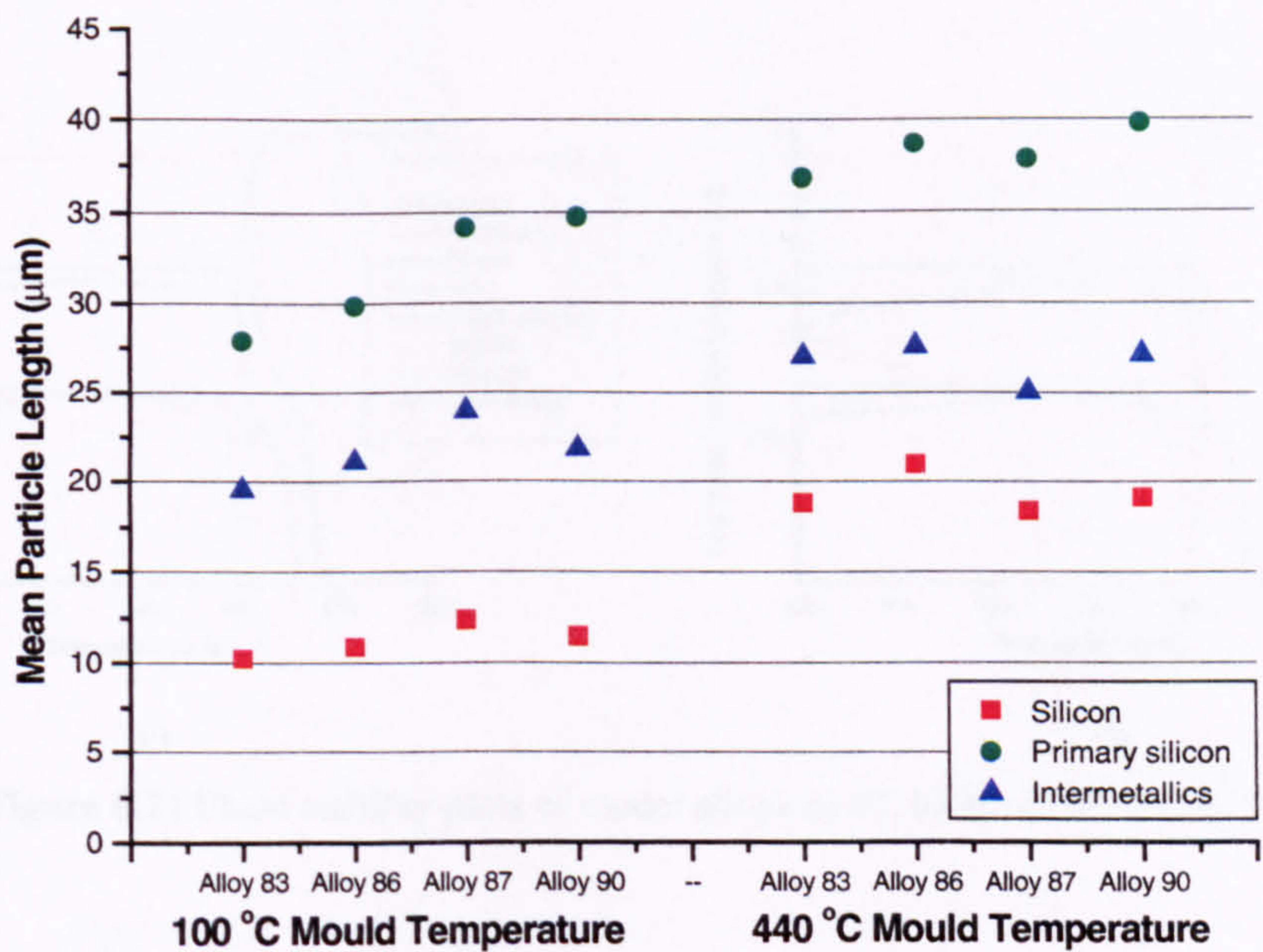


Figure 6.20 Mean particle lengths of phases in model alloys as determined by image analysis

In addition to phase stability plots, the mass fractions of the silicon and total intermetallic phases were calculated at 500 K (227 °C) to compare with the area fractions determined by image analysis. The graph in Figure 6.22 shows both predicted and measured fractions of phases, and it can be seen that the results compare well, with a slightly greater mass fraction of intermetallic phases predicted than observed. This can be explained by the fact that image analysis measures area fraction whilst thermodynamic predictions calculate the mass fraction of the phases.

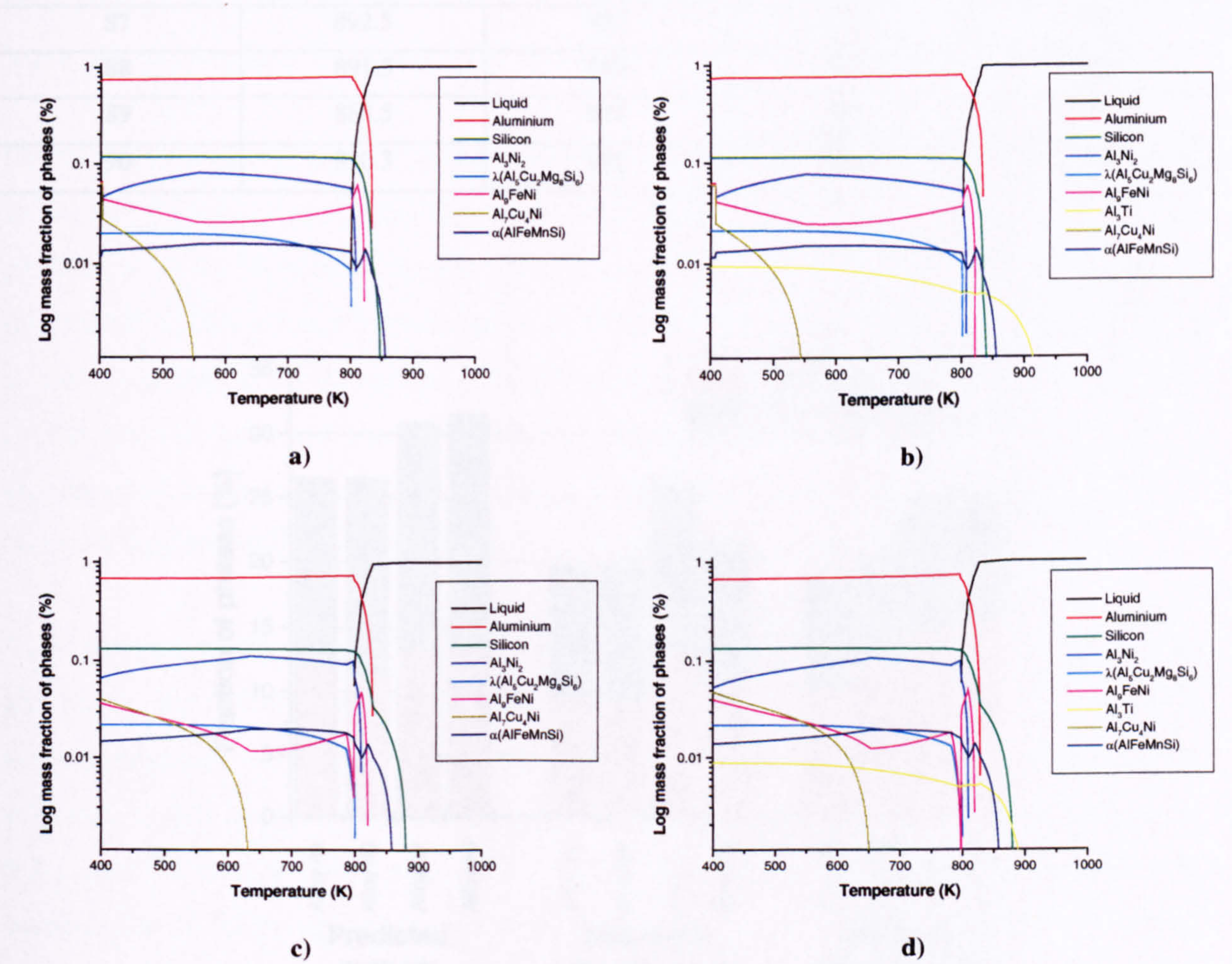


Figure 6.21 Phase stability plots of model alloys a) 83, b) 86, c) 87, and d) 90

Table 6.9 Measured (thermal analysis) and predicted (thermodynamic calculations) liquidus and solidus temperatures for model alloys 83, 86, 87 and 90

Alloy	Liquidus (K)		Solidus (K)	
	Measured	Predicted	Measured	Predicted
83	848.5	859	828.8	799
84	846.5	861	829.4	799
85	846.5	861	830.4	799
86	845.5	928	833.9	800

87	892.5	882	823.1	798
88	891.5	883	823.5	798
89	888.5	882	823.2	797
90	890.3	903	824.6	798

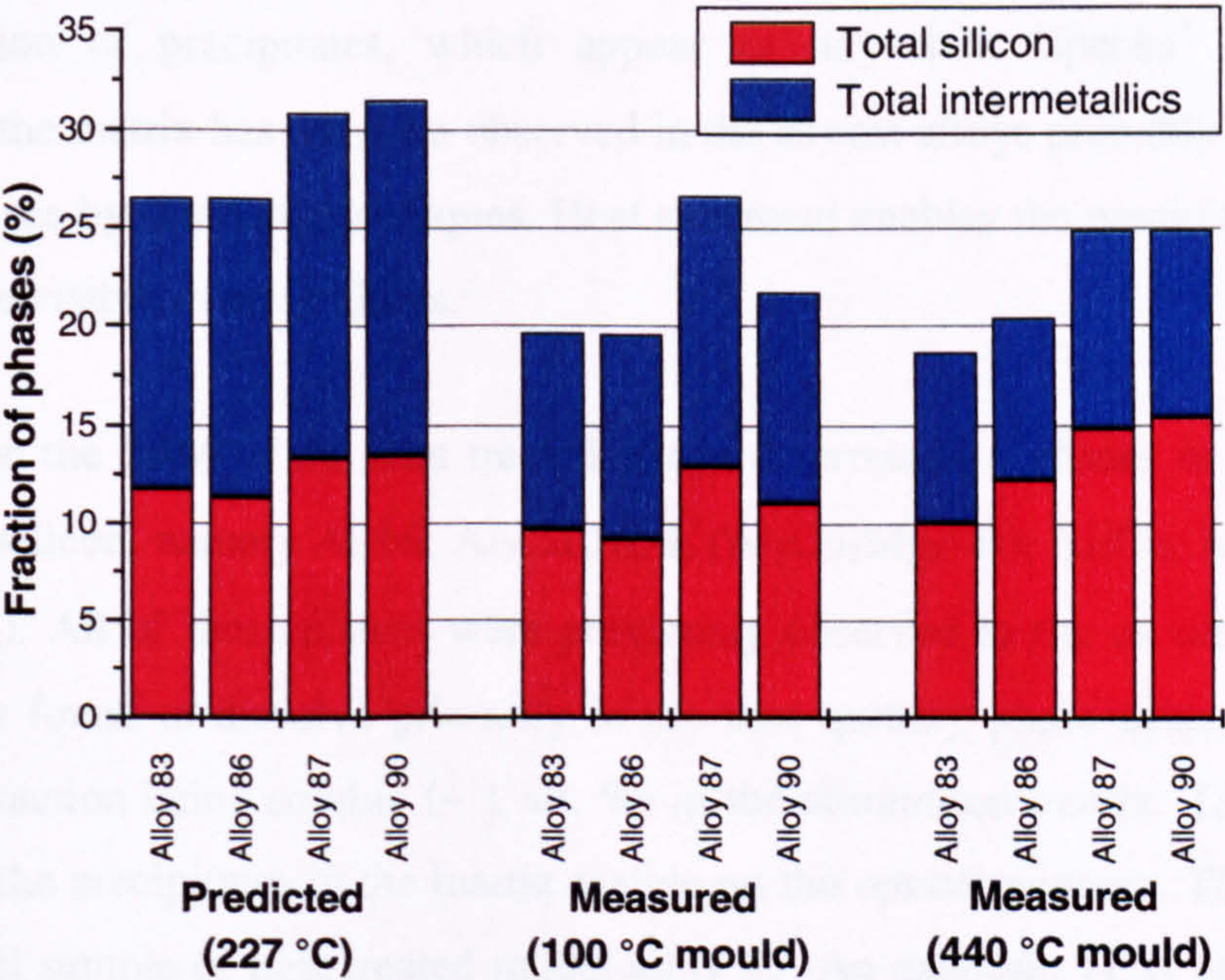


Figure 6.22 Measured (image analysis) and predicted (thermodynamic calculations) fractions of phases for model alloys 83, 86, 87 and 90

6.3.3 Heat Treated Model Alloys

Following characterisation of model alloys 83 to 90 with controlled additions of Ti, Zr and V, it was decided to carry out a series of heat treatments to determine firstly whether the as-cast alloys are representative of the in service structure, and secondly the effect of the heat treatment on solubility of the Zr. Zr is believed to improve fatigue properties at 350 °C as a function of time at this temperature, whilst still retaining its high temperature strength. However, as yet the mechanism behind this improvement in properties is unclear. In order to clarify the situation, two of the model alloys with and without Zr (+ V), 83 and 85 respectively, were heat treated at 350 °C for 100 hours to simulate in-service conditions. These alloys were then characterised by optical and electron microscopy.

Optical micrographs of the two alloys in both as-cast and in heat treated conditions are shown in Figures 6.23 a to d. In both alloys it can be seen that one effect of the heat treatment is to produce a more homogeneous microstructure of much larger particles, both silicon and intermetallic. This is more pronounced in alloy 85 than 83. In both heat treated alloys there is a clear indication of precipitates, which appear as tiny dark 'specks' in the matrix. Precipitation in the matrix has not been observed in the as cast alloys probably as the particles are too small to see by standard techniques. Heat treatment enables the precipitates to coarsen and thus they are visible in these alloys.

EDX analysis on the SEM of the heat treated alloys determined 6 phases in addition to the aluminium and silicon, namely Al_3Ni , $\text{Al}_7\text{Cu}_4\text{Ni}$, λ ($\text{Al}_5\text{Cu}_2\text{Mg}_6\text{Si}_5$), Al_2Cu , $\text{Al}_3(\text{Ni,Cu})_2$, and π ($\text{Al}_8\text{FeMg}_3\text{Si}_6$). All of these phases were previously observed in the as cast alloys (Table 6.7) and Zr was found to dissolve primarily in the new quinary phase described in Section 5.3.15, with a fraction being soluble (~ 1 wt. %) in the aluminium matrix. To determine the composition of the precipitates in the matrix visible on the optical pictures, TEM was carried out on a thin foil sample of heat treated model alloy 85. An example TEM image of an area containing a range of particles is given in Figure 6.24 with A and B indicating particles analysed, the compositions of which are summarised in Table 6.10. The majority of particles had a composition close to that of A which, taking into consideration pick up from the surrounding aluminium, is most probably the Al_2Cu phase. The particle denoted B has significantly less Cu content than A, but also contains small quantities of Si and Mg, and is likely therefore to be a derivative of the Mg_2Si phase, however conclusive identification was not possible.

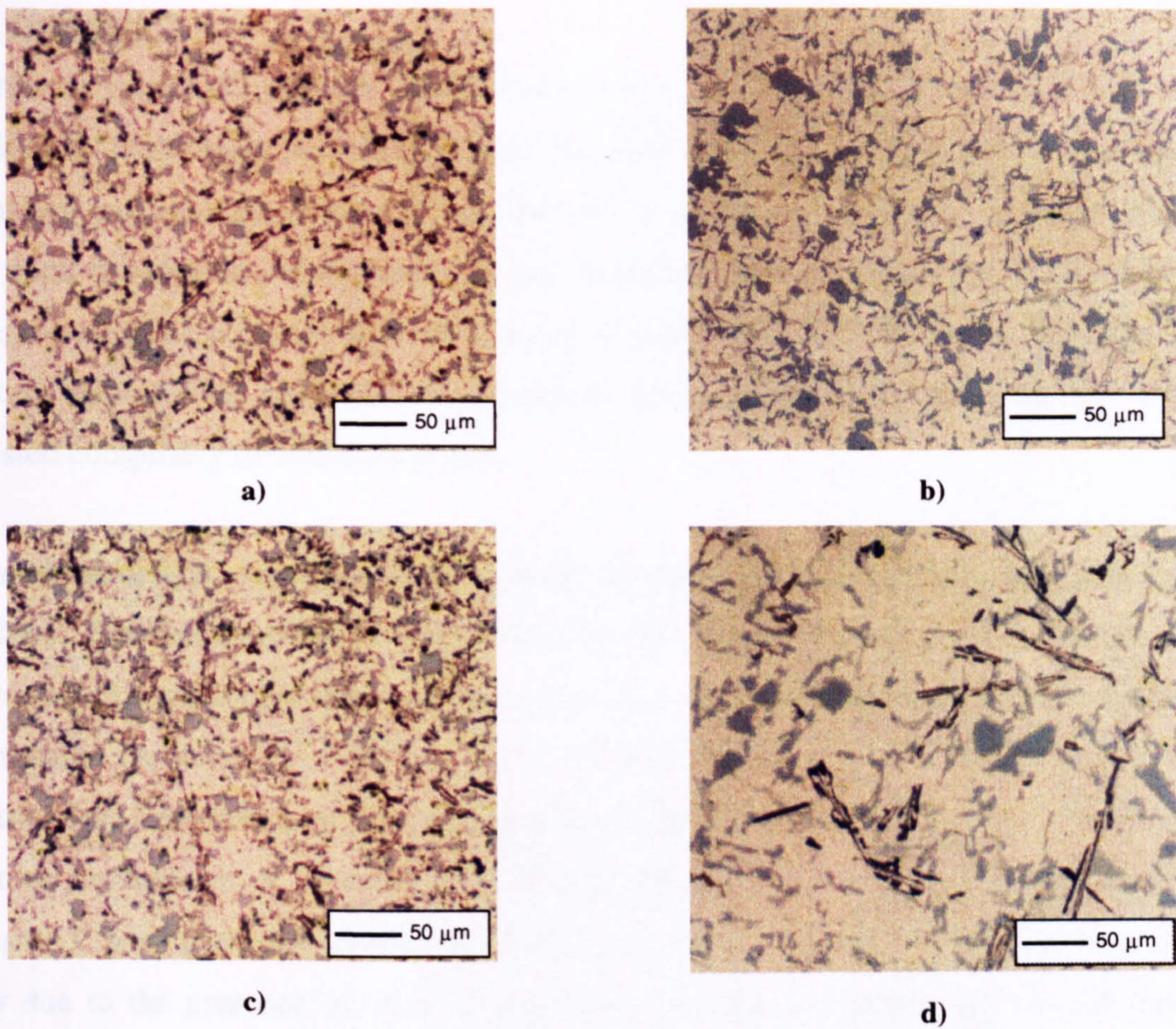


Figure 6.23 Optical micrographs of model alloy 83 (no additions) in the **a)** as cast and **b)** heat treated conditions, and model alloy 85 (Zr additions) in the **c)** as cast and **d)** heat treated conditions

Table 6.10 Composition of particles A and B (see Figure 6.24), heat treated model alloy 85

		Al	Cu	Si	Mg
A	Wt. %	75.5	24.6	-	-
	At. %	87.5	12.5	-	-
B	Wt. %	91.3	3.1	2.5	3.1
	At. %	92.7	1.3	2.5	3.5

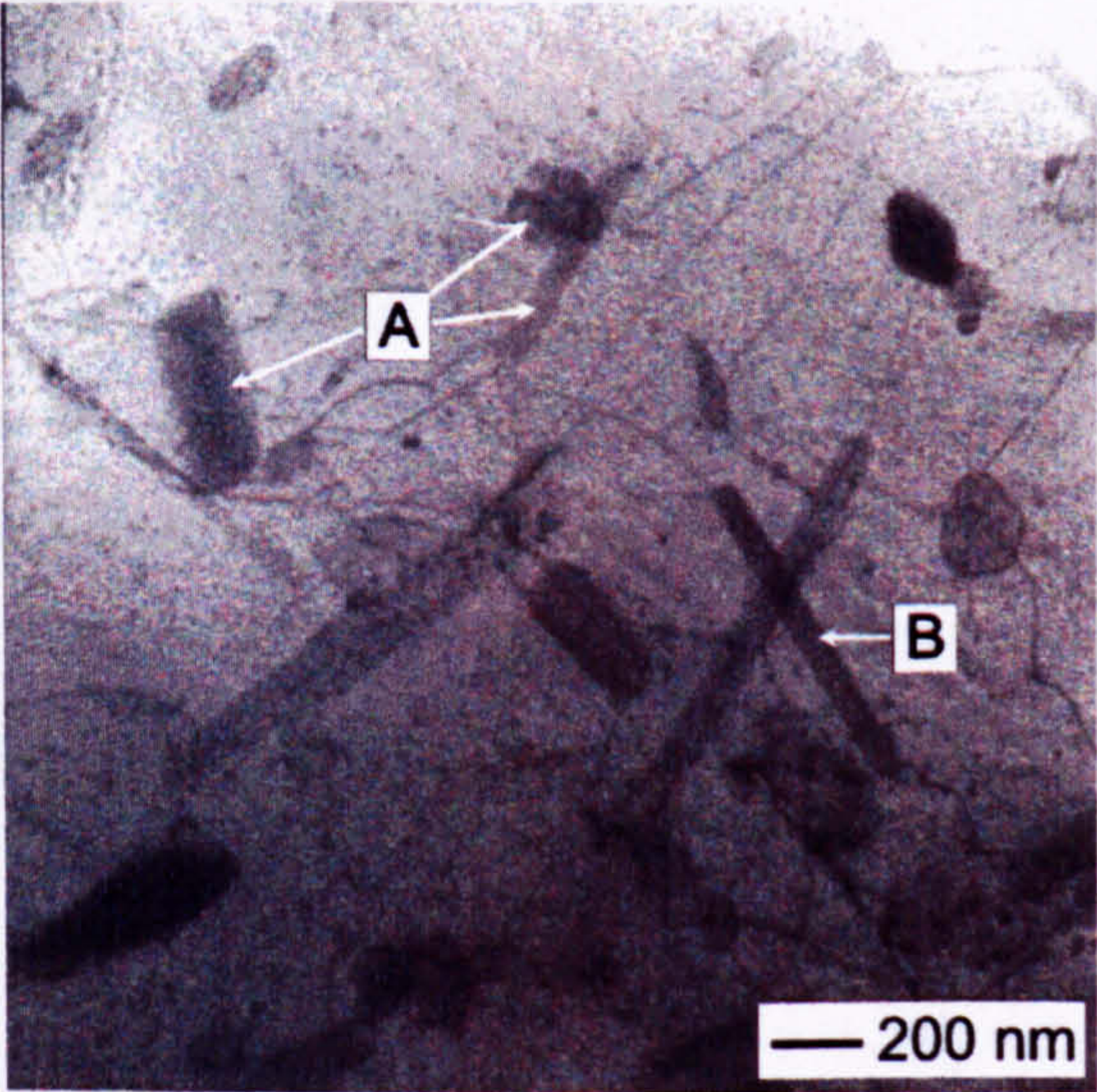


Figure 6.24 TEM image of matrix precipitates in heat treated model alloy 85

6.3.4 Summary

A series of model alloys were designed and cast to investigate the effect of Ti, Zr, and V additions to multicomponent Al-Si alloys. The castings were of a stepped mould shape and cast at two mould temperatures (100 and 440 °C) to additionally examine the effect of cooling rates upon the structure of the alloys. It was found that when no or Zr and V additions were made, the structure was columnar irrespective of cooling rate. However, on addition of Ti, the structure appeared to undergo a columnar to equiaxed transition, whereby the structure consisted completely of equiaxed grains.

The microstructure was seen to be affected by both the cooling rate and grain refining additions. The slower cooling rate produced by the thicker sections of the castings and the higher mould temperature, resulted in a much coarser microstructure with large silicon and intermetallic particles. The microstructures of faster cooled sections of the casting were seen to show clear dendritic growth of the aluminium, illustrative of the observed columnar grain structure. On addition of Ti to the alloy, the microstructure was seen to become much more segregated, with particular clustering of the silicon and intermetallic phases. This is most likely due to the presence of Al_3Ti in the melt, which acts as a nucleant for aluminium at higher temperatures. The aluminium would have had a longer time to grow before the secondary phases solidified due to constitutional effects between aluminium dendrites. Image analysis provided a quantitative measurements of the observed change in particle sizes, and it was also possible to directly compare area fraction of phases with the mass fractions predicted by thermodynamic calculations.

Finally, heat treatments representative of the commercial ‘soaking’ process were carried out on selected model alloys to determine any resultant changes in microstructure. The outcome was to produce a much coarser microstructure than the as-cast alloys, with the matrix precipitates coarsening to a large enough size for examination in the TEM. The composition of these precipitates was mainly Al-Cu indicating that they are most likely Al_2Cu , although small quantities of precipitates containing Si and Mg were also detected.

6.4 Keel Bar Alloys

14 alloys were designed and cast as keel bars based on the commercial alloy AE113 with varying additions of titanium, zirconium and vanadium, individually and in combination. In addition, several different types of Ti-containing refiner were looked at; in alloy 1/4 the titanium was added with a TiBA1 - TiB₂ grain refiner, in alloy 3/4 the titanium was added as Nucleant 70, a Foseco grain refining agent, and in alloys 4/1 to 4/3, an AlTi₆ master alloy was used to supply the titanium. Commercial AE113 stock already contains 0.15 wt. % Ti and 30 ppm phosphorus (nominally). The ideal compositions for the alloys were given in Table 4.4, but subsequent spark analysis enabled accurate compositions to be determined and these are given in Table 6.11.

Table 6.11 Chemical compositions, determined by spark analysis, of keel bar model alloys

Alloy	Composition (Wt.%)										P (ppm)
	Al	Si	Cu	Ni	Mg	Fe	Mn	Ti	Zr	V	
1/1	83.1	11.8	3.08	0.91	0.88	0.23	-	-	-	-	11
1/4	83.6	11.4	2.95	0.87	0.87	0.23	-	0.10	-	-	12
3/1	83.0	11.8	3.15	0.93	0.92	0.23	-	-	-	-	12
3/4	83.0	11.8	3.16	0.93	0.89	0.25	-	0.04	-	-	11
4/1	83.2	11.5	3.09	0.93	0.92	0.23	-	0.10	-	0.01	69
4/2	83.4	11.5	3.01	0.89	0.91	0.22	-	0.16	-	-	11
4/3	83.5	11.2	3.05	0.90	0.90	0.23	-	0.19	-	-	11
5/1	83.6	11.3	2.98	0.89	0.89	0.22	-	-	0.08	0.01	10
5/2	84.2	10.8	2.89	0.87	0.83	0.21	-	-	0.15	0.01	9
5/3	84.6	10.6	2.76	0.84	0.79	0.20	-	-	0.22	0.01	11
10/1	82.5	12.1	3.23	0.85	0.91	0.20	0.03	0.17	0.01	-	154
10/2	82.8	11.8	3.25	0.87	0.90	0.20	0.03	0.16	0.08	-	51
10/3	83.4	11.3	3.10	0.83	0.82	0.19	0.03	0.16	0.14	-	141
17/3	83.0	11.6	3.18	0.84	0.78	0.20	0.03	0.18	0.08	0.09	98

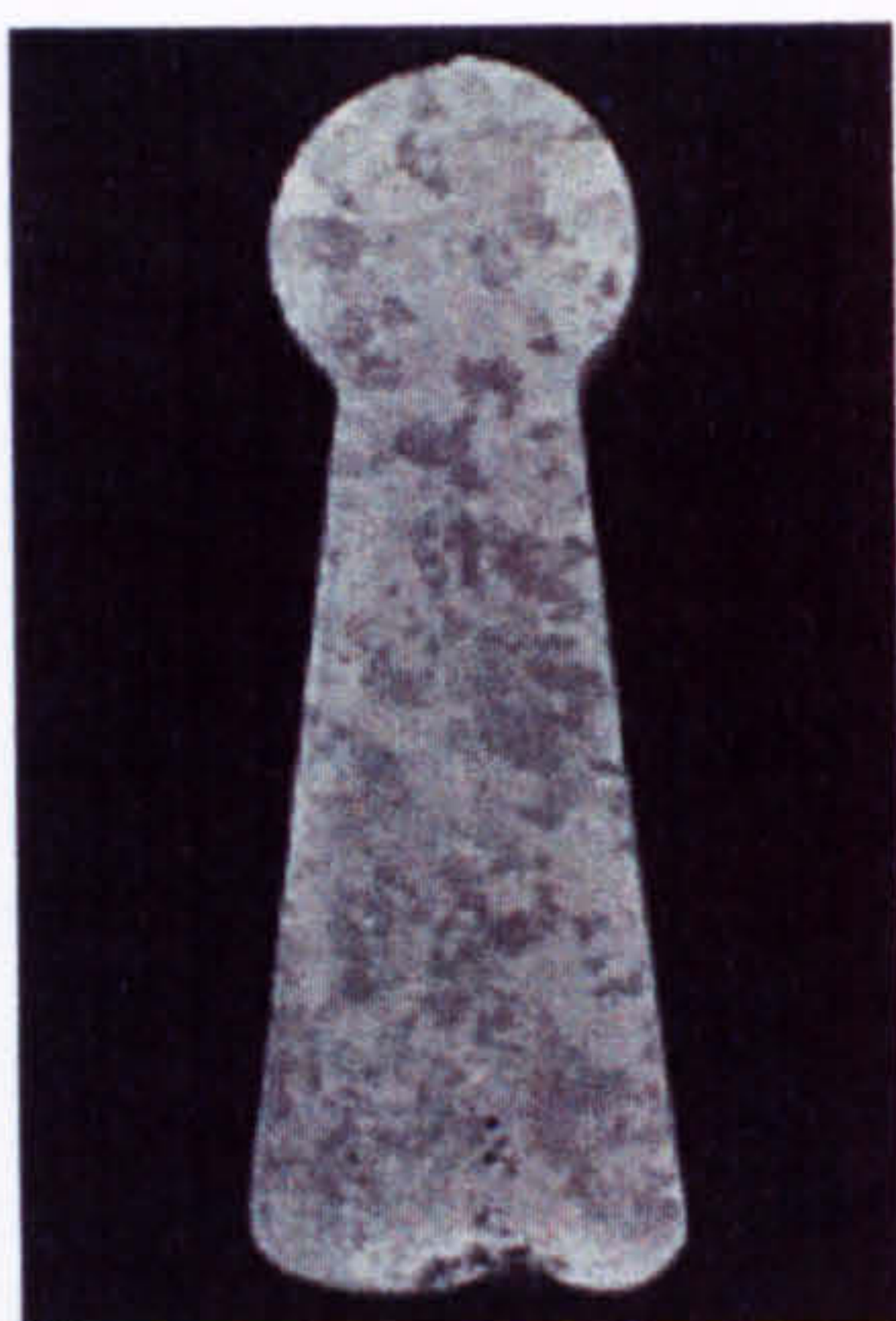
6.4.1 Grain Structures

Prior to the keel bars being sectioned for electron microscopy and spark analysis, they were polished and etched to reveal the macrostructures. The macrographs taken of the cross section of the keel bars are given in Figures 6.25 to 6.30, and from these pictures the variation in grain structure can be seen clearly.

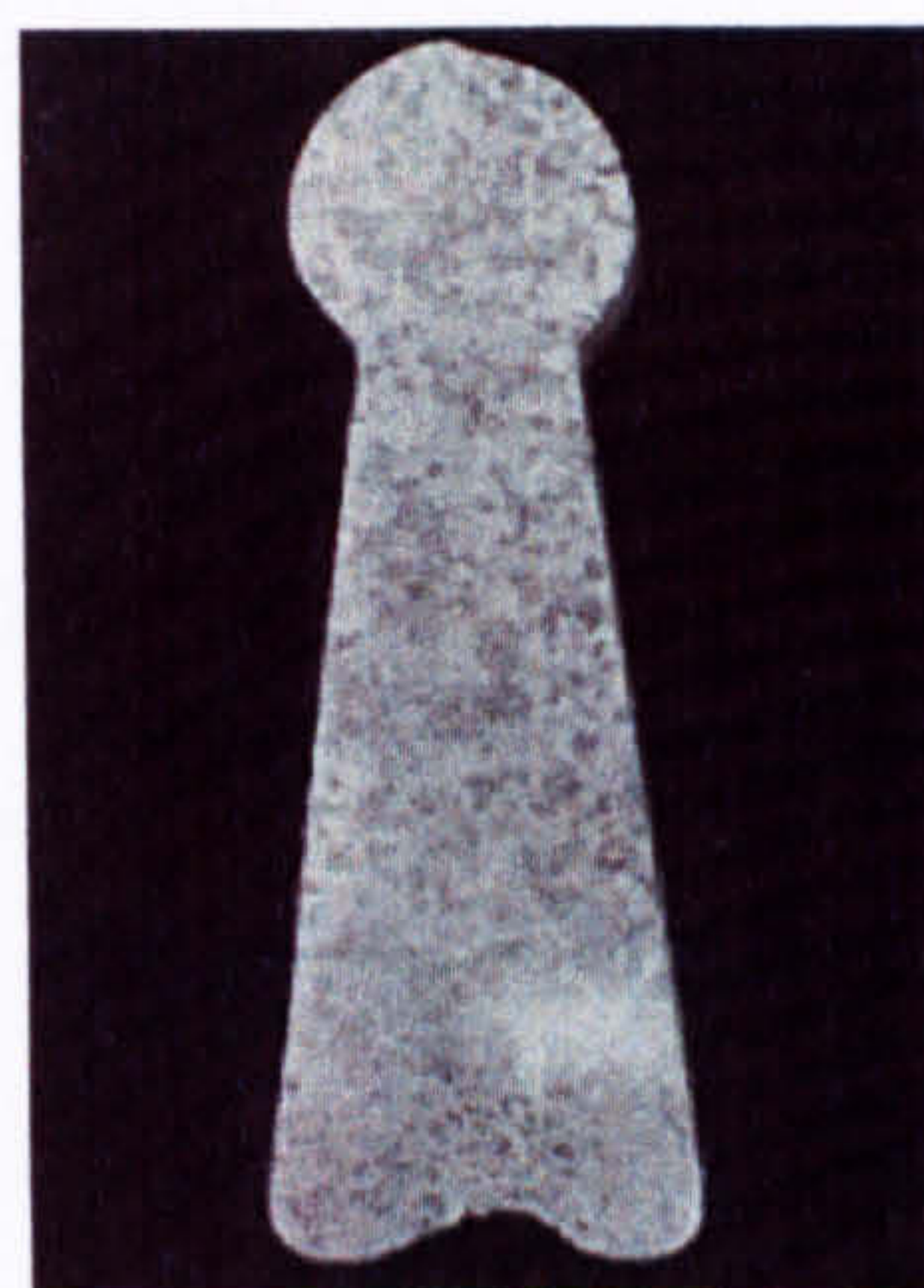
Looking first at the structures produced by addition of ~0.15 wt. % Ti through different grain refiners (alloys 1/4, 3/4, and 4/2, Figures 6.25 b), 6.26 b) and 6.27 b) respectively). It can be seen that alloy 4/2 has a finer and more evenly equiaxed grain structure than the other two alloys and thus addition of Ti by AlTi_6 appears to be the most efficient at this level. Looking at the effect of increasing Ti content in alloys 4/1 to 4/3 (Figures 6.27 a) to c)) it is seen that as the amount of Ti increases, so does the level of refinement. Alloy 4/3 has a much finer grain size than 4/1 or 4/2, with less columnar growth occurring at the edges, particularly around the top. A similar trend is observed when Zr is added (Figures 6.28 a) to c)) although it seems that 5/2 may have a slightly larger grain size than 5/1. However 5/3 is markedly finer than either 5/1 or 5/2 and so it is still believed that increasing amounts of Zr will decrease the grain size.

If the two different additions (Ti and Zr) are compared, it can be seen that the titanium appears to have a more significant effect than the zirconium for the same quantity of addition.

The series of alloys designated 10/1, 10/2 and 10/3 (Figures 6.29 a) to c)) investigated the effect of increasing Zr additions on an alloy containing a standard amount of Ti present in the alloy stock of approximately 0.15 wt. % Ti. It appears that the addition of Zr with Ti has a more marked effect than addition of either element individually, although the effect of increasing Zr content is not so pronounced. If V is then added in addition to the Ti and Zr, as in alloy 17/3 (Figure 6.30), the structure reverts to one of large grains and can be likened to those of unrefined alloys 1/1 and 3/1 (Figures 6.25 a) and 6.26 a)).

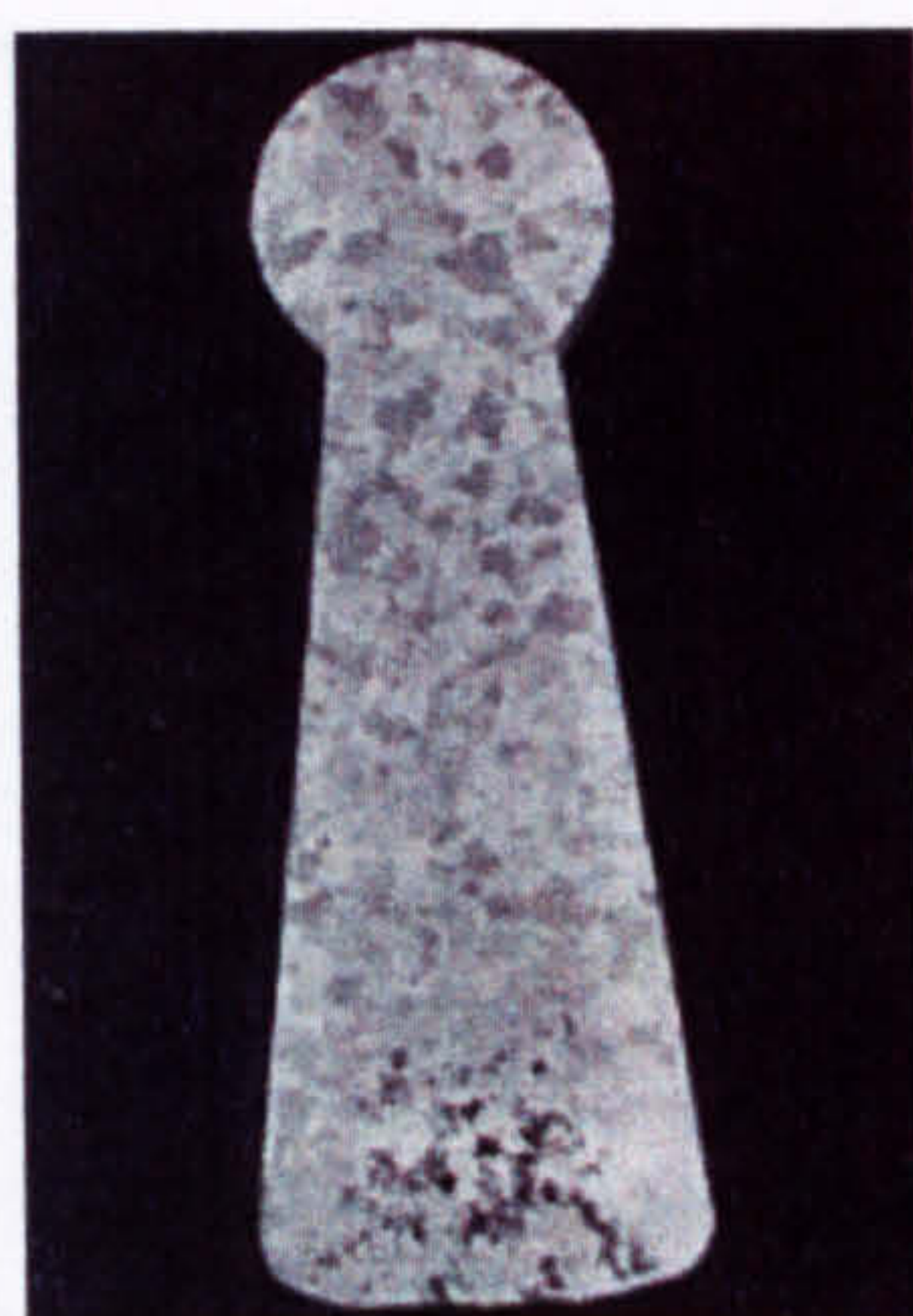


a)



b)

Figure 6.25 a) Alloy 1/1 (AE113 (no P or Ti)), and
b) Alloy 1/4 (1/1 + 0.15 wt.% Ti by TiBAl-TiB₂ grain refiner)

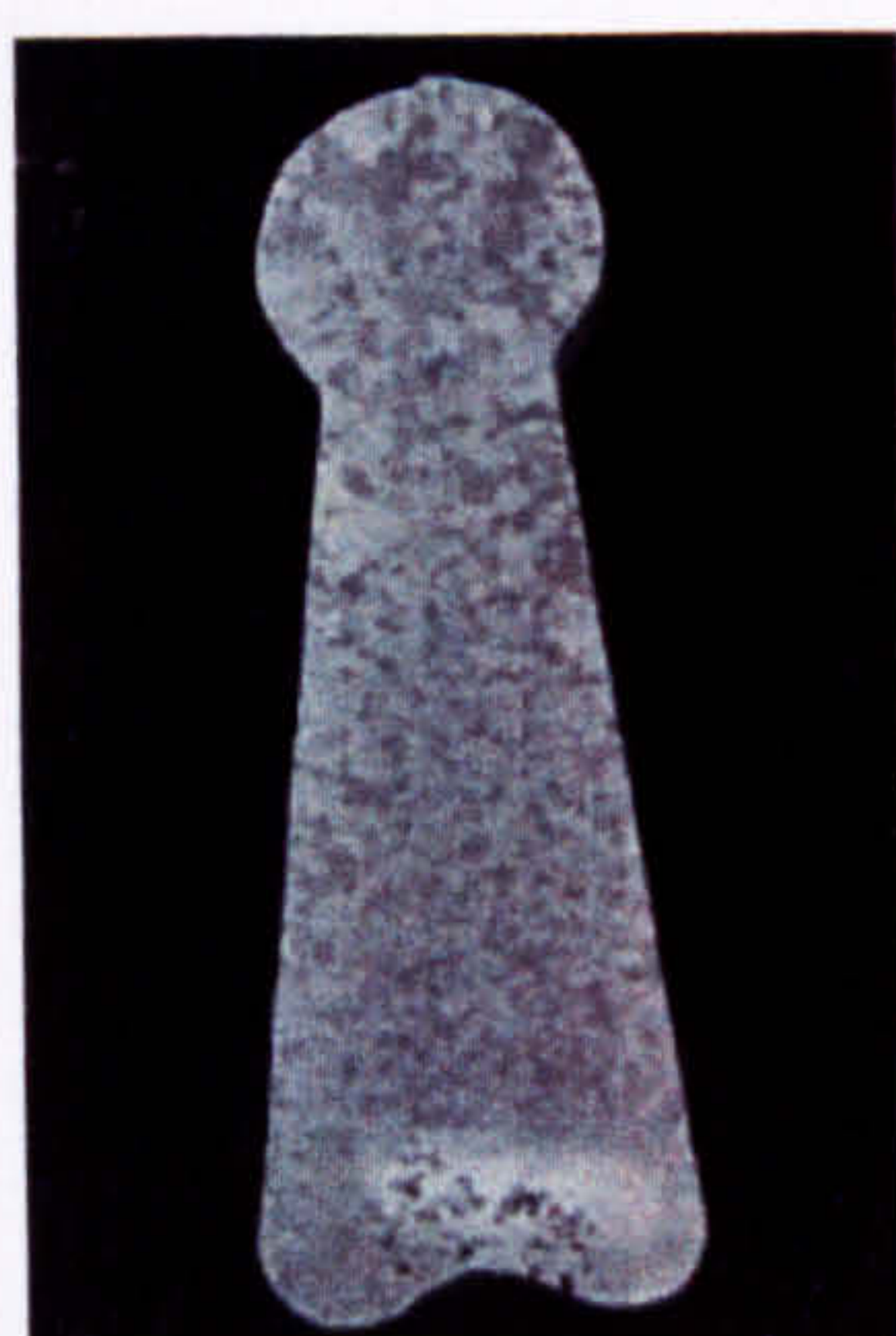


a)

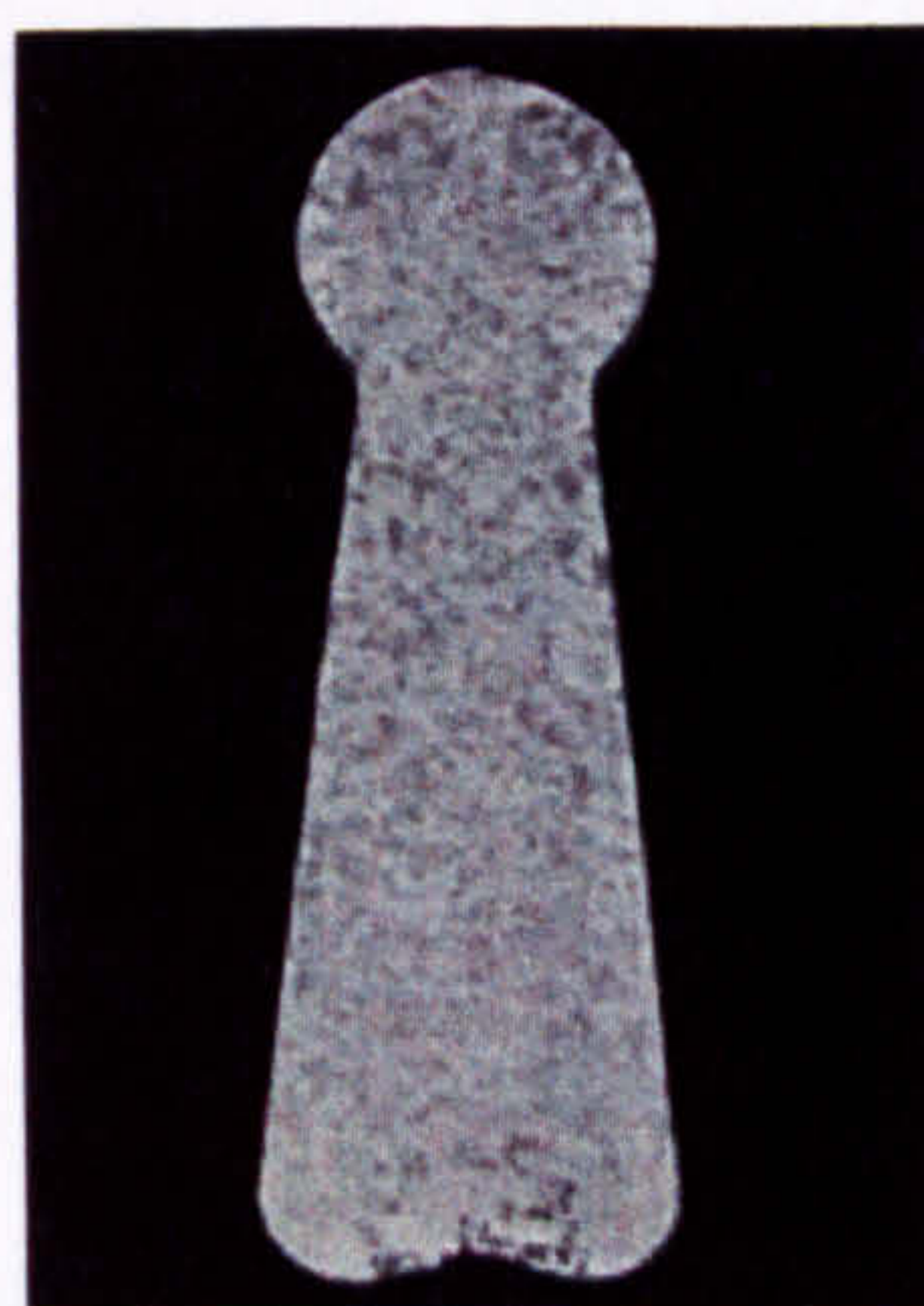


b)

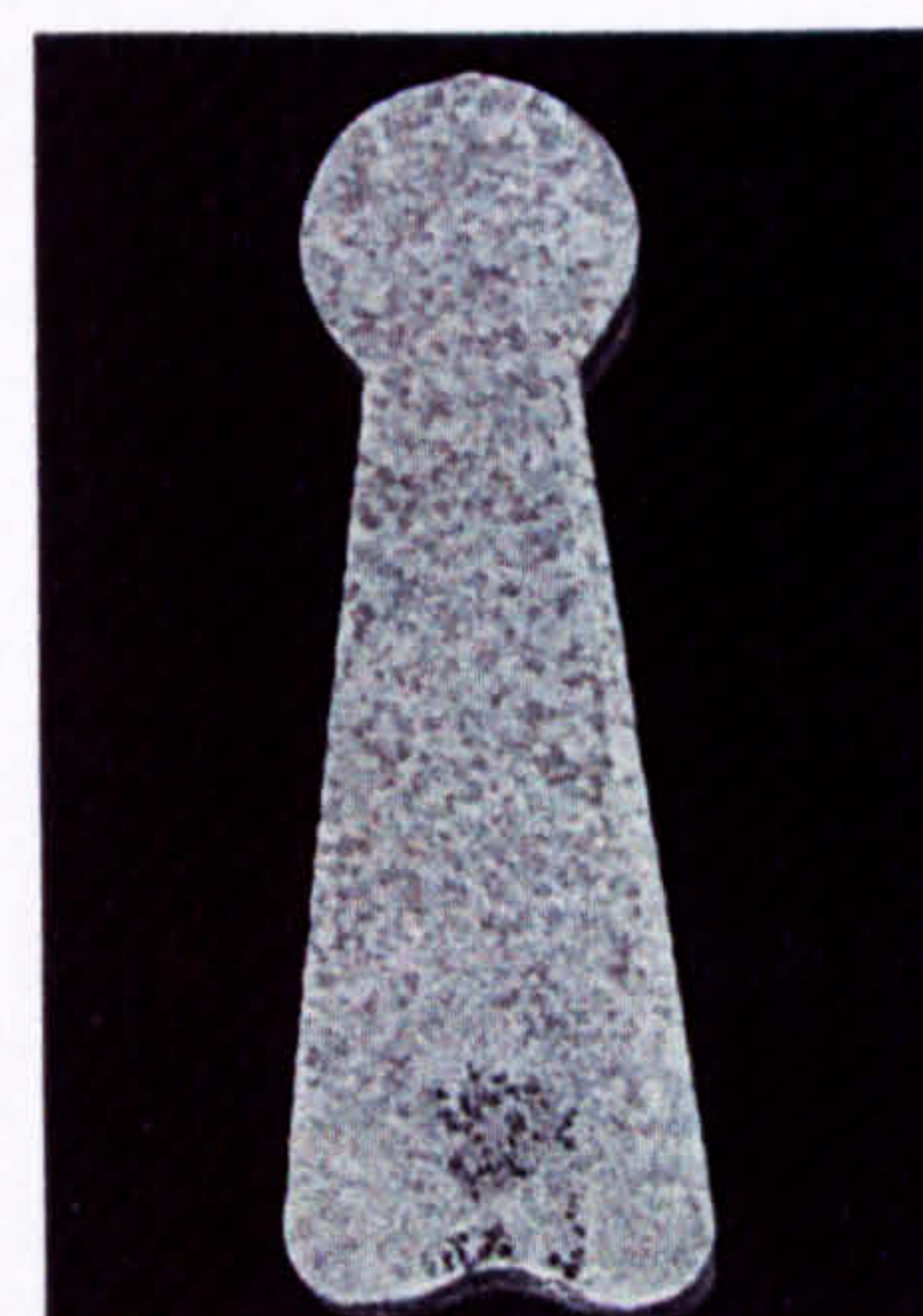
Figure 6.26 a) Alloy 3/1 (AE113 (no P or Ti)), and
b) Alloy 3/4 (3/1 + 0.15 wt.% Ti by Foseco Nucleant 70 grain refiner)



a)



b)



c)

Figure 6.27 AE113 (no P or Ti) a) alloy 4/1 (+ 0.1 wt.% Ti by Al-Ti₆ master alloy),
b) alloy 4/2 (+ 0.15 wt.% Ti by Al-Ti₆ master alloy), and c) alloy 4/3 (+ 0.2 wt.% Ti by Al-Ti₆ master alloy)

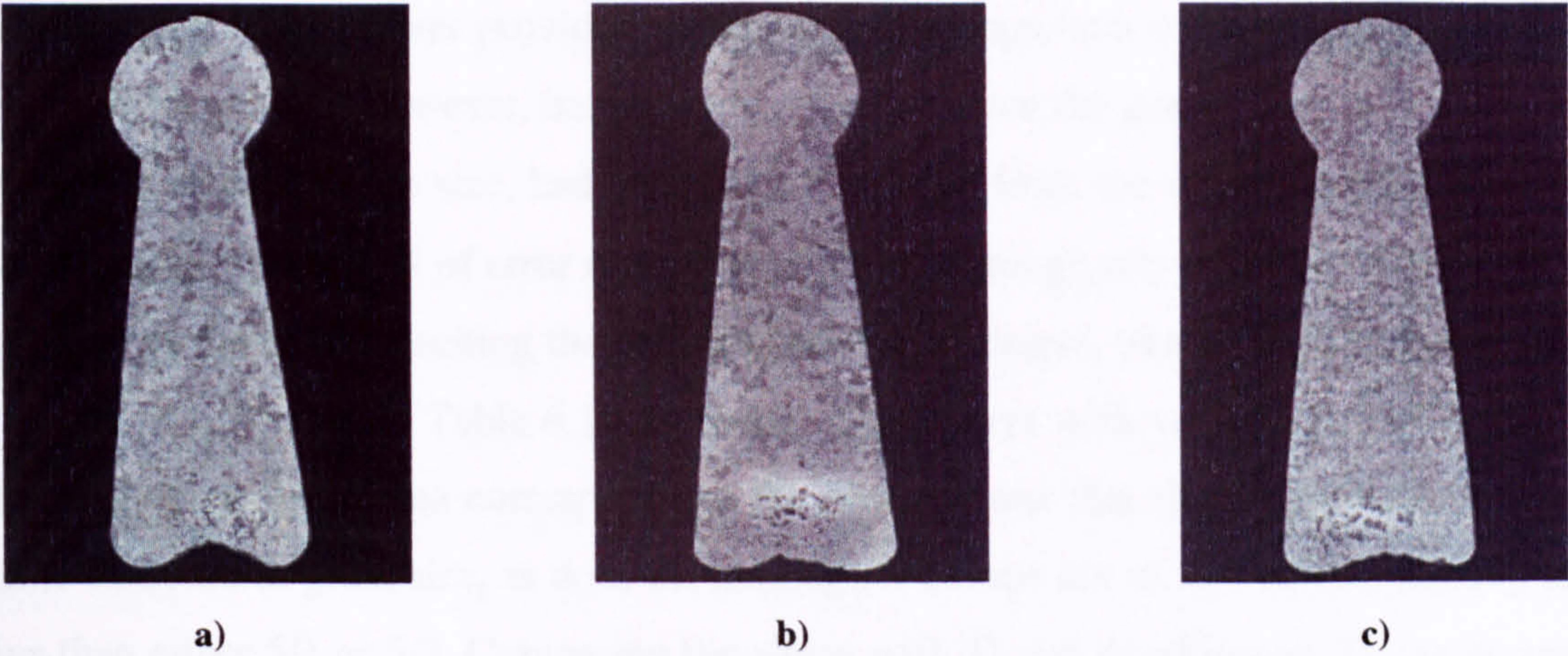


Figure 6.28 AE113 (no P or Ti) **a)** alloy 5/1 (+ 0.1 wt.% Zr by Al-5Zr master alloy), **b)** alloy 5/2 (+ 0.2 wt.% Zr by Al-5Zr master alloy), and **c)** alloy 5/3 (+ 0.3 wt.% Zr by Al-5Zr master alloy)

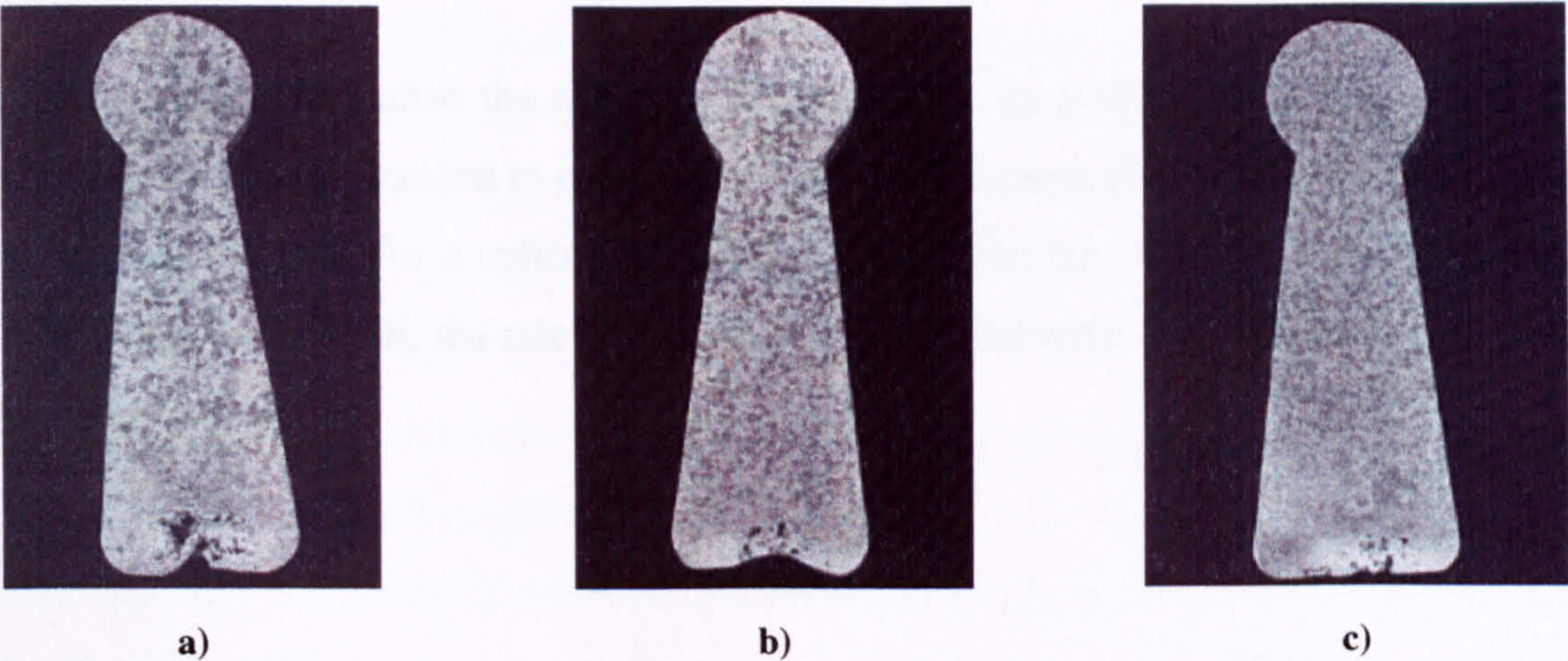


Figure 6.29 Commercial AE113 (P and ~0.15 wt.% Ti) **a)** Alloy 10/1 (+ 0.1 wt.% Zr by Al-5Zr master alloy), **b)** 10/2 (+ 0.2 wt.% Zr by Al-5Zr master alloy), and **c)** 10/3 – (+ 0.3 wt.% Zr by Al-5Zr master alloy)

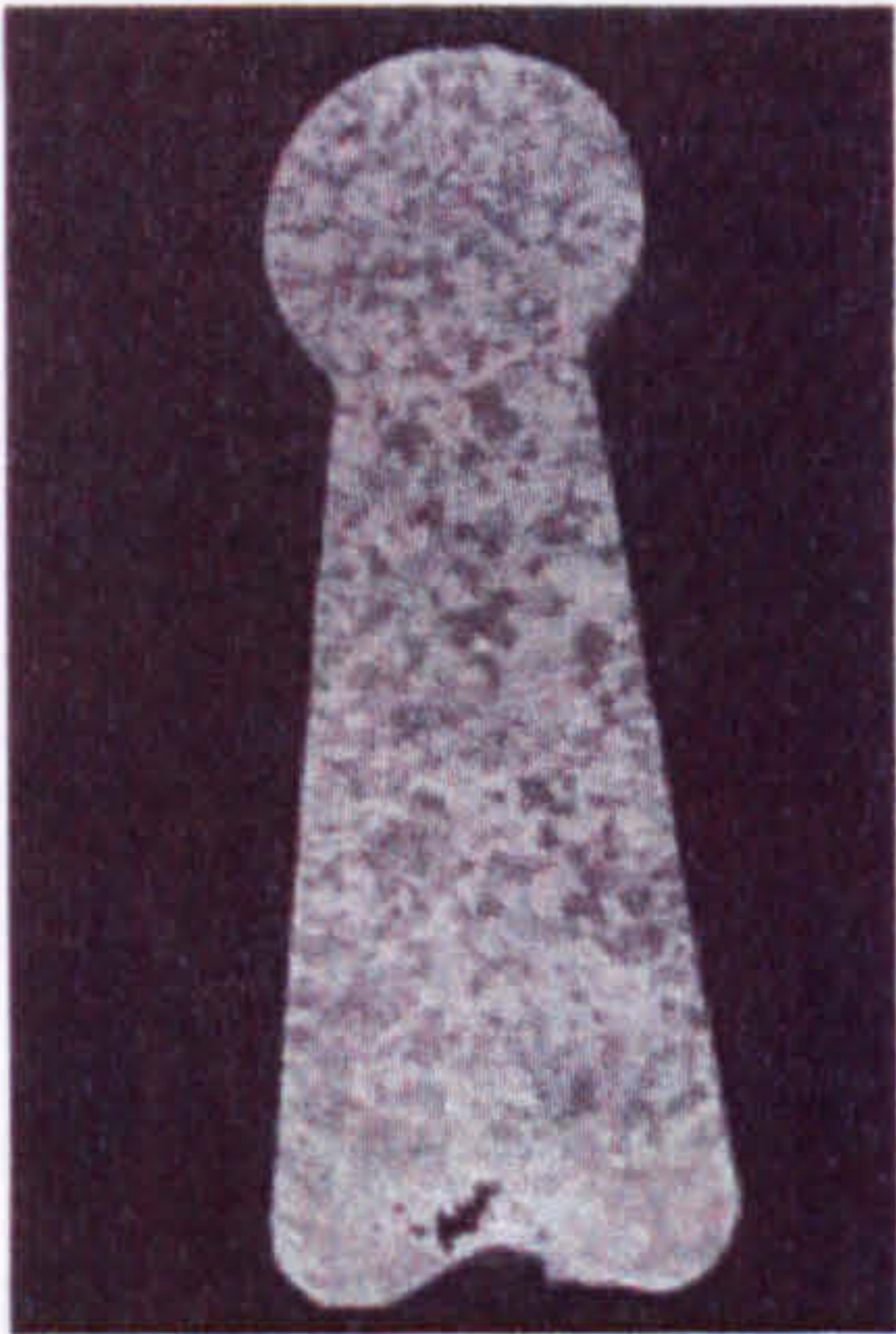


Figure 6.30 Alloy 17/3 (Commercial AE113 (P and ~0.15 wt.% Ti) + 0.1 wt.% Zr and 0.1 wt.% V by master alloys)

Image analysis of the alloys provided a quantitative comparison of the grain sizes after the various additions. It is, however, important to remember that the grains from which the image analysis has calculated the size, had been traced by hand from the macro photographs. There is undoubtedly a great deal of error using this method, although any excessive anomalies were eliminated by carefully checking the data created. Nevertheless, trends can be seen looking at the results as presented in Table 6.12. Looking at the alloys with varying Ti additions (4/1 – 4/3), the average grain area corresponds to the observations that the Ti additions produce a definite decrease in grain size, as does Zr, although 5/2 steps out of line having slightly larger grains than either 5/1 or 5/3. Comparing the alloys with Ti and Zr additions, Ti can be seen to have a larger grain refining effect than the Zr with grains measuring substantially smaller, as previously noted.

In order to try and formalise the effect of Ti, Zr and V on grain size as seen, and indeed quantified so far, it was decided to use growth restriction factors, fully described in Chapter 3, and in brief as follows. For a spherical crystal growing into the melt at a rate controlled by solute diffusion in the melt, the rate of growth at a given diameter is inversely proportional to a quantity Q , defined as:

$$Q = m(k - 1)C_0 = kP$$

where Q (K) is termed the growth restriction parameter, P (K) is the constitutional supercooling parameter, m (K wt.%⁻¹) is the liquidus slope, k is the equilibrium partition coefficient, and C_0 (wt.%) is the solute content in the alloy melt. The equilibrium partition coefficient k , is defined as:

$$k = \frac{C_s}{C_L}$$

where C_s and C_L are the mole fractions of solute in the solid and liquid in equilibrium at a given temperature respectively. For the simple case shown in Figure 6.31, k is independent of temperature. The same methodology applies to peritectic reactions (Al-Ti, Al-Zr and Al-V), although the analysis is made more complex by the small size of the liquid + FCC_Al region

magnified in Figure 6.32. The phases involved for Ti, Zr and V are Al_3Ti , Al_3Zr and Al_{10}V respectively.

In order to be confident of understanding the calculations and that thermodynamic modelling could reproduce reported results ^[Gre00], P and Q values for several of the solutes considered were recalculated using data produced by MTDATA¹. m , the liquidus slope, was calculated in the following way. Using the appropriate binary diagrams as a guide, stepping in temperature calculations at a set composition (0.1 wt.% addition) were carried out through MTDATA's MULTIPHASE module using the MTSOL database. The '*compute print brief print phase*' command presented the fraction of phases at each temperature step, from which the liquidus was determined. Initially a local gradient was calculated at compositions either side of the addition level used for determining k (0.1 wt.%) as in Figure 6.33 a). However, measurements from Greer ^[Gre00] appear to be an average gradient of the liquidus taken directly from the appropriate phase diagrams, and so calculations at either end of the liquidus were carried out (Figure 6.33 b)) and found to be closer to the values reported.

The equilibrium partition coefficient k was calculated by stepping the temperature at a set composition of 0.1 wt.% addition. Using the '*compute print brief print mol*' command the composition and fraction of phases was shown at each temperature step, from which the liquid and solid compositions were recorded. Using the data computed by MTDATA, values of m and k were calculated and once confident that thermodynamic simulations could produce the data needed to calculate the Q factor, solutes important to commercial alloys that had not been included in the report were determined, namely V and Zr. Table 6.13 presents values of P and Q for various solutes (at an addition level of 0.1 wt.%) taken from Greer ^[Gre00], those derived from data produced by Desnain *et. al.* ^[Des90], and produced in this work using MTDATA.

Using the alloy compositions determined by the spark analysis and given in Table 6.11, the growth restriction parameter was calculated for each alloy. The results are shown in Table 6.12 against grain size measurements from the image analysis. For the Ti containing alloys (4/1-4/3) the growth restriction parameter tends to increase slightly with increasing additions indicating there would be a decrease in grain size, as was both seen and measured optically. However, the zirconium containing alloys (5/1-5/3) tend to decrease slightly which would mean an increase in the grain size. A larger grain size was seen in 5/2 when compared with 5/1, however 5/3 appeared, and was quantified to be, finer than either. In order to give a better

idea of how the growth restriction parameter calculations relate to the measured grain size, the two variables were plotted against each other and can be seen in Figure 6.34. The resultant line of best fit illustrates how, as expected, the grain size decreases with increasing growth restriction parameter, although some scatter is present. This provides a method of quantifying the effects of the various additions.

6.4.2 Microstructural Characterisation

From the initial observations, it was decided to concentrate the remainder of the study on the effect of individual additions of Ti (alloys 4/1 to 4/3) and Zr (alloys 5/1 to 5/3) in both the as-cast and heat treated states (100 hours at 350 °C). These alloys were studied in closer detail by means of optical and electron microscopy. A series of optical photographs were taken to create a montage depicting the microstructure across the whole width of the keel bar. Little variation was found except that the structure in the centre of the casting was slightly coarser than that at the edges. This would be expected as the centre is the last place to solidify and therefore has the slowest solidification rate. Example micrographs are given in Figures 6.35 to 6.38, where it can be seen that there is very little difference between the microstructures whether containing Ti or Zr, although it appears that the heat treated samples may have a slightly less pronounced dendritic structure than the as cast, as expected due to gradual homogenisation.

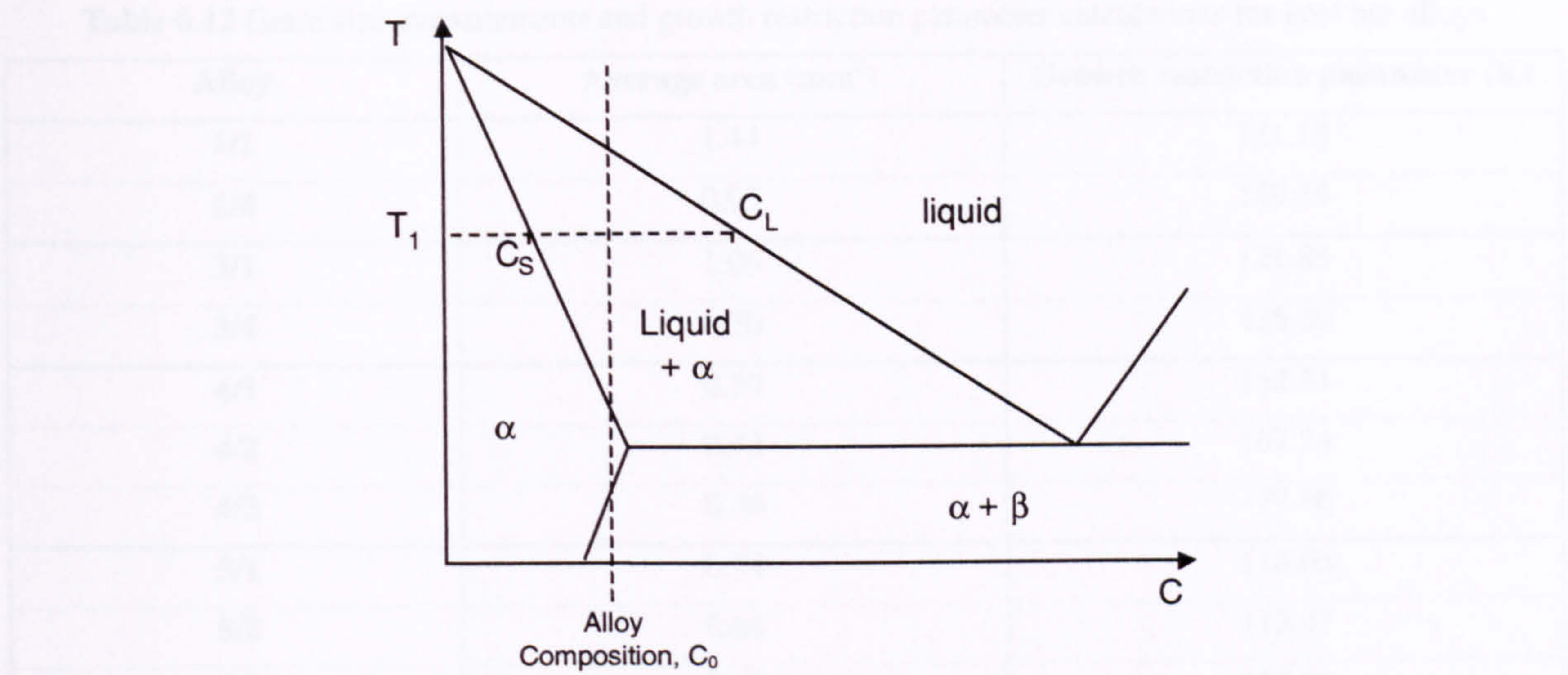


Figure 6.31 Hypothetical phase diagram illustrating $k = C_S/C_L$ as constant.

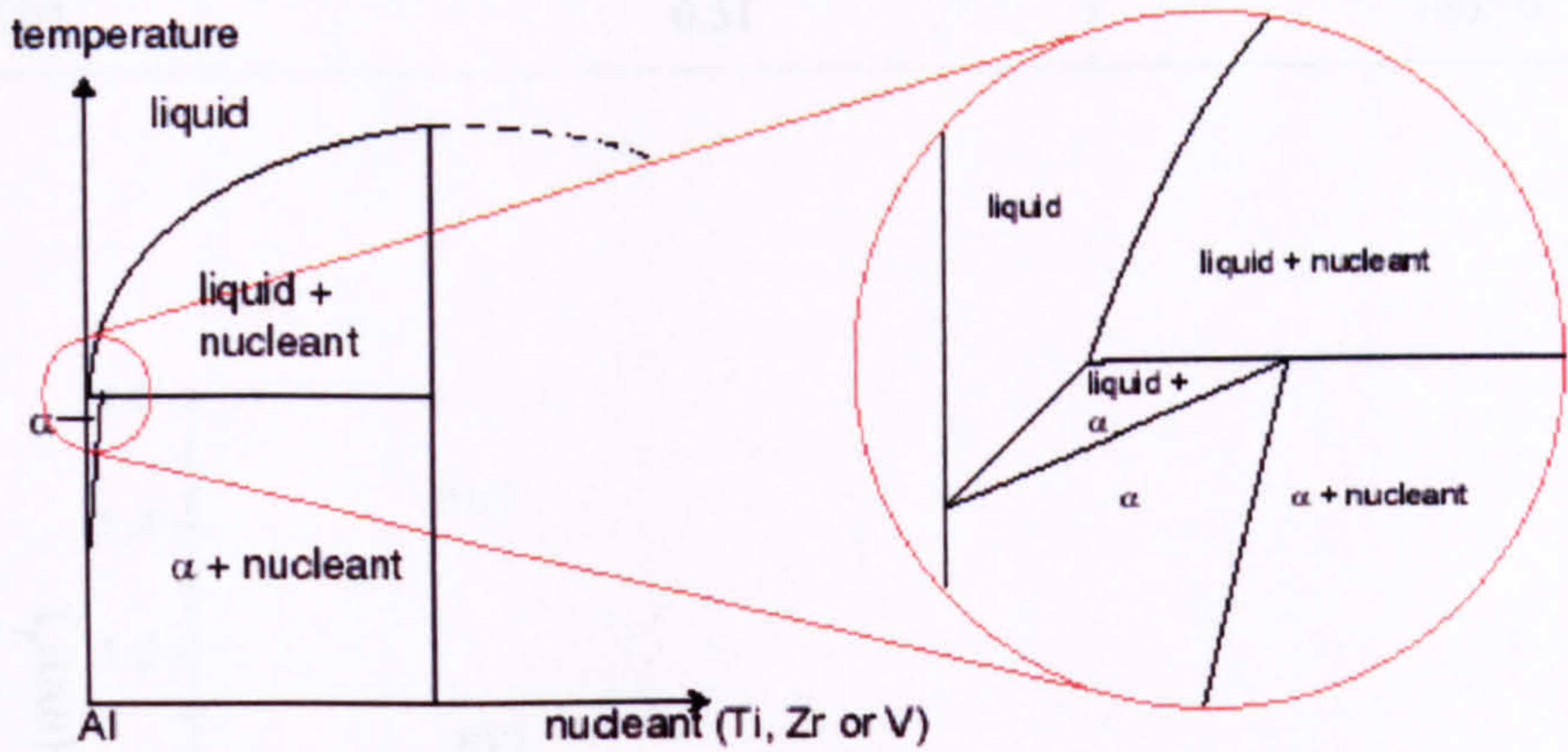


Figure 6.32 Magnification of peritectic reaction in Al-Ti, Al-Zr and Al-V systems.

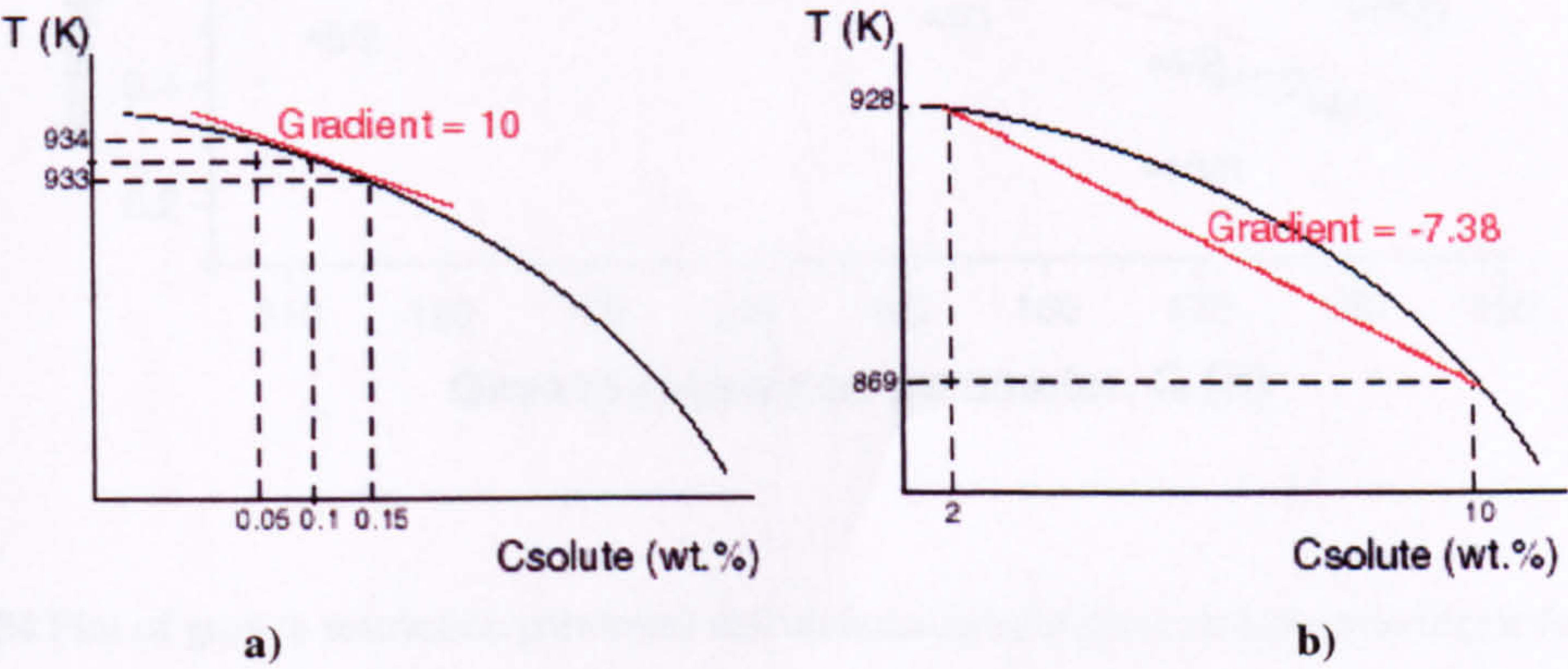


Figure 6.33 Calculation of m , liquidus slope for Al-Si system using a) local gradient, and b) average gradient

Table 6.12 Grain size measurements and growth restriction parameter calculations for keel bar alloys

Alloy	Average area (mm ²)	Growth restriction parameter (K)
1/1	1.44	121.18
1/4	0.95	149.59
3/1	1.06	121.85
3/4	0.70	135.09
4/1	0.50	152.51
4/2	0.43	167.34
4/3	0.36	177.66
5/1	0.74	118.05
5/2	0.81	113.47
5/3	0.48	111.81
10/1	0.54	179.59
10/2	0.39	171.53
10/3	0.25	167.02
17/3	0.51	180.50

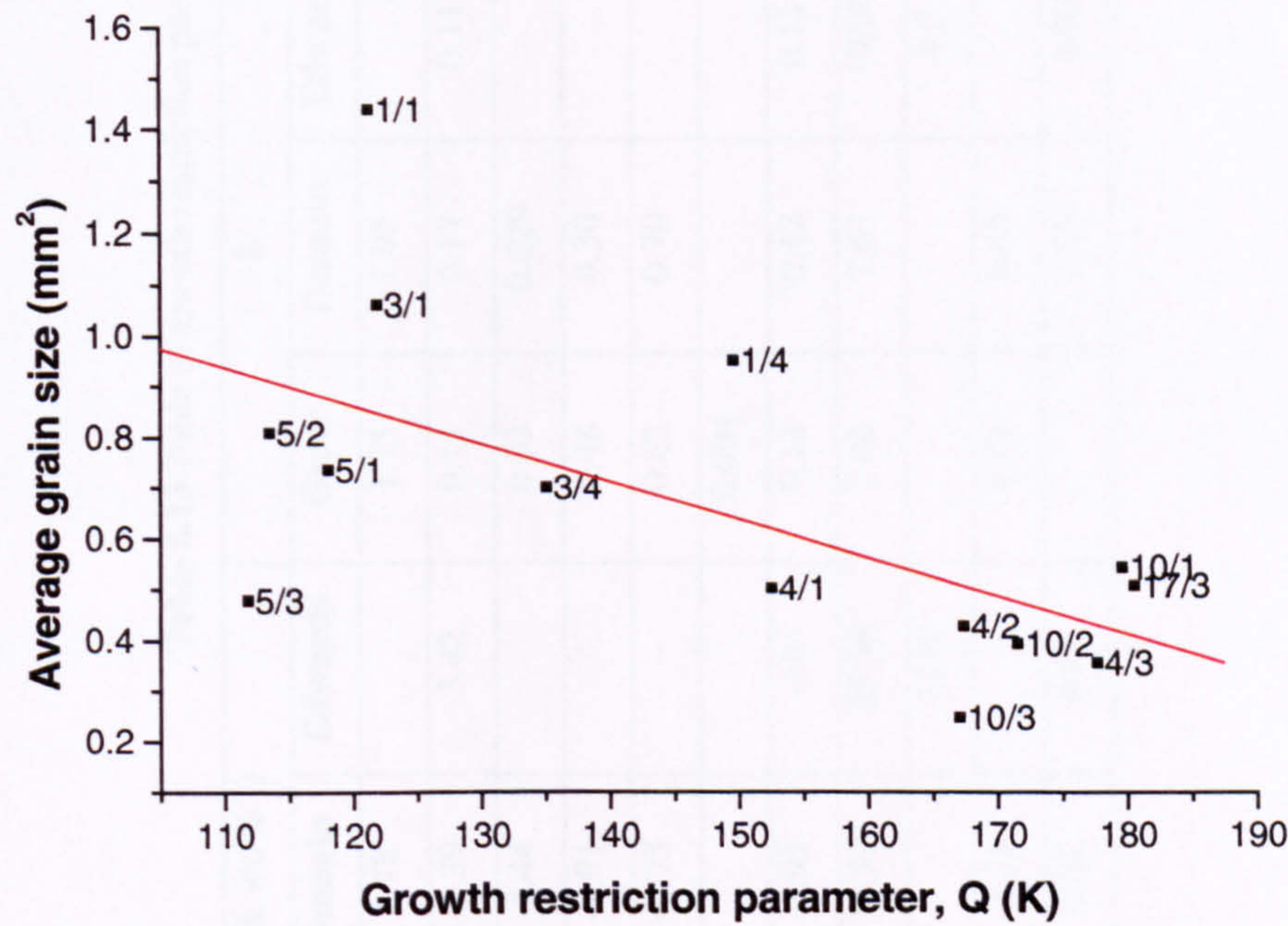
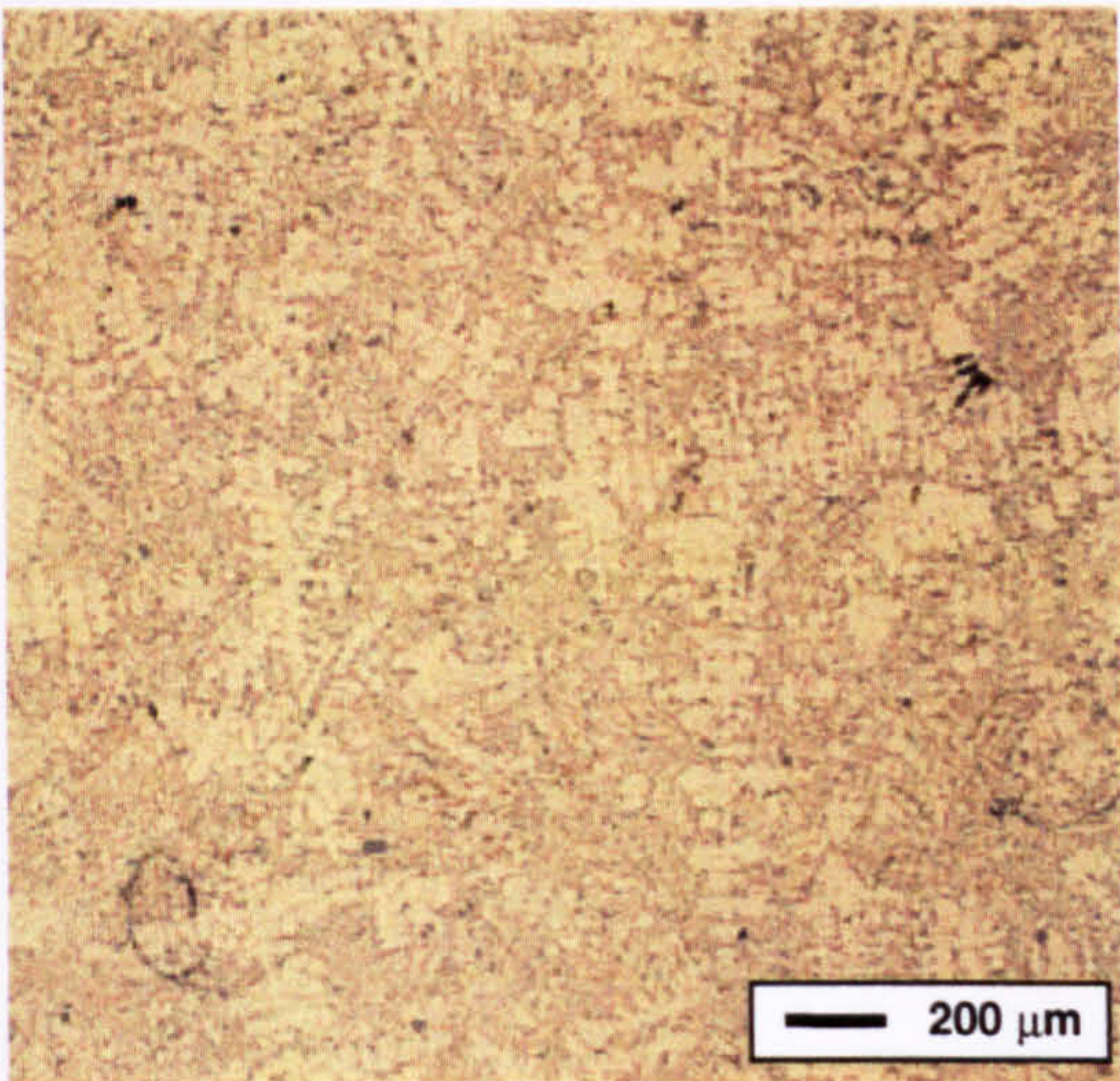


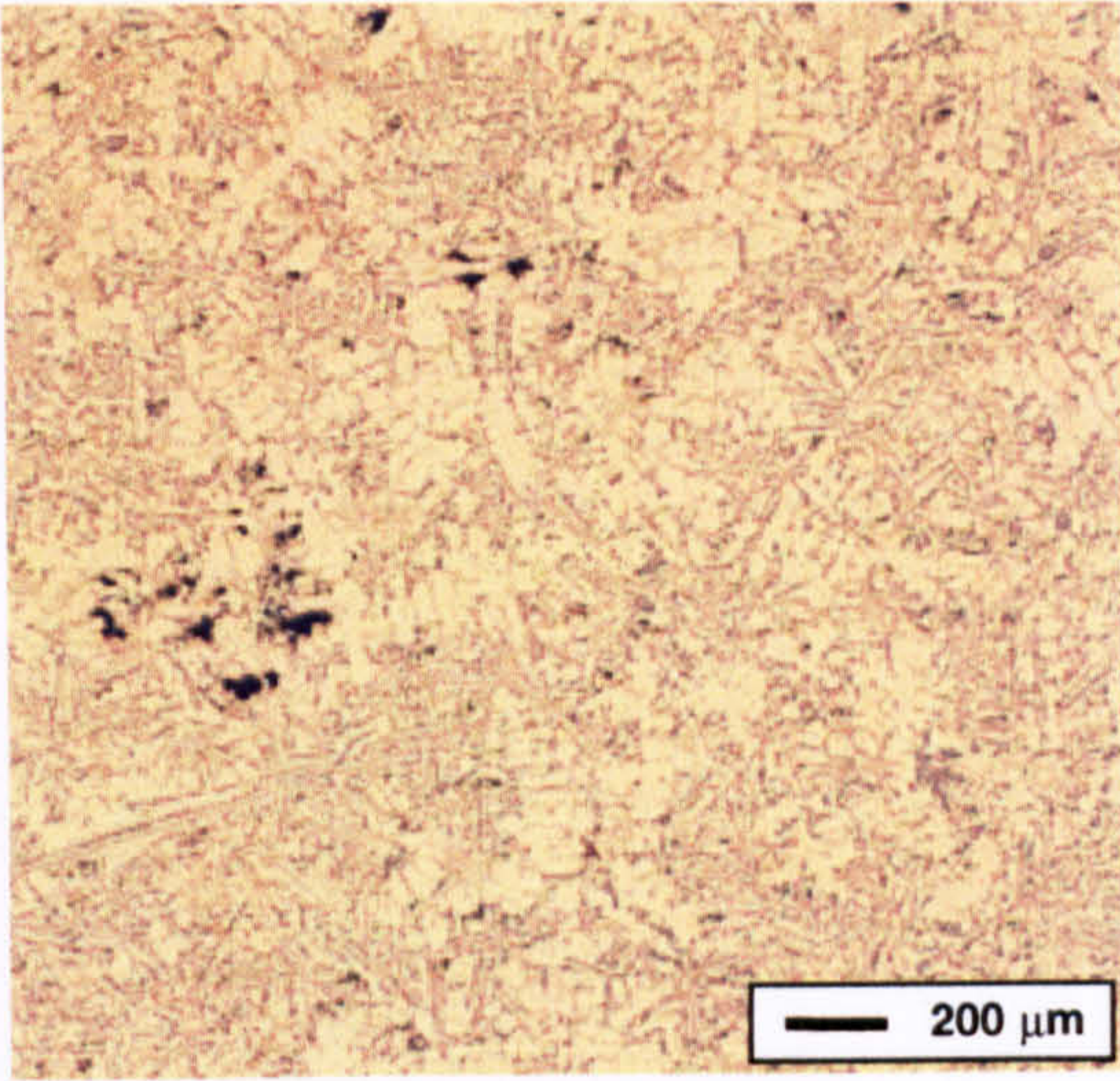
Figure 6.34 Plot of growth restriction parameter calculations against grain size measurements for keel bars

Table 6.13 Table of growth restriction parameters for various alloying additions

Solute	m (K wt.% ⁻¹)			k			P (K)			Q (K)		
	Greer	Desnain	Edwards	Greer	Desnain	Edwards	Greer	Desnain	Edwards	Greer	Desnain	Edwards
Cr	2.60	3.78		1.75	1.95		0.11	0.18		0.19	0.36	
Cu	-2.50	-3.39	-3.42	0.15	0.17	0.11	1.47	1.66	2.51	0.21	0.28	0.30
Fe	-2.93	-4.44		0.03	0.029		9.46	14.87		0.28	0.43	
Mg	-5.84	-4.91		0.48	0.30		0.63	1.15		0.30	0.34	
Mn	-1.20	-0.75		0.62	0.70		0.07	0.03		0.05	0.02	
Ni	-3.50			0.004			87.15			0.35		
Si	-6.62	-5.93	-10	0.13	0.12	0.11	4.85	4.35	5.97	0.58	0.52	0.66
Ti	25.63	33.33	35.56	7.00	7.67	10.00	2.20	2.90	3.20	15.38	22.23	32.00
V			11.8			4.3			0.91	2.11		3.89
Zn	-1.65	-3.21		0.43	0.45		0.22	0.39		0.09	0.18	
Zr		4.55	4.00		2.55	3.00		0.28	0.27		0.71	0.80

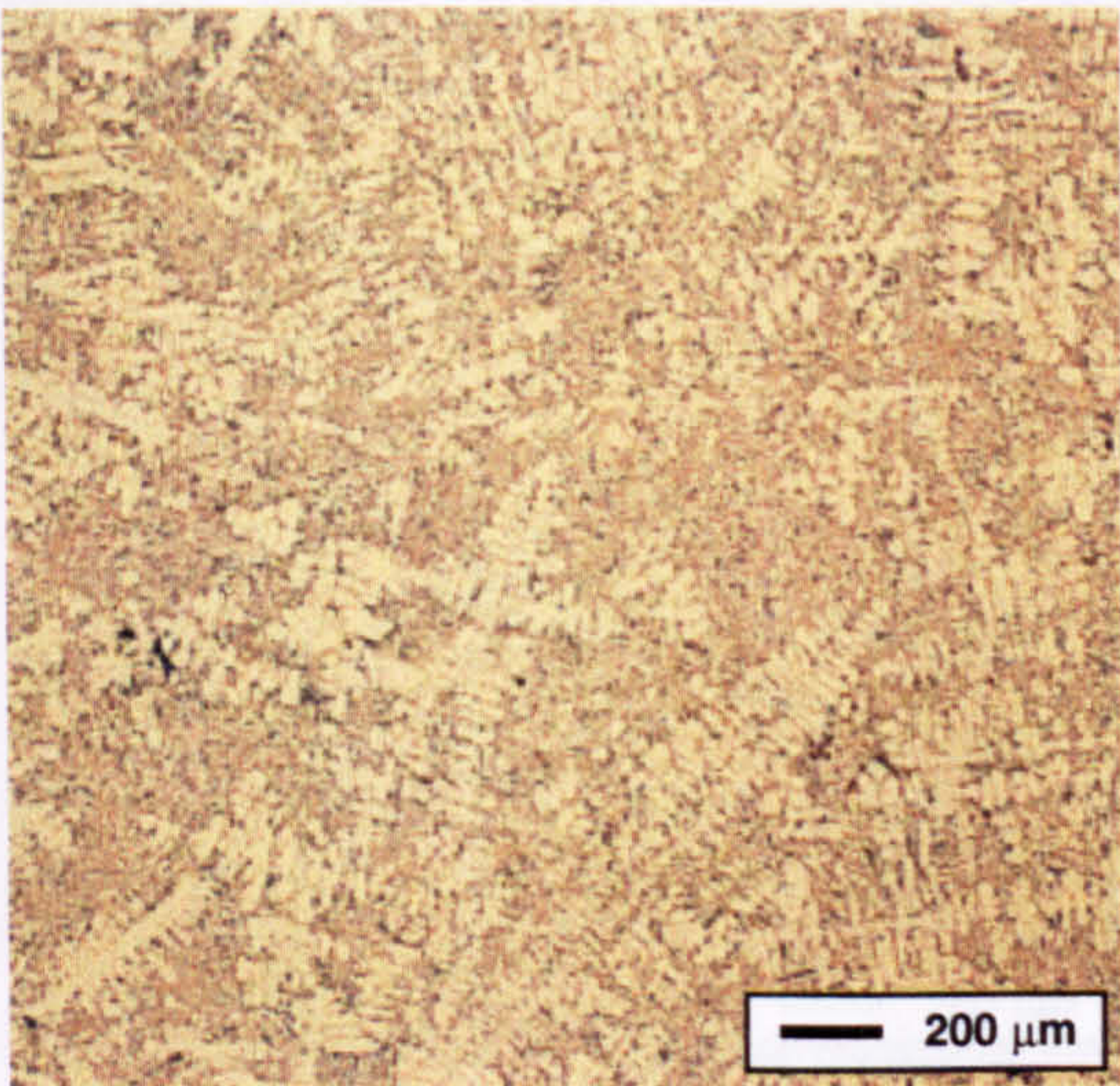


a)

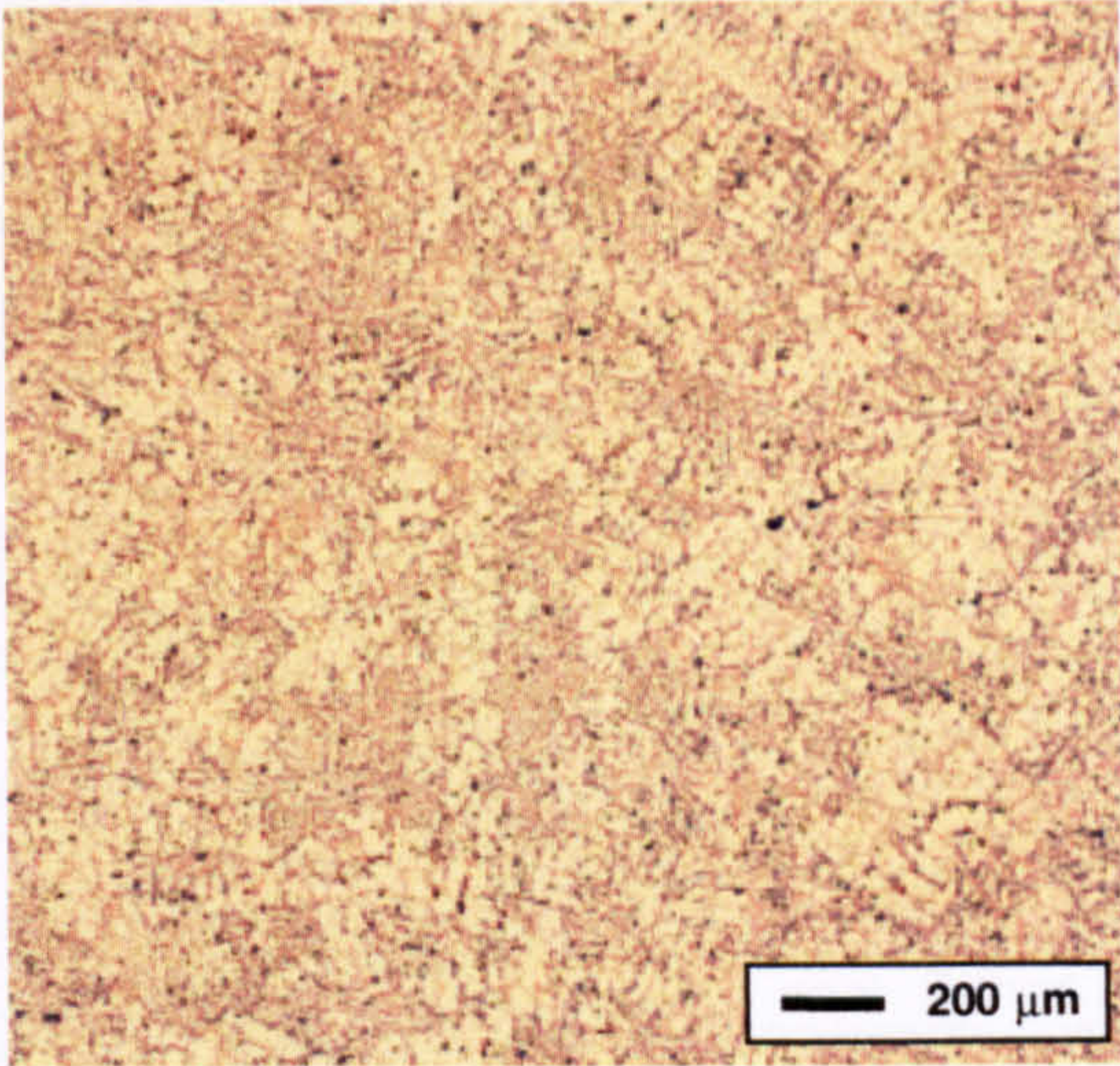


b)

Figure 6.35 Alloy 4/1 (AE113 (no P or Ti) + 0.1 wt.% Ti) **a)** as cast, and **b)** after heat treatment



a)



b)

Figure 6.36 Alloy 4/3 (AE113 (no P or Ti) + 0.2 wt.% Ti) **a)** as cast, and **b)** after heat treatment

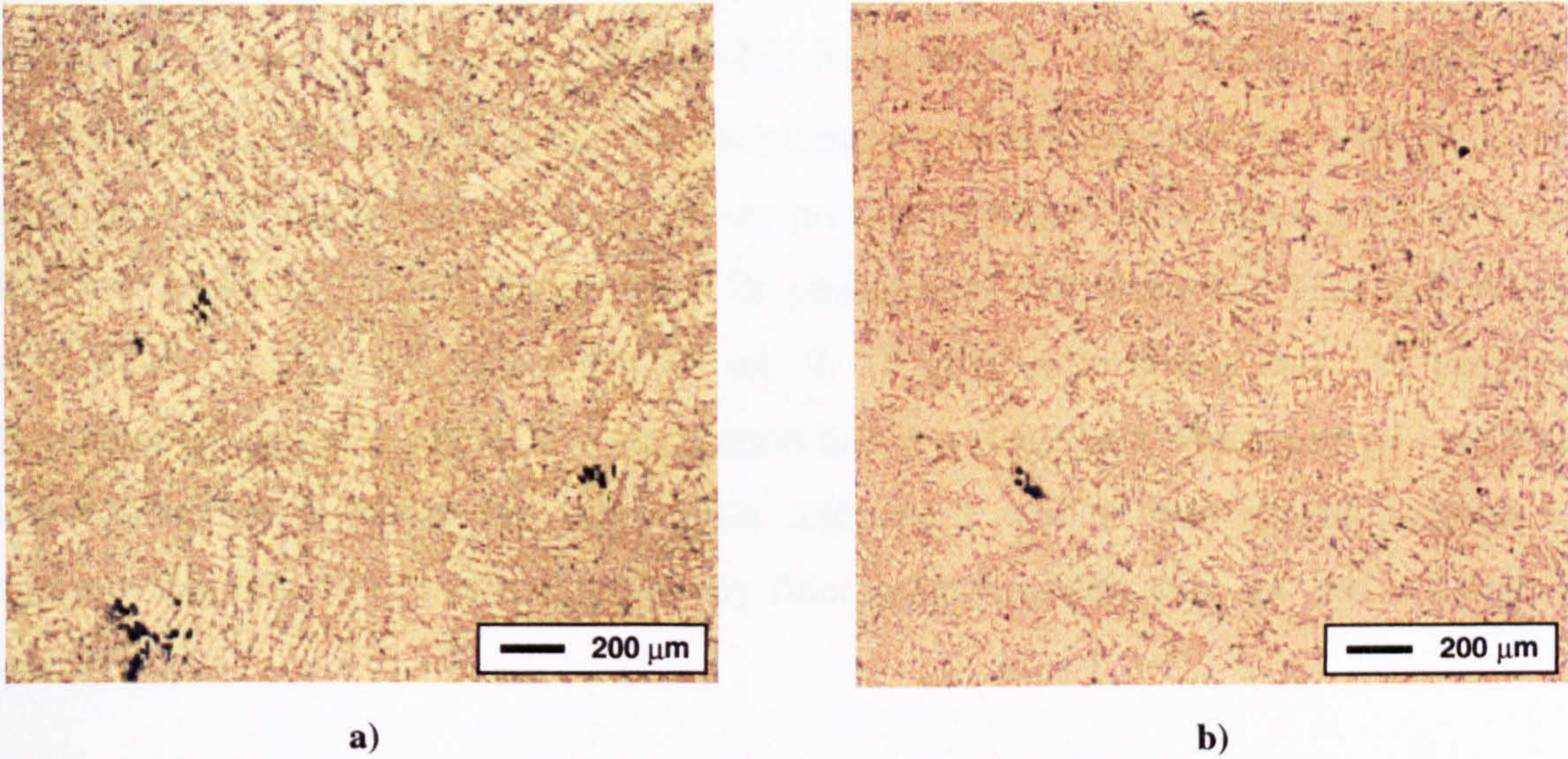


Figure 6.37 Alloy 5/1 (AE113 (no P or Ti) + 0.1 wt.% Zr) **a)** as cast, and **b)** after heat treatment

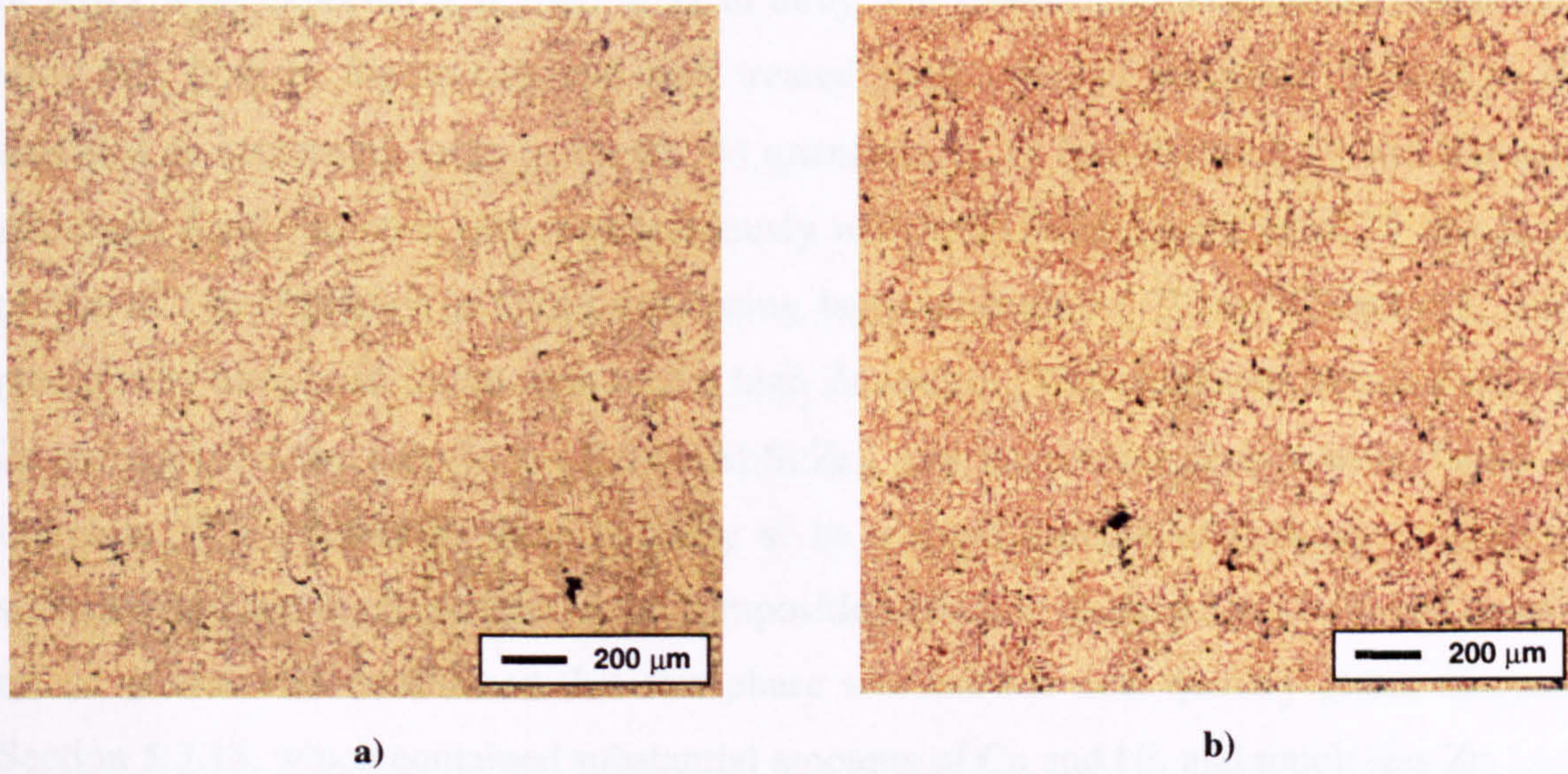


Figure 6.38 Alloy 5/3 (AE113 (no P or Ti) + 0.3 wt.% Zr) **a)** as cast, and **b)** after heat treatment

Standard EDX analysis was carried out on the SEM for the 8 alloys. In addition to the aluminium matrix and silicon particles several different intermetallic precipitates were identified, namely $\text{Al}_7\text{Cu}_4\text{Ni}$, $\pi(\text{Al}_8\text{FeMg}_3\text{Si}_6)$, Al_3Ni , $\text{Al}_3(\text{Ni,Cu})_2$, $\lambda(\text{Al}_5\text{Cu}_2\text{Mg}_6\text{Si}_5)$, Al_9FeNi , Al_2Cu , and Mg_2Si . None of these phases contained any quantity of the grain refining additions Ti or Zr, and furthermore, phases previously identified as having a high solubility for these elements, Al_3Ti and the high Zr phase, were not observed. This was surprising, particularly in alloy 4/3 where the 0.2 wt. % Ti addition is higher than that required for formation of the Al_3Ti phase. It is understood that it is this phase which acts as a nucleant for aluminium and therefore instigates grain refinement, and it was proven through image analysis that this alloy had a significantly finer grain structure than 4/1 and 4/2 with lesser additions.

A large reduction in grain size was also seen with increasing additions of Zr, and either Al_3Ti or Al_3Zr were expected at 0.3 wt. % Zr in alloy 5/3. Indeed, an intermetallic phase found in alloy 5/3, both in the as cast and heat treated states, was of particular interest as it was analysed as containing large (~ 60 wt. %) quantities of Zr (see Figure 6.39 and Table 6.14). Although Al_3Ti has been observed previously with substantial quantities of Ti and Zr, and a needle-like morphology in alloys containing large amounts of Ti (see Chapter 5), no such precipitates have been found with such a high Zr content. The calculated stoichiometry of the Zr particles can be seen to be 2:5:4 (Al:Si:Zr), and no similar phases were found in the literature ^[Han84]. Although there is likely to be a slight amount of pick up of Si from the surrounding area, the Si content in the composition given in Table 6.14 is believed to be a true effect. It was also established that this phase was not the new quinary phase discussed in Section 5.3.15, which contained substantial amounts of Cu and Ni, and much less Zr.

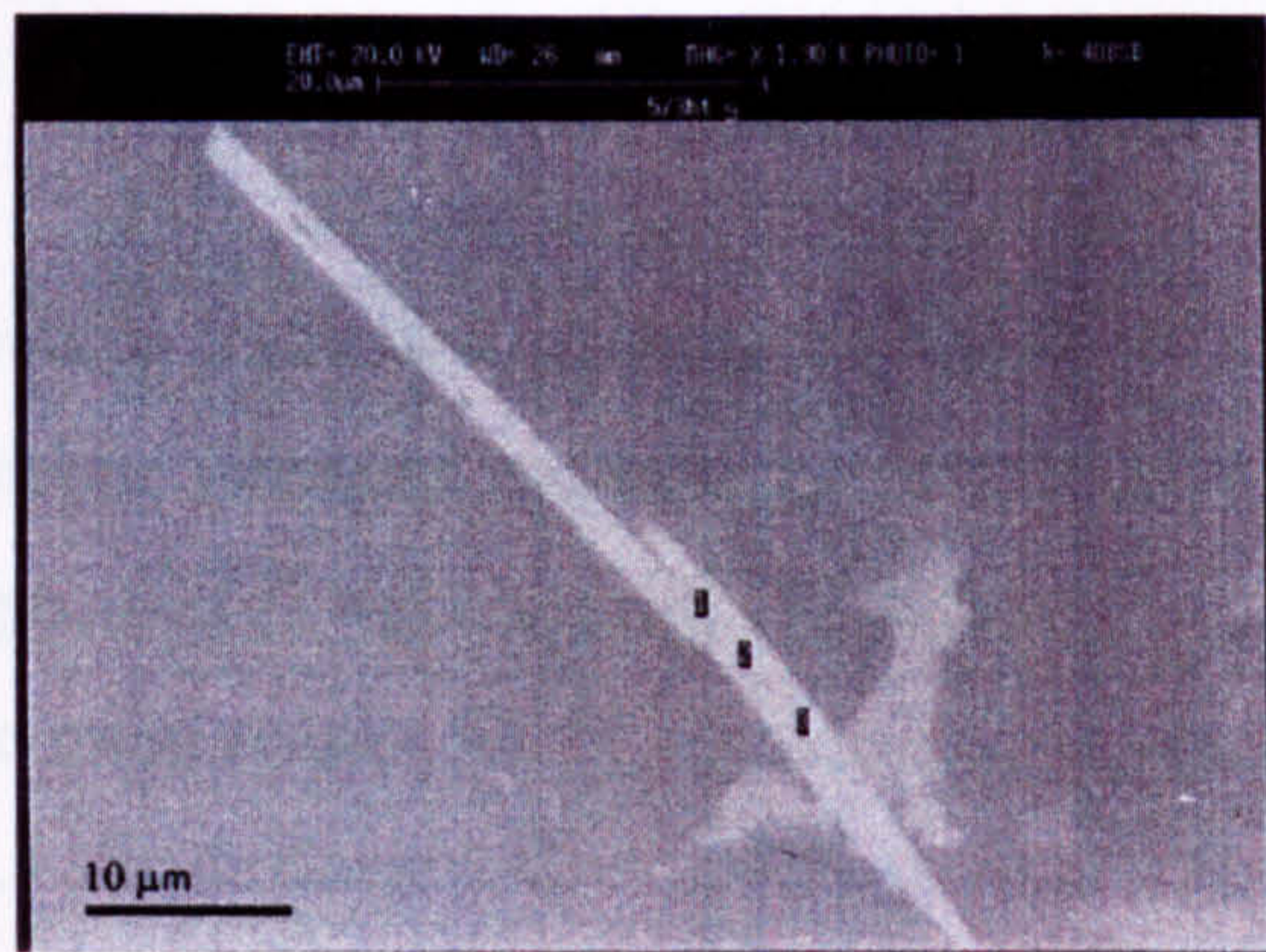


Figure 6.39 SEM image of a Zr rich particle

Table 6.14 Average composition of Zr rich particles observed in the SEM

	Wt. %	At. %
Al	10	19
Si	25	45
Zr	65	36

All other elements < 1% when present

6.4.3 Summary

A series of keel bar alloys were cast to investigate the effect of Ti and Zr additions, and the efficiency of the master alloys providing these grain refining elements. From observation of the grain structures, AlTi₆ appeared to be the most efficient master alloy for adding Ti to the melt producing a fine, equiaxed structure. Increasing the amount of refiner in the melt from 0.1 to 0.2 wt. % Ti, again by AlTi₆ master alloy, produced a very fine structure, much more refined than equivalent and higher addition of Zr. Image analysis of the grain structure provided a quantitative measurement of the effect of the various additions. In combination with calculation of the growth restriction parameters for each of the alloys, a relationship was established between grain size and growth restriction. The resultant plot (Figure 6.34) showed a clear trend linking an increase in Q with a decrease in grain size, thus providing a method of quantifying the effects of various additions.

Microstructurally, little difference was observed between as-cast and heat treated alloys. However, EDX analysis revealed a previously unreported phase in alloys containing large additions (0.22 wt. %) of Zr. The phase was found to include large amounts of Zr, of approximate stoichiometry SiZrAl_{0.5}, and was seen to adopt a similar morphology to that of Al₃Ti. This phase has not been observed before, presumably as the alloys of interest in this work do not usually contain such large additions of Zr, but is of particular interest as Zr is usually found to be soluble in the Al₃Ti phase. It can therefore be assumed that there is a specific quantity of Zr, above which the SiZrAl phase become stable instead of Al₃Ti, depending on the alloy composition.

6.5 Stepped Mould: Model Alloys 3/1 to 3/6

Previous trials investigating the effects of Ti, Zr and V additions to a number of model alloy systems (stepped moulds 83 to 90 and keel bars described in Sections 6.3 and 6.4 respectively) have proved inconclusive in determining the mechanism of grain refinement. The main reason for this appears to be that the large number of components (e.g. Cu, Fe, Ni etc.) also influence the solidification of a casting making the alloys too complicated to isolate the effect of Ti additions. Thus, a series of model alloys were designed based on calculations of growth restriction factors explained in Chapter 3, and used in section 6.4 in combination with image analysis to confirm the relationship between growth restriction and grain size. Consider again that for a spherical crystal growing into the melt at a rate controlled by solute diffusion in the melt, the rate of growth at a given diameter is inversely proportional to a quantity Q , defined as:

$$Q = m (k-1) C_0 = kP$$

Assuming that the liquidus slope, m , and equilibrium partition coefficient, k , are constant over the composition ranges of interest, the effect of Ti, Zr and V additions on the growth restriction parameter can be quantified as;

$$Q(\text{Al-Ti}) = 22.37 (10.37-1) C_{0\text{Ti}} \quad (\text{K})$$
$$Q(\text{Al-Zr}) = 4.0 (3.0-1) C_{0\text{Zr}} \quad (\text{K})$$
$$Q(\text{Al-V}) = 11.8 (4.3-1) C_{0\text{V}} \quad (\text{K})$$

This is illustrated in Figure 6.40 where it can be seen that, as expected, the Q factor is directly proportional to the solute content. The Ti additions can be seen to have a Q value around 4 times that of V, and considerably more than 4 times that of Zr. This, in theory, indicates that for equal quantities of Ti, Zr, and V additions, Ti would be the most efficient grain refiner. Alternatively, for Zr and V to have the same Q value as 0.1 wt.% Ti, they would have to be added at 2.62 and 0.54 wt. % respectively. Based on the latter of these assumptions equivalent Zr and V additions were calculated for Q values based on the range of Ti solute contents in Table 6.15.

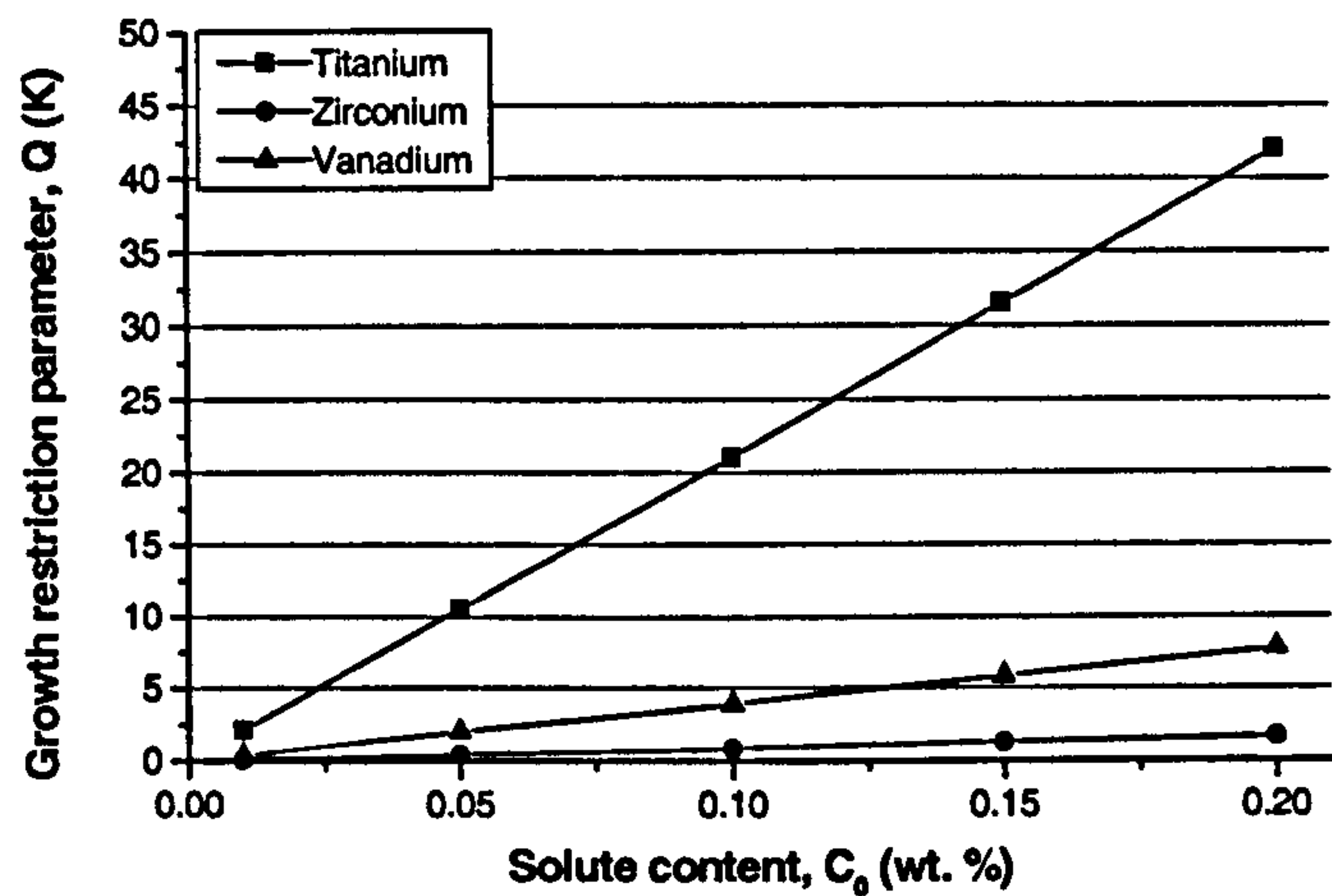


Figure 6.40 Relationship between growth restriction parameters and solute content of Ti, Zr and V

Table 6.15 Q calculations for various Ti contents, and Zr and V additions for the same Q

Ti content (wt.%)	Resultant Q (K)	Equivalent Zr content (wt.%)	Equivalent V content (wt.%)
0.01	2.10	0.26	0.05
0.05	10.48	1.31	0.27
0.1	20.96	2.62	0.54
0.15	31.44	3.93	0.81
0.2	41.92	5.24	1.08

In order to verify the theory quantified in Table 6.15 a series of ternary Al-Si-X (X = Ti, Zr and V) model alloys were designed and cast in stepped moulds. Model alloys 3/1, 3/2 and 3/3 were designed to contain 0.01, 0.05 and 0.15 wt. % Ti respectively, alloys 3/4 and 3/5 had Zr and V additions equivalent to 0.01 wt. % Ti (0.26 wt. % Zr and 0.05 wt. % V), and alloy 3/6 was aimed at investigating the effect of a combination of Zr and V, again equivalent to the growth restriction parameter of 0.01 wt. % Ti (0.12 wt. % Zr + 0.03 wt. % V). The actual compositions, as determined by spark analysis, are given in Table 6.16 and differ slightly from the intended elemental contents due to impurities (< 0.5 wt. %) in the melt stock. The alloys were cast in stepped moulds in order to provide an insight into the relationship between Ti (Zr and V) content, growth restriction and cooling rate.

Table 6.16 Composition of stepped mould model alloys 3/1 to 3/6

Alloy No.	Wt. %							
	Al	Si	Cu	Ni	Fe	Ti	Zr	V
3/1	Bal.	12.45	0.17	0.12	0.30	0.008	-	-
3/2	Bal.	12.49	0.17	0.13	0.31	0.051	-	-
3/3	Bal.	12.34	0.16	0.12	0.30	0.148	-	-
3/4	Bal.	12.20	0.09	0.10	0.38	0.007	0.221	-
3/5	Bal.	12.15	0.07	0.03	0.20	0.009	0.005	0.063
3/6	Bal.	12.11	0.12	0.08	0.22	0.009	0.142	0.020

6.5.1 Characterising the Structure

The macrographs taken of the stepped mould cross sections of all 6 alloys are presented in Figures 6.41 to 6.46. Consider first the difference between castings from the two different mould temperatures. In the smaller steps, at both mould temperatures, the structure is completely columnar due to the extremely fast cooling rates. However, in the larger steps it can be seen that in general the 440 °C mould temperature castings have much less columnar growth at the edges and a more equiaxed structure, with the size of the equiaxed grains appearing to be larger than those seen in the 100 °C castings. As was seen in model alloys 83 to 90, the slower cooling rates imposed by the heated mould enable longer growth times for the aluminium, and thus larger grains. In addition, it appears in these alloys that the slower cooling rate promotes a columnar to equiaxed transition, which is to be expected as the equiaxed grains in the centre of the casting have longer to establish themselves before they are impinged upon by the columnar growth.

However, of interest in this study is the effect of the elemental additions on the grain size and growth transitions, and so, after studying the macrographs closely, step 4 of the 100 °C MT castings were chosen to provide a direct comparison for further investigation.

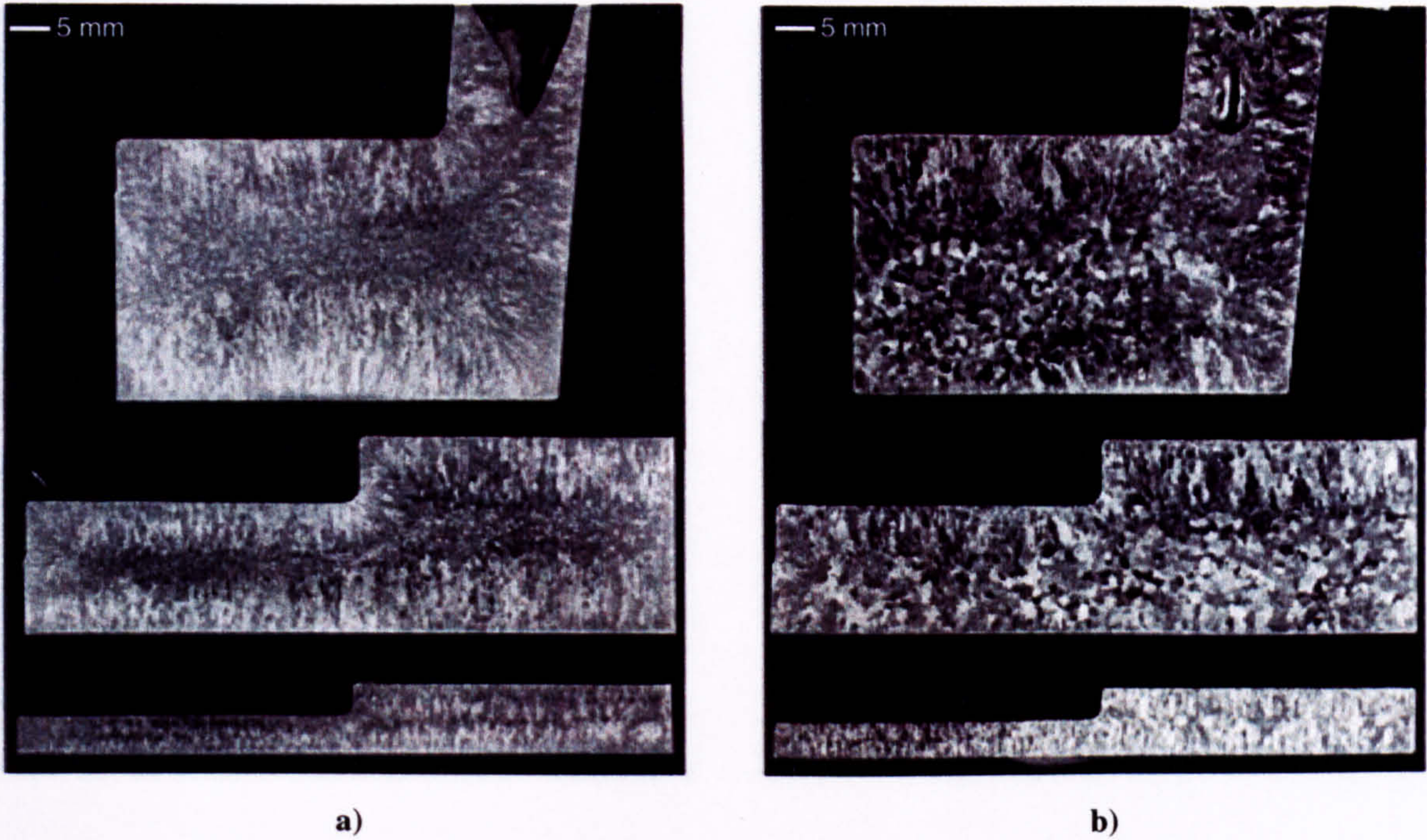


Figure 6.41 Optical macrographs of stepped mould: model alloy 3/1 (0.01 wt. % Ti), cast at **a)** 100 °C and **b)** 440 °C mould temperatures

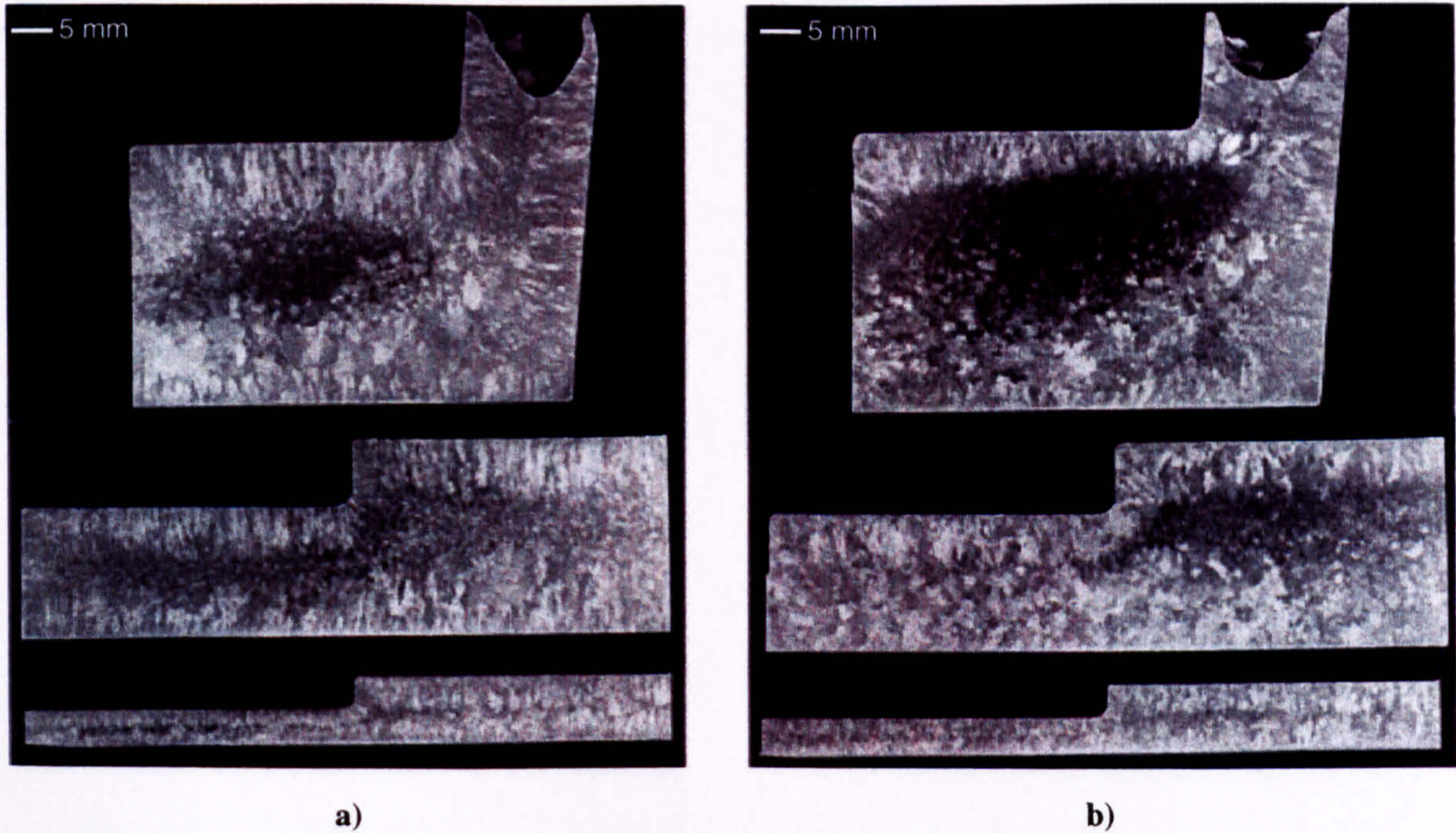


Figure 6.42 Optical macrographs of stepped mould: model alloy 3/2 (0.05 wt. % Ti), cast at **a)** 100 °C and **b)** 440 °C mould temperatures

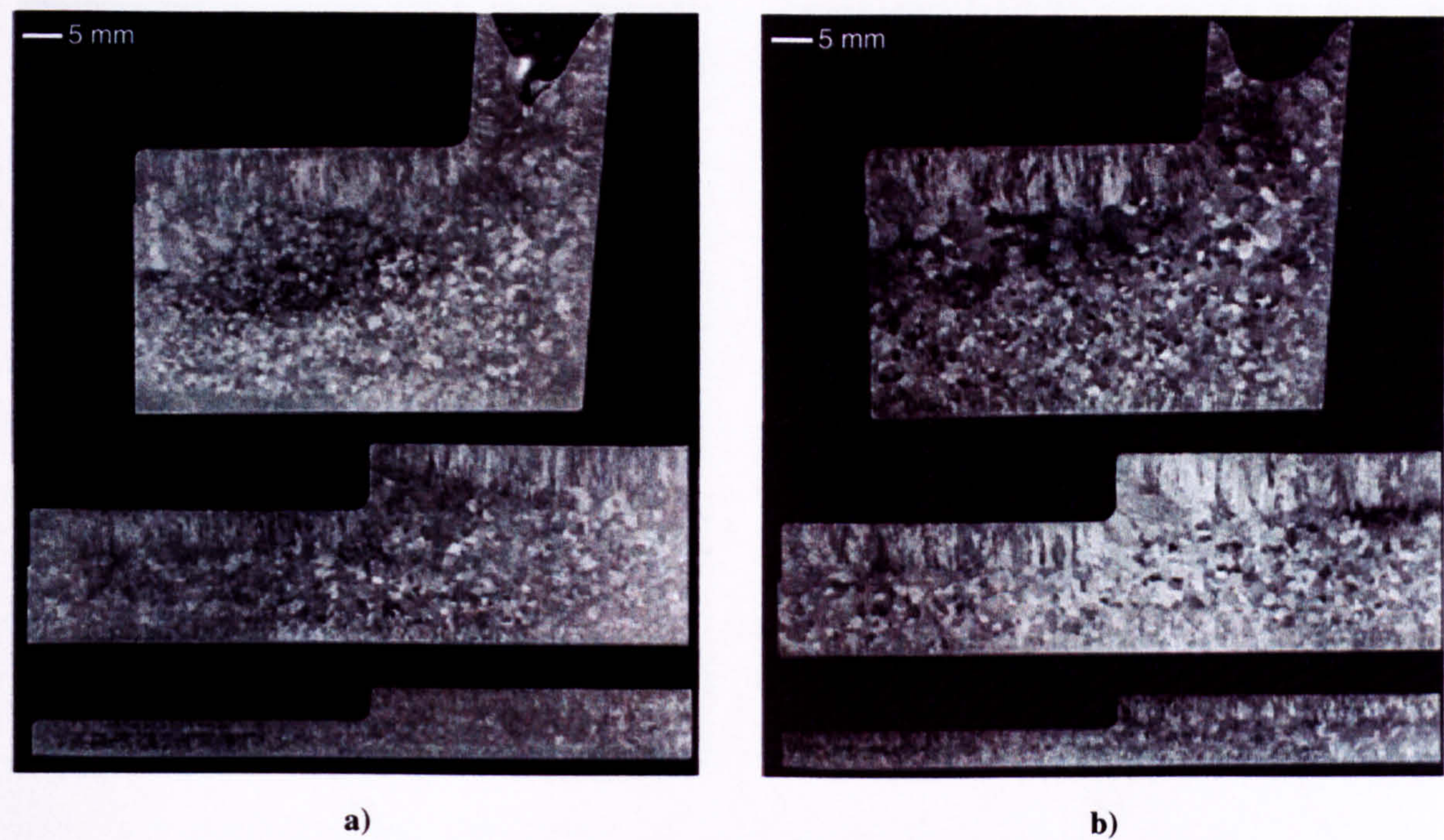


Figure 6.43 Optical macrographs of stepped mould: model alloy 3/3 (0.15 wt. % Ti), cast at **a)** 100 °C and **b)** 440 °C mould temperatures

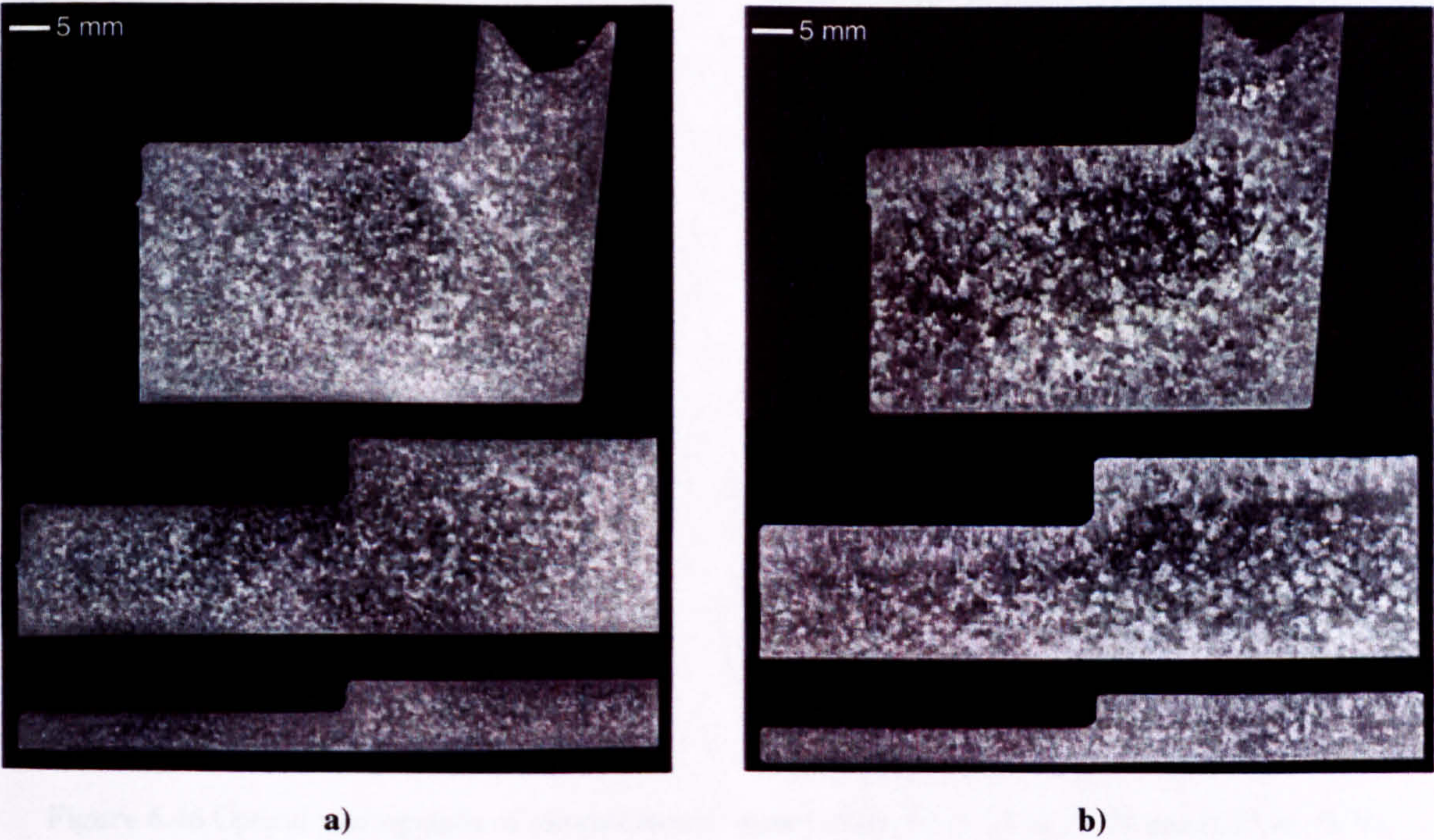
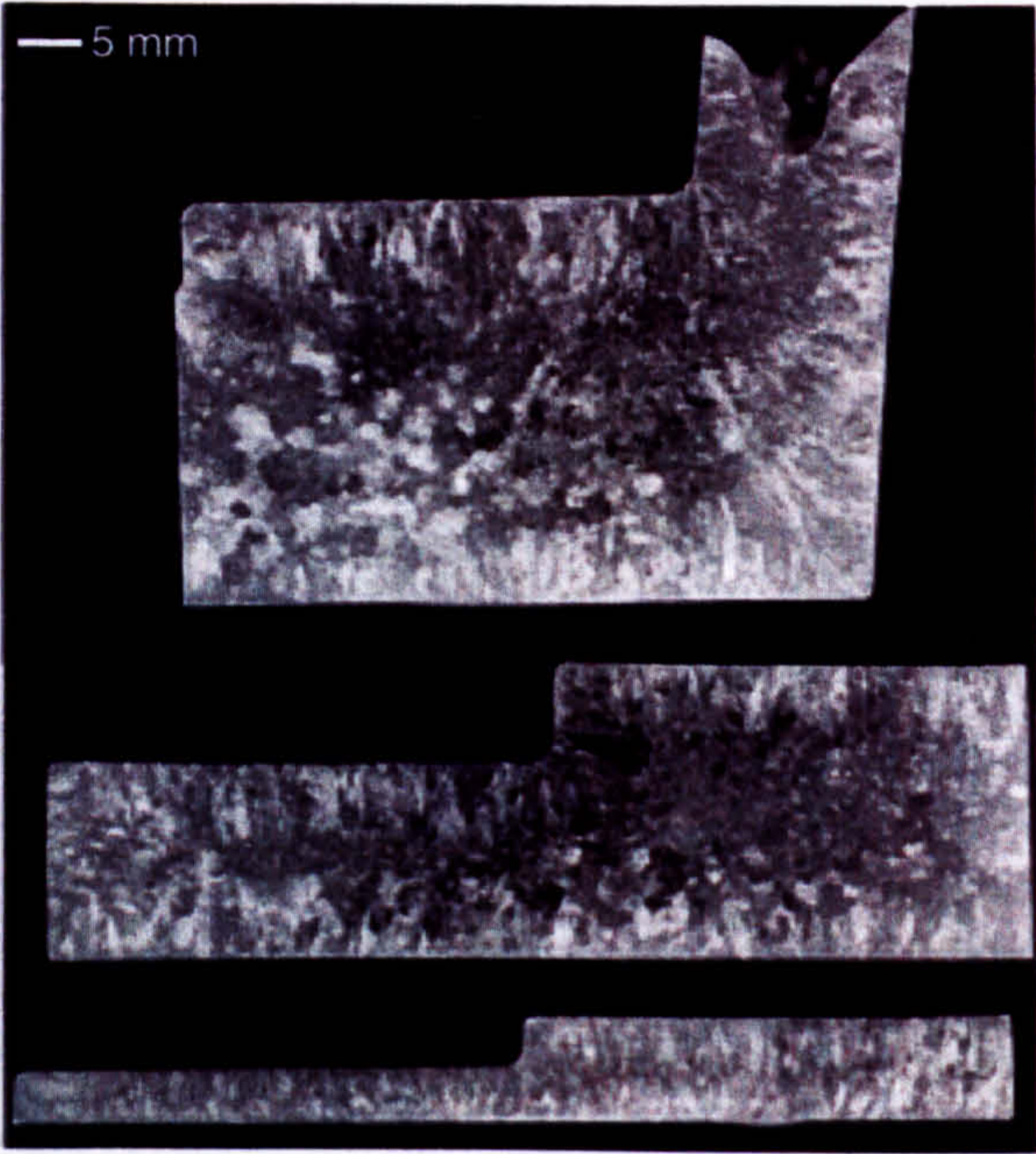
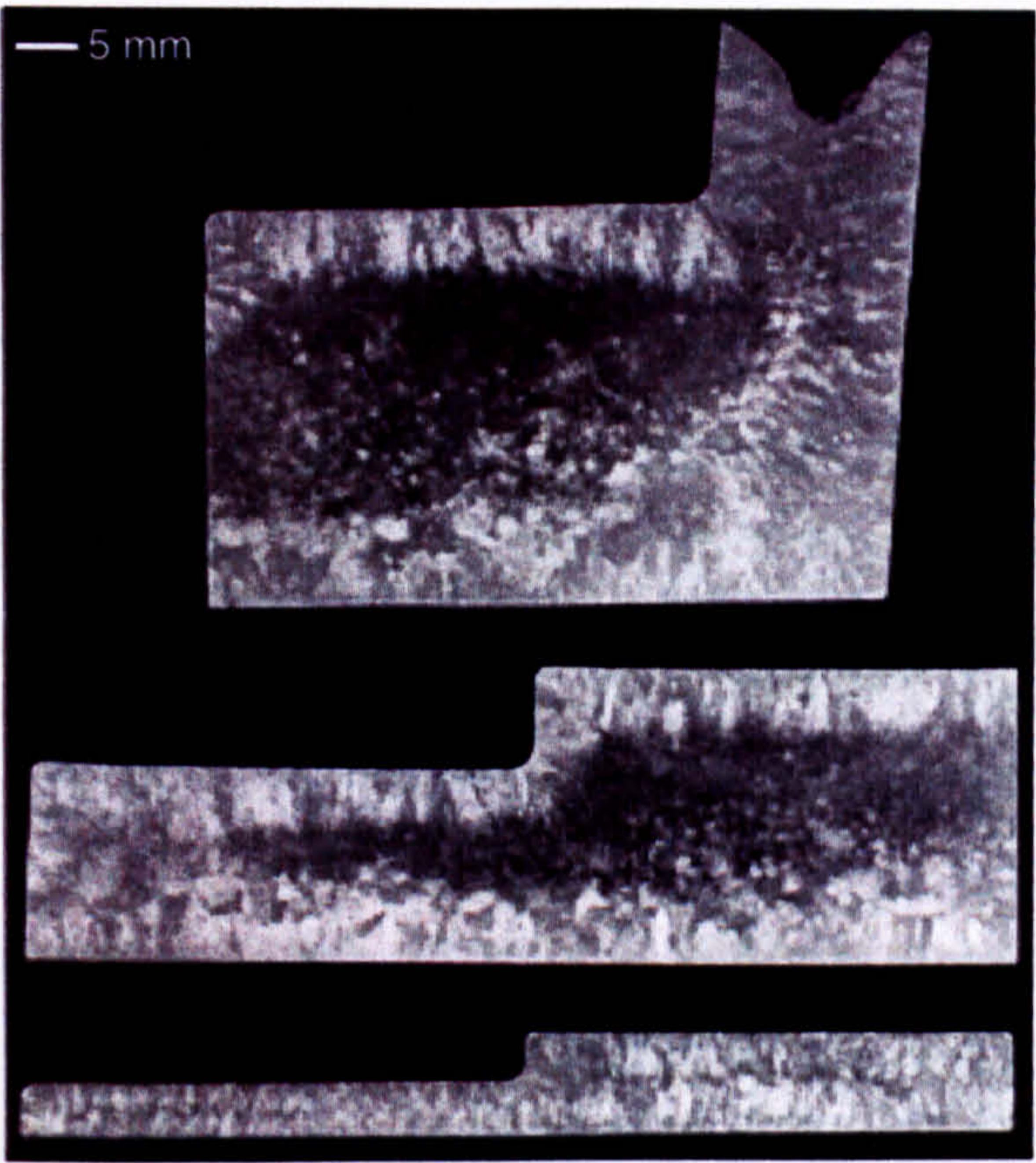


Figure 6.44 Optical macrographs of stepped mould: model alloy 3/4 (0.22 wt. % Zr), cast at **a)** 100 °C and **b)** 440 °C mould temperatures



a)



b)

Figure 6.45 Optical macrographs of stepped mould: model alloy 3/5 (0.005 wt. % Zr and 0.63 wt. % V), cast at **a)** 100 °C and **b)** 440 °C mould temperatures

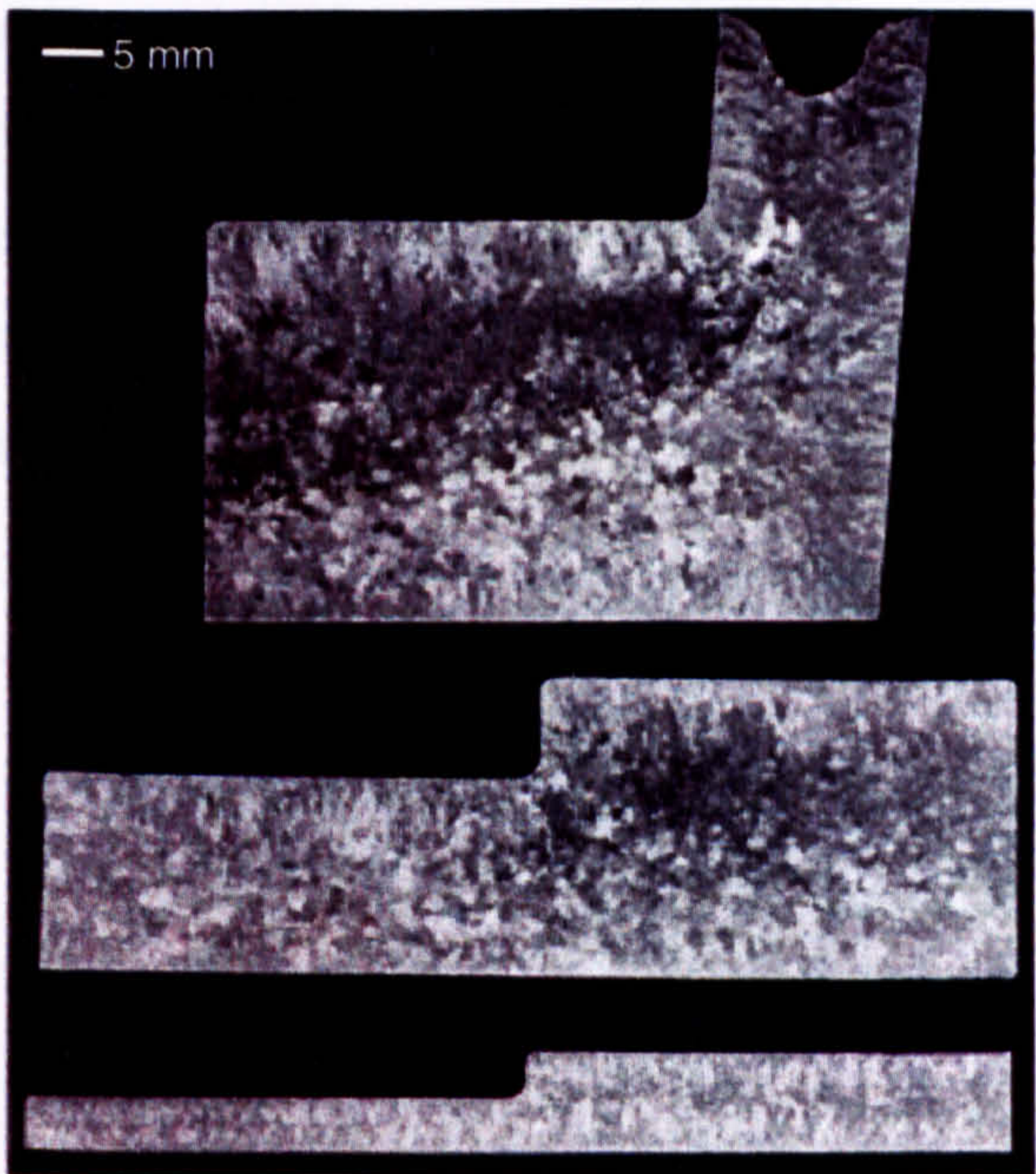
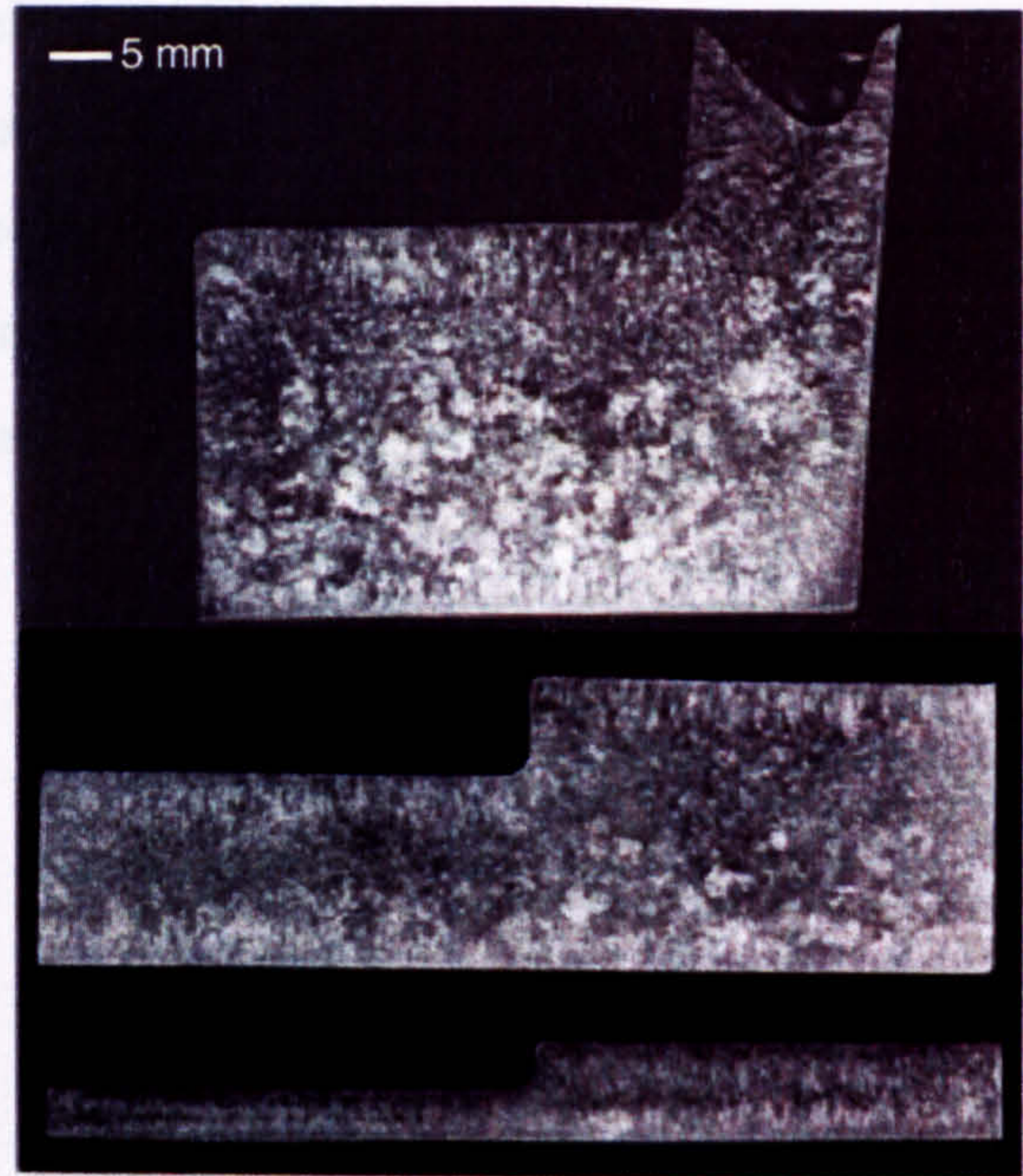


Figure 6.46 Optical macrographs of stepped mould: model alloy 3/6 (0.14 wt. % Zr and 0.02 wt. % V), cast at **a)** 100 °C and **b)** 440 °C mould temperatures

Pieces approximately $10 \times 15 \times 5$ mm were cut from step 4 of the 100 °C casting, to be ground, polished and etched for optical microscopy. To investigate the change in microstructure with grain structure, a series of low magnification (x 50) optical photographs were taken across the samples, from the chill zone down through the columnar and equiaxed zones to the other edge. These pictures were joined together to create a montage showing the microstructural change across the different regions. Due to the large size of these pictures, they are not included in this thesis, however they were used in conjunction with the macros to determine exactly where the growth transitions occurred and to relate microstructure with columnar or equiaxed growth.

Consider first the effect of Ti additions. The macrographs of step 4, 100 °C mould temperature casting of model alloys 3/1 and 3/3 are given in Figures 6.47 a) and b) respectively. The solid white line represents the area used for further microscopic analysis, as previously described, and the dashed white lines indicate where there is a change in microstructure as determined by the optical microscopy. There are two main points of interest arising from these pictures. The first is that for alloys 3/1 and 3/2, the columnar zones (from either side of the casting) are shown to extend to within the area used for microscopic investigation. In alloy 3/3, however, the columnar zone is much shorter and therefore only the columnar grain originating from the top of the casting are contained in the sample. Thus, with increasing Ti additions it appears that the range of the columnar zone is reduced, although the mechanism as to why this is remains unclear at this stage.

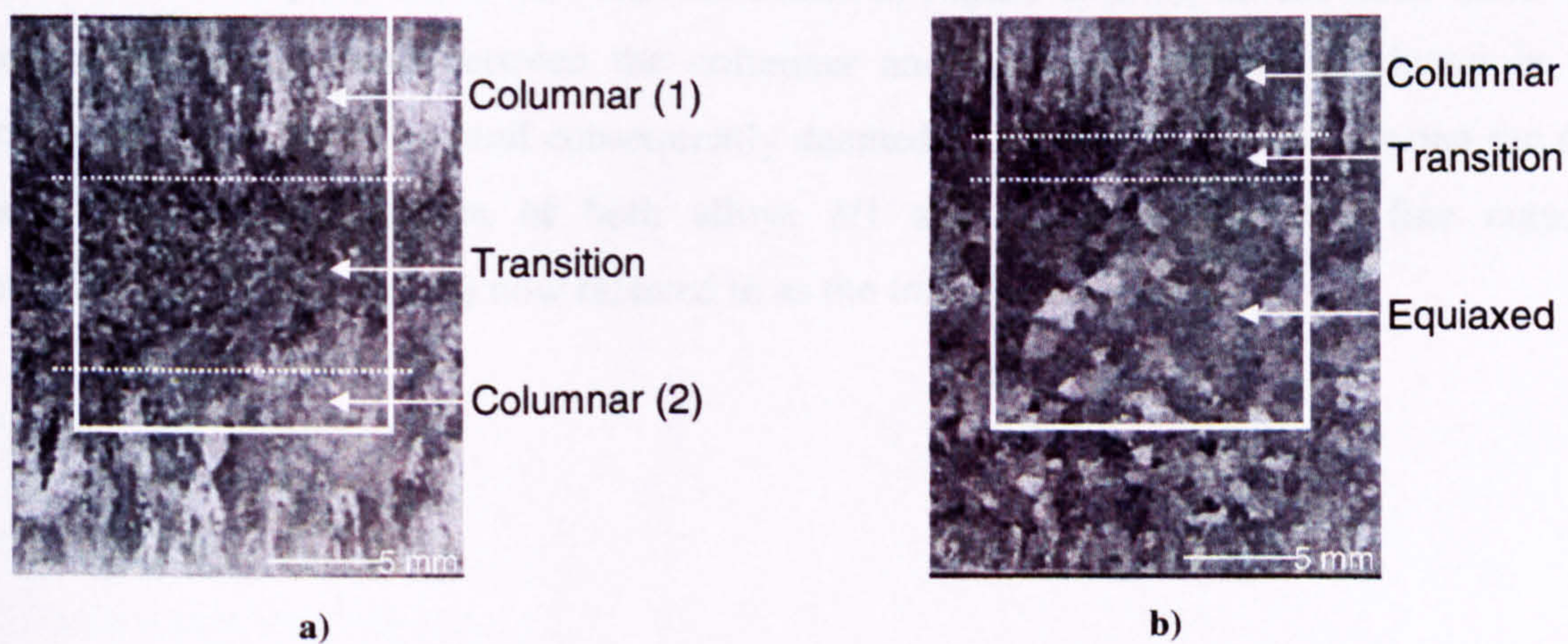
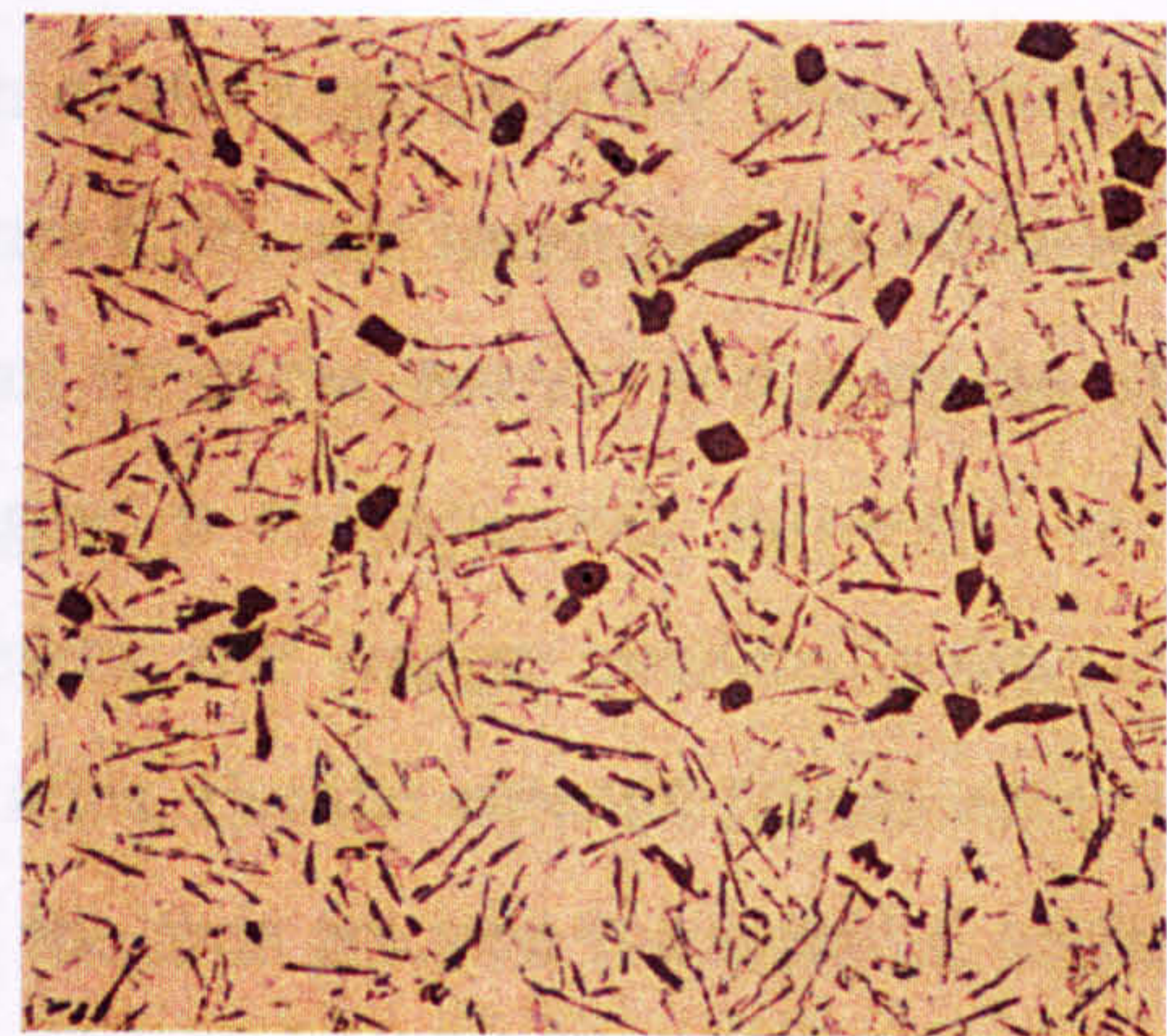


Figure 6.47 Optical macrostructures of step 4 from **a)** model alloy 3/1, representative also of 3/2 (0.01 and 0.05 wt. % Ti) and **b)** model alloy 3/3 (0.15 wt. % Ti), 100 °C mould temperature

The second observation is that there is a change in grain structure of the central region of the castings. The grains in the centre of the 3/1 and 3/2 castings are very small, whereas the grains in the centre of 3/3 are clearly equiaxed, and fairly large (~1mm) in size. It is now appropriate that the microstructures of the castings are considered. High magnification (x 200) pictures were taken and are given in Figures 6.48 and 6.49, and correspond to the areas marked by the dashed white lines on the macrographs in Figure 6.47.

In alloys 3/1 and 3/2 the same structures are seen: a coarse structure in the columnar zone consisting of primary silicon cuboids and large secondary silicon needles in an aluminium matrix (Figure 6.48 a); a very different structure in the equiaxed zone with primary silicon cuboids embedded in a fine dendritic aluminium-silicon matrix (Figure 3.48 b); and finally a return to the coarse columnar structure seen initially (Figure 6.48 c). However, in alloy 3/3, despite there being only two different zones visible on the macrograph, three different microstructures were observed. The columnar zone takes the same form as for the other alloys – silicon cuboids and coarse plates embedded in an aluminium matrix (Figure 6.49 a). The central zone, on the other hand, appears in fact to consist of two regions of two completely different microstructures where there is a change in morphology from that seen in the alloys 3/1 and 3/2 of a fine silicon structure (Figure 6.49 b), to a mixed structure of fine and coarse silicon surrounded by large areas of aluminium (Figure 6.49 c).

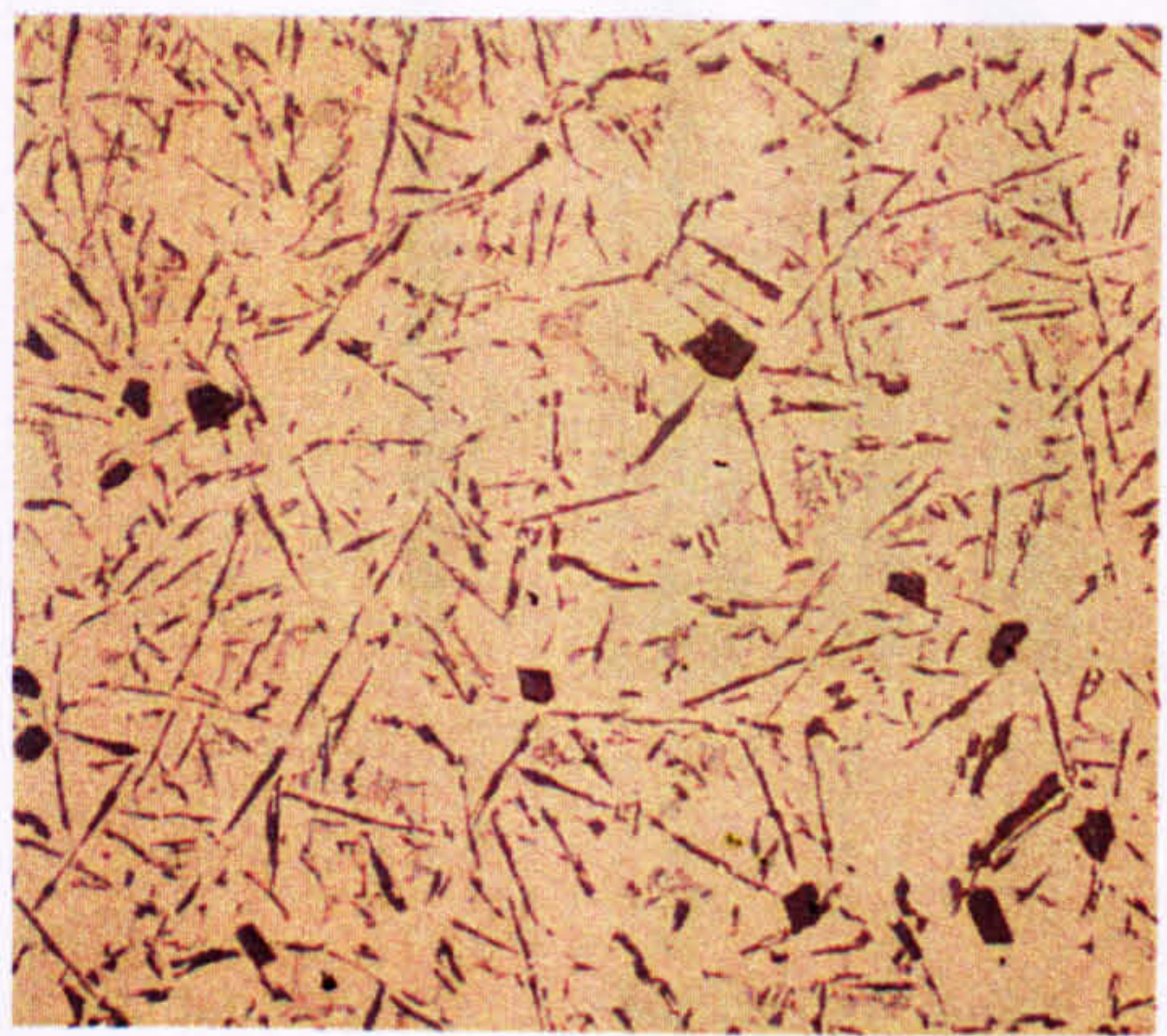
From the montage of optical micrographs of alloy 3/3, the area which Figure 6.49 c) represents was measured to fall exactly in the centre of the casting, where the grain structure is seen to be clearly equiaxed. The microstructure in Figure 6.49 b), on the other hand was observed to form a band between the columnar and equiaxed growth, as shown in the macrograph (Figure 6.47 b), and consequently deemed a transitional region between the two zones. However, the centres of both alloys 3/1 and 3/2 also have the fine eutectic microstructure (Figure 6.48 b) now referred to as the transitional region.



a)

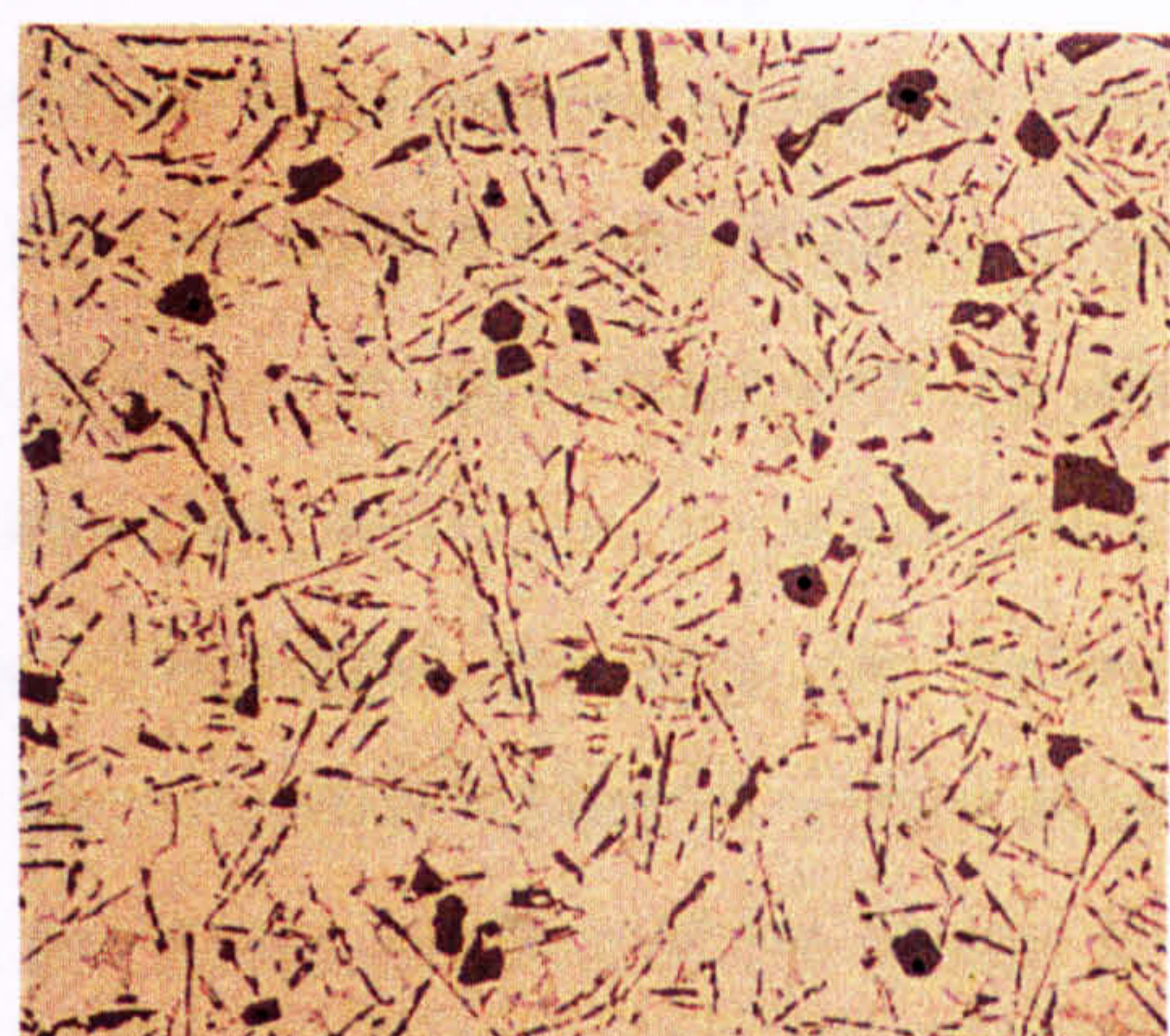


b)

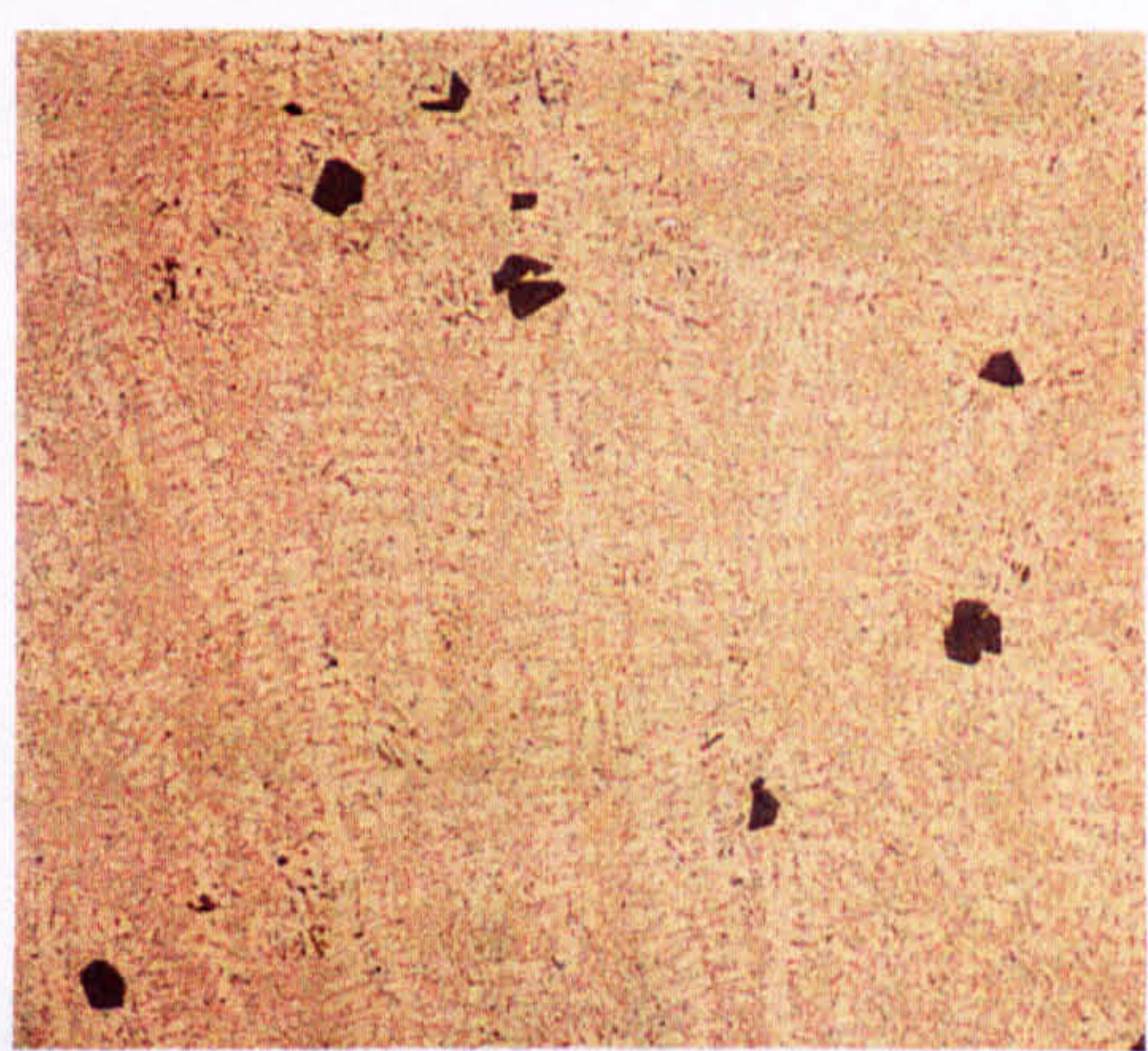


c)

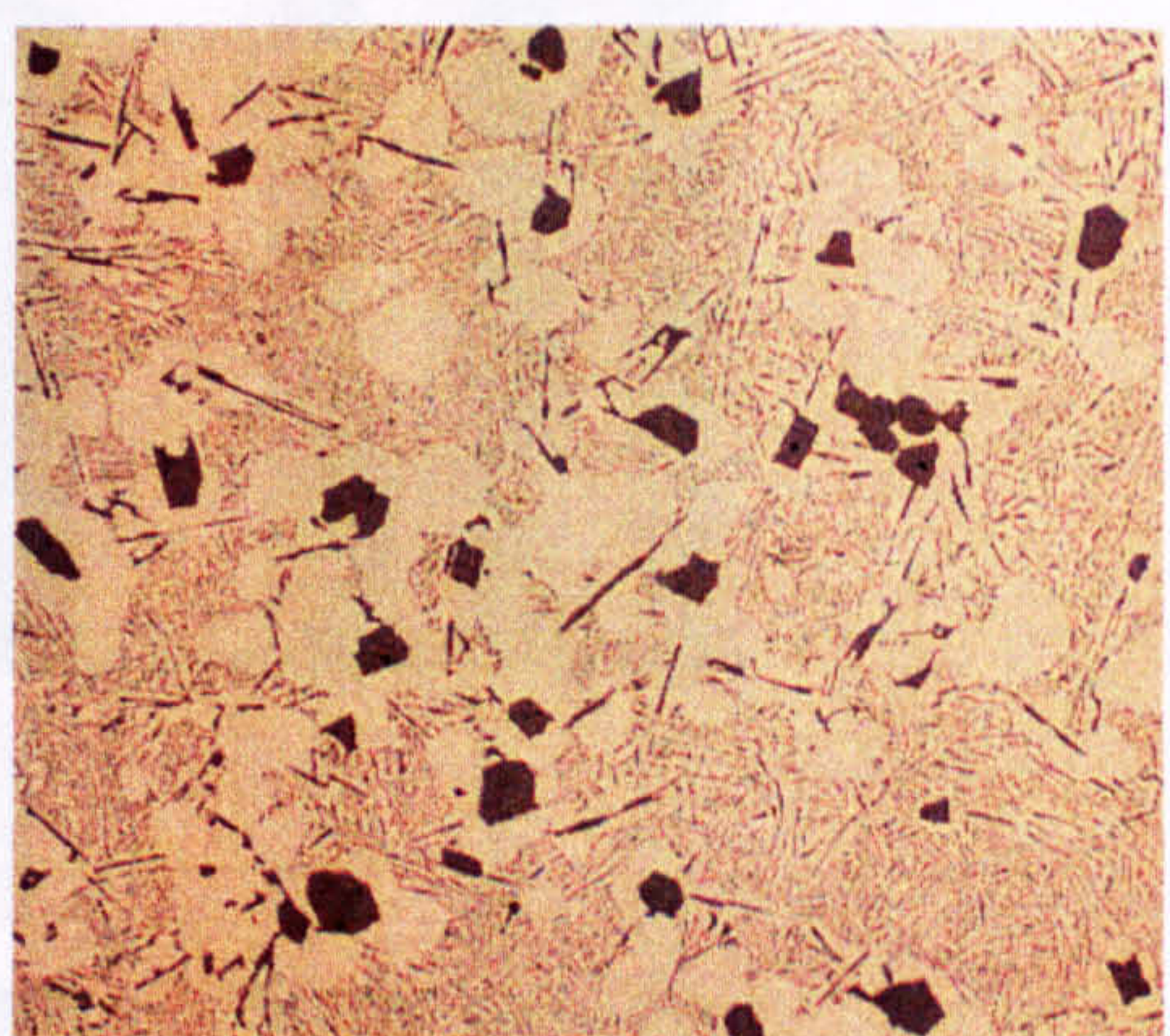
Figure 6.48 Optical micrographs representative of model alloys 3/1 and 3/2 (0.01 and 0.05 wt. % Ti) **a)** columnar zone (top of casting), **b)** transition zone, and **c)** columnar zone



a)



b)



c)

Figure 6.49 Optical micrographs representative of model alloy 3/3 (0.15 wt. % Ti) **a)** columnar zone (top of casting), **b)** transition zone, and **c)** equiaxed zone

To quantify changes in particle size between the zones, image analysis was carried out on each of the regions in the three alloys with resultant plots of area fraction of phases given in Figure 6.50, and mean particle sizes given in Figure 6.51. Clearly the largest fraction of phase (apart from the matrix) is that of the secondary silicon which is in agreement with the optical images. It is important, however, to take into account that when the particles are close together the image analysis software cannot always distinguish between the individual particles. For the eutectic silicon seen in the transition and equiaxed regions it is thus assumed that the area fraction measured is slightly higher than the actual fraction of the phase. It was also difficult to distinguish between the secondary silicon and intermetallics, the latter being present in trace amounts. The primary silicon can be seen to present in the highest fraction in the columnar and equiaxed regions, again in correspondence with the optical images. The fraction of primary silicon is lowest and the fraction of secondary silicon highest in the transitional region.

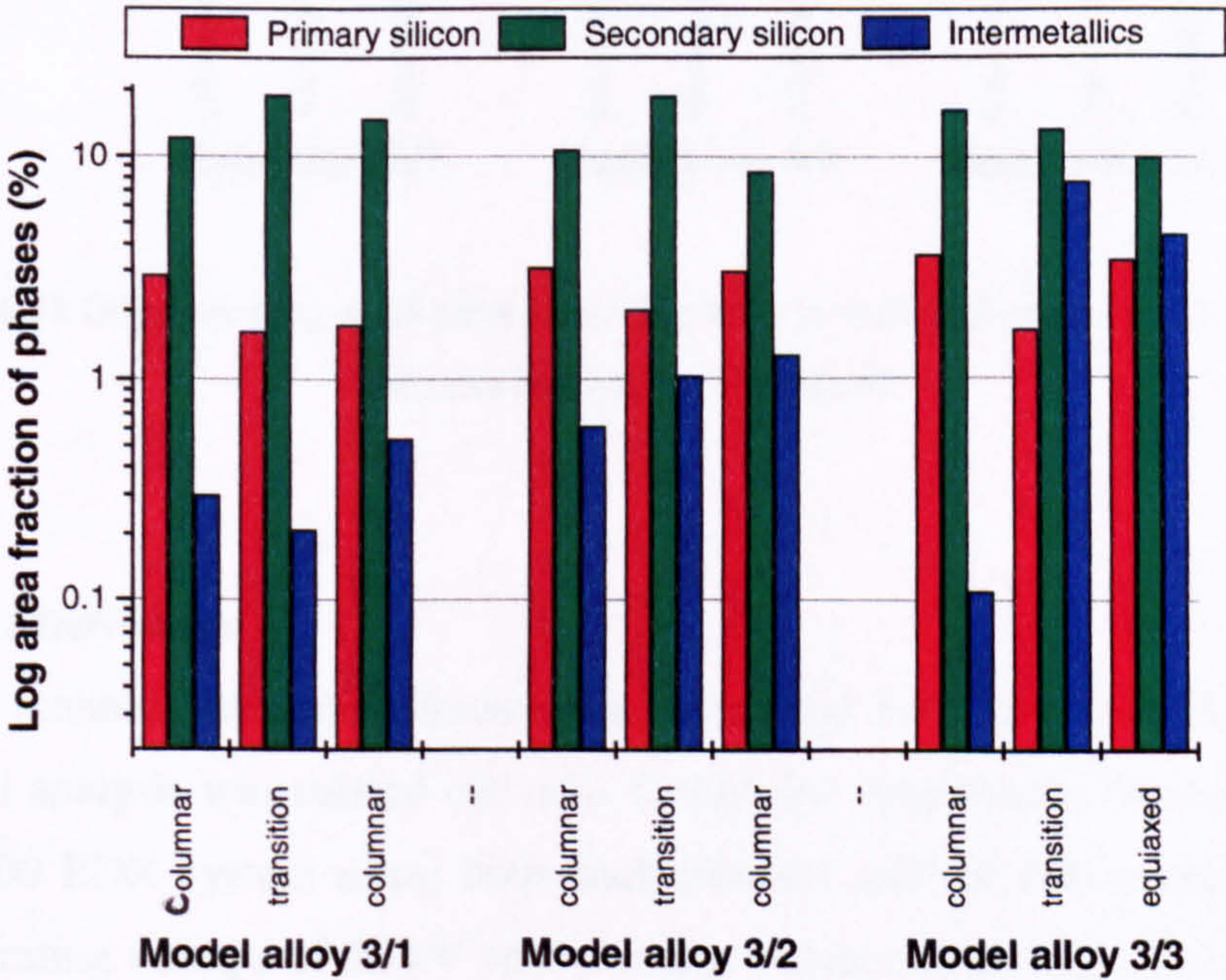


Figure 6.50 Graph showing log area fraction of phases in each of the three structure regions for model alloys 3/1, 3/2 and 3/3

With regards to mean particle size (Figure 6.51), the primary silicon phase is of most interest as these particles were clearly seen to change in size in the different growth zones. Those seen

in the columnar zones were slightly coarser than those in the transition regions, but the primary silicon crystals in the equiaxed zone in alloy 3/3 were seen, and measured to be the largest. This is in keeping with the theory that the solidification rate was slower in this area enabling longer growth times and therefore larger particles.

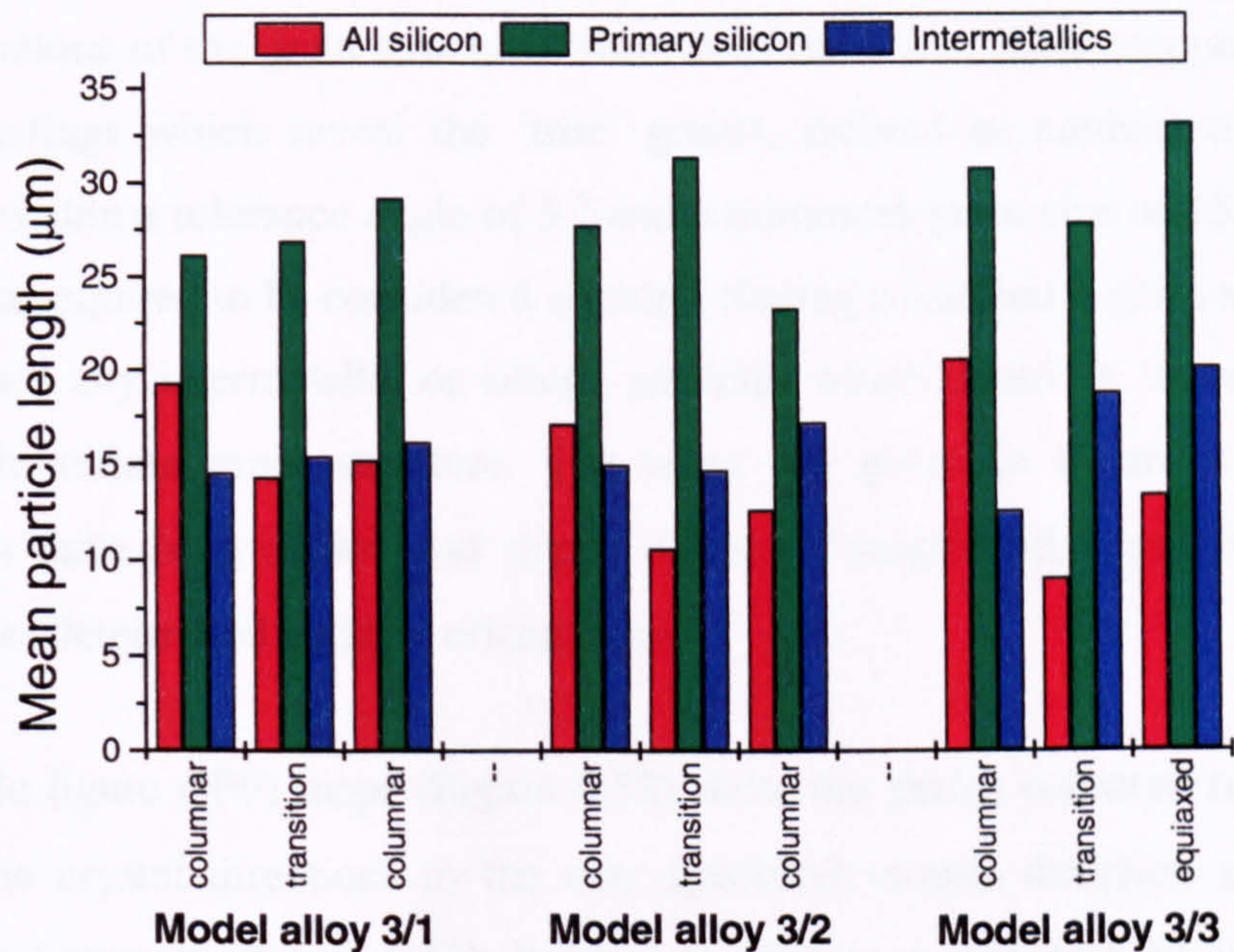


Figure 6.51 Graph showing mean particle size of phases in each of the three structure regions for model alloys 3/1, 3/2 and 3/3

6.5.2 Electron Microscopy

Two different scanning electron microscopes were used for characterisation in this work. Basic chemical analysis was carried out on a Cambridge Instruments Stereoscan 360 with a LINK AN10000 EDX system using both backscattered and secondary electron techniques with an accelerating voltage of 20 kV and working distance of 25 mm. Electron backscatter diffraction (EBSD) was carried out in collaboration with TSL/EDAX, Utah, using their Phillips XL30 FEG SEM, comprising energy dispersive X-ray (EDX) equipped with an ultra-thin window and electron back scattered diffraction (EBSD). The EBSD patterns were obtained and indexed using the orientation imaging microscopy (OIM) system of TSL Inc. The points for which the EBSD patterns were automatically indexed corresponded to a hexagonal grid with a 1 μm step size. Large scans were carried out to provide orientation

information about a substantial area of the specimen in each of the regions (e.g. columnar, equiaxed), and the data was then analysed using TSL's OIM Analysis program.

From the optical analysis three different regions were identified in the model alloys, namely columnar (all model alloys), transition (all model alloys), and equiaxed (model alloy 3/3 only). Since alloy 3/3 contained all three of the regions further work was concentrated on this sample. Observations of the grain structures were confirmed by EBSD mapping of the same areas of the castings which reveal the 'true' grains, defined as connected and similarly oriented points within a tolerance angle of 5° and a minimum grain size of 15 (the minimum number of points required to be considered a grain). Stating a minimum grain size enables the maps to disregard any intermetallic or silicon particles which cause an 'interference' when studying the aluminium grain structure. The maps are given in Figure 6.52, and grain boundary traces have been drawn and depict a line of neighbouring points belonging to separate grains as determined by their orientations.

The inverse pole figure (IPF) maps (Figure 6.52) show the grains coloured according to the alignment of the crystal directions to the user specified sample direction as defined in a colour-coded unit triangle (Figure 6.53). In the columnar zone (Figure 6.52 a) it can be seen that the majority of grains are coloured green indicating a [101] crystal direction is aligned with the sample normal direction (ND). There are also some red coloured grains representative of the [001], as well as randomly coloured, generally small grains scattered throughout the scan. The transition and equiaxed regions are also predominantly [101] orientation (green) although there is also a substantial amount of [111] (blue). There are only a few small grains of the [001] alignment indicating no preference towards this orientation.

For a two dimensional projection of the scanned areas $\langle 100 \rangle$ pole figures were plotted and can be seen in Figure 6.54. In Figure 6.54 a), the columnar region can be observed as having distinct concentrations of points indicative of preferred orientation. Indeed, there is some evidence of a cube ((100)[001]) texture. This is clear from the high density of points at the centre of the pole figure and at the ends of both the TD and RD axes. This means that one $\langle 100 \rangle$ pole lies parallel to the ND and perpendicular to the TD and RD. The other poles lie parallel to the TD and RD but perpendicular to the ND. The concentrated points do appear to be slightly off the axes but this is most likely a result of the sample not being exactly aligned in the SEM chamber because if the sample was rotated 1 or 2 degrees about the normal then

the poles would be correctly aligned. As the plane parallel to the TD and RD is the (100) then the sample direction is [001], hence the (100)[001] texture most commonly referred to as cube (not to be mistaken for cubic crystal structure). This is consistent with the [001] orientations seen in the inverse pole figure map as red-coloured grains.

In the columnar pole figure there is also a symmetrical pair of points along the RD which, together with the high densities at the ends of the TD axis, indicate a $\langle 011 \rangle$ orientation. Since the points along the RD are positioned between the centre and the edges of the projection these poles must be situated at 45 degrees to both the RD and ND, whilst lying perpendicular to the TD. Thus, in the columnar zone it is likely that there is both a $\{100\}\langle 001 \rangle$ and a $\{100\}\langle 011 \rangle$ texture as was suggested from the IPF maps.

The pole figure of the transition region (Figure 6.54 b) is very interesting and there are several points to note. Firstly, there is clearly some degree of random orientation seen as the scattering of points around the outside of the projection. Secondly, there is a concentration of points forming almost a 'ring' in the projection which could be the result of [111] orientation as was seen in the IPF map, however, it is unclear what the exact texture is and a three dimensional plot is required to resolve this. Finally, there are almost no points at all in the centre of the pole figure which indicates that there is definitely no [001] texture in this region. If this is compared with the IPF map these findings are consistent with the small numbers of [001] (red) grains. The equiaxed region (Figure 6.54 c) appears to have a small amount of random texture but mainly consists of high density spots across the projection. Again it is impossible solely from these pole figures to distinguish any texture although it is interesting to note that there is a particular concentration of points in the same area of the circle as was seen for the transition zone, possibly the [111], and no points to suggest a [001] texture in this region. This commonality suggests that there is some relationship between these two zones.

Two orientation distribution function (ODF) sections for each zone are presented in Figure 6.55 and essentially describe the orientation and direction of crystals rather than the crystal plane as in the case of pole figures. A three dimensional representation is required to accommodate the three Euler angles, and this is provided in the form of orientation space which show the orientation density as contour plots of parallel sections at 0 and 45 degrees. Thus, in combination with the texture charts it was possible to relate the orientation positions to textures of the form (hkl)[uvw]. In the columnar region (Figures 6.55 a) and d)) there is

some evidence of the (100)[001] texture (seen previously in the pole figures) as there are density concentrations at the corners of the 0 degree plots and in the top and bottom centres of the 45 degree plot. There are also two high density spots along the $\langle 110 \rangle$ parallel to the ND axis (present in both sections). One orientation appears to be of the form $\{110\}\langle 011 \rangle$ and the other is difficult to identify exactly, however, this confirms that there is a $\langle 011 \rangle$ component to the texture of the columnar zone as was discussed previously with respect to the IPF maps and pole figures. The $\langle 011 \rangle$ texture is further evident in the ODF's for both the transition and equiaxed regions (Figures 5.5 b, c, e, and f). The ODF for the transition region shows a very high density along the $\langle 110 \rangle$ parallel to the ND with some degree of orientation along the whole axis, and the equiaxed zone also has a strong orientation in this direction.

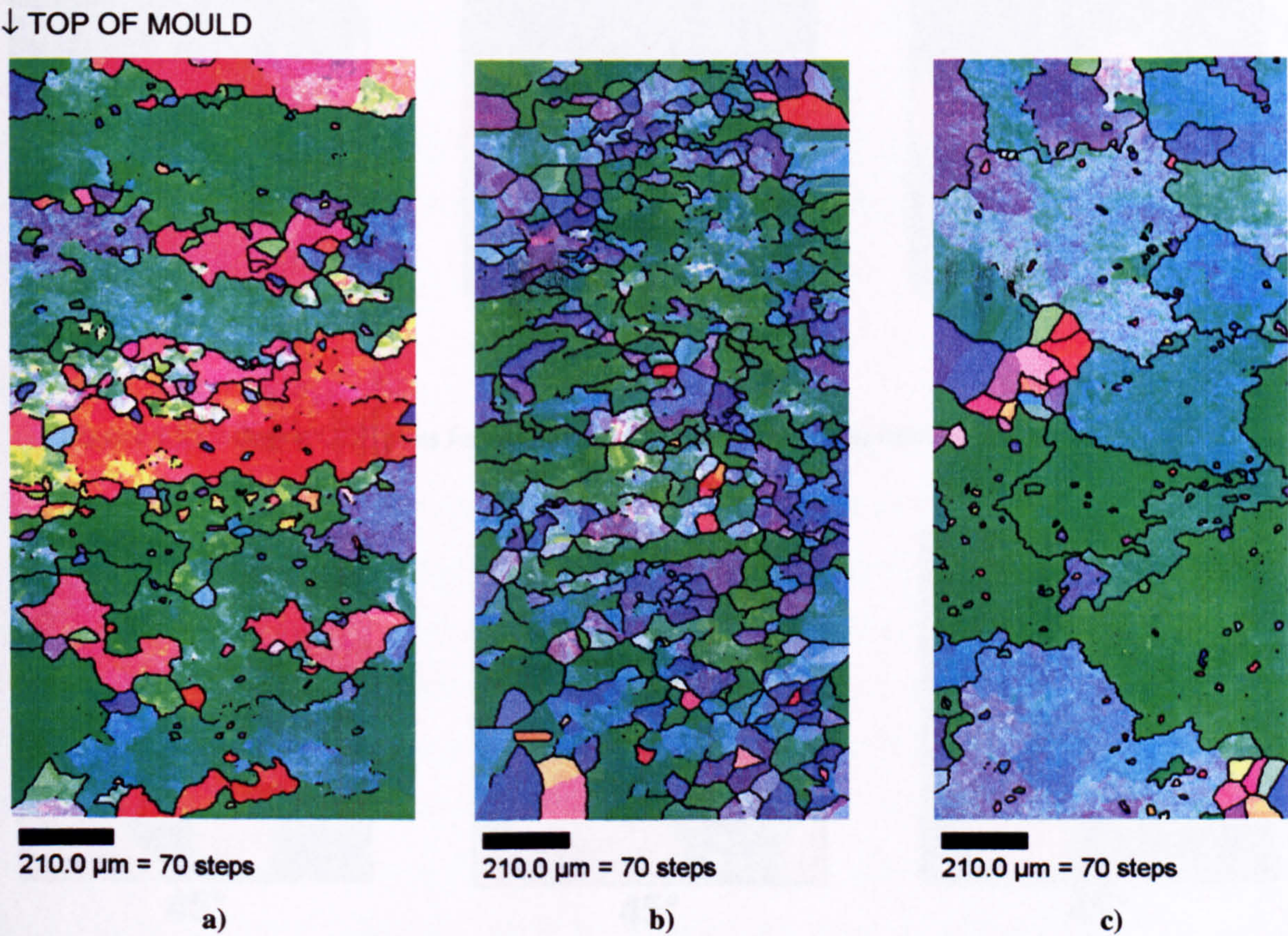


Figure 6.52 Inverse pole figure maps of the a) columnar, b) transition, and c) equiaxed regions in model alloys 3

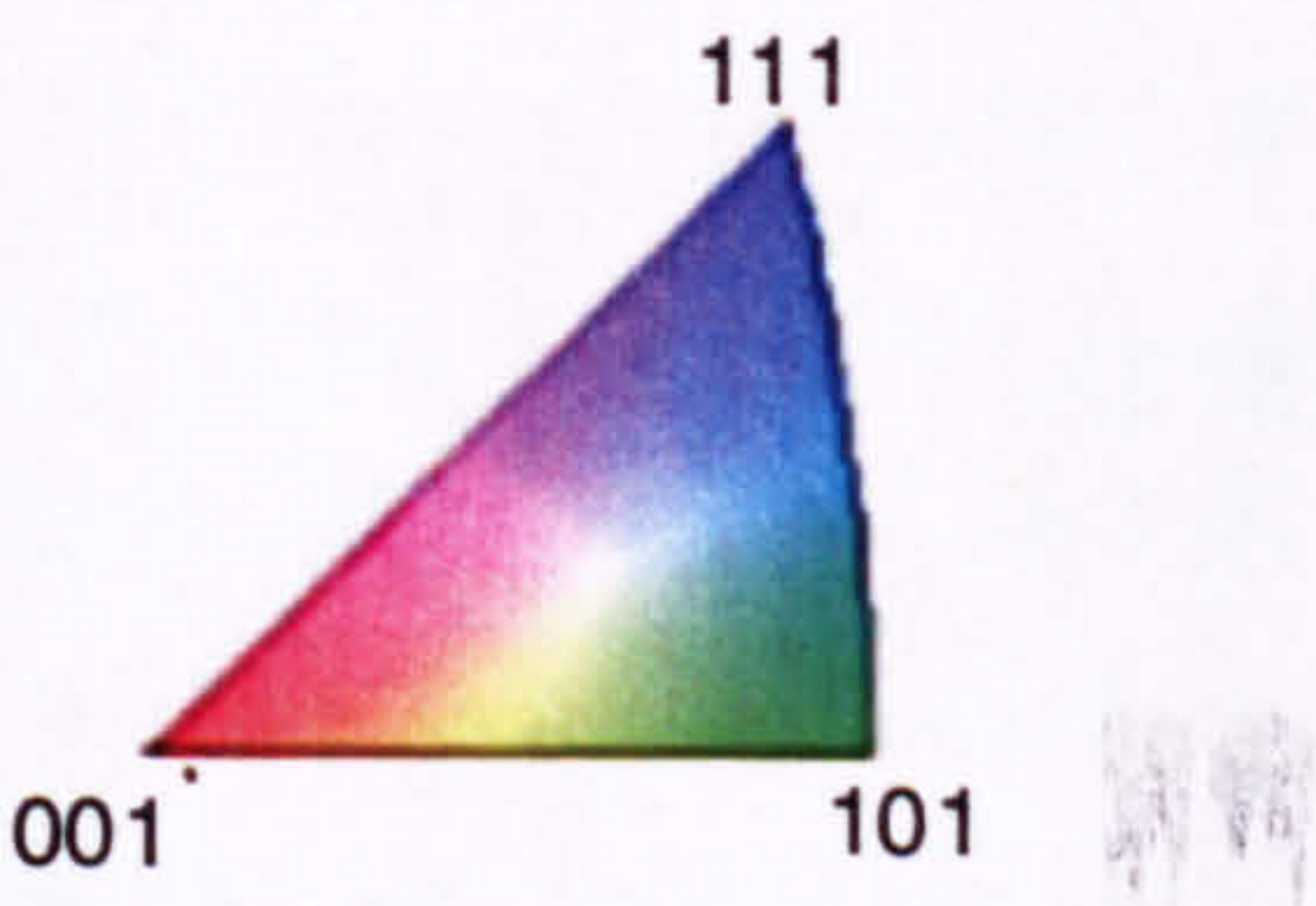


Figure 6.53 Colour coded unit triangle for the IPF maps in Figure 6.52

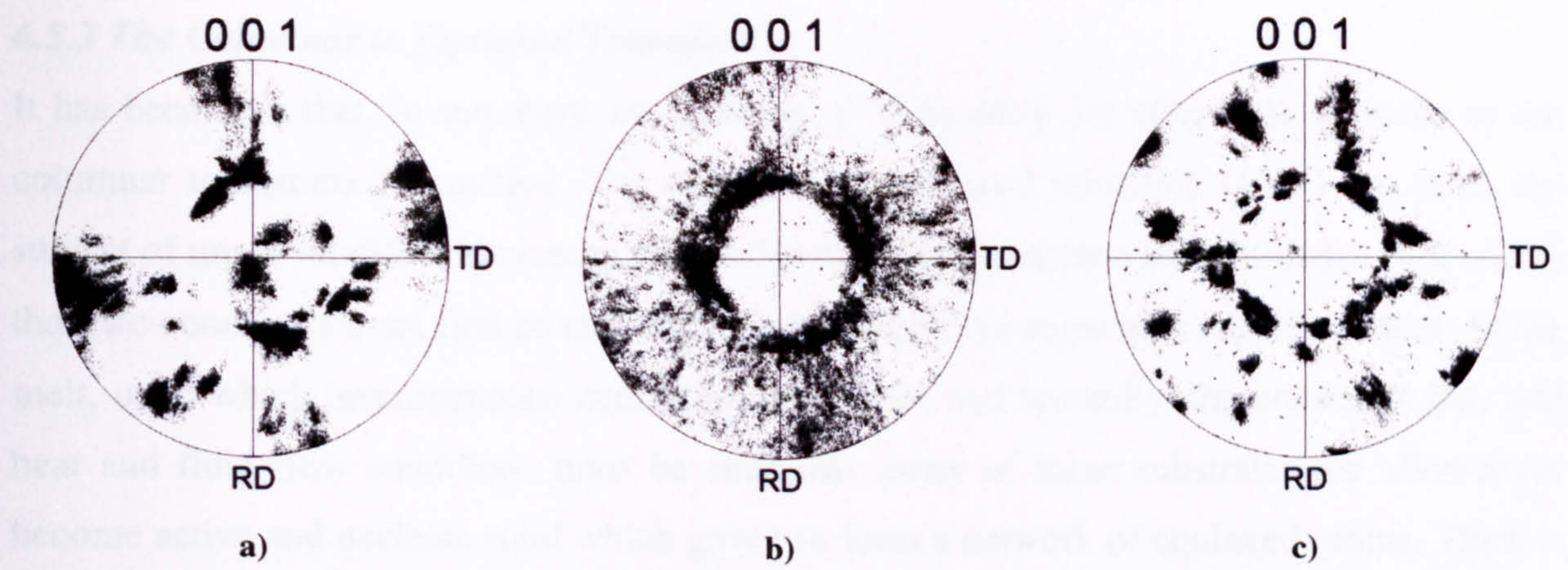


Figure 6.54 Pole figures for a) columnar, b) transition, and c) equiaxed regions of alloy 3/3

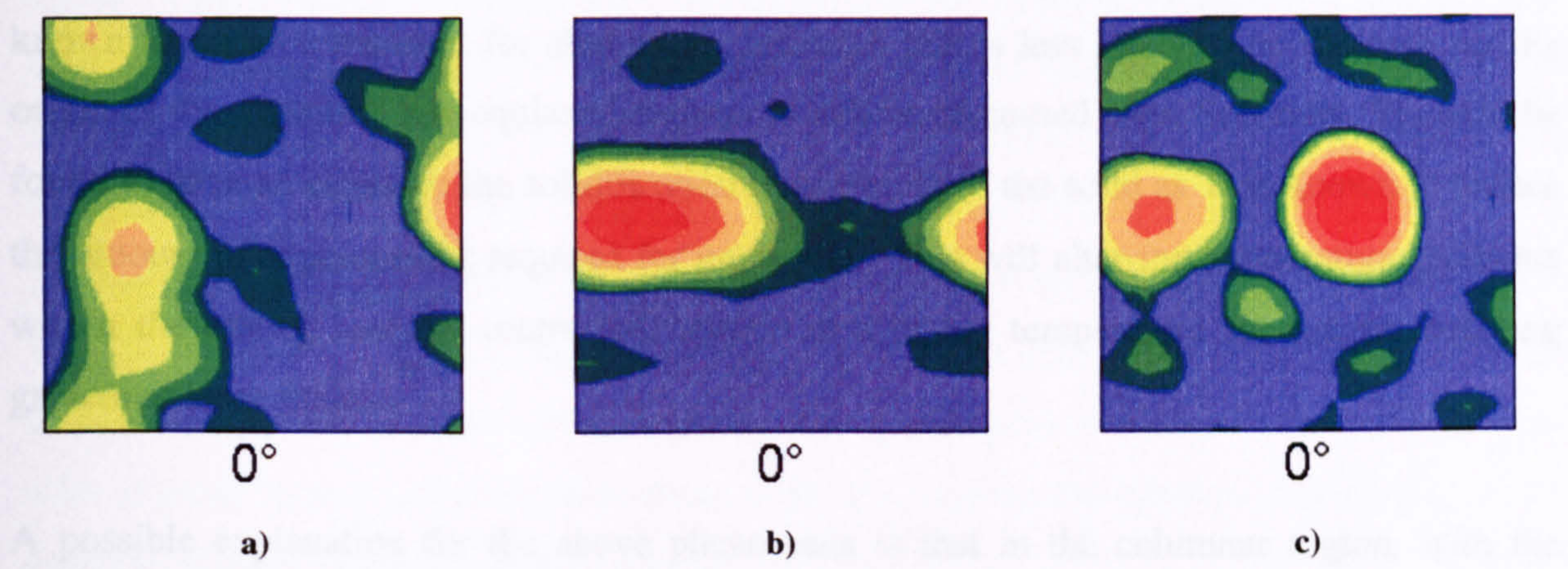


Figure 6.55 0 degree ODF plots for a) columnar, b) transition, and c) equiaxed regions of alloy 3/3

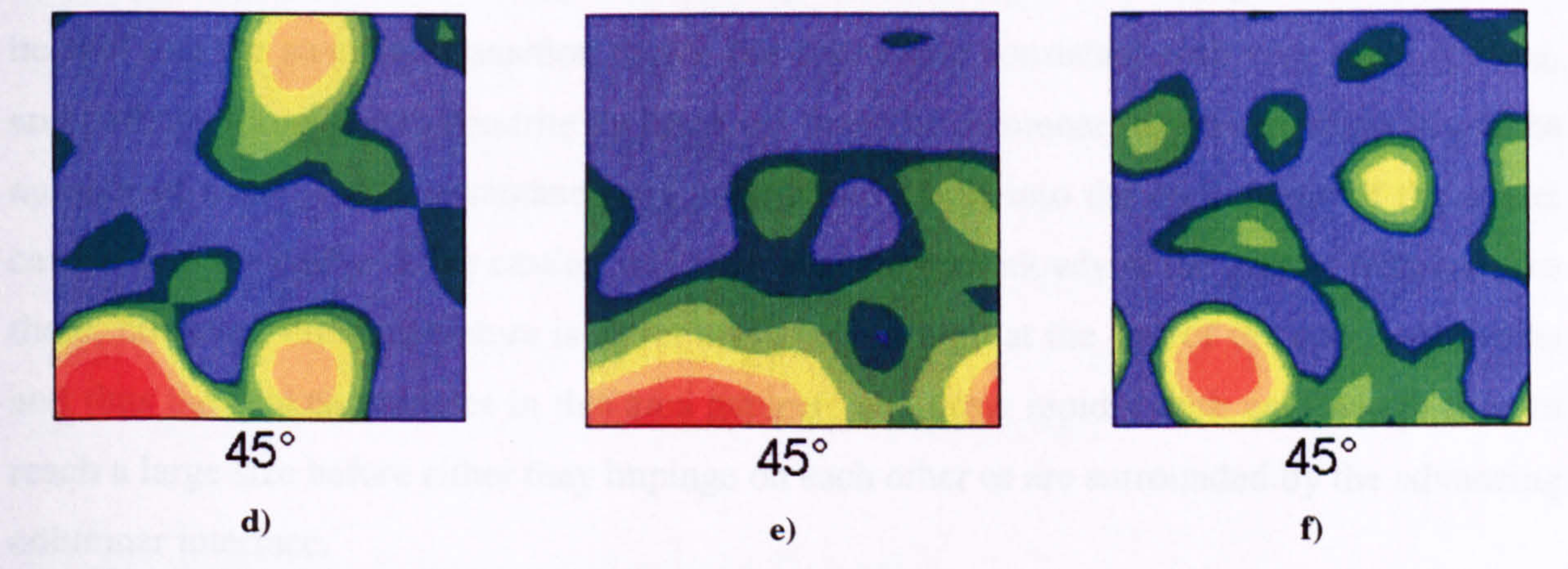


Figure 6.55 45 degree ODF plots for d) columnar, e) transition, and f) equiaxed regions of alloy 3/3

6.5.3 *The Columnar to Equiaxed Transition*

It has been seen that, in summary, the addition of Ti in alloy 3/3 affects the position of the columnar to equiaxed transition. The columnar to equiaxed transition (CET) has been the subject of much solidification research to understand the parameters that influence it. It seems that two conditions must first be met. First, numerous potent substrates must be present in the melt, upon which heterogeneous nucleation can occur, and secondly, the constitutional, and heat and fluid flow conditions must be such that many of these substrates are allowed to become active and nucleate solid which grows to form a network of equiaxed grains. Thus, it appears that the Ti may be affecting both of these parameters. Firstly, through addition of the Ti using a master alloy, numerous Al_3Ti particles are introduced into the melt which are known to act as a nucleant for aluminium, although this is less likely to be the case for the origin of the transition and equiaxed regions as will be discussed later. Secondly, Ti could be found to have an effect on the solidification temperature of the solid as Ti is known to reduce the amount of supercooling required for nucleation. This will alter the temperature gradients within the casting and the centre will remain at a higher temperature for longer, enabling growth of large grains.

A possible explanation for the above phenomena is that in the columnar region, with the highest cooling rates, nucleation of primary Si and the subsequent growth of the anomalous eutectic structure proceeds as expected. From previous analysis of cooling rate effects, it can be said that the so-called transition region has a structure consistent with very rapid cooling, and perhaps forms due to dendrite tip break off from the columnar regions resulting in a large number of nuclei being instantaneously present and swept into the melt. Most of the nuclei carried into the centre of the casting will nucleate and grow slowly at the greater temperatures there, however, the temperature is lower and gradient high at the tips of the columnar grains and thus the broken particles in this area nucleate and grow rapidly with not enough time to reach a large size before either they impinge on each other or are surrounded by the advancing columnar interface.

In the equiaxed region at the centre of the casting which has cooled more slowly, it is assumed that the primary Si nucleates initially. This is followed by the nucleation of Al in a Si-depleted region, and enhanced by the additional presence of Ti in alloy 3/3, which is able to grow still at relatively high temperatures. Finally a relatively coarse eutectic structure forms. This would be consistent with the lower fraction of silicon (both primary and

secondary) in the transitional zone, although it is doubtful that there would be a big enough solute build up ahead of the solidifying front to cause this. However, if the dendrite tip break off theory is operative, and the temperature in the centre of the casting is such that these broken pieces survive and nucleate at the lesser supercooling required from the Ti additions and begin to grow very slowly, then a large equiaxed structure would be expected, as was seen.

The columnar grains are shown clearly to grow in the direction of the temperature gradient as seen in both optical and EBSD analysis. Many of the columnar grains were found to exhibit a $\langle 100 \rangle$ texture which is the preferred orientation for fcc crystals. However, a strong $\langle 011 \rangle$ texture was also found to be evident and although this is not the usual preferred orientation it is in agreement with another work where dendritic aluminium grains grow along the $\langle 110 \rangle$ direction [Hen98]. In that work, the change in growth direction was attributed to a change in surface tension and/or attachment kinetics anisotropy as a result of solute additions and/or solidification conditions (e.g. high solidification rate). The growth competition is believed to be the same for $\langle 110 \rangle$ as for $\langle 100 \rangle$ whereby the crystals grow in competition with each other with crystals in the preferred orientation along the temperature gradient, developing at the expense of those less favourably oriented.

From the orientation information it is clear that there is some relationship between the three zones. This was seen initially in the IPF maps by the common $\langle 011 \rangle$ orientation in all three zones which was subsequently confirmed by the ODF plots which enabled a three dimensional view of the texture of the material. If the nucleation of grains in the transition and equiaxed regions is a result of dendrite tip break off from the columnar zone, as could be feasible if the melt conditions are favourable, then it is possible that the established orientation of those dendrite tips will preside over further growth.

6.5.4 Modelling the Columnar to Equiaxed Transition

The columnar to equiaxed transition (CET) was discussed extensively in Chapter 3, from which an explanation of the CET was produced [Bur74]. If there is a sufficient density of slowly growing equiaxed dendrites just ahead of the growing columnar front, then the equiaxed grains should generate a sufficient thermal gradient to increase the columnar supercooling, so allowing more rapid equiaxed growth and thus an increased gradient which will further impede columnar growth leading to the CET [Doh77].

Work by Hunt^[Hun84] incorporated these factors in an attempt to model columnar and equiaxed growth under realistic casting conditions. The columnar front usually associated with, but not necessarily exclusively, directional growth was rejected in favour of simple steady state equiaxed growth (which assumes that at each temperature the number and size of the equiaxed grains remains unchanged with time) for both dendritic and eutectic systems. Equiaxed grains were assumed to have nucleated heterogeneously and the subsequent growth and interaction with the columnar front was examined using an approximated analytical solution and a more accurate numerical integration of the heat flow equation. A simple expression predicting when fully equiaxed structures should occur was developed, a full derivation of which can be found in Appendix A.

The critical gradient condition for fully equiaxed growth is given approximately by

$$G < 0.617 \cdot N_0^{1/3} \cdot \left[1 - \frac{(\Delta T_N)^3}{(\Delta T_c)^3} \right] \cdot \Delta T_c \quad [6.1]$$

where G is the temperature gradient, N_0 the total number of heterogeneous substrate particles originally available per unit volume, ΔT_N is the supercooling at the heterogeneous nucleation temperature, and ΔT_c is a supercooling equal to that of the columnar growth front temperature. Similarly, assuming that a fully columnar structure results when the volume fraction ahead of the front is less than 1 % of the value required for a fully equiaxed one, leads to the condition for fully columnar growth being derived as

$$G > 0.617 \cdot (100 \cdot N_0)^{1/3} \cdot \left[1 - \frac{(\Delta T_N)^3}{(\Delta T_c)^3} \right] \cdot \Delta T_c \quad [6.2]$$

Initial investigations into using Hunt's model as a method of predicting the columnar to equiaxed transition in Al-Si alloys were carried out, first through validating the calculation method, and then by using the calculations with parameters adapted for Al-Si.

In order to verify the model procedure, calculations were performed for an Al - 3 wt. % Cu system using Equations 6.1 and 6.2 from which Figure 6.56 was drawn^[Hun84]. The solid lines illustrate the columnar and equiaxed regions calculated using the approximate analysis, and

the dashed lines represent calculated results using the more accurate analysis. Only the transition from a fully equiaxed structure is shown. The value of A , used in Equation A7, is taken from experimental results ^[Bur74] as $300 \mu\text{m s}^{-1} (\text{wt. \%})^{-1} \text{K}^{-2}$. The number of sites, N_0 , is assumed to be one per cubic millimetre ($N = 1000 \text{ cm}^{-3}$) and ΔT_N is taken to be 0.75 K . The blue dashed lines represent the values obtained by the author whilst trying to verify the calculations and can be seen to be consistent with those plotted by Hunt.

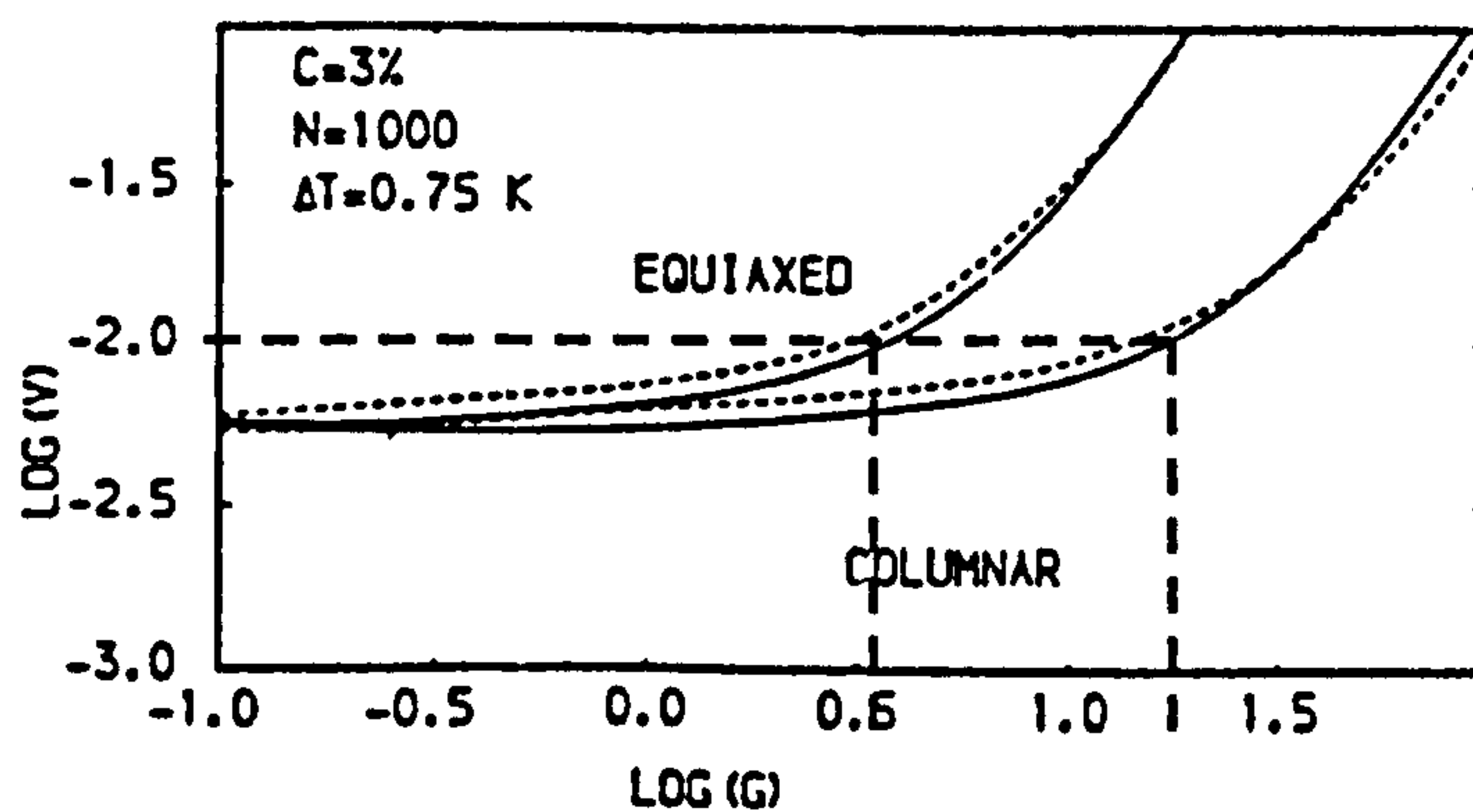


Figure 6.56 Plot of growth velocity V (cm s^{-1}) against temperature gradient G (K cm^{-1}) for Al-3 wt. % Cu, after Hunt ^[Hun84], with the blue lines representing verification by the author

Calculating the CET for Al-Si

Having validated the calculation methodology an attempt was made to recalculate the plot of growth velocity against temperature gradient for an Al - 12 wt. % Si system, using Al-Si parameters where possible. The first calculation was to determine ΔT_C ; the supercooling equal to that of the columnar growth front, defined as

$$\Delta T_C = \left(\frac{V' C_0}{A} \right)^{1/2} \quad [6.3]$$

V' , the real interface velocity was taken from plots by Hunt and found to range between 5×10^{-3} to 0.1 . Thus the first calculation was carried out using $V' = 0.01 \text{ cm s}^{-1}$. C_0 is the alloy composition, in this case 12 wt. % Si. A is a constant for any particular system, it being a function of liquidus slope, distribution coefficient and solid-liquid surface energy, which for Al-Si was derived to be $0.05 \text{ cm}^{-1} (\text{wt. \%})^{-1} \text{K}^{-2}$. Thus,

$$\Delta T_c = \left(\frac{0.01 \times 12}{0.05} \right)^{1/2} = 1.6$$

For calculating fully equiaxed growth (Equation 6.1) or fully columnar growth (Equation 6.2) the following parameters were required: N_0 is the total number of heterogeneous substrate particles originally available per unit volume, which being variable and impossible to measure was estimated at ranging from 10 to 100000 cm^{-3} . The first calculation was started at 1 particle per mm^3 (1000 cm^{-3}), although subsequent calculations show the change in growth conditions with different numbers of nucleants. ΔT_N , the supercooling of heterogeneous nucleation, was again speculated to range from 0 to 2.25 K, using an initial start temperature of 0.75 K.

Using Equations 6.1 and 6.2, and ranging the real interface velocity, V' , from 5×10^{-3} to 0.1 a plot of growth velocity against temperature gradient was drawn for an Al - 12 wt. % Si system, and is given in Figure 6.57.

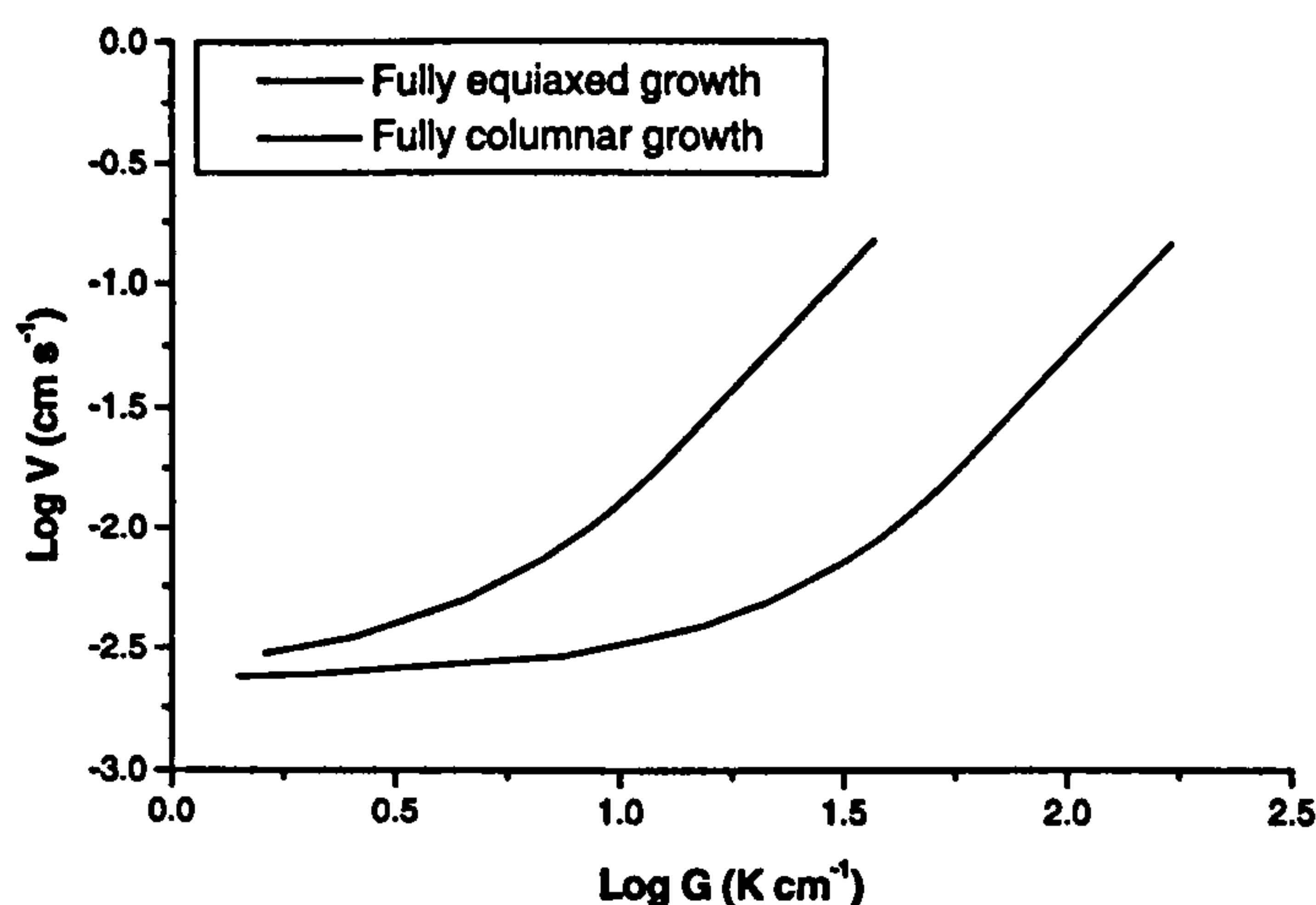


Figure 6.57 Plot of growth velocity, V (cm s^{-1}), against temperature gradient, G (K cm^{-1}), for Al-12wt.%Si ($N_0=1000 \text{ cm}^{-3}$ and $\Delta T_N=0.75 \text{ K}$)

The plot in Figure 6.57 provides an indication that, from initial investigations, Hunts model has the potential to predict the columnar to equiaxed growth transition, however, this depends on many parameters being known in order to calculate the relevant plots. Furthermore, the growth velocity and temperature gradients of the individual alloys are required to utilise the

resultant graphs. It can be seen that although the results for the Al-Si calculations appear promising, a lot more work is needed to develop the theory for this system. In particular, the different types of growth mechanism between Al-Cu and Al-Si (faceted and non-faceted) should be taken into consideration.

6.5.5 Summary

It can be concluded that the formation of both the transition and equiaxed zones is most likely a result of nucleation of broken-off dendrite tips from the columnar zone when casting conditions are favourable. Thus the $\langle 110 \rangle$ texture adopted initially by the columnar grains presides in the transition and equiaxed regions also. The addition of Ti acts to reduce the supercooling necessary for nucleation and growth at the centre of the casting, increasing the nucleation temperature with increasing Ti content. When there is a small amount of Ti the supercooling required at the centre of the casting is greater and the spontaneous growth of the broken tips occurs producing a large number of small particles, such as in the transition region. In alloy 3 where there was a large amount of Ti added, the nucleation temperature at the centre of the casting remained at a higher temperature so that two effects were seen; the transition region formed at the columnar interface where the melt was cooling rapidly, whilst in the centre broken tips were slowly growing into large equiaxed grains.

6.6 Discussion

This final section draws together the findings from the previously detailed experimental programs, in order to discuss the effect of grain refining additions on Al-Si casting alloys. As mentioned in Chapter 3, although grain refiners, such as Ti, are used widely in refinement of casting alloys, the approach is borrowed completely from wrought aluminium practice. In casting practice, a master alloy containing inoculant particles embedded in an Al matrix is added to the melt prior to pouring where it typically dissolves completely apart from the inoculant particles which are dispersed in the melt.

The most common grain refiner is Ti, and the particles are usually of the form Al_3Ti . It is assumed that casting conditions are such that Al_3Ti particles remain in the melt after addition by the master alloy, and subsequently act as nucleants for the aluminium phase during solidification. For Ti levels above the peritectic, 0.15 wt. % Ti in the Al-Ti binary system,

Al_3Ti is expected to be the first phase to form on solidification, and therefore master alloy additions will remain stable. Indeed, an Al_3Ti intermetallic phase was described in Chapter 5 and was most likely a result of excessive growth to form such a large particle. A similar phase was found in the keel bar alloy 5/3 after addition of Zr by an Al_5Zr master alloy, and although the particle was found to contain large quantities of Si, it is still believed to be residue from the master alloy addition.

According to phase diagram theory of equilibrium conditions, however, Al_3Ti is not stable at hypoperitectic (< 0.15 wt. %) compositions. This would mean that on addition to the melt the Al_3Ti dissolves completely leaving no nucleant particles except at very short holding times (equilibrium conditions). Grain refinement must therefore be due to non-equilibrium conditions, whereby the kinetics of dissolution mean that Al_3Ti can exist at non-equilibrium for a long time and thus can still be an active nucleant particle. In addition, the alloy systems are not simple Al-Ti binaries, and the effect of additional alloying elements is believed to change the peritectic point of Al_3Ti .

The casting alloys examined in this work were all multicomponent Al-Si alloys, that is they contained quantities of Mg, Cu, Ni, and Fe, as well as the elements added for the investigation of grain refinement (Ti, Zr, and V). It is known that certain elements enhance the efficiency of Al_3Ti , whilst others reduce the efficiency, or 'poison', the grain refiner. The mechanisms behind the effect of the alloying additions is less clear. From the stepped mould model alloys 86 and 90, a comparison can be made to determine the effect of the higher silicon and copper additions in alloy 90. Both alloys have similar quantities of Ti, Zr and V which are predicted to be soluble in Al_3Ti , and it is this phase which is predicted by thermodynamic calculations to be the first to form on solidification. However, the temperature of the liquidus in each alloy is different, being 928 in alloy 83 and 903 in alloy 90. This suggests that increased Si and Cu additions reduce the stability of the Al_3Ti phase, and consequently the liquidus temperature of the alloy.

As well as Ti, Zr and V are often added, both individually and in combination, as grain refiners. In this work, additions of V and Zr were both predicted and observed to stabilise the Al_3Ti phase in which these elements are predominantly soluble. Additions of V below the Al-V peritectic (0.1 wt. % V) are known to have little or no enhancement, and this was found to be the case in model alloys 24 and 25. Model alloy 38 was also observed to have little change

in structure, despite containing 0.12 wt. % V, therefore above the peritectic composition at which grain refinement is efficient. However, the grain refinement, in this case, was attributed to the formation of the Al_{10}V phase at hyperperitectic compositions, a phase not observed in the model alloys as all the V is believed to be soluble in Al_3Ti .

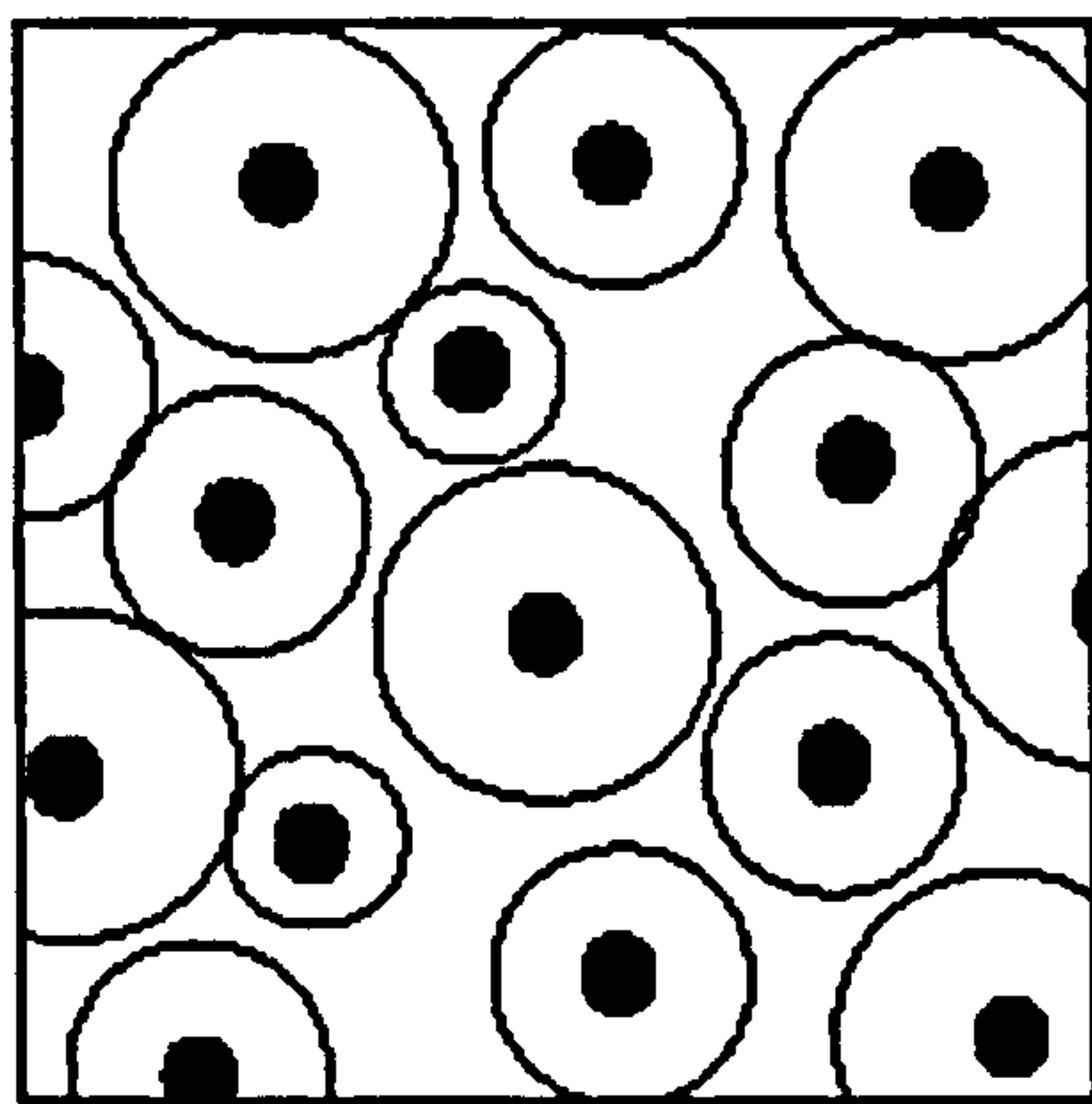
Zr is also proven to be an efficient grain refiner by formation of Al_3Zr when no Ti is present. This was evident in the study of the keel bar alloys where 5/1 to 5/3 contained Zr added at various hyperperitectic (> 1 wt. % Zr) amounts by an Al_5Zr master alloy. The additions were seen to produce an equiaxed grain structure, slightly coarser than that seen for equivalent Ti additions. At hypoperitectic additions the Zr alone is believed not to produce any refinement, although, in addition to Ti there is a combined effect to restrict the growth and promote grain refinement. However, when large amounts of Zr are added to a Ti-containing alloy, the Zr acts to change the lattice parameters of Al_3Ti in the basal plane, making the phase less effective and poisoning the grain refiner results.

The thermodynamic calculations illustrate the effect of theoretical combinations of Ti + V, Ti + Zr, and V + Zr additions, and show that Al_3Ti is predicted to increase in stability with increasing additions. The Ti + V combinations were seen to have the highest fraction of Al_3Ti , which was also the first phase to form on solidification resulting in a high liquidus temperature. However, Ti + Zr and V + Zr combinations were found to have a lower fraction of Al_3Ti , which was not the first phase to form at low additions, and the alloys had a much lower liquidus temperature than was seen for the Ti-V combination. This is consistent with the discussion regarding individual additions of Zr, where the Al_3Ti is poisoned by Zr which acts to change the lattice parameters of Al_3Ti in the basal plane. The efficiency of all three grain refiners was confirmed by growth restriction parameter calculations, which were proven to be a quantitative measurement for assessing grain refinement, and as such will be used in Chapter 9 to investigate new alloying additions.

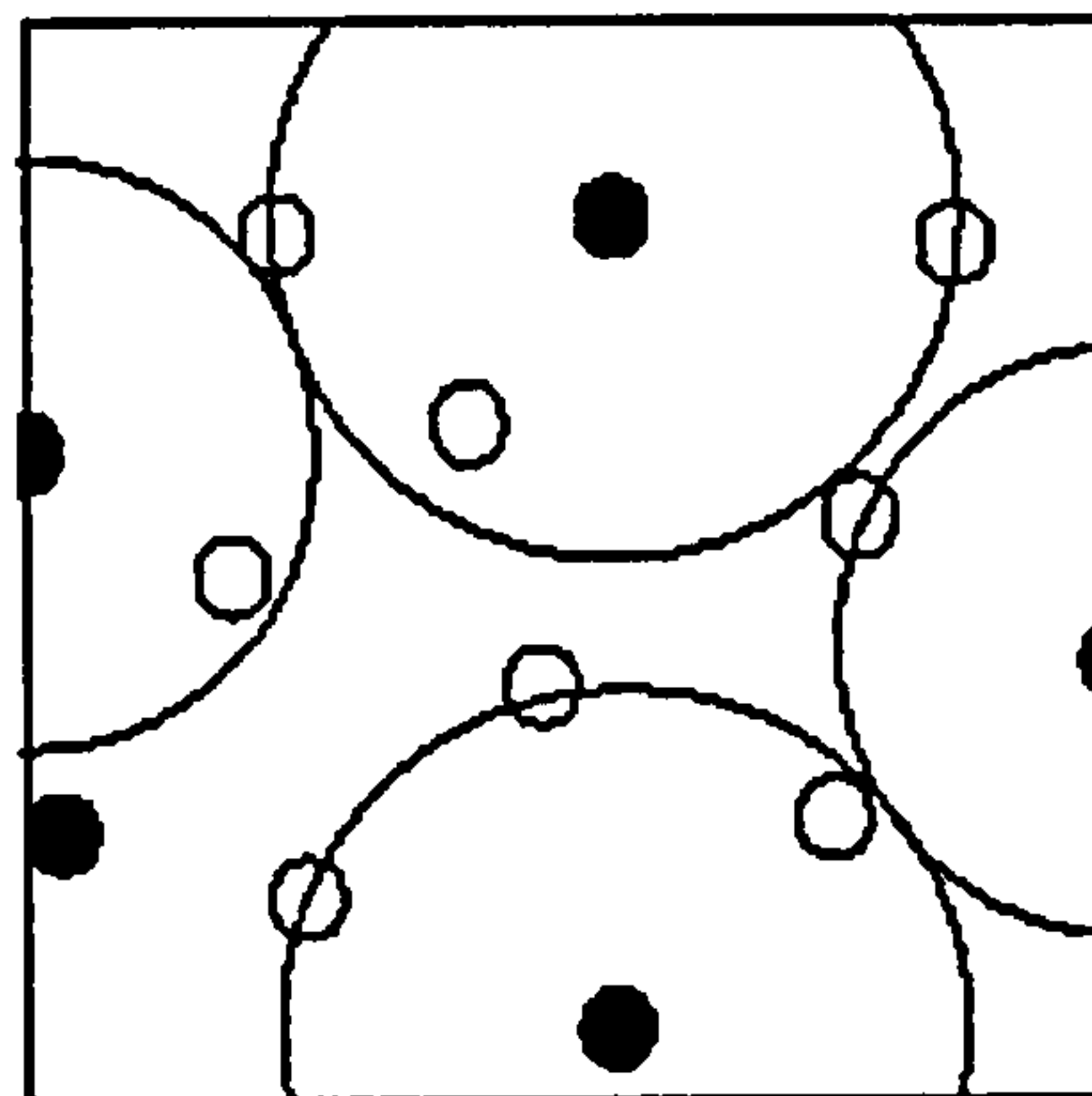
Assuming that numerous nucleant particles are present in the alloy melt, their efficiency to nucleate and promote a finely equiaxed structure will also depend on the casting conditions, such as mould temperature and dimensions. Throughout this work several investigations have considered alloys cast into stepped moulds to explore the effect of cooling rate and temperature gradients on final grain size and shape. To do this two different mould temperatures were used, one at 100 °C and the other at 440 °C.

Ignoring the effect of Ti (Zr and V), in general, the 100° mould temperature will generate the faster cooling rate due to the higher temperature gradient between the melt and mould wall. In thin sections the cooling rate is so fast that the melt solidifies almost instantaneously producing a fully columnar structure along the direction of the temperature gradient. In the thicker sections, growth will initially be columnar along the large temperature gradient between mould wall and liquid in the centre, although equiaxed growth may develop in the centre of the thicker sections if the temperature in the centre of the casting is supercooled sufficiently for nucleation to occur before the columnar grains impinge. At a 440 °C mould temperature there is a lower temperature gradient, and therefore a slower growth rate is expected. The thin sections will still solidify almost instantly forming columnar grains, and in the thick sections heat dissipation is slow, temperature gradient is reduced, and growth is slower. Although the columnar grains are growing slower, the liquid in the centre of the casting also takes longer to cool down enough for nucleation before the columnar grains impinge.

The effect of Ti (Zr and V) additions on the solidification process is to provide nucleation sites for aluminium to nucleate on at a lesser supercooling than is required otherwise. Thus, if sufficient nucleants are present in the melt, there will be spontaneous nucleation of the aluminium on pouring, as the temperature of the melt reaches the new solidification temperature more rapidly. Once the particles have nucleated, the size of the resultant grains is dependant on the rate of growth, which in turn hinges on the speed at which the heat is dissipated. For example, in the 100 °C casting the temperature gradient is high, and so most of the nucleated particles solidify rapidly producing fine equiaxed grains, as seen in Figure 6.58 a. The 440 °C casting, on the other hand cools more slowly, and therefore the growth rate is slower. As some grains grow to a large size they may encroach upon other nucleant particles, preventing them from growing, and enabling large grain sizes to be realised.



a)



b)

Figure 6.58 a) fast and b) slow growth of nucleated particles

Whatever the size of the equiaxed grains, the process of changing the growth mechanism from columnar to equiaxed is of particular interest when considering the effect of grain refiners. In stepped mould model alloys 3/1 to 3/3 it was shown that Ti additions appear to promote the CET. However, the microstructures related to the different growth zones indicated that the primary silicon, rather than the aluminium phase was in fact first to form on solidification. It was stated at the beginning of this chapter that significant amounts of P are present as an impurity in the alloys, which form the compound AlP. AlP acts as a nucleant for primary silicon and is therefore in competition with the nucleation of aluminium by Al_3Ti . In order to try and clarify the solidification process in stepped mould model alloys 3, a series of DSC experiments were run[†] to ascertain the cooling curves for each alloy. The curves can be seen in Figure 6.59 (alloys 3/1 to 3/3, increasing Ti additions) and Figure 6.60 (alloys 3/4 to 3/6, Zr and V additions), and were repeated to confirm their reproducibility.

From Figure 6.59 it can be seen that at low Ti additions (alloy 3/1) the silicon is nucleated at a around 595 °C, whereas at high Ti additions (alloy 3/3) the temperature is lower, at around 580 °C, close to the nucleation temperature of the aluminium. This would appear to indicate that for low Ti additions, the AlP is more efficient at nucleating the silicon at higher temperatures, with scope to continue growing over the increased temperature difference before the aluminium forms. However, at high Ti additions, the Ti appears to affect the

nucleating potency of the AlP, and the silicon and aluminium nucleation peaks become closer. The closer these peaks are, the more uniform, and closer to the eutectic, the structure is likely to be. The size of the silicon particles might be expected to be larger for low Ti additions, having had longer time to grow, however, image analysis results in Figure 6.51 proved inconclusive in quantifying this. A more detailed investigation of the size and number of silicon particles is a subject for further work.

The plot in Figure 6.60 shows the effect of Zr and V additions (alloys contain ~ 0.01 wt. % Ti) on the cooling curve of model alloys 3/4 to 3/6. It can be seen that the V additions (alloys 3/5 and 3/6) appear to have a similar effect to the Ti, by reducing the efficiency of AlP in nucleating silicon to a temperature close to that of aluminium nucleation. The Zr additions alone (alloy 3/4), on the other hand, appear to have very little effect on AlP, with silicon particles nucleating at around 590 °C and having the opportunity to grow over the increased temperature difference before the aluminium forms. This is in keeping with the common perception that Zr leads to larger and less uniformly distributed silicon particles, however it is important to remember that there are further competing effects of cooling rate not considered here.

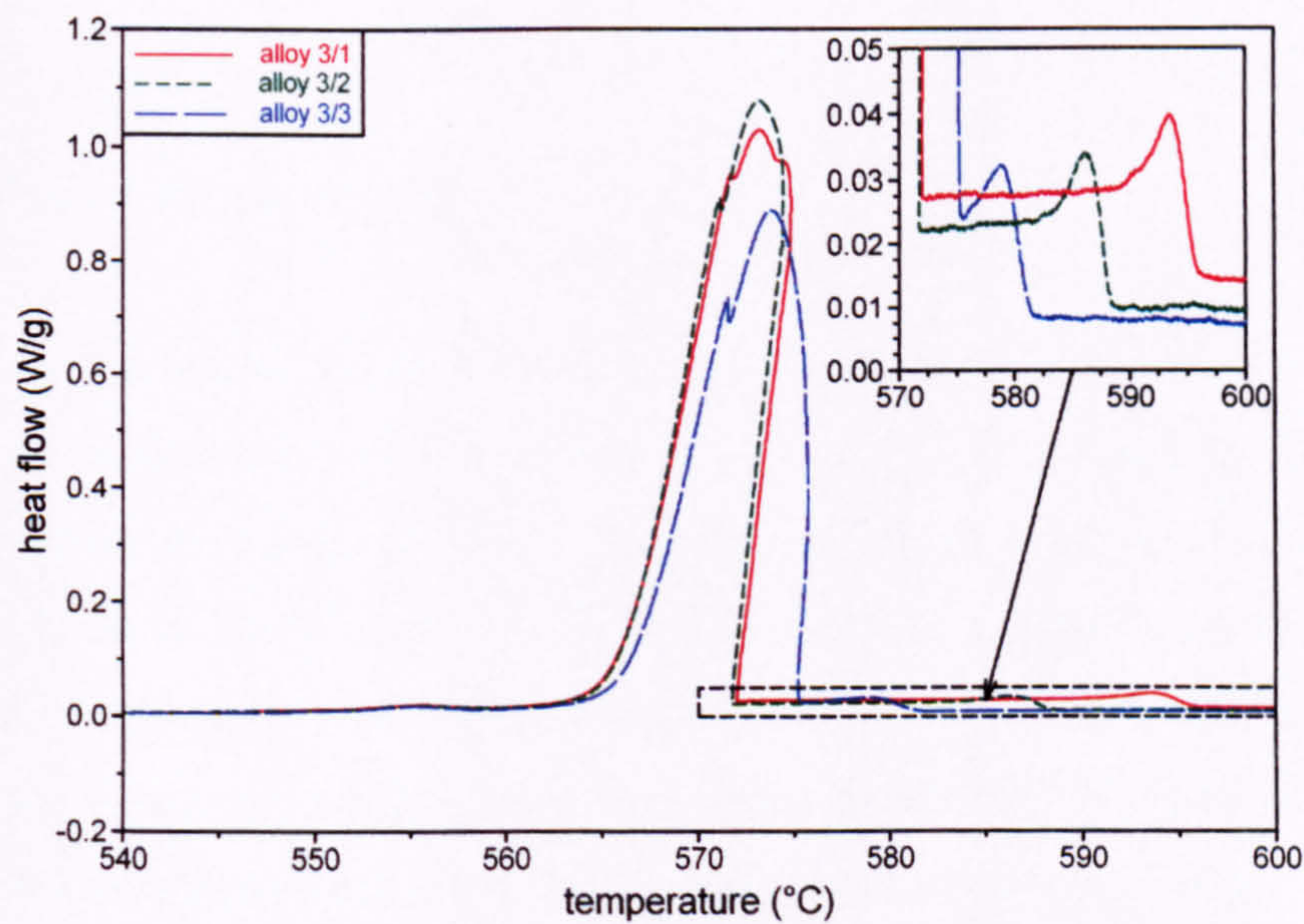


Figure 6.59 DSC cooling curves (1 °C/min) for stepped mould model alloys 3/1 (0.01 wt. % Ti), 3/2 (0.05 wt. % Ti), and 3/3 (0.15 wt. % Ti)

† This work was carried out by Mr. D. Price

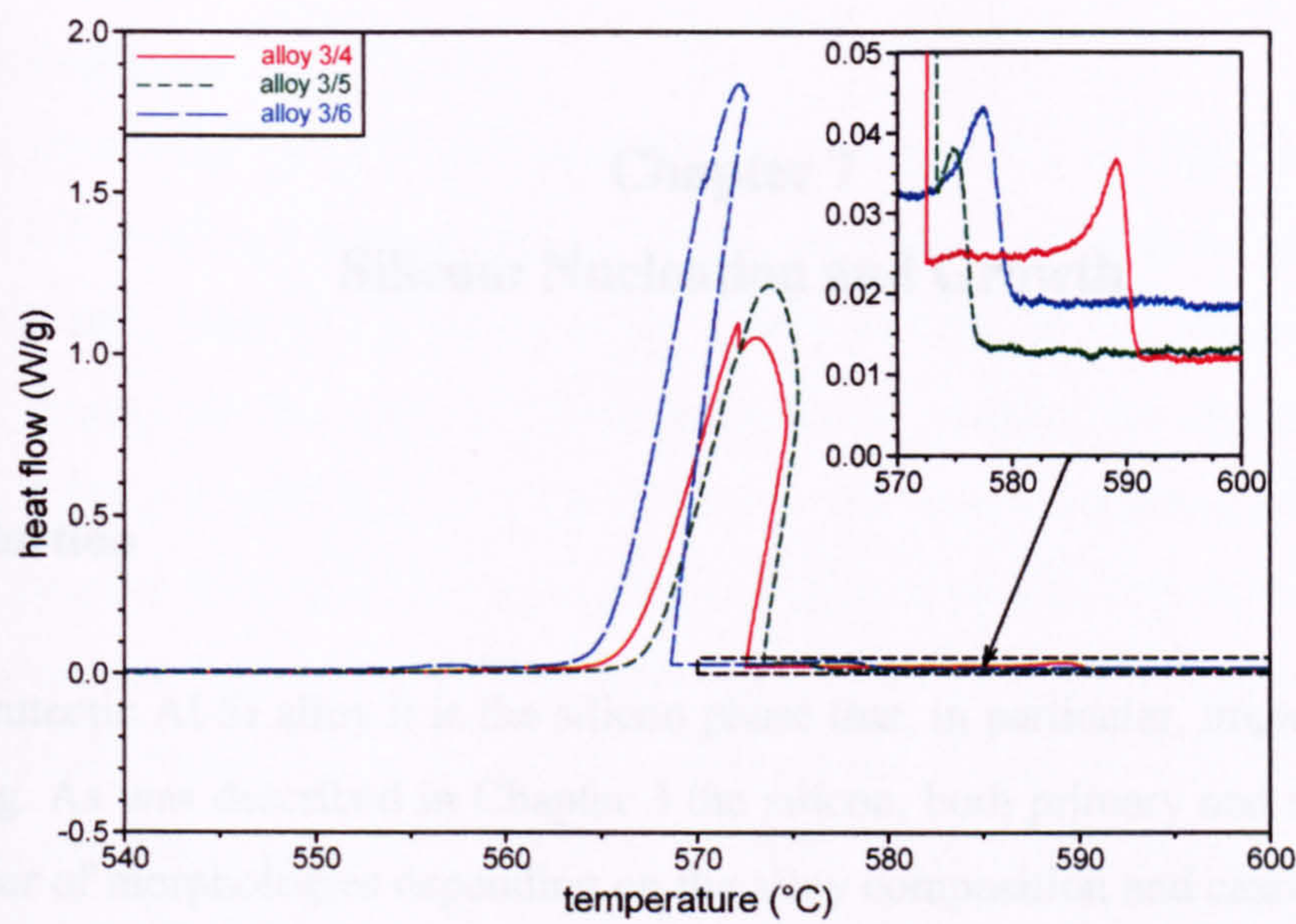


Figure 6.60 DSC cooling curves (1 °C/min) for stepped mould model alloys 3/4 (0.2 wt. % Zr), 3/5 (0.63 wt. % V, 0.005 wt. % Zr), and 3/6 (0.02 wt. % V, 0.14 wt. % Zr)

In conclusion, its has been shown that the final structure of a casting is a combination of both nucleation and growth issues, the nature and efficiency of the grain refiner added, and is further complicated by the competing effects of casting conditions.

Chapter 7

Silicon: Nucleation and Growth

7.1 Introduction

In a near-eutectic Al-Si alloy it is the silicon phase that, in particular, imparts wear resistance to a casting. As was described in Chapter 3 the silicon, both primary and secondary can take on a number of morphologies depending on the alloy composition and casting conditions. The secondary, or eutectic silicon phase has, in the past, been studied in detail due to its improvement in properties as a result of modification. However, the primary silicon phase has not been investigated to the same extent. In this chapter it is hoped to elucidate some of the questions regarding both the nucleation and growth mechanisms of silicon, and furthermore, how the morphology and structure of silicon particles relate to mechanical properties, in this case specifically fatigue behaviour. Electron backscatter diffraction (EBSD) on the SEM has been particularly useful in both phase identification and describing the orientation of the crystals.

7.2 Nucleation of Silicon Crystals

The process of inoculation in Al-Si alloys is that of providing large numbers of particles to act as heterogeneous nucleation sites on which silicon can easily grow, promoting the formation of a larger number of smaller particles. The most commonly used material for the inoculation of primary silicon in Al-Si alloys is AlP. AlP is naturally present in most aluminium-silicon alloys when phosphorous reacts with aluminium to form small, insoluble particles of AlP which then act as nuclei on which the silicon forms. Additional amounts of phosphorous may be added to the melt before casting to further improve the nucleating effect. AlP has an fcc B3 type lattice with lattice parameter $a = 0.5428$ nm, whilst silicon has a diamond type lattice with lattice parameter $a = 0.5202$ nm. Thus, the lattice mismatch between the AlP and Si is small, increasing the possibility of epitaxial growth.

7.2.1 Identification of AlP Particles

Despite the knowledge that AlP nucleates silicon, such particles are difficult to characterise in situ as the AlP seeds are washed, pulled or fall out during preparation leaving just the hole from whence they came in the centre of the silicon particle. In this work a sample of model alloy 24 (composition in Table 4.1) was prepared for optical and electron microscopy by grinding to 1200 grit, polishing to 6 μm diamond, and finally polishing to 0.06 μm colloidal silica on a Bhueler Vibromet. The time spent on each stage was kept to a minimum to avoid relief of the phases, and as a result it was possible to obtain a Kikuchi pattern from a trace of the AlP nucleant remaining in the central cavity of the silicon particle shown in Figure 7.1. The silicon has been outlined to show its faceted, polygonal morphology as there is little contrast between the silicon and surrounding aluminium, and the points from which EBSD patterns were obtained are indicated.

Kikuchi diffraction patterns were collected for the AlP and surrounding silicon particle, both of which were automatically indexed from the user database containing the material files created during the extensive phase analysis described in Chapter 5. The indexed patterns are given in Figures 7.2 a) and b), and correspond to the silicon and AlP phases respectively. The Euler angles for the patterns are also given. It is well established that silicon nucleates on the AlP, believed to be due to epitaxial growth as a result of the two phases having similar lattice structures and parameters. However, it is not possible to determine solely from the Kikuchi patterns whether there is any crystallographic relationship between the AlP and silicon, as would be expected. However, using a program called ORICONV[†] it was possible to plot the three Euler angles, identified during automatic indexing of the patterns, on stereographic projections for both phases. These are given in Figure 7.3, from which it is possible to compare the orientations of both. It can be seen that both crystals have virtually the same orientation and it can therefore be concluded that the silicon does indeed grow epitaxially on the AlP particle.

[†] ORICONV v1.0 by Pete Bate

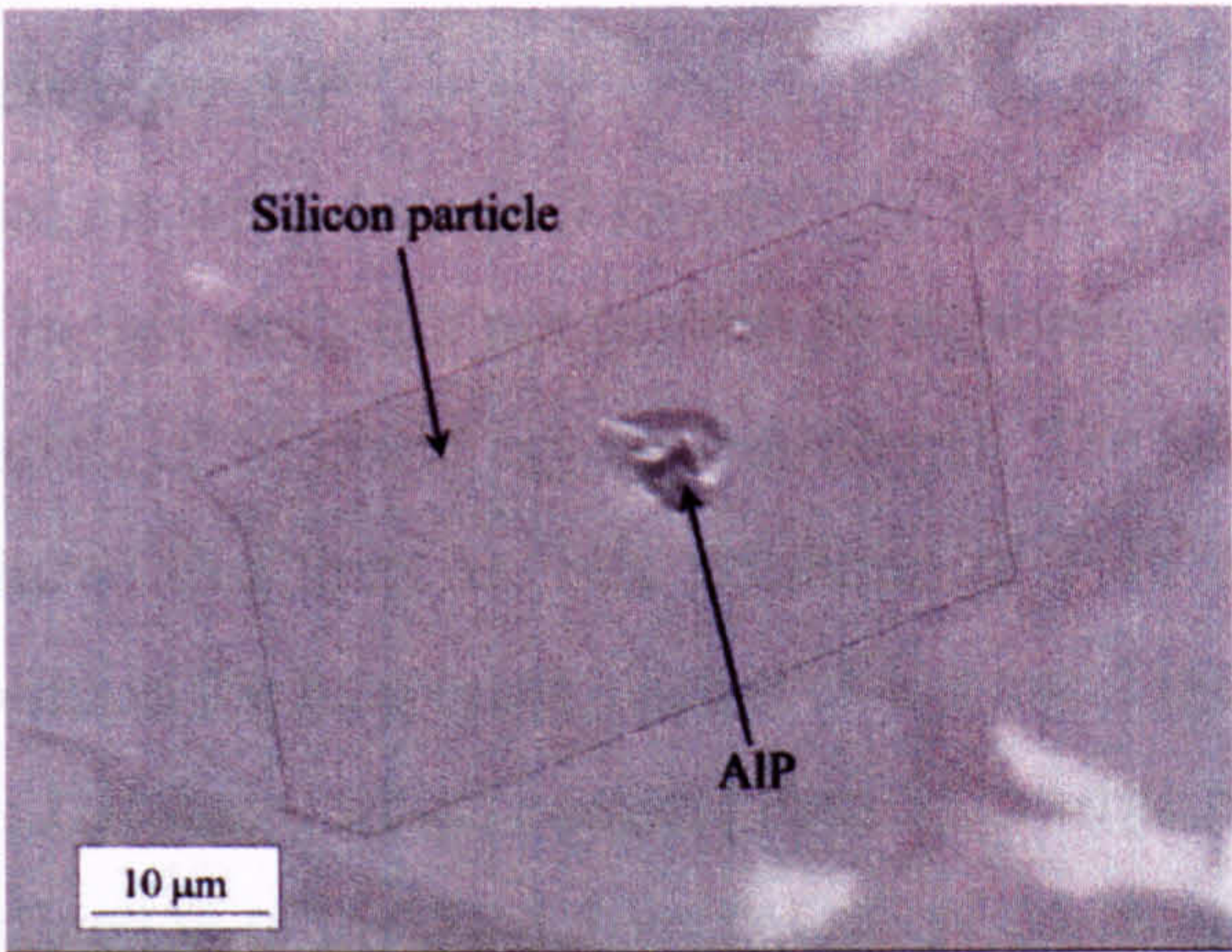
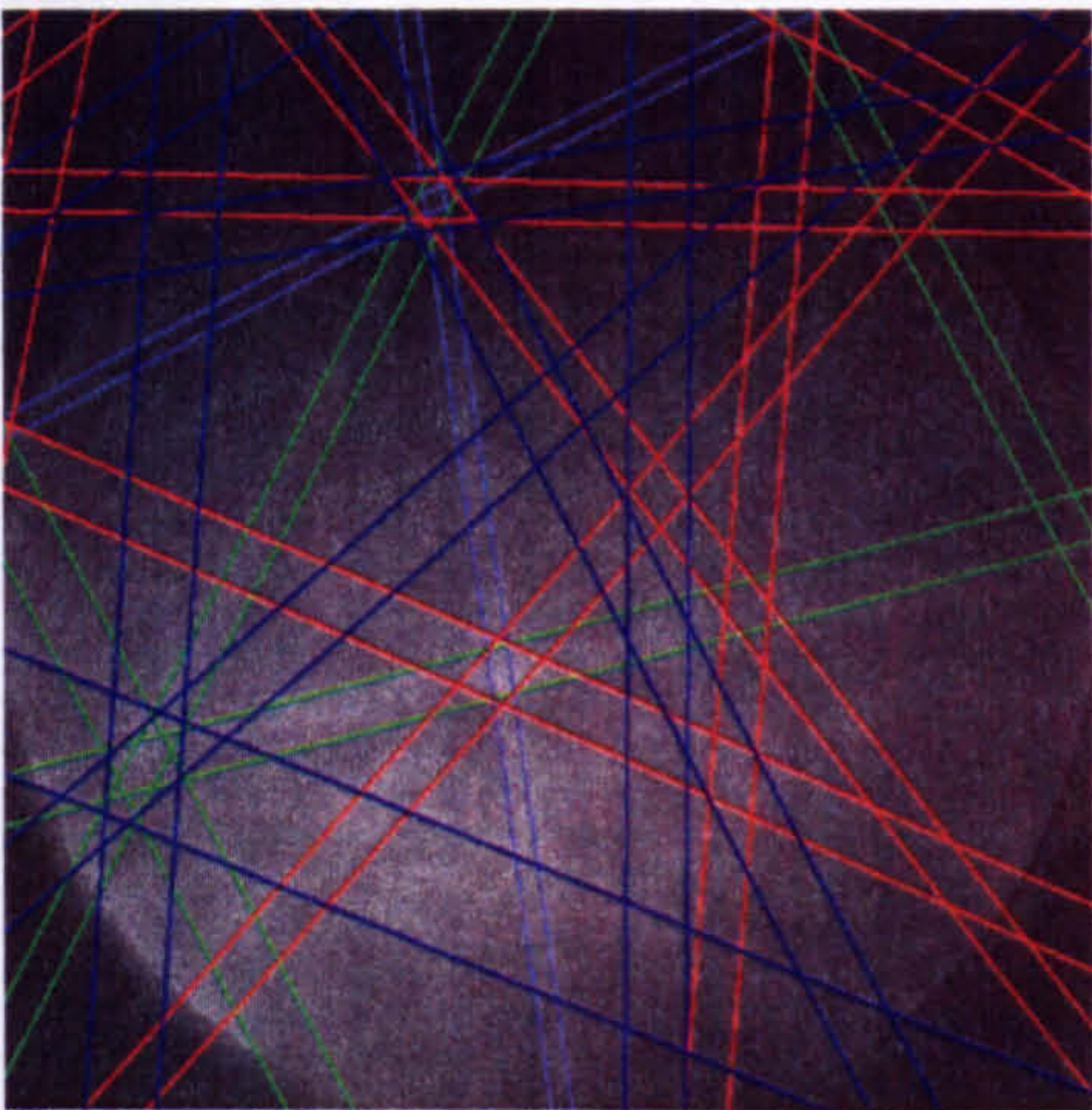
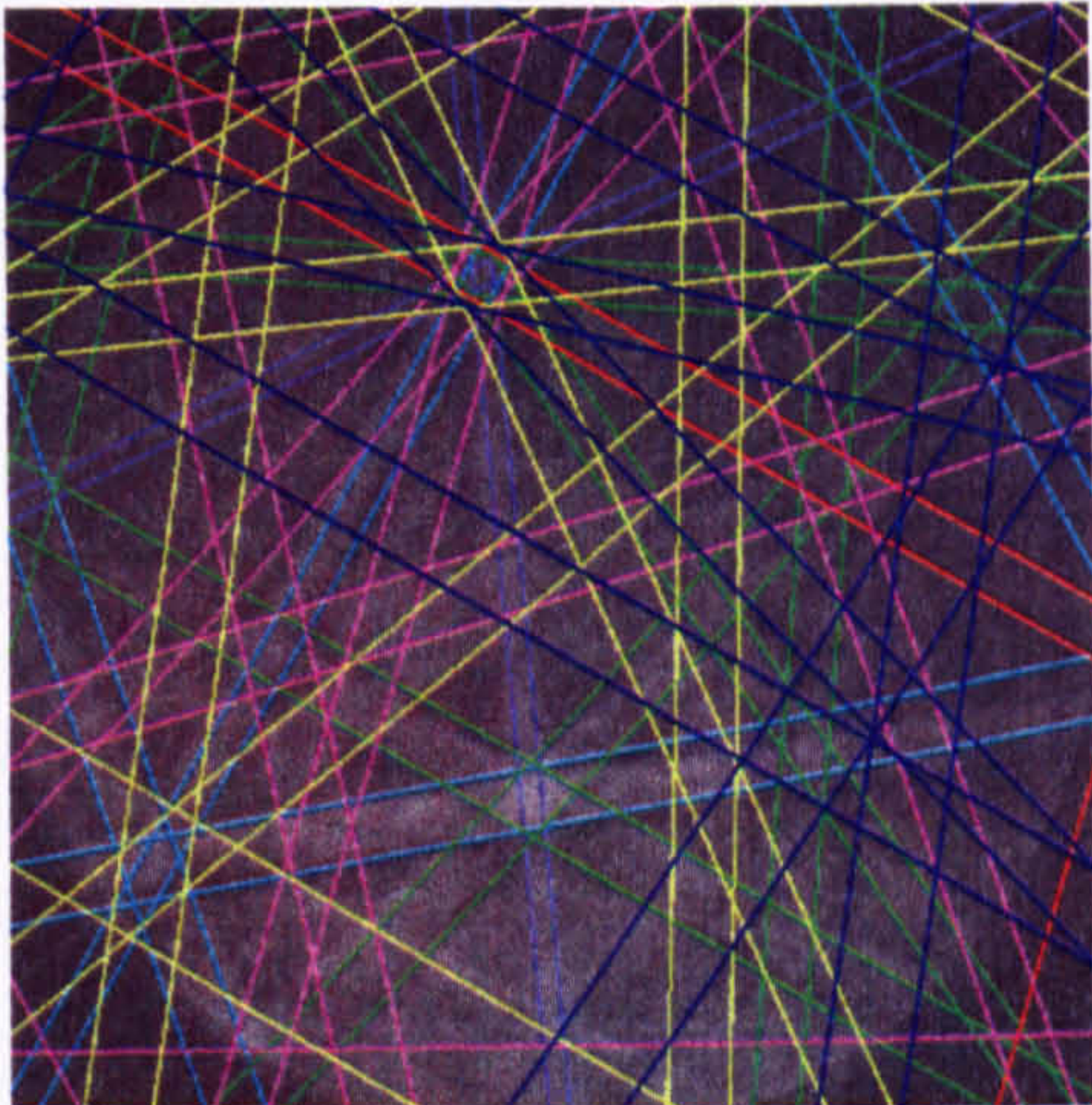


Figure 7.1 Secondary electron SEM image of a silicon particle with AlP particle in the centre



Euler angles: $\phi_1 = 128.7$, $\Phi = 119.3$, $\phi_2 = 346.0$

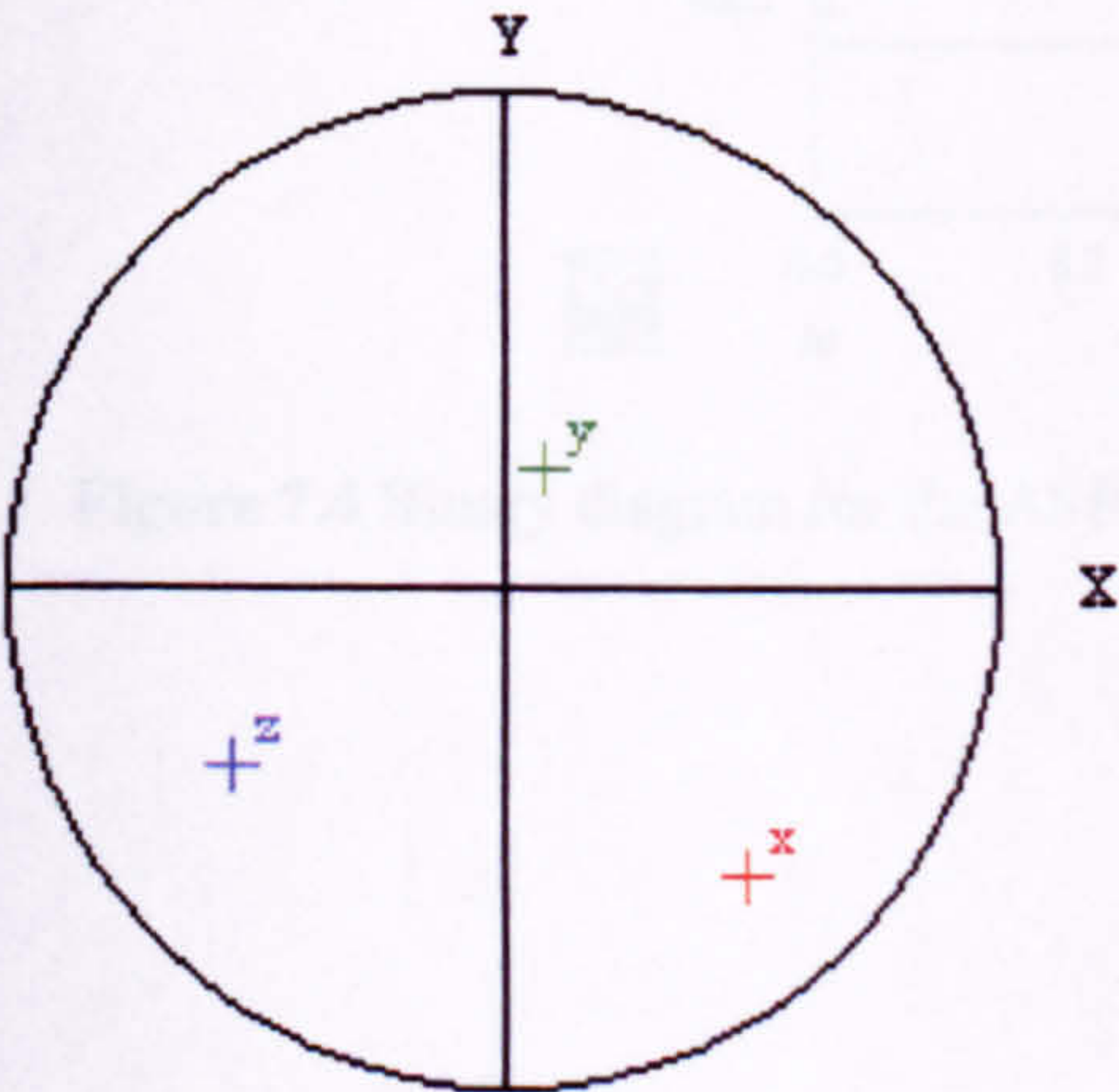
a)



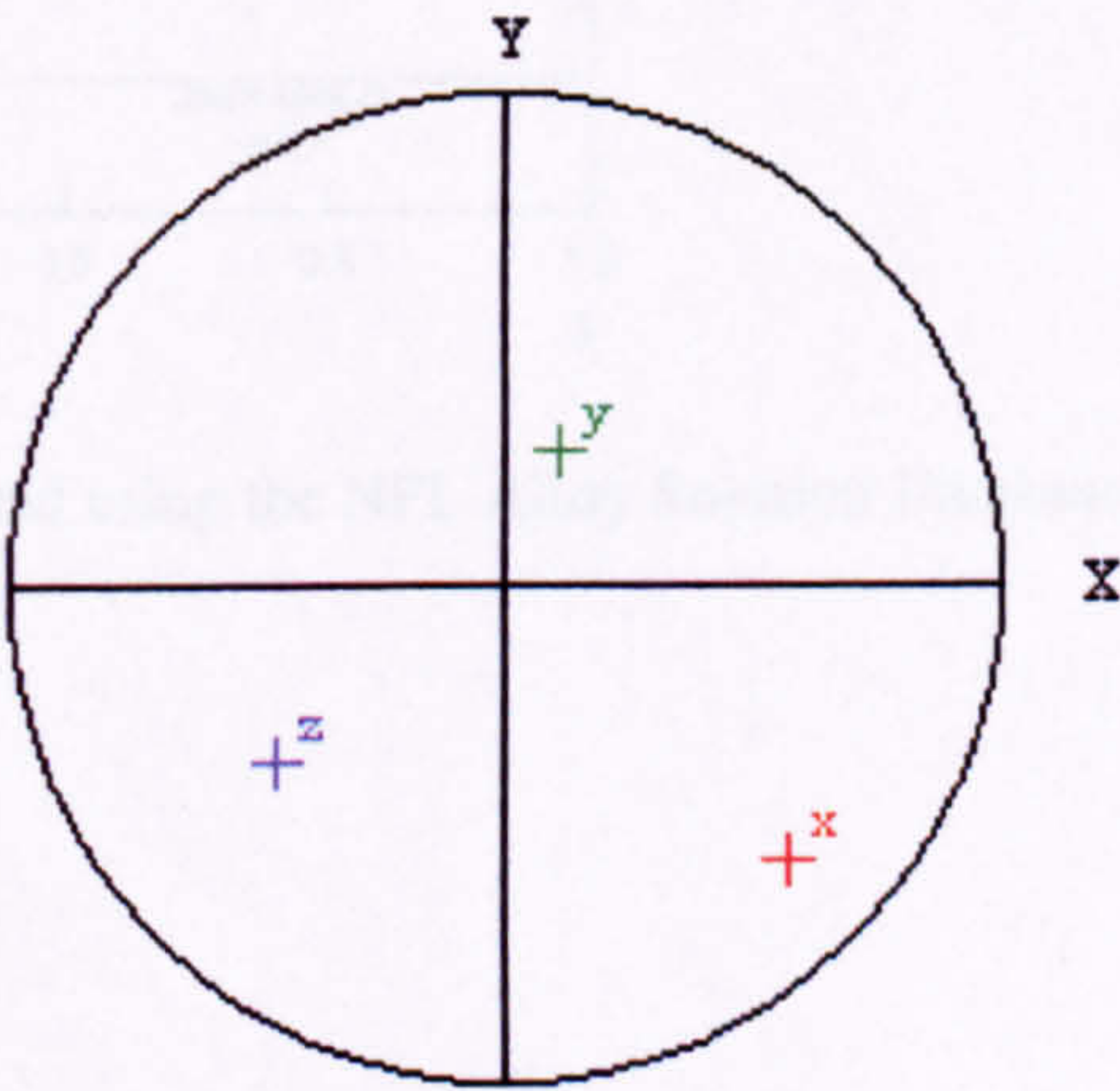
Euler angles: $\phi_1 = 123.8$, $\Phi = 113.2$, $\phi_2 = 344.0$

b)

Figure 7.2 Indexed EBSD patterns and Euler angles from the a) AlP, and b) silicon



a)



b)

Figure 7.3 Stereographic projections of Euler angles from a) AlP, and b) silicon phases

7.2.2 Thermodynamic Data for AlP

Thermodynamic calculations were discussed extensively in Chapter 5, however, it was noted that the databases used in this work did not contain phosphorus, and therefore the AlP phase important in the nucleation of Si could not be considered. The binary Al-P phase diagram, shown in Figure 7.4 shows that there is little solubility of P in Al and that AlP, with the zincblende structure, forms in the temperature range of interest. Figure A was calculated using the NPL Alloy Solution Database, which contains data for a large number of unary and some binary phases. A magnification of the Al-rich end of the phase diagram is presented in Figure 7.5, calculated using the 'isopleth' macro within MTDATA in order to obtain the necessary resolution. The diagram indicates that a very small eutectic exists at approximately 0.02 weight fraction P and 660 °C, above which the gradient of the liquidus rises steeply.

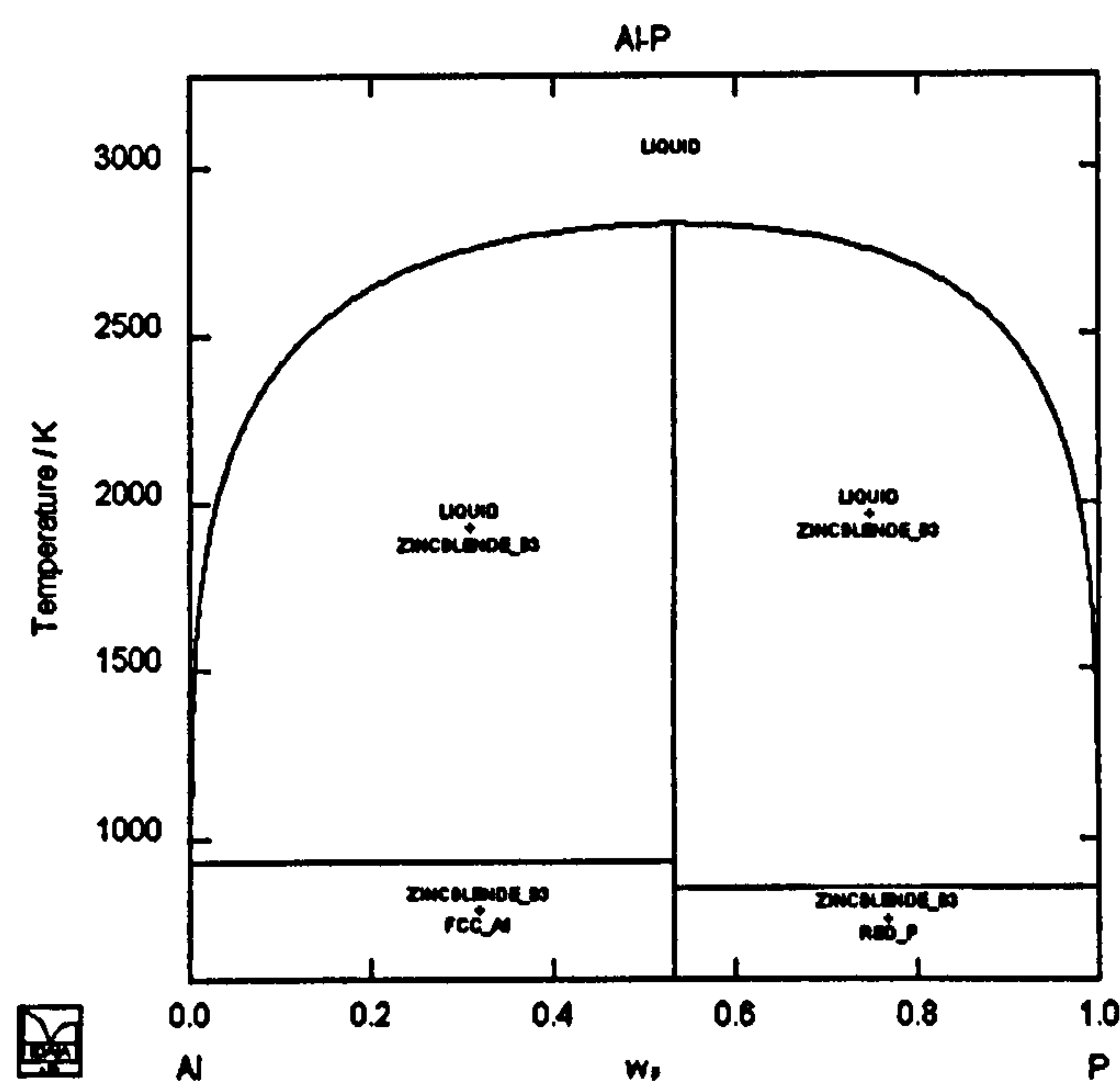


Figure 7.4 Binary diagram for the Al-P system calculated using the NPL Alloy Solution Database

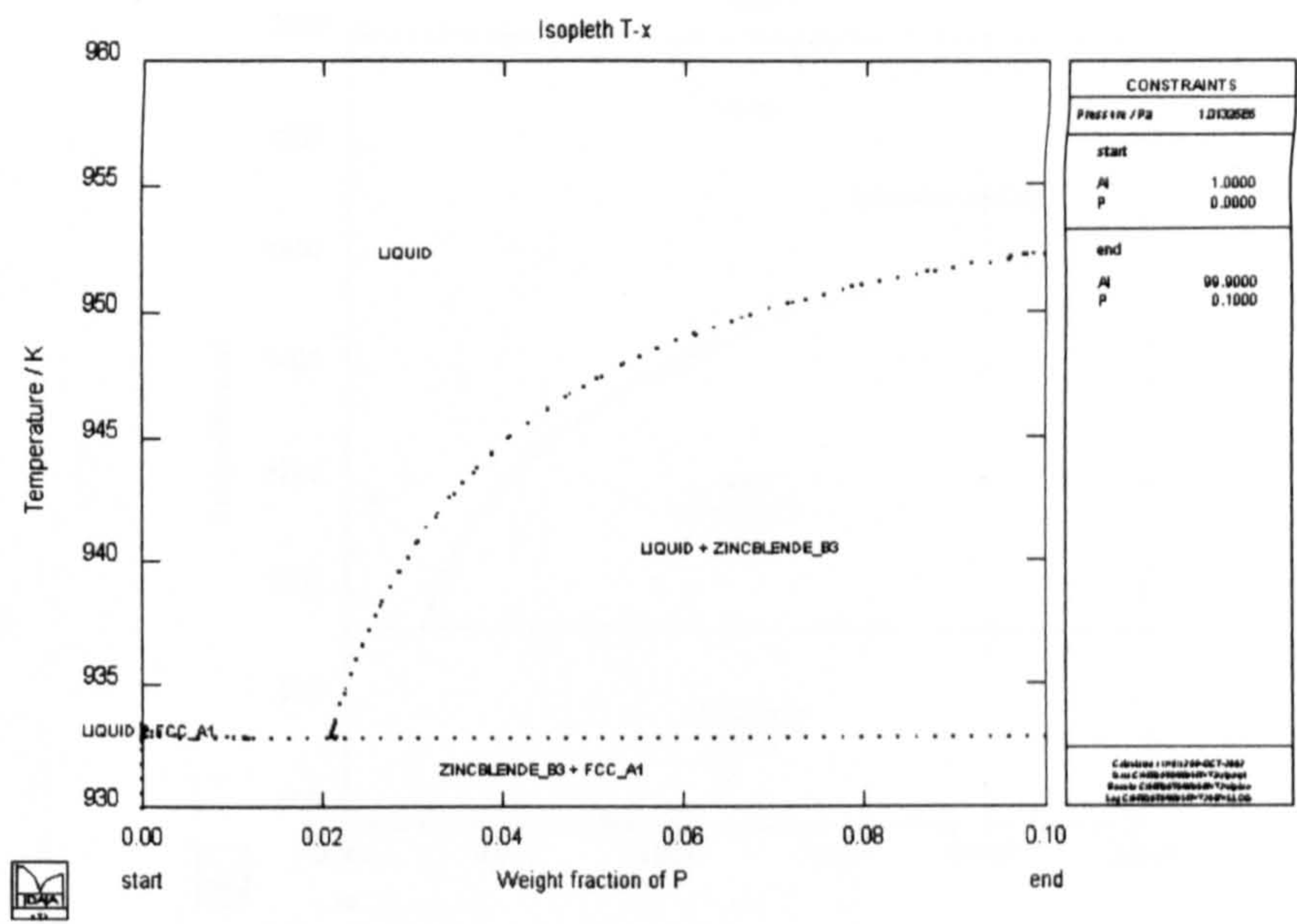


Figure 7.5 Magnification of the Al-rich end of the Al-P diagram, calculated using ‘isopleth’

As with previous work, it was decided to compare the thermodynamic predictions with experimentally determined values. Such small quantities of P are difficult to quantify and therefore by measuring the P content in an original melt and comparing with that in the filtered metal it is possible to determine the level of P present as AlP in the melt at the temperature of the test. Therefore, the amount of P in solution, P_s , in the alloy at a specific temperature, T , can be determined. Measurements carried out within Federal-Mogul have resulted in the formula

$$P_s = 0.0011 \exp (0.014T)$$

[7.1]

in which the P content has units of parts per million and the temperature is in degrees Celsius.

Figure 7.6 presents the Al-rich region of the calculated Al-P phase diagram superimposed with experimental points determined from the above formula. It is clear that the experimental points indicate an even lower solubility of P in Al than indicated by the calculations.

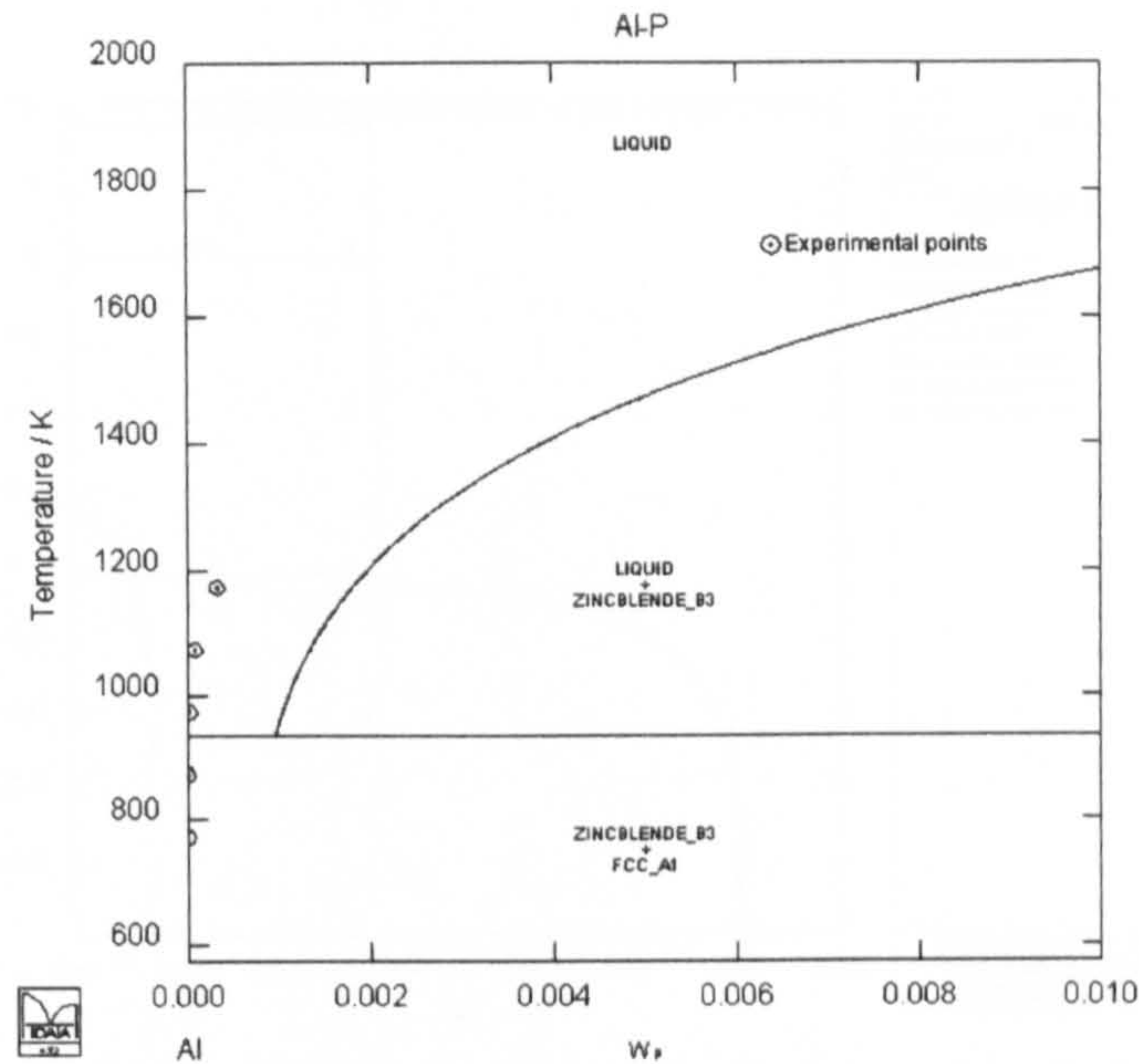


Figure 7.6 Calculated binary phase diagram compared with experimental data points

In order to explore the combined effect of both Si and Ti additions with AlP, a thermodynamic database was then created using the above P data in conjunction with AlData³. The new datafile was treated with a degree of caution in the light of the above data, nevertheless, it was hoped that it would provide a useful insight into the interaction of Si, Ti, P and Al. Initially all possible phases were allowed to exist, however, this led to the prediction of a number of Si and Ti binary phases (e.g. SiTi, Si₂Ti) which had not been observed in practice and were therefore disallowed in subsequent calculations. The results of two such calculations are presented in Figures 7.7 and 7.8 for Al-12 Si-0.15Ti and 0.05 and 0.01 wt. % P respectively. It can be seen that the AlP phase is indeed predicted to form, in addition to Al and Si, although it is perhaps a little surprising that Al₃Ti is predicted to be stable at relatively low temperatures. It is also of interest that the dissolution temperature of AlP appears from a comparison of Figures 7.7 and 7.8 to be very dependent on the P content. This is consistent with the very steep liquidus curve observed in Figure 7.4. The P levels used in these calculations are an order of magnitude larger than those typically used, however, a shift in the position of the liquidus as indicated in Figure 7.6 puts the actual values of dissolution temperatures into question, nevertheless it is clear that the amount of P present plays an important part in the volume fraction and dissolution temperature of any AlP formed within the microstructure.

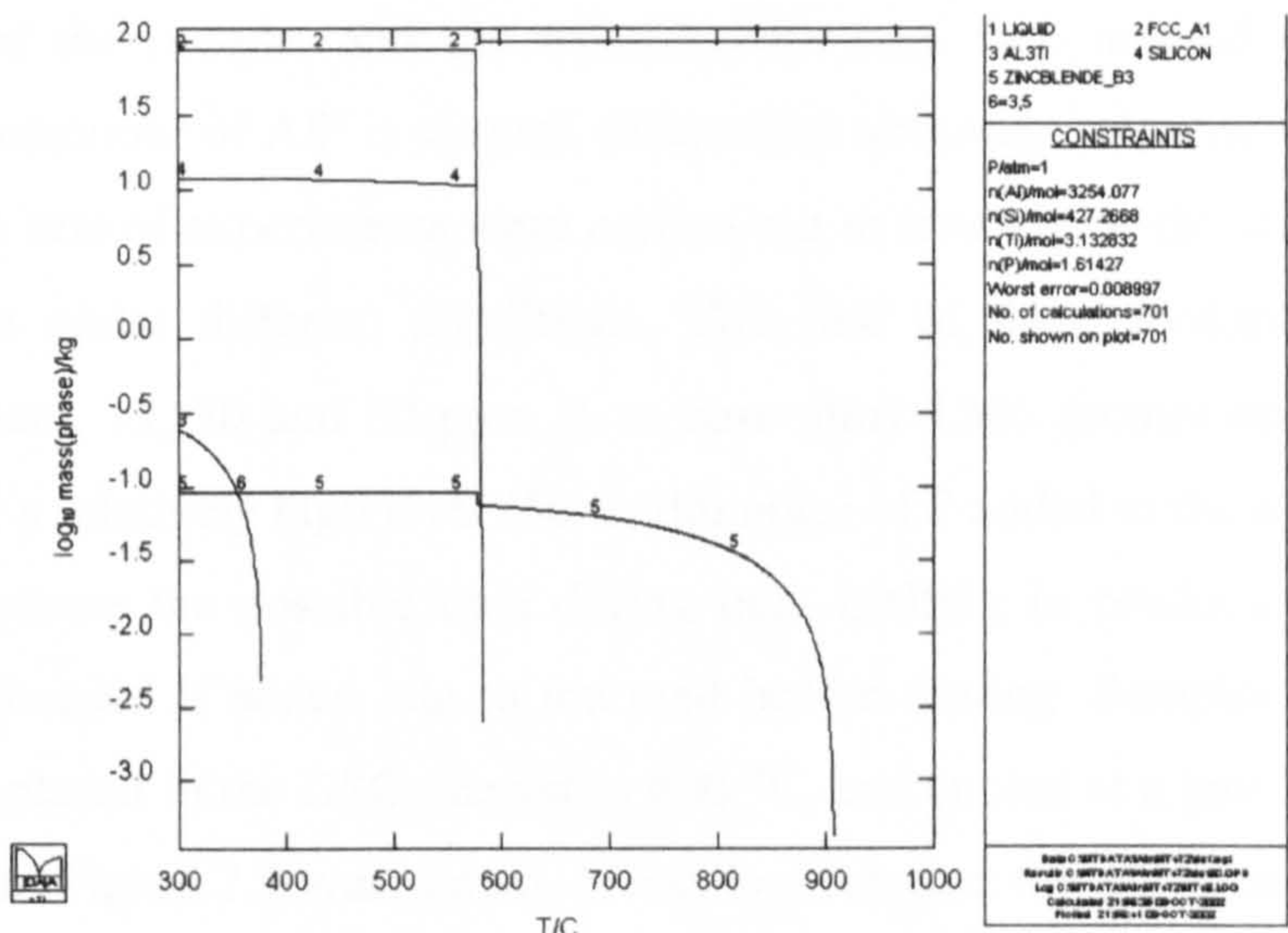


Figure 7.7 Phase stability plot for Al-12 Si-0.15Ti-0.05P wt.% alloy

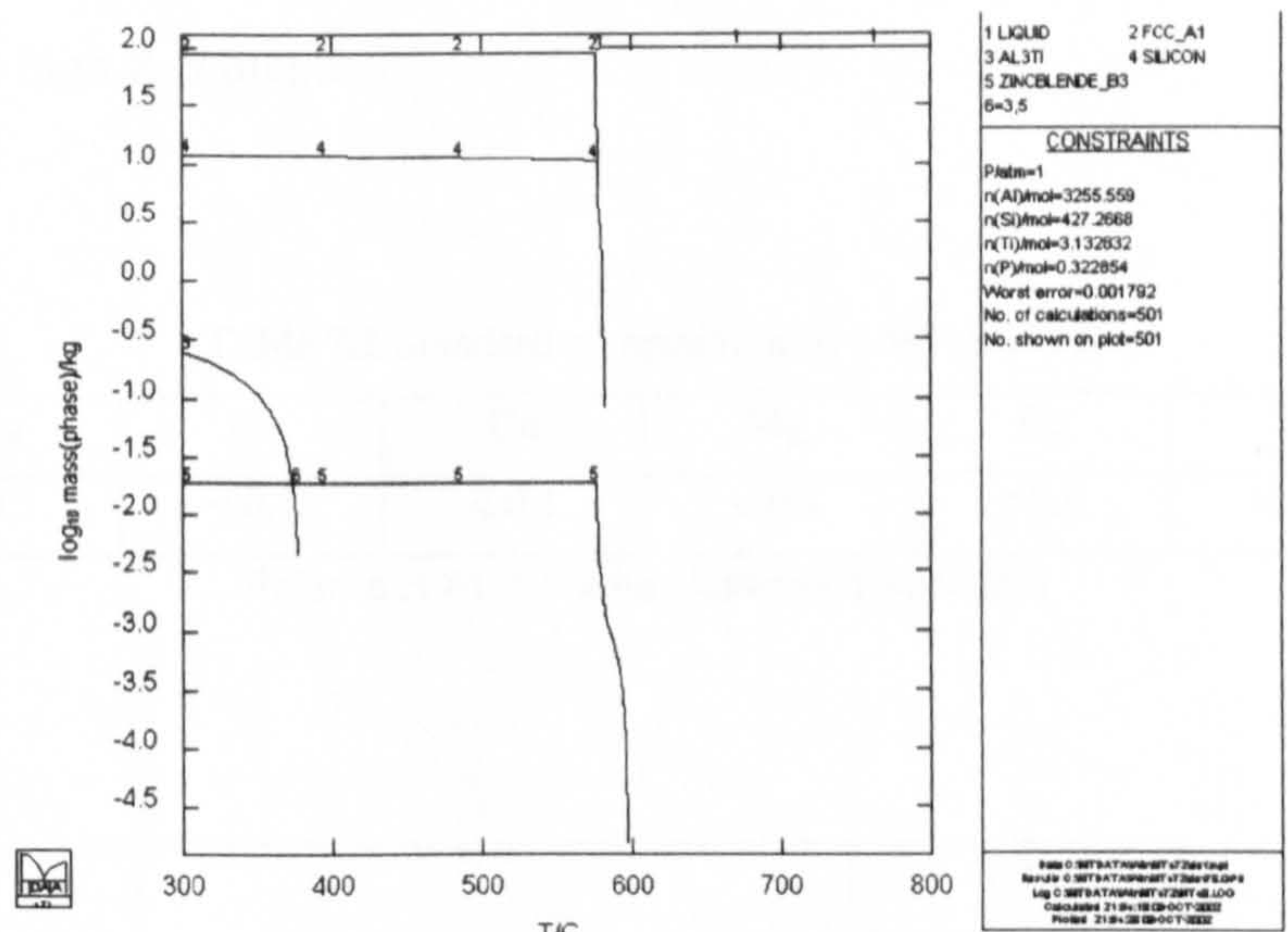


Figure 7.8 Phase stability plot for Al-12 Si-0.15Ti-0.01P wt.% alloy

A more exhaustive data assessment is required for not only the Al, Si, Ti, P system, but also to consider the potential interaction of P with other alloying elements typically present in multicomponent alloys. This should be the subject of future work.

It is known that the effectiveness of P for nucleating silicon depends on the P level, the thermal history of the sample, and the solidification rate. One method of examining the thermodynamic behaviour of AlP is through differential scanning calorimetry (Section 4.3.6). In this work three sets of experiments were carried out to investigate the efficiency of AlP at nucleating silicon under different conditions. The first of these looked at the effect of increasing P content, 15, 30 and 60 ppm P, to base alloy LM6 (composition in Table 7.1). There is normally a relatively high level (50 to 100 ppm) of P added to the alloys of interest in this work to overcome the possible fade during bulk melting in production, although only about 10 ppm is needed if added late to the melt before casting. Samples from each of the three alloys were placed in the DSC, heated to 600 °C, and cooled at a rate of 1 °C/min, from which the curve in Figure 7.9 was drawn. It can be seen that the all three P additions have similar cooling curves, with no clear indication that increased P increases the efficiency of AlP at nucleating silicon. It is noted, however, that because of the low silicon content there does not appear to be any nucleation of primary silicon, although some might have been expected with the high P contents.

Table 7.1 Standard composition of LM6 (wt. %)

Si	Mn	Ni	Cu	Mg	Fe	Zn	Pb
10 - 13	< 0.5	< 0.1	< 0.1	< 0.1	< 0.6	< 0.1	< 0.1

Balance is Al, all other elements unspecified

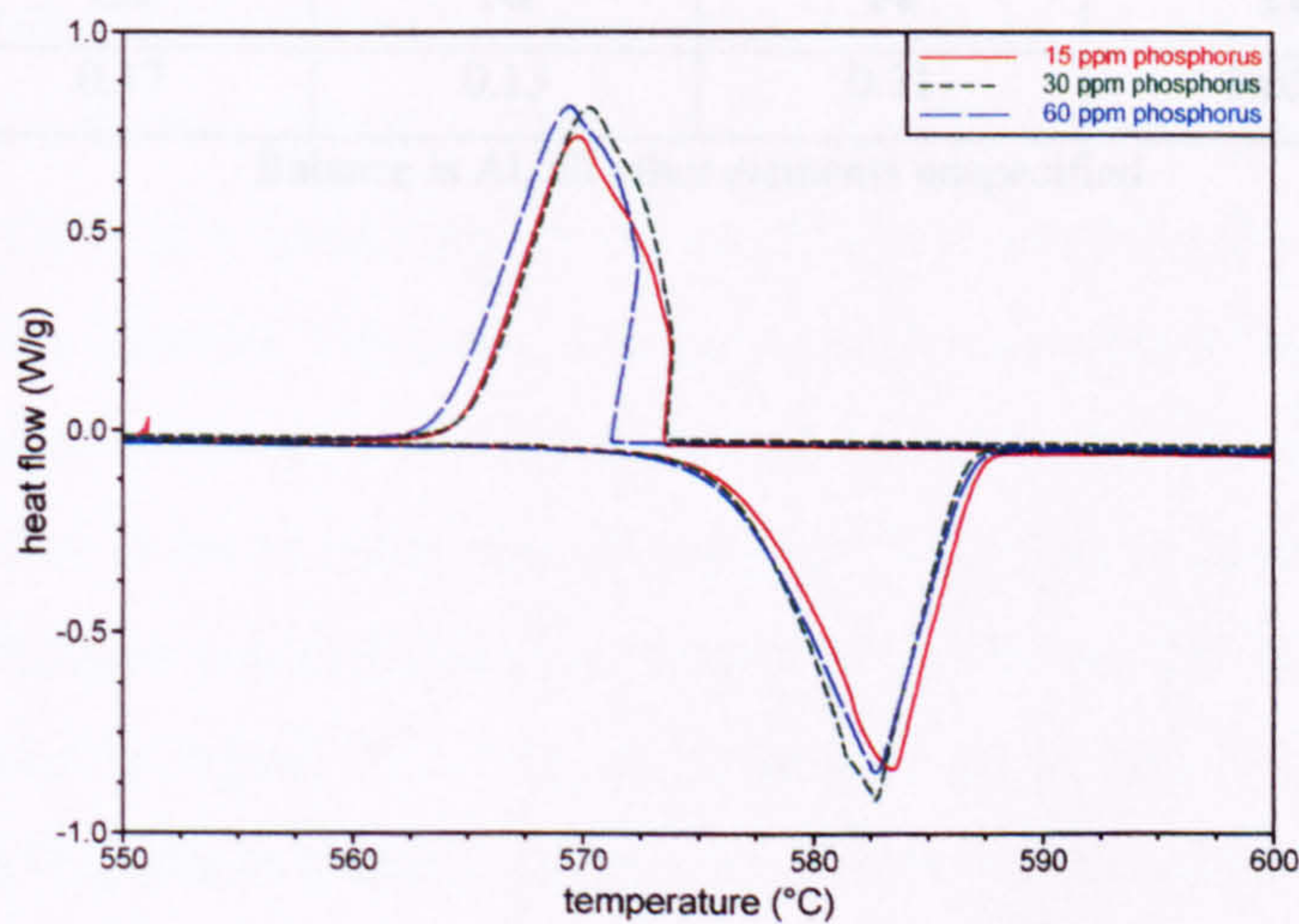


Figure 7.9 DSC curve showing the effect of increasing P additions on the solidification of alloy LM6

The second investigation looked at the effect of thermal history of an alloy, in this case stepped mould model alloy 2 (composition in Table 7.2). The low P content is due to impurities in the melt stock, as no additional P was added to the melt. It is known that continuous re-melting and re-solidification reduces the effectiveness of the P and so a DSC experiment was set up to study the effect of repeated melting and solidification at increasingly higher temperatures. The sample was progressively raised to higher temperatures from 750 °C to 1000 °C, always cooling at a rate of 1 °C/min. The resultant trace can be seen in Figure 7.10, with the inset showing the solidification exotherm of the primary silicon.

It is in the solidification of silicon that the effect of increasing temperature can be seen, as a clear change in exotherm when cooled from below 900 and 950 °C. It appears that between these two temperatures something happens to the AlP to make it more efficient at nucleating at a slightly higher temperature. It is believed that the reason for the difference is due to the fact that AlP requires a high temperature to put the P back into solution. Below this temperature, the P remains as AlP and is stable at temperatures above the melting point for AlP according to the Al-P phase diagram. However, above the critical temperature, which appears to fall between 900 and 950 °C as indicated by the DSC trace, the P goes back into solution and on solidification forms new AlP particles. These particles are more effective at nucleating the silicon at a higher temperature.

Table 7.2 Composition of stepped mould model alloy 3/2 (wt. %)

Si	Cu	Ni	Fe	Ti	P (ppm)
12.49	0.17	0.13	0.31	0.051	16

Balance is Al, all other elements unspecified

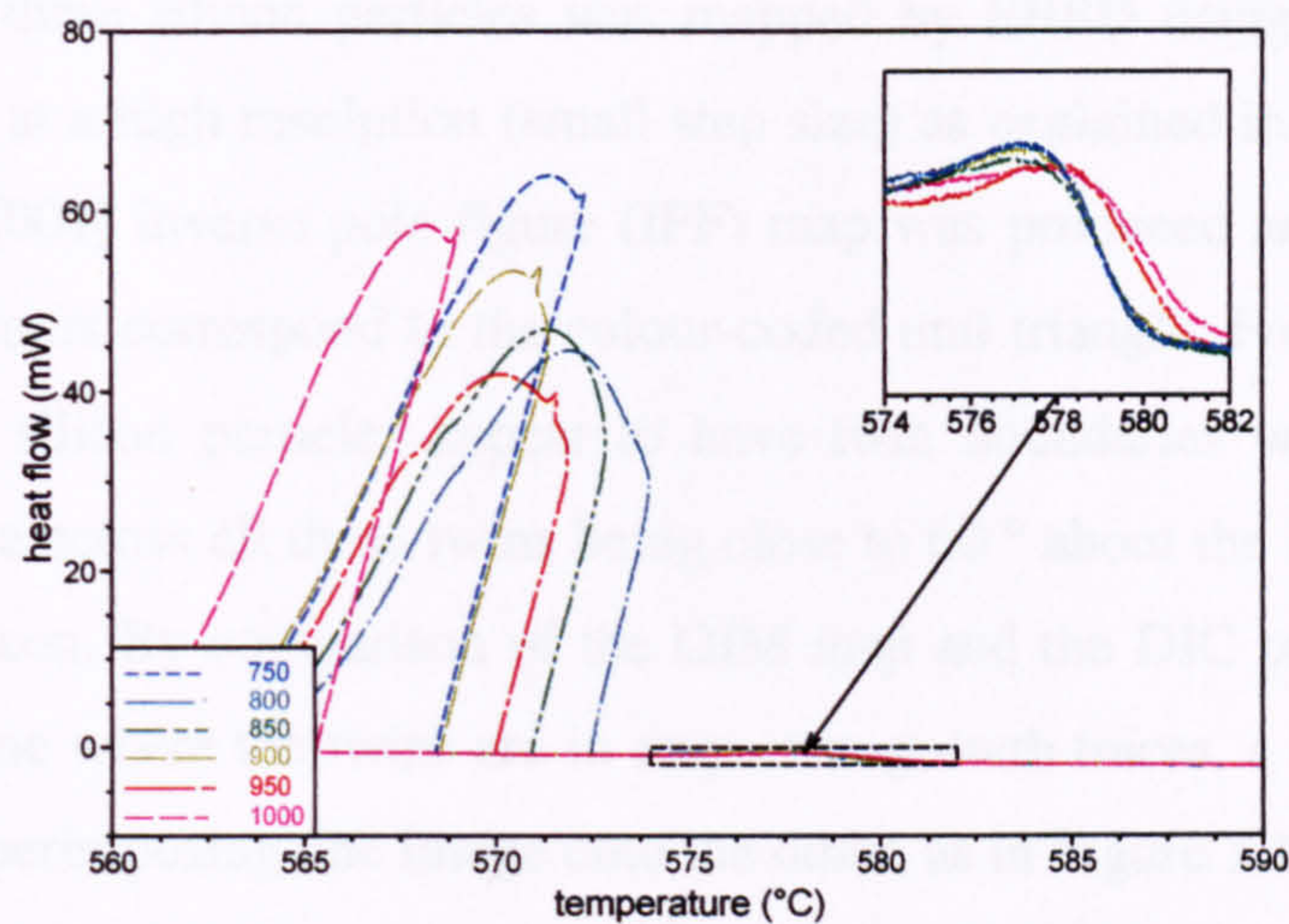


Figure 7.10 DSC curves showing the effect of cooling from progressively higher temperatures for stepped mould model alloy 3/2

The rate of solidification is known ^[Bar02] to also have an effect on the effectiveness of the ALP nucleant. If the cooling rate is high, the nucleation action of the ALP will be ineffective and nucleation will occur on any surface in the melt. On the other hand, if the cooling rate is too slow, the ALP particles can agglomerate together in the melt and not be effective nuclei. This is an area for further investigation.

7.3 Silicon Growth

To try and establish the mechanism of growth of silicon particles, several samples were analysed using electron backscatter diffraction in the SEM. The samples were first prepared by grinding to 1200 grit, polishing to 6 µm diamond, and finally polishing to 0.06 µm colloidal silica on a Bhueler Vibromet. The polishing times were kept to a minimum to avoid relief of the phases, however, on viewing the microstructure in the SEM, growth markings were clearly seen as relief in many silicon particles. Subsequent optical microscopy used the differential interference contrast (DIC) technique to emphasize the striations, and a resultant micrograph be seen in Figure 7.11. The concentric striations can be seen in all three silicon particles running in patterns parallel to the edge facets, undoubtedly the {111} as this is the densely packed cleavage plane in the diamond cubic structure as was described in Chapter 3.

The same area of three silicon particles was mapped by EBSD using orientation imaging microscopy (OIM) at a high resolution (small step size) as explained in Chapter 4. From the data collected, an [001] inverse pole figure (IPF) map was produced and is given in Figure 7.12, where the colours correspond to the colour-coded unit triangle. From the map it can be seen that all three silicon particles appear to have twin boundaries within them, with the misorientation angle across all these twins being close to 60° about the $\{111\}$, as is expected for twinning in silicon. By comparison of the OIM map and the DIC picture it is just about possible to determine where the twins are in respect to growth traces, a relationship which is made clearer by superimposing one image onto the other, as in Figure 7.13.

In each of the three silicon particles a single twin can be seen to dissect the crystal, close to the centre where AIP nuclei are visible. It appears that the twin plane reentrant (TPRE) mechanism plays no part in the continuous growth of these silicon particles, which is in agreement with the literature where a minimum of two parallel twins must be present to promote the TPRE mechanism of growth. Indeed it is clear from both the polyhedral morphology of the particles and the growth markings on them that growth was controlled by surface nucleation on the $\{111\}$ planes which is slower than that at the re-entrant edges and controlled by layer deposition involving step propagation across the liquid-solid interface. This is in agreement with the literature, which explains the presence of the growth spirals as a result of segregation to the base of the each layer forming striations parallel to the $\{111\}$ plane, and revealed by etching.

Considering the silicon particles individually, each has been drawn schematically by tracing the outlines of the optical image (Figure 7.11), and are shown in Figure 7.14. It is interesting to note the re-entrant edge and corresponding ridge in particle 2 (Figure 7.14 b), which have angles of 225° and 146° respectively, are close to those detailed in the earlier schematic of a twinned 'spinel' crystal (Figure 3.10). This is consistent with findings by Wang^[Wan95], where octahedral crystals were found to be frequently modified by the presence of twins. Indeed, referring back to the image in Figure 7.13, it is possible to see that the growth traces appear to change direction slightly as they pass over the twin boundary. Particles 1 and 3 (Figures 7.14 a) and c)), on the other hand, both appear to have two parallel twin boundaries, indicating the existence of the TPRE mechanism at an early stage of growth with a change in growth mechanism occurring resulting in the polyhedral crystal shapes seen.

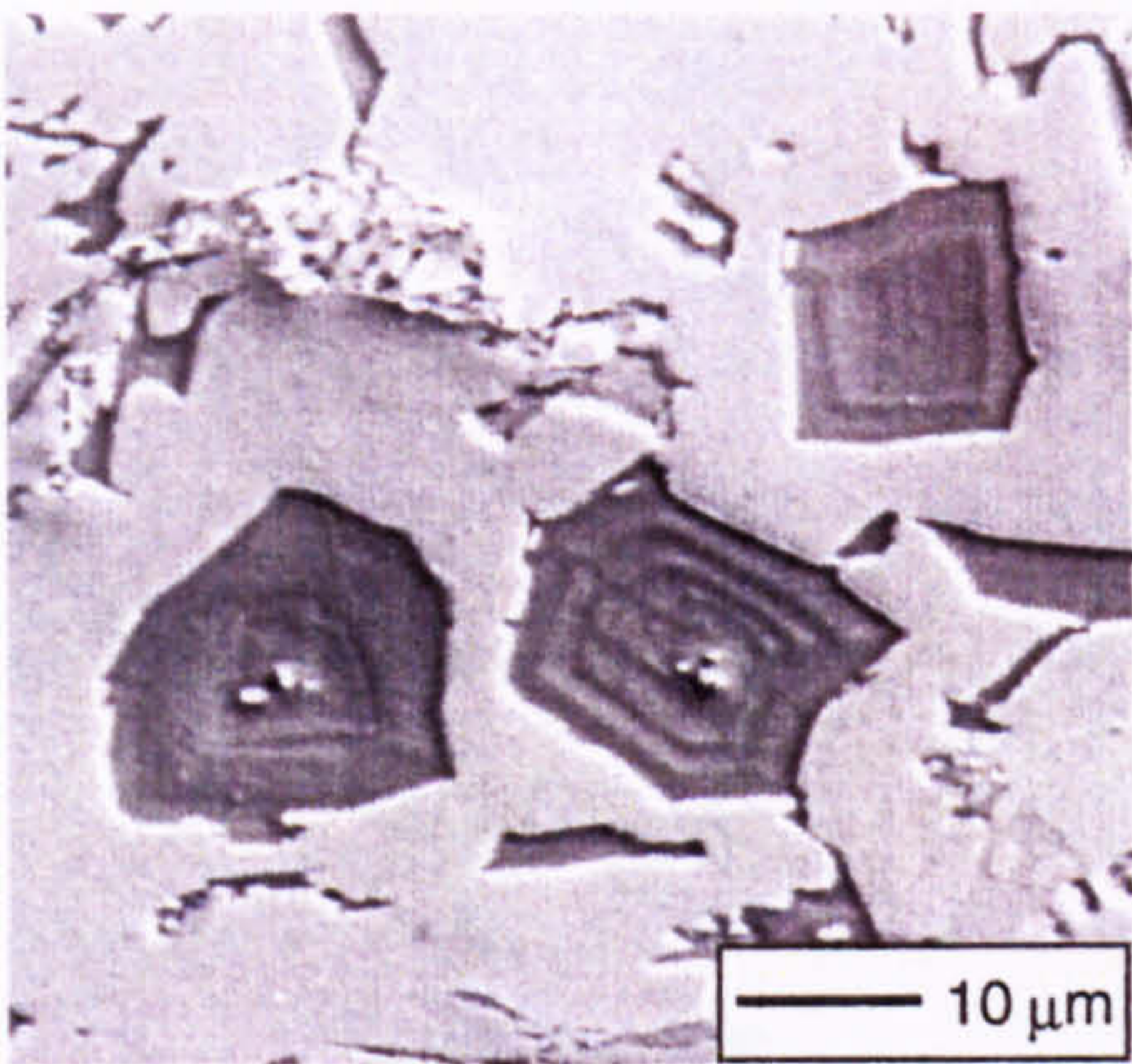


Figure 7.11 Optical micrograph of silicon particles taken using differential interference contrast mode

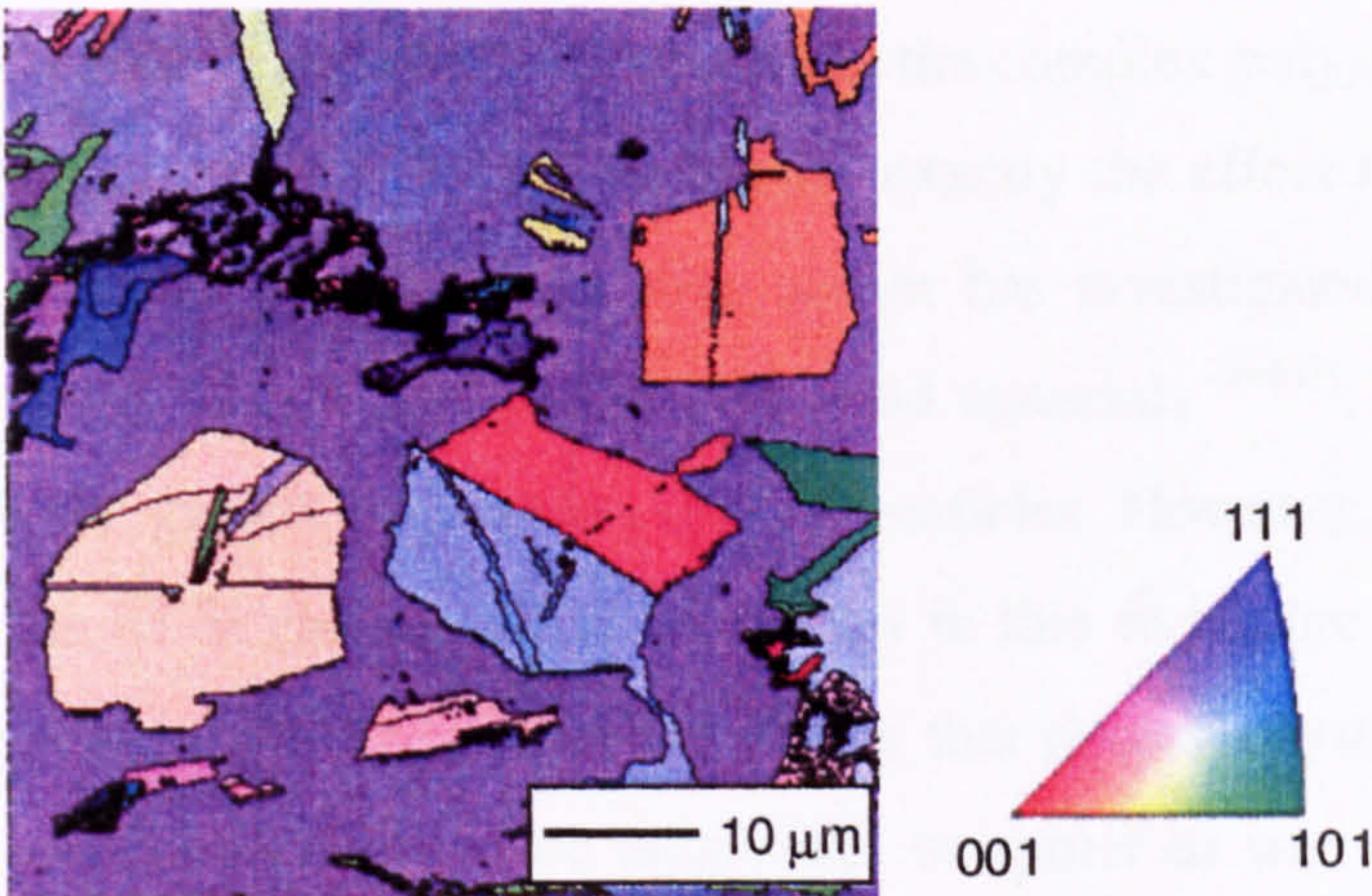


Figure 7.12 [001] inverse pole figure map from OIM with corresponding colour coded unit triangles for silicon

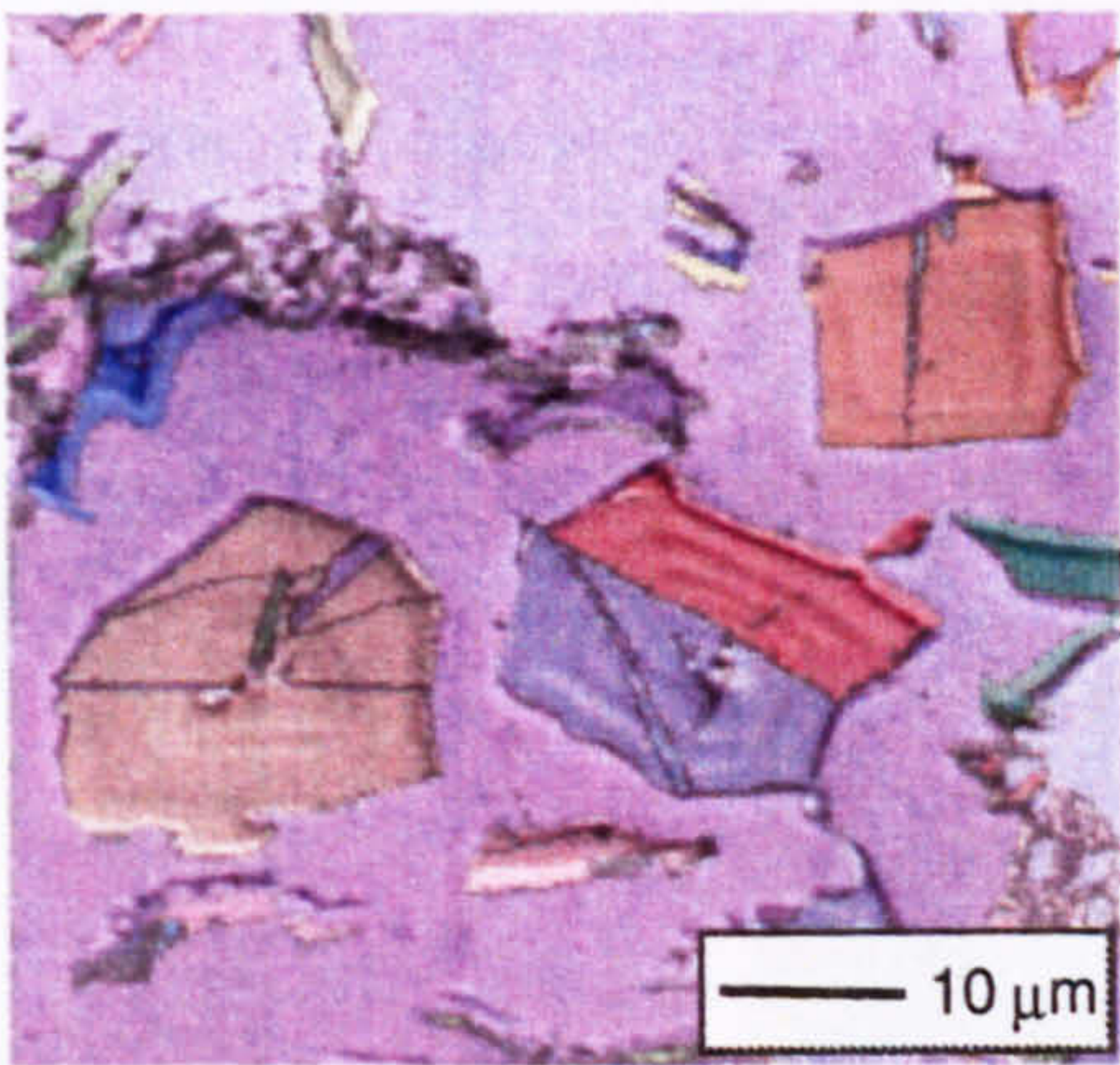


Figure 7.13 OIM IPF map (Figure 7.7) superimposed onto the DIC optical micrograph (Figure 7.6)

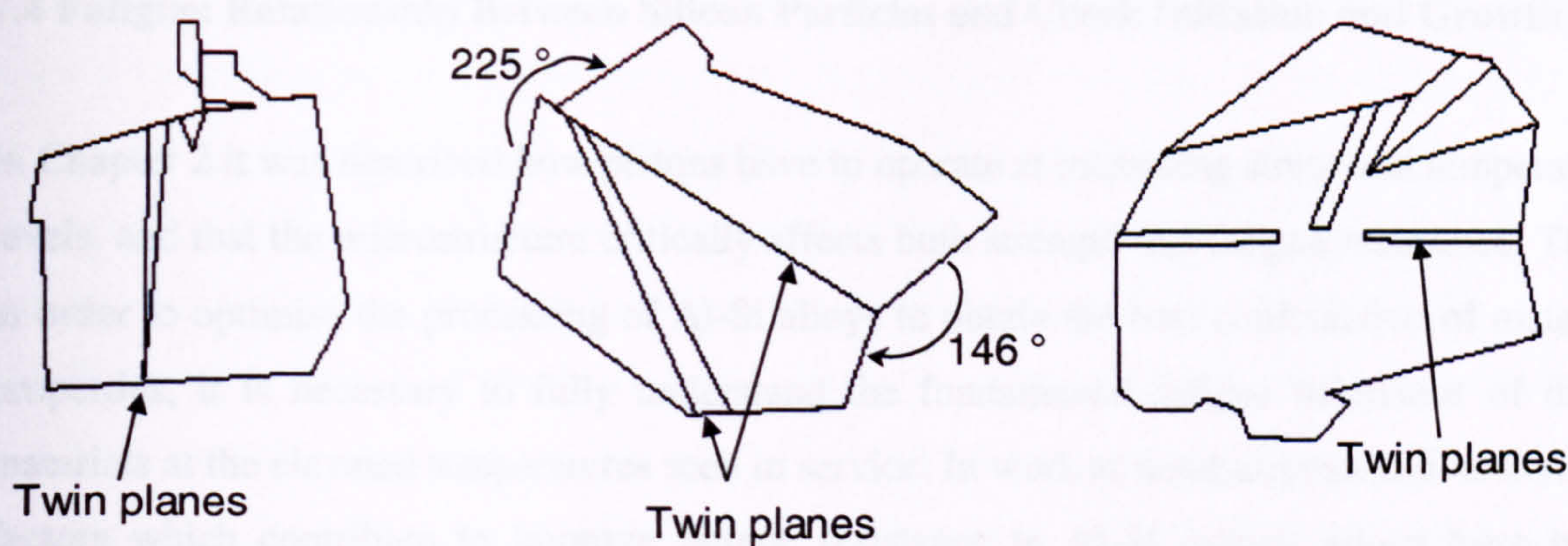


Figure 7.14 Schematic representation of the three twinned particles in Figure 7.11

Although the primary silicon is widely reported with respect to the complex polygonal shapes, as yet no work has been published using EBSD to determine exactly the effect twinning has on the crystal morphology of silicon in cast alloys. One author has investigated the growth mechanisms of five-fold branched silicon particles in laser clad materials ^[Pei01], and through EBSD has been able to prove the growth mechanism in such particles. However, the primary silicon particles common in the Al-Si casting alloys of interest in this work, are generally in the form of cuboids or hexagons, in agreement with the theory that normal crystal growth of the diamond cubic structure of silicon tends to be octahedral or spinel as was explained in Section 3.3. Sectioning of an octahedral at random angles gives rise to the various crystal shapes observed, including hexagonal and twinned (Figure 7.11), as well as the polyhedral which tend to be clusters of several crystals (Figures 7.15 and 7.16).

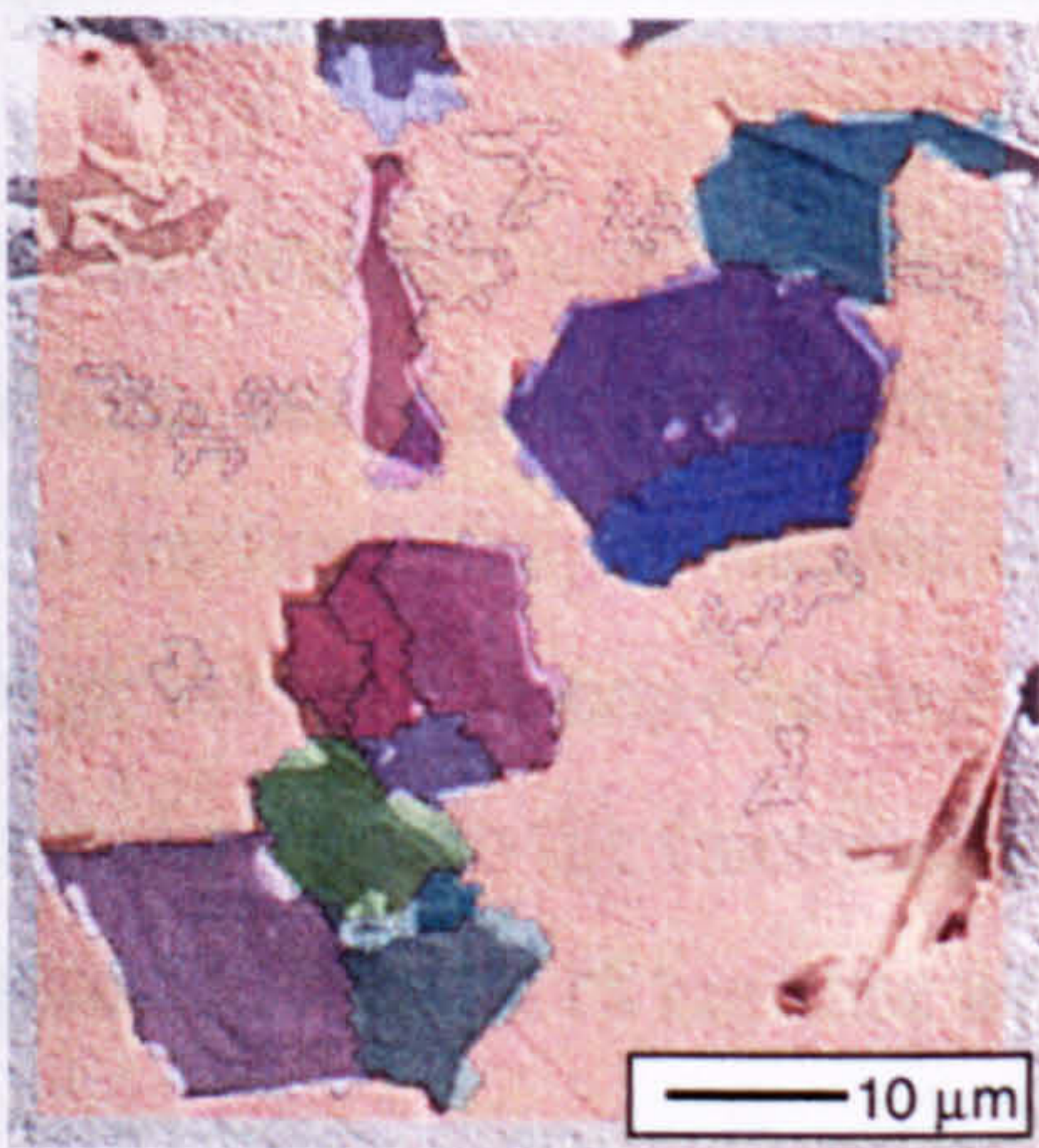


Figure 7.15

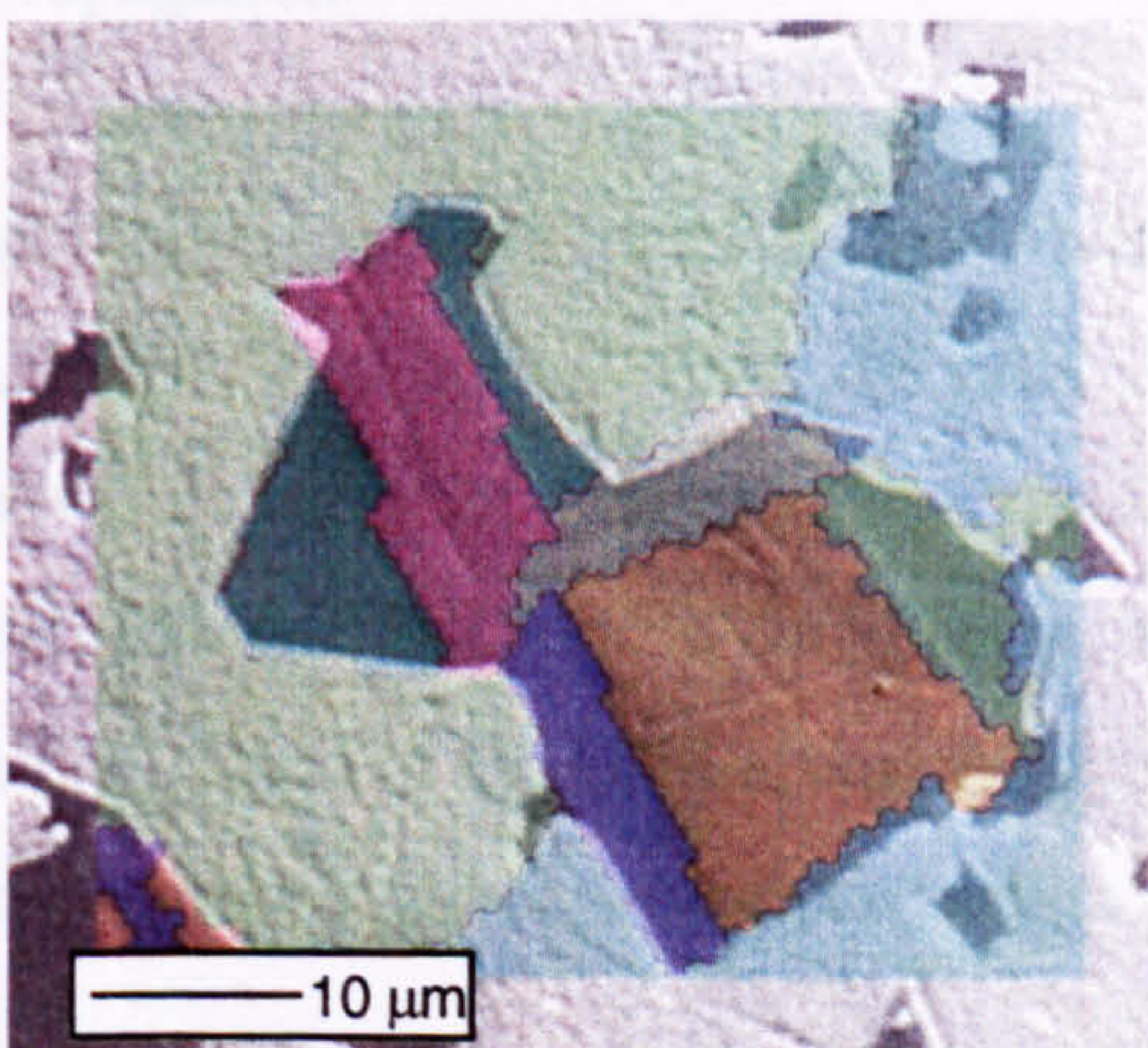


Figure 7.16

Figures 7.15 and 7.16 OIM inverse pole figure maps super-imposed onto
DIC optical micrographs of silicon particles

7.4 Fatigue: Relationship Between Silicon Particles and Crack Initiation and Growth

In Chapter 2 it was described how pistons have to operate at increasing stress and temperature levels, and that the microstructure critically affects both strength and fatigue resistance. Thus, in order to optimise the processing of Al-Si alloys to obtain the best combination of material properties, it is necessary to fully understand the fundamental fatigue behaviour of these materials at the elevated temperatures seen in service. In work at Southampton University, the factors which contribute to improve fatigue resistance in Al-Si casting alloys have been assessed to establish the fatigue initiating microstructural features as well as those contributing to crack growth.

Short crack fatigue tests were carried out to study the initiation and early growth behaviour of fatigue cracks. Plain bend bars, approximately $12 \times 12 \times 10$ mm in dimension, were machined from the crown of an AE413 small piston casting (composition in Table 4.1). The surface of the sample was prepared by polishing to 0.25 μm diamond, and was not etched. The test was performed at a frequency of 15 Hz at room temperature. It was found ^[Joy02] that initiation behaviour at room temperature is generally associated with cracking or debonding of primary silicon particles, and occasionally at clusters of intermetallics. There was no indication of a particle shape dependency, although the cracked or debonded silicon particles did appear larger than the background population. Furthermore, primary silicon was also found to be important in fatigue crack propagation with it appearing to be sought out by the propagating fatigue cracks. Again, the failure was seen to be due to both Si fracture, leading to fast propagation, and Si decohesion, resulting in slow propagation.

To try and establish any correlation between morphology, twinning, or crystal orientation in Si particles and crack propagation through them, EBSD and optical analyses were carried using a fractured fatigue sample as described above, courtesy of Southampton University. Although the main fracture surface could not be analysed by EBSD due to the roughness of it, microcracks close to the fractured surface were studied. Two of the OIM scans are presented in Figures 7.17 and 7.18 together with the optical micrographs and superimposed images.

In Figure 7.17, two silicon particles can be seen to have microcracks across them, although the cracks do not extend outside the silicon and must, therefore, have originated within the silicon crystal. One of the particles has a very large AIP 'hole' in the centre, from which it

appears to be grow. It is likely that the presence of the AlP nucleant in the centre of the crystal creates a stress concentration, which then acts as a point of weakness during fatigue testing and initiates the microcrack seen. The crack can then be observed to grow along the twin boundaries on either side, indicating that under certain conditions the twin boundary will provide a weak path for crack propagation. A similar effect is seen in Figure 7.18, where again the crack is seen to initiate at the void, albeit apparently filled with Al, in the centre of the silicon particle. However, in this case the crack does not propagate along the twin boundary, as it does not intersect with the hole in the centre. Instead, the crack grows away from the centre in both directions parallel to the twin. The second microcrack in Figure 7.17 b) also appears to travel straight across the silicon particle, however, the superimposed image in Figure 7.17 c) shows that, in fact, the crack changes direction slightly as it passes through the twin boundary.

This indicates that when aligned with the crack growth direction, the twin plane will provide a weak path for further propagation. However, if the twin plane is not in line with the crack, propagation will occur straight along the crystal plane closest to the direction of the applied stress. The twin plane appears then to act as a boundary, across which the crack will change direction to continue travelling along the crystal plane

7.5 Summary

Through EBSD it has been possible to identify both nucleation and growth mechanisms of primary silicon particles in an Al-Si casting. Having characterized the AlP phase in detail in Chapter 5, from which a material file was created, the crystallographic data was used in this work to ascertain that the nucleant at the centre of many of the silicon particles was indeed AlP. By considering the Euler angles of the AlP and its silicon particle, it was also possible to confirm that the silicon grows epitaxially on the AlP. The growth mechanisms were then examined through EBSD mapping and optical analysis. Nearly all the silicon particles studied contained at least one twin boundary which is believed to influence the initial stages of growth, and modify the shape of the crystal during further growth. However, the TPPE mechanism does not appear to be operative in the primary silicon in these alloys.

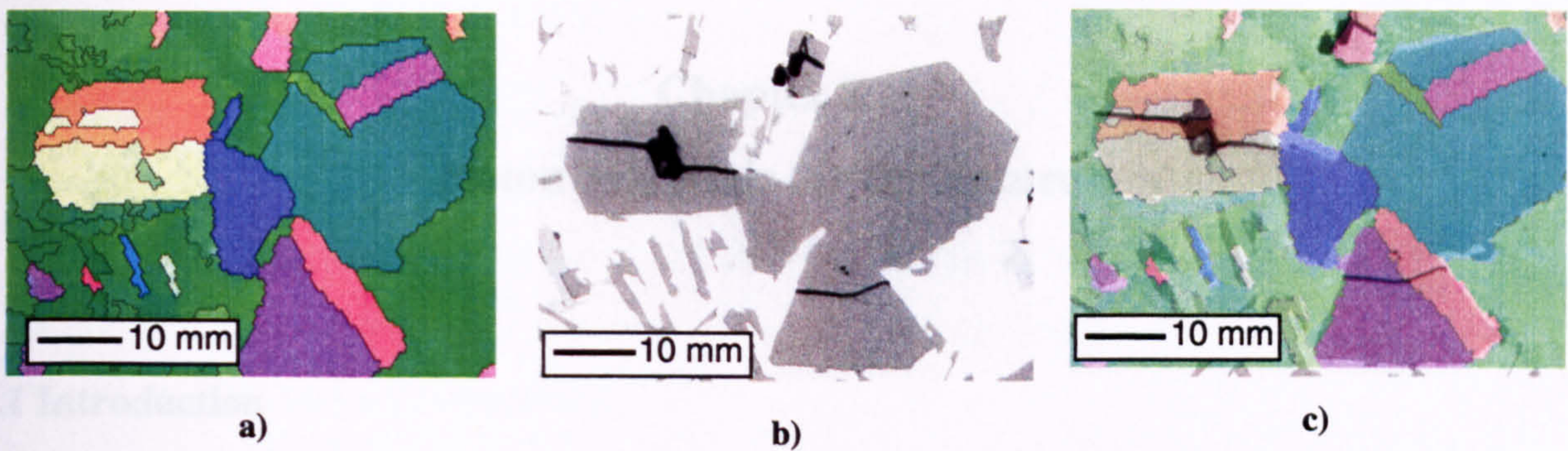


Figure 7.17 a) OIM IPF map, b) optical micrograph, and c) superimposed images, of a silicon particle containing a microcrack after fatigue testing

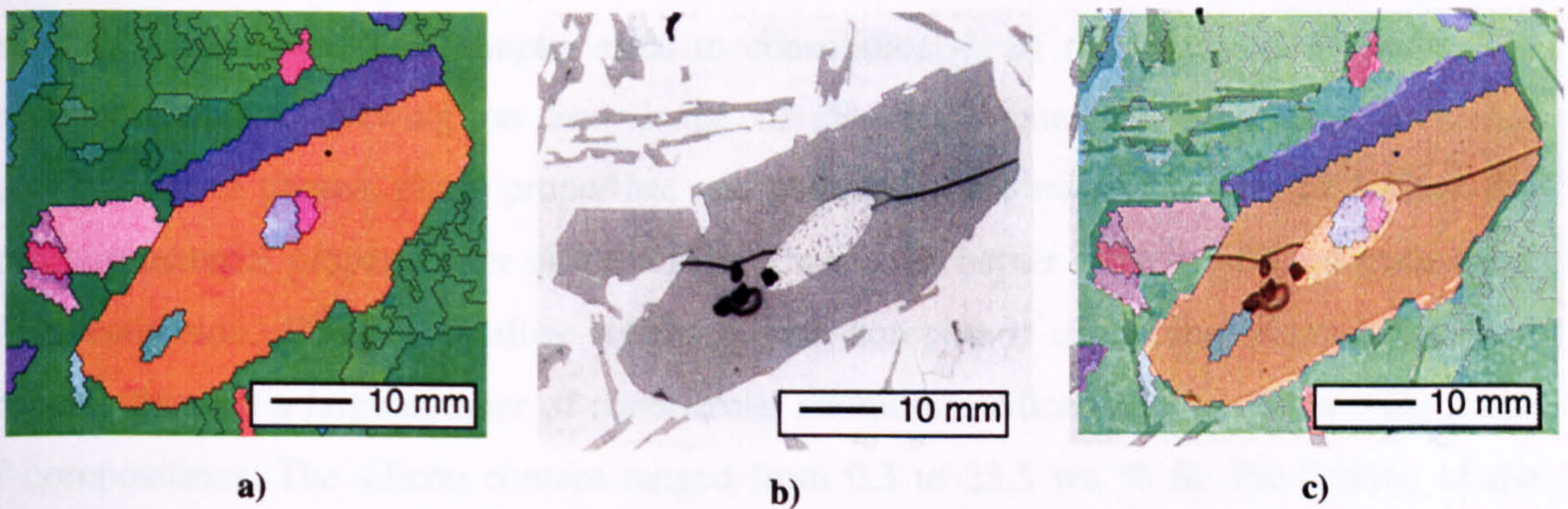


Figure 7.18 a) OIM IPF map, b) optical micrograph, and c) superimposed images, of a silicon particle containing a microcrack after fatigue testing

EBSD carried out on a fatigued sample concentrated on the relationship between the primary silicon particles and crack initiation and growth. It was concluded that the AIP hole in the centre of many of the silicon particles appears to act as a stress concentration point, often leading to initiation of microcracks during fatigue testing. However, the subsequent propagation of the crack appeared to follow the direction of the applied stress, and travelled along crystal planes. Only if a twin plane was aligned with the direction of stress did it appear to provide a weak path for crack growth. Thus, EBSD has been proven to be a novel and relatively simple technique to use for determining nucleation and growth mechanisms in silicon particles.

Chapter 8

Piston Materials for the Future

8.1 Introduction

The development of existing commercial alloys is essential in industry in order to improve in-production pistons whilst utilising existing plant investments and minimising capital outlay to keep the costs down. This chapter aims to consolidate all of the information obtained in previous chapters, drawing on knowledge of desired mechanical properties, elemental contributions to phases, phase properties, and controlling the microstructure, to achieve the optimum material properties for piston alloys. Thus, this chapter consists of three main areas of investigation. Firstly, an alloy database was composed, containing composition and property data for a large number of commercial aluminium-silicon alloys, with a wide range of compositions. The silicon content ranged from 0.3 to 23.5 wt. % Si. Predictions of the phases present have been made and are then linked to specific properties and trends identified. Secondly, with an awareness of the effect of phases on the properties of an Al-Si casting alloy, thermodynamic phase predictions of systematic additions of the major alloying elements Si, Cu, Ni, Fe and Mn to an existing piston alloy are considered. Finally, an elemental database investigating basic properties of existing and potential alloying elements is discussed, and suggestions made for new generation alloy compositions.

8.2 Alloy Database

An extensive database was compiled containing compositions, mechanical and physical property data for a large number of commercial aluminium alloys. Using the alloy compositions, thermodynamic phase predictions were calculated using Al-Data³ from which it was possible to relate the expected phases to alloy properties. The full database is given in Appendix G.

8.2.1 Mechanical Properties

From the database, plots were drawn to illustrate the effect of predicted mass fraction of phases (log scale) on the hardness, room temperature ultimate tensile strength, and endurance limit of the Al-Si alloys contained in the database. A line of best fit was determined using a simple linear regression, and has been added to indicate trends. The graphs are given in Figures 8.1, 8.2 and 8.3 respectively.

It was discussed in Chapter 2 that pure aluminium has a low tensile strength which decreases with increasing temperature, and furthermore, has little resistance to wear and scores easily. Certain elements can be alloyed with aluminium to improve the properties, in particular, Si is added to increase the wear resistance by formation as primary silicon. Cu, Ni, Mg and Mn are also added to form hard intermetallic phases which not only increase the strength over the large operating temperature range, but also increase the resistance to wear. In Figure 8.1, the hardness can be seen as a function of fraction of phases. As expected, the hardness is predicted to increase with decreasing amounts of the aluminium, and increasing fractions of all the secondary phases. Most evident are the silicon phase and the θ (Al_2Cu). The silicon, as discussed, is added primarily to increase the wear resistance of the Al alloy, however, the increased fraction of θ (Al_2Cu) appears also has a significant effect on the hardness. This is believed to be a result of the formation of fine precipitates in the matrix, as was discussed in Section 6.3, which are known to be partly responsible for strengthening in commercial Al-Si alloys. However, in Figure 8.2 showing tensile strength as a function of mass fraction of phases, it can be seen that θ (Al_2Cu) is predicted to result in a slight decrease in the room temperature ultimate tensile strength of the alloy, contrary to experimental findings. In fact, the changes in strength appear not to be as affected by the presence of secondary phases as the other properties considered here; silicon appears to be the only phase to actually improve the room temperature strength with increasing mass fraction.

Figure 8.3 shows the endurance limit as a function of mass fraction of phases, where again it can be seen that the silicon and θ (Al_2Cu) phases greatly affect the material properties. The endurance limit, also referred to as the fatigue limit, is the maximum stress amplitude level below which a material can endure an essentially infinite number of stress cycles and not fail. As silicon increases and θ (Al_2Cu) decreases the endurance limit is predicted to increase. However, it is important to remember that these data consider only material properties,

whereas the mechanical properties of a cast component will additionally depend on temperature, component geometry, and soundness of casting etc. For example, the geometry of a piston casting is relatively complex and provides many points for stress concentration, as do the inhomogeneities and imperfections, such as porosity, on a microscopic scale. These stress concentrations then act as points of weakness for premature failure. It should be noted here that changes in chemical composition can also bring about changes in casting characteristics, for example freezing range, which in turn can affect macroscopic properties through their influence on melt feeding and solidification rates.

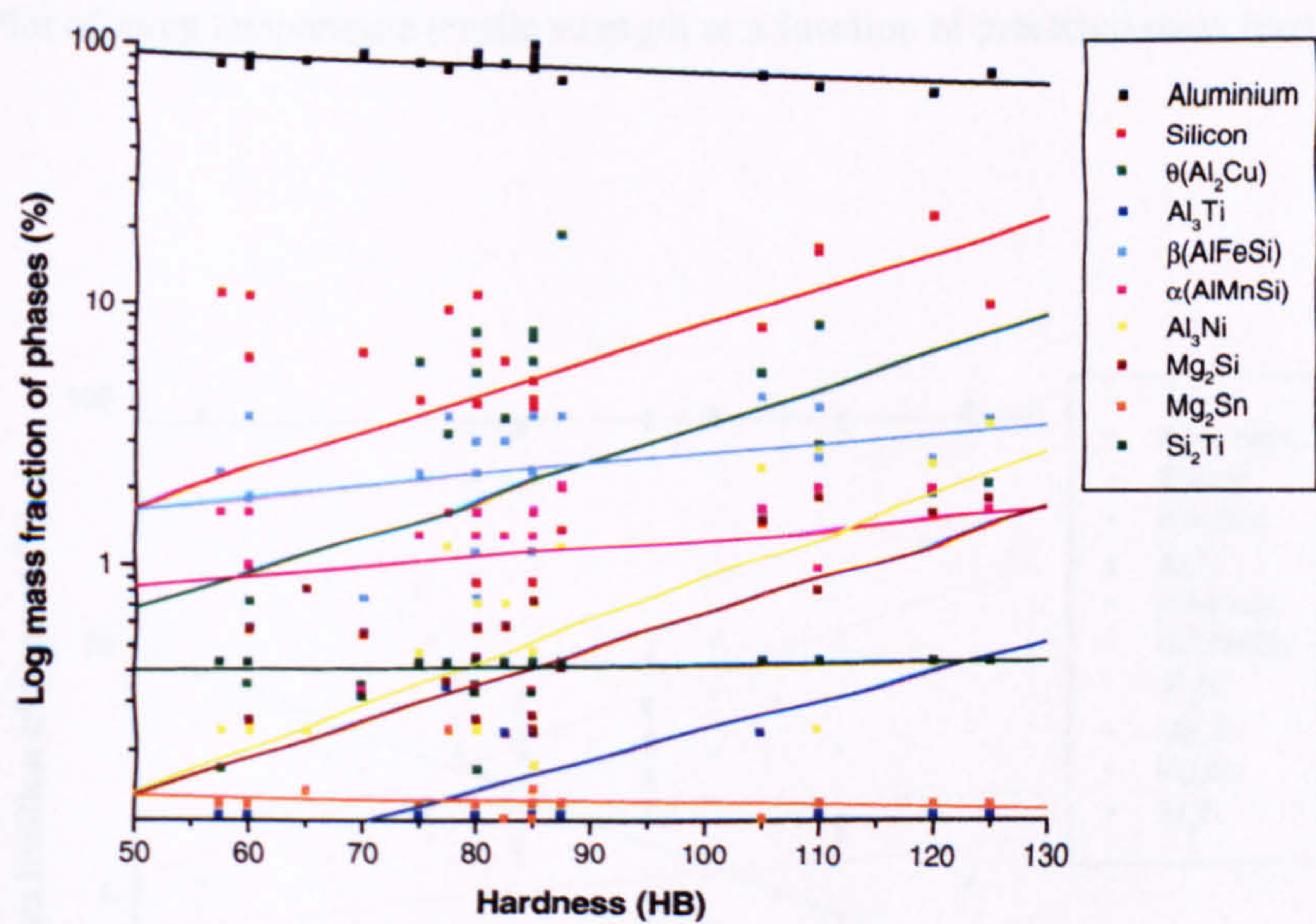


Figure 8.1 Plot of hardness as a function of predicted mass fraction of phases

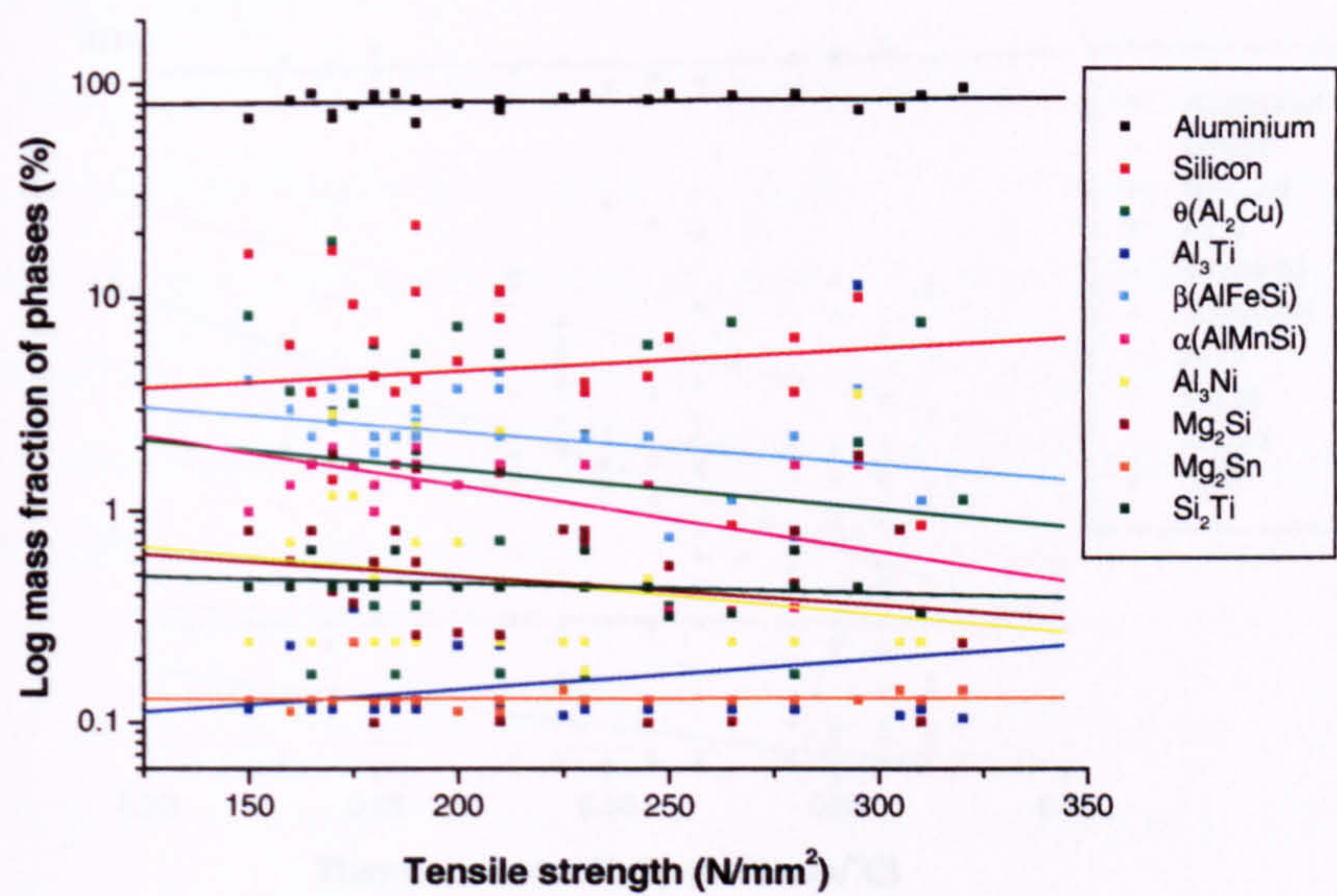


Figure 8.2 Plot of room temperature tensile strength as a function of predicted mass fraction of phases

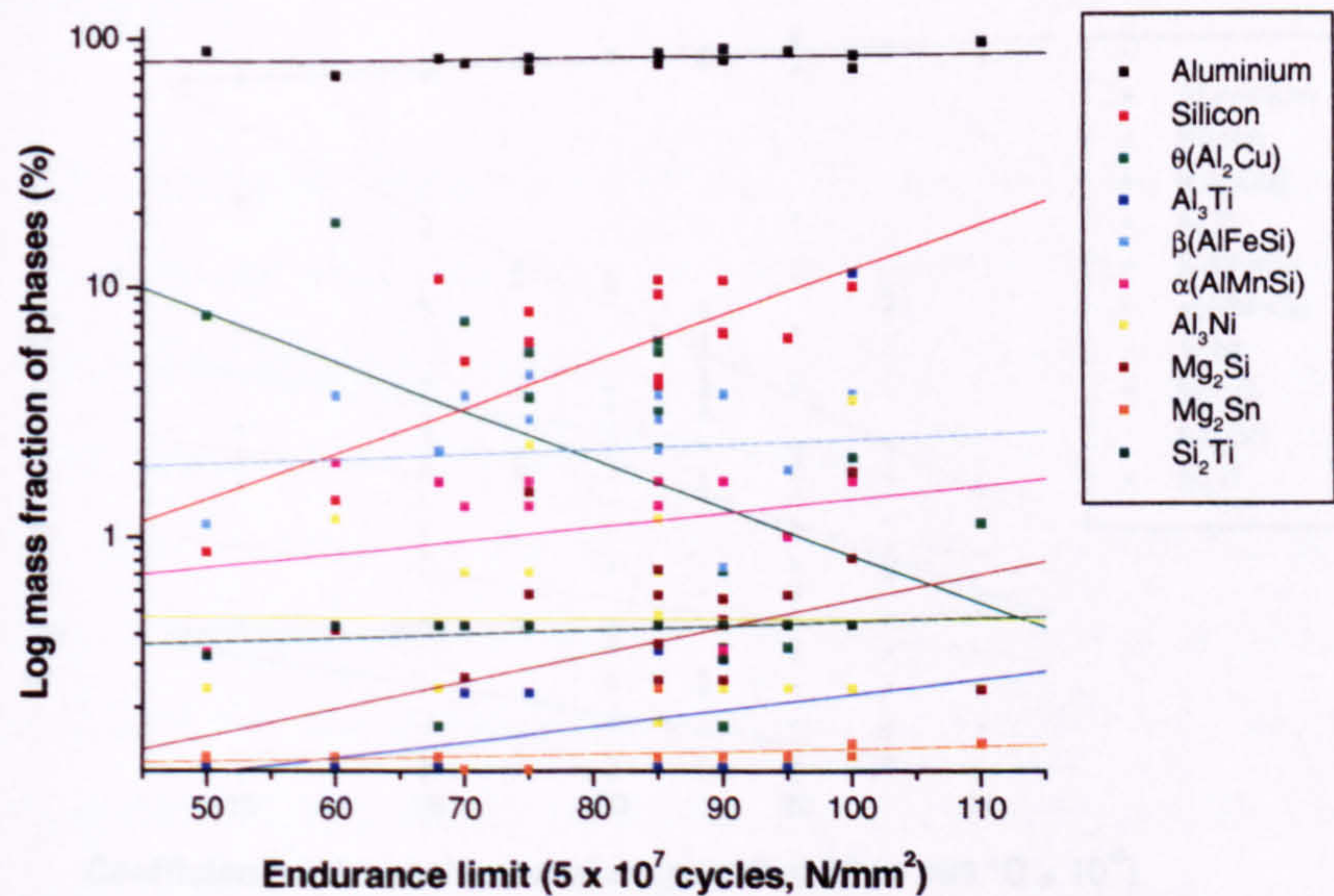


Figure 8.3 Plot of endurance limit as a function of predicted mass fraction of phases

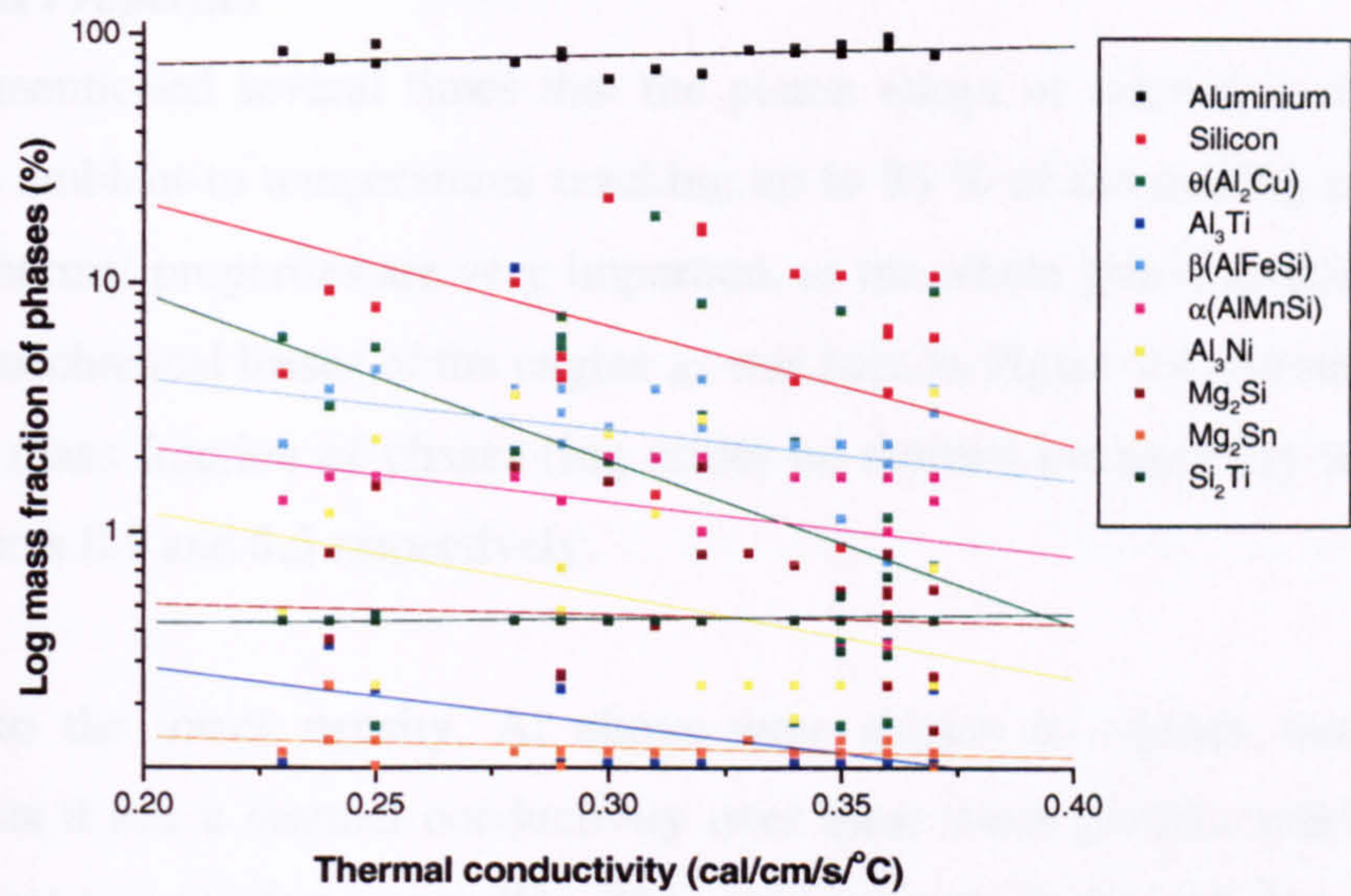


Figure 8.4 Plot of thermal conductivity as a function of mass fraction of phases

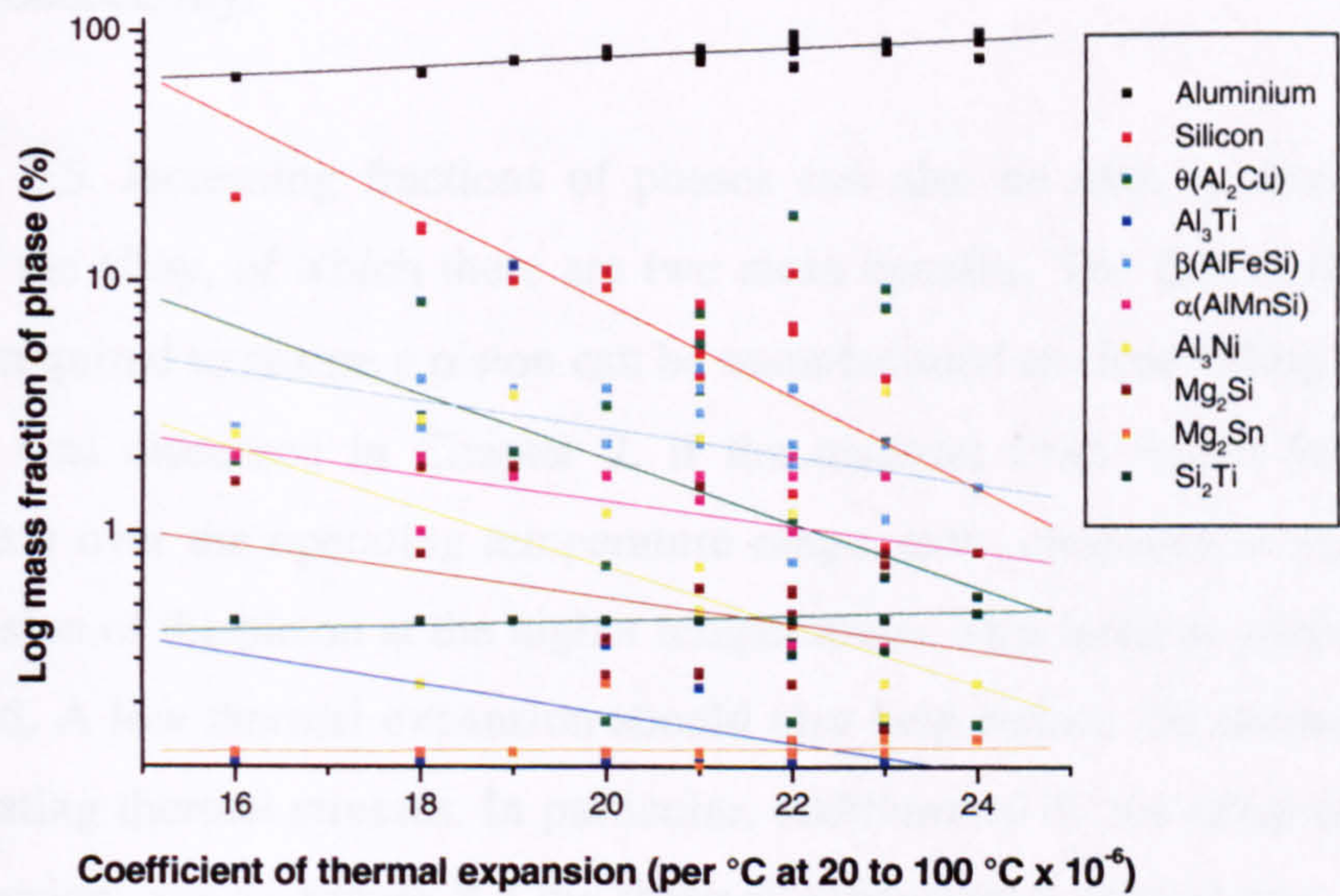


Figure 8.5 Plot of thermal expansion as a function of mass fraction of phases

8.2.2 Physical Properties

It has been mentioned several times that the piston alloys of interest in this work have to operate from ambient to temperatures reaching up to 85 % of the melting point of the alloy. Indeed, the thermal properties are very important, as the whole piston assembly absorbs 50 to 60 % of the mechanical losses of the engine as was seen in Figure 2.4. As such, plots showing the effect of mass fraction of phases (log scale) on thermal conductivity and expansion are given in Figures 8.4 and 8.5 respectively.

In addition to the lower density, Al alloys were chosen to replace cast iron for piston applications as it has a thermal conductivity over three times greater, making it efficient at conducting heat away as fast as possible. This means that there is a reduction in the maximum operating temperature of the piston, although the piston crown can still reach temperatures in excess of 450 °C in diesel engine pistons. The thermal conductivity is plotted in Figure 8.4 against mass fraction of phases, and can be seen to decrease with increasing secondary phases. This is expected as pure aluminium is a good conductor and any additions to this will decrease its conductivity.

From Figure 8.5, increasing fractions of phases can also be seen to decrease the thermal expansion of the alloy, of which there are two main benefits. The first is that a low thermal expansion is required to ensure a piston can be manufactured as close fitting to the cylinder as possible. As was discussed in Chapter 2, if the material from which the piston is made expands greatly over the operating temperature range, extra clearance is required to account for the expansion of the piston at the higher temperatures. This leads to piston ‘slap’ when the engine is cold. A low thermal expansion should also help reduce the thermal fatigue caused by the fluctuating thermal stresses. In particular, additions of Ni are often made to lower the thermal expansion, and in Figure 8.5 the thermal expansion is indeed seen to decrease with lower fractions of the Ni containing phase, Al_3Ni , although this trend is characteristic of all the secondary phases.

8.3 Thermodynamic Phase Predictions

This investigation used equilibrium thermodynamic calculations to predict the effect of systematic additions of the major alloying elements, Cu, Fe, Mn, Ni and Si (individually), to the phases predicted in commercial piston alloy FMS2N. The base composition of FMS2N was used, see Table 8.1, with the alloying additions modelled at a range of amounts based on the commercial content; for example, Cu is simulated to be added at 1 % increments between 2.5 and 6.5 wt.% Cu.

Table 8.1 Base composition of commercial alloy FMS2N (Wt. %)

Al	Si	Cu	Ni	Mg	Fe	Mn	Ti	Zr	V
Bal.	12.3	3.6	2.5	1.0	0.5	0.2	0.05	0.16	0.08

From the resulting data two types of graphs were produced in this case. Firstly, a phase stability plot was drawn for the base alloy, FMS2N, to show changes in predicted mass fraction of phases with respect to temperature at equilibrium (Figure 8.6). Secondly, phase stability data at 500 K for each of the additions were collated, from which plots of phase stability as a function of elemental content were produced (Figures 8.7 to 8.10). It should be noted that a number of other useful parameters could be obtained by such calculations, e.g. freezing range, however the focus of this section is the effect of alloy composition on the phases present. Therefore, this should enable a complete understanding of the effect alloying additions have on properties through the formation of intermetallic phases.

8.3.1 FMS2N

Calculations were performed for FMS2N (composition in Table 8.1) as a basis for comparison with subsequent results after differing amounts of Cu, Fe, Mn, Ni and Si additions had been made. The resultant phase stability plot can be seen in Figure 8.6. In addition to the aluminium and silicon, the equilibrium simulation predicted six intermetallic phases to form, namely $\text{Al}_3(\text{Cu,Ni})_2$, α (AlMnFeSi), λ ($\text{Al}_5\text{Cu}_2\text{Mg}_8\text{Si}_6$), $\text{Al}_7\text{Cu}_4\text{Ni}$, Al_9FeNi , and Al_3Ti . The fractions of these phases at 500 K are given in Table 8.2.

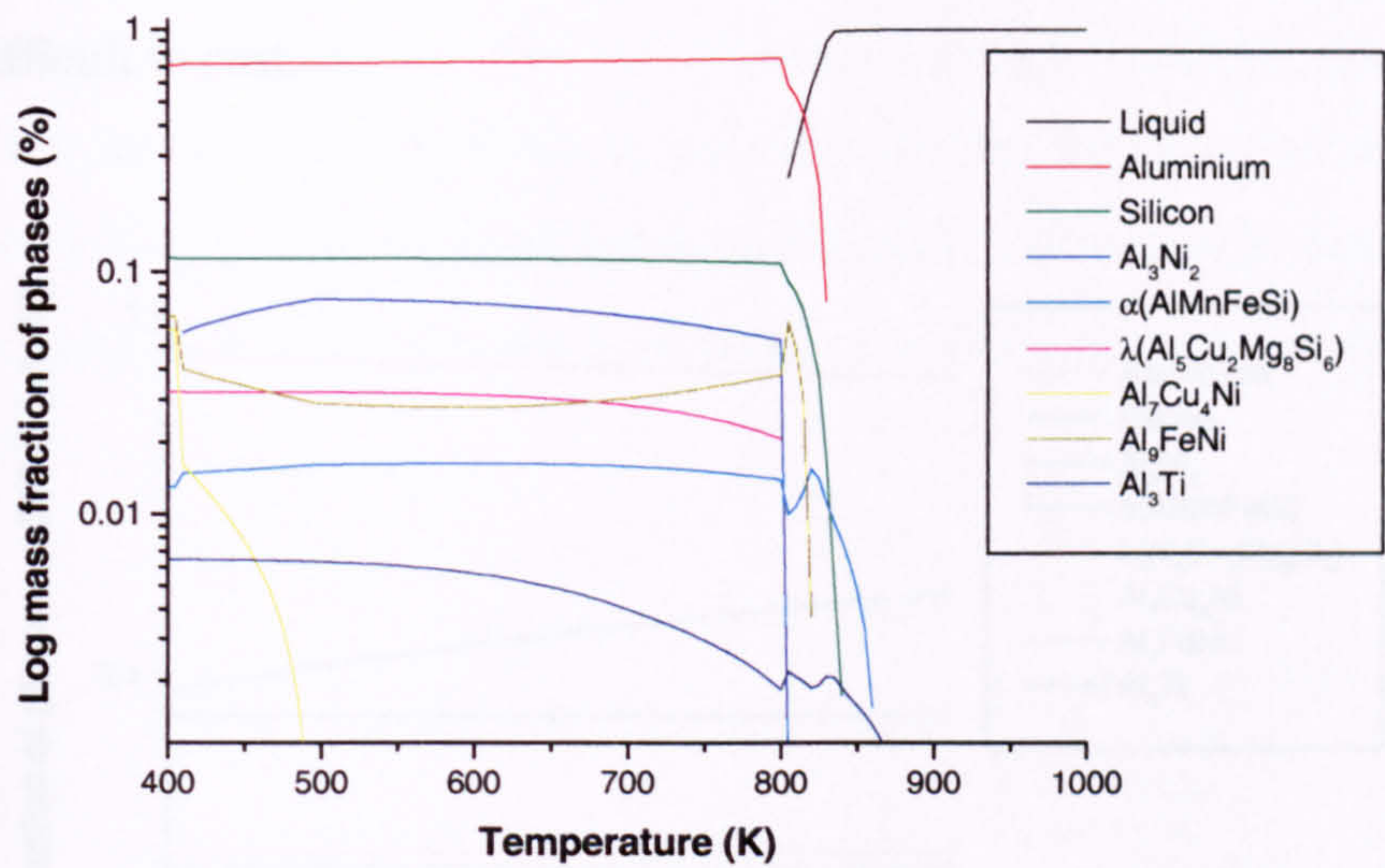


Figure 8.6 Phase stability plot for FMS2N

Table 8.2 Predicted mass fraction of phases in FMS2N at 500 K

Al	Si	Al ₃ (Cu,Ni) ₂	α (AlFeMnSi)	λ (Al ₅ Cu ₂ Mg ₈ Si ₆)	Al ₉ FeNi	Al ₃ Ti
72.71	11.29	7.71	1.58	3.20	2.88	0.63

8.3.2 Addition of Silicon

The addition of Si is typically carried out at near-eutectic levels (~ 12 wt. %) to impart wear resistance and fluidity to the aluminium. As was seen in Section 8.2, increasing the fraction of the silicon phase tends to have positive effects on the mechanical properties and a reduction in thermal expansion, although the thermal conductivity is also greatly reduced. The silicon phase has been observed and predicted (Section 5.3.2) to be predominantly Si, with most of the Si additions being soluble in this phase. This is supported by the graph in Figure 8.7 of mass fraction of phases (log scale) as a function of increasing Si content from 10 to 18 wt. %, which shows the silicon phase to form at a higher fraction with increasing Si additions. Thus, it would appear from these findings that higher additions of Si will form more silicon phase, and produce an alloy with improved properties. However, the casting of high silicon alloys becomes complex as the solidification temperature of hypereutectic composition alloys

changes according to the phase diagram in Figure 3.9, to an extent that the alloys become increasingly difficult to cast.

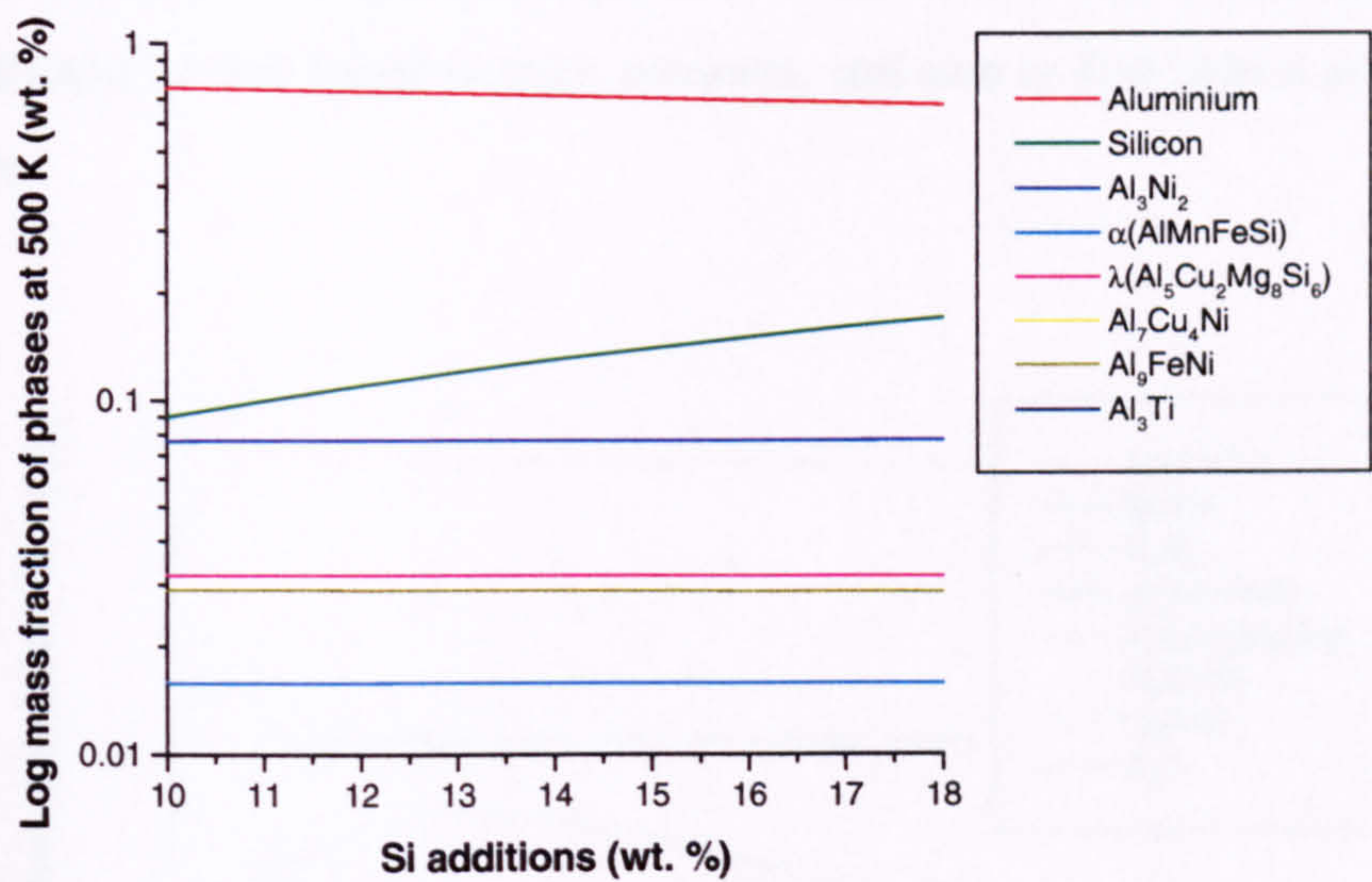


Figure 8.7 Fraction of phases predicted at 500 K as a function of Si content

8.3.3 Addition of Copper

FMS2N contains 3.6 wt.% Cu, and so for the purpose of investigating the effect of Cu additions, calculations were made with 1.0 wt.% additions between 2.5 and 6.5 wt.% Cu. Cu is added to Al-Si alloys to form intermetallic phases and improve the material properties. Of particular interest is the phase θ (Al₂Cu) which was discussed in Section 5.3.5 as requiring at least 5.7 wt. % Cu to form, although it was observed experimentally in alloys containing around 3 wt. % Cu. This phase is particularly desirable when it forms as fine matrix precipitates which are believed to be partly responsible for strengthening the alloy. However, in Section 8.2 it was shown that the θ (Al₂Cu) (and other intermetallics) appear to in fact decrease the tensile strength with increasing fraction of phases, although it is noted that there is significant scatter in the data, possibly due to the sizes of particles present in the different alloying additions.

The thermodynamic predictions, on the other hand, do not calculate the θ (Al₂Cu) phase to be stable at all in this alloy, forming instead Al₃(Cu,Ni)₂ and Al₇Cu₄Ni. From Figure 8.8 it can be seen that at low additions of less than 4 wt. % Cu, the stability of the Al₃(Cu,Ni)₂ phase is

predicted to increase at the expense of Al_9FeNi , whilst at high additions (> 4 wt. %) the $\text{Al}_3(\text{Cu,Ni})_2$ becomes less stable as $\text{Al}_7\text{Cu}_4\text{Ni}$ forms. Although neither of these phases were predicted to form in the commercial alloys contained in the database discussed previously, both were observed in the alloys investigated in Chapter 5 in a greater fraction than the θ (Al_2Cu). The θ (Al_2Cu) was found in trace amounts, and also as fine matrix precipitation after heat treatments.

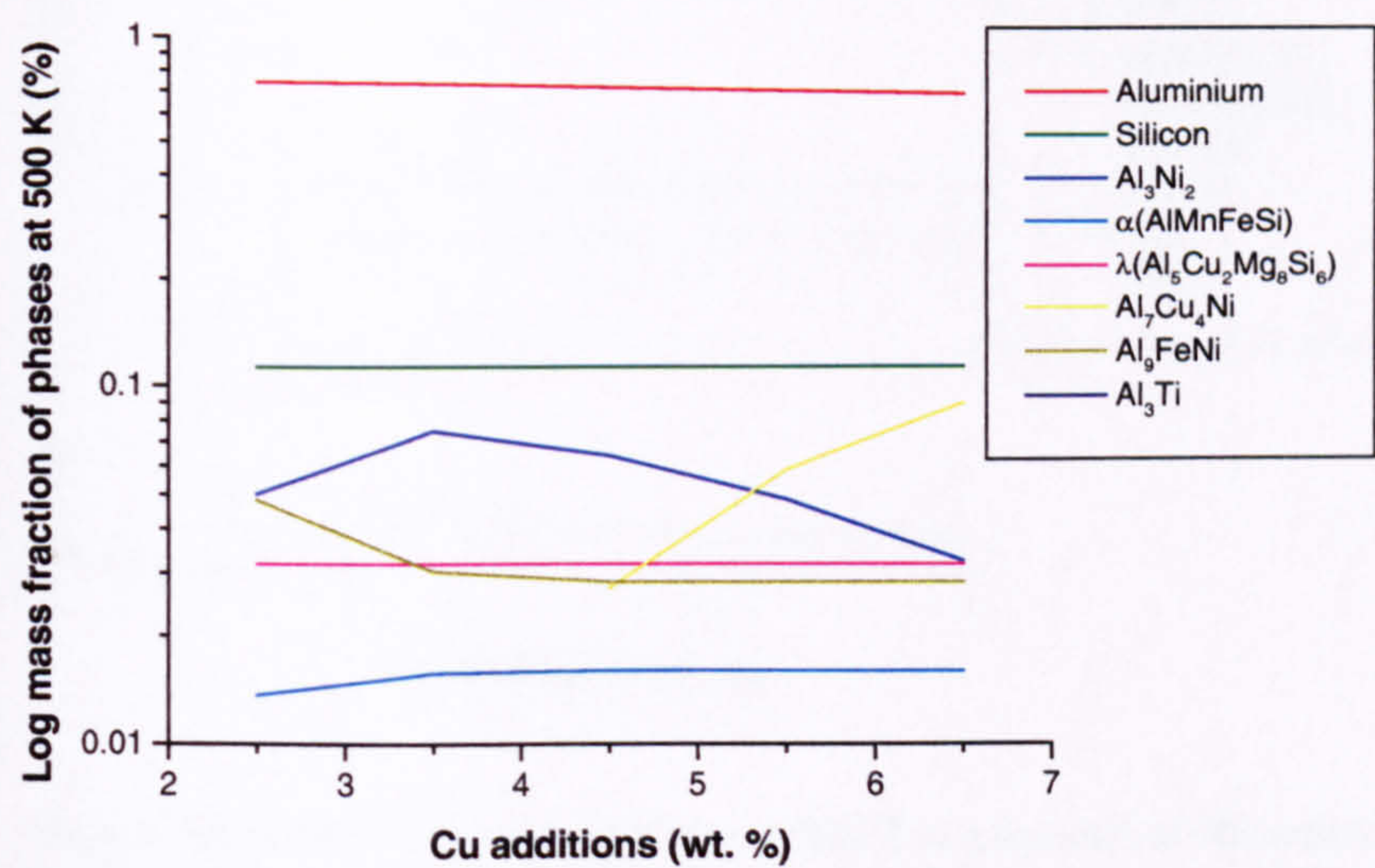


Figure 8.8 Fraction of phases predicted at 500 K as a function of Cu content

8.3.4 Addition of Nickel

Ni is added to Al-Si alloys to promote the formation of intermetallic phases and hence improve the strength and wear characteristics. Commercial addition levels are around 2 to 3 wt. % Ni, and so for the thermodynamic predictions the Ni content was simulated at 2 to 5 wt. % Ni in 1 % intervals. The resultant plot of mass fraction of phases at 500 K is given in Figure 8.9 and shows three phases to be predominantly effected by the Ni content, namely $\text{Al}_3(\text{Cu,Ni})_2$, Al_9FeNi , and Al_3Ni . All were observed in the analysis presented in Chapter 5, and found to contain substantial amounts of Ni. It appears from the graph that initial increases in Ni content up to 2.5 wt. % Ni increases the stability of the $\text{Al}_3(\text{Cu,Ni})_2$ phase, after which the Al_9FeNi phase increases at the expense of the α (AlMnFeSi). At 4.5 wt. % Ni, the phase Al_3Ni forms. Of these Ni containing phases, only Al_3Ni was predicted in the database of commercial alloys, and was found to follow the trends of the majority of intermetallics.

However, Ni is believed to enhance properties at elevated temperatures particularly when combined with Cu. The high temperature effect of the phases contained in the database is not taken into account, and it may therefore be postulated that the increased fraction of phases containing Ni will be beneficial at the operating temperature of the piston.

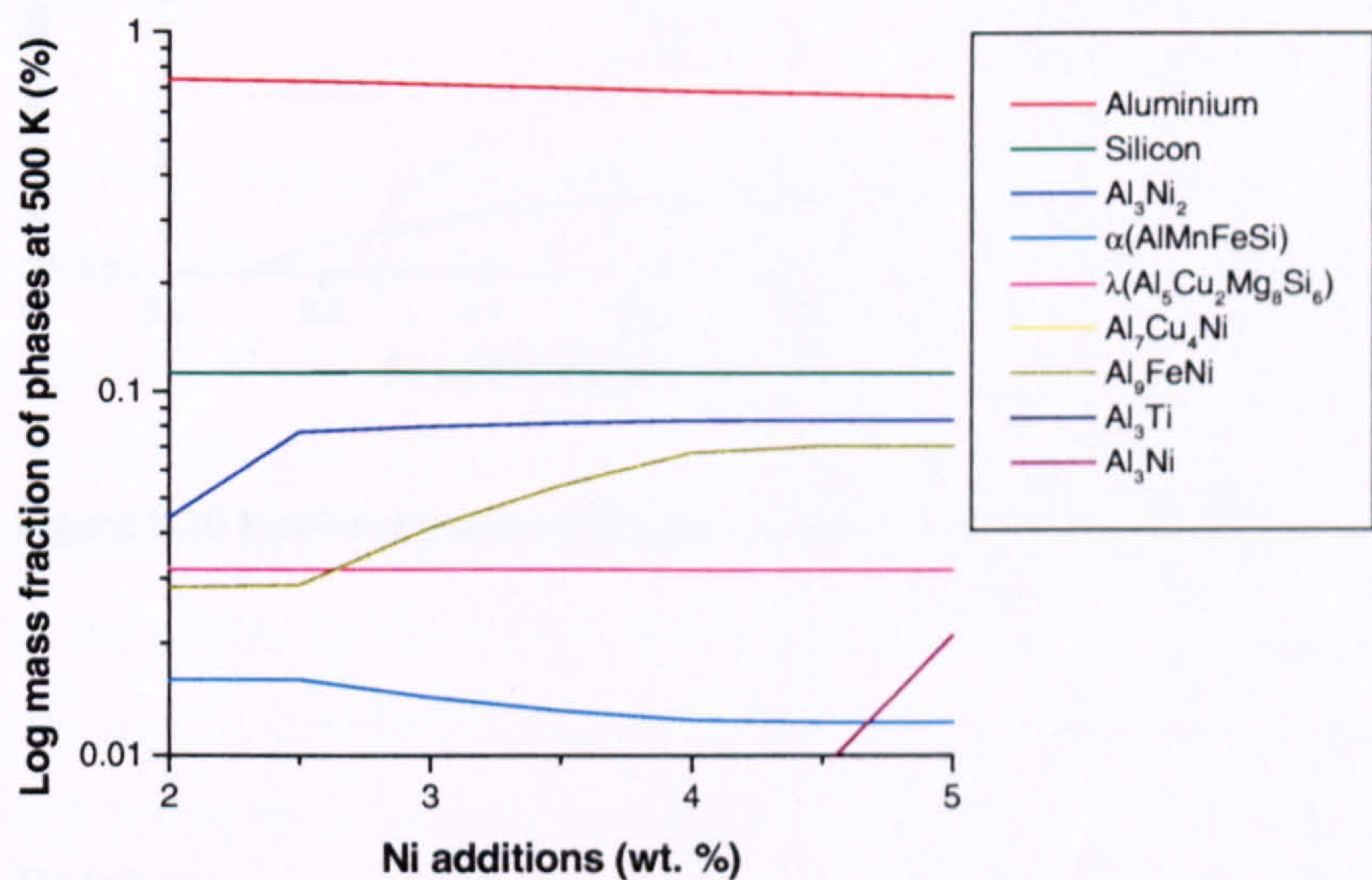


Figure 8.9 Predicted fraction of phases at 500 K as a function of Ni content

8.3.5 Addition of Iron

Fe is believed to improve hot tear resistance and strength at high temperatures, although it is rarely added intentionally to Al-Si casting alloys as high Fe contents severely decrease castability due to the formation of sludge phases, as described in Chapter 2. However, Fe occurs as the main impurity, usually at levels below 0.5 wt. % Fe, and to counteract the detrimental effect of the Fe content additional elements, such as Ni, are added to control intermetallic formation and to some extent rectify the deterioration in castability. Thus, thermodynamic predictions were carried out to investigate the effect on phase formation of increasing Fe additions from 0.1 to 1.0 wt. % Fe. From the plot in Figure 8.10 it can be seen that a small increase in the Fe content has a dramatic effect on the stability of several phases, particularly above 0.5 wt. % Fe. For example, both the Al₉FeNi and α (AlFeMnSi) phases increase in mass fraction with increasing additions, as does Al₇Cu₄Ni above 0.6 wt. % Fe, whilst the Al₃Ni decreases. This supports the theory that the Ni acts as a stabiliser for the Fe containing phases.

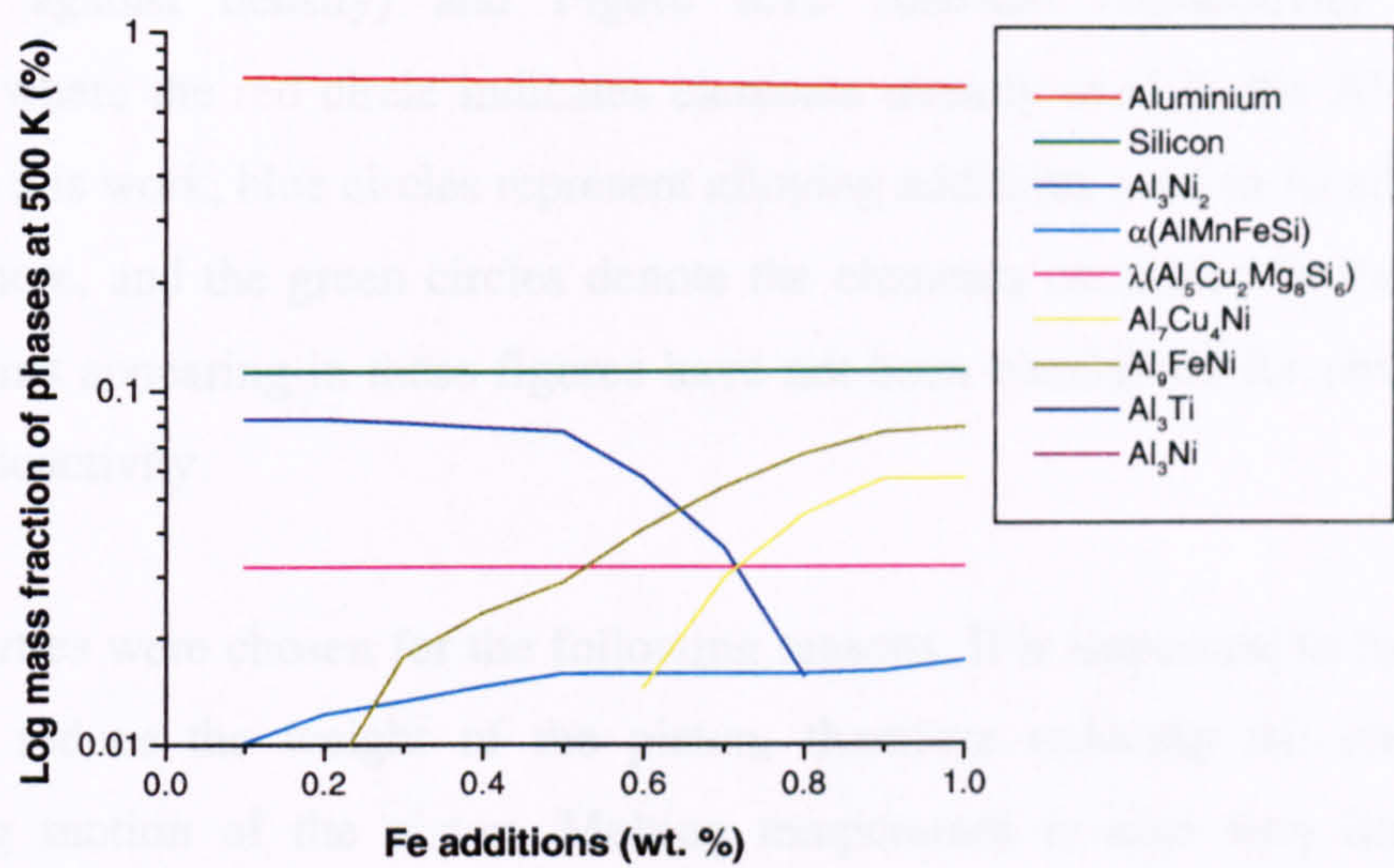


Figure 8.10 Predicted fraction of phases at 500 K as a function of Fe content

8.4 Elemental Database

New alloys would most probably need to be cast by the existing production route, gravity die casting, at least in the short term because introducing a new process would mean huge investment and expense. Therefore, the easiest way to improve the properties of an Al-Si alloy is through increased alloying additions. There are, however, several concerns with increasing the element content. Firstly, additions are expensive, and therefore there must be reasonable justification for their addition. Secondly, some elements added to improve the material properties have a resultant effect in decreasing the castability and fluidity of the alloy. This is particularly important as the castability of the alloys needs to be good, particularly for the intricate piston geometry, to reduce porosity and minimise shrinkage. Imperfections, e.g. porosity, provide stress concentration points which provide points of weakness for mechanical properties such as fatigue.

In order to investigate possible new elements (i.e. those previously not considered) for addition to Al-Si casting alloys, an elemental database was compiled. Data included crystal structures, densities, melting points and physical property data of elements where available. To narrow down the range of elements available, four of the most important physical properties were plotted against one another. The plots are given in Figures 8.11 (melting

temperature against density) and Figure 8.12 (thermal conductivity against thermal expansion), where the red circle indicates elements already used in the Al-Si casting alloys examined in this work, blue circles represent alloying additions used in Al alloys but not those considered here, and the green circles denote the elements examined further in this section. Some elements appearing in these figures have not been considered for obvious reasons, for example radioactivity.

These properties were chosen for the following reasons. It is important to have a low density in order to reduce the weight of the piston, therefore reducing the energy lost in the reciprocating motion of the piston. Melting temperature is also very important as alloy development trends towards higher working environments for pistons. Thermal conductivity is required to permit heat flow away from the piston at the greatest rate, keeping the temperature of the piston, particularly in the crown area, to a minimum. Thermal expansion must be kept as low as possible so that the piston can be cast as close to the net shape as possible without having to account for excessive expansion and contraction; this large change in dimensions due to heat can also lead to thermal fatigue.

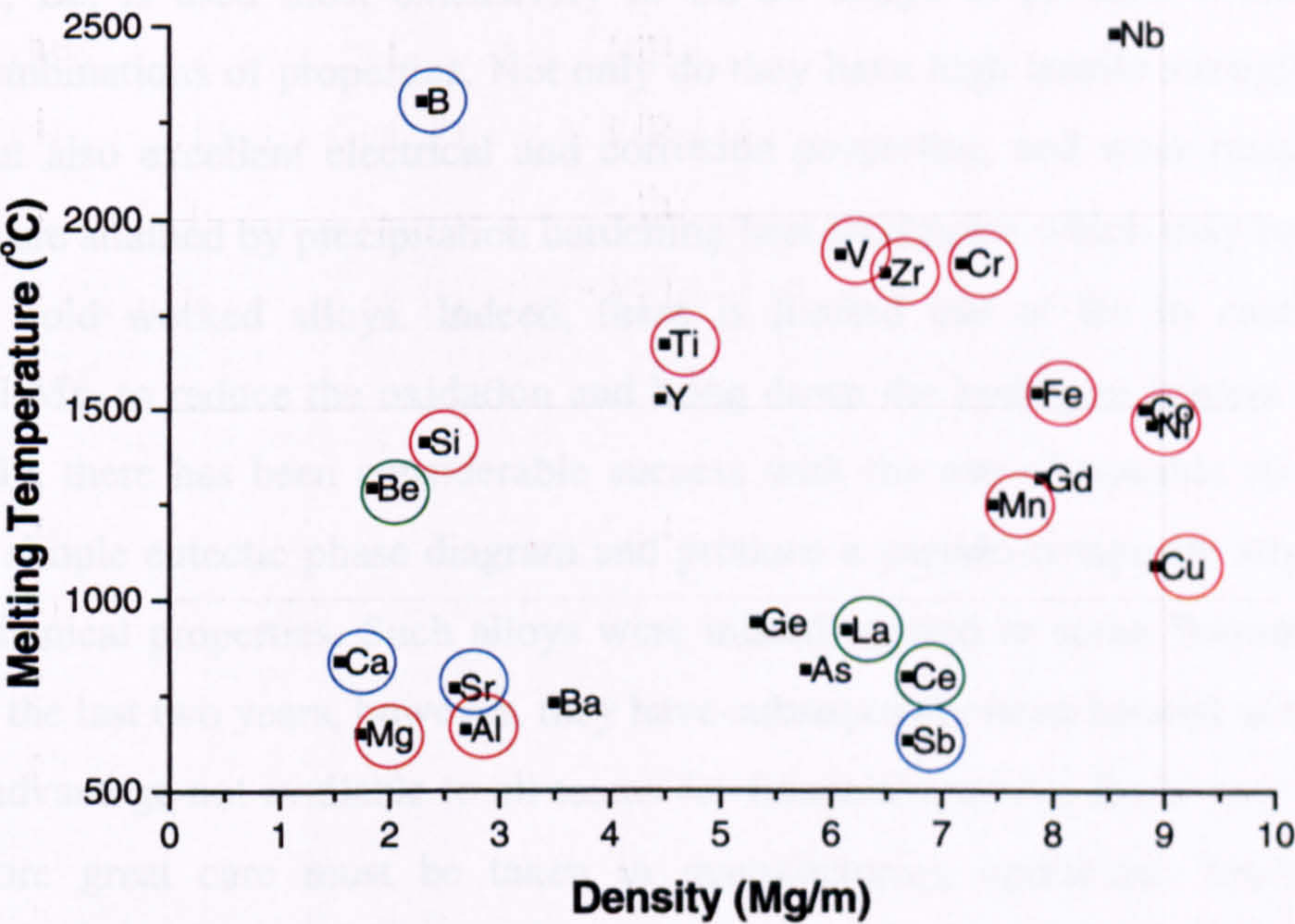


Figure 8.11 Plot of density against melting temperature

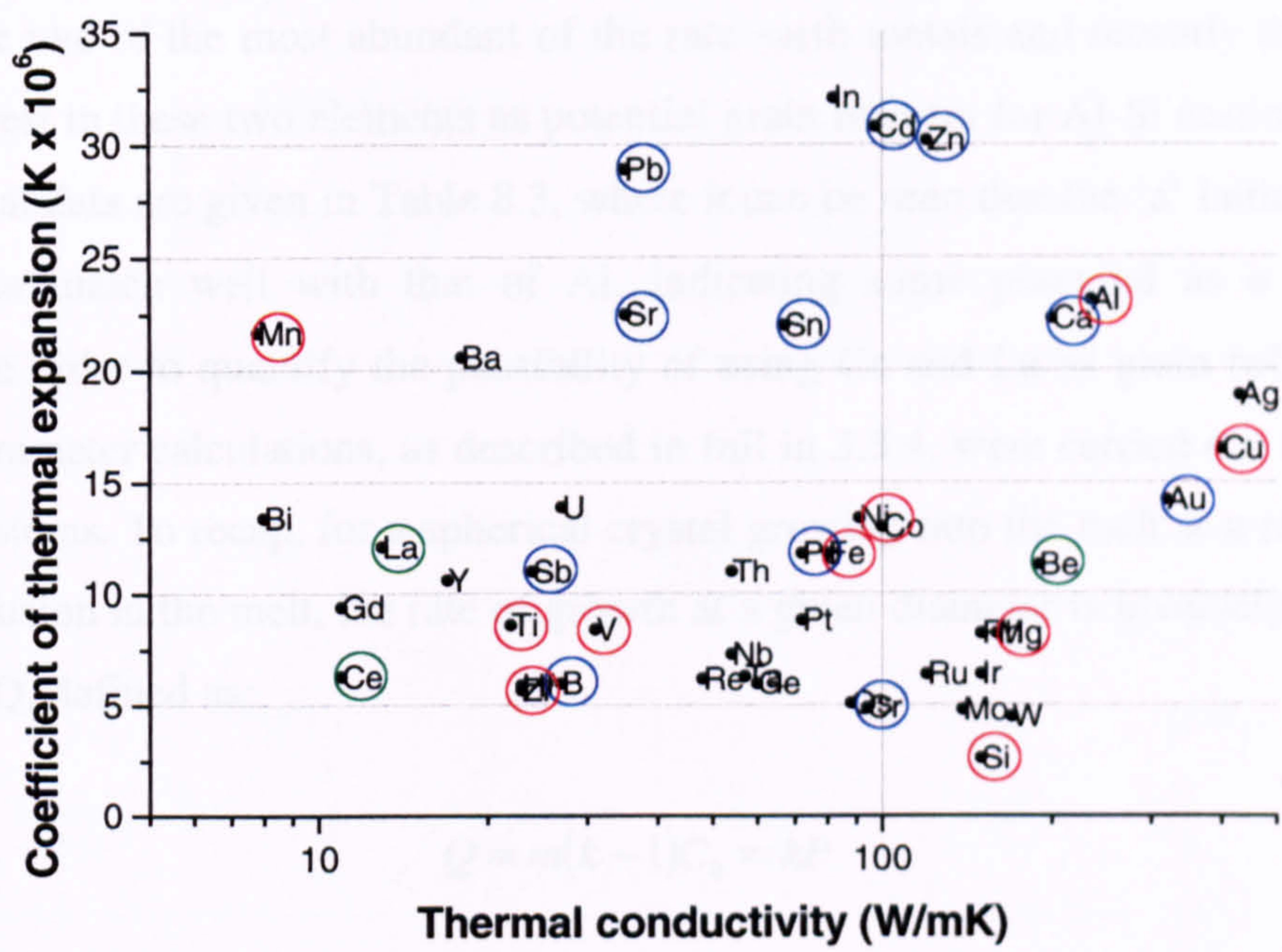


Figure 8.12 Plot of thermal conductivity against thermal expansion

8.4.1 Beryllium

A light metal, Be, is used most extensively in Cu-Be alloys to produce a material with remarkable combinations of properties. Not only do they have high tensile strengths of up to 1400 MPa, but also excellent electrical and corrosion properties, and wear resistance. The high strengths are attained by precipitation hardening heat treatments which may be applied to cast, hot and cold worked alloys. Indeed, there is limited use of Be in casting alloys, particularly Al-Mg, to reduce the oxidation and bring down the hydrogen content of the cast metal. Recently, there has been considerable success with the use of castable Al-Be alloys, which have a simple eutectic phase diagram and produce a pseudo-composite structure with excellent mechanical properties. Such alloys were indeed utilised in some Formula 1 racing car engines in the last two years, however, they have subsequently been banned as they gave a performance advantage not available to all teams for financial reasons. Be is very expensive, and furthermore great care must be taken in manufacturing operations because of the potentially toxic nature of BeO. It is therefore hard to see Be finding extensive use in mass market piston alloys.

8.4.2 Rare Earth Additions

Ce and La are two of the most abundant of the rare earth metals and recently there has been renewed interest in these two elements as potential grain refiners for Al-Si casting alloys. The relevant crystal data are given in Table 8.3, where it can be seen that the 'a' lattice parameters of Ce and La match well with that of Al, indicating some potential as a nucleant for aluminium. In order to quantify the possibility of using Ce and La as grain refiners, growth restriction parameter calculations, as described in full in 3.5.4, were carried out for the Al-Ce and Al-La systems. To recap, for a spherical crystal growing into the melt at a rate controlled by solute diffusion in the melt, the rate of growth at a given diameter is inversely proportional to a quantity Q , defined as:

$$Q = m(k - 1)C_0 = kP$$

where Q (K) is termed the growth restriction parameter, P (K) is the constitutional supercooling parameter, m (K wt.%⁻¹) is the liquidus slope, k is the equilibrium partition coefficient, and C_0 (wt.%) is the solute content in the alloy melt. The equilibrium partition coefficient k , is defined as:

$$k = \frac{C_s}{C_L}$$

where C_s and C_L are the mole fractions of solute in the solid and liquid in equilibrium at a given temperature respectively. The relevant portions of the binary diagrams are presented in Figure 8.13 from which the parameters were taken for the calculations.

The resultant growth restriction parameters were thus calculated to be 0.26 and 0.13 for Ce and La respectively. If these values are compared with those previously derived for grain refining additions of Ti, Zr, and V ($Q = 32.00, 0.80, 3.89$) it can be seen that the effect of Ce and La is expected to be much less. This was confirmed by casting trials at Federal-Mogul in which Ce and La were added to a basic alloy composition. The result was that extremely large amounts of these rare earths would be required to achieve the desired grain refinement.

Table 8.3 Crystal data for Al, Ce and La

Element	Crystal Structure	Lattice parameters (Å)	
		a	c
Al	FCC	0.4049	-
Ce	HCP	0.3081	1.186
La	HCP	0.3774	1.217

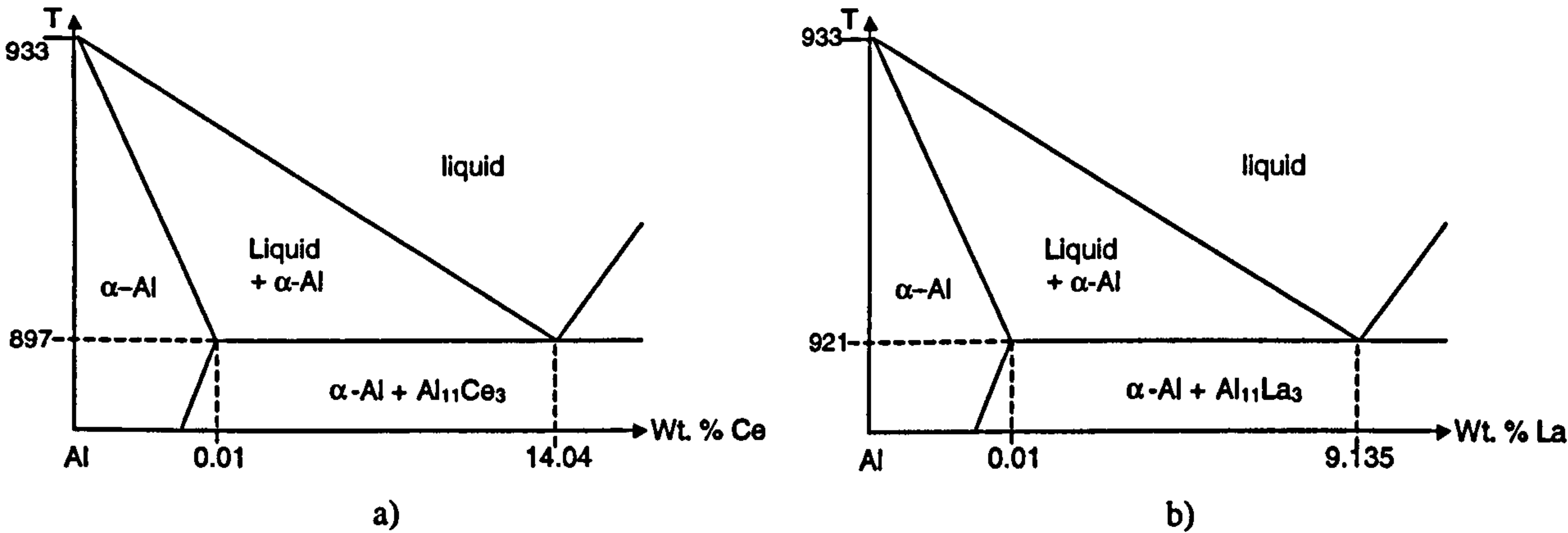


Figure 8.13 Binary phase diagrams for the a) Al-Ce system, and b) Al-La system

8.5 Summary

A number of issues have been addressed in this chapter concerning the possible ways forward in the development of piston alloys. From the work carried out on the alloy database, trends in both room temperature mechanical and physical properties as a function of composition have been identified. Furthermore, it is clear that thermodynamic calculations are now at a stage where they can play a vital role in alloy development, having the capability to predict, with reasonable accuracy, the fraction and composition of phases present in a given alloy system. However, modifications are still required to incorporate additional elements such as P.

In general, it was found that increasing the amount of a particular element will promote the formation of associated phases, e.g. the addition of Ni stabilises the Al₉FeNi and Al₃Ni phases. The consequences of increasing the content of a particular alloying element in respect of properties such as freezing range can also be addressed. The studies using the elemental database have indicated that Be and rare earth additions are not likely to be of significant benefit in a high volume industrial manufacturing environment.

The types of calculations and strategy presented in this chapter have already led to the development of the alloy AE160 from AE413, and have also been useful in harmonising the composition of FMS2N. In time, future advancements in piston alloys are likely to come from the use of composites, perhaps utilising selective reinforcements. However, it is hoped that this chapter has provided a focus for what may be possible within the current commercial constraints.

Chapter 9

Conclusions and Further Work

9.1 Conclusions

Multicomponent Al-Si piston alloys have been shown to be complex materials consisting of many different phases, the majority of which were found to be non-stoichiometric and containing several elements. The components that make up the microstructure are important not only with regards to the processing of these alloys, but in the final mechanical properties of the casting.

Thermodynamic calculations, both equilibrium and non equilibrium (Scheil), have been proven to be representative of the fraction and composition of the major phases occurring in the microstructures of as cast piston alloys. The Scheil simulation also has the potential to predict phases forming in segregated regions.

A detailed analysis identified the many intermetallic phases present in multicomponent Al-Si alloys to provide a thorough understanding of the morphology, composition, and stability of both primary and secondary phases. Electron backscatter diffraction (EBSD) was used to collect and identify diffraction patterns of the many phases, from which a comprehensive user database was compiled consisting of data for the phases present in these alloys. Furthermore, simultaneous EBSD and EDX were used to map large areas of the microstructure collecting both electron diffraction and chemical data. Using the data collected, maps were generated to illustrate grain orientation, phase identification, and elemental distribution of the scanned area. It is now possible to fully characterise the microstructures of multicomponent Al-Si casting alloys used in piston applications in this way.

The EBSD technique was also used in the identification of nucleation and growth mechanisms of the silicon phase. It was found that silicon nucleates epitaxially on AlP particles. The silicon particles were observed to contain twin boundaries of 60° about the $\{111\}$ plane, which indicates that the initial growth of the crystal may occur by the twin plane

reentrant mechanism. However, continuous growth was controlled by surface nucleation, although twinning was observed to influence the shape of the crystal.

In the investigation into grain refinement through a number of different model alloys, it was found that additions of Ti, Zr and V are primarily soluble in the Al_3Ti phase. This phase was seen to act as a grain refiner for the aluminium matrix, although the presence of Zr in combination with Ti was found to be detrimental, making Al_3Ti less effective at nucleation by changing its lattice parameters in the basal plane. The final structure was attributed to both nucleation and growth of the aluminium, the nature and efficiency of the grain refiner added, and complicated by the competing effects of casting conditions. A simple model for quantifying the efficiency of grain refiners through growth restriction parameter calculations was validated and then used as a predictive tool for signifying the growth restriction of new elements.

There is a strong competition between the nucleation of aluminium by Al_3Ti and nucleation of primary Si by AlP. This was also investigated by differential scanning calorimetry, where increasing additions of Ti were found to reduce the nucleating potency of the AlP, bringing the nucleation temperature of the aluminium and silicon phases closer together. In order to predict the effect of both Ti and P additions by thermodynamic calculations, P data were added to the thermochemical database.

9.2 Further Work

Several areas of further work have arisen from the investigations described in this thesis. These are discussed below.

Electron backscatter diffraction (EBSD) is now established as a powerful technique for both orientation and phase identification, with capability to characterise large areas of microstructure relatively simply. However, it is felt that the use of EBSD for phase analysis has yet to be exploited to its full capacity. Further development of the EBSD technique as a tool for phase identification is required for use without the need for previous knowledge of the phases, and for recognition of previously unreported phases. For example, of particular interest during the phase analysis was a new quinary phase previously unreported, which,

from diffraction data was suggested to be a derivative of the $\text{Al}_7\text{Cu}_4\text{Ni}$. It is believed that the Si and Zr content affect the stacking sequence of the crystal, and more work is therefore required to identify this phase completely.

It was also established that there is a strong competition between the effects of grain refiners and P, with the formation of Al_3Ti reducing the nucleating efficiency of AlP to silicon. Through differential scanning calorimetry the effect of P and Ti additions on the solidification of Al-Si alloys was shown to be complex. Although it has been demonstrated that this occurs, the mechanism remains unclear. This is clearly an area for future investigation, because this is particularly critical to the processing of Al-Si alloys, especially if Si contents are changed to significantly higher hypereutectic compositions.

Now that a thorough understanding of the microstructure has been established, further work is necessary to relate composition, fractions of phases, and grain structures to mechanical properties. The nanohardness of the individual phases present within the microstructure could be useful in the development of future models, especially if this can be determined as a function of temperature. High temperature properties are critical to a component, such as a piston, operating at high temperatures, and expansion of the alloy database to include properties such as creep-fatigue interactions is required to completely understand the behaviour of multicomponent alloys.

References

- Abd89 Abdel-Hamid A.A., *Zeitschrift Metallkund*, 1989, 80, 566
- Ana02 <http://www.anasys.co.uk>
- Ans94 Ansara I., *COST 507 - Thermochemical Database for Light Metal Alloys*, 1994
- Arj97 Arjuna Rao A., Murty B.S. and Chakraborty M., *Materials Science and Technology*, 1997, 13, 769
- Ask96 Askeland D.R., *The Science and Engineering of Materials*, London: Chapman and Hall, 1996
- Ata84 Atasoy. O.A., Yilmaz F. and Elliott R., *Journal of Crystal Growth*, 1984, 66, 137
- Ata87 Atasoy. O.A., *Zeitschrift Metallkund*, 1987, 76, 177
- Bac86 Backerud L., Chai G. and Tamminen J., *Solidification characteristics of Aluminium Alloys: Volumes 1 and 2*, Tangen Trykk A/S, Oslo, 1986
- Bac90 Backerud L., Chai G. and Tamminen J., *Solidification Characteristics of Aluminium Alloys*, AFS/SKANALUMINIUM, 1990
- Bal90 Bale C.W. and Eriksson G., *Canadian Metallurgical Quarterly*, 1990, 29, 2, 105
- Bal93 Ball R.G. J., *Journal of Nuclear Materials*, 1993, 201, 238
- Bar93 Barry T.I., Dinsdale A.T. and Gisby J.A., *Journal of Materials*, 1993, 45, 4, 32
- Bar02 Barnes S.I., Federal-Mogul, Cawston, *Personal communication*, 2002
- Bau83 Bauser, E. and Strunk, H. Max-Planck-Inst. fuer Festkoerperforschung, Stuttgart 1983
- Bil68 Biloni H. and Chalmers B., *Journal of Materials Science*, 1968, 3, 139
- Boo98 Boone G.W., Carver R.F. and Seese R.G., *Modern Castings*, 1998, 52
- Bra02 Brain M., How Car Engines Work, <http://www.howstuffworks.com>, 2002
- Bro66 Brody H.D. and Flemings M.C., *Transactions of the Metallurgical Society of AIME*, 1966, 236, 615
- Bun98 Bunn A.M., *Grain Refinement in Aluminium Alloys*, PhD Thesis, University of Cambridge, 1998
- Bun99 Bunn A.M., Schumacher P., Kearns M.A., Boothroyd C.B. and Greer A.L., *Materials Science and Technology*, 1999, 15, 1115
- Bur74 I Burden M.H. and Hunt J.D., *Journal of Crystal Growth*, 1974, 22, 99
-

-
- Bur74 II Burden M.H. and Hunt J.D., *Journal of Crystal Growth*, 1974, 22, 109
- Cha92 Chart T.G., *COST 507: A Database for the Development of New Light Alloys*, MTDS Note CST1, 1992
- Cha63 Chalmers B., *The Journal of the Australian Institute of Metals*, 1963, 8, 3, 255
- Chave R.A., *Concepts for Advanced Fatigue Life prediction of Pistons*, Technical Report, T&N Technology, 1995
- Cha99 Chart T.G., *EurAl Project Interim Report*, Chart Associates report, 1999
- Chr75 Christian J.W., *The Theory of Transformations in Metals and Alloys*, Pergamon, Oxford, 1975
- Cib49 Cibula A., *Journal of the Institute of Metals*, 1949, 76, 321
- Cib51 Cibula A., *Journal of the Institute of Metals*, 1951, 80, 1319
- Cla89 Clapham L. and Smith R.W., *Acta Metallurgica*, 1989, 37, 1, 303
- COS94 *COST 507 - Thermodynamic Database for Light Metal Alloys*, Ansara I. (Ed.), European Commission, 1994
- Cro51 Crossley P.B. and Mondolfo L.F., *Transactions of the Metallurgical Society of AIME*, 1951, 191, 1143
- Cro66 Crossley P.B. and Mondolfo L.F., *Modern Castings*, 1966, 89
- Dav63 Davies V. de L. and West J.M., *Journal of the Institute of Metals*, 1963, 92, 175
- Dav89 Davies R.H., Dinsdale A.T., Gisby J.A. and Hodson S.M., *MTDATA Handbook: Documentation for the NPL Metallurgical and Thermochemical Databank*, National Physical Laboratory, Teddington, 1989
- Dav90 Davies R.H., Dinsdale A.T., Chart T.G., Barry T.I. and Rand M.H., *High Temperature Science*, 1990, 26, 251
- Day68 Day M.G. and Hellawell A., *Proceedings of the Royal Society A*, 1968, 305, 473
- Day98 Daykin C.R.S., *Microstructural Modelling of Commercial Aluminium-Silicon Alloys for Piston Applications*, PhD Thesis, University of Cambridge, 1998
- Des90 Desnain P., Fautrelle Y., Meyer J. L., Riquet J. P. and Durand F., *Acta Metallurgica et Materialia*, 1990, 38, 8, 1513
- Deu97 Deuber A., Hofmann L., Obermeier-Wagner K. and Schearz R., *Patent No. 596013*, 1997
- Din97 Dingley D.J. and Field D.P., *Materials Science and Technology*, 1997, 13, 69
- Din88 Dinsdale A.T., Hodson S.M., Barry T.I. and Taylor J.R., *The Institute of Metals*, 1989, 246
-

- Din91 Dinsdale A.T., *CALPHAD*, 1991, 15, 4, 317
- Din95 Dinsdale A.T., Gisby J.A., Barry T.I. and Davies A.L., *International Minerals and Metals Technology*, 1995, 150
- Din96 Dinsdale A.T., NPL, Teddington, *Private Communication*, 1996
- Din97 Dinsdale, A.T., *Data Assessment and Modelling*, presented at MTDATA User Group Meeting, National Physical Laboratory, Teddington, Middlesex, U.K., 1997
- Doh77 Doherty R.D., Cooper P.D., Bradbury M.H. and Honey F.J., *Metallurgical Transactions A*, 1977, 8A, 397
- Eas99 Easton M. and StJohn D., *Metallurgical and Materials Transactions A*, 1999, 30A, 1613
- Edw23 Edwards J.D. and Archer R.S., *UK Patent Number 171997*, 1923
- Ell83 Elliott R., *Eutectic Solidification Processing*, First Edition, BMM, 1983
- Ell84 Elliott R., *Materials Science and Engineering*, 1984, 65, 85
- Ema93 Emadi D., Pekguleryuz M. and Gruzleski J.E., *Metallurgical Transactions B*, 1993, 24, 1055
- Fat89 Fat-Halla N., *Journal of Materials Science*, 1989, 24, 2488
- Flo81 Flood S.C. and Hunt J.D., *Metal Science*, 1981, 15, 287
- Flo86 Flood S.C. and Hunt J.D., *Conference Proceeding of the Metallurgical Society /AIME*, 1986, 607
- Flo87 Flood S.C. and Hunt J.D., *Journal of Crystal Growth*, 1987, 82, 543
- Fre72 Fredriksson H. and Hillert M., *Metallurgical Transactions*, 1972, 3, 565
- Fre73 Fredriksson H., Hillert M. and Lange N., *Journal of the Institute of Metals*, 1973, 101, 285
- Fuc95 Fuchsle K., *Internationale Anmeldung Veroffentlicht Nach Dem Vertrag Uber Die Internationale Zusammenarbeit Auf Dem Gebiet Des Patentwesens (PCT)*, 1995
- Gho64 Ghosh S., *Modern Castings*, 1963, 43, 17
- Gho93 Ghomashchi M.R., *Scandinavian Journal of Metallurgy*, 1993, 22, 2, 61
- Gis93 Gisby J.A., *Computer Software in Chemical and Extractive Metallurgy*, Metallurgical Society of the Canadian Institute of Mining, Metallurgy and Petroleum, 1993, 41
- Gis97 Gisby J.A., *Data Assessment and Modelling*, presented at MTDATA User Group Meeting, National Physical Laboratory, Teddington, Middlesex, U.K., 1997

-
- Gre00 Greer A.L., *Grain Refinement of Aluminium Alloys - Current Academic Studies*, Report No. 2 from MEBSP Sub-Group 1, 2000
- Gwy24 Gwyer A.G.C. and Phillips H.W.L., *U.K. Patent No. 219346*, 1924
- Gwy26 Gwyer A.G.C. and Phillips H.W.L., *Journal of the Institute of Metals*, 1926, **36**, 283
- Hag83 Hague M.M., *Metals Forum*, 1983, **6**, 1, 54
- Ham60 Hamilton D.R. and Seidensticker R.G., *Journal of Applied Physics*, 1960, **31**, 1165
- Han84 Hanna M.D., Lu S.Z. and Hellawell A., *Metallurgical Transactions A*, 1984, **15A**, 459
- Hei99 Heisler H., *Vehicle and Engine Technology*, Arnold, 2nd Edition, 1999
- Hen98 Henry S., Rappaz M. and Jarry P., *Metallurgical and Materials Transactions A*, 1998, **29**, 11, 2807
- Ho95 Ho C.R. and Cantor B., *Journal of Materials Science*, 1995, **30**, 1912
- Hog87 Hogan L.M. and Song H., *Acta Metallurgica*, 1987, **35**, 3, 677
- Hun66 Hunt J.D. and Jackson K.A., *Transactions of the Metallurgical Society of AIME*, 1966, **236**, 843
- Hun84 Hunt J.D., *Materials Science and Engineering*, 1984, **65**, 75
- Jac66 Jackson K. A. and Hunt J. D., *Transactions of the Metallurgical Society of AIME*, 1966, **236**, 88, 1129
- Jan93 B. Jansson, *Computer Software in Chemical and Extractive Metallurgy*, Metallurgical Society of the Canadian Institute of Mining, Metallurgy and Petroleum, 1993
- Joh94 Johnsson M., *Zeitschrift Metallkund*, 1994, **85**, 11, 786
- Joy02 Joyce M.R., Styles, C.M. & Reed P.A.S. *Materials Science Forum*, 2002, **396-402**, 3, 1261
- Kar98 Karantzalis A.E. and Kennedy A.R., *Materials Science and Technology*, 1998, **14**, 1092
- Kea96 Kearns M.A., Thistlethwaite S.R. and Cooper P.S., *125th Annual Meeting*, London and Scandinavian Metallurgical Co Limited, Anaheim, 1996
- Kea97 Kearns M.A. and Cooper P.S., *Materials Science and Technology*, 1997, **13**, 650
- Kha93 Khan S. and Elliott R., *Acta Metallurgica et Materialia*, 1993, **41**, 8, 2433
- Kim63 Kim C.B. and Heine R.W., *Journal of the Institute of Metals*, 1963, **92**, 367
- Kob85 Kobayashi K.F. and Hogan L.M., *Journal of Materials Science*, 1985, **20**, 1961
-

- Koe96 Koehnert M.H.J. and Issler W., Presented at the SIA conference "*Diesel Engine: Evolution and Changes*", Lyon, April 1996
- Kur79 Kurz W. and Fisher D.J., *International Materials Reviews*, 1979, 5, 177
- Kur86 Kurz W. and Fisher D.J., *Fundamentals of Solidification*, Trans Tech Publications Ltd., Switzerland, 1986
- Lar01 Larsen R.J. and Marx M.L., *An Introduction to Mathematical Statistics and its Applications*, London: Prentice Hall International, 2001
- Mag91 Magnin P., Mason J.T. and Trivedi R., *Acta Metallurgica et Materialia*, 1991, 39, 4, 469
- Mah93 Mahanti R.K., *Materials Transactions, JIM*, 1993, 34, 12, 1207
- Mah98 Mahle, *Mahle Group Pamphlet*, 1998
- Maj89 Major J.F. and Rutter J.W., *Materials Science and Technology*, 1989, 5, 645
- Mar71 Marcantonio J.A. and Mondolfo L.F., *Metallurgical Transactions*, 1971, 2, 465
- Max75 Maxwell I. and Hellawell A., *Acta Metallurgica*, 1975, 23, 229
- McC89 McCartney D.G. and Hunt J.D., *Acta Metallurgica*, 1989, 29, 11, 1851
- Moh95 Mohanty P.S. and Gruzleski J.E., *Acta Metallurgica et Materialia*, 1995, 43, 5, 2001
- Moh96 Mohanty P.S. and Gruzleski J.E., *Acta Metallurgica*, 1996, 44, 9, 3749
- Mon76 Mondolfo L.F., *Aluminium Alloys, Structure and Properties*, Butterworths, 1976
- Mon87 Mondolfo L.M., *Metallography of Aluminium Alloys*, Wiley, 1987
- Mor66 Morizane K., Witt A.F. and Gatos H.C., *Journal of the Electrochemical Society*, 1966, 113, 1, 51
- Mor70 Morando R., Biloni H., Cole G.S. and Bolling G.F., *Metallurgical Transactions*, 1970, 1, 1407
- Nun98 Nunney M.J., *Light and Heavy Vehicle Technology*, Butterworth-Heinemann, Third Edition, 1998
- OIM02 *OIM Analysis Handbook*, TexSEM Laboratories, 2002
- Ota26 Otani B., *Journal of the Institute of Materials*, 1926, 36, 243
- Pac21 Pacz A., *U.S. Patent No. 1387900*, 1921
- Par94 Paray F. and Gruzleski J.E., *Materials Science and Technology*, 1994, 10, 757
- Par95 Parton D.P., *16th Aalener Giessereisymposium*, Aalen, 1995
- Pei01 Pei Y. T. and De Hosson J. Th. M., *Acta Materialia*, 2001, 49, 561
- Plu57 Plumb R.C. and Lewis J.E., *Journal of the Institute of Metals*, 1957, 86, 393

- Pol89 Polmear I.J., *Light Alloys, Metallurgy of the Light Metals*, Second Edition, Edward Arnold, 1989
- Pol95 Polmear I.J., *Light Alloys, Metallurgy of the Light Metals*, Arnold, Third Edition, Edward Arnold, 1995
- Por81 Porter D.A. and Easterling K.E., *Phase Transformation in Metals and Alloys*, 1st edition, Chapman and Hall, London, 1981
- Por92 D.A. Porter and K.E. Easterling, *Phase Transformation in Metals and Alloys*, 2nd edition, Chapman and Hall, London, 1992
- Sau96-1 Saunders N., *Phase Diagram Calculations for Commercial Al-alloys*, presented at 5th International Conference on Al-alloys, Grenoble, France, 1996
- Sau96-2 Saunders N., *Al-Data Information*, Thermotech Ltd., Surrey Technology Centre, 40 Occum Road, The Surrey Research Park, Guildford, Surrey, U.K., 1996
- Sau96-3 Saunders N., *Materials Science Forum*, 1996, 217, 667
- Sau98 Saunders N. and Miodownik A.P., *CALPHAD*, Pergamon Materials Series, First edition, 1998
- Sch95 Schumacher P. and Greer A.L., *Light Metals*, 1995, 869
- Sch98 Schumacher P., Greer A.L., Worth J., Evans P.V., Kearns M.A., Fisher P. and Green A.H., *Materials Science and Technology*, 1998, 14, 394
- Sha86 Shamsuzzoha M. and Hogan L.M., *Philosophical Magazine A*, 1986, 54, 4, 459
- Sha89 Shamsuzzoha M. and Hogan L.M., *Journal of Materials Science*, 1989, 24, 2849
- Sig84 Sigworth G.K., *Metallurgical Transactions A*, 1984, 15, 277
- Sma82 Smart R.F., Bacon M.C., Coldrick G.M. and Parkin J.R., *Materials Aspects of Piston Reliability*, Conference Proceedings of the AE Symposium, 1982
- Sou67 Southin R.T., *Transactions of the Metallurgical Society of AIME*, 1967, 239, 221
- Sou78 Southin R.T. and Chadwick G.A., *Acta Metallurgica*, 1978, 231
- Spi97 Spittle J.A. and Brown S.G.R., *Light Metals*, 1997, 795
- Ste72 Steen H.A.H. and Hellawell A., *Acta Metallurgica*, 1972, 20, 363
- Sty00 Styles C.M. and Reed P.A.S., Southampton University, *Unpublished Work*, 2000
- Sun85 Sundman B., Jansson B. and Anderson J.O., *CALPHAD*, 1985, 9, 2, 153
- Sun88 Sundman B., *CIM Bulletin*, 1988, 81, 914, 79
- Tar71 Tarshis L.A., Walker J.L. and Rutter J.W., *Metallurgical Transactions*, 1971, 2, 2589
- Tas76 Tassa M. and Hunt J.D., *Journal of Crystal Growth*, 1976, 34, 38

- Tay93 Taylor J.R. and Dinsdale A.T., *Zeitschrift Metallkd.*, 1993, 84, 5, 335
- Tel88 Telli A.I. and Kisakurek S.E., *Materials Science and Technology*, 1988, 4, 153
- Tri94 Trividi R. and Kurz W., *International Materials Reviews (UK)*, 1994, 39, 2, 49
- Tro01 Tronche A. and Greer A.L., *Philisophical Magazine Letters*, 2001, 81, 5, 321
- Wan95 Wang R.Y., Lu W.H. and Hogan L.M., *Materials Science and Technology*, 1995, 11, 441
- Wan97 Wang R., Lu W.H. and Hogan L.M., *Metallurgical and Materials Transactions A*, 1997, 28A, 1233
- Wan99 Wang R., Lu W.H. and Hogan L.M., *Journal of Crystal Growth*, 1999, 207, 43
- Wag60 Wagner R.S., *Acta Metallurgica*, 1960, 8, 57
- Win54 Winegard W.C. and Chalmers B., *Transactions of the ASM*, 1954, 46, 1216
- Yil84 Yilmaz F. and Elliott R., *Metal Science*, 1984, 18, 362
- Zho94 Zhao H.X. and Jun C., *Journal of Materials*, 1994, 42
-

Appendix A

Columnar to Equiaxed Growth Model ^[Hun84]

Nucleation

According to Christian ^[Chr75] the nucleation rate per unit volume is assumed to be of the form

$$I = N_s \nu \exp\left(\frac{\Delta g^+}{kT}\right) \exp\left(\frac{\Delta G_c}{kT}\right) \quad [\text{A1}]$$

where N_s is the number of atoms in contact with the substrate, ν is the vibrational frequency, Δg^+ is the diffusional activation energy, ΔG_c is the energy of formation of the critical nucleus, k the partition coefficient, and T temperature. Equation A1 may be written as

$$I = (N_0 - N) I_0 \exp\left(\frac{\Delta G_c}{kT}\right) \quad [\text{A2}]$$

where N_0 is the total number of heterogeneous substrate particles originally available per unit volume, N is the number that have already nucleated, and I_0 is a constant. A value for I_0 may be estimated from Equation A1 using the liquid diffusion coefficient $D \approx a^2 \nu \exp. (-\Delta g^+/kT) \approx 10^{-9} \text{ m}^2 \text{ s}^{-1}$, the atomic diameter $a \approx 0.4 \text{ nm}$ and the substrate particle size $1\text{-}100 \text{ }\mu\text{m}$, giving $I_0 \approx 10^{18}\text{-}10^{22} \text{ s}^{-1}$. In work by Hunt ^[Hun84], I_0 is taken to be 10^{20} ; for small supercoolings it can be shown that ΔG_c is proportional to $1/(\Delta T)^2$ where ΔT is the supercooling. Thus, the nucleation rate is assumed to be

$$I = (N_0 - N) 10^{20} \exp\left\{-\frac{u}{(\Delta T)^2}\right\} \quad [\text{A3}]$$

where u is a constant for the substrate concerned. A value for u may be estimated from the heterogeneous nucleation temperature. If this temperature is defined as the temperature where

there is an initial nucleation rate of one nucleus per cubic centimetre per second, u may be calculated from

$$u = -(\Delta T_N)^2 \ln(N_0 \times 10^{20}) \quad [\text{A4}]$$

where ΔT_N is the supercooling at the heterogeneous nucleation temperature. Because of the large size of the pre-exponential term in Equation A3, once nuclei form, the nucleation rate increases very rapidly with decrease in temperature. The ratio $\Delta T_I/\Delta T_{I0}$ of the supercooling ΔT_I for one nucleus per second to the supercooling ΔT_{I0} for ten nuclei per second, on the assumption that $N_0 - N = 1000$, is $20/21 \approx 1.05$; thus site saturation will often occur very rapidly.

Growth

Dendrites have been shown to grow with a tip supercooling which depends on growth velocity, temperature gradient, and alloy composition. Empirically ^[Bur74], it is found that

$$\Delta T = \frac{GD}{V} + A'(C_0 V)^{1/2} \quad [\text{A5}]$$

where G is the temperature gradient, D the liquid diffusion coefficient, C_0 the alloy composition, V the velocity and A' a constant. Two approximate analyses have developed equations of this form ^[Bur74, Hun79]. One of these gives

$$\Delta T = \frac{GD}{V} + 2 \left\{ -\frac{2m(1-k_0)C_0 V \Gamma}{D} \right\}^{1/2} \quad [\text{A6}]$$

where m is the liquidus slope, k_0 the partition coefficient and Γ is the Gibbs-Thomson parameter, the ratio of solid-liquid interfacial energy to entropy of melting. The first term on the right hand side becomes appreciable when the gradient is high and the velocity is very low. In this work, discussion is restricted to regions where $GD/V \ll A'(C_0 V)^{1/2}$ so that from Equation A5 it is assumed that

$$\Delta T = \left(\frac{V' C_0}{A} \right)^{1/2} \quad [\text{A7}]$$

It is assumed that Equation A7 applies for both the columnar and equiaxed front where V' refers to the real interface velocity. Behind the dendrite tips and within the equiaxed grains the fraction g_L that is liquid is assumed to vary with liquid composition as in the Scheil equation

$$C_L = C_0 g_L^{k_0-1} \quad [\text{A8}]$$

where C_L is determined by the local temperature. Equation A8 may be written as

$$g_L = \left(\frac{T}{T_E} \right)^{1/(k_0-1)} \quad [\text{A9}]$$

where $T_E = mC_0$ is the equilibrium liquidus temperature for the alloy, the liquidus line is assumed straight and zero temperature is the melting point of the pure material. For eutectic growth an equation

$$\Delta T = \left(\frac{V}{A} \right)^{1/2} \quad [\text{A10}]$$

might be expected to apply according to Jackson ^[Jac66]. The fraction that is liquid behind the front would, of course, in this case be zero.

Simple Analytic Expression

Equiaxed crystals are assumed to be nucleated and then grown at a velocity determined by their local temperature. Their growth will be stopped when the grains impinge or are passed by the columnar front. Three steady state growth conditions may occur: a) fully columnar, b) columnar plus equiaxed and c) fully equiaxed. The type of growth depends on the volume fraction of equiaxed crystals present when the columnar front passes. Fully equiaxed growth

is considered to occur if the volume fraction ϕ is greater than 0.49, whereas the structure is assumed to be fully columnar if ϕ is 1% of this value. The reason for the choice of 0.49 is rather arbitrary and justification is as follows.

The average distance grown by a columnar dendrite is clearly a function of the volume fraction of equiaxed crystals. If all the equiaxed crystals have a radius R , there must be no equiaxed crystal centres in the volume C (Figure A1) for the dendrite at A to grow a distance b . There can be no centre in volume B for the columnar dendrite to be initially present at A . If there is just one centre in the length L of the cylinder, the probability that it is in C is

$$\frac{\pi R^2 b}{\pi R^2 L} = \frac{b}{L} \quad [\text{A11}]$$

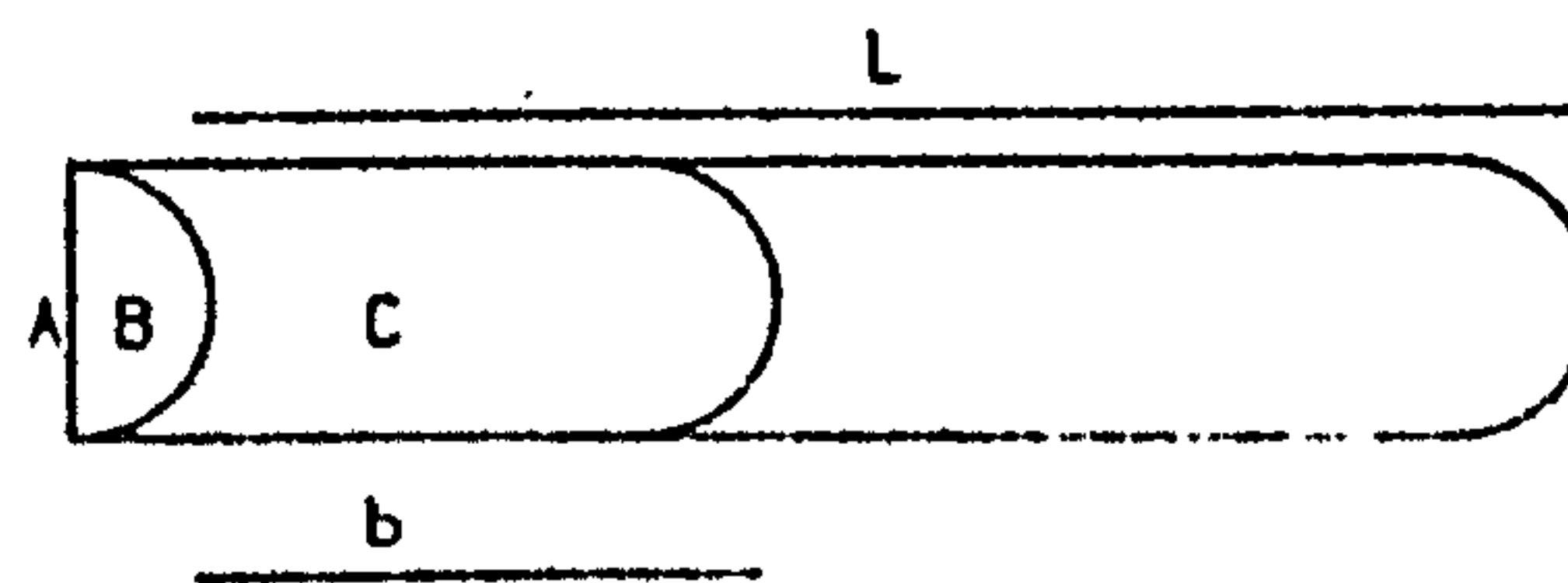


Figure A1 Average distance grown by a columnar dendrite, after Hunt ^[Hun84]

The probability that it is not in C is $1-b/L$. If there are N centres per unit volume, there are $N\pi R^2 L$ centres in the volume $\pi R^2 L$. The probability that none of these is in C is

$$F(b) = \left(1 - \frac{b}{L}\right)^{\pi R^2 L N} \quad [\text{A12}]$$

This is the probability that a dendrite gets at least as far as b . The quantity $-dF(B) = f(B) db$ is the number of dendrites that stop between b and $b + db$. The mean distance grown is thus

$$\bar{b} = \int_0^L b f(b) db \quad [\text{A13}]$$

Substituting

$$f(b) = \frac{dF(b)}{db}$$

$$= -\pi R^2 N \left(1 - \frac{b}{L}\right)^{\pi R^2 L N - 1}$$

and integrating Equation A13 by parts gives

$$\bar{b} = \frac{1}{\pi R^2 N + 1/L} \quad [A14]$$

and, as $L \rightarrow \infty$,

$$\bar{b} = \frac{1}{\pi R^2 N} \quad [A15]$$

The extended volume $\phi_E = 4\pi R^3 N/3$; therefore

$$\frac{\bar{b}}{R} = \frac{4}{3\phi_E} \quad [A16]$$

It is suggested that if $\bar{b}/R > 2$ there would be sufficient directionality to recognise partly columnar growth. Under these conditions a dendrite which was originally part of an equiaxed crystal would grow an average of $2R$ with the columnar front, i.e. the length in the heat flow direction would become $4R$. If \bar{b}/R is taken to be equal to 2, the extended volume fraction ϕ_E equals 0.66 and ϕ equals 0.49.

Since the nucleation sites are arranged randomly, a correction for the impingement of equiaxed grains may be made using the well-known concept of an extended volume fraction ϕ_E [Jac66]. In a small time interval,

$$d\phi = (1 - \phi)d\phi_E \quad [A17]$$

or

$$\phi = 1 - \exp(-\phi_E) \quad [A18]$$

so that when $\phi = 0.49$ then $\phi_E = 0.66$.

A very simple discussion of the various growth conditions may be made if it is assumed that all the available nucleation sites operate as soon as the heterogeneous nucleation temperature is reached and that the heat evolved during growth does not appreciably affect the temperature gradient. These assumptions are not made in the more detailed numerical treatment of the problem to be given later. The results from the two methods, however, turn out to be very similar. Since all the grains form at the same time, the radius of the equiaxed grains after time t is given by

$$r = \int_0^t V_e dt \quad [A19]$$

where V_e is the equiaxed velocity given by Equation A6 as $V_e = A(\Delta T)^2/C_0$. Since growth is at a steady state, then $dT/dt = -VG = -d(\Delta T)/dt$ where V is the steady state velocity, G the imposed temperature gradient which is assumed constant and ΔT the local supercooling. On substitution for V_e and dt , Equation A19 becomes

$$\begin{aligned} r &= \int_{\Delta T_N}^{\Delta T} \frac{A(\Delta T)^2}{VGC_0} d(\Delta T) \\ &= \frac{A\{(\Delta T)^3 - (\Delta T_N)^3\}}{3VGC_0} \end{aligned} \quad [A20]$$

where ΔT_N is the supercooling at the heterogeneous nucleation temperature. Fully equiaxed growth occurs when the extended volume fraction

$$\phi_E = \frac{4\pi r^3 N_0}{3} > 0.66 \quad [\text{A21a}]$$

at a supercooling equal to that of the columnar growth front temperature $\Delta T_c = (VC/A)^{1/2}$. Rearranging Equation A21a gives

$$r > 0.54 \left(\frac{1}{N_0} \right)^{1/3} \quad [\text{A21b}]$$

Using Equation A20 and the relationship for ΔT_c , Equation A21b becomes

$$G < 0.617 N_0^{1/3} \left\{ 1 - \frac{(\Delta T_N)^3}{(\Delta T_c)^3} \right\} \Delta T_c \quad [\text{A22}]$$

The structure is fully columnar when $\phi_E < 0.0066$ or when

$$G > 0.617 (100 N_0)^{1/3} \left\{ 1 - \frac{(\Delta T_N)^3}{(\Delta T_c)^3} \right\} \Delta T_c \quad [\text{A23}]$$

The Heat Flow Equation

The assumption that nucleation was complete at ΔT_N and that the temperature gradient was almost constant need not be made when the heat flow is examined in more detail. If a unit area box at steady state is considered, the heat going in at $x = 0$ must equal that leaving at x .

$$VH_x + K \left(\frac{dT}{dx} \right)_x = VH_{x=0} + K_{x=0} \left(\frac{dT}{dx} \right)_x \quad [\text{A24}]$$

where H is the heat content and K the conductivity at x or 0. Making the imposed temperature gradient $G = (dT/dx)_{x=0}$ and writing $K_x = K_{x=0} = K$ gives

$$\left(\frac{dT}{dx}\right)_x = \frac{V(H_{x=0} - H_x) + KG}{K} \quad [\text{A25}]$$

Equation A25 can be integrated numerically. In the present work it was written as

$$\begin{aligned} \delta T &= K^{-1} \{V(H_{x=0} - H_x) + KG\} \delta x \\ &= VK^{-1} \{V(H_{x=0} - H_x) + KG\} \delta t \end{aligned} \quad [\text{A26}]$$

Since the process is of a steady state nature, the interval on the right hand side may be considered to be a distance δx or a time δt . A small enough value of δt was chosen and δT calculated. If the quantities with primes refer to the previous values, then

$$T = T' + \delta T \quad [\text{A27}]$$

If T is known, a new value of $H = H' + \delta H$ could be calculated and the process repeated. It was found that a value of δt giving $\delta T \approx 0.001\text{K}$ produced sufficiently accurate results. The integration was started at T_E (the equilibrium liquidus temperature). At T_E ,

$$H_{x=0} = c_p T_E + L \quad [\text{A28}]$$

where c_p is the specific heat and L the latent heat per unit volume. Elsewhere

$$H = c_p T + g_L' L \quad [\text{A29}]$$

where g_L' is the fraction that is totally liquid. The fraction completely solid is given by

$$\begin{aligned} g_s' &= 1 - g_L' \\ &= \phi(1 - g_L) \end{aligned} \quad [\text{A30}]$$

where, as before, ϕ is the volume fraction of equiaxed crystals and g_L is the fraction of the semisolid that is liquid (given by Equation A9). Nucleation is assumed to be random so that the impingement of equiaxed crystals may be allowed for using the extended volume ϕ_E discussed earlier. δH is obtained by differentiating Equation A29 using Equation A30:

$$\delta H = \left\{ c_p + \frac{L\phi g_L}{T(k_0 - 1)} \right\} \delta T - L(1 - g_L)\delta\phi \quad [\text{A31}]$$

since, from Equation A9,

$$\frac{dg_L}{dT} = \frac{g_L}{(k_0 - 1)T}$$

To obtain $\delta\phi_E$ (or $\delta\phi = (1 - \phi) \delta\phi_E$) without keeping track of the size of each grain, values of the quantities n , $n \bar{r} = \sum_i n_i r_i$, $n \bar{r}^2 = \sum_i n_i r_i^2$, $n \bar{r}^3 = \sum_i n_i r_i^3$ were calculated at each position or time. Here, n is the total number of equiaxed crystals present per unit volume and r_i is the radius of the i th crystal. For a small change in δ the change in radius is $\delta r = V_e \delta$ where V_e is the equiaxed velocity given by Equation A7 ($V_e = A(\Delta T)^2/C_0$). If the quantities with primes refer to previous values, then

$$n = n' + I dt \quad [\text{A32a}]$$

$$n \bar{r}' + n dr \quad [\text{A32b}]$$

$$n \bar{r}^2 = n \bar{r}^2' + 2n \bar{r} dr \quad [\text{A32c}]$$

$$n \bar{r}^3 = n \bar{r}^3' + 3n \bar{r}^2 dr \quad [\text{A32d}]$$

The extended volume fraction is then

$$\phi_E = \frac{4}{3} \pi \sum_i n_i r_i^3 \quad [\text{A33}]$$

The actual number of equiaxed crystals was also recorded:

$$N = N' + (1 - \phi) \int dt \quad [A34]$$

The integration was stopped either side when the structure was fully equiaxed or when the temperature was low enough for the columnar front to grow. The volume fraction chosen as fully equiaxed was taken, as before, to be $\phi = 0.49$ ($\phi_E = 0.66$). When ϕ_E was 1% of this value, the structure was considered to be fully columnar.

Appendix B

Image Analysis Data Collection Macro

```
#-----  
# initialize  
#-----  
imgdelete "*"   
showwindow "Display",1  
Gclear 0  
showwindow "Gallery",1  
showwindow "Messages",1  
wait 100  
update  
wtime = 2000  
write "@"  
nfieldx = 20  
nfieldy = 20  
# -----  
# set shading correction with a standard sample  
# -----  
write  
write " put shading correction sample on microscope"  
tvlive  
tvinput 1  
! tvwbalance 1  
tvinput 1  
imgload "d:\sib\shade4.tif",2  
# tvinput 2  
    # imgdisplay 2  
    # lowpass 1,2,49,34  
imgprotect 2,1
```

```
# write
# write "place piston sample back on microscope"
# write " Please select stage file and magnification"
# write " and define home position and focus plane"
# write " by the following function"
STopen "Stage1"
STsethome
# use lenses 1.25x and 20x
# STmove "XYZ",45864,35064,140,0,0,1
STselmag
write " Enter the number of fields in x- and y-direction"
write " and start defining the focus plane of the meander!"
STgetprop "MeaFieldsX",nfieldsx
STgetprop "MeaFieldsY",nfieldsy
! STsetfields nfieldx,nfieldy,1,1
STsavemeander "sibmeal"

imgsetpath "d:\sib\ascan\b2h13049p2"
i = 1
#-----
# scan meander and measure
#-----

STloadmeander "sibmeal"
STmovepos 1,1
next := _STATUS
while next == 1
    STgetprop "MoveField",field
    STwaitpos
    write "Displaying meander field nr: ",i
tvinput 1
    # imgdisplay 1
    shadcorr 1,2,3,1,250
```

```
imgcopy "3[1,1]",4
```

```
imgdisplay 4
```

```
s1 = "image"
```

```
s2 = ".tif"
```

```
imgname = s1 + string(i) + s2
```

```
imgsave 4, imgname
```

```
i = i + 1
```

```
STmovepos 2,1
```

```
next = _STATUS
```

```
endwhile
```

```
# end of macro
```

```
stop
```

Appendix C

Image Analysis Data Analysis Macro

```
#-----  
# initialize  
#-----  
imgdelete "*"   
showwindow "Display",1  
Gclear 0  
showwindow "Gallery",1  
showwindow "Messages",1  
wait 100  
MSload "c:\sib\macros_macsys\sibsil.ms"  
update  
wtime = 2000  
write "@"  
DBdelete "RtotSI"  
DBdelete "rprimsi"  
DBdelete "rints"  
DBdelete "FtotSI"  
DBdelete "fprimsi"  
DBdelete "fints"  
MSsetprop "SCALEX",0.661  
MSsetprop "SCALEY",0.661  
  
#-----  
# load images and measure  
#-----  
imgsetpath "d:\wendy\83_100"  
i = 1  
while 1
```

```
write "Displaying field nr: ",i

s1 = "image"
s2 = ".tif"
imgname = s1 + string(i) + s2
imgload imgname, 1
i = i + 1

MSsetprop "FRAMEMODE",0

# -----
# Segment, process and measure total Si
# -----

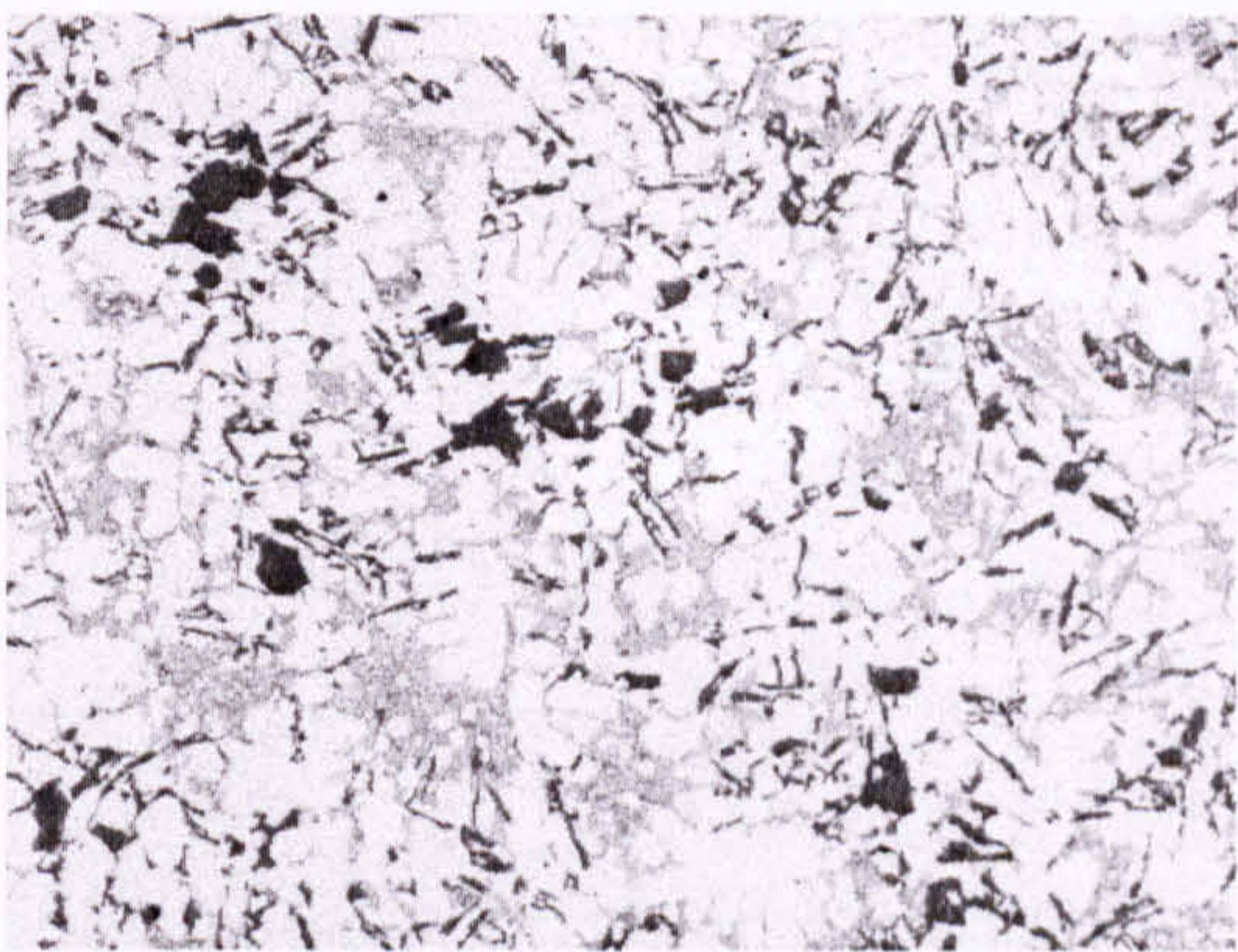
# imgdisplay 1
# lowpass 1,"shade",49,50
# shadcorr 1,"shade",1,1,0

imgdisplay 1

dislev 1,2,75,141,1
binscrap 2,3,0,10,0
binclose 3,4,5,1
# imgdisplay 4
MSmeasmask 4,1,"RtotSI",1,1,10
MSmeasmask 4,1,"ftotsi",1,2,10
MSsetprop
"DRAWFEAT","DRCONTOURU"
MSdrawmask 4,1
imgdisplay 1

# -----
# Detach ligaments from primary Si particles
# -----

binerode 4,5,5,3
binudilate 5,6,5,10
```



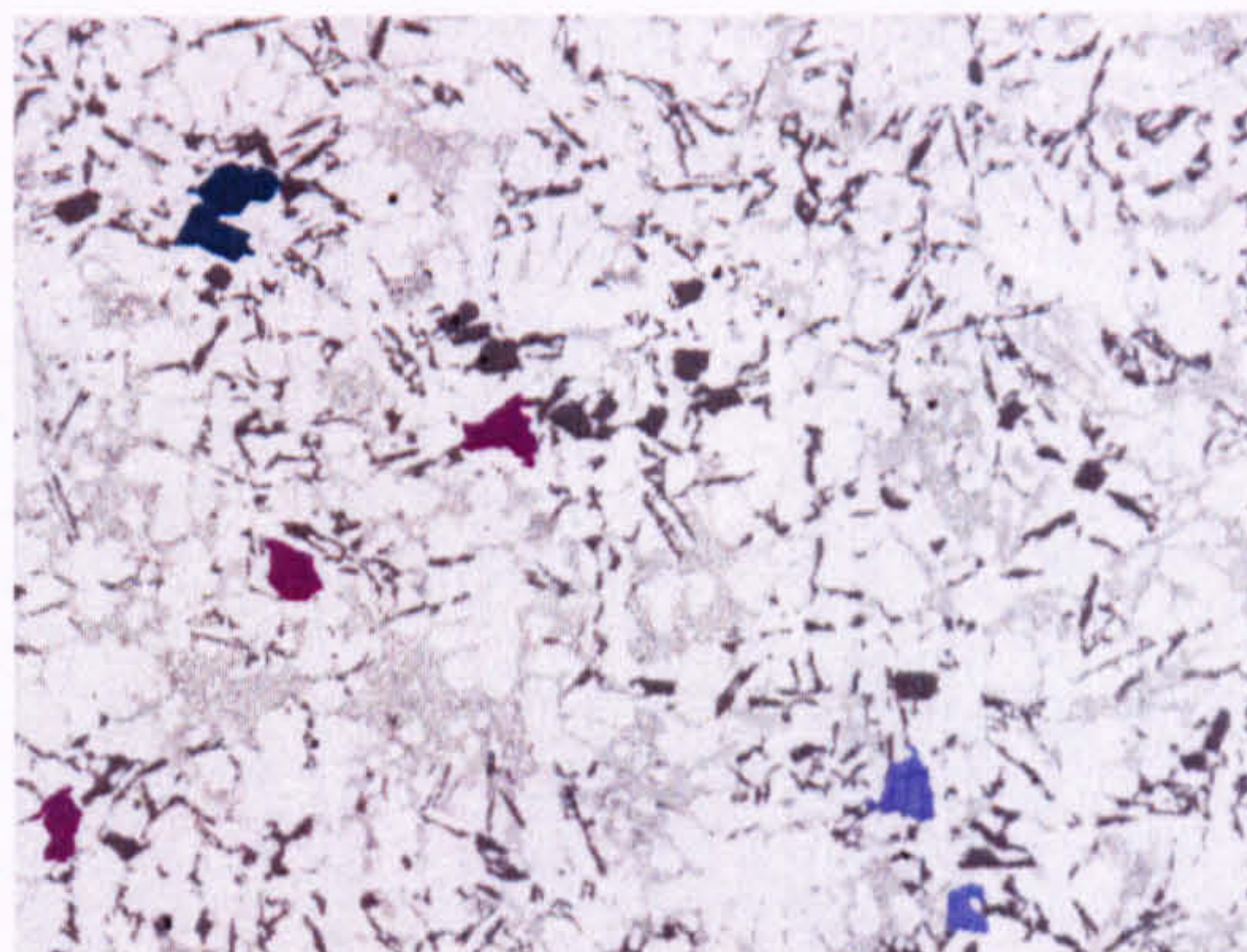

```

binand 4,6,7
# -----
# Select primary Si Particles and measure
# -----
write
write "Select Agglomerated Primary Si
Particles"
binfill 7,8
MSsetprop
"CONDITION","AREA>200&&1/FERETR
ATIO<4"
MSmeasmask 8,1,"rprimsi",1,1,10
MSmeasmask 8,1,"fprimsi",1,2,10
MSsetprop
"DRAWFEAT","DRLABELU,"
MSdrawmask 8,1
imgdisplay 1

Gclear 0

# -----
# Intermetallics
# -----
# Segment all phases
# -----
# imgdisplay 1
dislev 1,9,75,210,1
binscrap 9,10,0,5,0
# -----
# subtract dilated total Si from all phases
# to obtain intermetallics
# -----
bindilate 4,11,5,2

```



subtract 10,11,12,2

binscrap 12,14,0,50,0

MSsetprop "CONDITION",1

MSmeasmask 14,1,"rints",1,1,10

MSmeasmask 14,1,"fints",1,2,10

MSsetprop

"DRAWFEAT","DRCONTOURU"

MSdrawmask 14,1

imgdisplay 1

Gclear 0

if i >400 : break

endwhile

#-----

display results

#-----

datalist "rtotsi",0,1

datalist "rprimsi",0,1

datalist "rints",0,1

datalist "ftotsi",0,1

datalist "fprimsi",0,1

datalist "fints",0,1

end of macro

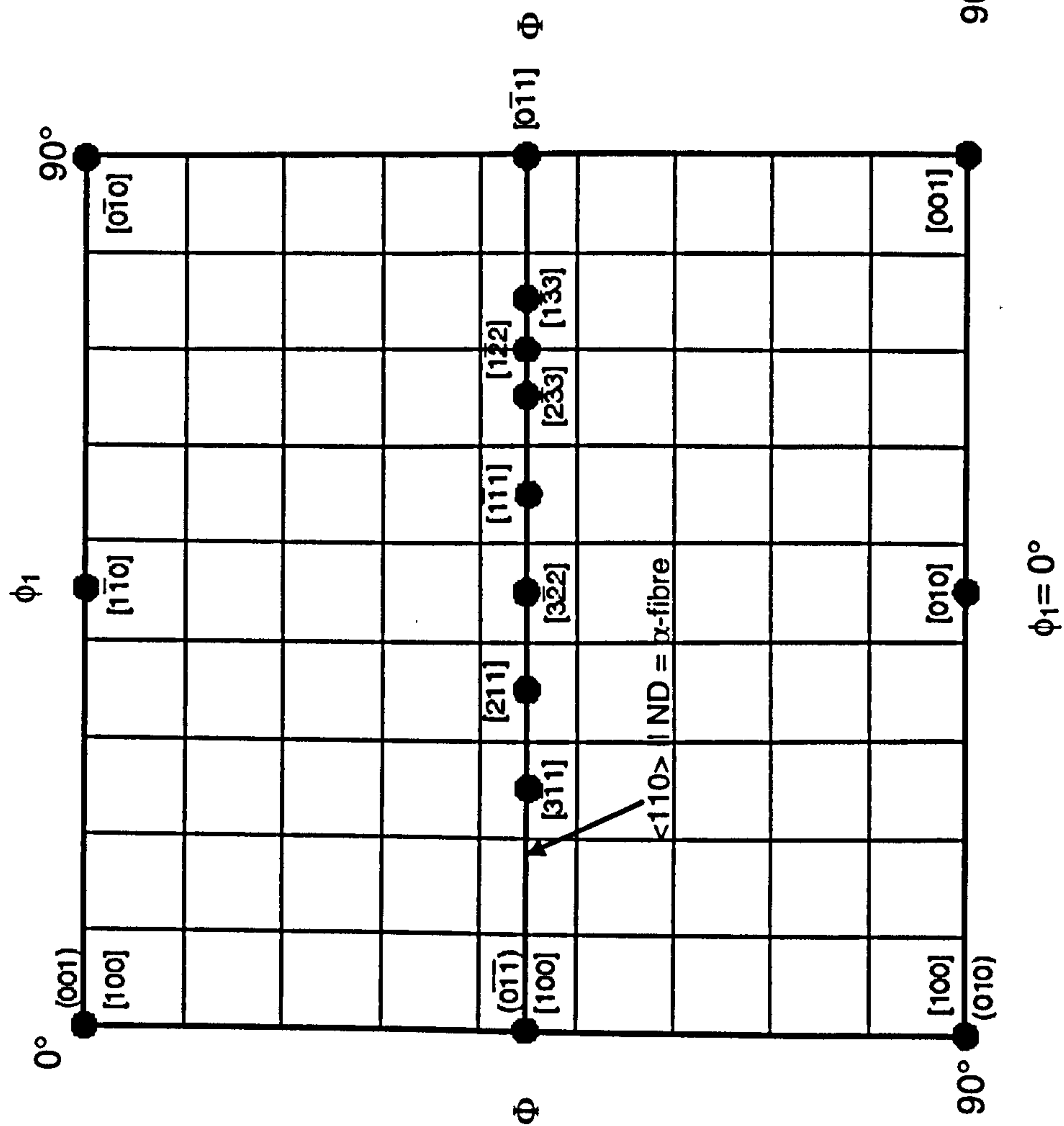
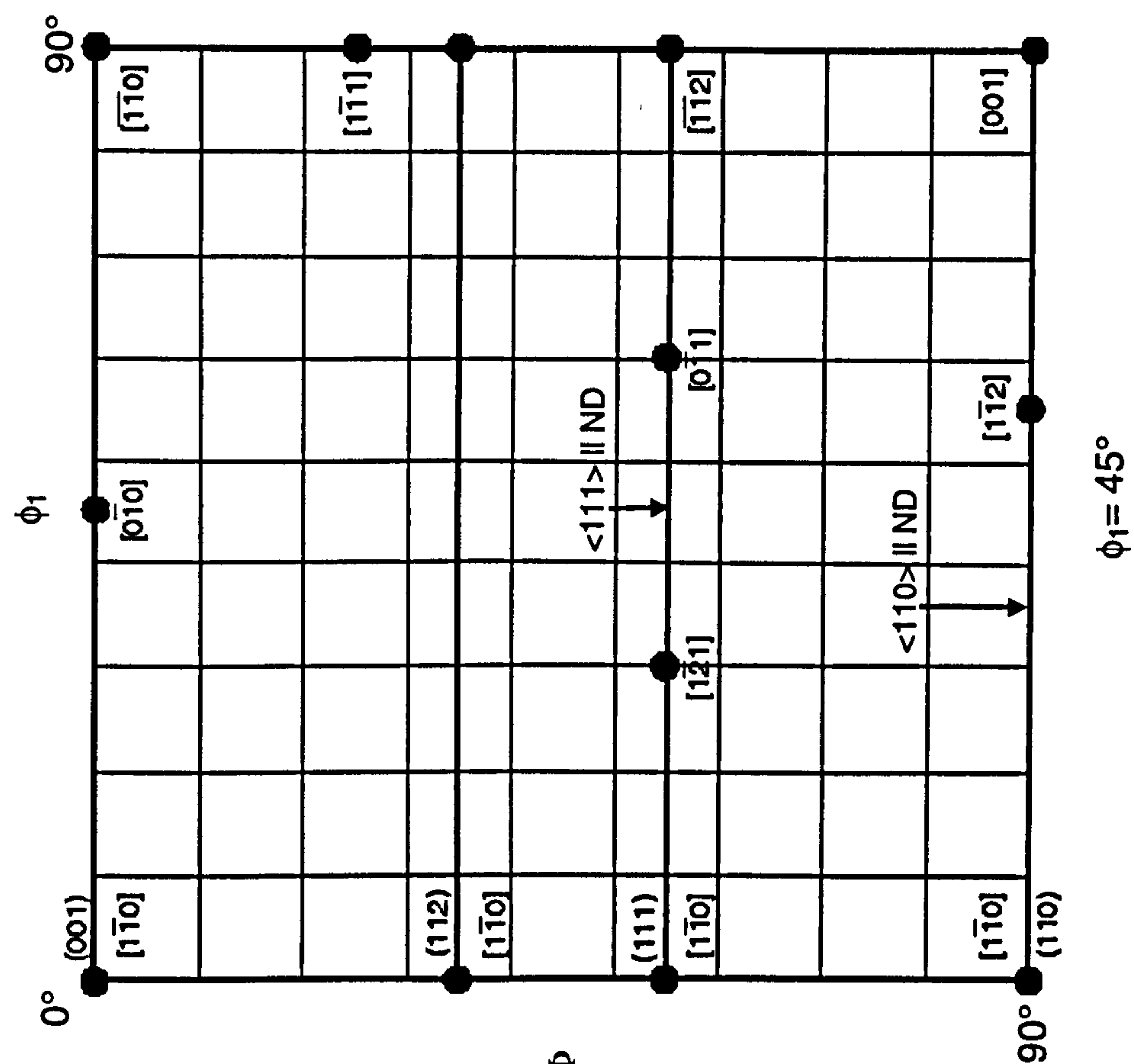
stop

Appendix D

Image Analysis t-Table ^[Lar01]

Degrees of Freedom	Confidence level					
	90%	95%	98%	99%	98.8%	99.9%
1	6.31	12.71	31.82	63.66	318.31	636.62
2	2.92	4.30	6.97	9.92	22.33	31.60
3	2.35	3.18	4.54	5.84	10.21	12.92
4	2.13	2.78	3.75	4.60	7.17	8.61
5	2.02	2.57	3.37	4.03	5.89	6.87
6	1.94	2.45	3.14	3.71	5.21	5.96
7	1.89	2.36	3.00	3.50	4.79	5.41
8	1.86	2.31	2.90	3.36	4.50	5.04
9	1.83	2.26	2.82	3.25	4.30	4.78
10	1.81	2.23	2.76	3.17	4.14	4.59
11	1.80	2.20	2.72	3.11	4.03	4.44
12	1.78	2.18	2.68	3.06	3.93	4.32
13	1.77	2.16	2.65	3.01	3.85	4.22
14	1.76	2.15	2.62	2.98	3.79	4.14
15	1.75	2.13	2.60	2.95	3.73	4.07
16	1.75	2.12	2.58	2.92	3.69	4.02
17	1.74	2.11	2.57	2.90	3.65	3.97
18	1.73	2.10	2.55	2.88	3.61	3.92
19	1.73	2.09	2.54	2.86	3.58	3.88
20	1.72	2.08	2.53	2.85	3.55	3.85
25	1.71	2.06	2.49	2.78	3.45	3.72
30	1.70	2.04	2.46	2.75	3.39	3.65
40	1.68	2.02	2.42	2.70	3.31	3.55
60	1.67	2.00	2.39	2.66	3.23	3.46
120	1.66	1.98	2.36	2.62	3.16	3.37
Infinity	1.64	1.96	2.33	2.58	3.09	3.29

Appendix E
Orientation Space Charts



Cube = {100} <001>
 Goss = {110} <001>
 Brass = {110} <112>
 Copper = {112} <111>
 Taylor = {4 4 11} <8 8 11>

Appendix F
Image Analysis Results
(Stepped Mould Model Alloys 83, 86, 87 and 90)

Model Alloy	Mould Temp. (°C)	% Silicon	Mean Si Length (µm)	Max. Si Length (µm)	90% Si Length	% Primary Silicon	Mean Prim. Si length (µm)	Max. prim. Si Length (µm)	90% Prim. Si Length	% Intermetallics	Mean Ints. Length (µm)	Max. Ints Length (µm)	90% Ints. Length
83	100	9.74 (0.15)	10.21 (0.06)	87.11 (0.00)	18.22 (0.12)	0.92 (0.02)	27.93 (0.05)	69.48 (0.00)	35.49 (0.04)	9.87 (0.65)	19.54 (0.23)	163.79 (0.15)	34.41 (0.76)
86	100	9.24 (0.55)	10.86 (0.16)	93.56 (0.15)	20.73 (0.32)	2.20 (0.11)	29.87 (0.12)	86.18 (0.29)	39.02 (0.25)	10.31 (1.06)	21.11 (0.39)	251.11 (12.94)	37.49 (1.13)
83	440	10.08 (0.90)	18.79 (1.23)	210.52 (0.00)	38.66 (2.95)	2.82 (0.22)	36.81 (0.12)	105.66 (0.00)	49.80 (0.26)	8.57 (1.13)	27.06 (1.76)	356.29 (74.01)	54.27 (6.91)
86	440	12.30 (0.29)	21.00 (0.31)	232.30 (0.00)	43.83 (0.75)	6.06 (0.11)	38.72 (0.09)	159.90 (0.06)	55.31 (0.20)	8.06 (1.35)	27.60 (1.51)	349.03 (29.55)	53.67 (4.49)
87	100	12.93 (0.67)	12.32 (0.29)	148.17 (2.27)	24.41 (0.51)	6.09 (0.22)	34.20 (0.26)	104.70 (0.00)	48.44 (0.53)	13.69 (4.13)	23.96 (2.01)	302.62 (69.53)	45.86 (6.25)
90	100	11.07 (1.29)	11.44 (0.13)	173.20 (2.75)	22.40 (0.39)	5.96 (0.39)	34.77 (0.61)	172.44 (0.35)	49.99 (1.17)	10.59 (1.99)	21.86 (0.96)	377.00 (15.22)	38.33 (2.52)
87	440	14.85 (0.57)	18.33 (0.45)	183.01 (0.52)	37.06 (0.94)	8.04 (0.26)	37.85 (0.18)	143.85 (0.43)	55.54 (0.41)	10.02 (0.54)	25.07 (0.94)	281.07 (12.80)	49.86 (6.64)
90	440	15.41 (2.02)	19.12 (0.70)	177.47 (5.52)	40.09 (1.68)	9.20 (0.70)	39.84 (0.57)	150.06 (0.81)	60.35 (1.00)	9.46 (1.70)	27.16 (2.38)	308.80 (49.33)	52.54 (6.64)

Appendix G
Alloy Database

Alloy
LM0
LM1
LM2
LM4
LM5
LM6
LM9
LM10
LM12
LM13
LM14
LM16
LM18
LM20
LM21
LM22
LM24
LM25
LM26
LM27
LM28
LM29
LM30
LM31
BS2L99
BSL119
BSL154
BSL155
BSL169
BSL173
BSL174
DTD716B
DTD722B
DTD727B
DTD735B
DTD5008B
DTD5018A

Composition (Wt.%)										
Si	Cu	Mg	Fe	Mn	Ni	Zn	Pb	Sn	Ti	Cr
0.3	-	-	0.4	-	-	0.1	-	-	-	-
3.0	4.0	0.1	1.2	0.5	0.4	1.0	-	-	0.3	-
10.3	1.6	0.3	1.0	0.5	0.5	2.0	0.3	0.2	0.2	-
5.0	3.0	0.2	0.8	0.4	0.3	0.5	0.1	0.1	0.2	-
0.3	0.1	4.0	0.6	0.5	0.1	0.1	0.1	0.1	0.2	-
11.5	0.1	0.1	0.6	0.5	0.1	0.1	0.1	0.1	0.2	-
11.5	0.2	0.4	0.6	0.5	0.1	0.1	0.1	0.1	0.2	-
0.3	0.3	10.0	0.3	0.2	-	0.2	-	-	0.3	-
2.5	10.0	0.3	1.0	0.6	0.5	0.8	0.1	0.1	0.2	-
11.5	1.1	1.2	1.0	0.5	1.5	0.5	0.1	0.1	0.2	-
0.7	4.0	0.3	1.0	0.4	2.0	0.4	-	-	0.4	0.3
5.0	1.3	0.5	0.6	0.5	0.3	0.1	0.1	0.1	0.2	-
5.0	0.6	0.1	0.8	0.5	-	0.5	-	-	0.3	0.3
11.5	0.4	0.2	1.0	0.5	0.1	0.2	0.1	0.1	0.2	-
6.0	4.0	0.2	1.0	0.4	0.3	2.0	0.2	0.1	0.2	-
5.0	3.0	0.1	0.6	0.4	0.2	0.2	0.1	0.1	0.2	-
8.5	3.5	0.3	1.3	0.5	0.5	3.0	0.3	0.2	0.2	-
7.0	0.2	4.0	0.5	0.3	0.1	0.1	0.1	0.1	0.2	-
9.5	3.0	1.0	1.2	0.5	1.0	1.0	0.2	0.1	0.2	-
7.0	2.0	0.4	0.8	0.4	0.3	1.0	0.2	0.1	0.2	-
18.5	1.6	1.2	0.7	0.6	1.2	0.2	0.1	0.1	0.2	0.6
23.5	1.1	1.1	0.7	0.6	1.1	0.2	0.1	0.1	0.2	0.6
17.0	4.5	0.6	1.1	0.3	0.1	0.2	0.1	0.1	0.2	-
0.3	0.1	0.7	0.5	0.1	0.1	5.0	0.1	0.1	0.3	0.5
7.0	0.1	0.3	0.2	0.1	0.1	0.1	0.1	0.1	0.2	-
0.3	5.0	0.1	0.5	0.3	1.5	0.1	-	-	0.2	-
1.3	4.2	0.1	0.3	0.1	0.1	0.1	0.1	0.1	0.2	-
1.3	4.2	0.1	0.3	0.1	0.1	0.1	0.1	0.1	0.2	-
0.1	0.7	0.2	0.1	0.1	0.1	0.1	0.1	0.1	0.2	-
7.0	0.2	0.4	0.2	0.1	-	0.1	-	-	0.1	-
7.0	0.2	0.4	0.2	0.1	-	0.1	-	-	0.1	-
4.8	0.1	0.6	0.6	0.5	0.1	0.1	0.1	0.1	0.3	-
4.8	0.1	0.6	0.6	0.5	0.1	0.1	0.1	0.1	0.3	-
4.8	0.1	0.6	0.6	0.5	0.1	0.1	0.1	0.1	0.3	-
4.8	0.1	0.6	0.6	0.5	0.1	0.1	0.1	0.1	0.3	-
0.3	0.1	0.7	0.5	0.1	0.1	5.0	0.1	0.1	0.3	0.5
0.3	0.2	7.7	0.4	0.2	0.1	1.2	0.1	0.1	0.3	0.0

Fraction of Predicted Phases (%)										
Aluminum	Silicon	θ (Al ₂ Cu)	Al ₃ Ti	β (AlFeSi)	α (AlMnSi)	Al ₃ Ni	Mg ₂ Si	Mg ₂ Sn	Si ₂ Ti	
98.4	0.10	-	-	1.50	-	-	-	-	-	-
82.8	1.84	7.38	-	4.51	0.17	0.95	0.16	-	-	0.65
79.4	9.40	3.22	0.34	3.76	1.67	1.19	0.36	0.24	0.43	0.43
84.3	4.20	5.53	0.11	3.01	1.34	0.71	0.26	0.13	0.43	0.43
86.0	-	-	0.11	-	-	0.24	0.82	0.14	-	-
83.9	10.9	0.17	0.11	2.25	1.67	0.24	0.10	0.13	0.43	0.43
83.5	10.8	0.35	0.11	2.25	1.67	0.24	0.57	0.13	0.43	0.43
72.6	-	-	-	-	-	-	0.82	-	-	-
72.1	1.42	18.5	0.11	3.76	2.01	1.19	0.42	0.13	0.43	0.43
76.3	10.1	2.11	0.12	3.76	1.67	3.57	1.84	0.13	0.43	0.43
80.1	-	7.38	-	-	-	4.76	0.39	-	0.87	0.87
87.6	4.08	2.29	0.11	2.25	1.67	0.17	0.73	0.13	0.43	0.43
88.5	4.26	1.09	-	3.01	1.67	-	0.16	-	0.65	0.65
82.00	10.7	0.72	0.11	3.76	1.67	0.24	0.26	0.13	0.43	0.43
80.6	5.13	7.38	0.23	3.76	1.34	0.71	0.26	0.11	0.43	0.43
84.7	4.36	6.09	0.11	2.25	1.34	0.48	0.10	0.13	0.43	0.43
84.71	4.36	6.09	0.11	2.25	1.34	0.48	0.10	0.13	0.43	0.43
89.0	6.30	0.35	0.11	1.88	1.00	0.24	0.57	0.13	0.43	0.43
75.52	8.08	5.53	0.23	4.51	1.67	2.38	1.53	0.11	0.43	0.43
83.8	6.12	3.68	0.23	3.01	1.34	0.71	0.58	0.11	0.43	0.43
69.1	16.7	2.95	0.11	2.63	2.01	2.86	1.84	0.13	0.43	0.43
65.55	21.9	1.93	0.11	2.63	2.01	2.50	1.60	0.13	0.43	0.43
68.7	16.1	8.30	0.11	4.13	1.00	0.24	0.81	0.13	0.43	0.43
90.8	-	0.16	0.10	-	-	0.24	-	0.14	0.54	0.54
90.8	6.58	0.17	0.11	0.75	0.35	0.24	0.45	0.13	0.43	0.43
83.2	-	9.23	-	-	-	3.69	0.15	-	0.43	0.43
89.0	0.86	7.75	0.11	1.13	0.33	0.24	0.10	0.13	0.33	0.33
89.0	0.86	7.75	0.11	1.13	0.33	0.24	0.10	0.13	0.33	0.33
97.0	-	1.14	0.10	-	-	0.24	0.24	0.14	-	-
91.1	6.60	0.35	-	0.75	0.33	-	0.55	-	0.32	0.32
91.1	6.60	0.35	-	0.75	0.33	-	0.55	-	0.32	0.32
90.3	3.68	0.17	0.11	2.25	1.67	0.24	0.81	0.13	0.65	0.65
90.3	3.68	0.17	0.11	2.25	1.67	0.24	0.81	0.13	0.65	0.65
90.3	3.68	0.17	0.11	2.25	1.67	0.24	0.81	0.13	0.65	0.65
90.3	3.68	0.17	0.11	2.25	1.67	0.24	0.81	0.13	0.65	0.65
90.9	-	0.16	0.10	-	-	0.24	-	0.14	0.46	0.46
78.1	-	-	0.11	-	-	0.24	0.82	0.14	-	-

Alloy	Properties									
	0.2% Proof Stress(N/mm ²)	Tensile Stress (N/mm ²)	Elongation (%)	Brinell Hardness	Endurance Limit (5x10 ⁷ cycles;N/mm ²)	Modulus of Elasticity (x10 ³ ; N/mm ²)	Coef. Of Thermal Expansion (per °C at 20-1000C x 10 ⁻⁶)	Thermal Conductivity (cal/cm ² /cm ² C at 25°C)	Electrical Conductivity (% copper standard at	Density (g/cm ³)
LM0	30.0	80.0	40.0	25.0		69.0	24.0	0.5	57.0	2.7
LM1										
LM2	210.0	175.0	2.5	77.5	85.0	71.0	20.0	0.2	26.0	2.7
LM4	95.0	190.0	3.0	80.0	85.0	71.0	21.0	0.3	32.0	2.8
LM5	105.0	225.0	5.0	65.0	100.0	71.0	23.0	0.3	31.0	2.7
LM6	75.0	210.0	7.0	57.5	68.0	71.0	20.0	0.3	37.0	2.7
LM9	107.5	190.0	4.0	80.0	85.0		22.0	0.4	38.0	2.7
LM10										
LM12	155.0	170.0	1.0	87.5	60.0	71.0	22.0	0.3	33.0	2.9
LM13	285.0	295.0	1.0	125.0	100.0	73.0	19.0	0.3	29.0	2.7
LM14										
LM16	145.0	230.0	3.0	85.0	85.0	71.0	23.0	0.3	36.0	2.7
LM18										
LM20	75.0	210.0	5.0	60.0	90.0	71.0	20.0	0.4	37.0	2.7
LM21	110.0	200.0	2.5	85.0	70.0	71.0	21.0	0.3	32.0	2.8
LM22	115.0	245.0	8.0	75.0	85.0	71.0	21.0	0.3	32.0	2.8
LM24	110.0	180.0	1.5	85.0	85.0	71.0	21.0	0.2	24.0	2.8
LM25	90.0	180.0	3.0	60.0	95.0	71.0	22.0	0.4	39.0	2.7
LM26	175.0	210.0	1.0	105.0	75.0	71.0	21.0	0.3	26.0	2.8
LM27	100.0	160.0	2.0	82.5	75.0	71.0	21.0	0.4	27.0	2.8
LM28		170.0	0.5	110.0		82.0	18.0	0.3		2.7
LM29	170.0	190.0	0.5	120.0		88.0	16.0	0.3		2.7
LM30	175.0	150.0		110.0		82.0	18.0	0.3	20.0	2.7
LM31							24.0	0.4	35.0	2.8
BS2L99	200.0	280.0	5.0	80.0	90.0	71.0	22.0	0.4	39.0	2.7
BSL119							23.0	0.4	36.0	2.8
BSL154	165.0	265.0	13.0	80.0	50.0	71.0	23.0	0.4	34.0	2.8
BSL155	200.0	310.0	9.0	85.0	50.0	71.0	23.0	0.4	34.0	2.8
BSL169	240.0	320.0	4.0	85.0	110.0	72.0	22.0	0.4	39.0	2.7
BSL173	190.0	250.0	5.0	70.0	90.0	71.0	22.0	0.4	39.0	2.7
BSL174							22.0	0.4	39.0	2.7
DTD716B	85.0	165.0	3.0				23.0	0.4	39.0	
DTD722B	130.0	185.0	2.0				23.0	0.4	39.0	
DTD727B	110.0	230.0	5.0				23.0	0.4	39.0	
DTD735B	215.0	280.0	2.0				23.0	0.4	39.0	
DTD5008B							24.0	0.3	25.0	
DTD5018A	170.0	305.0	10.0				24.0	0.2	24.0	